DISSECTING TRADITIONAL MEDICINE VIA CHEMICAL AND BIOCHEMICAL TECHNIQUES: ADVANCED ANALYTICS AND NOVEL PARADIGMS

EDITED BY: Yi Wang, Peng Li and Mirko Baruscotti
PUBLISHED IN: Frontiers in Pharmacology

frontiers Research Topics

ISSN 1664-8714
ISBN 978-2-83250-761-2
DOI 10.3389/978-2-83250-761-2

About Frontiers

Frontiers is more than just an open-access publisher of scholarly articles: it is a pioneering approach to the world of academia, radically improving the way scholarly research is managed. The grand vision of Frontiers is a world where all people have an equal opportunity to seek, share and generate knowledge. Frontiers provides immediate and permanent online open access to all its publications, but this alone is not enough to realize our grand goals.

Frontiers Journal Series

The Frontiers Journal Series is a multi-tier and interdisciplinary set of open-access, online journals, promising a paradigm shift from the current review, selection and dissemination processes in academic publishing. All Frontiers journals are driven by researchers for researchers; therefore, they constitute a service to the scholarly community. At the same time, the Frontiers Journal Series operates on a revolutionary invention, the tiered publishing system, initially addressing specific communities of scholars, and gradually climbing up to broader public understanding, thus serving the interests of the lay society, too.

Dedication to Quality

Each Frontiers article is a landmark of the highest quality, thanks to genuinely collaborative interactions between authors and review editors, who include some of the world's best academicians. Research must be certified by peers before entering a stream of knowledge that may eventually reach the public - and shape society; therefore, Frontiers only applies the most rigorous and unbiased reviews.
Frontiers revolutionizes research publishing by freely delivering the most outstanding research, evaluated with no bias from both the academic and social point of view. By applying the most advanced information technologies, Frontiers is catapulting scholarly publishing into a new generation.

What are Frontiers Research Topics?

Frontiers Research Topics are very popular trademarks of the Frontiers Journals Series: they are collections of at least ten articles, all centered on a particular subject. With their unique mix of varied contributions from Original Research to Review Articles, Frontiers Research Topics unify the most influential researchers, the latest key findings and historical advances in a hot research area! Find out more on how to host your own Frontiers Research Topic or contribute to one as an author by contacting the Frontiers Editorial Office: frontiersin.org/about/contact

DISSECTING TRADITIONAL MEDICINE VIA CHEMICAL AND BIOCHEMICAL TECHNIQUES: ADVANCED ANALYTICS AND NOVEL PARADIGMS

Topic Editors:
Yi Wang, Zhejiang University, China
Peng Li, University of Macau, China
Mirko Baruscotti, University of Milan, Italy

Citation: Wang, Y., Li, P., Baruscotti, M., eds. (2022). Dissecting Traditional Medicine via Chemical and Biochemical Techniques: Advanced Analytics and Novel Paradigms. Lausanne: Frontiers Media SA. doi: 10.3389/978-2-83250-761-2

Table of Contents

frontiers in Pharmacology

EDITORIAL
published: 08 February 2022
doi: 10.3389/fphar.2022.839004

Editorial: Dissecting Traditional Medicine *via* Chemical and Biochemical Techniques: Advanced Analytics and Novel Paradigms

Yi Wang[1]*, *Peng Li*[2] *and Mirko Baruscotti*[3]

[1]College of Pharmaceutical Sciences, Zhejiang University, Hangzhou, China, [2]State Key Laboratory of Quality Research in Chinese Medicine, Institute of Chinese Medical Sciences, University of Macau, Taipa, China, [3]Department of Biosciences, University of Milano, Milan, Italy

Keywords: Chinese medicine, LC-MS, ethnopharmacology, system biology, traditional Chinese medicine

Editorial on the Research Topic

Dissecting Traditional Medicine via Chemical and Biochemical Techniques: Advanced Analytics and Novel Paradigms

Traditional medicine (TM) plays an important role in the healthcare system and is increasingly used worldwide for managing various chronic diseases and promoting well-being. Although huge progresses have been achieved to reveal major compounds in well-known botanical drugs, such as *Salvia miltiorrhiza* Bunge, the identification of major active constituents remains extremely challenging due to the complexity of chemical composition and the elusive mechanisms of action. One major barrier to solving such problems is the lack of feasible techniques and strategies to distinguish those active compounds from those which make no or only a minor contribution to the activity of TM.

Often ubiquitous or widely distributed compounds are then claimed to be "actives" for major disease conditions. Moreover, it is difficult to judge whether certain components or compounds identified by a specific cellular model or target-based assays can exert a pharmacological effect *in vivo* in the context of biological network or in a real-life clinical setting. Therefore, it is time to dedicate greater efforts in either improving the capability of bioassays or developing novel paradigms to refresh our toolbox for dissecting TMs. The aim of this research topic is to improve the quality of such studies, accelerate the pace of screening and identification of active compounds from TMs, and to facilitate the expansion of screening assays from cellular tissue levels to organs and *in vivo* models.

In the past 3 decades, bioactivity-guided screening has become a mainstream workflow for lead discovery from TMs. With the aid of modern analytical approaches such as LC-MS, GC-MS, and NMR, it allows us to identify multiple constituents in active components found by phenotypes or target-based assays. However, synergistic effects among multiple compounds of TMs are difficult to recognize during conventional phytochemical isolation, which requires repeated purification steps to obtain a single compound from mixtures of TM. In this research topic, four articles are dedicated to develop novel analytical or preparing approaches to uncover the chemical composition of TM. Nie et al. used the emerging microscopic mass spectrometry imaging technique to reveal the distribution of phytochemicals in the dried root of *Isatis tinctoria* L. With the aid of the chemometric method, different samples from four habitats were successfully clustered. Chang YX and co-workers Yang et al. established a rapid high throughput vibration and vortex-assisted matrix solid phase dispersion method for simultaneous extraction of four isoflavones from *Glycine* max (L.) Merr. With satisfied recovery and a linear range, the approach was applied in the quality control of SSP.

OPEN ACCESS

Edited and reviewed by:
Michael Heinrich,
University College London,
United Kingdom

***Correspondence:**
Yi Wang
zjuwangyi@zju.edu.cn

Specialty section:
This article was submitted to Ethnopharmacology, a section of the journal Frontiers in Pharmacology

Received: *19 December 2021*
Accepted: *10 January 2022*
Published: *08 February 2022*

Citation:
Wang Y, Li P and Baruscotti M (2022) Editorial: Dissecting Traditional Medicine via Chemical and Biochemical Techniques: Advanced Analytics and Novel Paradigms. Front. Pharmacol. 13:839004. doi: 10.3389/fphar.2022.839004

As the mainstream technique for analyzing complex extracts of TM, LC-MS was also widely used in metabolite profiling. Zhang et al. analyzed the major compounds of the Buxue Yimu granule (BYG) and the serum endogenous metabolites regulated by the BYG. By integrating the metabolomic and biochemical data, they concluded that the BYG exerts a potential protective role in the intervention of incomplete abortion by anti-inflammation, promotes endometrial repair, and regulates the metabolic disorders. The study by Houriet et al. presented a comprehensive MS-based analytical workflow that allowed a generic and unbiased selection of specific and abundant markers and the identification of multiple related sub-markers, which is critical for metabolite profiling of TM. In a clinical study by Li et al., the serum metabolic profiles of 45 healthy controls and 124 patients with psoriasis vulgaris (PV) were analyzed. A total of 14 biomarkers related to syndrome differentiation and psoriasis types were identified, which might be potential biomarkers for diagnosis. Except for the metabolomics study, the gut microbiome is another hot topic in pharmacology of TM Cui et al. investigated the protective effects of Da-Chai-Hu decoction (DCH) against nonalcoholic fatty liver disease (NAFLD). 16S rRNA sequencing and untargeted metabolomics suggested that DCH regulated the arachidonic acid (AA), glycine/serine/threonine, and glycerophospholipid metabolic pathways and altered the abundance of several key gut microflora.

Multiple novel pharmacological techniques, e.g., high-throughput screening and high-content screening, provide opportunities to compare the efficacy of components singularly and as a whole on a larger scale. The screening models are shifting from the conventional biochemical and cellular assay to co-culture models, 3D-cultured organoid, organ-on-a-chip, and *in vivo* zebrafish model (small animal models).

Li et al. identified two representative compounds i.e., cryptotanshinone and senkyunolide I from the botanical drug Guanxinning Table. Their findings showed that the synergistic anti-thrombotic effect of two compounds from different herbs can be attributed to the regulation of thrombi formation at different levels *via* multiple signaling pathways, including oxidative stress, platelet activation, and coagulation cascade. Ma et al. also utilized *in vivo* zebrafish to evaluate anti-thrombosis effects of Xuesaitong injection (XST); another widely used botanical drug consisted of several saponins from *Panax notoginseng* (Burkill) F.H.Chen. They found that XST downregulates the expression of the fibrinogen alpha chain (fga) gene to inhibit the coagulation cascade during thrombosis, while it can be applied to evaluate the batch-to-batch consistency of XST. The study by Zhang et al. established a xenograft zebrafish model to investigate the anticancer effects of theaflavin (TF), a major active pigment of tea. Combined with *in vitro* effects, they demonstrated that TF possessed cytotoxic pro-apoptotic and tumor-inhibitory effects on A375 cells through activations of P53 and JNK pathways.

This issue also contains several articles focused on active substances of TM for various diseases. Berberine is a well-known benzylisoquinoline alkaloid in *Coptis chinensis* Franch. The study by Zhai et al. demonstrated for the first time that berberine directly binds to PLA2G4A and inhibits the MAPK/JNK signaling pathway to inhibit the PLA2G4A activity in inflammatory status. Chen et al. investigated the protective effect of pure total flavonoids from citrus (PTFC) against non-steroidal anti-inflammatory drug (NSAID)-induced intestinal injury *in vivo* and *in vitro*. They found PTFC promoted autophagy through the PI3K/Akt signaling pathway to protect the intestinal barrier integrity. Another study by Liu et al. evaluated the anti-hepatoma compound in *Heptapleurum heptaphyllum* (L.) Y.F.Deng by the component knock-out strategy. The compound A exerts the anticancer effect by regulating the levels of ROS and Bcl-2 family protein in the mitochondrial apoptosis pathway. Lu et al. identified a class of unique cyclic-peptide from *Pseudostellaria heterophylla* (Miq.) Pax, which is a commonly used TM for treating lung diseases. It is the first report of those cyclic peptides that improve the pulmonary ventilation function in the rat model of chronic obstructive pulmonary disease (COPD). The mechanism of action is attributed to inhibiting the abnormal activation of the TLR4-MyD88-JNK/p38 pathway.

In summary, the combined use of abovementioned novel methods and strategies will prompt the efficacy of modern research of TM. We hope that readers will find inspiration from this research topic. Therefore, the discovery of active compounds in TM will move further away from the systematic isolation and bioassay-guided isolation to programmed/targeted isolation to find those parts with equivalent effects as a whole, improving our pharmacological understanding of complex mixtures.

AUTHOR CONTRIBUTIONS

All authors listed have made a substantial, direct, and intellectual contribution to the work and approved it for publication.

ACKNOWLEDGMENTS

We would like to thank the authors for submitting their insightful and interesting research or review for publication and the reviewers for sharing their expertise, constructive critiques, and their contributions to improve the manuscript. Y.W. is supported by the Innovation Team and Talents Cultivation Program of National Administration of Traditional Chinese Medicine (No. ZYYCXTD-D-202002).

Conflict of Interest: The authors declare that the research was conducted in the absence of any commercial or financial relationships that could be construed as a potential conflict of interest.

Publisher's Note: All claims expressed in this article are solely those of the authors and do not necessarily represent those of their affiliated organizations, or those of the publisher, the editors, and the reviewers. Any product that may be evaluated in this article, or claim that may be made by its manufacturer, is not guaranteed or endorsed by the publisher.

frontiers in Pharmacology

ORIGINAL RESEARCH
published: 09 June 2020
doi: 10.3389/fphar.2020.00850

Cyclic Peptide Extracts Derived From *Pseudostellaria heterophylla* Ameliorates COPD *via* Regulation of the TLR4/MyD88 Pathway Proteins

Feng Lu[1,2†], *Han Yang*[1†], *Si-ding Lin*[1], *Li Zhao*[3], *Chang Jiang*[3], *Zhi-bin Chen*[2], *Ying-ying Liu*[2], *Yong-jun Kan*[3], *Juan Hu*[1,2*] *and Wen-sheng Pang*[1*]

[1] School of Pharmacy, Fujian University of Traditional Chinese Medicine, Fuzhou, China, [2] Respiratory Department, The Second Affiliated Hospital of Fujian Traditional Chinese Medical University, Fuzhou, China, [3] Institute of Materia Medica, Fujian Academy of Traditional Chinese Medicine, Fuzhou, China

OPEN ACCESS

Edited by:
Peng Li,
University of Macau, China

Reviewed by:
JianLi Gao,
Zhejiang Chinese Medical University, China
Ao Li,
Chongqing University of Technology, China

***Correspondence:**
Juan Hu
huj@fjtcm.edu.cn
Wen-sheng Pang
pws@fjtcm.edu.cn

[†]These authors have contributed equally to this work

Specialty section:
This article was submitted to Ethnopharmacology, a section of the journal Frontiers in Pharmacology

Received: 08 January 2020
Accepted: 22 May 2020
Published: 09 June 2020

Citation:
Lu F, Yang H, Lin S-d, Zhao L, Jiang C, Chen Z-b, Liu Y-y, Kan Y-j, Hu J and Pang W-s (2020) Cyclic Peptide Extracts Derived From Pseudostellaria heterophylla Ameliorates COPD via Regulation of the TLR4/MyD88 Pathway Proteins. Front. Pharmacol. 11:850. doi: 10.3389/fphar.2020.00850

We have explored the method of extraction and purification of cyclic-peptide extract (CPE) from *Pseudostellaria heterophylla* (Miq.) Pax. (Taizishen, TZS), characterized the structure about cyclic-peptide compounds and investigated the biological activity of CPE attenuating chronic obstructive pulmonary disease (COPD) in rats. The CPE from TZS was obtained by ethyl acetate, petroleum ether, hot water extraction, and alcohol-precipitation. Cyclic-peptide structures were distinguished using ultra-high performance liquid chromatography-quadrupole time-of-flight tandem mass spectrometry (UPLC-Q-TOF-MS/MS). Rats were induced by solid combustibles smoke (SCS) for the COPD model, and the anti-COPD activity of CPE was detected using lung airway resistance and dynamic lung compliance, as well as pulmonary tissue hematoxylin and eosin (HE) staining. The relevant inflammatory cytokines were assayed by enzyme-linked immunosorbent assay (ELISA). CPE obtained from TZS contained 12 cyclic-peptide constituents; the purity was up to 92.94%. CPE (200, 400, or 500 mg/kg/day) was given to SCS-induced COPD model rats orally for 15 days. The results showed that in rats given CPE (400 mg/kg/day) there was a sharp fall in lung airway resistance but a rise in dynamic lung compliance. The image analysis of lung tissue sections suggested that CPE could decrease the degree of alveolar destruction ($p < 0.05$), alleviate lung inflammation, increase alveolar space, and improve the infiltration of inflammatory cells. CPE was found to reduce the levels of TNF-α, but increase IL-10, adjusting multiple cytokines in rat serum; the TLR4 mRNA, MyD88 mRNA and AP-1 mRNA levels, the expressing levels of p-JNK, p-p38 and p-TAK1 protein were significantly down regulated in rat alveolar macrophages. CPE intervention could improve the pulmonary ventilation function on COPD rats, which may be related to its effect in inhibiting the abnormal activation of the TLR4-MyD88-JNK/p38 pathway. This is the first report that the CPE of TZS lessens the severity of COPD episodes. The new preparation process of CPEs implements the anticipated goal, which is to refine CPE and actualize quality control.

Keywords: ***Pseudostellaria heterophylla*, cyclic peptide, monomer structure, TLR4-MyD88-JNK/p38 pathway, anti-chronic obstructive pulmonary disease**

INTRODUCTION

Chronic obstructive pulmonary disease (COPD) is a noteworthy public health problem due to its morbidity and mortality (Lindberg et al., 2012). COPD exhibits symptoms of airflow blockage and breathlessness and includes emphysema, chronic bronchitis, or even asthma. Diagnosis of COPD can be best addressed by a combination of morphology and function. The morphological imaging of the lung parenchyma and airways can be detected using the three-dimensional high-resolution computed tomography (CT) technique. The image information obtained by functional imaging is perfusion, lung mechanics, and ventilation by magnetic resonance imaging (MRI). The comprehensive diagnostics of CT complemented with MRI are able to achieve a more sensitive detection (Ley et al., 2008). The development of COPD is mainly attributable to smoking, but genetic factors and respiratory infections are some of the most common causes of asthma; air pollution can aggravate asthma. In developing countries, air quality is thought to have a larger role in the progression of COPD (David and Victor, 2006).

COPD is closely correlated with a chronic inflammatory response, which is characterized by an increased amount of macrophages, neutrophils, and T lymphocytes in the small airways and lung parenchyma (Pelaia et al., 2006). In contrast to asthma, the inflammatory mediators involved in COPD are not clear, but inflammation comprises many mediators, factors, and pathways such as inflammatory peptides, lipid mediators, active oxygen, and cytokines that cause alveolar destruction and small airway fibrosis. Recognizing the inflammatory factors and understanding the interaction mechanism is crucial for anti-inflammatory treatments of COPD (Barnes et al., 2004).

COPD is a non-specific inflammatory disease, and an abnormal immune response plays an important role. Toll-like receptors (TLRs) have been studied that are a cornerstone of the innate immune system and play a pluripotent role in stable COPD. Myeloid differentiation primary response protein 88 (MyD88) is a critical adaptor protein involved in the TLR family signaling pathway and regulates immune responses and inflammation. Targeting MyD88 is one way to treat COPD (Di Stefano et al., 2017; Franco et al., 2018).

Coughing and wheezing can be treated with drugs. Patients who have low blood oxygen concentrations are often given supplemental oxygen. Even though the overall prognosis of COPD patients has shown some improvement, the mortality rate remains high (Bruno and Valenti, 2012).

China has a long history of traditional medicines; the treatment of lung disease focuses the lung deficiency syndrome on purging the lung and dissolving phlegm. Many Chinese herbals have been used for several thousand years to treat respiratory diseases such as cough, asthma, bronchial ailments, and pneumonia (Jiangsu New Medical College, 1977; Lin, 2004; Wang and Ng, 2006; Zhou, 2005; Hsu et al., 2013).

In traditional Chinese medicine (TCM), *Pseudostellaria heterophylla* (TZS) can moisten the lung, cough, and is a spleen tonic. TZS is a mild herb that strengthens the Qi to tone up the body and resist pulmonary diseases (Yan, 2008). Some studies indicate that TZS possesses immunologic enhancement and antioxidant properties (Wong et al., 1994; Ng et al., 2004; Zhou, 2005; Huang et al., 2005). The ethyl acetate extract of TZS relieves cough and improves lung function *via* adjustment of the levels of multiple cytokines (Pang et al., 2011). The ethyl acetate extract of TZS contains cyclic-peptide compounds; the activity of these cyclic-peptide fractions is not clear.

In this paper, according to the clinical use of this herb in TCM (Murărescu et al., 2008), the present study was undertaken to evaluate cyclic-peptides separated from the ethyl acetate extract of TZS attenuating a COPD rat model induced by solid combustibles smoke (SCS), and also characterize the structures of the cyclic peptide monomer. Enzyme-linked immunosorbent assay (ELISA) was used to detect tumor necrosis factor (TNF-α) and interleukin-10 (IL-10), quantitative real-time polymerase chain reaction (q-PCR) and western blotting (WB) were used to detect the TLR4 mRNA, MyD88 mRNA and AP-1 (activator protein-1) mRNA meanwhile the downstream protein expression of p-p38 (phosphorylated protein 38), p-JNK (phosphorylated c-jun amino terminal kinase), IKK (inhibitor of nuclear factor κB kinas), p-IκB (phosphorylated inhibitor of NF-κB), and TAK1 (transforming growth factor beta-activated kinase 1) of the TLR4 pathway, regulated by CPE, to clarify its mechanism of action. Some particular molecules of cyclic-peptides are naturally present in *P. heterophylla* but their activity was seldom reported. It is of profound interest to elucidate this substance class.

MATERIALS AND METHODS

Chinese TZS and Chemicals

Zheshen No. 2 P. *Heterophylla* (Miq.) Pax Chinese herbal was purchased from Ningde Nanling Agricultural Co., Ltd. Zherong County of the Ningde region of the Fujian Province in China is the advocate producing area of TZS. The TZS was cut into pieces and then dried below 60°C.

Chromatographic pure methanol was purchased from Merck KGaA (Darmstadt, Germany). Chromatographic pure acetonitrile was purchased from Fisher Scientific UK Ltd. (Leicestershire, England). Analytical grade reagents including petroleum ether, ethyl acetate, ethanol, n-butanol, ammonia, and chloroform were bought from Xilong Scientific Co., Ltd. (Shantou, China). Interleukin-10 (IL-10) and tumor necrosis factor (TNF-α) enzyme linked immunosorbent assay (ELISA) kits were purchased from cloud-clone corp.

Instruments

A high performance liquid chromatography (HPLC) system with a 2996 photodiode-array detector (PDA) and an auto-sampler was used (Waters Technologies, USA). Liquid chromatography tandem mass spectrometry (LC-MS/MS) was performed with an Agilent 1290 ultra-high performance liquid chromatography (UPLC) combined with an AB Sciex Triple time of flight (TOF) 4600 MS system. A SpectraMax Plus384 multimode micro-plate reader (Molecular Devices, USA) and a Milli-Q-Plus ultra-pure water system (Millipore, Bedford, MA, USA) were used.

CPE Preparation and Purification

The TZS was crushed to a powder (through 60 meshes) and was extracted using ethyl acetate as the solvent. According to the properties of the substance, the crude extract was purified by selecting the appropriate solvent to obtain the refined CPE.

Previous research of our group found that the ethyl acetate extract of TZS is rich in amino acids, cyclic peptides, and free fatty acids. Using several solvents to remove impurities, the process of CPE purification consisted of three steps: the ethyl acetate extract of TZS was degreased with petroleum ether, amino acids were removed with hot water, and polysaccharide and other impurities were removed with alcohol-precipitation. The purified cyclic-peptide powder was freeze-dried by lyophilization (**Figure 1**).

Ethyl Acetate Crude Extracts Preparation and HPLC-Fingerprint Analysis

TZS (60 mesh) was extracted with ethyl acetate using the Soxhlet extraction method for 2 h at 90°C. The extract was restored at room temperature, evaporated to dryness, and the ethyl acetate was removed in a rotary evaporator under reduced pressure. The residue was dissolved with chromatographic grade methanol, filtered through a 0.45 μm filter before analysis by HPLC. HPLC fingerprint analysis showed that the ethyl acetate extract contained three kinds of substances: amino acids, cyclic peptides, as well as free fatty acids. Thus, if pure cyclic peptides were to be obtained, the ethyl acetate extract needed to be further purified.

Removal of Fat-Soluble Substances

The ethyl acetate extract was degreased by mixing with petroleum ether (material: liquid = 1:30) to extract fat-soluble substances using ultrasonic extraction for 1 h at room temperature. The extract was filtered and the petroleum ether was discarded; the residue was degreased with petroleum ether in triplicate. The solvent was evaporated from the residue and ethanol was added (material: liquid = 1:30) for ultrasonic extraction at 60°C for 1 h. The extract was filtered, restored at room temperature, evaporated to dryness and alcohol was removed in a rotary evaporator under reduced pressure.

Removal of Amino Acids

The above-mentioned residue was fully dissolved in 50 ml hot water and extracted with ethyl acetate thrice (volume ratio 1:2)

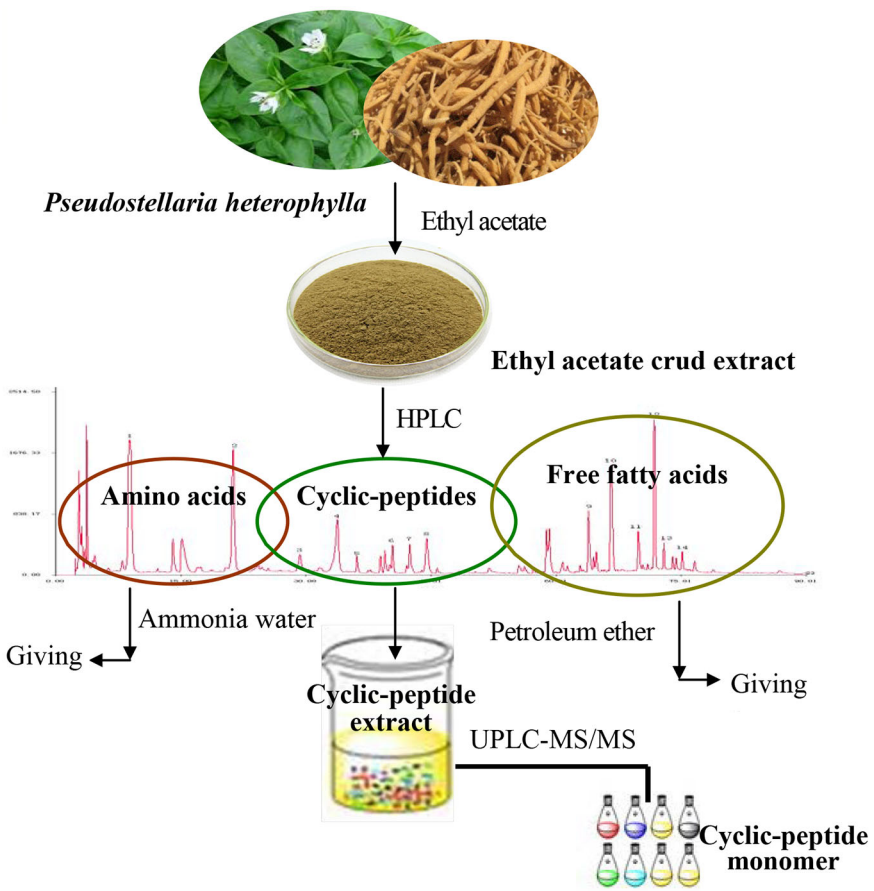

FIGURE 1 | Diagrammatic sketch of cyclic-peptide extract preparation and purification.

with a separating funnel; 100 ml of ethyl acetate was added each time. After the ethyl acetate phase was concentrated and dried, 50 ml hot water was added to the funnel to dissolve the residue, and 50 ml water-saturated n-butanol was added (volume ratio 1:1) and extracted thrice. The combined n-butanol extraction solution was poured into a separating funnel, 150 ml 40% ammonia test solution (volume ratio 1:1) was added to the n-butanol extraction, and the mixture was agitated well, and extracted thrice. The ammonia test solution extracts were discarded and the n-butanol phase was concentrated and dried. The residue was fully dissolved in 25 ml hot water, 50 ml chloroform was added (volume ratio 1:1) and extracted thrice. The chloroform phase was removed under reduced pressure, and the extract was concentrated and dried.

Removal of Polysaccharide and Other Impurities

The alcohol precipitation method was used to remove polysaccharides and other impurities. The above residue was placed in a beaker, dissolved with a proper amount of 85% ethanol, set for a period, filtered, and the resulting filtrate was a clear alcohol solution.

The above alcohol solution was placed in a beaker and mixed with distilled water (volume ratio 1:1) to obtain a 50% alcohol solution (freezing point −25°C). After pre-freezing at −80°C, a yellow powder was obtained by freeze-drying in a vacuum freeze-dryer.

Chemical Analysis of the Freeze-Dried Powder

A little powder was dissolved in methanol and filtered with a 0.22 μm microporous membrane. This paper deals with optimization of the chromatographic fingerprint of CPE to carry out HPLC analysis. The characteristic vibration cyclic-peptide bands showed the best responses at a wavelength of 203 nm, so 203 nm was successfully used to detect the target components. At the retention time of 25–60 min, 40 compounds with a peak area above 0.01% showed a better absorbance. For 16 of the 40 components, sixteen peaks were labeled with an area more than three ten thousand and the 40 components accounted for 96.9% of the total area (**Figure 2**).

HPLC-Fingerprint Analysis of Extracts

The chromatography was carried out with a Hypersil ODS column (4.6 mm × 250 mm, 5 μm) made by Dalian Elite Analytical Instruments Co., Ltd. (Dalian, China). The mobile phase, flow rate and column temperature were optimized to obtain better resolution and establish an HPLC method to determine the fingerprint of the CPE. The mobile phase was acetonitrile (A) and 0.2% orthophosphoric acid aqueous solution (B).

The gradient elution program included five steps: From 0 to 40 min, the ratio of acetonitrile was increased from 10 to 40%; from 40 to 60 min, the ratio of acetonitrile was increased from 40 to 70%; from 60 to 75 min, the ratio of acetonitrile was increased from 70 to 100%; from 75 to 90 min, the acetonitrile was maintained at 100%. The detection wavelength was set at 203 nm; the flow rate was 1.0 ml/min, sample size was 20 μl, and the column temperature was 30°C.

Cyclic-Peptide Ingredient Structure by LC-MS/MS Identification

UPLC-MS/MS determination was achieved on a SB C_{18} (2.1 × 100 mm, 1.8 μm) column. The velocity was 0.4 ml/min. The temperature of the auto-sampler and column were both maintained at 30°C. Both positive and negative electrospray ionization (ESI) modes were applied. The different instrument parameters including ion source temperature, collision energy, and collision energy spread were designed and optimized for high-quality fragment ions of the mass spectra (**Table 1**).

COPD Rat Model Preparation and Treatment

SPF grade Wistar adult rats, male and female (50:50) weighing 200 ± 25 g were purchased from Shanghai Laboratory Animals Center (Shanghai, China) and fed in the animal center of our institution. The ambient temperature was 25°C and humidity 70%. Rats were allowed free access to tap water and were given a rodent diet.

Some 60 Wistar rats were randomly divided into six groups. The rats were exposed to the admixture of 40 g of cigarette and

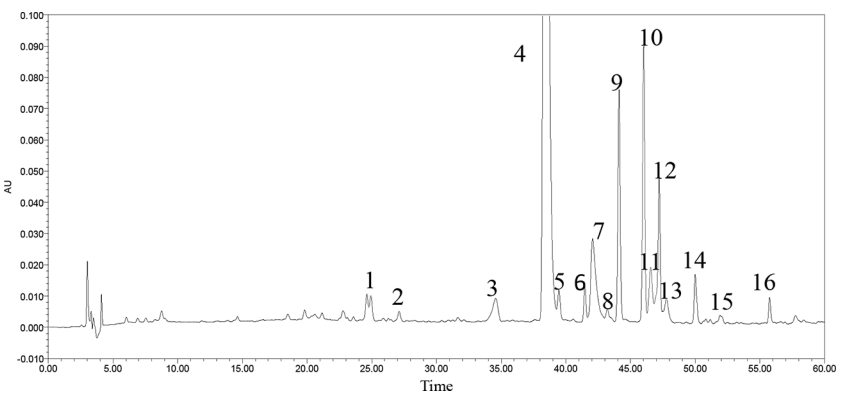

FIGURE 2 | HPLC-fingerprint of cyclic-peptide extract.

TABLE 1 | CPE UPLC-MS/MS analysis conditions.

Chromatographic conditions		Mass spectrometry conditions	
Chromatographic column	SB C18 (2.1× 100 mm, 1.8 μm)	Polarity	Positive/Negative ion mode
Flow rate	0.4 ml/min	TOF mass range	Min 100, Max 1,500
Detective wavelength	203 nm	Ion Source	Gas 50, Curtain Gas 35
Sample size	1 μl	Ion Source Temp	500°C
Column temperature	30°C	Ion Spray Voltage Floating	5,020/−4,500
Mobile phase	0.1% glacial acetic acid aqueous solution (A)- acetonitrile (B)	Collision Energy (CE)	±40
Gradient program	0-11-12-17-19-20-23 min, 10-50-70-100-100-10-10 B%	Collision Energy Spread (CES)	20

300 g of wood chips. The exposure was performed in a 1 m^3 fume cupboard with a flow rate of 0.1 m^3/h and 60 min daily, for 60 days. Attention was paid to control the velocity of the flow of smoke, to properly ventilate, and to avoid accidental death of the animals. The control groups, consisting of 10 rats were unexposed to pollutants. Physiological saline was used as solvent to prepare suspension of CPE. Rats were orally given CPE at the low dose of 200 mg/kg (CPE-LD), medium dose of 400 mg/kg (CPE-MD), and high dose of 500 mg/kg (CPE-HD) for 15days.

Guilong Kechuanning capsule is a classical proprietary Chinese medicine (license number Z20053135). Guilong Kechuanning capsule is effective for lung diseases such as COPD and acute or chronic bronchitis, and for the improvement of immunological function and cellular cytokines such as IL-8 and TNF-α in patient with COPD (Huang and Cai, 1993; Li et al., 2005). In this study, rats were orally given physiological saline suspension of Guilong Kechuanning capsule (450 mg/kg/day) for 15 days that as a positive control.

The vehicle control and model control groups were given an equal amount of physiological saline by gastric perfusion, respectively.

Pulmonary Function Assessment

Changes in the lung function of rats were observed using MedLab after treatment with CPE. Rats were anesthetized with pentobarbital sodium at a dose of 30 mg/kg and placed in a plethysmograph. Airway flow (V), tidal volume (V_t), and trans-pulmonary pressure (Ptp) were monitored for 30 min and changes in each parameter were recorded. The effect of CPE was determined by comparing the COPD model changes in lung airway resistance (R_L) and dynamic compliance (Cdyn) (Pang et al., 2011).

Image Analysis of Lung Tissue Sections

Pulmonary tissue sections were made for pathological examination. A certain thickness of pulmonary tissue was made of random sections according to Valença et al. (Weibel and Gomez, 1962; Valença et al., 2004). Lung tissue sections were stained with hematoxylin and eosin (HE) and were studied morphologically under the light microscope. Dilated alveolar spaces and alveolar morphological characteristics were counted and identified using the 100× field of view for each group.

Rat Serum Preparation, Alveolar Macrophage (AM) Isolation and Identification

When the CPE treatment was concluded, rats were given 1% pentobarbital sodium as an anesthetic. About 5 ml of blood was collected from inferior vena cava and was centrifuged for 20 min at 3,000 r/min to prepare serum was stored at −80°C for ELISA detection. The trachea and lungs were exposed and pulmonary alveolar macrophages (AMs) from each group were separated by bronchoalveolar lavage fluid (BALF) extraction. Briefly, a 2 mm diameter tube was inserted into the bronchus and 5 ml sterile saline was pumped in and then removed along with the fluid and cells; this was repeated four times. To amalgamate BALFs, the fluid was centrifuged for 15 min at 1,000 r/min. Cell precipitates were used to prepare single cell suspension by a floating and sinking process with RPMI-1640 medium containing 10% FBS, 100 U/ml penicillin, and 100 U/ml streptomycin. Giemsa stain was used to confirm AM purity >90% and trypan blue staining identified a cell survival rate ≥95%. AMs were inoculated in a culture dish at a concentration of 1×10^9/ml under an atmosphere of 37°C, 5% CO_2 for 2 h to gain the adherent cells. AMs were stored in liquid nitrogen for PCR and WB detection (Huang et al., 2015; Yu et al., 2018).

Cytokine Measurement by ELISA

The levels of TNF-α and IL-10 in serum and the supernatant of AMs were detected by ELISA kits, respectively. The operation manual was read carefully before testing.

Q-PCR Assay

RNA extraction of AMs was performed using a RNA Fast Mini kit (GK3016, Generay, Shanghai, China). According to the manufacturer's instructions, RNA was extracted and stored at −80 °C. Reverse transcription was performed using the HiScript-II Q RT SuperMix for qPCR (Vazyme, Nanjing, China). A CFX connect Real-Time PCR System (Bio-Rad Laboratories, USA) was used to assay the gene expression of TLR4, MyD88, and AP-1 in AMs.

The PCR primers for TLR4, MyD88 and the internal reference, GAPDH, were designed based on DNA gene sequences from the GenBank website. The three pairs of primers were:

TLR4: F 5′- GACACTTTATCCAGAGCCGTTG -3′,
R 5′- GGACTTCTCCACTTTCTCAAGG -3′

MyD88: F 5′- CAACCAGCAGAAACAGGAGTCT -3′,
R 5′- ATTGGGGCAGTAGCAGATGAAG -3′
AP-1: 5′ -AAACGACCTTCTACGACGATG-3′,
5′-TCGGAGGTGCGGCTTCAGATT-3′
GAPDH: F 5′- TATGACTCTACCCACGGCAAGT -3′,
R 5′- ATACTCAGCACCAGCATCACC -3′

The PCR amplification reaction contained 10 μl 2× ChamQ SYBR Color qPCR Master Mix, 0.6 μl 10 μM forward primer, 0.6 μl 10 μM reverse primer, 2 μl template cDNA, and distilled water (dH_2O) was added to 20 μl. PCR was conducted with the following reaction conditions: 95°C for 30 s, and 40 cycles of 95°C for 10 s, 59°C for 30 s, and 60 °C for 30 s. A melting curve was performed from 70 to 95 °C in increments of 0.5°C for 5 s.

Western Blotting Analysis

The cells were harvested after treatment for 12, 24, and 48 h. AM lysate protein was extracted and analyzed by 12% sodium dodecyl sulfate polyacrylamide gel electrophoresis (SDS-PAGE) that was transferred to a polyvinylidene difluoride (PVDF) membrane, and then blocked for 1 h with 5% non-fat milk. The membrane was incubated overnight with the following primary antibodies: JNK, p38, IKK, IκB, TAK1, and AP-1 (1:1,000), and GAPDH (1:5,000). Membranes were immersed in 1× TBST buffer, washed on a shaker three times for 10 min, incubated with secondary antibodies (1:10,000) for 1 h, and the membranes were washed with TBST. The bands were quantified by image software.

RESULTS

Freeze-Dried Powder Identification by UPLC-MS/MS Analysis

Both positive and negative ESI modes were applied, and the positive ESI response was much better than the negative ESI response. ESI^+ mode, (positive ions) such as $[M + H]^+$ and $[M + NH_4]^+$, were measured in mass in a full scan. Molecular and characteristic fragment ions of 16 chemical components are seen in **Table 2**. Their structures were investigated through

TABLE 2 | Peak area information of freeze-dried powder methanol solution.

HPLC-fingerprint analysis					UPLC-MS/MS analysis					
Marking peak no.	**RT (min)**	**Peak area (μAμ)**	**Peak area percentage (%)**	**CP peak area percentage (%)**	**RT (min)**	**m/z (M + H)**	**Mass Error (ppm)**	**Fomula**	**MW.**	**Name**	**MS/MS**
1	24.62	116,498	0.77	–	4.40	432.2817 (M+NH4)	-5.9	$C_{19}H_{34}N_4O_6$	414.25	Leu Pro Val Ser	265.1616; 177.1112 133.0851; 89.0588
2	27.12	48,684	0.32	0.32	6.72	488.2504	-0.5	$C_{24}H_{33}N_5O_6$	487.24	Heterophyllin J	460.2562; 297.1904 169.1322; 70.0646
3	34.58	220,233	1.45	1.45	7.48	502.2660	-1	$C_{25}H_{35}N_5O_6$	501.26	Pseudostellarin A	474.2715; 361.1877 233.1282,70.0652
4	38.39	9,829,954	64.56	64.56	7.62	564.2817	-0.8	$C_{30}H_{37}N_5O_6$	563.27	new pseudostellarin	536.2865; 318.1449 155.0812,70.0650
5	39.46	141,146	0.93	0.93	8.62	683.3511	-0.2	$C_{33}H_{46}N_8O_8$	682.34	Pseudostellarin B	665.3406; 570.2670 212.1389
6	41.47	131,686	0.86	0.86	8.83	785.4192	-2.4	$C_{38}H_{56}N_8O_{10}$	784.41	Pseudostellarin F	757.4240; 672.3340 308.1957
7	42.07	741,190	4.87	4.87	9.45	779.445	-2.1	$C_{40}H_{58}N_8O_8$	778.44	Heterophyllin B	751.4508; 405.2494
8	43.20	37,451	0.25	0.25	10.02	813.4505	1.5	$C_{40}H_{60}N_8O_{10}$	812.44	Pseudostellarin C	795.4441; 471.2972 358.2137
9	44.11	912,328	5.99	5.99	10.09	714.4185	1	$C_{36}H_{55}N_7O_8$	713.41	Pseudostellarin D	686.4253; 601.3354 573.3397; 211.1442
10	46.01	1,049,294	6.89	6.89	10.61	728.4341	0.6	$C_{37}H_{57}N_7O_8$	727.43	Heterophyllin A	710.4245; 615.2519 310.2149; 197.1280
11	46.56	340,299	2.24	–	10.67	498.2459	-2.7	$C_{24}H_{31}N_7O_5$	497.24	His Gly Trp Val	212.1178; 110.0709
12	47.21	649,931	4.27	4.27	11.00	817.4243	-0.2	$C_{42}H_{56}N_8O_9$	816.42	Pseudostellarin G	799.4176; 555.2935; 467.2297; 332.1605
13	47.77	176,064	1.16	1.16	11.30	878.5135	0.6	$C_{45}H_{67}N_9O_9$	877.51	Pseudostellarin E	765.4313; 674.4264; 365.2195; 308.1971
14	49.99	211,700	1.39	1.39	12.10	665.3657	0.3	$C_{35}H_{48}N_6O_7$	664.36	Heterophyllin D	647.3575; 387.2019; 288.1325
15	51.92	57,081	0.37	–	16.13	279.2319	-0.2	$C_{18}H_{30}O_2$	278.22	Octadecatrinoic acid	149.0231; 95.0852; 81.0700; 67.0546
16	55.75	88,005	0.58	–	19.93	277.2173 (M-H)	0.3	$C_{18}H_{30}O_2$	278.42	Linolenic acid	N/A
Area proportion			**96.9**	**92.94**							

fragmentation reactions of mass spectrum and compared with the existing literature (Fu et al., 2012; Hua et al., 2017). $[M + H]^+$ at *m/z* 432.2817 (M + NH4), *m/z* 488.2504, *m/z* 502.266, *m/z* 564.2817, *m/z* 683.3511, *m/z* 785.4192, *m/z* 779.445, *m/z* 813.4505, *m/z* 714.4185 *m/z* 728.4341, *m/z* 498.2459, *m/z* 817.4243, *m/z* 878.5135, *m/z* 665.3657, *m/z* 279.2319, *m/z* 277.2173(M–H), respectively. Peaks 1–16 was identified as Leu-Pro-Val-Ser molecules, Heterophyllin J, Pseudostellarin A, new Pseudostellarin, Pseudostellarin B, Pseudostellarin F, Heterophyllin B, Pseudostellarin C, Pseudostellarin D, Heterophyllin A, His-Gly-Trp-Val molecules, Pseudostellarin G, Pseudostellarin E, Heterophyllin D, octadecatrinoic acid, and linolenic acid/α-linolenic acid, respectively. There were 12 cyclic peptide monomer components of the 16 compounds; peak 4 was tentatively identified as one cyclic peptide compound and its structure must be further confirmed. The structures of 11 cyclic peptide monomers are shown in **Figure 3**. The relative contents in percentage were calculated using the area normalization method, after the ethyl acetate crude extract was purified to remove naturally occurring impurities, which indicated that the cyclic-peptides content in freeze-dried powder was up to 92.94%. Freeze-dried powder was the refined CPE.

TZS Cyclic Peptide Anti-COPD Activity

The Safety Preliminarily Evaluating by Feeding Rats With CPE for 28 Days

According to the State Food and Drug Administration (SFDA) "Technical guidelines for repeated drug administration toxicity testing", we tested the toxicity through twenty-eight days feeding study. A total of 100 SPF grade Wistar weaning rats, weighted (80 ± 10) g were divided randomly into five groups, 10 male rats and 10 female rats in each group, namely blank control group, vehicle control group, 200, 400 and 500 mg/kg/d dose of CPE group. Rats were fed the corresponding dose of drug or vehicle. On the 30th day, samples of blood were collected for hematological and biochemical analysis. Livers, spleens, kidneys and testicles (ovariesy) from all rats were weighed, furthermore, and the ratio of these organs to body weight was determined. The liver, kidneys, spleen, stomach, duodenum, testicles, ovariesy were removed for histopathological examinations. The tested animals were generally in good condition that both experimental groups and control group grown healthy and there was no abnormal change in body weight. Pathological examination of the experimental groups was negative. The results of hematological and biochemical indexes showed that all the indexes were in the normal range, the recommended dose of CPE was given to animals, and no toxicity was observed, results were listed **Tables 3A**, **B**.

CPE Improves Pulmonary Function

Pulmonary ventilation function is an important index in COPD diagnosis and treatment. Results are increased lung airway resistance (R_L) but decreased dynamic compliance (Cdyn). R_L and Cdyn are commonly measured by relating airflow and driving pressure. These data were calculated by measuring airway flow (V), tidal volume (V_t), and trans-pulmonary pressure (Ptp) by the formula R_L = Ptp/V, Cdyn = V_t/Ptp. The breathing rate of rats was recorded by the MedLab system for 30 min and the test waveforms are shown in **Figures 4A–C**. Compared with the vehicle control group, V and V_t were decreased in the COPD model rat, but led to a rise in Ptp. CPE (200, 400, or 500 mg/kg/day) was given orally for 15 days and the results showed that 400 mg/kg/day dose was the best dose. The V, and Vt were markedly increased (p <0.01) and Ptp was effectively lower (p <0.05) after treatment (**Figures 4D–F**). Compared with the vehicle control group, model group rats R_L increased by 67.12% (p <0.01) and Cdyn decreased by 75.14% (p <0.01). In the Guilong Kechuanning capsule positive group compared with the model group, R_L decreased by 26.02% and Cdyn increased by 140.40% (p <0.01). In the 400 mg/kg dose of CPE group compared with the model group, R_L decreased by 36.29% and Cdyn increased by 171.30% (p <0.01). Experimental results showed that CPE could decrease airway resistance and increased dynamic compliance in rats with COPD (**Table 4**).

Image Analysis of Lung Tissue Sections

Rats were killed to obtain lung tissues when the CPE treatment concluded and the pulmonary tissue pathology was observed with HE staining. Crucial gas exchange takes place in the alveoli. There were full alveoli, respiratory ducts, peripheral, small airways that were normally present in the pulmonary parenchyma in the control group (**Figure 5A**). The number of alveoli was significantly decreased in the SCS group; rats with COPD had significant inflammation that was caused by inflammatory cell infiltration and damage to alveoli structure. The lung lesions were characterized by interstitial edema, the alveolar wall was thickened and there was less alveolar space. There was extensive necrotic changes of the alveoli and partial consolidation, and infiltration of inflammatory cells (**Figure 5B**). The lung damage treated with Guilong Kechuanning capsule (450 mg/kg/day) and CPE (400 mg/kg/day, orally) was lower than that in the model group. Image analysis suggested that CPE could decrease the degree of alveolar destruction (p < 0.05), alleviate lung inflammation, increase alveolar space, and improve infiltration of inflammatory cells in airway inflammation (**Figures 5C, D**).

Effect of CPE on the Expression of Toll-Like Receptors and the Downstream Signaling Transduction Pathway in Rat AMs

Effect of CPE on the Proliferation of Rats Alveolar Macrophage

CPE of different concentrations was used to treat the cells at the 24, 48 and 72 h, and cell proliferation was observed using MTT method to evaluate the cytotoxicity of CPE to AMs. AMs proliferation rates were 100% 72 h at the CPE of 50 μg/ml, 99.73% 72 h at the concentration of 100 μg/ml (P <0.05), 99.55% 72 h at the concentration of 200 μg/ml (P <0.05), 99.28% 72 h at the concentration of 500 μg/ml (P <0.05), 95.83% 72 h at the concentration of 1,000 μg/ml (P <0.05), and 88.08% 72 h at the

concentration of 2,000 μg/ml (P <0.05). When the concentration of CPE was lower than 1000 μg/mL, the CPE showed no toxicity on AMs.

Cytokine Measurement by ELISA in Serum and Cell Supernatants

Medication group rats were treated with intragastric administration of CPE (200, 400, and 500 mg/kg) once daily for 15 days. Orbital plexus blood samples were collected; serum was isolated and assayed by ELISA. AMs of each group were separated by bronchoalveolar lavage.

TNF-α and IL-10 cytokine in the serum were measured using ELISA. COPD model group, the level of TNF-α inflammatory cytokine was increased in the serum when compared to the vehicle control group (145.34 ± 16.92 pg/ml *vs* 97.72 ± 6.94 pg/ml, p <0.01). Treatment with CPE resulted in significant differences (p <0.01) in that the concentration of TNF-α dropped from 145.34 ± 16.92 to 100.47 ± 8.01 pg/ml. However, the concentration of IL-10 anti-inflammatory cytokine was also increased in the serum of model rats (36.57 ± 1.63 pg/ml *vs* 29.80 ± 0.85 pg/ml, p <0.01). Guilong Kechuanning capsule and CPE groups, the levels of serum IL-10 were markedly

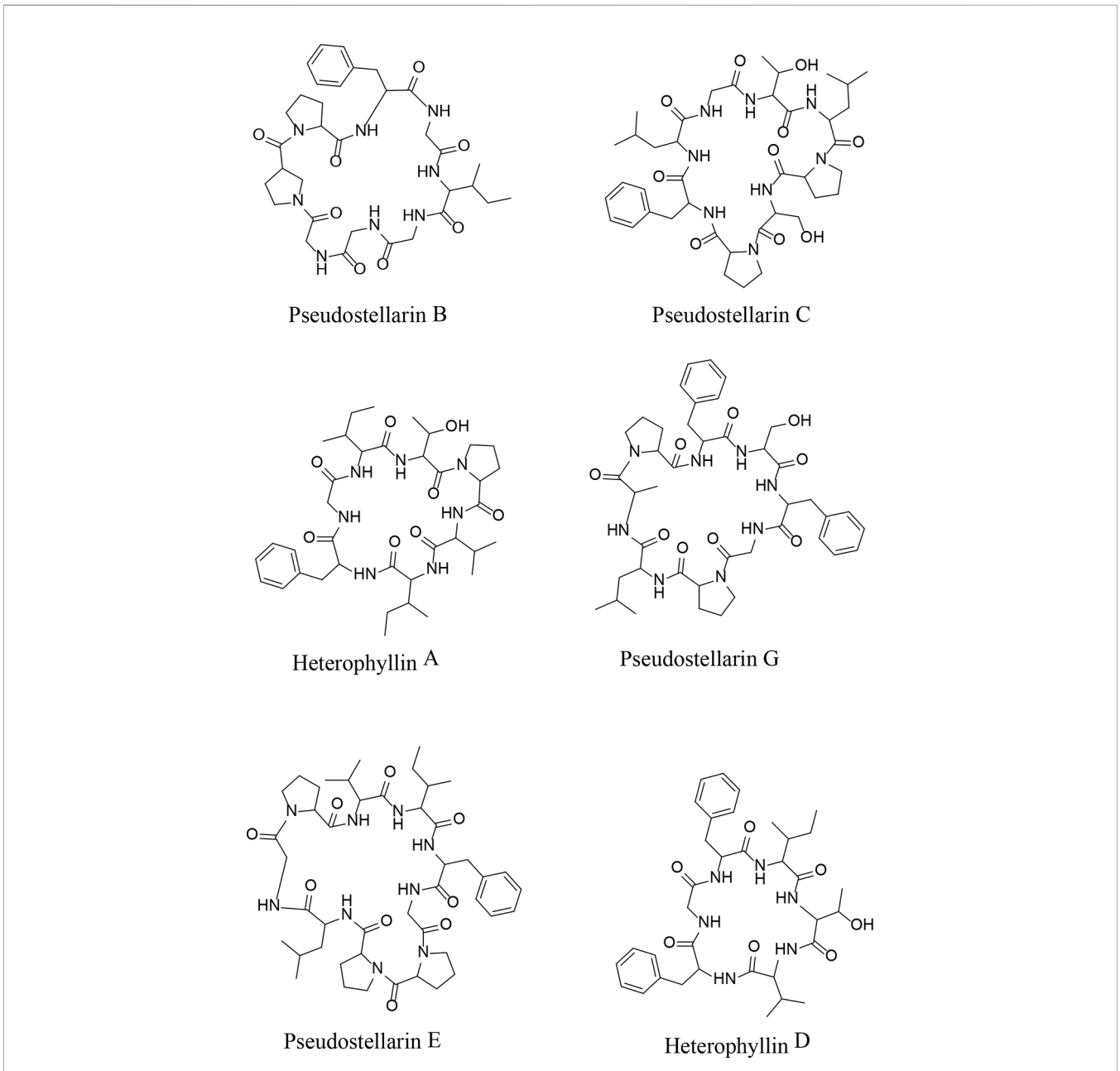

FIGURE 3 | Continued

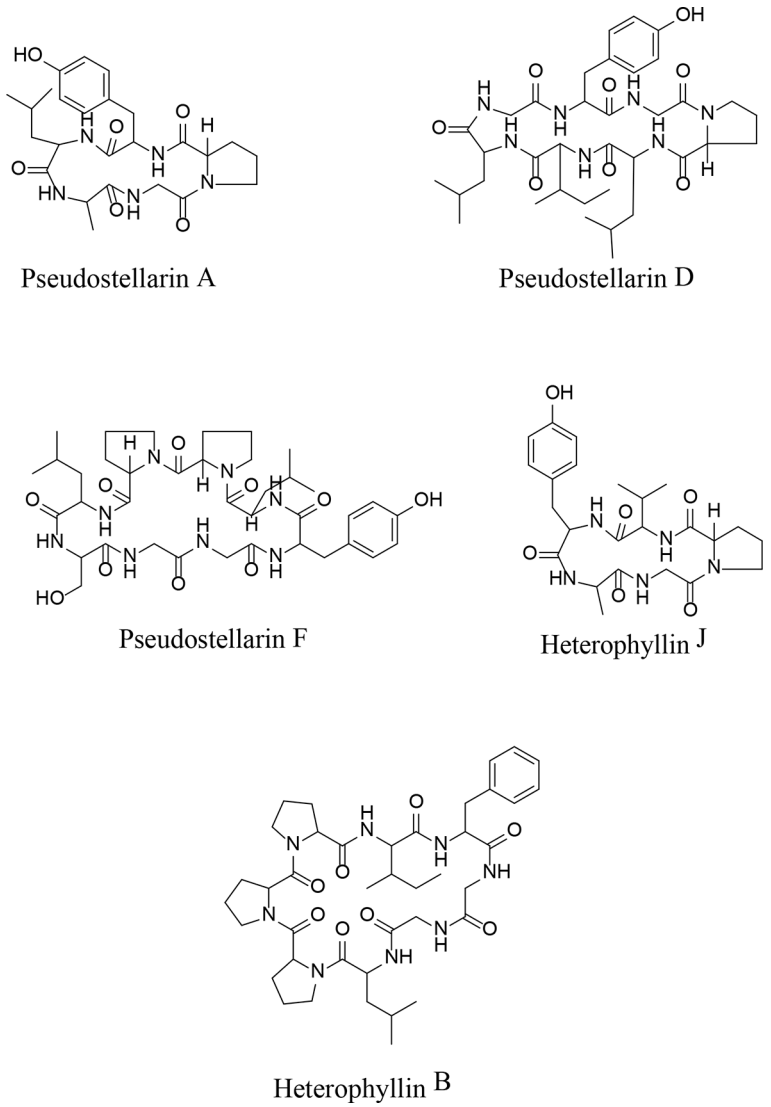

FIGURE 3 | The structures of 11 kinds of cyclic peptide monomers.

TABLE 3A | Effects of CPE on hematological indexes in rats ($\bar{x} \pm sd$).

Sex	Dose (mg/kg·bw/d)	n	Leucocyte count ($\times 10^9$/L)	Red-cell count ($\times 10^{12}$/L)	Hemoglobin (g/L)	Lymphocyte (%)	Neutrophil (%)	Monocyte (%)	Eosinophil (%)	Basicyte (%)
Female	Blank control	10	7.4 ± 1.9	7.3 ± 0.4	138 ± 4	85.0 ± 3.4	10.1 ± 3.9	3.12 ± 0.78	0.54 ± 0.19	0.19 ± 0.09
	Vehicle control	10	6.3 ± 1.8	7.4 ± 0.3	139 ± 5	84.1 ± 3.2	11.1 ± 2.8	3.30 ± 0.87	0.58 ± 0.18	0.13 ± 0.05
	200	10	7.5 ± 2.1	6.9 ± 0.6	132 ± 10	84.6 ± 3.6	10.9 ± 4.0	3.15 ± 0.71	0.42 ± 0.21	0.11 ± 0.07
	400	10	6.9 ± 1.7	7.2 ± 0.4	135 ± 8	85.0 ± 5.3	9.9 ± 4.2	3.37 ± 1.09	0.55 ± 0.20	0.13 ± 0.05
	500	10	6.0 ± 1.5	7.4 ± 0.3	140 ± 7	84.5 ± 2.6	10.3 ± 2.6	3.35 ± 0.84	0.68 ± 0.25	0.15 ± 0.07
Male	Blank control	10	6.8 ± 1.0	7.3 ± 0.3	138 ± 4	84.3 ± 2.8	11.7 ± 2.7	2.67 ± 0.49	0.54 ± 0.29	0.15 ± 0.07
	Vehicle control	10	6.3 ± 1.9	7.3 ± 0.4	137 ± 8	83.6 ± 3.3	12.4 ± 3.2	2.80 ± 0.91	0.52 ± 0.33	0.11 ± 0.07
	200	10	5.9 ± 1.5	7.5 ± 0.5	134 ± 6	82.6 ± 3.0	12.2 ± 2.7	2.72 ± 0.98	0.68 ± 0.39	0.13 ± 0.05
	400	10	7.0 ± 1.2	7.3 ± 0.2	138 ± 4	84.8 ± 3.3	11.0 ± 3.0	2.74 ± 0.93	0.58 ± 0.19	0.12 ± 0.04
	500	10	7.6 ± 1.2	7.3 ± 0.2	138 ± 3	83.8 ± 3.4	11.3 ± 3.1	3.27 ± 0.79	0.62 ± 0.17	0.18 ± 0.04

TABLE 3B | Effects of CPE on blood biochemical indexes in rats ($\bar{x} \pm sd$).

Sex	Dose (mg/kg·bw/d)	n	Alanine transaminase (U/L)	Aspertate Aminotransferase (U/L)	Total protein (g/L)	Albumin (g/L)	Blood urea nitrogen (mmol/L)	Creatinine (μmol/L)	Total cholesterol (mmol/L)	Triglyceride (mmol/L)
Female	Blank control	10	32 ± 2	115 ± 18	54.2 ± 1.9	32.9 ± 1.9	5.84 ± 0.91	33 ± 5	1.88 ± 0.32	0.40 ± 0.09
	Vehicle control	10	34 ± 6	112 ± 20	53.3 ± 2.7	32.7 ± 1.5	5.79 ± 0.85	33 ± 4	1.93 ± 0.27	0.37 ± 0.17
	200	10	31 ± 5	95 ± 19	54.2 ± 3.0	33.1 ± 1.3	5.86 ± 1.03	36 ± 6	1.96 ± 0.29	0.31 ± 0.05
	400	10	30 ± 3	102 ± 10	55.1 ± 1.5	33.4 ± 1.0	5.47 ± 1.08	32 ± 6	1.98 ± 0.33	0.39 ± 0.09
	500	10	32 ± 4	112 ± 15	54.4 ± 2.3	33.1 ± 1.1	5.86 ± 0.84	33 ± 6	2.04 ± 0.35	0.33 ± 0.07
Male	Blank control	10	39 ± 4	129 ± 32	53.2 ± 1.2	31.9 ± 0.6	4.65 ± 0.59	24 ± 2	1.39 ± 0.28	0.48 ± 0.06
	Vehicle control	10	41 ± 8	142 ± 34	54.1 ± 1.6	32.3 ± 0.7	5.21 ± 0.82	28 ± 9	1.46 ± 0.29	0.43 ± 0.27
	200	10	44 ± 2	159 ± 41	52.7 ± 1.9	31.6 ± 0.8	5.86 ± 1.03	36 ± 6	1.96 ± 0.29	0.31 ± 0.05
	400	10	37 ± 4	127 ± 20	54.3 ± 1.6	32.3 ± 0.6	4.84 ± 0.52	25 ± 3	1.36 ± 0.30	0.47 ± 0.08
	500	10	38 ± 7	134 ± 21	54.5 ± 1.8	32.4 ± 1.0	4.83 ± 0.68	26 ± 2	1.40 ± 0.35	0.45 ± 0.07

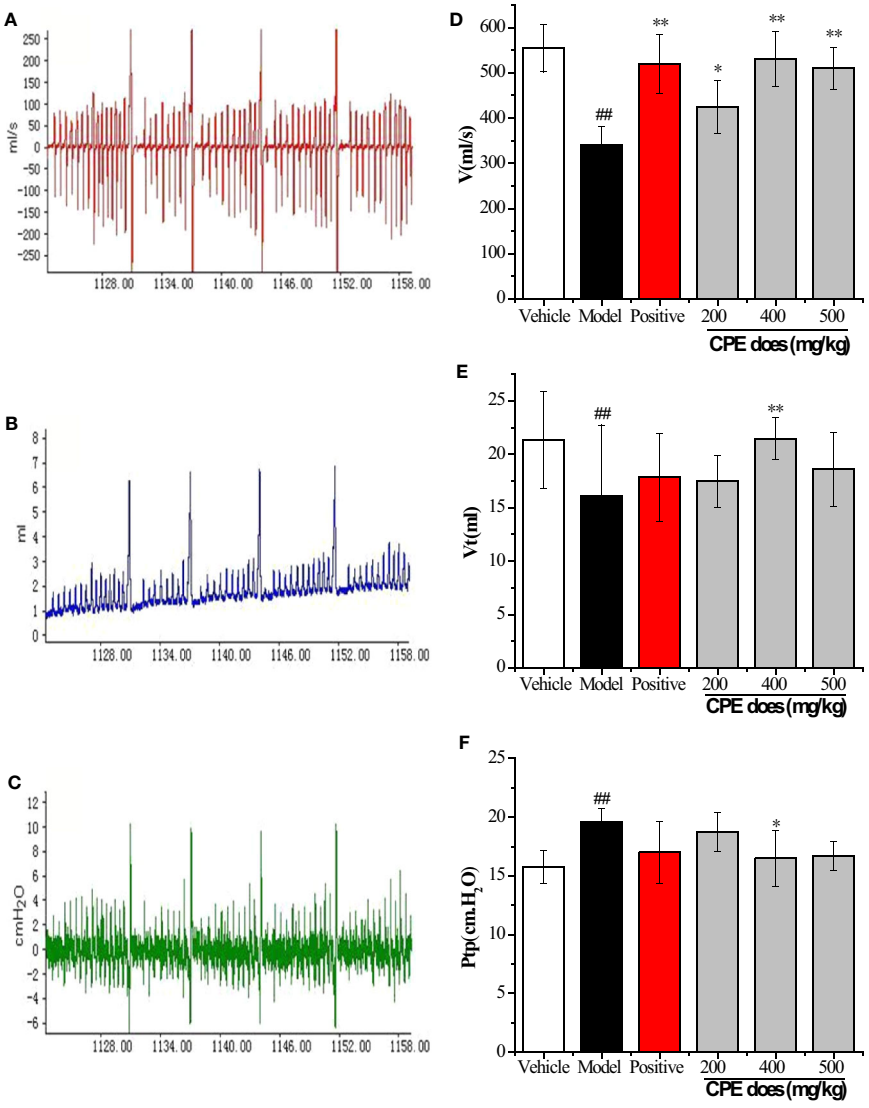

FIGURE 4 | Results of pulmonary function parameters test. **(A)** The test waveforms of airway flow, **(B)** tidal volume, and **(C)** trans-pulmonary pressure; **(D)** the test results in airway flow, **(E)** tidal volume, and **(F)** trans-pulmonary pressure; The measurements were used to calculate R_L and Cdyn. *p < 0.05, **p < 0.01, compared with COPD model; #p < 0.05, ##p < 0.01, compared with vehicle control, ($\bar{x} \pm sd$, n = 10).

TABLE 4 | Changes of airway resistance and dynamic compliance in rats.

Groups	V (ml/s)	Vt (ml)	Ptp (cm·H2O)	R_L (cm·H_2O·s/ml)	Cdyn (ml/cm·H_2O)
Vehicle	554.23 ± 53.96	21.31 ± 4.42	15.77 ± 1.39	0.028 ± 0.001	1.351 ± 0.459
Model	340.82 ± 39.30▲▲	16.13 ± 6.59▲▲	19.60 ± 1.05▲▲	0.057 ± 0.005▲▲	0.823 ± 0.269▲▲
Positive	519.85 ± 63.82**	17.84 ± 4.06	16.70 ± 3.01*	0.033 ± 0.007**	1.050 ± 0.279*
CPE-LD	514.56 ± 73.71**	17.46 ± 2.36	18.72 ± 1.74	0.036 ± 0.006*	0.933 ± 0.422*
CPE-MD	530.96 ± 60.12**	21.45 ± 2.00**	16.49 ± 2.37*	0.031 ± 0.005**	1.301 ± 0.337**
CPE-HD	509.98 ± 44.23**	18.59 ± 3.41*	16.70 ± 1.21*	0.033 ± 0.008**	1.113 ± 0.471*

Values are expressed as $\bar{x} \pm sd$, n = 10.
▲ *P ≤0.05 vs vehicle control,* ▲▲ *P ≤0.01 vs vehicle control.*
**P ≤0.05 vs COPD model, **P ≤0.01 vs COPD model.*

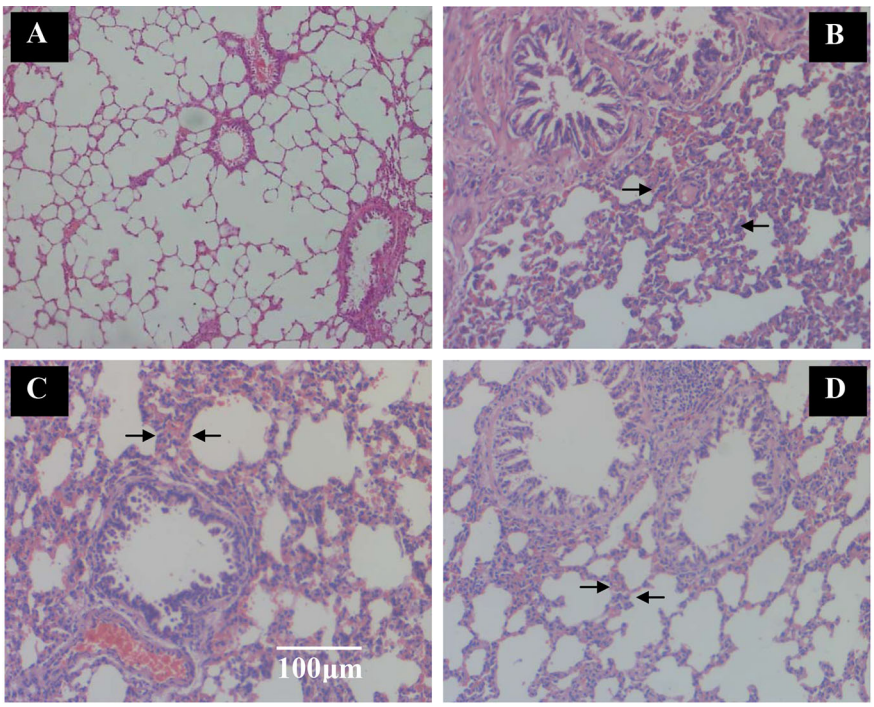

FIGURE 5 | The effect of TZS extracts on alveoli and inflammatory cell infiltration in lungs in SCS-induced rats (hematoxylin and eosin stain). Vehicle control group and model group rats treated with saline, positive control group rats treated with Guilong Kechuanning capsule (450mg/kg/day) and drug group treated with CPE (400 mg/kg/day, orally) was given to SCS-induced rats, tissue histological examination were assessed. **(A)** Vehicle control group, **(B)** SCS model group, **(C)** positive control group and **(D)** CPE treatment group. Arrows indicate alveoli space and inflammatory cell infiltration. With CPE medication, alleviate the lung inflammation, more alveolar space and the infiltrations of inflammatory cells were improved, magnification ×100.

increased to 43.13 ± 2.70 and 55.72 ± 2.67 pg/ml, respectively (p <0.01). For treatment with the positive control and CPE, levels of TNF-α decreased, but IL-10 increased, suggesting that they have obvious anti-inflammatory effects. A CPE dose of 400 mg/kg was the best and its curative effect was better than the positive control (**Figure 6A**).

After treatment of CPE, pulmonary alveolar macrophages (AMs) of all experiment group rats were separated by bronchoalveolar lavage fluid extraction. AMs were stimulated with lipopolysaccharide (LPS) (end concentration 0.1 μg/ml) and cultured with RPMI-1640 containing 10% FBS medium for different time (12, 24, or 48 h), AMs separated by normal and model groups rat served as controls. The levels of TNF-α and IL-10 in the AMs supernatant were detected by ELISA. The level of TNF-α was decreased treatment with CPE, but increased level of IL-10 in supernatant. AMs isolated from rats were treated with 400 mg/kg of CPE (CPE-MD) and cultured for 24 h that it was the best results. The concentration of TNF-α and IL-10 in the supernatant of AMs (vehicle or model group) was 26.37 ± 2.10, 96.79 ± 3.18, 244.59 ± 8.43, and 142.77 ± 6.28 pg/ml. CPE-MD group, they were 27.94 ± 2.15 and 241.57 ± 7.20 pg/ml; respectively. More detailed data are illustrated in **Figures 6B, C**.

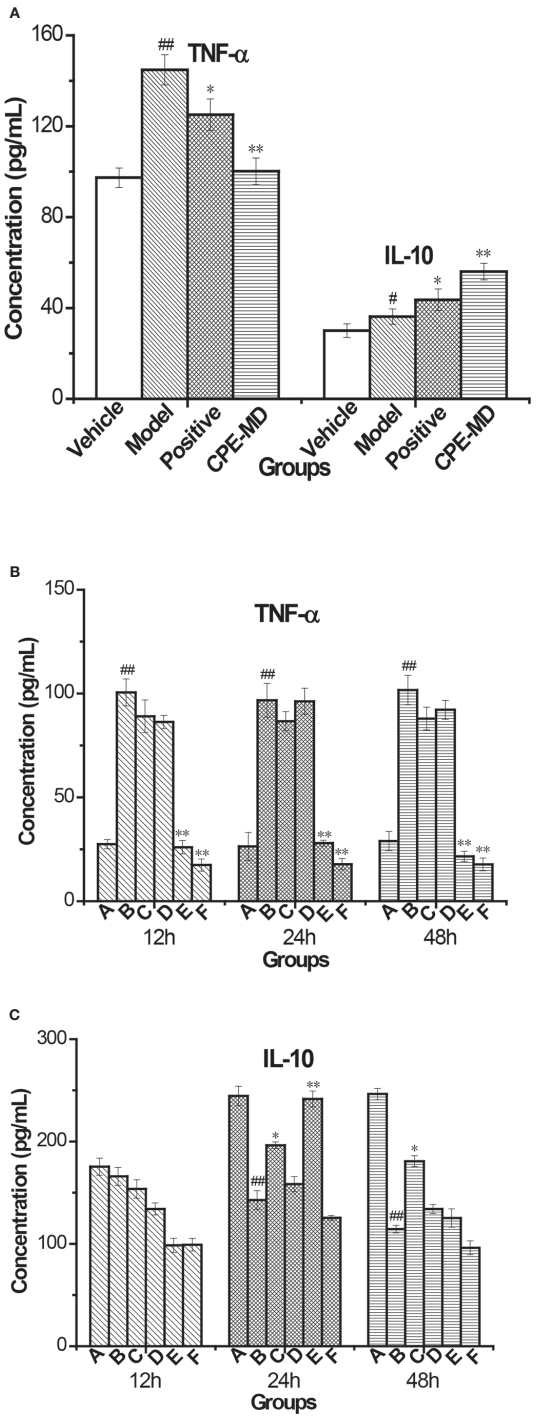

FIGURE 6 | Changes of cytokine in rat serum and supernatant of AMs with COPD model treatment with CPE. **(A)** TNF-α and IL-10 level in rat serum ($\bar{x} \pm sd$, n = 10). **(B)** TNF-α level and **(C)** IL-10 level in supernatant of AMs. *p < 0.05, **p < 0.01, compared with COPD model; #p < 0.05, ##p < 0.01, compared with vehicle control; **A**—Vehicle control, **B**—COPD model + LPS, **C**—positive + LPS, **D**—CPE-LD + LPS, **E**—CPE-MD + LPS, **F**—CPE-HD + LPS; *p < 0.05, **p < 0.01, compared with COPD model; #p < 0.05, ##p < 0.01, compared with vehicle control, ($\bar{x} \pm sd$, n = 6).

Expression of TLR4 mRNA and MyD88 mRNA of AMs by RT-PCR

An AM cell line was stimulated with LPS and cultured with RPMI 1640 containing 10% FBS medium. Twenty-four hours later, RNA of AMs was extracted and TLR4 mRNA MyD88 mRNA, and AP-1 mRNA levels were determined with relative quantification using the $2^{-\triangle\triangle Ct}$ method.

TLR4 mRNA expression in the COPD model group was 2.98 ± 0.13, which was remarkably increased compared to the vehicle control group (1.00 ± 0.00, p <0.01). CPE could attenuate the expression of TLR4 mRNA in COPD rats. TLR4 mRNA levels were 2.09 ± 0.18 for the CPE-LD group, 1.10 ± 0.10 for the CPE-MD group, and 1.09 ± 0.22 for the CPE-HD group. TLR4 mRNA expression was decreased (p <0.01) after using CPE-MD or CPE-HD, while it increased in the CPE-LD group (p <0.05).

MyD88 mRNA expression in AMs of the COPD rats (3.08 ± 0.22) was increased compared to that of vehicle groups (1.26 ± 0.28). In the CPE-LD group it was 2.58 ± 0.26, 1.33 ± 0.16 in the CPE-MD group, and 1.57 ± 0.10 in the CPE-HD group. The MyD88 mRNA expression was decreased (p <0.01) after using CPE-MD or CPE-HD, while it increased in the CPE-LD group (p <0.05).

AP-1 mRNA expression in AMs of the COPD rats (1.22 ± 0.05) was increased compared to that of vehicle groups (1.00 ± 0.00). In the CPE-LD group it was 1.13 ± 0.05, 1.08 ± 0.11 in the CPE-MD group, and 1.09 ± 0.08 in the CPE-HD group. The AP-1 mRNA expression was decreased (p <0.05) after using CPE-MD or CPE-HD, but not significantly difference with CPE-LD group.

CPE reduced the mRNA level of TLR4, MyD88, and AP-1 exerted anti-inflammatory effects, and simultaneously resistance LPS infection to stimulus. Vehicle control values of TLR4, MyD88 and AP-1 were expressed as 1.0. Results were listed in **Table 5**.

Levels of p-p38, p-JNK, p-IKK, p-IκB, p-TAK1, and AP-1 in AMs by WB

An AM cell line was stimulated with LPS and cultured with RPMI 1640 containing 10% FBS medium. Twenty-four hours later, total protein was extracted. Western blot was used to determine the total protein levels of p38, JNK, IKK and levels of phosphorylated IKK, JNK, and p38 in whole-cell lysates. The expression of p-IκB protein was unstable in AMs. Compared with the vehicle control group, the protein levels of p-p38, p-JNK, p-IKK, p-TAK1, and AP-1 were significantly increased in the COPD model group while the expression of p-IKK in the CPE group was not significantly

TABLE 5 | Effect of CPE on the expression of TLR 4 mRNA, MyD88 and AP-1 mRNA in AMs.

Groups	$2^{-\triangle\triangle ct}$(TLR4)	$2^{-\triangle\triangle ct}$ (MyD88)	$2^{-\triangle\triangle ct}$ (AP-1)
Vehicle	1.00 ± 0.00	1.00 ± 0.00	1.00 ± 0.00
Model	2.98 ± 0.13▲▲	2.44 ± 0.17▲▲	1.22 ± 0.05▲
Positive	1.74 ± 0.19**	1.41 ± 0.12**	1.19 ± 0.07
CPE-LD	2.09 ± 0.18*	2.05 ± 0.21*	1.13 ± 0.05
CPE-MD	1.10 ± 0.10**	1.06 ± 0.13**	1.08 ± 0.11*
CPE-HD	1.09 ± 0.22**	1.25 ± 0.08**	1.09 ± 0.08*

Values are expressed as $\bar{x} \pm sd$, n = 6.
▲P ≤0.05 vs vehicle control, ▲▲P ≤0.01 vs vehicle control.
**P ≤0.05 vs COPD model, **P ≤0.01 vs COPD model.*

decreased compared to the model group (p >0.05). p-JNK proteins in the CPE-LD, CPE-MD, and CPE-HD groups were significantly decreased compared with the COPD model group (p <0.01) and p-p38 proteins in the CPE-MD, and CPE-HD groups were significantly decreased compared with the COPD model group (p <0.01). AP-1 protein in the CPE-MD group was decreased compared with the COPD model group (p <0.05). p-TAK1 proteins in the CPE-MD and CPE-HD groups were significantly decreased compared with the COPD model group (p <0.01).

CPE reduced the proteins level of p-JNK, p-p38, p-TAK1, and AP-1 exerted anti-inflammatory effects, and simultaneously resistance LPS infection to stimulus. The levels of p-IKK, p-JNK, p-p38, p-TAK1, and AP-1 have been normalized by the levels of the corresponding total protein and expressed relative to the phosphorylation ratio in vehicle-treated cells (see in **Figures 7** and **8**).

DISCUSSION

COPD is a public health problem. It exhibits symptoms of chronic bronchitis and emphysema, which causes the characteristic narrow airways and shortness of breath in patients. COPD drug therapy, including bronchodilators, anti-inflammatory agent, antioxidant, protease inhibitors, antibiotics, etc; but has a poor prognosis, at present there is no specific way to make COPD are completely curable. The primary aim of COPD treatment is to

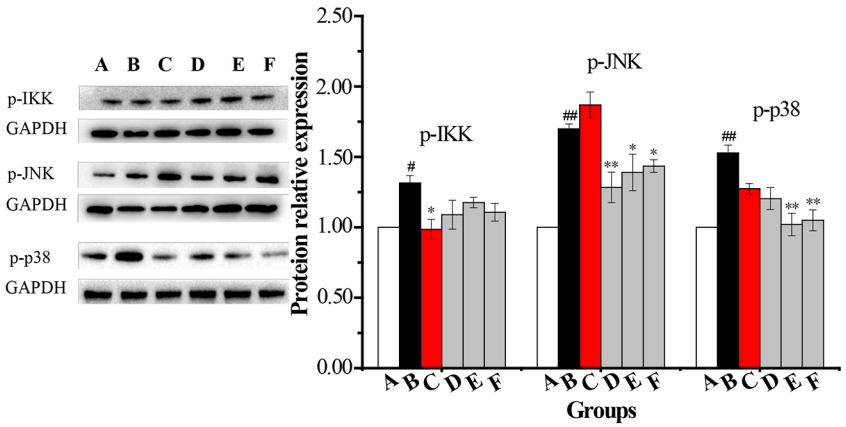

FIGURE 7 | The changes in expression levels of p-IKK, p-JNK and p-p38 in rat alveolar macrophages after the treatment with CPE. **A**—vehicle control, **B**—COPD model + LPS, **C**—positive + LPS, **D**—CPE-LD + LPS, **E**—CPE-MD + LPS, **F**—CPE-HD + LPS; *p < 0.05, **p < 0.01, compared with COPD model; #p < 0.05, ##p < 0.01, compared with vehicle control, ($\bar{x} \pm sd$, n = 6).

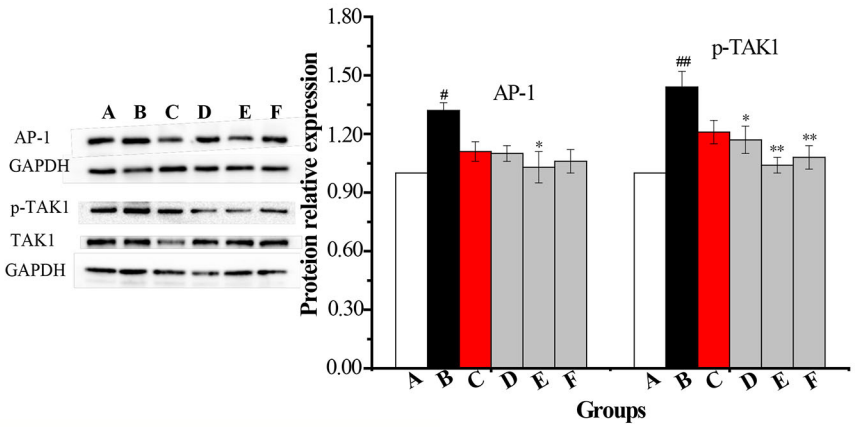

FIGURE 8 | The changes in expression levels of AP-1 and p-TAK1 in rat alveolar macrophages after the treatment with CPE. **A**—vehicle control, **B**—COPD model + LPS, **C**—positive + LPS, **D**—CPE-LD + LPS, **E**—CPE-MD + LPS, **F**—CPE-HD + LPS; *p < 0.05, **p < 0.01, compared with COPD model; #p < 0.05, ##p < 0.01, compared with vehicle control, ($\bar{x} \pm sd$, n = 6).

control symptoms, reduce the rate of deterioration and mortality, and improve the quality of life of patients (Fujii et al., 1999; Puljic et al., 2007; Wollin and Pieper, 2010; Zeng et al., 2010).

TNF-α is a pro-inflammatory cytokine that is closely correlated with pulmonary inflammation caused by COPD. IL-10 decreases pulmonary neutrophilia and also suppresses the expression of TNF-α, IL-6, and IL-8 (Pelaia et al., 2006). TLR4 mediates pathogen-induced NF-κB activation in endothelial cells through the homologous structure of the intracellular interleukin-1 receptor (IL-1R) followed by downstream signaling of MyD88, which then secretes immune inflammatory cytokines, and thereby causes COPD. With better understanding of the COPD inflammatory mechanisms, broad spectrum anti-inflammatory drugs may be more effective, such as inhibitors of PDE4, p38 MAPK and NF-κB, some data suggest that anti-inflammatory therapies might provide a way to prevent COPD condition worsens (Barnes, 2008).

Natural medicinal or Chinese medicine displays a unique chemical diversity and diversity of the biological activities which is one of the most important resources of novel lead compounds especially for the critical diseases. The research on active constituent of natural or traditional medicine is known as one of important means of developing new drugs.

TZS is a Chinese herb that resists pulmonary diseases. We previously showed that the ethyl acetate extract of TZS relieves cough and improves lung function *via* adjustment of the levels of multiple cytokines (Pang et al., 2011). The ethyl acetate extract of TZS is rich in cyclic-peptides; the activity of these cyclic-peptide fractions is not clear.

Cyclic peptides are the substances which are Head-totail cyclization refers to the formation of an amide bond between the C-terminal carboxylic acid and N-terminal amine of the peptide. Cyclic peptides possess diverse biological activities such as antibacterial, anticancer, antifungal, antiviral, and anti-inflammatory properties. More than 40 cyclic peptide drugs have been clinically approved, the most of which are derived from natural world. But some cyclic peptides there are problems with the metabolic stability and oral absorption limits their development as drug candidates (Jing and Jin, 2020).

In this paper, the ethyl acetate extract of TZS was purified that degreased with petroleum ether, amino acids were removed with hot water, and polysaccharide and other impurities were removed with alcohol-precipitation. The purity of CPE after purification is up to 92.94%.

Our research provides further evidence for *P. heterophylla* (Miq.) Pax. CPE prevents alveolar destruction and alleviating lung inflammation in COPD rats induced by SCS. The release of the pro-inflammatory cytokine TNF-α was significantly inhibited, while the anti-inflammatory cytokine IL-10 was increased in serum. These results are closely associated with airflow limitation in the COPD rat.

TLR4 and MyD88 expression was determined using SYBR Green I by real-time PCR. AMs were stimulated by LPS, the expressions of TLR4, MyD88 and p-JNK and p-p38 were enhanced, showing remarkably higher in COPD groups than normal control groups. Upon activation by LPS, TLR4 can form a dimer to recruit MyD88 and/or TRIF, and then bind with IRAK4 to enable IRAK1 to recruit TRAF6. The IRAK1–TRAF6 complex phosphorylates TAB2/TAB3 and TAK1 and thus activates the IKK and MAPK signaling pathways. JNK and p38 MAPK activation initiate the transcriptional potential of c-Jun or c-fos, a critical part of AP-1. After medication, the expression levels of TLR4 mRNA and MyD88 mRNA, and p-JNK and p-p38 were significantly down-regulated. Our experiments have proved that CPE inhibited TAK1 phosphorylation and effectively down-regulating the expression of AP-1. CPE intervention could improve pathological changes of the pulmonary ventilation function in COPD rats, which may be related to its effect in inhibiting abnormal activation of the TLR4-MyD88-JNK/p38 signal transduction pathway.

CONCLUSION

In conclusion, we studied the CPE of TZS that it prevented alveolar destruction and alleviated lung airway inflammation by inhibiting inflammatory cytokine levels *via* the regulation of the TLR4/MyD88 pathway and its related proteins in COPD rats. This is the first report on cyclic peptides extracted from *P. heterophylla* lessens the severity of COPD episodes. The results of studies will be helpful to develop potential anti-COPD cyclic peptide drugs and solve tricky medical problems by stealing an idea from nature.

DATA AVAILABILITY STATEMENT

The datasets generated for this study are available on request to the corresponding authors.

ETHICS STATEMENT

The animal study was reviewed and approved by Ethics committee on experimental animals of Fujian Academy of Traditional Chinese Medicine No. FJATCM-IAEC2017012.

AUTHOR CONTRIBUTIONS

FL: research. HY: separation experiment. S-DL: HPLC analysis and pharmacological experiments. LZ: UPLC/MS/MS analysis and pharmacological experiments. CJ: HPLC analysis and pharmacological experiments. Z-BC: statistical analysis. Y-YL: cell experiment and q-PCR assay. Y-JK: The safety evaluating and western blotting analysis. JH: project management and thesis writing. W-SP: CPE preparation methodology research.

FUNDING

The authors gave thanks to Project 81673575, supported by the National Natural Science Foundation of China; the authors gave thanks to Project 2019YFC1710504, supported by the National Key R & D Plans.

REFERENCES

Barnes, P. J. (2004). Mediators of Chronic Obstructive Pulmonary Disease. *Pharmacol. Rev.* 56 (4), 515–548. doi: 10.1124/pr.56.4.2

Barnes, P. J. (2008). Frontrunners in novel pharmacotherapy of COPD. *Curr. Opin. Pharmacol.* 8 (3), 300–307. doi: 10.1016/j.coph.2008.03.001

Bruno, C. M., and Valenti, M. (2012). Acid-Base Disorders in Patients with Chronic Obstructive Pulmonary Disease: A Pathophysiological Review. *J. Biomed. Biotechnol.* 2012, 1–8. doi: 10.1155/2012/915150. Article ID 915150,.

David, M. M., and Victor, A. K. (2006). Changing the burden of COPD mortality. *Int. J. Chronic. Obstr.* 1 (3), 219–233. doi: 10.2147/copd.2006.1.3.219

Di Stefano, A., Ricciardolo, F. L. M., Caramori, G., Adcock, I. M., Chung, K. F., Barnes, P. J., et al. (2017). Bronchial inflammation and bacterial load in stable COPD is associated with TLR4 overexpression. *Eur. Respir. J.* 49 (5), 1602006–1602006, 11. doi: 10.1183/13993003.02006-2016

Franco, D. P., Valerie, F. J. Q., and Bernhard, R. (2018). MyD88 as a therapeutic target for inflammatory lung diseases. *Expert. Opin. Ther. Tar.* 22 (5), 401–408. doi: 10.1080/14728222.2018.1464139

Fu, X. S., Liu, X. H., Xu, H., Zhou, Y. Z., and Chen, F. (2012). Research status and trends of pseudostellariae radix. *Chin. J. New Drugs* 21 (7), 757–760.

Fujii, T., Otsuka, T., Tanaka, S., Kanazawa, H., Hirata, K., Kohno, M., et al. (1999). Plasma endothelin-1 level in chronic obstructive pulmonary disease: relationship with natriuretic peptide. *Respiration* 66 (3), 212–219. doi: 10.1159/000029380

Hsu, D. Z., Liu, C. T., Chu, P. Y., Li, Y. H., Periasamy, S., and Liu, M. Y. (2013). Sesame Oil Attenuates Ovalbumin-Induced Pulmonary Edema and Bronchial Neutrophilic Inflammation in Mice. *BioMed. Res. Int.* 2013, 1–7. doi: 10.1155/2013/905670. Article ID 905670,.

Hua, Y. J., Wang, S. N., Chai, C., Liu, Z. X., Liu, X. H., Zou, L. S., et al. (2017). Quality Evaluation of Pseudostellariae Radix Based on Simultaneous Determination of Multiple Bioactive Components Combined with Grey Relational Analysis. *Molecules* 22 (1), 13–28. doi: 10.3390/Molecules22010013

Huang, X. X., and Cai, J. K. (1993). Effect of Guilong Kechuanning on 1468 Cases of Pulmonary Diseases. *Jiangsu J. Tradit. Chin. Med. Sum* 495 (11), 15.

Huang, W. Z., Liu, Y., Qin, M. J., and Dou, C. G. (2005). The evaluation of immunifaction of extract from Pseudostellaria heterophylla in mice. *Res. Pract. Chin. Med.* 19 (6), 35–37.

Huang, C. Y., Pan, L. H., Lin, F., Qian, W., and Li, W. (2015). Alveolar macrophage TLR4/MyD88 signaling pathway contributes to ventilator-induced lung injury in rats. *Chin. J. Cell. Mol. Immunol.* 31 (2), 182–189.

Jiangsu New Medical College (1977). *Encyclopedia of Chinese Materia Medica (Appendix)* (Shanghai, China: Shanghai People's Press), 595–596.

Jing, X. S., and Jin, K. (2020). A gold mine for drug discovery: Strategies to develop cyclic peptides into therapies. *Med. Res. Rev.* 40 (2), 753–810. doi: 10.1002/med.21639

Ley, Z. J., Ley, S., and Kauczor, H. U. (2008). Morphological and functional imaging in COPD with CT and MRI: present and future. *Eur. Radiol.* 18, 510–521. doi: 10.1007/s00330-007-0772-1

Li, T. Z., Chen, Z. T., and Peng, J. (2005). Effect of the therapy Shenyi capsules and Guilongkechuanning capsules on the cellular immunologic function and cytotines in patients with chronic obstructive pulmonary disease. *Chin. Chongqing Med.* 34 (1), 78–82.

Lin, G. M. (2004). Progress in study of Chinese herb Taizishen. *Chin Wild Plant Resour.* 23 (6), 15–17.

Lindberg, A., Larsson, L. G., Muellerova, H., Rönmark, E., and Lundbäck, B. (2012). Up-to-date on mortality in COPD-report from the OLIN COPD study. *BMC Pulm. Med.* 12, 1–7. doi: 10.1186/1471-2466-12-1

Murărescu, E. D., Eloae-zugun, F., and Mihailovici, M. S. (2008). Experimental COPD induced by solid combustible burn smoke in rats: a study of the emphysematous changes of the pulmonary parenchyma. *Rom. J. Morphol. Embryo.* 49 (4), 495–505.

Ng, T. B., Liu, F. H., and Wang, X. (2004). The antioxidant effects of aqueous and organic extracts of Panax quinquefolium, Panax notoginseng, Codonopsis pilosula, Pseudostellaria heterophylla and Glehnia littoralis. *J. Ethnopharmacol.* 93 (2), 285–288. doi: 10.1016/j.jep.2004.03.040

Pang, W. S., Lin, S. D., Dai, Q. W., Zhang, H. C., and Hu, J. (2011). Antitussive Activity of Pseudostellaria heterophylla (Miq.) Pax Extracts and Improvement in Lung Function via Adjustment of Multi-Cytokine Levels. *Molecules* 16, 3360–3370. doi: 10.3390/molecules16043360

Pelaia, G., Vatrella, A., Gallelli, L., Renda, T., Caputi, M., Maselli, R., et al. (2006). Biological targets for therapeutic interventions in COPD: clinical potential. *Int. J. Chronic. Obstr.* 1 (3), 321–334. doi: 10.2147/copd.2006.1.3.321

Puljic, R., Benediktus, E., Plater-Zyberk, C., Baeuerle, P. A., Szelenyi, S., Brune, K., et al. (2007). Lipopolysaccharide-induced lung inflammation is inhibited by neutralization of GM-CSF. *Eur. J. Pharmacol.* 557 (2-3), 230–235. doi: 10.1016/j.ejphar.2006.11.023

Valença, S. S., de Souza da Fonseca, A., da Hora, K., Santos, R., and Porto, L. C. (2004). Lung morphometry and MMP-12 expression in rats treated with intraperitoneal nicotine. *Exp. Toxicol. Pathol.* 55 (5), 393–400. doi: 10.1078/0940-2993-00322

Wang, H. X., and Ng, T. B. (2006). Concurrent isolation of a Kunitz-type trypsin inhibitor with antifungal activity and a novel lectin from Pseudostellaria heterophylla roots. *Biochem. Bioph. Res. Co.* 342 (1), 349–353. doi: 10.1016/j.bbrc.2006.01.109

Weibel, E. R., and Gomez, D. M. (1962). A principle for counting tissue structures on random sections. *J. Appl. Physiol.* 17 (2), 1343–1348. doi: 10.1152/jappl.1962.17.2.343

Wollin, L., and Pieper, M. P. (2010). Tiotropium bromide exerts anti-inflammatory activity in a cigarette smoke mouse model of COPD. *Pulm. Pharmacol. Ther.* 23 (4), 345–354. doi: 10.1016/j.pupt.2010.03.008

Wong, C. K., Leung, K. N., and Fung, M. C. (1994). The induction of cytokine gene expression in murine peritoneal macrophages by Pseudostellaria heterophylla. *Immunopharm. Immunot.* 16 (3), 347–357. doi: 10.3109/08923979409007098

Yan, C. G. (2008). The research and application of medicinal plants Pseudostellaria heterophylla (Miq.) Pax. *Res. Pract. Chin. Med.* 22 (2), 61–65.

Yu, X., Hu, J. T., Lai, J., Wang, R. Z., Ma, L. L., and Tang, Z. H. (2018). Comparison of the biological characteristics of primary rat macrophages extracted by three methods. *Chin. J. Tissue Eng. Res.* 22 (24), 3863–3868.

Zeng, L. X., Dong, J. C., Yu, W. Q., Huang, J. H., Liu, B. J., and Feng, X. T. (2010). Baicalin attenuates inflammation by inhibiting NF-κB activation in cigarette smoke induced inflammatory models. *Pulm. Pharmacol. Ther.* 23 (5), 411–419. doi: 10.1016/j.pupt.2010.05.004

Zhou, Z. R. (2005). Fufangtaizishenzhikeyiqisan were used to treatment of bronchial asthma 2180 examples. *J. Med. &Pharmacy Chin. Minorities* 11 (5), 12–13.

Conflict of Interest: The authors declare that the research was conducted in the absence of any commercial or financial relationships that could be construed as a potential conflict of interest.

frontiers in Pharmacology

ORIGINAL RESEARCH
published: 31 August 2020
doi: 10.3389/fphar.2020.01317

Theaflavin Induces Apoptosis of A375 Human Melanoma Cells and Inhibits Tumor Growth in Xenograft Zebrafishes Through P53- and JNK-Related Mechanism

Lei Zhang[1], *Bo Yan*[1], *Shijie Meng*[2], *Li Zhou*[2], *Yiqiao Xu*[3], *Wenxi Du*[2]* *and Letian Shan*[2]*

[1] School of Biological and Chemical Engineering, Zhejiang University of Science and Technology, Hangzhou, China, [2] The First Affiliated Hospital, Zhejiang Chinese Medical University, Hangzhou, China, [3] Research and Development Department, Hunter Biotechnology, Inc., Hangzhou, China

OPEN ACCESS

Edited by:
Peng Li,
University of Macau, Macau

Reviewed by:
Xiuping Chen,
University of Macau, China
Xiaoying Wang,
Tianjin University of Traditional Chinese Medicine, China

***Correspondence:**
Wenxi Du
purpleraineer@163.com
Letian Shan
letian.shan@zcmu.edu.cn

Specialty section:
This article was submitted to Ethnopharmacology, a section of the journal Frontiers in Pharmacology

Received: 11 May 2020
Accepted: 07 August 2020
Published: 31 August 2020

Citation:
Zhang L, Yan B, Meng S, Zhou L, Xu Y, Du W and Shan L (2020) Theaflavin Induces Apoptosis of A375 Human Melanoma Cells and Inhibits Tumor Growth in Xenograft Zebrafishes Through P53- and JNK-Related Mechanism. Front. Pharmacol. 11:1317. doi: 10.3389/fphar.2020.01317

Theaflavin (TF) is a major active pigment and polyphenol of tea, possessing anti-cancer activities. However, little is known about its activity and mechanism on melanoma cells. To fill this gap, we conducted *in vitro* experiments (cell viability assay, morphology observation, DAPI staining, and flow cytometry) and *in vivo* experiment by using a xenograft model of larval zebrafishes. Real-time PCR (qPCR) and Western blot (WB) analyses were conducted to explore the mechanism of TF. The *in vitro* data showed that TF exerted significant anti-proliferative and pro-apoptotic effects on A375 cells in a concentration-dependent manner. *In vivo*, TF significantly inhibited A375 tumor growth in larval zebrafishes at 0.67 and 2.0 μg/ml (1.3 to 3.9 μM). qPCR and WB data showed that TF significantly activated the P53 pathway-related proteins (ATM, CHK1/2, P53, and CASP8/3) and the JNK pathway-related proteins (ASK1, JNK, and C-JUN) through phosphorylation and cleavage, followed by activation of pro-apoptotic molecules (PARP, *BAX*, *BIM*, *PUMA*, and *P53*). In sum, TF possessed cytotoxic pro-apoptotic and tumor-inhibitory effects on A375 cells through activations of P53 and JNK pathways. This is the first report on TF regarding its effects and mechanism on A375 cells, making it a promising candidate of natural products for clinical treatment of melanoma.

Keywords: green tea, theaflavin, melanoma, zebrafish, P53, JNK

Abbreviations: DAPI, 4'-6-diamidino-2-phenylindole; DMEM, Dulbecco's modified Eagle's medium; DMSO, dimethyl sulfoxide; dpf, days post fertilization; FBS, fetal bovine serum; FI, fluorescence intensity; LSD, Fisher's least significant difference; NOAEL, no observed adverse effect level; MTT, 3-(4,5-dimethylthiazol-2-yl)-2,5-diphenyltetrazolium bromide; PARP, poly ADP-ribose polymerase; SDS-PAGE, denaturing sodium dodecyl sulfate polyacrylamide gel electrophoresis; TCM, theaflavin; TF, Traditional Chinese medicine.

INTRODUCTION

Melanoma is a fatal type of skin cancer, with high metastatic potential and intractability (Yang et al., 2018). Melanoma patients at advanced stages are always unresectable and have a worse prognosis (Leonardi et al., 2018). Chemotherapy is a mainstay of clinical treatment for melanoma, but the efficacies of chemotherapeutics are limited due to their side effects on healthy tissues (Oliveira Pinho et al., 2019). Recently, several immunotherapies, including CTLA-4 or PD-1 receptor inhibitors, have been developed as new options for treating melanoma, but their efficacies are unreliable and their side effects are still non-negligible (Rodríguez-Cerdeira et al., 2017). Therefore, new strategies with satisfactory effectiveness and safety are urgently needed. Traditional Chinese medicine (TCM) is a complementary approach and has been clinically applied for thousands of years, possessing certain efficacy and fewer side effects. According to the TCM theory, cancer is associated with body accumulation of phlegm, toxins or inflammation, and the anti-phlegm, anti-toxic, or anti-inflammatory herbs may possess anti-cancer effects (Wang and Cheng, 2019). The theory has been supported by many cases. For example, curcumin in *Rhizoma Curcumae longae* exerted cytotoxic effects by inducing apoptosis and inhibiting angiogenesis of melanoma cells (Mirzaei et al., 2016), and vitexin in *Vitex negundo* suppressed melanoma cell growth by inducing DNA damage and increasing ROS levels (Liu et al., 2018). Therefore, TCM herbal components have great potential for treatment of cancers, such as melanoma.

Tea [*Camellia sinensis* (L.) O. Kuntze] is one of the most prevalent beverages in the world. It is well-known not only for the peculiar flavor but also for the benefits to health. Due to the difference of process, tea has three main types, including unfermented green tea, partially fermented *oolong* tea, and fully fermented black tea or *pu-erh* tea (Kuo et al., 2005). Tea leaves have been characterized as a TCM herb with anti-phlegm and anti-toxic properties, indicating its anti-cancer potential. Modern studies have reported that tea drink is effective in preventing and treating cancers (Jin et al., 2018). Recently, tea polyphenols have been found to possess anti-cancer activity, which have superior effect to tea drink (Mao et al., 2019). Theaflavin (TF) is such a polyphenol component produced by oxidation of catechins of tea leaves during fermentation, acting as a main pigment for the color, flavor and bioactivity of tea (Roberts et al., 1957). It is capable of inducing apoptosis in a variety of cancer cell lines, such as human breast carcinoma cell lines (MCF-7, MDA-MB-231, T47D, and ZR-75-1), colon carcinoma cell lines (HCT-15 and HT-29), and hepatic carcinoma cell lines (HCCLM3 and Huh-7), indicating anti-cancer potential (Adhikary et al., 2009; Lahiry et al., 2010; Li et al., 2012; Shao et al., 2016). Nevertheless, little attention has been given to its effect towards melanoma as yet.

In view of the reported pro-apoptotic effects of TF on many cancer cell lines (Lahiry et al., 2008), we put forward a hypothesis that TF exerts pro-apoptotic effects on melanoma cells. To verify this, the present performed *in vitro* experiments to evaluate the cytotoxic pro-apoptotic effect of TF on human melanoma cells and conducted *in vivo* experiment by using a xenograft model in larval zebrafishes to determine its tumor-inhibitory effect. Moreover, the mechanism of TF was also explored.

MATERIALS AND METHODS

Materials and Chemicals

Theaflavin (TF, >95% of purity) was provided by Theabio Co., Ltd (Hangzhou, China) (Batch number: 20181211061). Dulbecco′s modified Eagle′s medium (DMEM) containing high glucose (4.5 g/l) was obtained from HyClone Laboratories (UT, USA). Fetal bovine serum (FBS) was obtained from Cell Max (Beijing, China). Trypsin (0.25%) were obtained from Gibco (NY, USA). 3-(4,5-dimethylthiazol-2-yl)-2,5-diphenyltetrazolium bromide (MTT) and dimethyl sulfoxide (DMSO) were obtained from Sigma (St. Louis, MO, USA). Annexin-V: FITC apoptosis detection kit was obtained from BD Biosciences (CA, USA). 4'-6-diamidino-2-phenylindole (DAPI) staining solution was obtained from Thermo Fisher Scientific (MA, USA). Primary antibodies were obtained from Cell Signaling Technology (MA, USA). Trizol reagent and real time polymerase chain reaction (real time PCR) kit were obtained from TaKaRa (Dalian, China).

Cell Line Preparation

Human HFF-1 skin fibroblast and A375 melanoma cell line were obtained from Shanghai Cell Bank of Chinese Academy of Sciences (Shanghai, China), and human A875 melanoma cell line was obtained from Kunming Cell Bank of Chinese Academy of Sciences (Kunming, China). These cell lines were cultured in DMEM medium containing 10% FBS at 37°C in a humidified 5% CO_2 incubator. The medium was daily changed, and the cells were treated with TF in their logarithmic growth phase.

Zebrafish Preparation

Wild-type AB strain of zebrafishes was obtained from the China Zebrafish Resource Center, Institute of Hydrobiology, China Academy of Science (Wuhan, China) and accredited by the Association for Assessment and Accreditation of Laboratory Animal Care International (SYXK 2012-0171). Larval zebrafishes at 2 dpf (days post fertilization) were produced by natural pair-mating and housed in a light-controlled aquaculture facility with a standard 14:10 h day/night photoperiod and fed with live brine shrimp twice a day and fry flakes once a day.

Cell Viability Assay and Morphological Observation

MTT assays were conducted to determine the inhibitory effects of TF on melanoma cell lines, as previously described (Zhou et al., 2017). Cells were seeded into 96-well plates at 6×10^3 cells/well in 200 μl medium for 24h adherence, followed by treatment with TF at concentrations of 0, 50, 100, 150, 200, 250, 300, and 400 μg/ml for 24, 48, and 72 h. Then 20 μl of MTT solution (5.0 mg/ml) was added to each well and incubated at 37°C for 4h. DMSO (150 μl) was added in each well and the optical density value (OD value) was measured at 490 nm with Biorad microplate reader (CA, USA). Inhibitory rate (%) = [1-(TF-treated OD/untreated OD)] × 100%. The 50% inhibitory concentrations (IC_{50}) for 24, 48, and 72 h were calculated by regression analysis. Accordingly, 120, 240, and 360 μg/ml (232.3, 464.7, and 697.0 μM) were designated as low, middle, and high doses of TF. Then, HFF-1, A375, and A875 cell lines were seeded

into 96-well plates as above, and treated with middle dose of TF at 24 h. The cell morphology of A375 cells was observed under Carl Zeiss fluorescence microscope (Göttingen, Germany).

Apoptosis Analysis by DAPI Staining and Flow Cytometry

Cell apoptosis was determined by DAPI staining and annexin-V/PI staining-based flow cytometry. For DAPI staining, A375 cells were seeded into 96-well plates and treated with TF at low, medium, and high concentrations for 24 h, followed by fixation with 4% paraformaldehyde in PBS for 30 min at room temperature and staining with DAPI for 10 min in dark. After thrice wash, cells were observed using five coverslips under Carl Zeiss fluorescence microscope (Göttingen, Germany) and the apoptotic cells were counted. Flow cytometry was conducted according to the manufacturer′s instruction. Briefly, A375 cells were seeded into 6-well plates at 3×10^5 cells/well for 24 h and treated with TF at low, medium, and high concentrations for another 48 h. Afterwards, the cells were washed twice and labeled with annexin V-fluorescein isothiocyanate solution and PI in binding buffer. Fluorescence intensity of the cells was detected by BD C6 flow cytometry (CA, USA). The analysis was replicated and the early apoptotic and late apoptotic cell rates (%) were calculated.

Xenograft Animal Assay

For determining the dose range of TF, totally 300 larval zebrafishes at 3 dpf were used and randomly cultured into 6-well plates with 30 fishes each. TF were dissolved into each well at 0, 3.47, 10.4, 31.25, 62.5, 125, 250, 500, 1,000, and 2,000 μg/ml, respectively, for 24 h. Afterwards, fishes in each group were observed under a stereoscopic microscope to record mortality and adverse events. As described by our previous study, no observed adverse effect level (NOAEL) of TF was estimated, and 1/9 NOAEL, 1/3 NOAEL and NOAEL were applied as the low, middle, and high doses for the following experiment (Jin et al., 2018).

To establish the xenograft model, A375 cells were stained with CM-Dil (red fluorescence) at a dilution of 1:1,000 and microinjected into the yolk sac of larval zebrafishes (2 dpf) at a dose of 200 cells/fish. After tumor growth for 24 h, all fishes were observed under a fluorescent microscope (AZ100, Nikon, Tokyo, Japan) for model verification. The A375-bearing fishes were grouped into 5 groups (30 fishes each) and treated with 0 μg/ml, 1/9 NOAEL, 1/3 NOAEL, and NOAEL of TF, as well as 15 μg/ml (50 μM) of cisplatin, respectively, for 24 h. The fluorescence intensity (FI) of A375 cell mass of zebrafishes was detected and the inhibitory rate was calculated as: inhibitory rate (%) = [1–(FI of treated group/FI of untreated group)] × 100%.

Real Time PCR (qPCR) Analysis

To reveal the molecular actions of TF on A375 cells, qPCR was employed on an ABI QuantStudio™ 7 Flex Real-Time PCR System (Applied Biosystems, CA, USA). The total RNA of A375 cells was extracted using Trizol reagent and synthesized to cDNA *via* reverse transcription. The qPCR reaction system had a 20.0 μl volume: 10 μl SYBR® Premix Ex Taq II (Tli RnaseH Plus), 0.8 μl PCR forward primer, 0.8 μl PCR reverse primer, 2.0 μl template cDNA, 0.4 μl ROX reference dye, and 6.0 μl ddH_2O. The qPCR reaction condition was set to 95°C for 30 s initial denaturation, 40 cycles of 95°C for 5 s denaturation, 60°C for 34 s annealing, and 72°C for 40 s extension. At the end of each reaction, a melting curve analysis was performed. *β-ACTIN* was used as the reference gene and the $2^{-\Delta\Delta CT}$ method was applied to analyze the relative expression of each gene (**Table 1**).

Western Blot (WB) Analysis

The protein expression of A375 cells with TF treatment at 0 μg/ml and 120 μg/ml (232.3 μM) was analyzed by WB analysis. The total proteins were extracted using a lysis buffer (50 mM Tris-HCl pH 7.4, 150 mM NaCl, 1 mM EDTA, 1% Triton, 0.1% SDS, 5 μg/ml leupeptin, and 1 mM PMSF) for 30 min on ice with repeated freezing and thawing. Targeted proteins were separated using denaturing sodium dodecyl sulfate polyacrylamide gel electrophoresis (SDS-PAGE) (8~12%) and then transferred onto a polyvinylidene fluoride (PVDF) membrane (Millipore, MA, USA). The membrane was blocked with 5% non-fat milk for 2 h, followed by overnight incubation at 4°C with the antibodies against: ACTIN, ASK1, ATM, phosphorylated ATM (*p*-ATM), ATR, phosphorylated ATR (*p*-ATR), cleaved caspase 3 (*c*-CASP3), cleaved caspase 8 (*c*-CASP8), CHK1, CHK2, phosphorylated CHK1 and CHK2 (*p*-CHK1 and *p*-CHK2), JNK, phosphorylated JNK (*p*-JNK), C-JUN, phosphorylated C-JUN (*p*-C-JUN), cleaved PARP (poly ADP-ribose polymerase), P53, and phosphorylated P53 (*p*-P53). After incubation with the secondary antibody, these proteins were visualized with an enhanced chemiluminescence kit (Amersham Pharmacia Biotech, Little Chalfort, UK) and detected using a chemiluminescence analyzer.

TABLE 1 | Primer sequences used for qPCR analysis.

Gene	Forward primer	Reverse primer
β-ACTIN	5′-CATGTACGTTGCTATCCAGGC-3′	5′-CTCCTTAATGTCACGCACGAT-3′
BAX	5′-CCTTTTCTACTTTGCCAGCAAAC-3′	5′-GAGGCCGTCCCAACCAC-3′
BCL-2	5′-ATGTGTGTGGAGAGCGTCAACC-3′	5′-TGAGCAGAGTCTTCAGAGACAGCC-3′
BIM	5′-ACCAAACCAAAGCCGTCATCA-3′	5′-GGAGCCAGTAAACGTATTGGAAG-3′
C-MYC	5′-GCCACGTCTCCACACATCAG-3′	5′-TGGTGCATTTTCGGTTGTTG-3′
P21	5′-GGCAGACCAGCATGACAGATT-3′	5′-GCGGATTAGGGCTTCCTCT-3′
P53	5′-TCAACAAGATGTTTTGCCAACTG-3′	5′-ATGTGCTGTGACTGCTTGTAGATG-3′
PUMA	5′-GACCTCAACGCACAGTACGAG-3′	5′-AGGAGTCCCATGATGAGATTGT-3′

Statistical Analysis

Data were expressed as mean values ± SD and subjected to one-way ANOVA, followed by Fisher's least significant difference (LSD) comparison. All analyses were performed using an updated version of DPS software (Tang and Zhang, 2013).

RESULTS

Anti-Proliferative Effect of TF

As shown in **Figure 1A**, TF at 50 μg/ml (96.8 μM) significantly inhibited the viability of A375 cells, and the inhibitory rates were increased with increasing TF concentrations from 50 to 400 μg/ml (96.8 to 744.4 μM) (each $P < 0.01$ vs. normal level), indicating a concentration-dependent manner. The inhibitory rates were also increased with TF treatment from 24 to 72 h, with IC_{50} of 218.9 to 84.9 μg/ml (423.8 to 164.4 μM), respectively. Then, we applied 120, 240, and 360 μg/ml (232.3, 464.7, and 697.0 μM) as the doses of TF-L, TF-M and TF-H, respectively. As shown in **Figure 1B**, TF-M obviously inhibited the viability of A375 and A875 cells but exerted little effect on HFF-1 cells. As shown in **Figure 1C**, the morphology of A375 cells was obviously altered and the living cell number was decreased with TF treatment at increasing concentrations.

Pro-Apoptotic Effect of TF

DAPI staining and flow cytometry were performed to evaluate the pro-apoptotic effect of TF on A375 cells. The result of DAPI staining showed apoptotic morphology, including shrunken shape, karyopyknosis, and nuclear fragmentation, in A375 cells with TF treatment from 120 to 360 μg/ml (232.3 to 697.0 μM) (**Figure 2A**). The apoptotic cell numbers were significantly increased with TF treatment at 240 and 360 μg/ml (464.7 and 697.0 μM) (each $P < 0.01$ vs. NC) (**Figure 2C**). The result of flow cytometry showed TB-induced early apoptosis and late apoptosis of A375 cells (**Figure 2B**). The numbers of early and late apoptotic cells were increased with TF treatment from 120 to 360 μg/ml (232.3 to 697.0 μM) (**Figure 2B**), and their proportions were significantly higher with TF treatment at 360 μg/ml (697.0 μM) ($P < 0.01$ and $P < 0.05$ vs. normal level) (**Figures 2D, E**). The results indicated that TF induced apoptosis of A375 cells in a concentration-dependent manner.

In Vivo Effect of TF on Xenograft Zebrafishes

The curves of mortality and adverse events of zebrafishes with TF treatment were shown in Fig. 3A. Fish death was caused by TF at 31.25 μg/ml (60.5 μM), and no fish was survived with TF at 125 μg/ml (242.0 μM), indicating the maximum non-lethal dose of TF less than 31.25 μg/ml (60.5 μM). The adverse events, including abnormal body roll over and edema, were observed with TF treatment from 3.47 μg/ml (6.7 μM) to its higher doses, indicating the NOAEL of TF less than 3.47 μg/ml (6.7 μM). After replicated tests, the NOAEL was finally estimated as 2.0 μg/ml (3.9 μM). Thereby, 0.22, 0.67, and 2.0 μg/ml (0.4, 1.3, and 3.9 μM) were used as the low, middle, and high doses of TF for the subsequent experiment.

As shown in **Figure 3B**, a xenograft model of A375 cells was established in larval zebrafishes and the fluorescent intensities of the cell mass in the fishes were tested. After 24 h treatment, TF from 0.22 to 2.0 μg/ml (0.4, 1.3, and 3.9 μM) obviously inhibited the A375 tumor growth, with inhibitory rates from 1.0 to 46.4%.

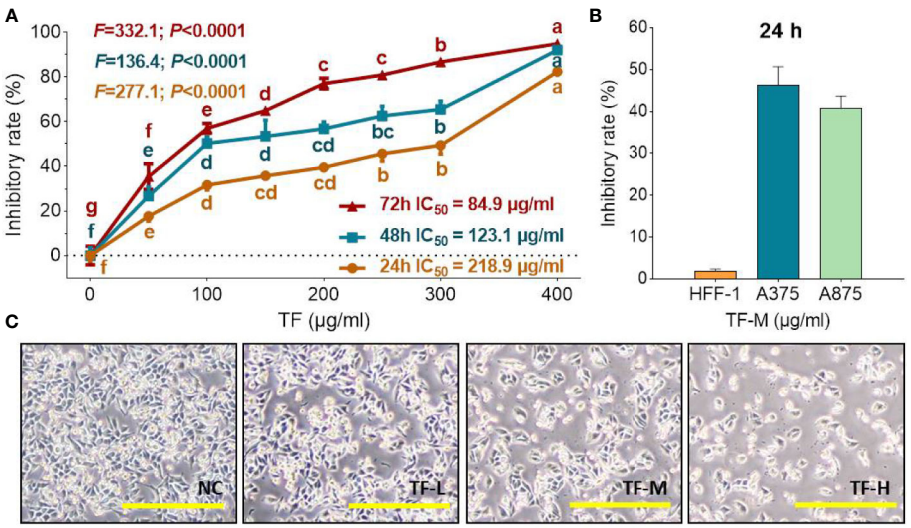

FIGURE 1 | Cell viability of A375 cells with TF treatment at 24, 48, and 72 h **(A)**, cell viability of HFF-1, A375, and A875 cells with TF treatment at 24 h **(B)**, and morphology of A375 cells with theaflavin (TF) treatment at 24 h **(C)**. Data were mean ± SD ($n = 5$). By means of Fisher's least significant difference (LSD) multiple comparisons, data (mean ± SD) with same lowercase letter (b vs. bc; bc vs. cd; c vs. c; cd vs. d; d vs. d) indicate no significant difference between each other, while data with different letters (a vs. b vs. c vs. b vs. e vs. f vs. g) indicate significant difference with each other. Scale bar = 200 μm.

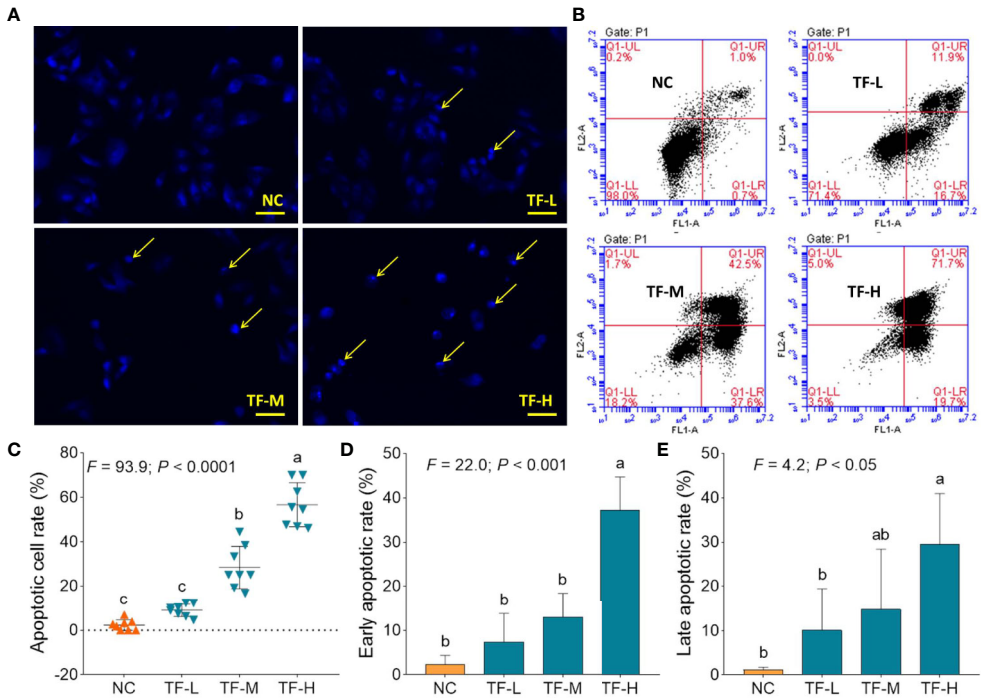

FIGURE 2 | DAPI staining observation **(A)** and flow cytometry analysis **(B)** on A375 cells with theaflavin (TF) treatment. Statistical analysis of apoptotic cell rate **(C)**, statistical analysis of early apoptotic rate **(D)** and statistical analysis of late apoptotic rate **(E)**. By means of Fisher's least significant difference (LSD) multiple comparisons, data (mean ± SD) with same lowercase letter (a vs. ab; ab vs. b; b vs. b; c vs. c) indicate no significant difference between each other, while data with different letters (a vs. b vs. c) indicate significant difference with each other. Scale bar = 100 μm.

The inhibitory effects of TF at 0.67 and 2.0 μg/ml (1.3 and 3.9 μM) were significant, if compared with the model group ($P < 0.01$), and the effect of TF at 2.0 μg/ml (3.9 μM) was even higher than that of cisplatin at its NOAEL (50 μM).

Molecular Action of TF on mRNA Expressions in A375 Cells

The relative mRNA expressions of TF-targeted genes were tested by qPCR assay. As shown in Fig. 4, the expressions of *BAX*, *BIM*, *C-MYC*, *P21*, *P53*, and *PUMA* were significantly up-regulated by TF (each $P < 0.01$ vs. NC level), except for that of *BAX* with TF treatment at its low concentration. Although the expression of *BCL-2* was up-regulated by TF, the ratios of *BAX/BCL-2* were significantly higher with TF treatment at its middle to high concentrations than that of NC level ($P < 0.01$), indicating the major role of *BAX* in the action of TF.

Molecular Action of TB on Protein Expressions in A375 Cells

WB was applied to determine the expression and phosphorylation of proteins targeted by TF. As shown in **Figure 5**, the expressions of ATM, *p*-ATM, CHK1, *p*-CHK1, *p*-CHK2, *p*-P53, *c*-PARP, ASK1, JNK, *p*-JNK, C-JUN (48 kd), *p*-C-JUN (Ser 63), *c*-CASP8, and *c*-CASP3 were significantly up-regulated by TF at 120 μg/ml (232.3 μM) (each $P < 0.01$ vs. NC level). Besides, the actions of TF on ATR, *p*-ATR, CHK2, P53, C-JUN (43 kd), and *p*-C-JUN (Ser 73) were insignificant (each $P > 0.05$ vs. NC level).

DISCUSSION

Although the anti-cancer activities of TF has been well documented (Sur and Panda, 2017; Takemoto and Takemoto, 2018; Sajadimajd et al., 2020), the knowledge of its effectiveness on melanoma is still little. To fill this gap, the present study conducted *in vitro* and *in vivo* experiments to study the effects and mechanism of TF against melanoma cells. For the first time, we demonstrated the cytotoxic pro-apoptotic and tumor-inhibitory effects of TF on melanoma A375 cells. Its mechanism was suggested to be associated with P53 and JNK pathways. The innovation of this study is the finding of TF′s anti-melanoma efficacy, while previous reports only focused on TF′s effects on other tumors (Lin, 2002; Sur and Panda, 2017). Furthermore, this is also the first report on the molecular action of TF on JNK pathway, while the P53 pathway-associated mechanism of TF′s pro-apoptotic effect on carcinoma cells has been previously reported (Lahiry et al., 2008).

Recently, xenograft tumor models using larval zebrafishes have attracted increasing attention for anti-cancer studies, owing to the advantages of larval zebrafishes compared to other animal models: (1) the lack of immune rejection against human cells

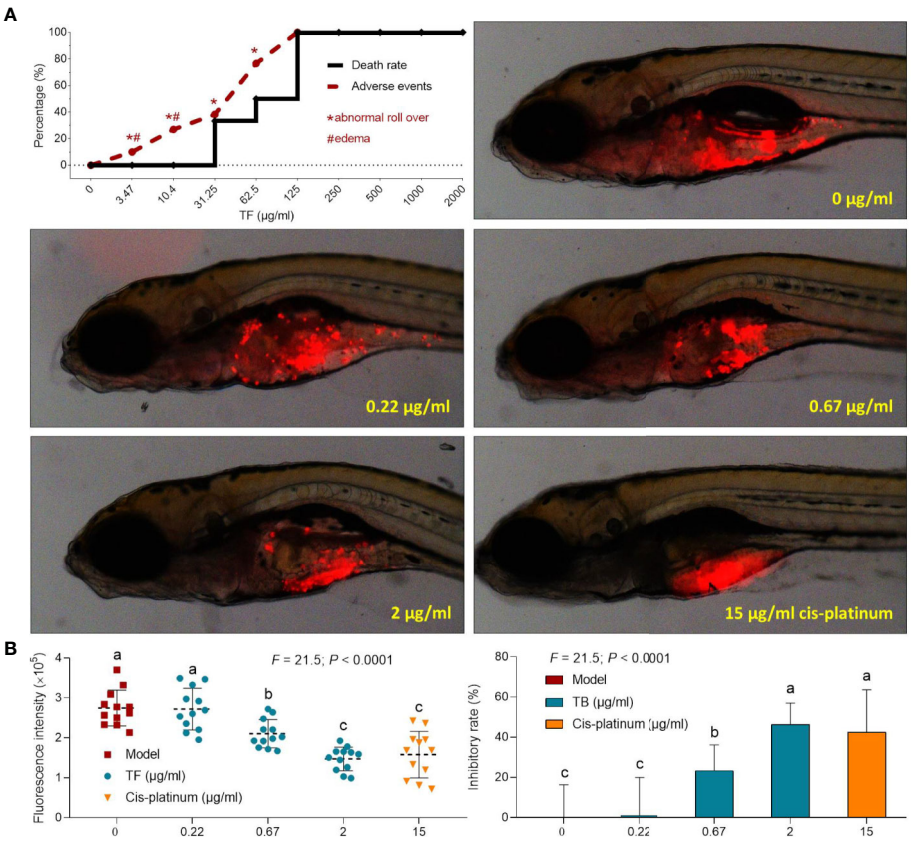

FIGURE 3 | Mortality and adverse events of larval zebrafishes induced by theaflavin (TF) and observation of larval zebrafishes xenotransplanted with A375 cells with treatment of TF or cisplatin **(A)** as well as the fluorescence intensity and inhibitory rates of TF **(B)**. Fluorescent area in red represents the A375 cell mass. By means of LSD multiple comparisons, data (mean ± SD) with same lowercase letter (a vs. a; c vs. c) indicate no significant difference between each other, while data with different letters (a vs. b vs. c) indicate significant difference with each other.

provides higher success rate for xenotransplantation; (2) body transparency provides *in vivo* visible observation of tumor growth and drug toxicity; and (3) large-scale generation and rapid organogenesis provides shorter experimental periods (Langheinrich, 2003; Pardo-Martin et al., 2010; Konantz et al., 2012). In this study, TF exerted dose-dependent inhibitory effect on A375 tumor mass in larval zebrafishes (**Figure 3B**), with inhibitory rate of 46.4% at its NOAEL (3.9 μM). The inhibitory rate was higher than that of cisplatin, indicating that TF was more effective than cisplatin within their respective safe dose range. Moreover, the inhibitory rate was higher than that of another tea pigment (theabrownin) (Jin et al., 2018), suggesting TF as the most effective component of tea. However, the effective *in vivo* dose range (1.3 to 3.9 μM) of TF is much lower than its effective *in vitro* dose range (96.8 to 774.4 μM). The reason for such difference may be that, after oral administration, the metabolized TF derivatives have higher effect than that of TF. It indicates that oral application may be more efficient than other routes for TF.

According to the dose conversion rule, the effective doses (1.3 and 3.9 μM) of TF in larval zebrafishes can be estimated as 0.03 to 0.09 mg/kg in human (Zhang et al., 2003). It suggests that oral administration of TF at such a low dose range may be effective in treating patients with melanoma, indicating a good cost-effectiveness of this compound. Up to our knowledge, there are only a few reports regarding the clinical application of TF. A double-blind, randomized, placebo-controlled, parallel-group trial has applied TF-enriched green tea extract to treat patients with mild to moderate hypercholesterolemia for 12 weeks (Maron et al., 2003). In that trial, the daily intake of TF was 75 mg in green tea extract, which significantly reduced total cholesterol, LDL-C, and triglyceride in hypercholesterolemic adults without observation of significant adverse events (Maron et al., 2003). In this study, the effective dose range of TF was much lower than the reported one, suggesting a greater potential of TF for melanoma treatment in clinic. However, although the effective dose range of TF was small, its lethal dose threshold to zebrafish larvae was also low (<60.5 μM) and was lower than other tea pigments (**Figure 3A**) (Jin et al., 2018), leaving a concern for the potential toxicity of TF to human beings. Interestingly, we found that TF exerted little effect on the normal cell line (HFF-1 skin fibroblast) (**Figure 1B**), suggesting a clinical feasibility for its external use which can avoid the potential toxicity of its internal use.

Our mechanistic experiment showed that TF activated ATM, CHK1/2, P53, CASP8/3 in P53 pathway and also activated ASK1, JNK, and C-JUN in JNK pathway, associating with A375 cell apoptosis. The apoptosis was determined by DAPI staining and flow cytometric analysis at cellular level (**Figure 2**) and mediated by the overexpression of pro-apoptotic genes (*P53*, *BAX*, *BIM*, and *PUMA*) and the activation of apoptosis-related proteins (caspases and PARP) at the molecular level (**Figures 4** and **5**). *P53* (*TP53*) encodes a DNA-binding nuclear phosphoprotein with tumor suppressor activity, which acts as transcription factor at the center of a network for the control of apoptosis in response to cellular stresses (Martin et al., 2002). It activates apoptosis by stimulating the transcription of Bcl-2 family genes, such as *BAX*, *BIM*, and *PUMA* (Levine and Oren, 2009). *BAX* and *BIM* encode pro-apoptotic members that provoke apoptosis and cell death by activating caspase cascade in response to apoptotic stimuli (Rossé et al., 1998; Youle and Strasser, 2008). *PUMA*, as a *P53* up-regulated modulator of apoptosis, encodes a BH3 domain-containing protein that localizes to the mitochondria, interacts with Bax and Bak, and activates the caspase cascade by cleavage of CASP3 (Nakano and Vousden, 2001; Letai, 2009). In this study, CASP8 and CASP3 were cleaved in response to P53 activation. CASP8 is an initiating caspase in the apoptotic cascade, which activates CASP3 for apoptotic DNA fragmentation, resulting in subsequent cleavage of PARP (*c*-PARP) to execute the apoptotic process (Jänicke et al., 1998; Stennicke et al., 1998; Boulares et al., 1999). PARP is responsible for DNA repair and cell viability in response to exogenous stress (Satoh and Lindahl, 1992). It can be cleaved by CASP3 and thereby facilitates the cellular disassembly in apoptosis (Oliver et al., 1998). Thus, the amount of cleaved PARP (*c*-PARP) can be used as marker of cell apoptosis.

In our previous studies, we have reported that DNA damage induction was associated with P53 pathway-mediated pro-apoptotic mechanism of theabrownin (Wu et al., 2016; Jin et al., 2018). However, although both TF and theabrownin activated P53 pathway and induced tumor cell apoptosis, we did not find DNA damage induction with TF treatment in this study. Alternatively, we found the activation of ASK1–JNK–C-JUN cascade, which also functions as apoptotic pathway. In this signaling module, ASK1 (apoptosis signal-regulating kinase 1) is a mitogen-activated protein kinase that plays a key role in cytokine- and stress-induced apoptosis by triggering mitochondria-dependent pathway (Matsuzawa and Ichijo, 2001; Zhang et al., 2003). It activates downstream JNK signaling in response to different types of stress, leading to cell apoptosis through C-JUN activation and subsequent overexpression of pro-apoptotic genes (Tobiume et al., 2001). Chemotherapeutics, such as cisplatin, docetaxel, and paclitaxel, have been reported to induce apoptosis of melanoma cells through the JNK pathway independent of the P53 pathway (Mandic et al., 2001; Mhaidat et al., 2008; Selimovic et al., 2008). This indicates that TF might have an advantage compared to these drugs due to its dual-pathway-mediated mechanism of action, which has been preliminarily demonstrated by the higher tumor-inhibitory effects of TF than that of cisplatin in this study. However, there are some limitations of this study as follows: (1) the actions of P53 and JNK pathways in the proposed dual-pathway-mediated mechanism of TF has not been verified; (2) the interaction between P53 and JNK pathways has not been investigated, and which pathway plays the main role is unknown; and (3) the *in vitro* dose range and the *in vivo* dose range are quite different, the reason of which has been explained but needs experimental evidence. To address these issues, further studies are needed in future. For instance, siRNAs or inhibitors of P53 and JNK should be used to verify the actions of these pathways and to explore the interaction between each other, and the serum metabolites of TF should be chemically analyzed and pharmacologically studied to test our hypothesis that the metabolized TF derivatives have

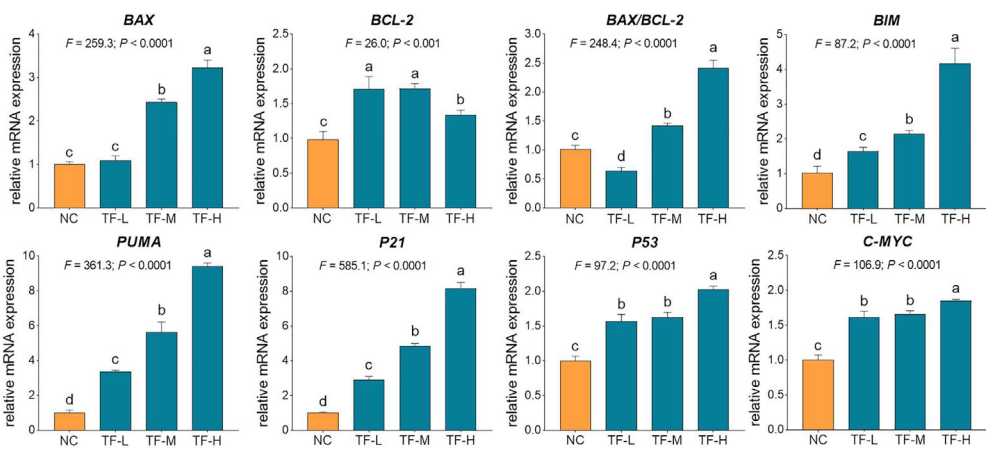

FIGURE 4 | Relative mRNA expression of theaflavin (TF)-targeted genes in A375 cells after 24 h treatment. By means of Fisher's least significant difference (LSD) multiple comparisons, data (mean ± SD) with same lowercase letter (a vs. a; b vs. b; c vs. c) indicate no significant difference between each other, while data with different letters (a vs. b vs. c vs. d) indicate significant difference with each other.

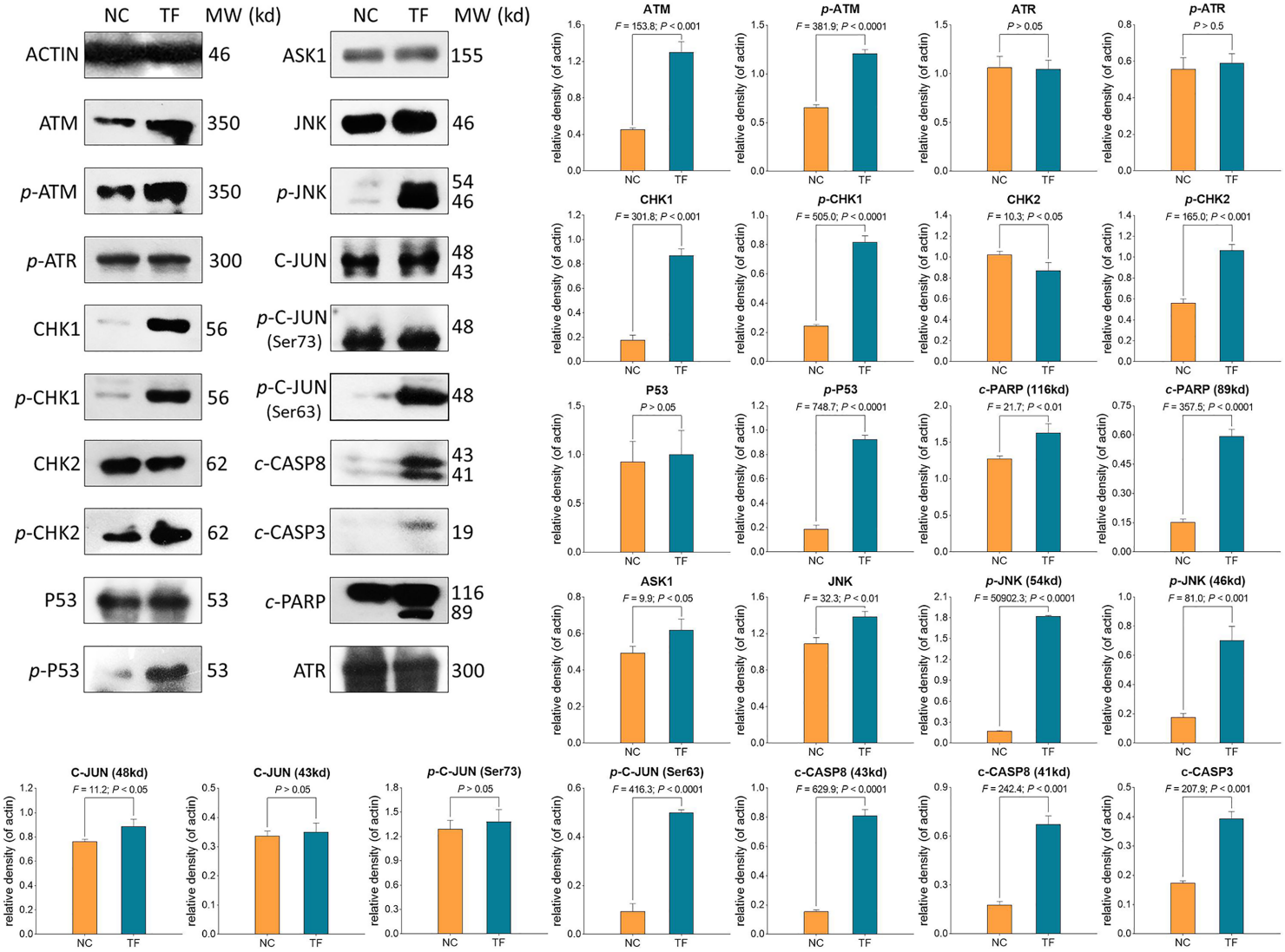

FIGURE 5 | Expression and phosphorylation of theaflavin (TF)-targeted proteins in A375 cells after 24 h treatment. Data (mean ± SD) with different lowercase letters are significantly different with each other at Fisher's least significant difference (LSD) multiple comparisons.

higher effect than that of TF. Moreover, since there are no clinical reports of TF for cancer treatment, the therapeutic efficacy and benefits of TF on cancer patients should be further studied.

CONCLUSION

Since the anti-cancer potential of TF has been well documented, it remains uncertain whether TF is effective in treating melanoma. In this study, by using melanoma cell line and xenograft zebrafish model, we found cytotoxic pro-apoptotic and tumor-inhibitory effects of TF on melanoma cells and revealed its mechanism in association with the activations of P53 and JNK pathways. This is the first study describing the effects and mechanism of TF against melanoma cells. Since the mechanism of TF was not only dependent on the P53 pathway, it can be expected that TF may be effective in treating P53-mutated cell lines. Further studies are warranted to verify this deduction. Altogether, this study provides evidence for the efficacy of TF against melanoma, which contributes to the development of TF-derived agents for melanoma therapy.

DATA AVAILABILITY STATEMENT

The raw data supporting the conclusions of this article are available from the corresponding author on reasonable request.

ETHICS STATEMENT

The animal study was reviewed and approved by the Ethics Committee of Zhejiang Chinese Medical University.

AUTHOR CONTRIBUTIONS

LeZ performed the main work of this paper. BY conducted the cellular and molecular experiments. LiZ and SM contributed to the writing of this manuscript. WD provided ideas and funding support to this work. YX conducted the zebrafish experiment. LS designed this work and drafted the manuscript. TE improved the design and draft of this paper. All authors contributed to the article and approved the submitted version.

FUNDING

This work was supported by the National Natural Science Foundation of China (Grant No. 81774331, 81873049, and 81973873), the Zhejiang Provincial Natural Science Foundation of China (Grant No. LY18H270004), the Zhejiang Provincial Science and Technology Project of Traditional Chinese Medicine of China (Grant No. 2016ZZ011), the Zhejiang Provincial Key Construction University Superiority Characteristic Discipline (Traditional Chinese Pharmacology), and the Opening Foundation of China (Grant No. ZYX2018006).

REFERENCES

Adhikary, A., Mohanty, S., Lahiry, L., Hossain, D. M., Chakraborty, S., and Das, T. (2009). Theaflavins retard human breast cancer cell migration by inhibiting NF-kappaB via p53-ROS cross-talk. *FEBS Lett.* 584 (1), 7–14. doi: 10.1016/j.febslet.2009.10.081

Boulares, A. H., Yakovlev, A. G., Ivanova, V., Stoica, B. A., Wang, G., Iyer, S., et al. (1999). Role of poly(ADP-ribose) polymerase (PARP) cleavage in apoptosis. Caspase 3-resistant PARP mutant increases rates of apoptosis in transfected cells. *J. Biol. Chem.* 274 (33), 22932–22940. doi: 10.1074/jbc.274.33.22932

Jänicke, R. U., Sprengart, M. L., Wati, M. R., and Porter, A. G. (1998). Caspase-3 is required for DNA fragmentation and morphological changes associated with apoptosis. *J. Biol. Chem.* 273 (16), 9357–9360. doi: 10.1074/jbc.273.16.9357

Jin, W., Zhou, L., Yan, B., Yan, L., Liu, F., Tong, P., et al. (2018). Theabrownin triggers DNA damage to suppress human osteosarcoma U2OS cells by activating p53 signalling pathway. *J. Cell. Mol. Med.* 22 (9), 4423–4436. doi: 10.1111/jcmm.13742

Konantz, M., Balci, T. B., Hartwig, U. F., Dellaire, G., André, M. C., Berman, J. N., et al. (2012). Zebrafish xenografts as a tool for in vivo studies on human cancer. *Ann. New Y. Acad. Sci.* 1266, 124–137. doi: 10.1111/j.1749-6632.2012.06575.x

Kuo, K. L., Weng, M. S., Chiang, C. T., Tsai, Y. J., Lin-Shiau, S. Y., and Lin, J. K. (2005). Comparative studies on the hypolipidemic and growth suppressive effects of oolong, black, pu-erh, and green tea leaves in rats. *J. Agric. Food Chem.* 53 (2), 480–489. doi: 10.1021/jf049375k

Lahiry, L., Saha, B., Chakraborty, J., Bhattacharyya, S., Chattopadhyay, S., Banerjee, S., et al. (2008). Contribution of p53-mediated Bax transactivation in theaflavin-induced mammary epithelial carcinoma cell apoptosis. *Apoptosis* 13 (6), 771–781. doi: 10.1007/s10495-008-0213-x

Lahiry, L., Saha, B., Chakraborty, J., Adhikary, A., Mohanty, S., Hossain, D. M. S., et al. (2010). Theaflavins target Fas/caspase-8 and Akt/pBad pathways to induce apoptosis in p53-mutated human breast cancer cells. *Carcinogenesis* 31 (2), 259–268. doi: 10.1093/carcin/bgp240

Langheinrich, U. (2003). Zebrafish: a new model on the pharmaceutical catwalk. *BioEssays News Rev. Mol. Cell. Dev. Biol.* 25 (9), 904–912. doi: 10.1002/bies.10326

Leonardi, G. C., Falzone, L., Salemi, R., Zanghi, A., Spandidos, D. A., McCubrey, J. A., et al. (2018). Cutaneous melanoma: From pathogenesis to therapy (Review). *Int. J. Oncol.* 52 (4), 1071–1080. doi: 10.3892/ijo.2018.4287

Letai, A. (2009). Puma strikes Bax. *J. Cell Biol.* 185 (2), 189–191. doi: 10.1083/jcb.200903134

Levine, A. J., and Oren, M. (2009). The first 30 years of p53: growing ever more complex. *Nat. Rev. Cancer* 9 (10), 749–758. doi: 10.1038/nrc2723

Li, B., Vik, S. B., and Tu, Y. (2012). Theaflavins inhibit the ATP synthase and the respiratory chain without increasing superoxide production. *J. Nutr. Biochem.* 23 (8), 953–960. doi: 10.1016/j.jnutbio.2011.05.001

Lin, J.-K. (2002). Cancer chemoprevention by tea polyphenols through modulating signal transduction pathways. *Arch. Pharmacal. Res.* 25 (5), 561–571. doi: 10.1007/BF02976924

Liu, N., Wang, K. S., Qi, M., Zhou, Y. J., Zeng, G. Y., Tao, J., et al. (2018). Vitexin compound 1, a novel extraction from a Chinese herb, suppresses melanoma cell growth through DNA damage by increasing ROS levels. *J. Exp. Clin. Cancer Res. CR* 37 (1), 269. doi: 10.1186/s13046-018-0897-x

Mandic, A., Viktorsson, K., Molin, M., Akusjärvi, G., Eguchi, H., Hayashi, S. I., et al. (2001). Cisplatin induces the proapoptotic conformation of Bak in a deltaMEKK1-dependent manner. *Mol. Cell. Biol.* 21 (11), 3684–3691. doi: 10.1128/MCB.21.11.3684-3691.2001

Mao, X., Xiao, X., Chen, D., Yu, B., and He, J. (2019). Tea and its components prevent cancer: A review of the redox-related mechanism. *Int. J. Mol. Sci.* 20 (21), 5249. doi: 10.3390/ijms20215249

Maron, D. J., Lu, G. P., Cai, N. S., Wu, Z. G., Li, Y. H., Chen, H., et al. (2003). Cholesterol-lowering effect of a theaflavin-enriched green tea extract: a randomized controlled trial. *Arch. Intern Med.* 163 (12), 1448–1453. doi: 10.1001/archinte.163.12.1448

Martin, A. C., Facchiano, A. M., Cuff, A. L., Hernandez-Boussard, T., Olivier, M., Hainaut, P., et al. (2002). Integrating mutation data and structural analysis of the TP53 tumor-suppressor protein. *Hum. Mutat.* 19 (2), 149–164. doi: 10.1002/humu.10032

Matsuzawa, A., and Ichijo, H. (2001). Molecular mechanisms of the decision between life and death: regulation of apoptosis by apoptosis signal-regulating kinase 1. *J. Biochem.* 130 (1), 1–8. doi: 10.1093/oxfordjournals.jbchem.a002947

Mhaidat, N. M., Thorne, R., Zhang, X. D., and Hersey, P. (2008). Involvement of endoplasmic reticulum stress in Docetaxel-induced JNK-dependent apoptosis of human melanoma. *Apoptosis Int. J. Program. Cell Death* 13 (12), 1505–1512. doi: 10.1007/s10495-008-0276-8

Mirzaei, H., Naseri, G., Rezaee, R., Mohammadi, M., Banikazemi, Z., Mirzaei, H. R., et al. (2016). Curcumin: A new candidate for melanoma therapy? *Int. J. Cancer* 139 (8), 1683–1695. doi: 10.1002/ijc.30224

Nakano, K., and Vousden, K. H. (2001). PUMA, a novel proapoptotic gene, is induced by p53. *Mol. Cell* 7 (3), 683–694. doi: 10.1016/S1097-2765(01)00214-3

Oliveira Pinho, J., Matias, M., and Gaspar, M. M. (2019). Emergent nanotechnological strategies for systemic chemotherapy against melanoma. *Nanomater. (Basel)* 9 (10), 1455. doi: 10.3390/nano9101455

Oliver, F. J., de la Rubia, G., Rolli, V., Ruiz-Ruiz, M. C., de Murcia, G., and Murcia, J. M. (1998). Importance of poly(ADP-ribose) polymerase and its cleavage in apoptosis. Lesson from an uncleavable mutant. *J. Biol. Chem.* 273 (50), 33533–33539. doi: 10.1074/jbc.273.50.33533

Pardo-Martin, C., Chang, T.-Y., Koo, B. K., Gilleland, C. L., Wasserman, S. C., and Yanik, M. F. (2010). High-throughput in vivo vertebrate screening. *Nat. Methods* 7 (8), 634–636. doi: 10.1038/nmeth.1481

Roberts, E. A. H., Cartwright, R. A., and Oldschool, M. (1957). The phenolic substances of manufactured tea. I. Fractionation and paper chromatography of water-soluble substances. *J. Sci. Food Agric.* 8, 72–80. doi: 10.1002/jsfa.2740080203

Rodríguez-Cerdeira, C., Carnero Gregorio, M., López-Barcenas, A., Sánchez-Blanco, E., Sánchez-Blanco, B., Fabbrocini, G., et al. (2017). Advances in immunotherapy for melanoma: A comprehensive review. *Mediators Inflammation* 2017, 3264217. doi: 10.1155/2017/3264217

Rossé, T., Olivier, R., Monney, L., Rager, M., Conus, S., Fellay, I., et al. (1998). Bcl-2 prolongs cell survival after Bax-induced release of cytochrome c. *Nature* 391 (6666), 496–499. doi: 10.1038/35160

Sajadimajd, S., Bahramsoltani, R., Iranpanah, A., Kumar Patra, J., Das, G., Gouda, S., et al. (2020). Advances on natural polyphenols as anticancer agents for skin cancer. *Pharmacol. Res.* 151, 104584. doi: 10.1016/j.phrs.2019.104584

Satoh, M. S., and Lindahl, T. (1992). Role of poly(ADP-ribose) formation in DNA repair. *Nature* 356 (6367), 356–358. doi: 10.1038/356356a0

Selimovic, D., Hassan, M., Haikel, Y., and Hengge, U. R. (2008). Taxol-induced mitochondrial stress in melanoma cells is mediated by activation of c-Jun N-terminal kinase (JNK) and p38 pathways via uncoupling protein 2. *Cell. Signal.* 20 (2), 311–322. doi: 10.1016/j.cellsig.2007.10.015

Shao, J., Meng, Q., and Li, Y. (2016). Theaflavins suppress tumor growth and metastasis via the blockage of the STAT3 pathway in hepatocellular carcinoma. *Oncotarg. Ther.* 9, 4265–4275. doi: 10.2147/OTT.S102858

Stennicke, H. R., Jürgensmeier, J. M., Shin, H., Deveraux, Q., Wolf, B. B., Yang, X., et al. (1998). Pro-caspase-3 is a major physiologic target of caspase-8. *J. Biol. Chem.* 273 (42), 27084–27090. doi: 10.1074/jbc.273.42.27084

Sur, S., and Panda, C. K. (2017). Molecular aspects of cancer chemopreventive and therapeutic efficacies of tea and tea polyphenols. *Nutrition* 43-44, 8–15. doi: 10.1016/j.nut.2017.06.006

Takemoto, M., and Takemoto, H. (2018). Synthesis of theaflavins and their functions. *Mol. (Basel Switzerland)* 23 (4), 918. doi: 10.3390/molecules23040918

Tang, Q.-Y., and Zhang, C.-X. (2013). Data Processing System (DPS) software with experimental design, statistical analysis and data mining developed for use in entomological research. *Insect Sci.* 20 (2), 254–260. doi: 10.1111/j.1744-7917.2012.01519.x

Tobiume, K., Matsuzawa, A., Takahashi, T., Nishitoh, H., Morita, K., Takeda, K., et al. (2001). ASK1 is required for sustained activations of JNK/p38 MAP kinases and apoptosis. *EMBO Rep.* 2 (3), 222–228. doi: 10.1093/embo-reports/kve046

Wang, J. Y., and Cheng, H. B. (2019). Analyses on the pathogenesis theory of cancer toxin and 'consolidating body resistance and clearing the source' theory. *China J. Trad. Chin. Med. Pharm.* 34 (10), 4687–4690.

Wu, F., Zhou, L., Jin, W., Yang, W., Wang, Y., Yan, B., et al. (2016). Anti-proliferative and apoptosis-inducing effect of theabrownin against non-small cell lung adenocarcinoma A549 cells. *Front. Pharmacol.* 7, 465. doi: 10.3389/fphar.2016.00465

Yang, K., Fung, T. T., and Nan, H. (2018). An epidemiological review of diet and cutaneous malignant melanoma. *Cancer Epidemiol. Biomarkers Prev.* 27 (10), 1115–1122. doi: 10.1158/1055-9965.EPI-18-0243

Youle, R. J., and Strasser, A. (2008). The BCL-2 protein family: opposing activities that mediate cell death. *Nat. Rev. Mol. Cell Biol.* 9 (1), 47–59. doi: 10.1038/nrm2308

Zhang, C., Willett, C., and Fremgen, T. (2003). Zebrafish: an animal model for toxicological studies. *Curr. Protoc. Toxicol.* Chapter 1:Unit1.7. doi: 10.1002/0471140856.tx0107s17

Zhou, L., Wu, F., Jin, W., Yan, B., Chen, X., He, Y., et al. (2017). Theabrownin inhibits cell cycle progression and tumor growth of lung carcinoma through c-myc-related mechanism. *Front. Pharmacol.* 8, 75. doi: 10.3389/fphar.2017.00075

Conflict of Interest: YX was employed by the company Hunter Biotechnology, Inc.

The remaining authors declare that the research was conducted in the absence of any commercial or financial relationships that could be construed as a potential conflict of interest.

frontiers in Pharmacology

ORIGINAL RESEARCH
published: 09 September 2020
doi: 10.3389/fphar.2020.01342

Anti-Hepatoma Compound Determination by the Method of Spectrum Effect Relationship, Component Knock-Out, and UPLC-MS^2 in *Scheflera heptaphylla* (L.)Frodin Harms and Its Mechanism

Xuqiang Liu[1,2], *Nan Jiang*[2], *Xiaoqing Xu*[1], *Cunyu Liu*[1], *Zhenhua Liu*[1,3*], *Yan Zhang*[4,5*] *and Wenyi Kang*[1,3*]

[1] National R & D Center for Edible Fungus Processing Technology, Henan University, Kaifeng, China, [2] School of Biomedical Sciences, Huaqiao University, Xiamen, China, [3] Joint International Research Laboratory of Food & Medicine Resource Function, Henan Province, Henan University, Kaifeng, China, [4] Hebei Food Inspection and Research Institute, Shijiazhuang, China, [5] College of Forensic Medicine, Hebei Medical University, Shijiazhuang, China

OPEN ACCESS

Edited by:
Yi Wang,
Zhejiang University, China

Reviewed by:
Liang Feng,
China Pharmaceutical University, China
Fatma Mohamady El-Demerdash, Alexandria University, Egypt

***Correspondence:**
Zhenhua Liu
liuzhenhua623@163.com
Yan Zhang
snowwinglv@126.com
Wenyi Kang
kangweny@hotmail.com

Specialty section:
This article was submitted to Ethnopharmacology, a section of the journal Frontiers in Pharmacology

Received: *30 June 2020*
Accepted: *11 August 2020*
Published: *09 September 2020*

Citation:
Liu X, Jiang N, Xu X, Liu C, Liu Z, Zhang Y and Kang W (2020) Anti-Hepatoma Compound Determination by the Method of Spectrum Effect Relationship, Component Knock-Out, and UPLC-MS^2 in Schefflera heptaphylla (L.)Frodin Harms and Its Mechanism. Front. Pharmacol. 11:1342. doi: 10.3389/fphar.2020.01342

Scheflera heptaphylla (L.)Frodin, a kind of Traditional Chinese Medicine, is commonly used in anti-inflammatory, analgesic, anti-viral, anti-tumor, and hemostasis. This study aimed to determine the anti-hepatoma components and its mechanism from the leaves of *S. heptaphylla*. The spectrum-effect relationships were analyzed by the method of Partial least squares, indicating that P1, P2, and P10 were positively correlated to inhibitory activity of Huh7 cells. Whereas others were negatively correlated. The technologies of component knock-out and UPLC-MS^2 were used to determine compounds as 3,4-Dicaffeoylquinic acid (P6), 3,5-Dicaffeoylquinic acid (P7), 3α-Hydroxy-lup-20(29)-ene-23,28-dioic acid (P10, named Compound A). The results forecasted that Compound A had the best correlation with inhibitory activity. The effects of Compound A on the activities of human hepatoma cells (Huh7, SMMC-7721, HepG 2) and normal hepatocytes (L0-2, Chang liver) were evaluated. Cell apoptosis was observed with inverted microscope and flow cytometer. In addition, the proteins, related to apoptosis, were detected by Western blot. The results showed that Compound A (400 nM) could significantly inhibit the activity of three hepatoma cells ($P < 0.001$) with slight toxicity to normal hepatocytes, and the IC_{50} values were 285.3 and 315.1 nM, respectively, which were consistent with the prediction of spectrum-effect relationships. After treatment with Compound A, the number of hepatoma cells decreased significantly. And the apoptosis rate of Huh7 cells increased significantly ($P < 0.001$) in Compound A (200, 400 nM) groups, SMMC-7721 and HepG 2 were directly necrotic. Compound A groups could significantly improve the level of intracellular reactive oxygen species (ROS) ($P < 0.05$, $P < 0.001$) in Huh7 with no effect on normal hepatocytes. The content of apoptotic protein (Bax and Bim) in mitochondria was significantly increased in Compound A groups ($P < 0.001$). On the contrary, the content of anti-apoptotic protein (Bcl-xL and Mcl-1) decreased significantly ($P < 0.001$).

These results demonstrated that Compound A was the main anti-hepatoma active component in the *S. heptaphylla* leaves. It achieved the effect of promoting apoptosis of Huh7 cells by regulating the levels of ROS and Bcl-2 family protein in mitochondrial apoptosis pathway.

Keywords: *S. octophylla*, spectrum-effect relationship, active ingredient, Huh7, mechanism

INTRODUCTION

Hepatocellular carcinoma (HCC) is one of the most common malignant tumors in the world, with high morbidity and mortality (Ally et al., 2017; Fukuda et al., 2017; Yang et al., 2017; Yang et al., 2019; Wu et al., 2020). Primary liver cancer is the second leading cause of death in the world, of which 70% to 85% are HCC. The incidence of liver cancer in China ranks first worldwide (LV et al., 2015; Yang and Hou, 2016; Zhu and Liu, 2018).

According to statistics, the incidence of liver cancer is still growing rapidly, and China is a "Large country of liver cancer." At present, the clinical treatment of liver cancer includes surgical treatment and non-operative treatment, and mainly choose the non-operative chemotherapy to improve the quality of life and prolong the life of patients (Julie et al., 2018). However, chemotherapeutic drugs could produce many side effects, such as myelosuppression, decreased immune function, organ damage, hair loss and so on, which significantly reduce the quality of life in patients. Ethnic drugs with wide efficacy and rich resources are widely used in the treatment of tumor, Such as *Eucommia* ulmoides Oliver, *Poria cocos* (Schw.) Wolf, and *Schisandra* chinensis (Turcz.) Baill (Li, 2011; Gui, 2012; Qian et al., 2019), which has the advantages of multi-target, multi-effect, little side effect, safety and effectiveness (Zhang et al., 2019). It could not only inhibit and kill tumor cells, but also has less toxicity to normal tissues and cells of the body. At the same time, it also can regulate the immune function of the body and improve clinical symptoms and signs (Wang and Hou, 2013). However, Traditional Chinses Medicine (TCM) is a whole concept in the process of treating diseases, it is difficult to determine the exact therapeutic components of TCM, which greatly restricts the application of TCM in clinical treatment of diseases.

Scheflera heptaphylla (L.)Frodin is commonly used as a hepatoprotective drug in Southeast Asia and has a significant anti-liver cancer effect. However, the anti-hepatoma effect of *S. heptaphylla* is not scientifically evaluated, and its active substances and mechanism are not clear. So, the anti-liver cancer active components of *S. heptaphylla* were investigated by the rapid method of "spectrum-effect relationship" (Wang et al., 2013), "knock-out technique," and high-resolution mass spectrometry.

In this manuscript, the fingerprint of *S. heptaphylla* leaves was established by high performance liquid chromatography (HPLC) method, and the anti-hepatoma activity of 10 batches of extracts was evaluated *in vitro*. 10 quantitative chromatographic peaks were selected to analyze the correlation between the spectral efficacy and the efficacy data, and the spectral efficiency analysis model was established (Zeng et al., 2015). The peaks of anti-liver cancer active compounds were screened by spectrum-effect correlation, the target components were knocked out by knock-out technology (Gong et al., 2015), and the structures of the target components were identified by high resolution mass spectrometry. The effect and mechanism on anti-hepatoma of the target component was evaluated.

RESULTS

Quantitative Determination of Chromatographic Peaks

Spectrum-effect relationship method was used to circumvent the weaknesses of the fingerprint technique and foster the strengths in TCM (Xu et al., 2014). The study of spectrum-effect relationship can reveal the material basis of the therapeutic values of TCM. This method has been widely applied in the researches of pharmacodynamic components, origins, harvest times, processing methods and batches of TCM (Hu et al., 2013; Zheng et al., 2014; Fang et al., 2016). Therefore, in order to accurately determine the material basis of their effects on anti-hepatoma activity, 10 batches of *S. heptaphylla* samples were selected to establish the fingerprint.

The chromatogram of *S. heptaphylla* ethanol extract was used as the reference spectrum, and the time window was set at 0.5. The chromatographic peaks with relatively high content and good separation in 10 batches of samples were selected for multi-point correction, and the average method was used to generate the control map by the software "Evaluation system of similarity of chromatographic fingerprint of traditional Chinese Medicine version 2004 1.0 A". 10 common peaks out of the 10 feature maps were selected, as shown in **Figure 1**. The chromatographic peak matching data of *S. heptaphylla* leaves were shown in **Table 1** and the similarity data were shown in **Table 2**.

Effect of Ethanol Extract From *S. heptaphylla* on the Viability of Huh7 Hepatoma Cells

In **Figure 2A**, the effects of 10 batches of *S. heptaphylla* ethanol extract on the viability of Huh7 showed when the concentrations of the extracts were 200, 400, 800 μg ·mL^{-1}, the 10 batches of samples significantly inhibited the cells viability of Huh7 ($P <$

Abbreviations: ROS, reactive oxygen species; HPLC, high-performance liquid chromatography; CCK-8, cell counting kit-8; IC_{50}, half-inhibitory concentration; DMSO, dimethyl sulfoxide; 5-FU, 5-fluorouracil; IRPA, radio immunoprecipitation assay; PVDF, polyvinylidene fluoride membranes; MTT, 3-(4,5)-dimethylthiahiazo (-z-y1)-3,5-di- phenytetrazolium bromide; DMEM, Dulbecco's modified eagle medium; TCM, Traditional Chinese Medicine; ECL, enhanced chemiluminescence; Compound A, 3α-hydroxy-lup-20(29)-ene-23,28-dioic acid; HCC, hepatocellular carcinoma; FBS, fetal bovine serum.

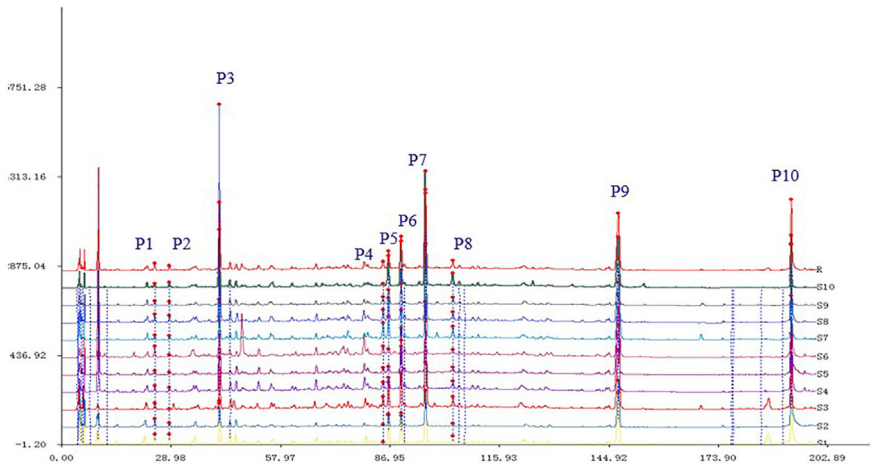

FIGURE 1 | The matching chromatograms characterized by HPLC.

TABLE 1 | The relative retention times and characteristic peak areas measured by HPLC (n = 10).

No.	Rt (min)	S1	S2	S3	S4	S5	S6	S7	S8	S9	S10
P1	24.651	4150363	3544788	2966786	2559433	1691232	4429168	2094106	3250961	1684673	1686005
P2	28.563	4685151	2096663	767523.3	2084688	1047507	1142884	1723123	2888822	1412197	2226924
P3	41.755	18577750	10369660	23167590	49942160	24822840	16189230	17097740	73437960	13291750	24401140
P4	85.11	592701.2	1457146	7990373	4320132	3009498	4750857	8561796	4586575	3546717	1556045
P5	86.568	13953340	5962813	14479290	5941413	3732601	4019646	10818650	10113450	6630262	13898410
P6	89.858	13179900	6474944	18474240	19940080	20712890	6278698	13510380	22922260	9318214	20823120
P7	96.315	38493880	20329800	64912050	39361480	23221780	16586590	48771280	57299430	29297410	55631030
P8	103.588	4301443	2003645	10780220	4782403	3473666	3193451	6878667	5054586	3843094	7659356
P9	147.446	32274540	30767130	53029030	52233150	54448330	53133420	51860980	48339290	31147070	37918510
P10	193.201	37645150	39480010	31020010	37507360	36340180	38904470	22636290	37593440	20405930	17547740

TABLE 2 | The similarity degree of characteristic peak areas (n = 10).

No.	S1	S2	S3	S4	S5	S6	S7	S8	S9	S10	Reference fingerprint
S1	1	0.93	0.895	0.876	0.82	0.61	0.9	0.859	0.935	0.893	0.94
S2	0.93	1	0.805	0.855	0.857	0.681	0.847	0.782	0.902	0.778	0.907
S3	0.895	0.805	1	0.862	0.783	0.554	0.931	0.844	0.931	0.929	0.926
S4	0.876	0.855	0.862	1	0.913	0.704	0.886	0.947	0.911	0.877	0.966
S5	0.82	0.857	0.783	0.913	1	0.879	0.837	0.805	0.864	0.772	0.933
S6	0.61	0.681	0.554	0.704	0.879	1	0.604	0.544	0.631	0.52	0.743
S7	0.9	0.847	0.931	0.886	0.837	0.604	1	0.863	0.974	0.956	0.952
S8	0.859	0.782	0.844	0.947	0.805	0.544	0.863	1	0.892	0.899	0.922
S9	0.935	0.902	0.931	0.911	0.864	0.631	0.974	0.892	1	0.949	0.972
S10	0.893	0.778	0.929	0.877	0.772	0.52	0.956	0.899	0.949	1	0.929
Reference fingerprint	0.94	0.907	0.926	0.966	0.933	0.743	0.952	0.922	0.972	0.929	1

0.001, 0.001 < P < 0.01, P < 0.05) in a dose-dependent manner compared with the blank group *in vitro*.

In **Figure 2B**, when the sample concentrations were at 1 g·mL^{-1} (equivalent to the original medicinal material), the IC_{50} values of 10 batches of *S. heptaphylla* on Huh7 cells showed a "W" shape, indicating that at this concentration, the anti-hepatoma effects of *S. heptaphylla* ethanol extract at different collection times were significantly different. The IC_{50} values were the lowest at S3 and S7, indicating that *S. heptaphylla* ethanol extracts had the best anti-liver cancer (Huh7) activity with no significant difference (P > 0.05).

Partial Least Square Regression Analysis

In recent years, spectrum-effect correlation analysis has been successfully applied to the analysis of active components of

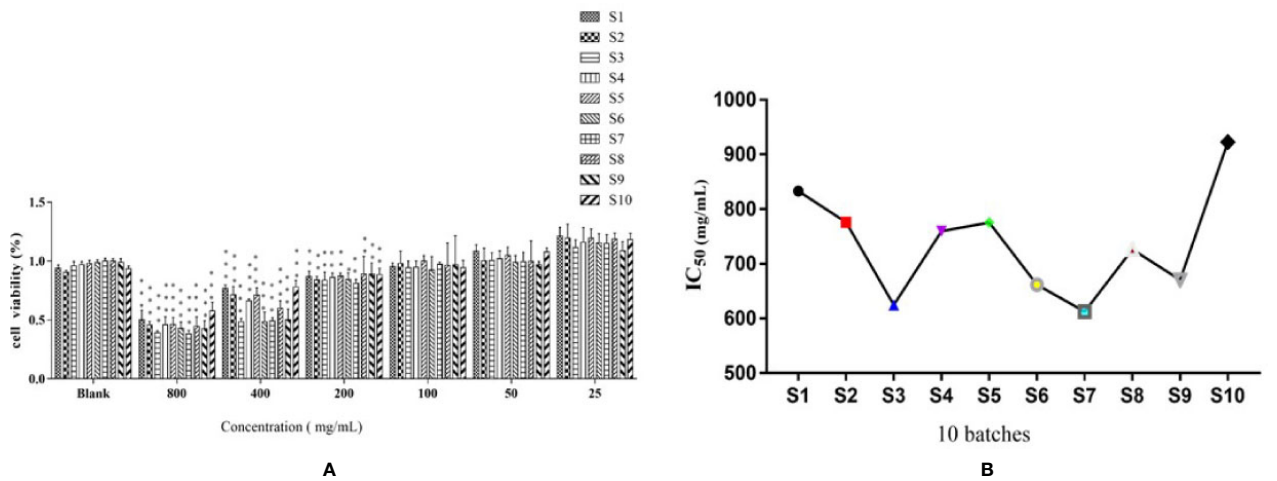

FIGURE 2 | Effects of of *S. heptaphylla* ethanol extracts on the viability of Huh7 cells **(A)** and its IC_{50} values **(B)** *in vitro*. ***$P < 0.001$, $0.001 < **P < 0.01$ vs. Blank group.

various traditional Chinese medicine. The main components of spectrum-effect relationship of traditional Chinese medicine include the establishment of fingerprint, pharmacodynamic evaluation and data processing of spectrum-effect correlation (Xu et al., 2014). The most common methods for establishing fingerprints are HPLC, UPLC, GC, and GC-MS (Zhou et al., 2008). Pharmacodynamics often uses experimental models *in vitro* or *in vivo* to obtain "efficacy" information (Zhang et al., 2012). The most common data processing methods are principal component analysis (PCA), canonical correlation analysis (CCA), partial least square analysis (PLSR) and grey correlation analysis (GRDA) (Zhao et al., 2004). Among them, the PLSR method is practical and stable, it can contain all the original fingerprint peaks, and the reaction information is more comprehensive (Alciaturi et al., 2014).

The IC_{50} values of anti-hepatoma activity of samples (equivalent to 1 g ·mL^{-1}) were taken as dependent variables and 10 quantitative characteristic chromatographic peak areas as independent variables. The data were averaged by DPS 7.05 statistical software, and then partial least square regression analysis was carried out. After data standardization, the square sum of model error R^2 increased with the increase of potential factor. When the potential factor reached 6, R^2 reaches the maximum, and the variance of the explained independent variable is 89.62%.

The regression equation was obtained as follows:

$$Y = 0.000000 - 0.44285x1 + 0.183478x2 - 0.112569x3 + 0.548834x4 - 0.183714x5 + 0.077159x6 - 0.245942x7 + 0.446524x8 - 0.682518x9 + 0.884567x10$$

The regression coefficient diagram of the partial least square regression equation was shown in **Figure 3**. P3 and P5, P6, P7, P8, and P9 were positively correlated with the IC_{50} of anti-liver cancer activity of *S. heptaphylla* ethanol extract. However, P1, P2, P4 and P10 were negatively correlated with the anti-hepatoma activity of *S. heptaphylla* ethanol extract. P10 had the strongest anti-liver cancer activity.

Composition Knock-Out Experiment

The Total Chromatogram of the Sample and the Chromatogram of the Knocked-Out Components

In **Figure 4A**, the full chromatogram of *S. heptaphylla* ethanol extract at 210 nm wavelength. **Figures 4B–F** are the chromatogram of the target components: P5, P6, P7, P9, and P10, respectively. According to the peak area normalization method, the purity of each target component was more than 85%, and the resolution was good (R > 1.5).

P6 (Rt = 89.858 min), the UPLC-MS^2 results of the knock-out component was shown in **Figure 5A**, in which the molecular formula was $C_{25}H_{24}O_{12}$. The results of secondary mass spectrometry showed that there were some ion fragments: 515.12/353.09/191.06/173.04/173.04/135.04. According to the reference (Yi, 2017), it was speculated to be 3,5-dicaffeoylquinic acid (**Figure 5B**). Moreover, the retention time of P6 was consistent with that of the reference substance.

P7 (Rt = 96.315 min), the UPLC-MS^2 results of the knock-out component was shown in **Figure 5C**, in which the molecular formula was $C_{25}H_{24}O_{12}$. The results of secondary mass spectrometry showed that there were some ion fragments: 515/353/191/179/173/135, 515/335.08/255.07/179.03/155.03/135.04, 515/335.1/317.07/299.06/173.04. According to the reference (Yi, 2017), it was speculated to be 3,4-dicaffeoylquinic acid (**Figure 5D**). In addition, the retention time was consistent with that of the reference substance.

P9 (Rt = 147.446 min), the UPLC-MS^2 results of the knock-out component was shown in **Figure 5E**, in which the molecular formula was $C_{48}H_{76}O_{19}$. According to the reference (Adam et al., 1982), it was speculated to be 3α-hydroxy-lup-20(29)- ene-23,28-dioic acid 28-*O*-[α-L-rhamnopyranosyl (1→4)-*O*-β-D-glucopyranosyl (1→ 6)]-β-D-glucopyrano-side (**Figure 5F**). In

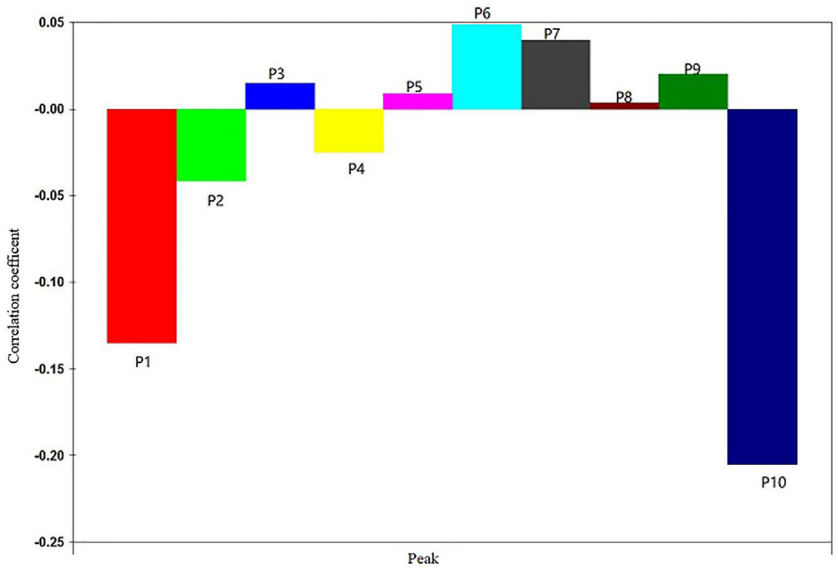

FIGURE 3 | Standardization regression coefficient of PLSR equations of HPLC.

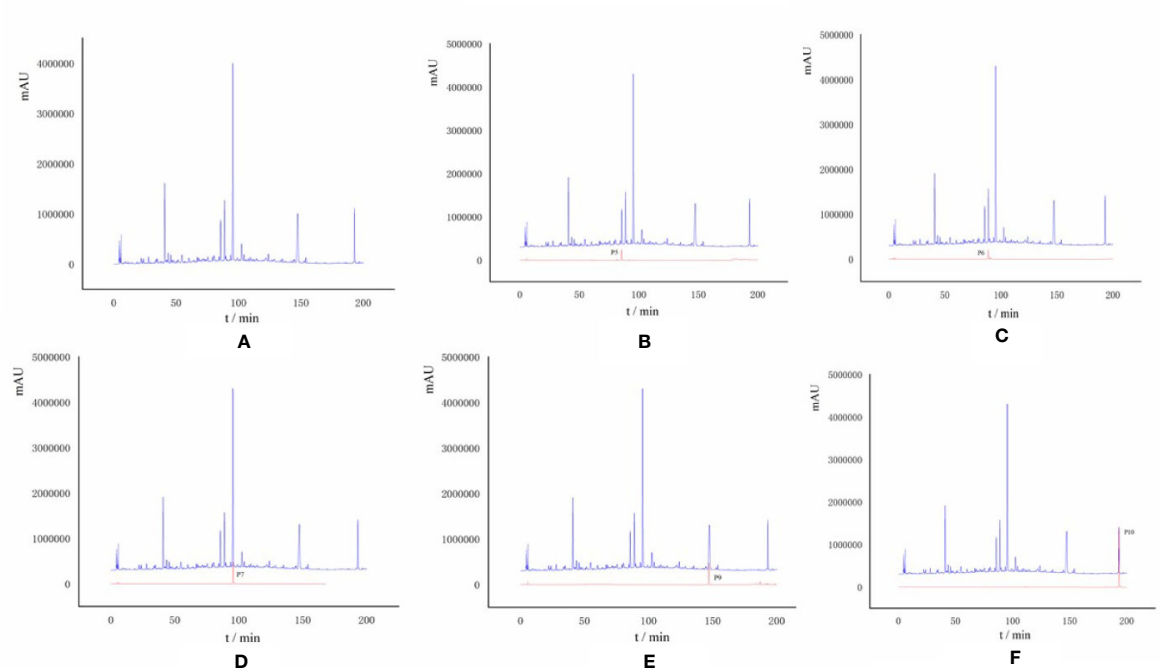

FIGURE 4 | (A) HPLC chromatogram of *S. heptaphylla* ethanol extract; **(B–F)** HPLC chromatogram of Knock-Out components.

addition, the retention time of P9 was consistent with that of the reference substance.

P10 (Rt = 193.201 min), the UPLC-MS^2 results of the knock-out component was shown in **Figure 5G**, in which the molecular formula was $C_{30}H_{46}O_5$. The results of secondary mass spectrometry showed that there were some ion fragments: 485.33/467.32/439.32/423.33/, According to the reference (Adam et al., 1982), it was speculated to be 3α-hydroxy-lup-20 (29)-ene-23,28-dioic acid (**Figure 5H**). Moreover, the retention time was consistent with that of the reference substance.

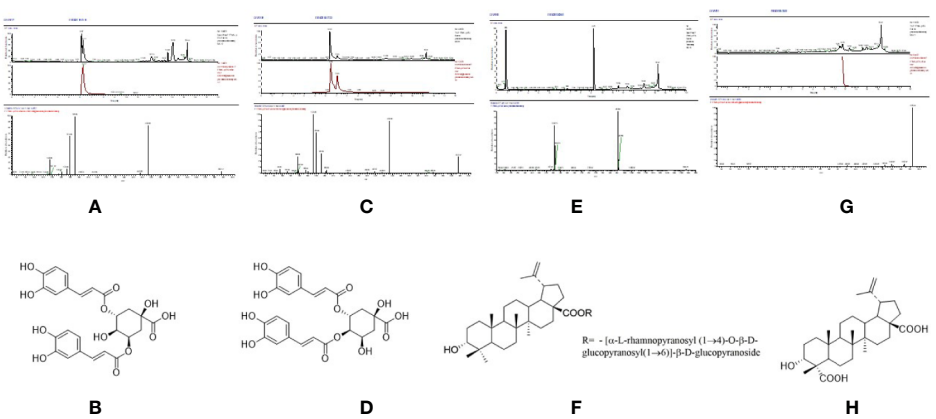

FIGURE 5 | The high resolution mass spectra and chemical structures of Peak 6, 7, 9, 10 **(A–H)** knocked-out components.

Effect of Compound A on the Viability of Normal Hepatocytes and Hepatocellular Carcinoma Cells

Compound A had the strongest anti-hepatoma activity, the effects of different concentrations of Compound A on the cell viability of normal hepatocyte lines (L0-2, Chang liver) and two hepatoma cell lines (Huh 7, HepG 2) after 24, 48, 72 h were detected by CCK-8 method. In **Figure 6A**, when the concentration of Compound A was higher than 125 nM, and 48 h treatment, Compound A had a slight inhibitory effect on human normal hepatocytes (L0-2), while the positive drugs showed significant cytotoxicity to normal hepatocytes in a time-dependent manner. In **Figure 6B**, after 24 h treatment, when the concentration of Compound A was higher than 500 nM, Compound A had significant cytotoxicity to Chang liver cells, compared with the blank group. After 48 h treatment, when the concentration of Compound A was higher than 62.5 nM, Compound A had significant cytotoxicity. The positive drug had significant cytotoxicity after 48 h. Compared with positive drugs, Compound A had less effect on the viability of normal hepatocytes. In **Figure 6C**, for Huh 7 hepatoma cells, when the concentration of Compound A was higher than 25 nM, it showed significant inhibitory effect on Huh 7 cells in a dose-dependent manner. The values of IC_{50} at 24, 48, and 72 h were 249.9, 285.3, and 199.5 nM, respectively. In **Figure 6D**, Compound A had a significant inhibitory effect on HepG 2 cells when the concentration of Compound A was higher than 25 nM. The values of IC_{50} at 24, 48, and 72 h were 657.7, 315.1, and 186.1 nM, respectively. The results showed that Compound A could significantly inhibit the viability of hepatoma cells, which was consistent with the results predicted by partial least square method. Then, the mechanism of Compound A against hepatoma cells was investigated.

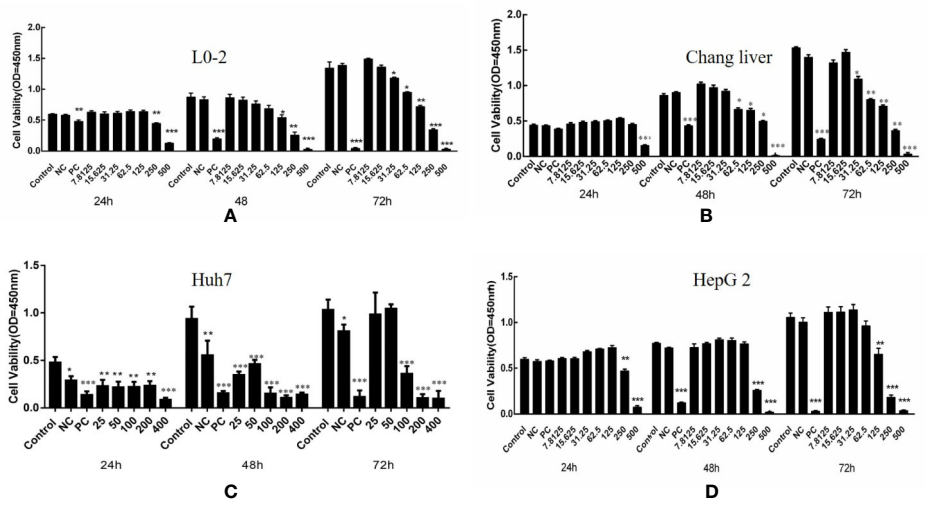

FIGURE 6 | Effects of compound A on the activity of normal hepatocytes and hepatoma cells: L0-2 **(A)**; Chang liver **(B)**; Huh7 **(C)**; HepG2 **(D)**. ***$P < 0.001$, $0.001 < **P < 0.01$, *$P < 0.05$ vs. control group.

Effects of Compound A on the Morphology of Two Kinds of Hepatoma Cells

The morphological changes of cells are closely related to the physiological phenomena such as cell proliferation, apoptosis and necrosis. Three concentrations of 100, 200, 400 nM were selected by CCK-8 experiment. HepG 2 and Huh7 hepatoma cells were treated with blank solvent, positive control drug (5-FU) and Compound A (100, 200, 400 nM) for 48 h, and then the morphological changes of HepG 2 and Huh7 hepatoma cells were observed by inverted microscope. Results were shown in **Figure 7**, the cells in the blank group were evenly spread over the bottom of the culture bottle, and the cells were regular, refractive and closely arranged, indicating that the cells were in good condition. While the number of cells in the positive control group and each concentration group of Compound A significantly decreased in a dose-dependent manner, and the cells showed morphological changes such as pseudopodia, deformation and floating.

Thus, the question is whether the inhibitory effects of Compound A on hepatoma cells were achieved by directly causing cell necrosis or by promoting apoptosis? It needs to be further verified.

Effects of Compound A on Apoptosis of Normal Hepatocytes and Hepatoma Cells

In order to explore the mechanism of Compound A on inhibiting the proliferation of hepatoma cells, the effects of Compound A on apoptosis of normal hepatocytes (Chang liver) and hepatoma cells (Huh 7, HepG 2 and SMMC-7721) were analyzed by Annexin V/PI double staining and flow cytometry. Normal hepatocytes (Chang liver) and hepatoma cells (Huh 7, HepG 2 and SMMC-7721) were treated with blank solvents, positive drug and different concentrations of Compound A for 48 h. In **Figure 8A**, Compound A (200, 400 nM) and positive control group (5-FU) could significantly promote the apoptosis of Huh7 cells ($P < 0.001$), and the effect of Compound A (400 nM) was significantly better than that of positive control (5-FU) ($P < 0.001$). Therefore, we speculated that the inhibitory effect of Compound A on Huh 7 cells might be through promoting apoptosis. In **Figures 8B, C**, Compound A had no significant effects on the apoptosis of other hepatoma cells (HepG 2 and SMMC-7721), but could inhibit the viability of hepatoma cells by directly causing cell necrosis. However, did Compound A also have effects on normal hepatocytes? In **Figure 8D**, Compound A has no significant

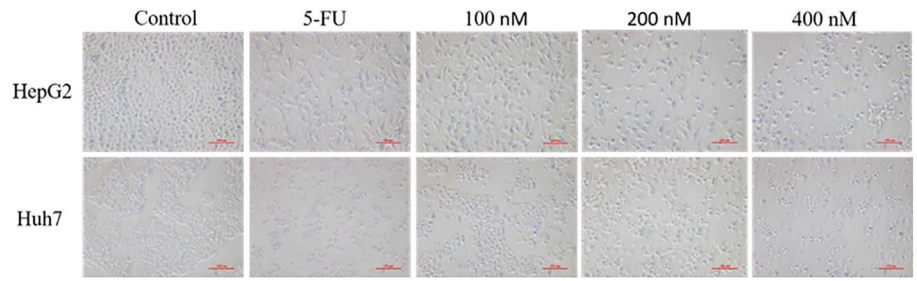

FIGURE 7 | Effects of compound A at different concentrations on the morphology of HepG 2 and Huh 7 cells.

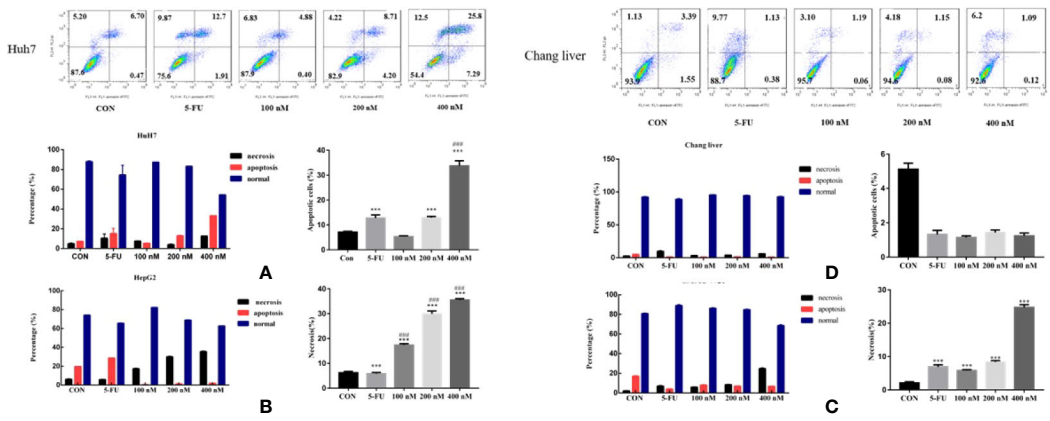

FIGURE 8 | Effects of Compound A on apoptosis of hepatoma cells [**(A)**: Huh 7; **(B)**: HepG 2; **(C)**: SMMC-7721] and normal hepatocytes [**(D)**: Chang liver]. $^{***}P < 0.001$ vs. control group; $^{###}P < 0.001$ vs. 5-FU group.

effect on the apoptosis and necrosis of normal hepatocytes, which further indicated that Compound A not only could inhibit hepatoma cells, but also has less toxic and side effects on normal hepatocytes. Then, we further studied the mechanism of Compound A in promoting apoptosis of Huh 7 cells.

Mechanism of Compound A on Promoting Apoptosis of Huh 7 Cells

Compound A Induces Apoptosis of Huh 7 Cells Through ROS

Cancer cells have a variety of apoptotic pathways, and ROS can affect mitochondrial metabolism and induce apoptosis (Masahiko and Masaya, 2013). Therefore, we studied whether Compound A induced apoptosis in Huh 7 cells by changing the level of reactive oxygen species (ROS). In **Figures 9A, B**, flow cytometry analysis showed that both the positive group (5-FU) and Compound A (100, 200, 400 nM) could significantly increase the level of intracellular ROS ($P < 0.05$, $P < 0.001$) compared with the blank group, in addition, the effects of Compound A (200, 400 nM) were significantly stronger than that of the positive control group (5-FU). For the normal hepatocytes (Chang liver), it was found that the positive control group (5-FU) could significantly increase the level of ROS ($P < 0.001$), compared with the blank group, while Compound A had no significant effect on the level of ROS in normal hepatocytes ($P > 0.001$), indicating that Compound A had less cytotoxicity to normal hepatocytes (Chang liver), and significantly lower than positive drugs (5-FU). It has been reported that the increase of intracellular ROS could induce the activation of mitochondrial apoptosis pathway. Then, the next study focused on the changes in the content of mitochondrial apoptotic proteins.

Regulatory Effect of Compound A on the Expression of Apoptosis-Related Proteins in Huh 7 Cells

The increase of intracellular ROS level can induce the activation of mitochondrial apoptosis pathway. In order to further explore the mechanism of Compound A-induced apoptosis in Huh 7 cells, the expressions of Bcl-2 family proteins were detected. The change in the content of pro-apoptotic proteins was shown in **Figure 10A**, Compound A (100, 200, 400 nM) could significantly increase the content of mitochondrial pro-apoptotic proteins Bax and Bim ($P < 0.001$) compared with the blank group, and the effects were better than that of positive drug (5-FU). As for the anti-apoptotic protein, in **Figure 10B**, Compound A (100, 200, 400 nM) could significantly decrease the contents of Bcl-xL and Mcl-1 ($P < 0.001$), with no significant effect on the content of Bcl-2 ($P > 0.001$) compared with the blank group. Because the ratio of Bcl-2 to Bax determines the permeability of mitochondrial membrane, when the ratio is low, the permeability of mitochondrial membrane increases and apoptotic factors are transferred from mitochondria to the nucleus, which in turn induces cell apoptosis. On the contrary, it is difficult for apoptotic factors to transfer to the nucleus. In **Figure 10C**, Compound A (100, 200, 400 nM) and the positive control group (5-FU) significantly decreased the proportion of Bcl-2/Bax protein compared with the blank group ($P < 0.001$), and the effects of Compound A (100, 200, 400 nM) were significantly better than

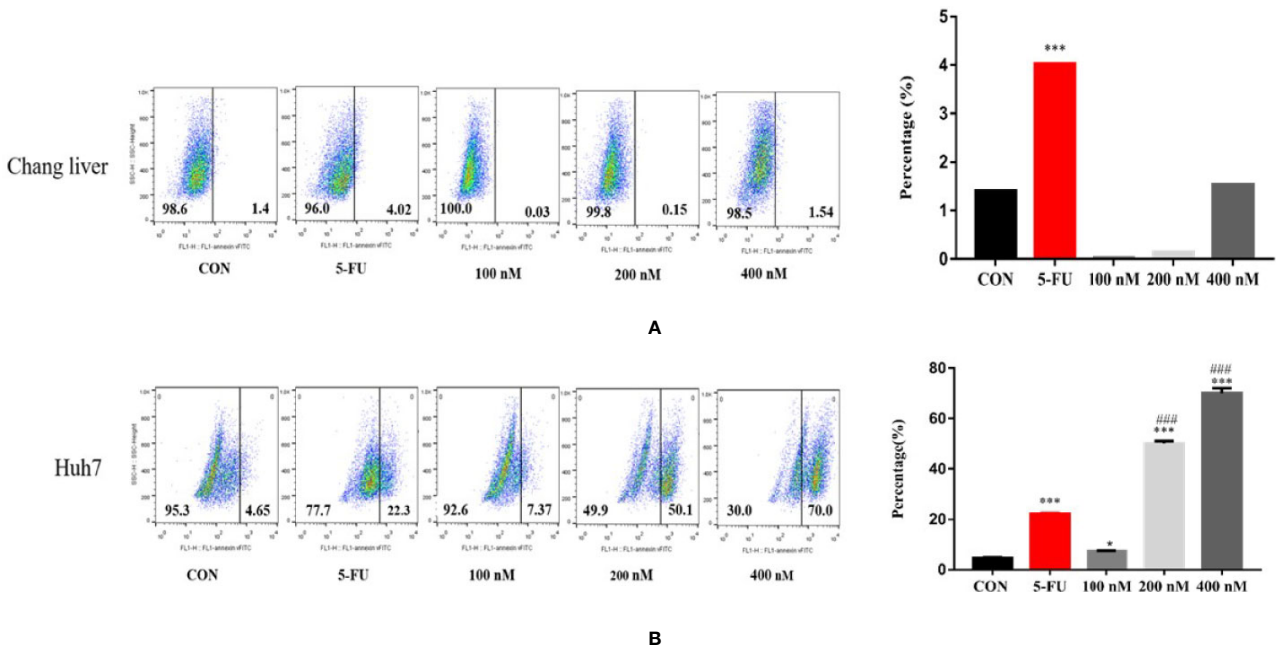

FIGURE 9 | Effects of Compound A at different concentrations on ROS levels in Chang liver **(A)** and Huh 7 **(B)** cells. $^{***}P < 0.001$, $^{*}P < 0.05$ vs. control group; $^{\#\#\#}P < 0.001$ vs. 5-FU group.

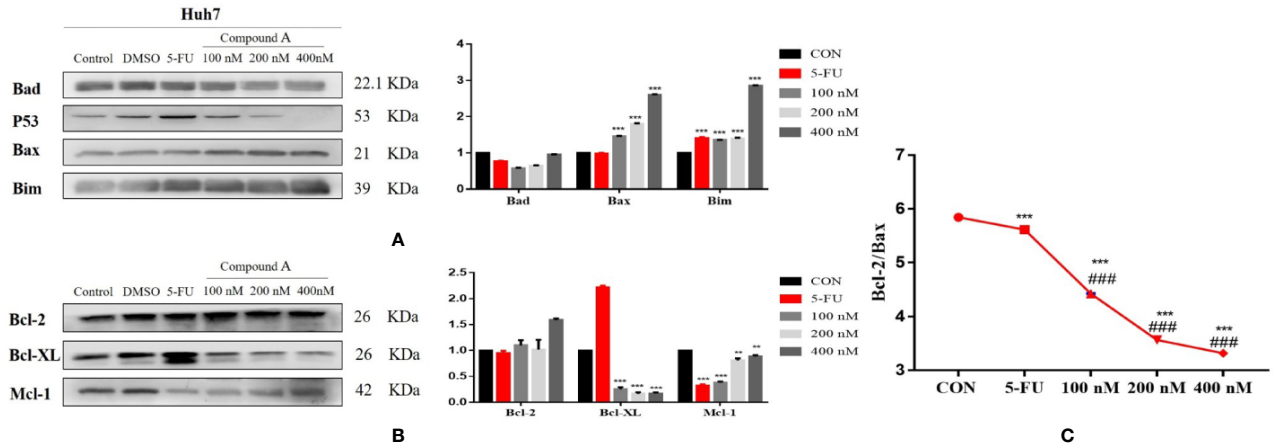

FIGURE 10 | The regulatory effect of Compound A on the expression of apoptosis related proteins in Huh7 cells. **(A)** pro-apoptotic protein; **(B)** anti-apoptotic protein; **(C)** ratio of Bcl-2 to Bax. $^{***}P < 0.001$,$^{**}P < 0.01$ vs. control group; $^{###}P < 0.001$ vs. 5-FU group.

that of the positive control group (5-FU). It was inferred that Compound A might induce apoptosis of Huh 7 cells by regulating the expression of mitochondrial apoptotic proteins.

MATERIALS AND METHODS

General

Shimadzu High-Performance Liquid Chromatograph (Japan Shimadzu Co., Ltd). Thermo Ultimate 3000 UHPLC, Q Exactive (Thermo Scientific, US). chromatographic column Purospher® STAR LP RP-18 (Merck KGaA, Germany). MultiskanMK3 Full wavelength enzyme marker (Thermo Electron, US). GRP-9270 Constant temperature incubator (Sen xin Experimental instrument Co., Ltd, Shanghai). AB135-S Electronic balance (Mettler-Toledo Instruments Co., Ltd., Switzerland). Rotary evaporation meter (Tokyo physical and Chemical Instruments Co., Ltd.), Centrifuge precipitator (Shanghai Surgical Instruments Factory). Flow cytometry (Becton Dickinson, BD, US). Multicolor fluorescence, chemiluminescence and visible light imager (ProteinsiMpleFluorcheM Q). Electrophoretic apparatus (EPS600 Tanon); Inverted microscope (Nikon ECLiPSETS100).

Drugs and Reagents

Acetonitrile was purchased from Fisher (HPLC, US); pure water was obtained from Wahaha Group (Hangzhou); Dulbecco's modified eagle medium (DMEM), Penicillin and streptomycin, Penicillin and streptomycin and PVDF membrane were purchased from Beijing Solarbio Science & Technology Co., Ltd. non-fat milk powder, Trypsin, EDTA, CCK-8 Kit, 6/96 well cell culture plate, Annexin V-FITC/Pl, Bax、Bcl-2、BID、Bcl-XL、Bak、Bim、β-actin and corresponding antibody were purchased from Becton Dickinson (BD, US); BCA protein quantitative Kit and Acrylamide were obtained from biyuntian biological Co., Ltd (Shanghai); fetal bovine serum (FBS) was purchased from Gibco (Grand Isoland, US); Thiazolyl blue(MTT) was purchased from Hualan Chemical Technology Co., Ltd (Shanghai).

Plant Material

10 batches of *S. heptaphylla* leaves were collected from the foothills of Qingyuan Mountain in Quanzhou City, Fujian Province, as detailed in **Table 3**. All the samples were identified as the leaves of *S. heptaphylla* by Professor Changqin Li (Henan University). The samples now were stored in the Medical College of Huaqiao University and the National

TABLE 3 | Collection of *S. heptaphylla* leaves.

NO.	Sample origin	Collection time
S1	Qingyuan Mountain, Quanzhou City (118°36' E, 24°58 ' N)	2017.03.15
S2	Qingyuan Mountain, Quanzhou City (118°36' E, 24°58 ' N)	2017.04.15
S3	Qingyuan Mountain, Quanzhou City (118°36' E, 24°58 ' N)	2017.05.15
S4	Qingyuan Mountain, Quanzhou City (118°36' E, 24°58 ' N)	2017.06.15
S5	Qingyuan Mountain, Quanzhou City (118°36' E, 24°58 ' N)	2017.07.15
S6	Qingyuan Mountain, Quanzhou City (118°36' E, 24°58 ' N)	2017.08.15
S7	Qingyuan Mountain, Quanzhou City (118°36' E, 24°58 ' N)	2017.09.15
S8	Qingyuan Mountain, Quanzhou City (118°36' E, 24°58 ' N)	2017.10.15
S9	Qingyuan Mountain, Quanzhou City (118°36' E, 24°58 ' N)	2017.11.15
S10	Qingyuan Mountain, Quanzhou City (118°36' E, 24°58 ' N)	2018.12.15

R & D Center for Edible Fungus Processing Technology, Henan University.

Experimental Methods

Sample Solution Preparation

10 batches of *S. heptaphylla* leaves were crushed (40 mesh), about 5.0 g, 10 times the amount of 70% ethanol, cold soaked for 3 times, each time for 3 days, combined with filtrate, decompressed and concentrated to obtain the total extract of *S. heptaphylla* leaves. The 200.00 mg extract was precisely weighed and dissolved in 10 mL 70% ethanol and filtered with a 0.22-μm micro porous membrane to prepare a solution, equivalent to 1 g· mL^{-1} of the original medicinal material.

Conditions for Fingerprint Analysis

Chromatographic conditions: RP-18 endcapped column (4.6 mm × 250 mm, 5 μm); mobile phase was acetonitrile (B)-0.1% phosphate water (D). The elution procedure was shown in **Table 4**. The flow rate was set at 0.6 mL/min, and the column temperature was 25 °C. The detection wavelength was set at 210 nm with the injection volume of 5 μL.

The Method of Knocking Out the Target Components

Under the optimal conditions of high performance liquid chromatography (HPLC), the 70% ethanol extract (equivalent to 1 g· mL^{-1}) was injected into 5 μL, and the chromatogram at 210 nm wavelength was recorded. According to the spectrum-effect relationship, the retention time of the chromatographic peaks related to the anti-hepatoma activity was analyzed, and the eluents of the corresponding peaks were collected and concentrated under reduced pressure to get the target compounds. Each target peak was prepared 10 times in liquid phase, and concentrated the eluate respectively. Dissolved with 0.3 mL 70% ethanol solution and passed through 0.22 μm microporous membrane to obtain the sample containing the target peak (marked as Px).

Mass Spectrometry Analysis

Chromatographic conditions: Watres BEHC-18 column (2.1 × 50 mm, 1.7 μm), mobile phase was acetonitrile (A)-0.1% formic acid aqueous solution (B), The elution procedure was follows: 0–5 min, (A)10%–(B) 90%; 5–30 min, (A) 95%–(B) 5%; 30 to 55 min, (A) 95% to (B) 5%; 55 to 56 min, (A) 10%–(B) 90%; 56–61 min, (A) 10%–(B) 90%. The flow rate was set at 0.3 mL/min, and injection 0.2 μL, determination.

TABLE 4 | Elution procedure.

Time (min)	B (%)	D (%)
0–50	5%–15%	95%–85%
50–100	15%–25%	85%–75%
100–135	25%–33%	75%–67%
135–145	33%–35%	67%–65%
145–165	35%–41%	65%–59%
165–200	41%–90%	59%–10%

Mass spectrometry conditions: sheath gas flow rate: 35 arb; auxiliary gas flow rate: 10 arb; spray voltage: 3.5 kV; capillary temperature: 320 °C, polarity: positive; full scan parameters: resolution 7000; AGC target: 3e6; Maximum IT: 100 ms; scanning range: 50-800 *m/z*. Second-level scanning parameters: resolution: 17500; AGC target: 1e5; Maximum IT: 50 ms; isolation window: 4.0 *m/z*; collision energy: 30.

Cell Culture

L0-2, Chang liver, HepG 2, SMMC-7721 and Huh 7 cells were cultured in the DMEM medium containing 10% FBS, 1% penicillin and streptomycin mixture and cultured in the incubator at 37 °C and 5% CO_2. Take logarithmic growth phase cells for follow-up experiment.

Microscopic Observation of Cell Morphology

After the cells were treated with different concentrations of drugs for 48 h, the cells were collected and randomly taken 5 visual fields under an inverted microscope to take pictures (20 × objective lens).

Cell Viability Detection

MTT

The cells of logarithmic growth phase were inoculated in 96-well plates (1×10^4 cells/well), and incubated in incubator at 37 °C and 5% CO_2 for 24 h. Thereafter, the supernatant was discarded by liquid transfer gun. The ethanol extracts of *S. octophylla* were diluted from 800 μg/mL to 800, 400, 200, 100, 50 and 25 μg/mL, respectively, and the blank control group was given DMEM medium with 6 compound holes in each concentration. Then incubated in 37 °C incubator for 24 h, 10 μL MTT solution was added to each well, then the supernatant was discarded after 4 h, and then DMSO solution was added to dissolve it. The absorbance was measured at 490 nm wavelength for 10 min.

CCK-8

Follow the operation steps of the CCK-8 test kit instructions. The logarithmic growth phase cells were inoculated into 96-well plates (2×10^3 cells/well). 12 h later, Compound A of different concentrations were added, and 6 compound holes were set up for each concentration. The cells were cultured at 37 °C for 24, 48 and 72 h, then the supernatant was discarded and washed with PBS twice. Then, 10% CCK-8 solution was added and cultured at 37 °C for 2 h. The absorbance was measured by enzyme labeling instrument at 450 nm wavelength.

Flow Cytometry Analysis

The apoptosis of related cells was detected by FITC Annexin V apoptosis detection kit. The cells in logarithmic growth phase were inoculated in 6-well plates (1×10^6 cells/well) and cultured for 24 h. The original culture medium was abandoned and Compound A (100, 200, 400 nM) solution was added. The blank control group was DMSO, positive control group was 5-fluorouracil (5-FU). Each group was provided with 3 multiple holes and incubated in an incubator at 37 °C and 5% CO_2 for 48 h. After discarding the original culture medium and washing with PBS for 3 times, the cells were digested with 0.25% trypsin,

centrifuged for 5 min, washed twice with 1 mL precooled PBS, re-suspended in 200 μL binding buffer, then mixed with 10 μL Annexin V-FITC, 15 min, and 300 μL binding buffer were added away from light at room temperature, finally, 5 μL PI was added away from light, staining for 15 min to determine the apoptosis rate of each sample by flow cytometry. The left upper quadrant (Q1) was necrotic cells, the right upper quadrant (Q2) was late apoptotic cells, the right lower quadrant (Q3) was early apoptotic cells, and the left lower quadrant (Q4) was normal cells. Results the average percentage of apoptotic cells was analyzed by FlowJo software.

Detection of the Expression of Related Proteins in Apoptosis Signal Pathway by Western Blot

The cells in logarithmic growth phase were evenly inoculated in 6-well plates (1×10^6 cells/well), and then treated with Compound A (20, 50, 100 nM), blank control group (DMSO) and positive control group (5-FU) for 48 h in an incubator at 37 °C and 5% CO_2. Then, cells were harvested and lysed on ice for 30 min in Radio Immunoprecipitation Assay (RIPA), and centrifuged at 4 °C, 12000 rpm for 20 min, to absorb the supernatant and transfer it to an EP tube. The protein concentration was measured by BCA protein concentration assay kit. Cell lysates were then loaded onto 10% SDS-PAGE for analysis of Bax、Bcl-2、BID、Bcl-XL、Bak、Bim, and β-actin. Proteins were transferred onto a polyvinylidene fluoride membranes (PVDF), which were blocked in 5% non-fat milk in Tris-buffered saline with 1% Tween 20 for 2 h. Then, the PVDF membrane was incubated with the primary antibody overnight at 4 °C. The membranes were washed thoroughly and incubated with horseradish peroxidase-conjugated secondary antibodies. After washing, protein bands were visualized using enhanced chemiluminescence (ECL) and use Imag J software to analyze the gray value of the protein.

Statistical Analysis

The partial least square regression analysis method was used to analyze the data of 10 quantitative characteristic maps and the anti-hepatoma activities of 10 batches *S. heptaphylla* extracts. The retention time of each peak of the characteristic spectrum of *S. heptaphylla* was corrected by using the software "similarity Evaluation system of chromatographic fingerprint of traditional Chinese Medicine version 1.0 A" recommended by Chinese Pharmacopoeia Committee, and the peak area was averaged. The data of 10 quantitative characteristic peaks were obtained. Using DPS 7.05 software to analyze the area of 10 quantitative characteristic peaks as independent variables, the IC_{50} values of (X), 10 batches of *S. heptaphylla* extract against liver cancer as dependent variables (Y), the partial least square regression equation was established, and the correlation between quantitative characteristic peaks and anti-hepatoma activity was screened.

The results were expressed by arithmetic mean and standard deviation, and the significant differences were compared by SPSS software single factor analysis of variance (One-Way ANOVA). All the pictures were drawn with Graphpad Prism 7.0.

DISCUSSION

"Spectrum-Effect Relationship" and "Component Knock-Out" technology has been successfully applied in screening the active ingredients of natural products (Shi et al., 2018 and Li et al., 2019). In this paper, partial least square method was used to analyze the correlation between 10 quantitative characteristic chromatographic peaks of *S. heptaphylla* and the anti-hepatoma activity (IC_{50} value) of *S. heptaphylla*. It was inferred that P10 had the strongest anti-liver cancer activity by spectral correlation analysis. Bioactive components of natural products can be isolated quickly and efficiently by using "component knock-out" technology, which has advantages of accuracy and efficiency. In this manuscript, based on spectral correlation analysis, P10 with anti-hepatoma activity was prepared rapidly by component knock technique, and P10 was determined as 3α-hydroxy-lup-20(29)- ene-23,28-dioic acid (Compound A) by "Component knock-out" method and high resolution mass spectrometry. HPLC comparison showed that the results were consistent with reference standard.

In this manuscript, the results of CCK-8 test showed that Compound A could significantly inhibit the viability of hepatoma cells Huh 7, HepG 2 and SMMC-7721, which was consistent with the results speculated by spectral correlation analysis. Compound A could inhibit the viability of liver cancer cells by directly necrotizing tumor cells or indirectly inducing tumor cell apoptosis? The morphological changes of cells are often closely related to necrosis, apoptosis and so on. We found that Huh7 cells showed typical apoptotic morphology, which was further verified. The apoptosis of three kinds of hepatocellular carcinoma cells and normal hepatocytes were analyzed by flow cytometry. It was found that the apoptotic proportion of Huh7 cells significantly increased after Compound A treatment, while the necrotic proportion of HepG 2 and SMMC-7721 cells increased significantly, but there was no significant effect on normal hepatocytes.

The classical cytological theory points out that apoptosis is a spontaneous way of cell death, which mainly includes exogenous and endogenous apoptosis pathways (Daugas, 2001; Alciaturi et al., 2014). Including mitochondrial apoptosis pathway, death receptor apoptosis pathway and endoplasmic reticulum apoptosis pathway (Fulda and Debatin, 2006). Among them, mitochondrial apoptosis pathway is the most common one (Ashkenazi and Salvesen, 2014), which is regulated by Bcl-2 protein family, Caspase family and other key factors. Among them, Bcl-2 family regulates the permeability of mitochondrial inner and outer membrane, thus affecting the process of cell apoptosis (Martinou and Youle, 2011). The Bcl-2 protein family is mainly composed of anti-apoptotic proteins and pro-apoptotic proteins (Tsukahara et al., 2006). Anti-apoptotic proteins include Bcl-xl, Mcl-l and so on, in which Bcl-2 protein is the main sensor of apoptosis (Hockenbery et al., 1990; Boise et al., 1993). Anti-apoptotic proteins can stabilize the mitochondrial membrane, prevent the release of many kinds of mitochondrial apoptotic proteins such as Cyt-c, and prevent the further activation of Caspase (Kutuk and Basaga, 2006). Pro-apoptotic proteins,

including Bax, Bak and Bad, could change the mitochondrial membrane potential and enhance the mitochondrial permeability. Cytochrome C (Cyt-c) is released from the mitochondria into the cytoplasm and further binds with apoptosis-related factors (Apaf-1) to form oligomers, which binds Pro-Caspase-9 to form apoptotic bodies to activate Caspase-9, and then activate Caspase-3, to lead cell apoptosis. In addition, the ratio of Bax to Bcl-2 protein may play a key role in the process of apoptosis (Liang and Cao, 2014). When the proportion is low, the permeability of the mitochondrial membrane increases, and the apoptotic factor is transferred from the mitochondria to the nucleus, which could induce the apoptosis. On the contrary, it is difficult to transfer the apoptotic factor to the nucleus. Intracellular ROS could affect mitochondrial metabolism (Masahiko and Masaya, 2013) and then activate the pathway of mitochondrial apoptosis.

It is reported that lupine pentacyclic triterpenes have strong and broad-spectrum anti-tumor activity, low toxicity and selectivity to tumor cells, and their mechanism is independent of p53 pathway, so they are expected to become excellent anti-tumor lead compounds (Wang et al., 2017). Betulinic acid can inhibit the proliferation of HepG 2 cells through Wnt pathway. Oleanolic acid inhibits proliferation and induces apoptosis of HepG 2 cells by regulating ROS and MMP (Miao et al., 2016). In addition, betulinic acid, 23-hydroxybetulinic acid, betulin and lupeol have significant anti-cancer activities through activating mitochondrial apoptosis pathway, and regulate the levels of Bcl-2 and ROS (Wang et al., 2017).

In order to further explore the mechanism of Compound A in promoting apoptosis of Huh7 cells. We detected the changes of apoptosis-related proteins of Bcl-2 family proteins and ROS in Huh7 cells. The results showed that Compound A (100, 200, 400 nM) could significantly increase the content of mitochondrial pro-apoptotic proteins Bax and Bim ($P < 0.001$), and its effect was better than that of positive drugs (5-FU). As for anti-apoptotic protein, Compound A (100, 200, 400 nM) could significantly reduce the content of Bcl-xL and Mcl-1 ($P < 0.001$), compared with the blank group, and Compound A (100, 200, 400 nM) and 5-FU could significantly reduce the proportion of Bcl-2/Bax protein ($P < 0.001$).

CONCLUSION

Spectrum Effect Relationship and Component Knock-Out were the rapid method to infer anti-hepatoma activity of compound in *S. heptaphylla* leaves and Compound A was determined to be one of the main anti-hepatoma active components. Compound A could significantly inhibit the proliferation of all kinds of hepatoma cells (Huh7, HepG2 and SMMC-7721), and had little toxicity to normal hepatocytes. It could promote the apoptosis of Huh7 cells by up-regulating the level of ROS in Huh7 cells, activating intracellular mitochondrial apoptosis pathway and regulating the level of Bcl-2 family proteins in mitochondrial apoptosis pathway.

DATA AVAILABILITY STATEMENT

All datasets presented in this study are included in the article/ supplementary material.

AUTHOR CONTRIBUTIONS

WK and YZ conceived the research subject. XL, NJ, XX, and CL conducted the experiments, collected the plant specimens, separated and analysis compounds, analyzed and interpreted the data, as well as prepared the first draft. WK and XL critically read and revised the paper. All authors contributed to the article and approved the submitted version.

FUNDING

This work was supported by Key Project in Science and Technology of Henan Province (192102110112).

REFERENCES

Adam, G., Lischewski, M., and Phiet, H. V. (1982). 3α-Hydroxy-lup-20(29)-ene-23, 28-dioic acid from Schefflera octophylla. *Phytochemistry* 21 (6), 1385. doi: 10.1016/0031-9422(82)80147-7

Alciaturi, C. E., Escobar, M. E., De La Cruz, C., and Rincón, C. (2014). Partial least squares (PLS) regression and its application to coal analysis. *Rev. Tècnica La Facultad Ingeniería Universidad Del Zulia.* 26 (3), 197–204.

Ally, A., Balasundaram, M., Carlsen, R., Chuah, E., Clarke, A., Dhalla, N., et al. (2017). Comprehensive and Integrative Genomic Characterization of Hepatocellular Carcinoma. *Cell* 169 (7), 1327–1341. e23. doi: 10.1016/j.cell.2017.05.046

Ashkenazi, A., and Salvesen, G. (2014). Regulated cell death: signaling and mechanisms. *Annu. Rev. Cell Dev. Biol.* 30, 337–356. doi: 10.1146/annurev-cellbio-100913-013226

Boise, L. H., González-García, M., Postema, C. E., Ding, L., Lindsten, T., Turka, L. A., et al. (1993). Bcl-x, a bcl-2-related gene that functions as a dominant regulator of apoptotic cell death. *Cell* 74, 597–608. doi: 10.1016/0092-8674(93)90508-n

Daugas, E. (2001). Essential role of the mitochondrial apoptosis-inducing factor in programmed cell death. *Nature* 410 (6828), 549. doi: 10.1038/35069004

Fang, C., Han, Z. H., Liu, X. H., Yang, Y. F., Lan, Z. H., and Feng, S. L. (2016). Spectrum-effect relationship of active fraction from Hedysari Radix on improving immunity. *Chin. Tradit. Herbal Drugs* 47, 101–105. doi: 10.7501/j.issn.0253-2670.2016.01.015

Fukuda, K., Okumura, T., Abei, M., Fukumitsu, N., Ishige, K., Mizumoto, M., et al. (2017). Long-term outcomes of proton beam therapy in patients with previously untreated hepatocellular carcinoma. *Cancer Sci.* 108 (3), 497–503. doi: 10.1111/cas.13145

Fulda, S., and Debatin, K. M. (2006). Extrinsic versus intrinsic apoptosis pathways in anticancer chemotherapy. *Oncogene* 25 (34), 4798. doi: 10.1038/sj.onc.1209608

Gong, A. G., Li, N., Lau, K. M., Lee, P. S., Yan, L., Xu, M. L., et al. (2015). Calycosin orchestrates the functions of DangguiBuxue Tang, a Chinese herbal decoction composing of Astragali Radix and Angelica Sinensis Radix: An evaluation by

using calycosin-knock out herbal extract. *J. Ethnopharmacol.* 168, 150–157. doi: 10.1016/j.jep.2015.03.033

Gui, J. F. (2012). *Study on antitumor activity of Poria cocos triterpene compositions and the quality analysis of Poria cocos medicinal materials [D]* (Wuhan: Hubei University of Chinese Medicine).

Hockenbery, D., Nunez, G., Milliman, C., Schreiber, R. D., and Korsmeyer, S. J. (1990). Bcl-2 is an inner mitochondrial membrane protein that blocks programmed cell death. *Nature* 348, 334–336. doi: 10.1038/348334a0

Hu, X. Y., Liu, M. H., Qin, S., and Zhang, S. J. (2013). Spectrum-effect relationship of antibacterial extracts from Isatidis Radix. *Chin. Tradit. Herb. Drugs* 44, 1615–1620. doi: 10.7501/j.issn.0253-2670.2013.12.018

Julie, K. H., Laura, M. K., and Richard, S. F. (2018). AASLD guidelines for the treatment of hepatocellular carcinoma. *Hepatology* 67 (1), 358–380. doi: 10.1002/hep.29086

Kutuk, O., and Basaga, H. (2006). Bcl-2 protein family: Implications in vascular apoptosis and atherosclerosis. *Apoptosis* 11 (10), 1661–1675. doi: 10.1007/s10495-006-9402-7

Li, W. J., Zhang, Y., Shi, S. J., Yang, G., Liu, Z. H., Wang, J. M., et al. (2019). Spectrum-effect relationship of antioxidant and tyrosinase activity with Malus pumila flowers by UPLC-MS/MS and component knock-out method. *Food Chem. Toxicol.* 133, 110754. doi: 10.1016/j.fct.2019.110754

Li, b. (2011). *Study on Separation and Purification Methods、Structural Identification and the Activity of Inhibiting Liver Cancer of Triterpenoid from Schisandra Chinensis (Turcz.) Baill [D]* (Shenyang: Shenyang Agricultural University).

Liang, K., and Cao, B. Z. (2014). Progress on cell apoptosis of mitochondrial regulation. *BME &Clin Med*. 18 (5), 501–505. doi: 10.13339/j.cnki.sglc.2014.05.049

LV, G. S., Chen, L., and Wang, H. Y. (2015). Research progress and prospect of liver cancer in China. *Chin. Bull. Life Sci.* 27 (3), 237–248. doi: 10.13376/j.cbls/2015034

Martinou, J. C., and Youle, R. J. (2011). Mitochondria in apoptosis: Bcl-2 family members and mitochondrial dynamics. *Dev. Cell.* 21, 92–101. doi: 10.1016/j.devcel.2011.06.017

Masahiko, T., and Masaya, H. (2013). HTLV-1 Tax oncoprotein stimulates ROS production and apoptosis in T cells by interacting with USP10. *Blood* 122, 715–725. doi: 10.1182/blood-2013-03-493718

Miao, J. Q., Wang, X. R., Dong, X. S., He, S. H., Liang, T. G., Li, Q. S., et al. (2016). Apoptosis-inducing effect of oleanlic acid on human hepatoma cell line HepG 2 and its mechanism. *Drugs Cli.* 7 (31), 934–938.

Qian, W. D., Tan, A. J., Li, S. M., Chen, B. L., Du, A. D., Wang, S. Y., et al. (2019). Pentacyclic triterpenoids from Eucommia ulmoides and their antitumor activities. *Chin. Tradit. Pat. Med.* 41 (5), 1059–1065.

Shi, M. J., Zhang, Y., Song, M. M., et al. (2018). Screening the Marker Components in Psoralea corylifolia L. with the Aids of Spectrum-Effect Relationship and Component Knock-Out by UPLC-MS². *Int. J. Mol. Sci.* 19 (11), 3439. doi: 10.3390/ijms19113439

Tsukahara, S., Yamamoto, S., Shwe, T.-T.-W., Ahmed, S., Kunugita, N., Arashidani, K., et al. (2006). Inhalation of low-level formaldehyde increases the Bcl-2/Bax expression ratio in the hippocampus of immunologically sensitized mice. *Neuroimmunomodulation* 13 (2), 63–68. doi: 10.1159/000094829

Wang, B., and Hou, W. (2013). A new target for TCM anti-tumor research. *Cancer Res. Prev. Treat.* 40 (12), 1200–1203.

Wang, J., Kong, H., Yuan, Z. M., Gao, P., Dai, W. D., Hu, C. X., et al. (2013). A novel strategy to evaluate the quality of traditional Chinese medicine based on the correlation analysis of chemical fingerprint and biological effect. *J. Pharm. Biomed. Anal.* 83, 57–64. doi: 10.1016/j.jpba.2013.04.035

Wang, Y. W., Xu, S. T., and Xu, J. Y. (2017). Advances in Research on Lupane-Type-Pentacyclic Triterpenes and Their Anti-tumor Activities. *Pharm. Clin. Res.* 25 (4), 336–342. doi: 10.13664/j.cnki.pcr.2017.04.016

Wu, M., Fu, T., Chen, J. X., Lin, Y. Y., Yang, J. E., and Zhuang, S. M. (2020). LncRNA GOLGA2P10 is induced by PERK/ATF4/CHOP signaling and protects tumor cells from ER stress-induced apoptosis by regulating Bcl-2 family members. *Cell Death Dis.* 11, 276. doi: 10.1038/s41419-020-2469-1

Xu, G. L., Xie, M., Yang, X. Y., Song, Y., Yan, C., Yang, Y., et al. (2014). Spectrum-Effect Relationships as a Systematic Approach to Traditional Chinese Medicine Research: Current Status and Future Perspectives. *Molecules* 19 (11), 17897–17925. doi: 10.3390/molecules191117897

Yang, W. T., and Hou, E. C. (2016). The research progress of primary hepatic carcinoma treatment. *Mod. Oncol.* 24 (21), 3495–3499.

Yang, J. D., Larson, J. J., Watt, K. D., Allen, A. M., Wiesner, R. H., Gores, G. J., et al. (2017). Hepatocellular Carcinoma Is the Most Common Indication for Liver Transplantation and Placement on the Waitlist in the United States. *Clin. Gastroenterol. Hepatol.* 15 (5), 767–775. e3. doi: 10.1016/j.cgh.2016.11.034

Yang, J. D., Hainaut, P., Gores, G. J., Amadou, A., Plymoth, A., and Roberts, L. R. (2019). A global view of hepatocellular carcinoma: trends, risk, prevention and management. *Nat. Rev. Gastroenterol. Hepatol.* 16, 589–604. doi: 10.1038/s41575-019-0186-y

Yi, Z. H. (2017). *Quantum Chemistry Study on ESI-ITMSn Fragmentation of Caffeoylquinic Acids* (Jiamusi: Jiamusi University).

Zeng, L. J., Lin, B., and Song, H. T. (2015). Progress in study of spectrum-effect relationship of traditional Chinese medicine and discussions. *China J. Chin. Mater. Med.* 40 (8), 1425–1432. doi: 10.4268/cjcmm20150801

Zhang, L., Yan, J., Liu, X. M., Ye, Z. G., Yang, X. H., Meyboom, R., et al. (2012). Pharmacovigilance practice and risk control of Traditional Chinese Medicine drugs in China: current status and future perspective. *J. Ethnopharmacol.* 140 (3), 519. doi: 10.1016/j.jep.2012.01.058

Zhang, X. P., Shao, J. J., Ma, D. L., Liu, F., and Liu, M. M. (2019). Research on antitumor active components and mechanisms of natural products. *Acta Pharm. Sin.* 54 (11), 1949–1957. doi: 10.16438/j.0513-4870.2019-0669

Zhao, X. P., Fan, X. H., Yu, J., and Cheng, Y. Y. (2004). A method for predicting activity of traditional Chinese medicine based on quantitative composition-activity relationship of neural network model. *China J. Chin. Mater. Med.* 29 (11), 1082.

Zheng, Q., Zhao, Y., Wang, J., Liu, T., Zhang, B., Gong, M., et al. (2014). Spectrum-effect relationships between UPLC fingerprints and bioactivities of crude secondary roots of Aconitum carmichaelii Debeaux (Fuzi) and its three processed products on mitochondrial growth coupled with canonical correlation analysis. *J. Ethnopharmacol.* 153, 615–623. doi: 10.1016/j.jep.2014.03.011

Zhou, J., Qi, L., and Li, P. (2008). Quality control of Chinese herbal medicines with chromatographic fingerprints. *Se Pu.* 26 (2), 153–159. doi: 10.1016/S1872-2059(08)60011-5

Zhu, X. S., and Liu, W. C. (2018). The progress in epidemiology and risk factors of primary liver cancer worldwide. *Mod. Oncol.* 26 (14), 2297–2301.

Conflict of Interest: The authors declare that the research was conducted in the absence of any commercial or financial relationships that could be construed as a potential conflict of interest.

frontiers in Pharmacology

ORIGINAL RESEARCH
published: 30 October 2020
doi: 10.3389/fphar.2020.590587

A Rapid High Throughput Vibration and Vortex-Assisted Matrix Solid Phase Dispersion for Simultaneous Extraction of Four Isoflavones for Quality Evaluation of *Semen Sojae Praeparatum*

Xuejing Yang[1,2†], Ali Sun[1,3†], Evans Owusu Boadi[1,3], Jin Li[1], Jun He[1,3], Xiu-mei Gao[1] and Yan-xu Chang[1,3]**

[1]State Key Laboratory of Component-based Chinese Medicine, Tianjin University of Traditional Chinese Medicine, Tianjin, China, [2]School of Pharmacy, Harbin University of Commerce, Harbin, China, [3]Tianjin Key Laboratory of Phytochemistry and Pharmaceutical Analysis, Tianjin University of Traditional Chinese Medicine, Tianjin, China

OPEN ACCESS

Edited by:
Yi Wang,
Zhejiang University, China

Reviewed by:
Simone Carradori,
University "G. d'Annunzio" of Chieti-Pescara, Italy
Yuelin Song,
Beijing University of Chinese Medicine, China
Chu Chu,
Zhejiang University of Technology, China

***Correspondence:**
Jin Li
Lijin@tjutcm.edu.cn
Yan-xu Chang
tcmcyx@tjutcm.edu.cn

†These authors have contributed equally to this work

Specialty section:
This article was submitted to Ethnopharmacology, a section of the journal Frontiers in Pharmacology

Received: 02 August 2020
Accepted: 08 October 2020
Published: 30 October 2020

Citation:
Yang X, Sun A, Boadi EO, Li J, He J, Gao X and Chang Y (2020) A Rapid High Throughput Vibration and Vortex-Assisted Matrix Solid Phase Dispersion for Simultaneous Extraction of Four Isoflavones for Quality Evaluation of Semen Sojae Praeparatum. Front. Pharmacol. 11:590587. doi: 10.3389/fphar.2020.590587

Isoflavones (daidzein, daidzin, genistein and genistin) were main chemical components and usually selected as markers for quality control of Traditional Chinese Medicine *semen sojae praeparatum* (SSP). High throughput vibration and vortex-assisted matrix solid phase dispersion and high performance liquid chromatography with diode array detection were developed to simultaneously extract and quantify four isoflavones in SSP. Some parameters influencing extraction efficiency of isoflavones by vortex-assisted matrix solid phase dispersion such as sorbent type, ratio of sample to sorbent, crushing time, vibration frequency, methanol concentration, eluting solvent volume and vortex time were optimized. It was found that the best extraction yields of four isoflavones were obtained when the sample (20 mg) and SBA-3 (40 mg) was crushed by ball mill machine for 2 min at vibration frequency of 800 times per minute. Methanol/water (1.5 ml, 8:2, *v/v*) solution was dropped into the treated sample and vortexed for 3 min. The recoveries of the four isoflavones ranged from 86.1 to 94.8% and all relative standard deviations were less than 5%. A good linearity ($r > 0.9994$) was achieved within the range 0.5–125 μg/ml. It was concluded that the high throughput vibration and vortex-assisted matrix solid-phase dispersion coupled with high performance liquid chromatography was user-friendly extraction and quantification method of multiple isoflavones for quality evaluation of SSP.

Keywords: isoflavones, high throughput ball mill, vibration and vortex-assisted MSPD, *semen sojae praeparatum*, high performance liquid chromatography

INTRODUCTION

Traditional Chinese medicines (TCMs) have been used to treat the diseases for thousands of years. Biological activities of TCMs with therapeutic or toxic effect largely attributed to multiple effects of numerous components in TCMs (Yang et al., 2011). From this perspective, the great attention should be paid to simultaneous extraction and purification of target components from TCM samples for purposes of guaranteeing their efficacy and safety. Furthermore, the procedure for sample preparation is a high-priority step in analytical methods owing to the complexity of TCMs matrices and relatively low active components in TCMs. Conventional sample pretreatment techniques for extracting components in TCM include ultrasonic extraction, heat reflux extraction, soxhlet extraction, solid phase extraction, liquid-liquid extraction and microwave-assisted extraction (Yang et al., 2011; Xiong et al., 2009; Wu et al., 2012; Xiong et al., 2012; Yue et al., 2018; Akbari et al., 2019). However, these procedures are usually time consuming, inefficient, costly and require large volumes of organic solvents. In view of these shortcomings, it is invaluable to develop a simple, green and efficient pre-concentration method for components analysis of TCMs.

Semen sojae praeparatum (SSP) is a famous TCM for treating febrile fever, cold fever, headache, irritability and chest tightness in the Chinese pharmacopoeia (Chinese Pharmacopoeia Commission, 2020). It is made from fermented matured seed of soybean (*Glycine max* (L.) Merr). It was also regarded as an important food material of the traditional Chinese diet by Chinese communities around the world (Guo et al., 2018). According to the Classic books of TCM "Jin-Kui-Yao-Lue" and "ShangHanLun," SSP was the main component of classical formula "Zhi-Zi-Da-Huang Tang," "Zhi-Shi-Zhi-Zi-Chi-Tang," and "Zhi Zi Chi Tang," which have been clinically utilized for the treatment of alcoholic hepatitis, abdominal distension and depression for more than thousand years (Qu et al., 2014; Chen et al., 2015; Wang et al., 2016; Wang et al., 2019). It was reported that SSP could reduce oxygen consumption in the heart muscle, improve microcirculation, and treat tumors and osteoporosis (Qu et al., 2007; Chai et al., 2019). Genistein, genistin, daidzin, and daidzein were the main isoflavones of SSP due to its extensive biological activities. Isoflavones were known as natural phytoestrogens because their structure is similar to the structure of estradiol. They could simulate the bidirectional regulation of endocrine levels (Chai et al., 2017; Yao et al., 2018). Phytoestrogens, especially distributed in legumes, could replace the role of estrogen and prevent the occurrence of adverse reactions to estrogen. Experience in TCM shows that the herbal medicine containing isoflavones were often used to treat the depressurization, hypoglycemic, lipid-lowering, prevent disease of heart head blood-vessel and atherosclerosis, etc. Phytoestrogens in prevention and treatment of menopausal syndrome, osteoporosis after menopause, etc., are similar to the positive role of estrogen replacement therapy (Vitale et al., 2013; Cederroth and Nef, 2009). Therefore, it was meaningful to develop the efficient extraction and quantitative determination method of these bioactive isoflavones for improvement of quality evaluation of SSP (Mocan et al., 2018).

Matrix solid-phase dispersion (MSPD) was proposed and pioneered by Barker (1989), which was a robust technology for simultaneous extraction and clean-up of target components from solid or semi-solid matrices in a single step (Barker et al., 1989). It has been widely applied to detection of various target components in plant matrices, animal tissues, food stuff, sludge, aquatic biota, soil and indoor dust samples (Dorota and Marta, 2019). MSPD is a modified solid-phase extraction (SPE) method that requires manual blending of sample with solid abrasive material before elution of target components with fitting solvent. This technique is too cumbersome to enhance efficiency as well as simplify the analytical procedures. Vortex-assisted MSPD (VA-MSPD), which is based on substitution of the SPE step for a vortex agitation procedure, has demonstrated satisfactory results (Caldas et al., 2013; Escarrone et al., 2014; Hertzog et al., 2015; Du et al., 2018). Subsequently, a vortex-homogenized MSPD (VH-MSPD) has been established to determine halogenated phenolic compounds in seafood (Chen et al., 2016a) and short chain chlorinated paraffin from indoor dust samples (Chen et al., 2016b). This modified MSPD used vortex agitation procedure as mixing and blending steps instead of mortar and pestle for blending and homogenization. Recently, a combination of these two simplified techniques termed as dual-vortex-assisted MSPD, has been used to determine nine parabens in door dust (Chung et al., 2019). In spite of these improvements which made operation more convenient, the aforementioned techniques require transfer procedure between extraction (blending) and clean-up (the SPE) steps, which may result in quantitative loss of analytes. Subsequently, new procedure, balls-in-tube MSPD was proposed and used to determine 133 pesticide residues in apple, peach pear and plum. In this method, all sample preparations were done directly in closed extraction tube with the assistance of steel balls (Kemmerich et al., 2019). Preprocessing process of balls-in-tube MSPD required manual operation which is less efficient and time consuming especially when large batch of samples need be processed. Accordingly, the more robust, high-efficiency and controllable blend method is in great request.

Vibrating ball mill also known as tissuelyser or mixer mill is an equipment with two high-speed large-amplitude arms which grinds, mixes and breaks cells in seconds or minutes through grinding balls impacting and friction within the bowl. It is suitable for milling and homogenizing soft, fibrous, hard and brittle materials in the wet and dry state. Various kinds of samples ranging from plants, food, tissue of human and animals, hair have been crushed using vibrating ball mill (Sun et al., 2018). In other literatures, sea foods and human hair were crushed with ball mill but grinding was manually done with mortar and pestle (Moreda-Pineiro et al., 2012; Miguez-Framil et al., 2013). The extraction (blending) step was accomplished by substituting manual grinding with ball milling.

In present study, it aimed at optimizing a rapid, high throughput MSPD technique for detection of genistein, genistin, daidzein and daidzin in SSP. A modified MSPD method named as high throughput vibration and vortex-assisted matrix solid phase dispersion (VVA-MSPD) was proposed and established to extract and determine four

isoflavones in SSP. All operations were performed in the same extraction tube in high throughput with ball mill machine vibration process. The vortex agitation was used to replace mixing, blending and SPE step, respectively. Besides minimization of manual grinding, the loss of analytes arising from transfer of mixed powder to SPE column or tube was reduced. Furthermore, ball mill has ability to handle dozens of simultaneous samples within seconds or a few minutes in which it might take hours by manual operation with great care and consistency. Additionally, main parameters affecting VVA-MSPD were systematically investigated to optimize this new method. In a nutshell, the newly established VVA-MSPD coupled with high performance liquid chromatography (HPLC) was successfully used to extract and detect the isoflavones for quality evaluation of SSP (**Figure 1**).

MATERIALS AND METHODS

Chemicals and Reagents

HPLC grade methanol and formic acid were purchased from Fisher (Leicestershire, United Kingdom). Genistein, genistin, daidzein and daidzin (purity on HPLC > 98%) were supplied by Chengdu Desite Bio-Technology (Chengdu, China). C18 and Silica were provided by Welch Materials (Chatham Road Ellocott City, United States). SBA-3, TS-1 and MCM-41 were obtained from Nanjing JCNANO Technology (Nanjing, China). Ultrapure water was purified by a Grindi-Q Academic ultra-pure water system (Grindipore, Milford, MA, United States). All other reagents were of analytical grade.

Herbal Plant

Five batches of SSP samples were obtained from the local pharmacy shops. All samples were identified as fermented processed product of matured seed of soybean [*Glycine max* (L.) Merr] by Prof. Yanxu Chang (Tianjin University Traditional Chinese Medicine). The material was ground through 65 mesh sieve, dried at 40°C and stored in a dryer.

Apparatus and HPLC Analysis

Blending was done with a ball mill machine (TJG-25, Techin, China) with an adapter of 2 × 24 well plate that was fixed by fastening device, ceramic beads of 5 mm diameter and 2.0 ml micro-centrifuge tube (Beijing Labgic Technology Co., Ltd., Beijing, China).

Analysis was carried out on Agilent 1260 system (Agilent, Santa Clara, CA, USA) coupled with photodiode array detector (Scanning range 210–400 nm). Separation was performed on an Agilent Eclipse Plus C18 column (4.6 mm × 100 mm, 1.8 μm) connected with a LC-18 guard column (4.6 mm × 12.5 mm, 5 μm) at 30°C. Linear gradient elution system with acetonitrile (A) and ultrapure water (B) was as follows: 5–20% A at 0–10 min, 20–25% A at 10–25 min, 25–45% A at 25–32 min, 45–62% A at 32–37 min, 62–95% A at 40–45 min. Flow rate was set at 0.3 ml/min, injection volume of 2 μL for each run and detection wavelength of 258 nm.

Preparation of Standard Solutions

Concentration of 1 mg/ml of each isoflavone (genistein, genistin, daidzein, and daidzin) in methanol solution (60%, v/v) was prepared. In addition, a mixed standard solution containing 0.25 mg/ml of each isoflavone was prepared and further diluted into range of concentrations for calibration curves.

Vibration and Vortex-Assisted MSPD Procedure

Twenty milligram pulverized SSP and 40 mg sorbent (C18, silica, MCM-41, SBA-3 and TS-1) were mixed in a 2 ml round bottom centrifuge tube. A small ceramic ball was added and the lid covered tightly. The centrifuge tube was put into the adapter and installed on the ball mill machine to homogenize the mixture. Vibration frequency and crushing time were set at 800 times per min and 2 min, respectively. Ceramic ball was removed from the tube after the power settled.

One and an half milliliter methanol/water (8:2, v/v) was gently dropped into the tube and vortexed for 3 min. Thereafter, the solution was centrifuged at 550 g for 10 min. The eluted solvent was then filtered with 0.22 μm nylon membrane before HPLC analysis.

Vibration-Forced MSPD Procedure

Initial procedures were same as outlined in VVA-MSPD method ("*Vibration and Vortex-Assisted MSPD Procedure*" section). After removal of ceramic ball, the mixture was transferred into an SPE column with a sieve plate at the bottom. Another sieve plate was gently blocked on the top with a glass rod. Methanol/water (8:2, v/v) was dropped into the tube to elute the volume to 1.5 ml after connection with a vacuum pump. The elute solvent was centrifuged at 550 g for 10 min and filtered with 0.22 μm nylon membrane before HPLC analysis.

Normal Vortex-Assisted MSPD Procedure

Instead of ball milling procedure, 20 mg pulverized SSP and 40 mg sorbent (SBA-3) were mixed in an agate mortar, ground for 2 min to attain a homogenous mixture and then transferred into a centrifuge tube. Subsequent procedures were same as outlined in VVA-MSPD method.

Ultrasonic Extraction

According to a previous study (Niu et al., 2010), 0.500 g SSP was ultrasonically extracted (40 kHz, 96% power) with 20 ml 50% (v/v) aqueous ethyl alcohol for 50 min. Thereafter, the lost weight was replenished with aqueous ethyl alcohol (50%, v/v) until reaction cooled down to room temperature. The solution was then filtered with 0.22 μm pore membrane before HPLC analysis.

Heating Reflux Extraction

Heating reflux extraction was also performed in accordance with a previous study (Chai et al., 2014). Briefly, 1.000 g SSP was mixed with 25 ml 75% (v/v) aqueous methanol solution in a conical flask. The mixture was weighed, heat refluxed for 30 min, cooled down to room temperature and reweighed. Lost weight was made with 75% methanol (v/v). The solution was then shaken and

transferred to a 25 ml volumetric flask and then brought to volume with 75% (v/v) aqueous methanol. The solution was filtered through a 0.22 μm pore membrane prior to chromatographic analysis.

Optimization of VVA-MSPD Parameters

In order to obtain higher precision, sensitivity and efficiency of extracting isoflavones from SSP, seven parameters which can influence VVA-MSPD procedure were optimized. Specifically, type of sorbent (C18, silica, MCM-41, SBA-3 and TS-1); ratio of sample to sorbent (1:0, 2:1, 1:1, 1:2, and 1:3); crushing time of ball mill (1, 2, 3, and 4 min); vibration frequency of ball mill (500, 800, and 1,000 times per min); concentration of methanol (50, 60, 70, 80, 90, and 100% v/v); volume of eluting solvent (0.5, 0.75, 1, 1.25, 1.5, and 1.75 ml); and vortex time (1, 2, 3, and 4 min) were investigated. Each optimized parameter was further analyzed. All analytical samples were also analyzed in triplicate.

RESULTS AND DISCUSSION

Effect of Related Factors in MSPD

Types of Sorbent

Sorbent type is usually the main factor influencing sensitivity and selectivity of extraction the pre-analytical stage. Normal-phase material (silica), reversed-phase material (C18) and three molecular sieves (MCM-41, SBA-3 and TS-1) were selected to optimize the preferred sorbent. As shown in **Figure 2A**, the efficient of C18 was the least when the same ratios of liquid to solid remained constant. Comparatively, efficiencies of MCM-41, TS-1 and silica were similar whereas the efficient SBA-3 was the most in extracting isoflavones. SBA-3 was the preferred sorbent for further MSPD extraction procedure. SBA-3 has been applied in separation and preconcentration of crystal violet in water sample by a solid phase preconcentration procedure (Azarkohan et al., 2013). However, it has not been used in plants samples and MSPD process. This study indicated that SBA-3 was a suitable molecular sieve sorbent for MSPD procedure. Molecular sieves are crystalline metal aluminosilicates comprising of three-dimensional interconnecting networks of tetrahedral oxides.

Mass Ratio of Sample to Sorbent

Mass ratio is related to both interface area of sample matrix and dispersant as well as elution process. Results shown in **Figure 2B** indicated that peak areas of each target isoflavone increased gradually as mass of SBA-3 increased from 0 to 40 mg (1:0–1:2). With increased amount of SBA-3, more surface area and crystal cavities are available to target isoflavone. Interaction between sample matrix and sorbent gets higher, however, extraction yields of target isoflavone were slightly lower at ratio of sample to sorbent (1:3). Excess sorbent may lead to incomplete elution for the four isoflavones. In this regard, optimal sample to sorbent ratio of 1:2 was selected for further tests.

Crushing Time of Ball Mill

Crushing procedure supplied external forces to pulverize samples and facilitated interactions between samples and sorbents. Results presented in **Figure 2C** showed that the highest extraction efficiency was achieved for 2 min crushing time whereas prolonged crushing (from 3 to 4 min) gradually decreased yields of all isoflavones. Increment of crushing time may cause stronger interaction force between the target isoflavones and the dispersing sorbents, which make elution more difficult. Crushing time of 2 min was adapted for subsequent analysis.

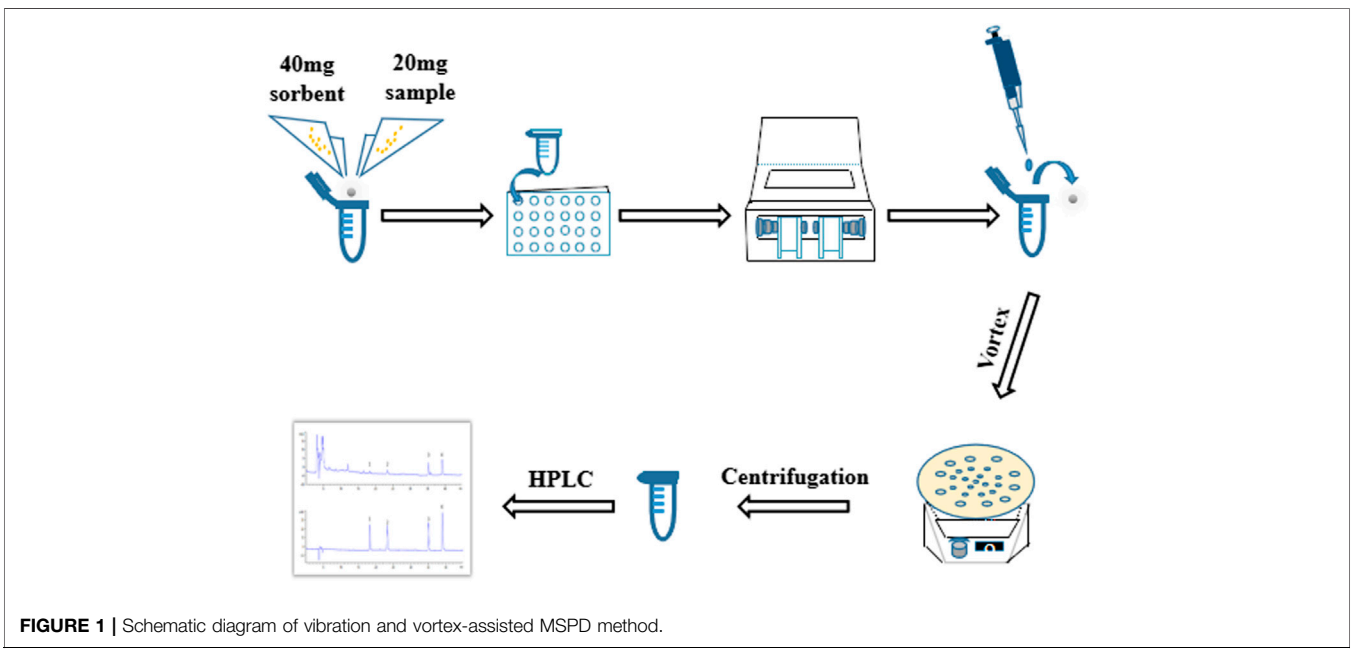

FIGURE 1 | Schematic diagram of vibration and vortex-assisted MSPD method.

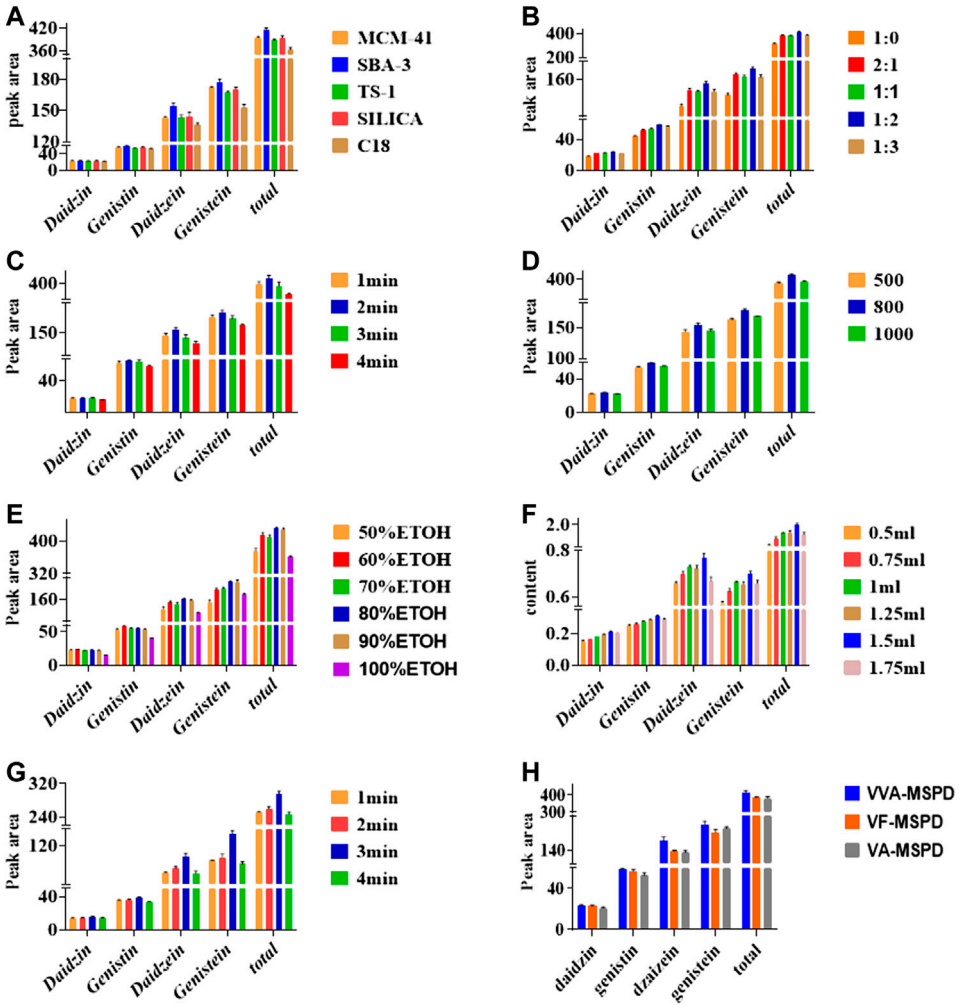

FIGURE 2 | Effects of parameters on extraction of four compounds by single factor using VVA-MSPD technique: **(A)** type of sorbent, **(B)** mass ratio of sample to sorbent, **(C)** crushing time of ball mill, **(D)** vibration frequency of ball mill, **(E)** Selection of Methanol with different concentration, **(F)** volume of eluting solvent, **(G)** vortex time, **(H)** comparison of VVA-MSPD with VF-MSPD and VA-MSPD method. The errors bars represent RSD (n = 3).

Vibration Frequency of Ball Mill

Figure 2D showed that the extraction efficiency of target isoflavones was increased as vibration frequency was enhanced from 500 to 800 times per min. However, frequency of 1,000 times per min reduced extraction efficiency of the four isoflavones. Thus, the optimum vibration frequency was set at 800 times/min.

Selection of Methanol With Different Concentration

Selective and efficient desorption of isoflavones in complex mixtures could be achieved by selecting appropriate solvent polarity. It was found that extraction efficiency of isoflavones increased as methanol/water concentration increased from 50 to 80% (**Figure 2E**). However, there was a slight decrease in yield with 90% methanol/water. Thus, methanol-water

TABLE 1 | Linearity, LOD, LOQ, repeatability and recovery.

Component	Calibration curve	Test range (μg/ml)	r	LOD (μg/ml)	LOQ (μg/ml)	Repeatability (RSD%)	Recovery	
							Average (%)	RSD (%)
Daidzin	y = 8.5072x–7.7909	0.5–125	0.9994	0.13	0.5	2.75	86.1	4.74
Genistin	y = 12.248x–11.247	0.5–125	0.9995	0.12	0.5	2.87	90.6	4.63
Daidzein	y = 11.532x–8.4018	0.5–125	0.9997	0.25	0.8	1.83	94.8	5.00
Genistein	y = 15.683x–11.247	0.5–125	0.9995	0.07	0.2	1.35	93.7	4.24

TABLE 2 | Accuracy and precison of intra-day and inter-day and stability for 24 h.

Component (μg/ml)	Concentration	Intra-day		Inter-day		Stability for 24 h	
		Accuracy (%)	RSD (%)	Accuracy (%)	RSD (%)	Remain (%)	RSD (%)
Daidzin	2	103	2.08	105	1.19	104	2.16
	5	104	4.25	105	2.31	104	3.41
	50	100	1.50	105	3.77	103	1.46
Genistin	2	102	1.66	104	1.06	103	1.73
	5	102	3.89	105	2.22	104	2.87
	50	97.0	1.47	100	1.39	98.7	1.36
Daidzein	2	94.8	3.38	100	1.83	97.30	1.96
	5	103	1.97	96.5	1.10	99.1	3.09
	50	96.2	0.64	96.1	1.61	96.2	1.56
Genistein	2	102	1.35	102	1.35	102	1.58
	5	102	4.82	102	4.32	102	4.85
	50	102	3.07	105	3.77	103	2.87

(80/20, v/v) was the best eluting solvent for VVA-MSPD procedure.

Volume of Eluting Solvent

Besides the choice of suitable solvent, moderate volume of eluting solvent during the desorption in VVA-MSPD procedure is also needed. The highest contents of all isoflavones were obtained when an elution volume was 500 μL (**Figure 2F**).

Vortex Time

Transfer of the target components from solid phase to liquid phase could be accomplished by using optimum vortex. **Figure 2G** showed that each isoflavone had the highest peak at 3 min whereas extraction yields declined at 4 min vortex time. Finally, vortex time was set at 3 min.

Method Validation

To verify the feasibility of the established VVA-MSPD coupled with HPLC-DAD method for determination of isoflavones in SSP, some parameters including limits of detection (LODs), limits of quantitation (LOQs), linearity, precision, repeatability, stability and recovery were estimated **(Tables 1**, **2)**. The established analytical technique was very sensitive with LODs (signal to noise ratio of 3:1) and LOQs (signal to noise ratio of 10:1) ranging from 0.25 to 0.40 μg/ml and 0.80–1.25 μg/ml, respectively. Good linearity ($r > 0.9994$) was achieved within the range 0.5–125 μg/ml. Intra-day precision at three level concentrations (2, 5, 50 μg/ml) ranged from 94.8 to 104% for accuracy and theirs RSDs were below 4.82% RSDs whereas inter-day precision results were 96.5–105% for accuracy and RSDs were below 4.32%. The sample stabilities varied from 96.2 to 104% and theirs RSDs were below 4.85%. The RSDs of repeatability was lower than 2.87%. The recoveries of target components ranged from 86.1 to 94.8% and theirs RSDs were below 5.00%. These results demonstrated that the proposed method could simultaneously quantify the four isoflavones in the sample of SSP.

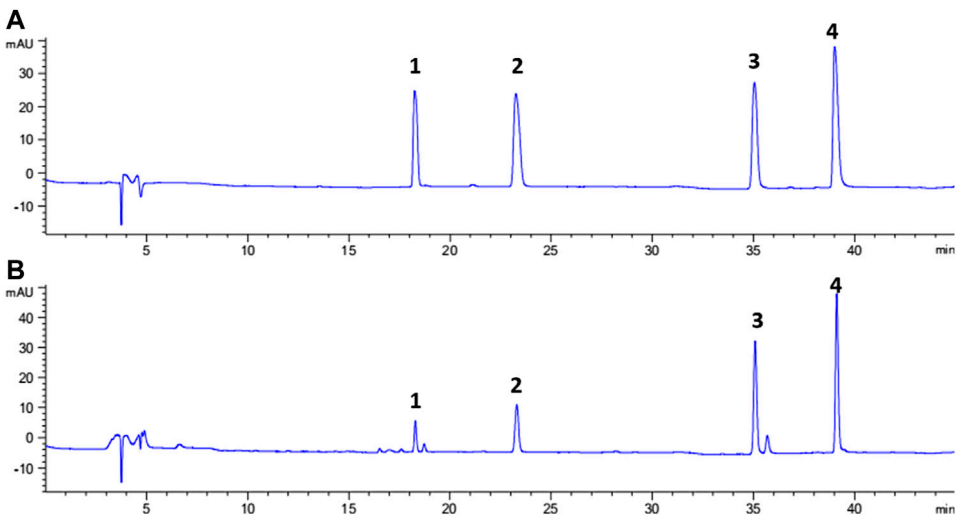

FIGURE 3 | Typical chromatograms of standard solution of four analytes **(A)** and sample solution **(B)**, peak 1: daidzin; peak 2: genistin; peak 3: daidzein; and Peak 4: genistein.

TABLE 3 | Contents of four components in semen sojae praeparatum samples by VVA-MSPD, Ultrasound and Heating reflux method (mg/g, n = 3).

samples	Daidzin	Genistin	Daidzein	Genistein
1	0.21 ± 0.01	0.31 ± 0.01	0.72 ± 0.01	0.76 ± 0.00
1[a]	0.14 ± 0.00	0.22 ± 0.00	0.59 ± 0.01	0.54 ± 0.01
1[b]	0.11 ± 0.00	0.17 ± 0.00	0.49 ± 0.01	0.44 ± 0.01
2	0.29 ± 0.00	0.46 ± 0.01	0.32 ± 0.00	0.47 ± 0.00
3	0.79 ± 0.01	1.30 ± 0.03	2.69 ± 0.05	2.41 ± 0.02
4	0.88 ± 0.02	1.17 ± 0.04	2.07 ± 0.10	1.08 ± 0.05
5	1.56 ± 0.04	1.73 ± 0.04	1.22 ± 0.05	0.82 ± 0.02

[a]*Ultrasound extraction.*
[b]*Heating reflux extraction.*

Comparing VVA-MSPD to Other MSPD Methods

Figure 2H illustrates the extraction efficiencies of the developed VVA-MSPD, VF-MSPD and VA-MSPD methods. Individual peak areas as well as the total contents of all four isoflavones were the highest with our proposed VVA-MSPD method. Comparison with VVA -MSPD and VA-MSPD revealed that homogenization procedure of crushing with ball mill yields better extraction efficiency compared to hand grinding. Moreover, unlike VF-MSPD method, there was no quantitative loss of isoflavones with our developed method due to the absence of a transfer step. Comparatively, extraction efficiency of VVA-MSPD was higher than that of VF-MSPD.

Sample Analysis and Comparison of VVA-MSPD With Traditional Extraction Methods

Representative chromatograms showing the separation of the isoflavones and their contents in each batch of SSP are presented in **Figure 3** and **Table 3**, respectively. Contents of four isoflavones in the five batches of different samples ranged from 0.21 to 1.56 mg/g for daidzin, 0.31–1.73 mg/g for genistin, 0.32–2.69 mg/g for daizein, and 0.48–2.41 mg/g for genistein, respectively. Furthermore, it was found that VVA-MSPD was higher than other conventional extraction methods such as ultrasonic assisted (Niu et al., 2010) and heating reflux (Chai et al., 2014) according to extraction efficiencies for all isoflavones in Samples 1, 1a, and 1b. Comparing to the corresponding yields by ultrasonic assisted extraction, extraction yields of daidzin, genistin daidzein and genistein were increased by 50%, 41%, 22% and 41% usingVVA-MSPD, respectively. The yields of daidzin, genistin daidzein and genistein by VVA MSPD extraction were 1.91, 1.82, 1.47 and 1.73 fold higher than those of daidzin, genistin daidzein and genistein by heating reflux method, respectively. It was concluded that the newly established VVA-MSPD method had outstanding extraction abilities for isoflavones in SSP. Genistein, genistin, daidzin, and daidzein are the main isoflavones of SSP. Among them, genistein is an effective anticancer substance, which could prevent, delay or block the occurrence of cancer through its multi-effect mechanism (Russo et al., 2016). Genistin has a variety of therapeutic effects, such as reducing the risk of osteoporosis and postmenopausal symptoms, anti-inflammatory, anticancer, heart protection, and antioxidant, etc (Liang et al., 2018; Islam et al., 2020). Daidzin could stimulate glucose uptake and has a hypoglycemic effect (Meezan et al., 2005). Daidzein has a protective effect on liver by inhibiting inflammation and oxidative stress and improving lipopolysaccharide induced hepatocyte injury (Yu et al., 2020). Therefore, it was of great significance to establish the efficient extraction and quantitative determination method of these bioactive isoflavones. The newly established VVA-MSPD method could provide an effective reference for the improvement of the quality standard of SSP.

CONCLUSION

A rapid, high throughput and effective VVA-MSPD based on SBA-3 method was successfully developed and extracted four isoflavones in SSP. Crushing sample by ball mill was introduced as a homogenization procedure whereas vortex agitation was used as SPE step in MSPD method. Combination of these two procedures ensured that all extraction processes occurred in the same tube. The quantitative loss of isoflavones was eliminated during transfer step as well as extraction efficiency was improved in the extraction procedure. It was demonstrated that VVA-MSPD coupled with high performance liquid chromatography is a rapid, high throughput and efficient method for extracting and determining the isoflavones and is a useful tool for quality evaluation of SSP.

DATA AVAILABILITY STATEMENT

All datasets presented in this study are included in the article/ supplementary material.

AUTHOR CONTRIBUTIONS

YC, JL, and XG designed the experiment. YC and XY analyzed the experimental data. AS, XY, EB, JL, and JH performed the experiment. YC and XY wrote the manuscript.

FUNDING

This research was supported by the National Key R&D Program of China (2019YFC1711000), National Natural Science Foundation of China (81973704 and 81374050), Science and Technology Program of Tianjin (No. 19ZYPTJC00060).

REFERENCES

Akbari, S., Abdurahman, N. H., and Yunus, R. M. (2019). Optimization of saponins, phenolics, and antioxidants extracted from fenugreek seeds using microwave-assisted extraction and response surface methodology as an optimizing tool. *Comptes Rendus Chimie* 22(11–12), 714–727. doi:10.1016/j.crci.2019.07.007

Azarkohan, A., Shemirani, F., Alvand, M., and Blin, J. L. (2013). Fast analysis of water samples for trace amount of crystal violet dye based on solid phase extraction using nanoporous SBA-3 prior to determination by fiber optic-linear array detection spectrophotometry. *J. Chem.* 2013, 1. doi:10.1155/2013/530843

Barker, S. A., Long, A. R., and Short, C. R. (1989). Isolation of drug residues from tissues by solid phase dispersion. *J. Chromatogr. A* 475, 353–361. doi:10.1016/S0021-9673(01)89689-8

Caldas, S. S., Bolzan, C. M., Menezes, E. J. D., Escarrone, A. L. V., Martins, C. M. G., Bianchini, A., et al. (2013). A vortex-assisted MSPD method for the extraction of pesticide residues from fish liver and crab hepatopancreas with determination by GC–MS. *Talanta* 112, 63–68. doi:10.1016/j.talanta.2013.03.054

Cederroth, C. R., and Nef, S. (2009). Soy, phytoestrogens and metabolism: a review. *Mol. Cell. Endocrinol.* 304 (1–2), 30–42. doi:10.1016/j.mce.2009.02.027

Chai, C., Cui, X. B., Dai, Z. L., Yu, S., Shan, C. X., Qi, H. W., et al. (2014). Content determination of isoflavones in semen sojae praeparatum and the optimization of the fermentation process. *Chin. J. Exp. Trad. Med. Formulae* 20, 72–76. doi:10.1109/CCM.2003.1194327

Chai, C., Cui, X., Shan, C., Yu, S., and Wen, H. (2017). Contents variation analysis of free amino acids, nucleosides and nucleobases in semen sojae praeparatum fermentation using UFLC-QTRAP MS. *Biomed. Chromatogr.* 31, e3985. doi:10.1002/bmc.3985

Chai, C., Cui, X., Shan, C., Yu, S., Wang, X., and Wen, H. 2019). Simultaneous characterization and quantification of varied ingredients from *sojae semen praeparatum* in Fermentation Using UFLC-TripleTOF MS. *Molecules* 24(10), 1864. doi:10.3390/molecules24101864

Chen, K. L., Bi, K. S., Han, F., Zhu, H. Y., and Yin, R. (2015). Evaluation of the protective effect of Zhi-Zi-da-Huang decoction on acute liver injury with cholestasis induced by α-naphthylisothiocyanate in rats. *J. Ethnopharmacol.* 172. doi:10.1016/j.j-ep.2015.06.04310.1016/j.jep.2015.06.043

Chen, Y.-H., Chang, C.-Y., and Ding, W.-H. (2016a). Vortex-homogenized matrix solid-phase dispersion for the extraction of short chain chlorinated paraffins from indoor dust samples. *J. Chromatogr. A* 1472, 129–133. doi:10.1016/j.chroma.2016.10.048

Chen, J.-M., Yang, C.-C., Chung, W.-H., and Ding, W.-H. (2016b). Vortex-homogenized matrix solid-phase dispersion coupled with gas chromatography—electron-capture negative-ion mass spectrometry to determine halogenated phenolic compounds in seafood. *RSC Adv.*, 6, 96510. doi:10.1039/c6ra20680h

Chinese Pharmacopoeia Commission (2020). *Pharmacopoeia of the People's Republic of China*, Vol. 1. Beijing, China: China Medical Science and Technology Press.

Chung, W. H., Lin, J. S., and Ding, W. H. (2019). Dual-vortex-assisted matrix solid-phase dispersion coupled with isotope-dilution ultrahigh-performance liquid chromatography-high resolution mass spectrometry for the rapid determination of parabens in indoor dust samples. *J. Chromatogr. A*. 1605, 460367. doi:10.1016/j.chroma.2019.4 60367

Dorota, W., and Marta, G. (2019). New insights into the application of MSPD in various fields of analytical chemistry. *Trac. Trends Anal. Chem.* 112, 29–51. doi:10.1016/j.trac.2018.12.028

Du, K. Z., Li, J., Bai, Y, An, M. G., Gao, X. M., and Chang, Y. X. (2018). A green ionic liquid-based vortex-forced MSPD method for the simultaneous determination of 5-HMF and iridoid glycosides from Fructus Corni by ultrahigh performance liquid chromatography. *Food Chem.* 244, 190–196. doi:10.1016/j.foodchem.2017.10.0.057

Escarrone, A. L. V., Caldas, S. S., Soares, B. M., Martins, S. E., Primel, E. G., and Maia Nery, L. E. (2014). A vortex-assisted MSPD method for triclosan extraction from fish tissues with determination by LC-MS/MS. *Anal. Methods* 6, 8306–8313. doi:10.1039/c4ay01518e

Guo, H., Zhang, Z., Yao, Y., Liu, J., Chang, R., Liu, Z., et al. (2018). A new strategy for statistical analysis-based fingerprint establishment: application to quality assessment of Semen sojae praeparatum. *Food Chem.* 258, 189–198. doi:10.1016/.foo-dchem.2018.03.06710.1016/j.foodchem.2018.03.067

Hertzog, G. I., Soares, K. L., Caldas, K. L., and Primel, E. G. (2015). Study of vortex-assisted MSPD and LC-MS/MS using alternative solid supports for pharmaceutical extraction from marketed fish. *Anal. Bioanal. Chem.* 407(16), 4793–4803. doi:10.1007/s00 216-015-8685-3

Islam, A., Islam, M., Hasan, M., and Akanda, M. (2020). The potential health benefits of the isoflavone glycoside genistin. *Arch Pharm. Res.* 434, 14–63. doi:10.1007/s12 272-020-01233-2

Kemmerich, M., Demarco, M., Bernardi, G., Prestes, O. D., Adaime, M. B., and Zanella, R. (2019). Balls-in-tube matrix solid phase dispersion (BiT-MSPD): an innovative and simplified technique for multiresidue determination of pesticides in fruit samples. *J. Chromatogr. A*. 110, 395–401. doi:10.1016/j.chroma.2019.460640

Liang, Y., Zhao, W., Wang, C., Wang, Z., Wang, Z., and Zhang, J. (2018). A comprehensive screening and identification of genistin metabolites in rats based on multiple metabolite templates combined with UHPLC-HRMS analysis. *Molecules* 23, 1862. doi:10.3390/molecules23081862

Meezan, E., Meezan, E. M., Jones, K., Moore, R., Barnes, S., and Prasain, J. K. (2005). Contrasting effects of puerarin and daidzin on glucose homeostasis in mice. *J. Agric. Food Chem.* 53, 8760–8767. doi:10.1021/jf058105e

Míguez-Framil, M., Cabarcos, P., Tabernero, M. J., Bermejo, A. M., Bermejo-Barrera, P., and Moreda-Piñeiro, A. (2013). Matrix solid phase dispersion assisted enzymatic hydrolysis as a novel approach for cocaine and opiates isolation from human hair. *J. Chromatogr. A* 1316, 15–22. doi:10.1016/j.chroma.2013.09.063

Mocan, A., Carradori, S., Locatelli, M., Secci, D., Cesa, S., Mollica, A., et al. (2018). Bioactive isoflavones from Pueraria lobata root and starch: different extraction techniques and carbonic anhydrase inhibition. *Food Chem. Toxicol.* 112, 441–447. doi:10.1016/j.fct.2017.08.009

Moreda–Pineiro, J., Alonso-Rodriguez, E., Romaris-Hortas, V., Moreda-Pineiro, A., Lopez-Mahia, P., Muniategui-Lorenzo, S., et al. (2012). Assessment of the bioavailability of toxic and non-toxic arsenic species in seafood samples. *Food Chem.* 130, 552–560. doi:10.1016/j.foodchem.2011.07.071

Niu, L. Y., Shi, S. Q., Liu, M. Y., Wang, F., and Wang, X. G. (2010). Processing of *semen sojae praeparatum*. *Chin. Trad. Patent Med.* 32, 1372–1376. doi:10.19540/j.cnki.cjcmm.20190321.301

Qu, K. K., Zhao, L. S., Luo, X. Y., Zhang, C. N., Hou, Y. P., Bi, K. S., et al. (2014). An LC–MS method for simultaneous determination of five iridoids from Zhi-zi-chi Decoction in rat brain microdialysates and tissue homogenates: towards an in depth study for its antidepressive activity. *J. Chromatogr. B* 965, 206–215 doi:10.1016/j.jchromb. 2014.03.032

Qu, L. P., Fan, G. R., Peng, J. Y., and Mi, H. M. (2007). Isolation of six isoflavones from Semen sojae praeparatum by preparative HPLC. *Fitoterapia* 78, 200–204. doi:10.1016/j.fitote. 2006.11.002

Russo, M., Russo, G. L., Daglia, M., Kasi, P. D., Ravi, S., Nabavi, S. F., et al. (2016). Understanding genistein in cancer: the "good" and the "bad" effects: a review. *Food Chem.* 196, 589–600. doi:10.1016/j.foodchem.2015.09.085

Sun, S., Yao, K., Zhao, S., Zheng, P., Wang, S., Zeng, Y., et al. (2018). Determination of aflatoxin and zearalenone analogs in edible and medicinal herbs using a group-specific immunoaffinity column coupled to ultra-high-performance liquid chromatography with tandem mass spectrometry. *J. Chromatogr. B*, 1092, 228–236. doi:10.1016/j.jchromb.2018.06.012

Vitale, D. C., Piazza, C., Melilli, B., Drago, F., and Salomone, S. (2013). Isoflavones: estrogenic activity, biological effect and bioavailability. *Eur. J. Drug Metab. Pharmacokinet.* 38 (1), 15–25. doi:10.1007/s13318-012-0112-y

Wang, H. Q., Zhu, Y. X., Liu, Y. M., Wang, R. L., and Wang, S. F. (2019). Rapid discovery and identification of the anti-inflammatory constituents in Zhi-Shi-Zhi -Zi-Chi-Tang. *Nat. Med. China* 17, 308–320. doi:10.1016/s1875-5364(19)30035-4

Wang, J., Shi, Q., Wu, C., and Feng, F. (2016). Dynamic metabolic profile of Zhi-Zi-Da-Huang decoction in rat urine based on hybrid liquid chromatography-mass spectrometry coupled with solid phase extraction. *J. Chromatogr. B* 1036–1037, 100–113. doi:10.1016/j.jchromb.2016.10.003

Wu, X., Zhu, B. H., Lu, L., Huang, W., and Pang, D. (2012). Optimization of a solid phase extraction and hydrophilic interaction liquid chromatography-tandem mass spectrometry method for the determination of metformin in dietary

supplements and herbal medicines. *Food Chem.* 133, 482–488. doi:10.1016/j.foodchem10.1016/j.foodchem.2012.01.005

Xiong, A.-Z., Yang, L., Zhang, F., Yang, X.-J., Wang, C.-H., and Wang, Z.-T. (2009). Determination of total retronecine esters-type hepatotoxic pyrrolizidine alkaloids in plant materials by pre-column derivatization high-performance liquid chromatography. *Biomed. Chromatogr.* 23, 665–671. doi:10.1002/bmc.1172

Xiong, H., Gong, X., and Qu, H. (2012). Monitoring batch-to-batch reproducibility of liquid-liquid extraction process using in-line near-infrared spectroscopy combined with multivariate analysis. *J. Pharm. Biomed. Anal.* 70, 178–187. doi:10.1016/j.jpba.2012.06.028

Yang, X., Yang, L., Xiong, A., Li, D., and Wang, Z. (2011). Authentication of *Senecio scandens* and *S. vulgaris* based on the comprehensive secondary metabolic patterns gained by UPLC-DAD/ESI-MS. *J. Pharm. Biomed. Anal.* 56, 165–172. doi:10.1016/j.jpba.2011.05.004

Yao, Y., Ma, X., Li, T., Guo, H., Chang, R., Liu, J., et al. (2018). Quantification of isoflavone glycosides and aglycones in rat plasma by LC-MS/MS: troubleshooting of interference from food and its application to pharmacokinetic study of *Semen Sojae Praeparatum* extract. *J. Pharm. Biomed. Anal.* 161, 444. doi:10.1016/j.jpba.2018.09.011

Yu, Z., Yang, L., Deng, S., and Liang, M. (2020). Daidzein ameliorates LPS-induced hepatocyte injury by inhibiting inflammation and oxidative stress. *Eur. J. Pharmacol.* 885, 173399. doi:10.1016/j.ejphar.2020.173399

Yue, Y., Qiu, Z.-D., Qu, X.-Y., Deng, A.-P., Yuan, Y., Huang, L.-Q., and Lai, C.-J. -S. (2018). Discoursing on Soxhlet extraction of ginseng using association analysis and scanning electron microscopy. *Journal of Pharmaceutical Analysis* 8, 312–317. doi:10.1016/j.jpha.2018.08.003

Conflict of Interest: The authors declare that the research was conducted in the absence of any commercial or financial relationships that could be construed as a potential conflict of interest.

frontiers in Pharmacology

ORIGINAL RESEARCH
published: 18 November 2020
doi: 10.3389/fphar.2020.558731

Metabonomics Study on Serum Characteristic Metabolites of Psoriasis Vulgaris Patients With Blood-Stasis Syndrome

Li Li[1], Dan-ni Yao[2], Yue Lu[1], Jing-wen Deng[2], Jian-an Wei[1], Yu-hong Yan[2], Hao Deng[2], Ling Han[1]* and Chuan-jian Lu[2]**

[1] Molecular Biology and Systems Biology Team of Chinese Medicine, Guangdong Provincial Hospital of Chinese Medicine (The Second Clinical College of Guangzhou University of Chinese Medicine, Guangdong Provincial Academy of Chinese Medical Sciences), Guangzhou, China, [2] Department of Dermatology, Guangdong Provincial Hospital of Chinese Medicine (The Second Clinical College of Guangzhou University of Chinese Medicine, Guangdong Provincial Academy of Chinese Medical Sciences), Guangzhou, China

OPEN ACCESS

Edited by:
Peng Li,
University of Macau, China

Reviewed by:
Helen Skaltsa,
National and Kapodistrian University of Athens, Greece
Xiansheng Meng,
Liaoning University of Traditional Chinese Medicine, China
Guoan Luo,
Tsinghua University, China

***Correspondence:**
Chuan-jian Lu
Luchuanjian888@vip.sina.com
Ling Han
Linghan36@163.com
Li Li
Lily_vvv@163.com

Specialty section:
This article was submitted to Ethnopharmacology, a section of the journal Frontiers in Pharmacology

Received: *03 May 2020*
Accepted: *16 September 2020*
Published: *18 November 2020*

Citation:
Li L, Yao D-n, Lu Y, Deng J-w, Wei J-a, Yan Y-h, Deng H, Han L and Lu C-j (2020) Metabonomics Study on Serum Characteristic Metabolites of Psoriasis Vulgaris Patients With Blood-Stasis Syndrome. Front. Pharmacol. 11:558731. doi: 10.3389/fphar.2020.558731

Psoriasis is a chronic, refractory, systemic inflammatory skin disease. Traditional Chinese medicine (TCM) shows unique advantage in the treatment of psoriasis based on syndrome differentiation. An untargeted high-throughput metabonomics method based on liquid chromatography coupled to mass spectrometry was applied to study the serum metabolic characteristics in different TCM syndrome types in patients with psoriasis vulgaris (PV), and to discover potential serum biomarkers for its pathogenesis on the endogenous metabolite differentiation basis. The serum metabolic profiles of 45 healthy controls and 124 patients with PV (50 in the blood-stasis group, 30 in the blood-heat group, and 44 in the blood-dryness group) were acquired. The raw spectrometric data were processed using multivariate statistical analysis, and 14 biomarkers related to TCM syndrome differentiation and psoriasis types were screened and identified. The blood-stasis syndrome group showed abnormal lipid metabolism, which was characterized by a low level of phosphatidylcholine (PC) and a high level of lysophosphatidylcholine (LPC). We propose that platelet-activating factor can be applied as a potential biomarker in clinical diagnosis and differentiation of PV with blood-stasis syndrome. The difference in the serum metabolites among PV types with different TCM syndromes and healthy control group illustrated the objective material basis in TCM syndrome differentiation and classification of psoriasis.

Keywords: metabonomics, psoriasis, traditional Chinese medicine syndrome, blood-stasis syndrome, biomarker

INTRODUCTION

Psoriasis is a chronic, refractory, systemic inflammatory skin disease, and it is also quite complex. The etiology and pathogenesis are unclear, and it is challenging to cure (Nestle et al., 2009). In China, long-term clinical practice has proved that traditional Chinese medicine (TCM) syndrome differentiation treatment of psoriasis vulgaris (PV) can achieve long-lasting effects, delay recurrence,

and thus improve quality of life (Lu et al., 2012). In recent years, psoriasis has been mostly treated by syndrome depending TCM therapy from the view of blood in clinical practice in China. According to the epidemiological investigation of modern medicine and the consensus of TCM, the TCM syndromes in PV mainly include blood-stasis syndrome, blood-heat syndrome, and blood-dryness syndrome (Zhang et al., 2002; Zhang et al., 2009; He et al., 2014). On the basis of clinical epidemiological investigation, 2651 cases of psoriasis vulgaris were analyzed by investigation, multicenter, and large sample study. The TCM syndromes in psoriasis vulgaris mainly include the 3 types, and other syndromes were rarely seen, covering 0.6%. The concurrent syndromes mainly involve dampness, heat, blood stasis, and toxin (Zhang et al., 2008). The literature research, in total, 920 qualified articles from 1979 to 2010, also shows the distribution of Chinese medical syndrome in PV (Lu et al., 2010). The TCM evidence-based clinical practice guide for psoriasis vulgaris issued by the dermatology branch of Chinese Association of traditional Chinese medicine (2013) is also classified and defined in this way (Dermatology branch of Chinese Association of traditional Chinese Medicine, 2013). In the Guangdong Provincial Bureau of quality and technical supervision: psoriasis vulgar syndrome differentiation standard of traditional Chinese medicine, local standards of Guangdong Province (Guangdong Provincial Bureau of quality and technical supervision, 2018), shows that psoriasis is treated by blood, and the basic syndrome types are blood heat syndrome, blood stasis syndrome, and blood dryness syndrome. Two or three syndrome types can appear simultaneously in clinic, and other concurrent syndromes can be combined. The TCM syndrome diagnosis system of psoriasis vulgaris has been established, which can be used by clinicians for free (website: http://183.62.15.51:8912/index.html).

TCM syndrome differentiation diagnosis in the clinic is based on the comprehensive judgment considering many factors, such as the color and thickness of the skin lesion, the status of the tongue, the mood and mental state of the patient, and the whole metabolic state of the patient. It relies on the doctor's clinical experience and subjective judgment. Therefore, it is necessary to study the objective basis of TCM syndrome differentiation in psoriasis. The development of omics techniques in systems biology provides powerful tools for understanding and interpretation of the TCM theory (Alessandro et al., 2012).

Metabonomics is a high-throughput omics technique, which is a new technique to analyze all low molecular weight metabolites in an organism or a cell qualitatively and quantitatively. Compared with other omics techniques, metabonomics reflects the final metabolic status of individuals more directly and comprehensively in response to pathophysiological stimuli or genetic modification (Nicholson et al., 1999). The systematic features of metabonomics are similar to the holistic view of TCM. Applying metabonomics approaches to material basis study of TCM syndrome differentiation is a beneficial attempt. Metabonomics technology research based on liquid chromatography coupled with mass spectrometry (LC-MS) and gas chromatography coupled with mass spectrometry (GC-MS) has been applied in the TCM syndrome differentiation studies and biomarker identification in coronary heart disease (Zhou et al., 2019) and rheumatoid arthritis (Gu et al., 2012). However, few studies were undertaken to explore the objective material basis of the TCM syndrome differentiation in patients with psoriasis. In this study, metabonomics strategy based on ultra-performance liquid chromatography coupled with quadruple-time-of-flight mass spectrometry (UPLC/Q-TOF-MS) was applied to investigate and compare the serum metabolic changes in patients with PV with different TCM syndrome types and healthy controls, as well as to discover the potential biomarkers to distinguish TCM syndromes.

MATERIALS AND METHODS

Human Serum Collection

Outpatients (124) confirmed to have PV were recruited from the dermatology outpatient department of Guangdong Provincial Hospital of Chinese Medicine from April 2014 to July 2015. Healthy volunteers (45) were recruited from the physical examination department of Guangdong Provincial Hospital of Chinese Medicine. According to the diagnosis of TCM syndrome type, all patients with PV were divided into blood-heat type, blood-stasis type, and blood-dryness groups. The diagnostic criteria were based on the Western medicine diagnosis referring to the Guidelines of psoriasis treatment (2008), recommended by the American Academy of Dermatology. The TCM syndrome differentiation criteria referred to the judgment standard of TCM syndromes of psoriasis according to the "People's Republic of China TCM Industry Standards" and "Principles of Clinical Research Guidelines for New Chinese Drugs." Patients with PV with moderate to severe lesions (PASI > 10 or BSA > 10%) who agreed to sign informed consent were included. The study protocol (No. B2010-08-01) was approved by the institutional ethics committee of Guangdong Provincial Hospital of Chinese Medicine, and all the patients included in this study understood and signed informed consent.

Serum samples (124) of patients with PV (50 cases of the blood-stasis syndrome, 44 cases of the blood-dryness syndrome, 30 cases of the blood-heat syndrome) and 45 serum samples of healthy controls were collected and included in the study. Clinical characteristics of patients and controls are described in **Table 1**. Serum (4 mL) from all volunteers was collected on an empty stomach from the elbow vein blood in the morning, centrifuged, and extracted. The upper serum layer was stored at -80°C for further tests.

TABLE 1 | Clinical characteristics of psoriasis vulgari patients with different TCM syndromes and healthy controls.

TCM Syndrome (Cases)	Male age (Average ± SD) (Cases)	Female age (Average ± SD) (Cases)
Blood-stasis(50)	42.0 ± 9.8 (30)	44.2 ± 10.9(20)
Blood-dryness(44)	42.9 ± 11.6 (26)	44.3 ± 13.6(18)
Blood-heat(30)	43.3 ± 9.4 (24)	51.2 ± 18.8 (6)
Healthy control(45)	40.1 ± 9.1 (24)	41.2 ± 8.1 (21)

Reagents and Instruments

Acetonitrile was purchased from Merck (HPLC grade, Darmstadt, Germany). Formic acid was purchased from Fluka (Analytical grade, Buchs, Switzerland). Ultrapure water (18.2 MΩ) was prepared using a Milli-Q water purification system (Millipore, Bedford, MA, USA).

An ultra-performance liquid chromatography (Waters ACQUITY UPLC, USA) coupled with quadruple-time-of-flight mass spectrometry (AB SCIEX Triple TOF™ 5600, USA) was applied for serum analysis. Vortex mixer was purchased from Qilinbeier (VORTEX-5, Jiangsu, China), and the centrifuge was purchased from Beckman Coulter (AllegraTM X-22, Beckman Coulter Corporation, USA). Analyst® TF (Version 1.5, AB SCIEX, USA), MarkerView™ (Version 1.2, AB SCIEX, USA), and Simca-P software (version 14.1, Umetrics, Umeå, Sweden) were applied.

Sample Preparation

The frozen serum samples were placed in the 4°C refrigerator for freeze-thawing and vortexed for 2–5 seconds. Serum (150 μL) was transferred into a 1.5 mL Eppendorf tube and kept on ice, 600 μL of pure ice-cold acetonitrile was added into the tube and vortexed for 2 min, then centrifuged at 13,000 rpm for 20 min at 4°C. The whole supernatant was transferred into a 96-well collection plate for LC-MS analysis.

LC-MS Analysis

Chromatographic separation was carried out using an ACQUITY BEH C18 analytic column (100× 2.1 mm, 1.7 μm, Waters); column temperature was set at 40°C. All metabolites were separated *via* linear gradient elution using water with 0.1% formic acid and acetonitrile with 0.1% formic acid as the mobile phase. The flow rate was 0.4 mL/min. The temperature of auto-sampler was set at 4°C and the sample injection volume was 2 μL.

The mass spectrometry parameters were as follows: MS scan range was set to m/z 100 to 1000 in positive electrospray ionization (ESI+) mode, ion source voltage flow (ISVF) was set to 5500, source temperature was set to 650°C, and collision energy (CE) was set to 10. The information-dependent acquisition function was enabled to obtain high resolution, high mass accuracy in the MS/MS spectra. All the acquired m/z data were real-time corrected using an independent reference to ensure higher accuracy.

Raw Data Processing and Statistical Analysis

The raw spectrometric data were collected using the Analyst® TF software. All of the raw data were imported to MarkerView™ software, and the metabolic profiling was processed for peak recognition and matching. Noise filtering, data normalization, and the peak list data were loaded to Simca-P software for multivariate statistical analysis. Unsupervised analysis (principal components analysis, PCA) and supervised analysis (partial least squares discriminate analysis, PLS-DA, and orthogonal signal correction partial least squares discriminate analysis, OPLS-DA) were applied to distinguish different TCM syndrome types of psoriasis.

Identification of Potential Biomarkers

According to the value of variable importance in the projection (VIP) in the PLS-DA model, combined with t-test results, the potential candidate biomarkers were selected. Compounds were identified according to mass spectrometry isotope matching and the results of a database search in the human metabolome database (HMDB).

RESULTS

Metabolic Profiling of Patients With PV With Different TCM Syndrome Types and Healthy Controls Was Established Using UPLC/Q-TOF-MS

UPLC/TOF-MS was applied to investigate the serum metabolic profiling of patients with psoriasis with different TCM syndrome types and healthy controls. The total ion chromatograms (TIC) operating under positive ion mode are shown in **Figure 1**. There were differences among the metabolic profiling of patients with PV with blood-stasis, blood-heat, and blood-dryness and the healthy control group. This suggested that there were a variety of metabolites in the serum related to the differentiation of TCM syndrome types in PV.

Methodology Investigation

The sample pool was prepared by mixing 10 μL serum from each sample of all groups. According to the sample preparation method, a quality control (QC) sample was prepared for precision and stability investigation. One sample was injected six times, 10 peaks were selected from the TIC, and the retention time and ion response were stable. The relative standard deviation (RSD) of the peak intensity and the number of peaks of the six injections were less than 10%, indicating that the precision of the instrument was good and met the analysis requirements.

QC sample was prepared for stability test. A QC sample was set for injection every 10–15 samples, and all metabonomics samples were continuously injected. RSD of peak intensity and peak number of the six injections was less than 15%, indicating that the instrument and method were stable and reliable.

The Multivariate Statistical Analysis Results for Patients With PV With Different TCM Syndrome Types

The raw data of all groups were processed using MarkerView software for peak recognition and matching. Noise filtering, data normalization, and 3982 retention time_mass-to-charge ratio (RT_m/z) variables were screened. Isotope peaks were removed to avoid repeated calculation, and 2454 variables were loaded to Simca-P software for multivariate statistical analysis. PCA and PLS-DA, OPLS-DA were applied to study the clustering of samples of different syndrome types. The score map shows the correlation of samples in the coordinate map and the samples with similar metabolic status accumulated together. In contrast, different samples were distributed in different areas separately;

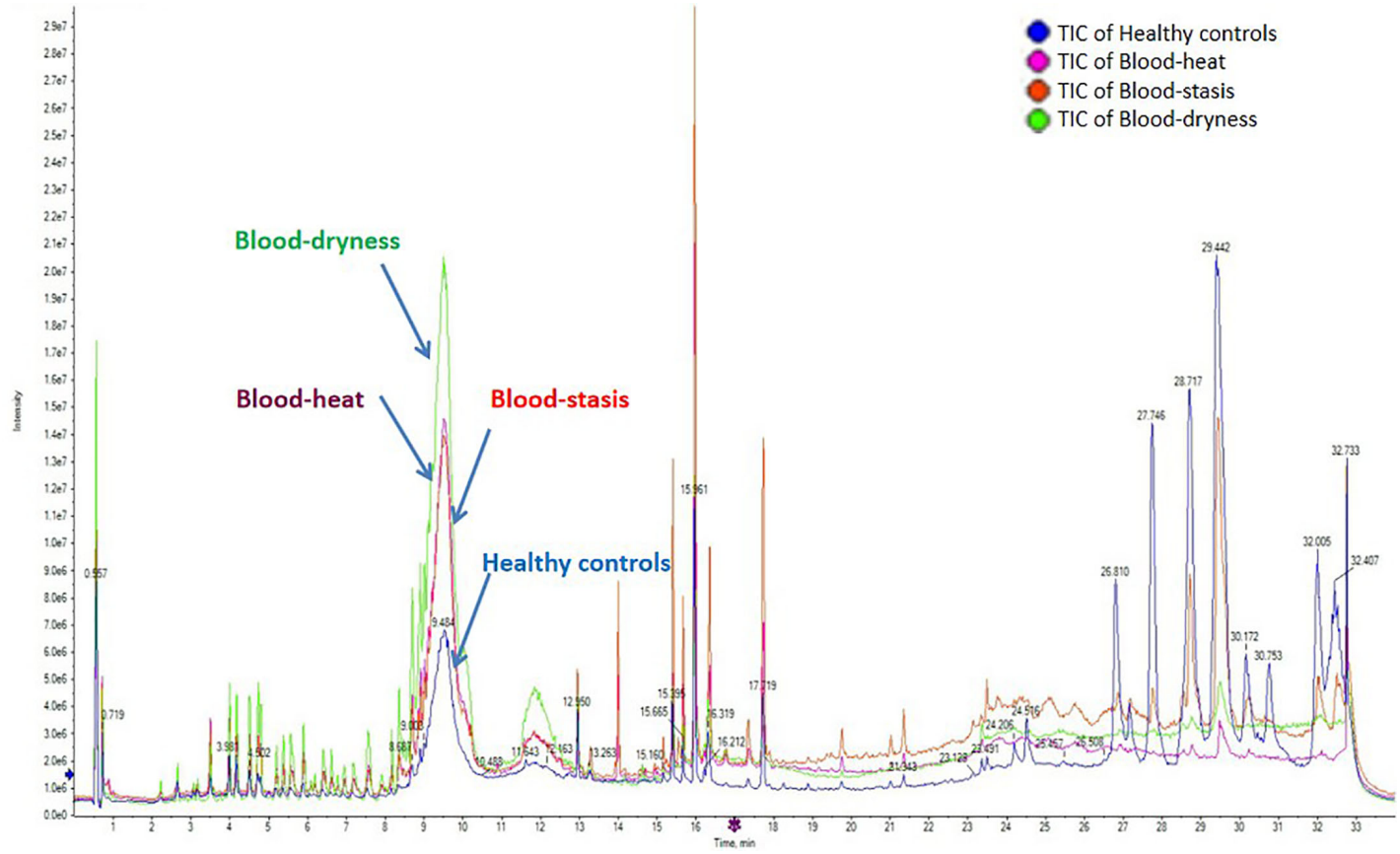

FIGURE 1 | The total ion chromatograms (TIC) operating under positive ion mode. There were differences among the metabolic profilings of psoriasis vulgaris patients groups with blood-stasis, blood-heat, and blood-dryness and healthy control group.

therefore, the scores map could classify the experimental group samples according to metabolic differences. As shown in **Figure 2A**, blood-stasis group, blood-heat group, blood-dryness group, and healthy control group were clustered separately, indicating that there were significant metabolic differences among these groups. Loading map could reveal the components that contributed to the classification. The farther away from the origin, the larger the number of components that contributed to the classification. These components could be considered as potential biomarkers that interfere with normal physiological metabolism. In **Figure 2C**, the dots far away from the origin in the loading map were screened as the potential biomarkers. Permutation test with 100 iterations results showed that the predictive ability of this model was excellent. The model was validated as not over-fitting (**Figure 2B**).

Potential Biomarker Screening and Identification

According to the PLS-DA pattern recognition results, the VIP values were sorted. Combined with the t-test, the significant difference ($P < 0.05$) of metabolites among the four groups were screened, and the candidate compounds from the loading map (**Figure 2C**) were identified. TOF-MS provided the precise molecular weight of the screened metabolites. The search for the compounds in the human metabolome database (HMDB), combined with isotopic molecular weight, mass spectrometry ionization fragmentation patterns, and biological significance, and the potential biomarkers were identified.

Fourteen significant metabolites in patients with psoriasis with different TCM syndromes and healthy controls were considered as potential biomarkers, as shown in **Table 2**. The compounds were mainly related to coagulation, mental function, inflammation, antibacterial action, and detoxification. Lipid compounds play an essential role in the development of psoriasis (Pietrzak et al., 2010; Pietrzak et al., 2019). In this study, all the psoriasis groups showed an abnormal lipid metabolism, which was characterized by the high level of lysophosphatidylcholine (LPC) (**Figure 3**) and low level of phosphatidylcholine (PC) (**Figure 3**) compared to the healthy control group.

Receiver Operating Characteristic Curve

One goal of metabonomic studies is biomarker discovery, which aims to identify a metabolite or a set of metabolites capable of classifying conditions or diseases with high sensitivity (true-positive rate) and specificity (true negative rate). ROC curve analysis is generally considered to be the gold standard for the assessment of biomarker performance. A compound was selected from the loading map (**Figure 2C**) and identified as the platelet-activating factor (PAF). PAF was evaluated using a classical ROC curve analysis. **Figure 4** shows the results of the ROC curve of PAF in the blood-stasis group. Compared to the healthy control group, the area under the curve (AUC) was 0.995 (**Figure 4A-1**), and the boxplot of two groups is shown in **Figure 4A-2**. Compared to the blood-dryness group, AUC was 0.962 (**Figure 4B-1**), and the boxplot of the two groups is shown in **Figure 4B-2**. Compared to the blood-heat group, AUC was 0.9 (**Figure 4C-1**), and the boxplot of the two groups is shown in **Figure 4C-2**. All AUC values were higher than 0.9, suggesting that PAF had good predictive ability in distinguishing the blood-stasis group from the other groups. PAF might be a valuable biomarker in patients with psoriasis with blood-stasis syndrome.

DISCUSSION

There were 14 potential biomarkers in **Table 2**, mainly involved in glycerophospholipid metabolism pathway, also related to

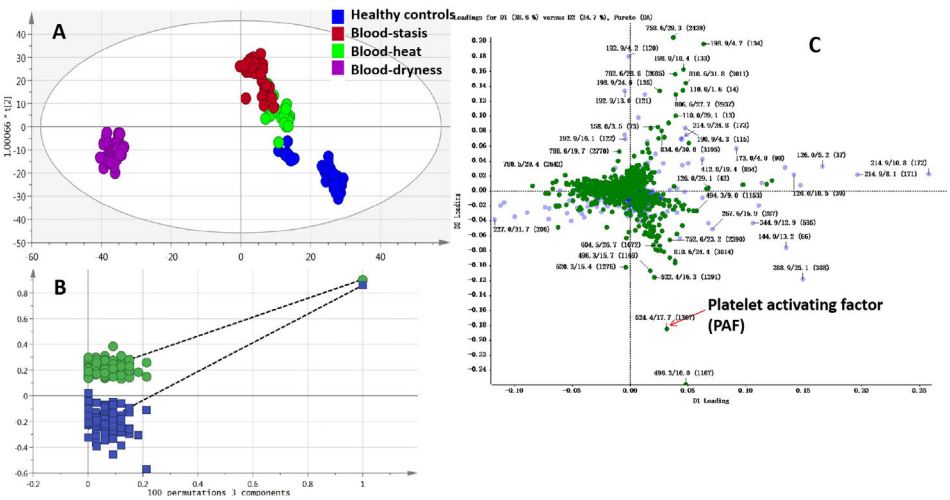

FIGURE 2 | Multivariate data analysis and permutation test **(A)** OPLS-DA scores map, **(B)** Permutation test of OPLS-DA, **(C)** Loading map of PLS-DA.

TABLE 2 | Potential biomarkers identification.

No.	m/z	Compound	Chemical Formula	Adducts	HMDB ID	Trend*
1	524.370	Platelet-activating factor	C26H54NO7P	M+H	HMDB0062195	↑
2	496.338	LysoPC(16:0)	C24H50NO7P	M+H	HMDB0010382	↑
3	520.337	LysoPC(18:2)	C26H50NO7P	M+H	HMDB0010386	↑
4	522.354	LysoPC(18:1)	C26H52NO7P	M+H	HMDB0002815	↑
5	550.385	LysoPC(20:1)	C28H56NO7P	M+H	HMDB10391	↑
6	544.340	LysoPC(20:4)	C28H50NO7P	M+H	HMDB10395	↑
7	835.528	PI(18:0/16:2)	C43H79O13P	M+H	HMDB09807	↑
8	613.393	Cholestane-3,7,12,25-tetrol-3-glucuronide	C33H56O10	M+H	HMDB10355	↑
9	782.570	PC(18:3/18:1)	C44H80NO8P	M+H	HMDB0008170	↓
10	806.571	PC(22:5/16:1)	C46H80NO8P	M+H	HMDB0008660	↓
11	810.601	PC(20:4/18:0)	C46H84NO8P	M+H	HMDB0008464	↓
13	806.561	Lactosylceramide (d18:1/12:0)	C42H79NO13	M+H	HMDB04866	↓
14	313.155	Phenylalanylphenylalanine	C18H20N2O3	M+H	HMDB13302	↓

**The trend was psoriasis groups compared to healthy control group.*

Fourteen significant difference metabolites were screened out to be the potential biomarkers according to the value of variable importance for projection (VIP) value in PLS-DA model.

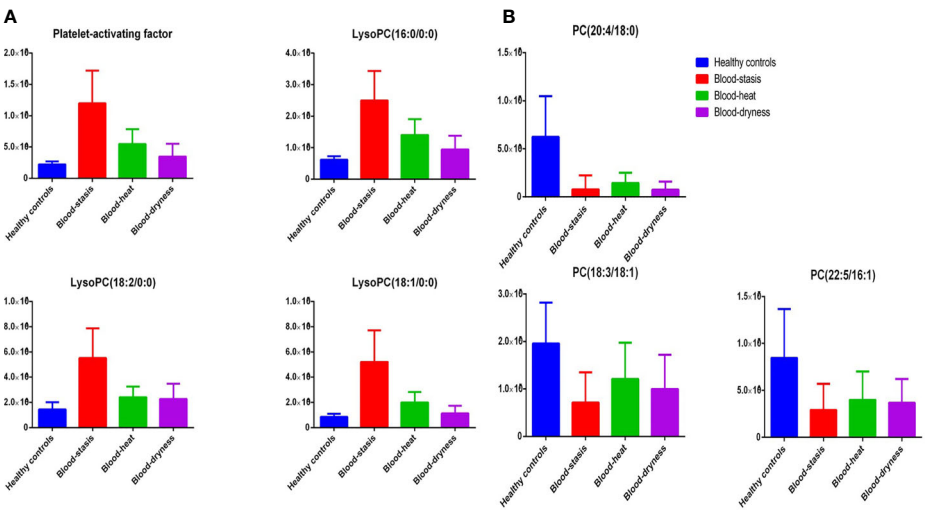

FIGURE 3 | Typical metabolites with significant alterations. The peaks area of potential biomarkers in serum of the four groups were shown.

linoleic acid metabolism, sphingolipid metabolism, arachidonic acid metabolism, and pentose and glucuronate interconversions. In recent years, lipid metabolism abnormalities have been reported in patients with psoriasis (Taheri et al., 2014). Psoriasis patients are prone to diabetes, hyperlipidemia, hypertension, and other metabolic diseases (Ribeiro et al., 2014), suggesting that psoriasis has a close relationship with metabolic syndromes, involving phospholipid, fatty acid, amino acid, arachidonic acid metabolisms, and other metabolic cycles.

In this study, all psoriasis groups showed an abnormal lipid metabolism, which was characterized by the high level of LPC and low level of PC compared to the healthy control group. The level of LysoPC(16:0), LysoPC(18:2), LysoPC(18:1), and LysoPC(20:1) in the serum of patients with psoriasis were significantly higher than that of healthy controls, whereas the level of PC(18:3/18:1), PC (22:5/16:1), and PC(20:4/18:0) were significantly higher than that of the healthy controls. The result was consistent with the previous lipidomics research on psoriasis (Zeng et al., 2017). LPC is the main active component of oxidized LDL, which has a wide range of biological effects, including the development of atherosclerosis. LPC is a degradation product of PC. It can induce inflammatory response, increase oxidative stress, interfere with vascular endothelial function, and destroy plaque stability. LPC plays an essential role in the prevention, diagnosis, and treatment of atherosclerosis. Brown adipose tissue (BAT) recently emerged as a potential therapeutic target in the treatment of obesity and associated disorders due to its fat-burning capacity. The concentrations of lysophosphatidylcholine-acyl (LysoPC-acyl) C16:1, LysoPC-acyl C16:0, and phosphatidylcholine-diacyl C32:1 show strong positive correlations with BAT volume as well as BAT activity (Boon et al., 2017).

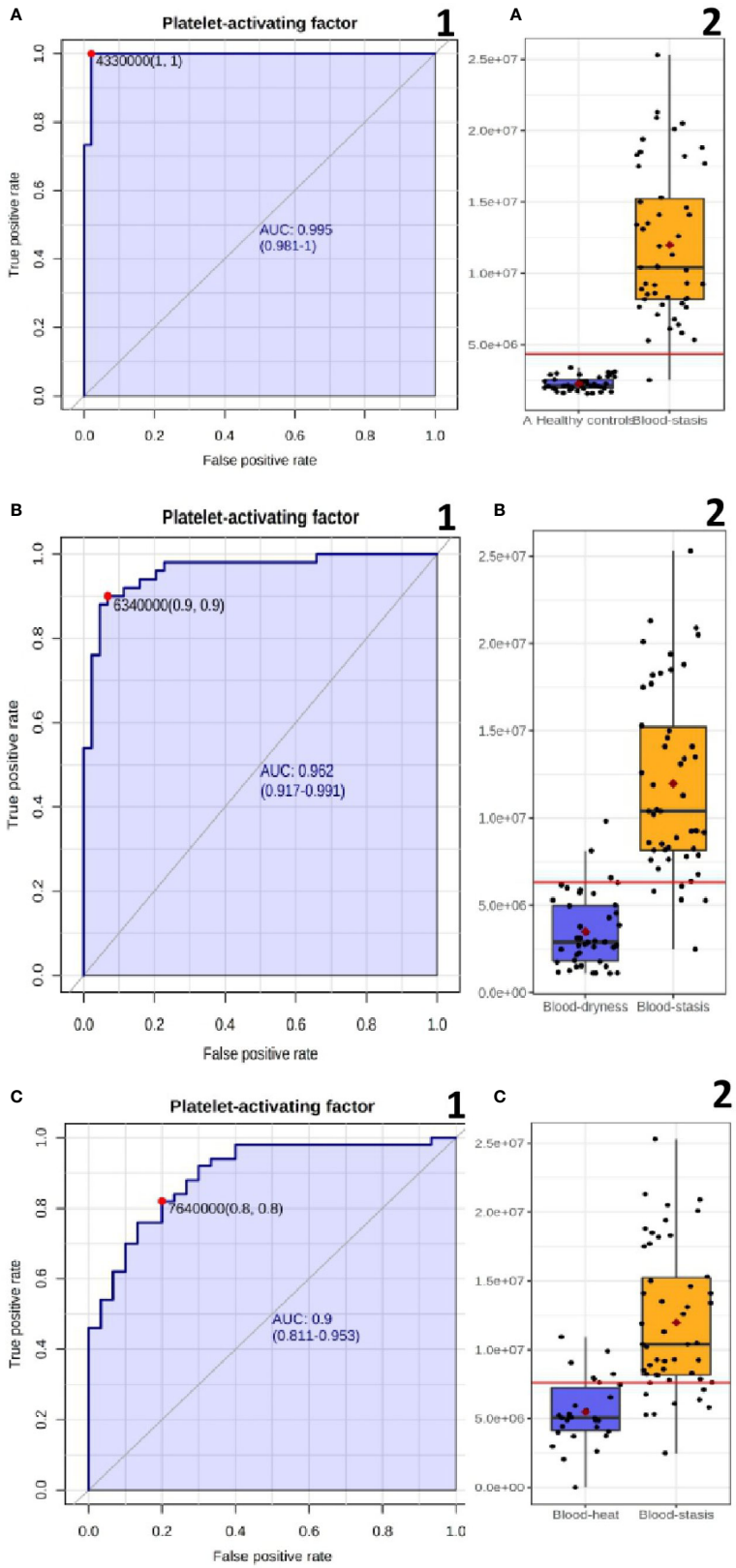

FIGURE 4 | The ROC curve plots and boxplot of PAF **(A)** Blood-stasis vs Healthy controls; **(B)** Blood-stasis vs Blood dryness; **(C)** Blood-stasis vs Blood-heat.

PAF, also known as PC(O-16:0/2:0), is a ubiquitous, potent phospholipid activator and mediator of inflammation that has an important role in the pathogenesis of inflammatory disorders and cardiovascular disease. PAF causes platelet aggregation and anaphylaxis. PAF is synthesized continuously in low quantities in many different types of cells, especially those involved in host defense, such as macrophages, monocytes, granulocytes, neutrophils, platelets, and endothelial cells. Platelet-activating factor receptor is a G-protein coupled receptor located on the cell membranes of a variety of cells. Once bound to its receptor, PAF mobilizes calcium and activates a wide range of signaling pathways. In our study, the PAF level of blood-stasis syndrome was significantly higher than that of non blood-stasis syndrome, and that of non blood-stasis syndrome was significantly higher than that of healthy controls (**Supplement Table 1**), and the ROC curve showed excellent predictive ability (**Figure 4A**). The relationship of PAF and psoriasis had been studied by several researchers previously (Judge et al., 1994; Lzaki et al., 1996; Greaves and Judge, 1997), but there were different comments about it. In recent years, it has been increasingly recognized that platelet activation seems to be a major pathogenic factor in psoriasis (Elbers et al., 2010), and platelet activation indexes generally suggest abnormal platelet function and are given an additional role in the diagnosis of psoriasis. Platelets are also immune cells that initiate and regulate immune and inflammatory processes, except as the principal mediator of hemostasis and thrombosis, and platelet dysfunction is deeply involved in the pathogenesis of psoriasis (Fan et al., 2020).The platelet activating factor has been reported in coronary heart disease with blood-stasis syndrome (Zheng et al., 2012) and primary dysmenorrhea with blood-stasis tongue figure (Yang and Chen, 2011), but there is no report in psoriasis with blood-stasis. PAF cannot be a characteristic diagnostic marker of psoriasis disease, but it is expected to be used as potential biomarkers for diagnosis and differentiation of blood-stasis syndrome in PV, and the increase of platelet-activating factor may be a pathogenesis of blood-stasis syndrome.

CONCLUSION

We developed an untargeted metabonomics method to investigate the differences among patients with psoriasis with different TCM syndromes and healthy controls. Fourteen potential biomarkers were screened and identified. Lower level of phosphatidylcholine (PC) and higher level of lysophosphatidylcholine (LPC) were shown in psoriasis patients. We propose PAF as a biomarker for diagnosis and differentiation of blood-stasis syndrome, levels of which show that there is an objective material basis in TCM syndrome differentiation of psoriasis.

DATA AVAILABILITY STATEMENT

The raw data supporting the conclusions of this article will be made available by the authors, without undue reservation.

ETHICS STATEMENT

The studies involving human participants were reviewed and approved by institutional ethics committee of Guangdong provincial hospital of Chinese medicine. The patients/participants provided their written informed consent to participate in this study. Written informed consent was obtained from the individual(s) for the publication of any potentially identifiable images or data included in this article.

AUTHOR CONTRIBUTIONS

C-jL and LH supervised the whole experiments. LL designed this study and performed the practical work and completed the experiments. D-nY, J-wD, Y-hY, and HD diagnosed patients and collected samples. YL and J-aW provided help during experiments. All authors contributed to the article and approved the submitted version.

FUNDING

This work was supported by natural science foundation of China (81302736), Guangdong natural science foundation (S2011040005849), Guangdong Province Science and Technology Planning Project (2017A050506041, 2017B030314166, 2019A1515010636, 2020B1111100006, 2020A1515010607), Guangdong Provincial Department of Education Project (2018KQNCX046), Guangzhou Science and Technology Project (201807010051), and Guangdong Provincial Hospital of Chinese Medicine Special Fund (YN2018HK01, YN2018ZD08, YN2018RBA02, YN2016XP02, YN2019QJ04, YN2019QJ08, 2019KT1313).

SUPPLEMENTARY MATERIAL

The Supplementary Material for this article can be found online at: https://www.frontiersin.org/articles/10.3389/fphar.2020.558731/full#supplementary-material

REFERENCES

Alessandro, B., Maria, L., Garcia, B., Enrica, B., Xu, Q. H., Li, H. G., et al. (2012). Omic techniques in systems biology approaches to traditional Chinese medicine research: Present and future. *J. Ethnopharmacol.* 140, 535–544. doi: 10.1016/j.jep.2012.01.055

Boon, M. R., Bakker, L. E. H., Prehn, C., Adamski, J., Vosselmanet, M. J., Jazet, I. M., et al. (2017). LysoPC-acyl C16:0 is associated with brown adipose tissue activity in men. *Metabolomics* 13, 48. doi: 10.1007/s11306-017-1185-z

Dermatology branch of Chinese Association of traditional Chinese Medicine (2013). Evidence based clinical practice guide of traditional Chinese medicine

for psoriasis vulgariVersion). *J. Tradit. Chin. Med.* 55, 76–82. doi: 10.13288/j.11-2166/r.2014.01.021

Elbers, M. E., Gerritsen, M. J., and Kerkhof, P. C. (2010). The effect of topical application of the platelet-activating factor-antagonist, Ro 24-0238, in psoriasis vulgaris–a clinical and immunohistochemical study. *Clin. Exp. Dermatol.* 19 (6), 453–457. doi: 10.1111/j.1365-2230.1994.tb01246.x

Fan, Z., Wang, L., Jiang, H., Yong, L., and Wang, Z. C. (2020). Platelet Dysfunction and Its Role in the Pathogenesis of Psoriasis. *Dermatology* 1–10. doi: 10.1159/000505536

Greaves, M. W., and Judge, M. R. (1997). Platelet activating factor in psoriasis. *Br. J. Dermatol.* 136 (3), 467. doi: 10.1111/j.1365-2133.1997.tb14968.x

Gu, Y., Lu, C., Zha, Q., Kong, H., Lu, X., Lu, A., et al. (2012). Plasma metabonomics study of rheumatoid arthritis and its Chinese medicine subtypes by using liquid chromatography and gas chromatography coupled with mass spectrometry. *Mol. Biosyst.* 8, 1535–1543. doi: 10.1039/c2mb25022e

Guangdong Provincial Bureau of quality and technical supervision (2018). "Psoriasis vulgar syndrome differentiation standard of traditional Chinese medicine," (Local standards of Guangdong Province: Guangdong Provincial Bureau of quality and technical supervision), DB44/T 2120–2018.

He, Z. H., Wang, D. M., Lu, C. J., and Ou, A. H. (2014). The Distribution of TCM Syndromes of Vulgaris Psoriasis:Correspondence Analysis of the Relationships Between TCM Syndromes and Disease Stages. *Chin. J. Dermatovenereol.* 28, 22–25. doi: 10.13735/j.cjdv.1001-7089.2014.0022

Judge, M. R., Barr, R. M., Mallet, A. I., Courtney, F., Black, A. K., and Greaves, M. W. (1994). Platelet activating factor (PAF) and lyso-PAF in psoriasis[J]. *Arch. Dermatol. Res.* 286 (7), 376–379. doi: 10.1007/BF00371796

Lu, C. J., Zeng, Z., Xie, X. L., and Ning, J. (2010). Distribution of Chinese Medical Syndrome in Ordinary Psoriasis: Literature from 1979 to 2010. *J. Tradit. Chin. Med.* 53, 959–961.

Lu, C. J., Yu, J. J., and Deng, J. W. (2012). Disease-syndrome combination clinical study of psoriasis: Present status, advantages, and prospects. *Chin. J. Integr. Med.* 18, 166–171. doi: 10.1007/s11655-012-1006-1

Lzaki, S., Yamamoto, T., Goto, Y., Lshimaru, S., and Matsuzakiet, M. (1996). Platelet-activating factor and arachidonic acid metabolites in psoriatic inflammation. *Br. J. Dermatol.* 134 (6), 1060–1064. doi: 10.1111/j.1365-2230.1994.tb01246.x

Nestle, F. O., Kaplan, D. H., and Barker, J. (2009). Psoriasis. *N. Engl. J. Med.* 361, 496–509. doi: 10.1056/NEJMra0804595

Nicholson, J. K., Lindon, J. C., and Holmes, E. (1999). 'Metabonomics': understanding the metabolic responses of living systems to pathophysiological stimuli via multivariate statistical analysis of biological NMR spectroscopic data. *Xenobiotica* 29, 1181–1189. doi: 10.1080/004982599238047

Pietrzak, A., Chodorowska, G., Szepietowski, J., Zalewska-Janowska, A., Krasowska, D., and Hercogová, J. (2010). Psoriasis and serum lipid abnormalities. *Dermatol. Ther.* 23, 160–173. doi: 10.1111/j.1529-8019.2010.01311.x

Pietrzak, A., Chabros, P., Grywalska, E., Kicinski, P., Franciszkiewicz-Pietrzak, K., Krasowska, D., et al. (2019). Serum lipid metabolism in psoriasis and psoriatic arthritis - An update. *Arch. Med. Sci.* 15, 369–375. doi: 10.5114/aoms.2018.74021

Ribeiro, B., Bittencourt, F. V., Gontijo, B., and Andrade, G. (2014). Comorbidities and cardiovascular risk factors in patients with psoriasis. *Anais Brasileiros Dermatol.* 89, 735–744. doi: 10.1590/abd1806-4841.20142874

Taheri, S. M., Hedayati, M. T., Shokohi, T., and Haj, H. Z. (2014). Serum lipids and lipoproteins in patients with psoriasis. *Arch. Iranian Med.* 17, 343–346. doi: 0141705/AIM.007

Yang, A. P., and Chen, Q. (2011). Correlation between blood-stasis tongue figure and platelet activating factor (PAF) and acetyl hydrolase of PAF (PAF-AH) in patients with primary dysmenorrhea. *Zhongguo Zhong XI Yi Jie He Za Zhi* 31 (3), 331–333. doi: 10.1097/MOP.0b013e328341d1da

Zeng, C., Wen, B., Hou, G., Lei, L., Mei, Z., Jia, X., et al. (2017). Lipidomics profiling reveals the role of glycerophospholipid metabolism in psoriasis. *Gigascience* 6, 1–11. doi: 10.1093/gigascience/gix087

Zhang, G., Wang, P., Wang, J., Jiang, C., Deng, B., and Li, P. (2008). Study on the distribution and development rules of TCM syndromes of 2651 psoriasis vulgaris cases. *J. Tradit. Chin. Med.* 29, 894–896.

Zhang, G. Z., Wang, J. S., Wang, P., Jiang, C. Y., Deng, B. X., Li, P., et al. (2009). Distribution and Development of the TCM Syndromes in Psoriasis Vulgaris. *J. Tradit. Chin. Med.* 29, 195–200. doi: 10.1016/S0254-6272(09)60064-9

Zhang, B. Z. (2002). Preliminary study on essence of TCM syndrome typing of psoriasis and its objective basis. *CJIM* 8, 254–255. doi: 10.1007/BF02934397

Zheng, G. H., Xiong, S. Q., Mei, L. J., Chen, H. Y., Wang, T., and Chu, J. F. (2012). Elevated Plasma Platelet Activating Factor, Platelet Activating Factor Acetylhydrolase Levels and Risk of Coronary Heart Disease or Blood Stasis Syndrome of Coronary Heart Disease in Chinese: A Case Control Study[J]. *Inflammation* 35 (4), 1419–1428. doi: 10.1007/s10753-012-9455-4

Zhou, H., Li, L., Zhao, H., Wang, Y., Du, J., Peng, J., et al. (2019). A Large-Scale, Multi-Center Urine Biomarkers Identification of Coronary Heart Disease in TCM Syndrome Differentiation. *J. Proteome Res.* 18, 1994–2003. doi: 10.1021/acs.jproteome.8b00799

Conflict of Interest: The authors declare that the research was conducted in the absence of any commercial or financial relationships that could be construed as a potential conflict of interest.

frontiers in Pharmacology

ORIGINAL RESEARCH
published: 19 November 2020
doi: 10.3389/fphar.2020.576496

Berberine Suppresses Colonic Inflammation in Dextran Sulfate Sodium–Induced Murine Colitis Through Inhibition of Cytosolic Phospholipase A2 Activity

Lixiang Zhai[1†], Tao Huang[1†], Hai-tao Xiao[2†], Pei-gen Wu[3], Cheng-yuan Lin[1], Zi-wan Ning[1], Ling Zhao[1], Hiu Yee Anna Kwan[1], Xian-jing Hu[1], Hoi Leong Xavier Wong[1], Xian-qian Li[2] and Zhao-xiang Bian[1,4*]*

[1]School of Chinese Medicine, Hong Kong Baptist University, Kowloon, Hong Kong, [2]School of Pharmacy, Health Science Center, Shenzhen University, Shenzhen, China, [3]School of Pharmaceutical Sciences, Guizhou Medical University, Guiyang, China, [4]Shenzhen Research Institute and Continuing Education, Hong Kong Baptist University, Shenzhen, China

OPEN ACCESS

Edited by:
Peng Li,
University of Macau, China

Reviewed by:
Lixin Zhu,
The Sixth Affiliated Hospital of Sun Yat-sen University, China
Ying Wang,
University of Macau, China

***Correspondence:**
Zhao-xiang Bian
bzxiang@hkbu.edu.hk
Hai-tao Xiao
xhaitao@szu.edu.cn

[†]*These authors share first authorship*

Specialty section:
This article was submitted to Ethnopharmacology, a section of the journal Frontiers in Pharmacology

Received: *26 June 2020*
Accepted: *08 October 2020*
Published: *19 November 2020*

Citation:
Zhai L, Huang T, Xiao H, Wu P, Lin C, Ning Z, Zhao L, Kwan HYA, Hu X, Wong HLX, Li X and Bian Z (2020) Berberine Suppresses Colonic Inflammation in Dextran Sulfate Sodium–Induced Murine Colitis Through Inhibition of Cytosolic Phospholipase A2 Activity. Front. Pharmacol. 11:576496. doi: 10.3389/fphar.2020.576496

Ulcerative colitis (UC) causes chronic inflammation and damage to the colonic mucosal layer. Recent studies have reported significant changes in phosphatidylcholine (PC) and lysophosphatidylcholine (LPC) in UC patients and oral administration of PC has considerable therapeutic effects against UC, suggesting the metabolism of phosphatidylcholine may be involved in the UC development. Our previous work has demonstrated that berberine effectively suppresses inflammation and protects colonic mucosa injury in DSS-induced colitic mice. However, whether the therapeutic effects of berberine are attributed to its action on the PC metabolism remains unknown. In the present study, we have shown that berberine significantly reduces the lysophosphatidylcholine (LPC) levels in the sera of DSS-induced experimental colitis mice and LPS-stimulated macrophage RAW 264.7 cells. The cytosolic phospholipase A2a (PLA2G4A), an enzyme for hydrolyzing PC to LPC, was found to be up-regulated in the colon tissue of experimental colitis mice and inflamed macrophage RAW 264.7 cells. We then demonstrated berberine inhibits the phosphorylation of cytosolic phospholipase A2a (PLA2G4A) in the colon tissue of experimental colitis mice and inflamed macrophage RAW 264.7 cells. Subsequently, we revealed berberine suppressed the expression of pro-inflammatory factors including TNF-alpha and IL-6 through regulating PLA2G4A dysfunction in macrophage RAW 264.7 cells. Mechanistically, we found that berberine directly binds to PLA2G4A and inhibits MAPK/JNK signaling pathway to inhibit PLA2G4A activity in inflammatory status. Therefore, we concluded that berberine inhibits colonic PLA2G4A activity to ameliorate colonic inflammation in experimental colitic mice, suggesting modulation of the PC metabolism via PLA2G4A might be beneficial for establishing new therapies strategy for UC.

Keywords: ulcerative colitis, macrophage, phospholipase A2, lysophosphatidylcholine, berberine

Abbreviations: BBR, berberine; DSS, dextran sulfate sodium; LPC, lysophosphatidylcholine; PC, phosphatidylcholine; PLA2, phospholipase A2; UC, ulcerative colitis.

INTRODUCTION

Ulcerative colitis (UC) and Crohn's disease (CD) are classified as severe and chronic inflammatory bowel disease (IBD) that causes inflammation and sores (ulcers) in the gastrointestinal tract, particularly in the large intestine (Kaplan, 2015). Lipid metabolism is in relation to chronic inflammation as one of the possible mechanisms involved in the pathogenesis of many inflammatory diseases (Parhofer, 2015). Notably, IBD patients have been found with dyslipidemia by several studies, suggesting lipid metabolism and signaling may play key roles in modulating inflammation in IBD (Biyyani et al., 2010; Karaahmet et al., 2013). In lipid metabolism and signaling, phosphatidylcholine (PC) is a phospholipid that has been shown to account for more than 70% of total phospholipids in the intestinal mucus layer. UC patients were found to have decreased PC content, while the clinical trial studies revealed PC supplementation to the colonic mucus alleviated the inflammation in UC patients. In contrast, lysophosphatidylcholine (LPC) is derived from PC which is hydrolyzed by phospholipase A2 in the circulation. LPC has been reported with pro-inflammatory (Olofsson et al., 2008; Qin et al., 2014) properties in macrophages and apoptotic effects on vascular endothelial cells (Aiyar et al., 2007; Song et al., 2010). Moreover, lipidomics investigation on IBD patients has revealed alterations of lysophosphatidylcholine (LPC) (Chen et al., 2008; Chander et al., 2014; Fan et al., 2015). Therefore, the PC and LPC alterations in lipid metabolism and signaling may be involved in the colonic inflammatory responses in IBD, and therapeutic approaches regulating the PC and LPC metabolism or its related enzymes are potentially beneficial for suppressing inflammation in colitis.

Berberine is a natural benzylisoquinoline alkaloid found in a wide variety of plants such as *Coptis chinensis* Franch. (Chinese goldthread), *Berberis vulgaris* L. (European barberry), and *Berberis aquifolium* Pursh. (Oregon grape). Recent studies along with our findings have suggested berberine alleviates experimental colitis by suppressing inflammatory responses in macrophages and T cells and maintaining intestinal barrier function (Li et al., 2015; Li et al., 2016; Zhang et al., 2017; Liu et al., 2018) via regulation of multiple signaling pathways (Cui et al., 2009; Jeong et al., 2009; Amasheh et al., 2010; Zhou et al., 2015). Besides, berberine exhibits modulatory abilities on phospholipid metabolism in metabolic diseases such as obesity and non-fatty liver disease (Zhang et al., 2011; Hu et al., 2012; Wei et al., 2016; Zhao et al., 2017). Since phospholipid metabolism plays an important role in IBD, we wondered whether the pharmacological mechanism of berberine action on IBD involves phospholipid metabolism and signaling. For this purpose, we first characterized the berberine action on phospholipid metabolism in an experimental colitis mice model. Second, we determined whether the anti-inflammatory effects of berberine in animal models of colitis are mediated by modulation of phospholipid-related targets.

MATERIALS AND METHODS

Regents

Berberine chloride was purchased from Shenzhen ChemStrong Scientific Co., Ltd. (Shenzhen, China) at the highest available purity (≥95%). Lipopolysaccharide (LPS), TNF-α, and endotoxin removal solution were purchased from SIGMA (St. Louis, MO, United States). Interferon-γ was obtained from Merck (EMD Millipore, MA, United States). cPLAα, p-cPLAα, JNK, and p-JNK antibodies were purchased from Cell Signaling (Danvers, MA, United States). Insulin was purchased from Life Technologies (Grand Island, NY, United States). Lipid standards, including SPLASH™ Lipidomix® Mass Spec Standard, and LPC standards were purchased from Avanti Polar Lipids (Alabaster, AL, United States). PLA2 activator, JNK inhibitor and activator, Mouse *Pla2g4*, and control siRNA were purchased from Santacruz (Dallas, TX, United States). The recombinant human PLA2G4A protein was obtained from R&D Systems (Minneapolis, MN, United States).

Cell Culture

RAW 264.7 macrophage cell line was obtained from ATCC (Manassas, VA, United States). RAW 264.7 cells were grown in DMEM (Gibco) supplemented with 10% fetal bovine serum (Gibco). RAW 264.7 cells were maintained at 37°C in a humidified atmosphere containing 5% CO_2. Berberine hydrochloride was dissolved in DMSO to prepare 50 mM stock solution. Other reagents were dissolved in 1× phosphate-buffered saline (PBS) as stock solution.

Animal Experiment

C57BL/6 background male mice were purchased from the Chinese University of Hong Kong. They were maintained in the animal laboratory of the School of Chinese Medicine, Hong Kong Baptist University (HKBU). The animals were kept in a standard living condition (room temperature 22°C, 12-h light/dark normal cycle, and constant humidity) with diet and water *ad libitum*. All experimental protocols and procedures were supervised by the Animal Care Ethics Committee of HKBU and the Department of Health, Hong Kong Special Administrative Region. Induction of colitis on mice was through 2.0% (w/v) dextran sulfate sodium (DSS) in drinking water. After 3 days of development, colitis mice were confirmed by fecal occult blood testing and randomly divided into two groups (model group and berberine treatment group). Mice in the berberine treatment group were administered berberine hydrochloride solution (suspended in water, dosage = 20 mg/kg) through oral gavage, while mice in the model group were administered water as parallel control. On day 7, the mice were anesthetized by 3% chloral hydrate through intraperitoneal injection. About 1 ml serum was collected through hemostasis from the heart to sacrifice the mice.

LIPIDOMICS STUDY

Lipidomics Profiling on Mice Serum and Colon Tissue

For lipidomics study on serum, 30 μL serum and 30 μL water were added with 240 μL Folch solvent (chloroform:methanol = 2:1) and vortexed vigorously. Two phases were formed after centrifugation at 8,000 rpm for 15 min at 4°C. For lipidomics study on colon tissue, about 10 mg frozen colon tissue was weighed and homogenized in 1× PBS with a 1:10 m/v ratio. Then, 60 μL homogenate was added with 240 μL Folch solvent (with internal standard) for lipid extraction. The samples were vortexed and centrifuged at 8,000 rpm for 15 min at 4°C to induce phase separation. About 150 μL down layer solution was collected and dried under a vacuum concentrator within 30 min at room temperature. The samples were stored in −80°C until analysis.

Lipidomics Profiling on RAW Cell Lines

RAW 264.7 cells were extracted according to a well-agreed protocol from LIPID MAPS using Bligh–Dyer (BD) extraction. In brief, cells from a 100-mm culture plate were washed twice with 5 ml ice-cold 1× PBS after aspirating the culture medium. Then, 10 ml 1× PBS was added to the plate, and the cells were scraped and transferred to 15-ml conical tubes. Then, 200 μL suspension was taken out for protein quantification by a protein BCA kit. Cell pellets were collected after centrifugation at 3,500 rpm for 10 min at 4°C. Then, the BD system: 1 ml of 80°C pre-cold 70% MeOH, 350 μL $CHCl_3$, 350 μL H_2O, and 350 μL $CHCl_3$ were added step by step and vortexed at each step to induce phase separation. After centrifugation at 4,000 rpm for 30 min at 4°C, the down layer (200 μL) was transferred to 1.5 ml tubes. The samples were dried under vacuum at room temperature within 30 min and stored at −80°C until analysis.

Before LC-MS analysis, the dried samples were dissolved with 200 μL of acetonitrile/isopropanol/H_2O (65:30:5, v/v/v) and centrifuged at 14,000 rpm for 10 min at 4°C. For LC-MS analysis, the liquid chromatogram was performed on an Agilent 1290 UPLC system and mass spectrometry was employed on an Agilent 6540 quadrupole time-of-flight mass spectrometry system. The Waters ACQUITY UPLC HSS C18 column (2.1 mm × 100 mm, 1.8-μm particle size) was used for separation at 40°C. Mobile phases A and B were prepared as 60:40 water/acetonitrile and 90:10 isopropanol/acetonitrile with 10 mM ammonium formate and 0.1% formic acid. The linear gradient was set as 0–32% B (0–0.8 min), 32–45% B (0.8–2 min), 45–52% B (2–2.5 min), 52–58% B (2.5–4 min), 58–66% B (5–5.5 min), 66–70% (5.5–7 min), 70–75% B (7–8.8 min), and 75–97% B (8.8–10.5 min); then maintained at 97% B from 10.5 to 15 min; and decreased to 32% B from 15 to 18 min. Lipids were detected and identified in both negative and positive ionization modes. The injection volume is 3 μL in the negative mode and 1 μL in the positive mode for each analysis. For lipid identification, the frame m/z values were used to search for information on LIPID MAPS and Human Metabolome Database (HMDB). The matches were confirmed by exact tandem mass (MS/MS) of lipids and retention time based on standards and databases.

Transfection Study on RAW Cell Lines

Neon® Transfection System (Life Technologies) was used following the instructions of the manufacturer for transfection study. For transfection on RAW 264.7 cells, 1×10^6 cells were transfected with 20 nM siRNA with one pulse of 1,680 V for 20 ms. After transfection, cells were seeded in a 6-well cell culture plate to recover overnight in antibiotics-free medium. Then, RAW 264.7 cells were incubated with berberine 10 μM for 2 h before challenged with stimuli (LPS) for 24 h. Mouse *Pla2g4* siRNA and matched control siRNA were transfected using the Neon Transfection System according to the manufacturer's instructions. Quantitative RT-PCR was used to detect transfection efficiency.

Quantitative RT-PCR Analysis

Total RNA was isolated from RAW 264.7 cells using TRIzol reagent (TAKARA, Japan) following the manufacturers' instruction, and cDNA was synthesized with a reverse transcriptase kit (TAKARA, Japan). For RT-PCR analysis, amplification was performed using SYBR Green for 40 cycles (94°C for 30 s, 57°C for 20 s, and 72°C for 20 s). The primers were designed and synthesized from Invitrogen. The primer sequences are provided in **Supplementary Table S1** (Ashley et al., 2016).

Western Blot Analysis

An equal amount of protein (10 μg) from each sample was separated on SDS-PAGE gels and transferred to nitrocellulose membranes. Blots were blocked with 5% non-fat milk in Tris-buffered saline with 0.1% Tween-20 (TBST, 25 mM Tris, pH 8.0, 137 mM NaCl, 2.7 mM KCl, and 0.1% Tween-20) at room temperature for 1 h, followed by overnight incubation with primary antibodies at 4°C. The primary antibodies were prepared with 5% bovine serum albumin (BSA). After being washed with TBST five times, the blots were hybridized with secondary antibodies conjugated with horseradish peroxidase (Bio-Rad, Hercules, CA, United States) in 5% non-fat milk dissolved in TBST at room temperature for 1 h and washed five times with TBST. The membranes were then incubated with enhanced chemiluminescence reagents and exposed to X-ray film (Fuji, Japan).

Nitric Oxide and ELISA Assay

NO production was evaluated measuring nitrite, the stable metabolite of NO, from the culture media of RAW 264.7 by a modified Griess reagent (Sigma) according to the manufacturers' instructions. Duplicates of 100 μL of supernatant or culture media were added to 96-well microtiter plates and mixed with 100 μL Griess solution. The plate was then read on a microtiter plate reader using 540-nm wavelength. TNF-α and IL-10 were measured from supernatants of RAW 264.7 cells through enzyme-linked immunosorbent assay (ELISA) analysis by using ELISA kits according to the manufacturer's protocol (eBioscience, San Diego, CA, United States). Duplicates of 100 μL of supernatant or culture media were added to 96-well

coating plates for ELISA analysis using 570-nm wavelength. The result obtained from the microtiter plate reader was normalized by measured protein.

Human PLA2G4A Assay

The PLA2G4A activity was measured by its ability to hydrolyze 1-hexadecanoyl-2-(1-pyrene-decanoyl)-sn-glycero-3-phosphocholine. The berberine was dissolved in DMSO (50 mM) as a stock solution to prepare the enzyme–inhibitor complex. The assay procedure was followed by the protocol online from R&D Systems.

Docking Study of PLA2G4A and Berberine

Homology modeling of "open lid" conformation of PLA2G4A: The "open lid" conformation of PLA2G4A catalytic domain was constructed by grafting the "open lid" in PLA2G4D (PDB ID: 5IXC) onto the "closed lid" structure of PLA2G4A (PDB ID: 1CJY). First, the catalytic domain structures of PLA2G4A (residue 141–749) and PLA2G4D (residue 277–810) were superposed based on main-chain atoms and refined with Gaussian distance weights in Molecular Operating Environment (MOE) version 2012.10 (Deeth et al., 2005; Maier and Labute, 2014). Second, the lid region in PLA2G4D and residue 530–575 were selected and used as override template. Third, the homology model of the "open lid" conformation of PLA2G4A was built with 1CJY as the main template and residue 530–575 in 5IXC as an override template, besides of using methyl gamma-linolenyl fluorophosphonate as environment ligand in MOE. Finally, the model was optimized with AMBER10: EHT force field and scored by GB/VI function.

Docking of berberine into the "open lid" conformation of PLA2G4A: The 3D structure of berberine was extracted from the crystal structure of the QacR–berberine complex (PDB ID: 3BTI). The whole docking study was performed with MOE: dock. The methyl gamma-linolenyl fluorophosphonate was used as a reference ligand to guide the berberine docking into the active site of PLA2G4A. The placement method was Triangle Matcher, and a flexible receptor was used during the refinement stage. The GBVI/WAS dG was selected as the final scoring function. Docking poses were ranked by the GBVI/WAS dG score and analyzed by manual observation as well as ligand interactions modules. All 3D structures were drawn with VMD 1.8.3 software (Humphrey et al., 1996).

Statistical Analysis

Results were from multiple, at least three times independent experiments. The lipidomics data were processed by the R package with XCMS. MetaboAnalyst was used for multivariate statistical analysis. Cytoscape was used to match the associated enzyme in the KEGG database. ImageJ was used to process Western blot results. Other data are expressed as average and SD value of at least triplicate samples. Significance p values were calculated using GraphPad Prism 6 from either Students' t-test or one-way ANOVA, and the p value less than 0.05 was regarded as statistically significant.

RESULTS

Berberine Reduces Lysophosphatidylcholine Level in Dextran Sulfate Sodium–Treated Colitis and Lipopolysaccharides-Stimulated RAW 264.7 Cells

We first investigated the effect of berberine on lipid metabolism in experimental colitic mice. DSS treatment caused a decrease in body weight, colon shortening, and increase in stool consistency as well as colonic bleeding. In contrast, treatment of berberine significantly ameliorated colon tissue injury and inflammatory responses in DSS-induced colitis mice (**Supplementary Figure S1**). To characterize and compare the lipid profiles of control, model, and berberine groups, biological samples including serum and colon tissues were collected and analyzed. Initially, we performed a lipidomics analysis of mouse serum to determine the changes in systemic lipid profiles. The score plot exhibited well-separated trends among the control group, model group, and berberine treatment group (**Figure 1A**). The heat map plot revealed that some LPC species significantly increased and PC species reduced in the model group compared with the control group (**Figure 1B**). Moreover, we found berberine treatment significantly reduced LPC and increased PC. This result indicated that berberine regulated the serum LPC level and PC level in DSS-induced colitis in mice.

Next, we studied the effects of berberine on inflammatory responses in LPS-treated RAW 264.7 macrophages (Qian et al., 2015). To investigate the regulatory effects of berberine on LPC species, we also determined the impact of berberine treatment on LPC profiles in LPS-treated RAW 264.7 macrophages. We first determined the anti-inflammatory effects of berberine on RAW 264.7 under pro-inflammatory stimulations (**Supplementary Figures S2, S3**). Berberine suppressed the expression of pro-inflammatory genes expression including *tnf-alpha*, *nos2*, *il6*, and *cxcl10* in the LPS-stimulated RAW 264.7 macrophages. Based on the results of cytotoxicity and anti-inflammatory effects of berberine on RAW 264.7 cells, berberine treatment at a concentration of 10 μM was chosen for lipidomics study. In RAW 264.7 cells, the score plot displayed clear classification among the control group, model group, and berberine treatment group, indicating that pro-inflammatory stimulations by LPS affect total lipid profiles. Berberine effectively reduced the elevated LPC levels in LPS-treated RAW 264.7 cells (**Figures 1C,D**). Subsequently, Cytoscape encoded with the KEGG database was used to address the related metabolic pathways of LPC. We found that phospholipase A2α is mainly responsible for the production of LPC (**Figure 1E**). Consistently, previous experimental findings have shown the involvement of phospholipase A2α in regulating inflammatory responses (Sun et al., 2010). Therefore, berberine treatment may inhibit phospholipase A2α activity in both DSS-treated colitis and LPS-stimulated RAW 264.7 cells.

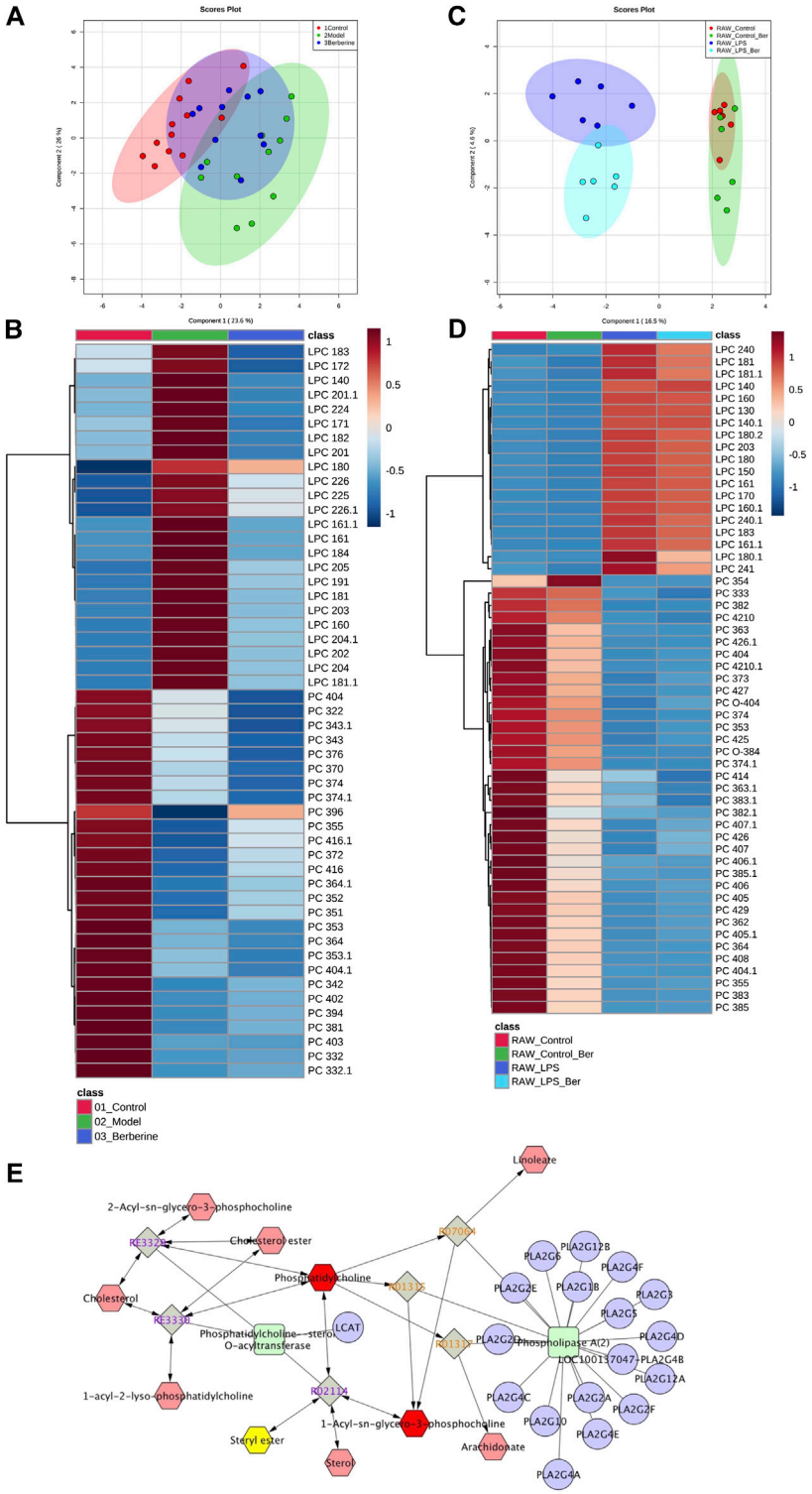

FIGURE 1 | Berberine reduces the LPC level in DSS-treated colitis and LPS-stimulated RAW 264.7 cells. **(A)** PCA score plot of berberine treatment based on lipidomics profiling of DSS-induced colitis mice serum (merged using negative and positive ionization modes, ESI –/ESI +). **(B)** Heat map of PC and LPC profiles in DSS-induced colitis mice serum. **(C)** PCA score plot of berberine treatment based on lipidomics profiling of LPS-treated RAW cells. **(D)** Heat map of PC and LPC profiles in LPS-treated RAW cells. **(E)** KEGG pathway map of the PC and LPC metabolism.

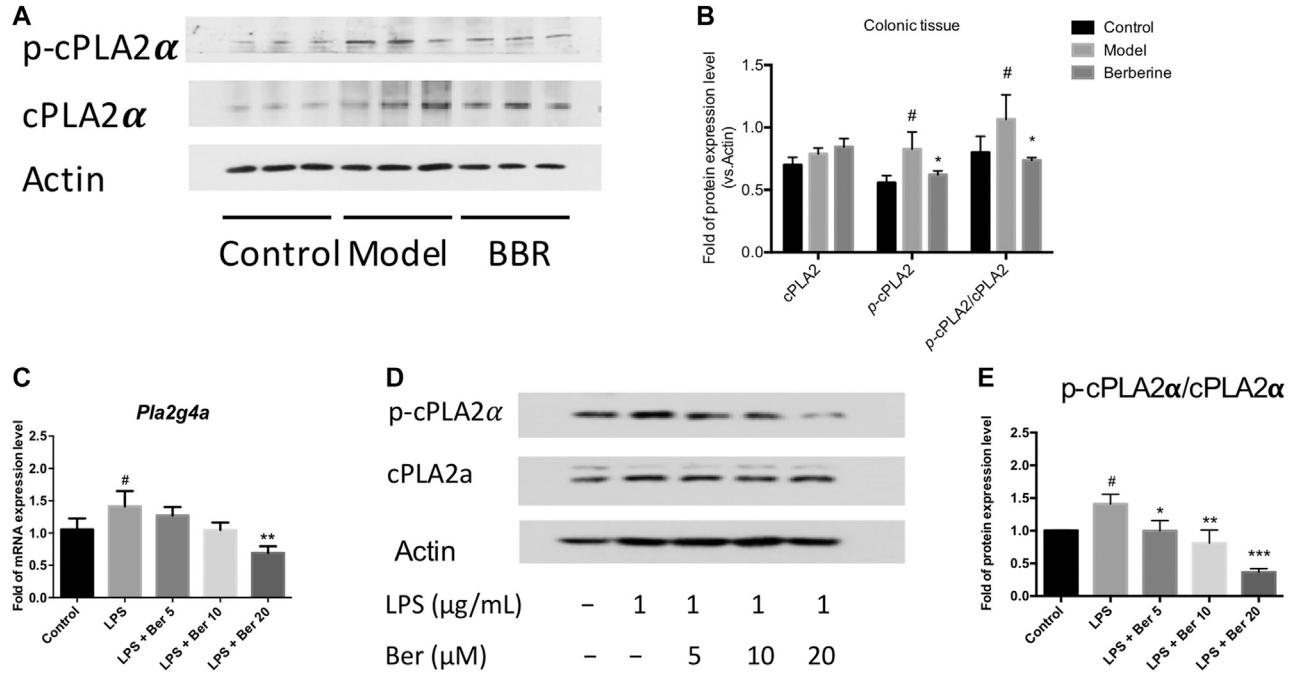

FIGURE 2 | Berberine regulates PLA2G4A (cPLA2α) dysfunction in DSS-treated colitis and LPS-stimulated RAW 264.7 cells. **(A,B)** Immunoblot and the semi-quantitative results of cPLA2α and p-cPLA2α in colon tissues of berberine treatment on DSS-induced colitis mice. **(C)** *Pla2g4a* mRNA expression level of berberine treatment on LPS-treated RAW cells. **(D,E)** Immunoblot and the semi-quantitative results of cPLA2α and p-cPLA2α of berberine treatment on LPS-treated RAW cells. Data are given in means ± SD. $^{*,\#}p < 0.05$, $^{**,\#\#}p < 0.01$, and $^{***,\#\#\#}p < 0.001$. # indicates comparisons between the control group and model group or LPS group. * indicates comparisons between the berberine group and model group or LPS group.

Berberine Regulates PLA2G4A Dysfunction in Dextran Sulfate Sodium–Treated Colitis and Lipopolysaccharides-Stimulated RAW 264.7 Cells

The cytosolic phospholipase A2α (PLA2G4A) activity has been shown to be increased in the colon biopsies of UC patients (Murase et al., 2016; Murase et al., 2017). Herein, we examined the expression of PLA2G4A and the effect of berberine on the PLA2G4A in experimental colitic mice. The phosphorylated forms of PLA2G4A (p-cPLA2α) was found up-regulated in the colon tissues of DSS-induced colitis mice and suppressed by berberine treatment (**Figures 2A,B**). Next, we examined the mRNA and protein expression levels of PLA2G4A in the RAW 264.7 macrophages under inflammatory conditions. The mRNA expression level of *Pla2g4a* and the protein expression level of *p*-cPLA2α all significantly increased after LPS stimulation. Berberine suppressed the up-regulation of PLA2G4A in LPS-stimulated RAW 264.7 macrophages in a dose-dependent manner (**Figures 2C–E**). Since PLA2G4A (cPLA2α) has been shown to be associated with the inflammation and PLA2G4A inhibitors significantly suppressed inflammatory responses in collagen-induced arthritis (Feuerherm et al., 2019), we wondered whether berberine suppresses the inflammatory responses by regulating PLA2G4A dysfunction.

Berberine Suppresses Inflammation via Regulating PLA2G4A Activity in Lipopolysaccharides-Stimulated RAW 264.7 Cells

Neon® Transfection System was used to establish transfection models using *Pla2g4a* and control siRNA. Together with the transfection models, a phospholipase A2 (PLA2) activator, namely, sc-3034 (from PLA2 activating protein PLAP, 50 μg/ml) was used for activating PLA2G4A. Subsequently, we determined the expression levels of pro-inflammatory genes in knockdown and activating models of PLA2G4A RAW 264.7. We found the expression of pro-inflammatory gene levels decreased in the *Pla2g4a* siRNA model but increased by sc-3034 treatment. Meanwhile, we found that knockdown of *Pla2g4a* promoted berberine-induced suppression of pro-inflammatory genes in LPS-activated RAW 264.7 cells. In contrast, activation of PLA2G4A by sc-3034 suppressed the anti-inflammatory effects of berberine on LPS-stimulated RAW 264.7 cells (**Figures 3A,B**). Therefore, the anti-inflammatory properties of berberine are PLA2G4A-dependent in RAW 264.7 cells.

Berberine Directly Inhibits PLA2G4A Activity

We then determined whether berberine directly binds to PLA2G4A by using a human PLA2G4A protein assay. Berberine exhibited an IC_{50} = 15 μM on PLA2G4A activity (**Figures 4A,B**). The crystal structure of both the C2- and the

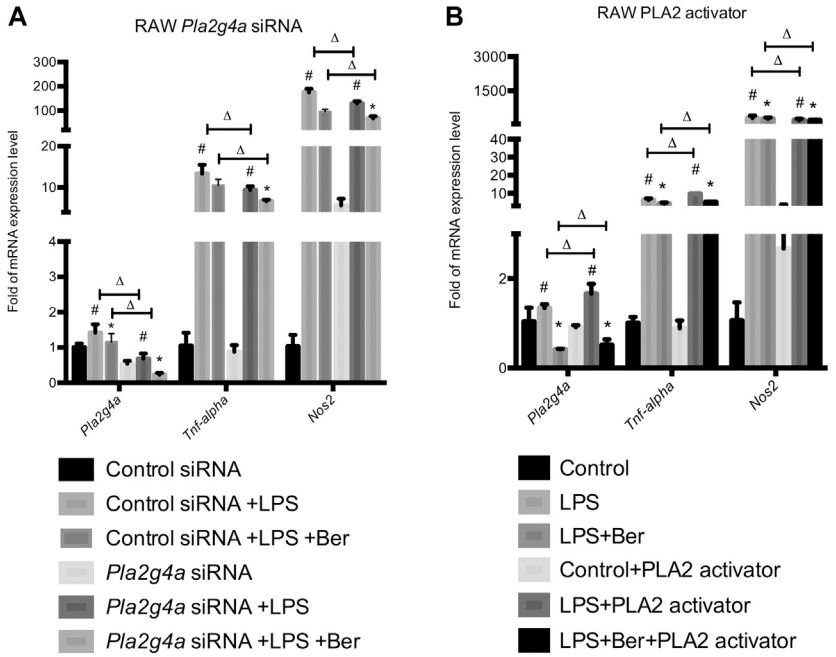

FIGURE 3 | Berberine suppresses inflammation via regulating PLA2G4A activity in RAW 264.7 cells. **(A)** The mRNA expression level of Pla2g4a, Tnf-alpha, and Nos2 in RAW cells transfected with Pla2g4a siRNA. **(B)** The mRNA expression level of Pla2g4a, Tnf-alpha, and Nos2 in RAW cells treated with PLA2 activator. *comparisons between the LPS group and treatment group; # comparison between the LPS group and control group; Δ comparisons in the normal group and knockdown/overexpressed models. Data are represented in means + SD (n = 4–6 independent measurements). $^{*,\#,\Delta}p < 0.05$, $^{**,\#\#,\Delta\Delta}p < 0.01$, and $^{***,\#\#\#,\Delta\Delta\Delta}p < 0.001$.

catalytic domain of PLA2G4A was published in 1999 (PDB ID: 1CJY) (Dessen et al., 1999). However, in this structure, the catalytic domain is ligand-free, and the active site was covered by the lid (residue 396–461) (**Supplementary Figure S4**), which makes it unsuitable for docking study. Meanwhile, the catalytic domain with the "open lid" conformation of another member in the phospholipase A2 group IV, PLA2G4D, was resolved in 2016 (PDB ID: 5IXC) (Wang et al., 2016a). The lid in PLA2G4D (residue 530–575) was rotated, and the active site was occupied by a substrate-like inhibitor, methyl gamma-linolenyl fluorophosphonate (**Supplementary Figure S4**). Therefore, to understand the binding mode of berberine on PLA2G4A, we performed molecular docking based on previous structural studies of PLA2G1D. By aligning the sequences and main-chain atom positions in these two structures (**Supplementary Figure S5**), we built a putative model of the "open lid" conformation of PLA2G4A with homology modeling (**Supplementary Figure S6A**). The model quality was reasonably good, and the backbone dihedral angles of most residues were within favorable and allowed regions (**Supplementary Figure S6B**). Based on this putative, "open lid," and holo-structure of PLA2G4A, we performed the docking study of berberine. The docking results showed berberine could insert into the active site of the catalytic domain of PLA2G4A (**Figures 4C–E**). The best docking pose was with a binding energy of −7.02 kcal/mol suggesting that berberine may have favorable interactions with the PLA2G4A catalytic domain. Interaction analysis based on structural observation indicated that residues I399, L400, L552, T680, and F683 may have hydrophobic interactions with berberine. However, neither hydrogen bond nor salt bridge interactions could be observed from the docking complex. Taken together, the docking study showed that berberine could be a moderate binder of the PLA2G4A catalytic domain.

Berberine Inhibits PLA2G4A Activity via Mitogen-Activated Protein Kinase/c-Jun N-Terminal Kinase Signaling Pathway

Since previous studies have shown PLA2G4A is regulated via the MAPK/JNK signaling pathway (Casas et al., 2009), we used JNK inhibitor SP600125 to investigate whether PLA2G4A is mediated by the JNK signaling pathway in RAW 264.7 cells. The protein expression levels of *p*-JNK and *p*-cPLAα were significantly increased in LPS-stimulated RAW 264.7 cells, which was suppressed by SP600125 (10 μM) (**Figures 5A,B**). Next, we used a nonspecific JNK activator PMA to investigate whether berberine can regulate the dysfunction of PLA2G4A via the JNK signaling pathway. We revealed that *p*-JNK and *p*-cPLAα were up-regulated significantly after treating RAW with PMA (**Figures 5C,E**), whilst berberine treatment suppressed the up-regulation of p-JNK and p-cPLA2α in LPS-treated RAW 264.7 cells (**Figures 5D,F**). Combining the results together, berberine treatment regulates PLA2G4A dysfunction via both direct binding and regulation of the

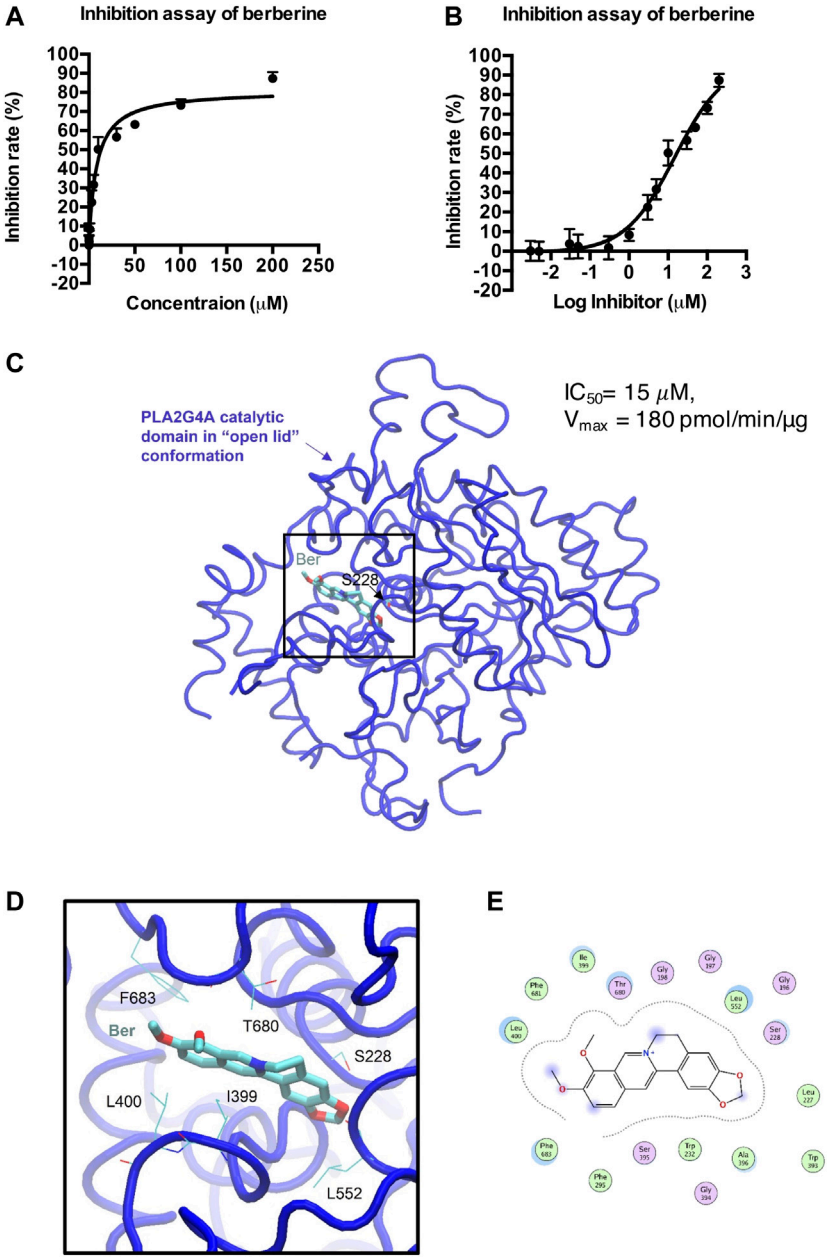

FIGURE 4 | Docking model of berberine (Ber) and PLA2G4A catalytic domain. **(A,B)** The inhibition rate (%) of berberine on PLA2G4A activity. **(C)** The overall 3D structure of the berberine–PLA2G4A complex. The backbone of protein is rendered in tube and colored in blue. Berberine is rendered in stick and colored by element. The nucleophilic residue serine (S228)is rendered inline and colored by element. **(D)** A close view of the active site binding with berberine. Key residues interacted with berberine are rendered inline and colored by element. **(E)** The 2D protein–ligand interaction diagram of berberine–PLA2G4A complex. Protein residues are rendered in circles and colored based on their properties: green, hydrophobic residue; purple, polar residue.

JNK signaling pathway in LPS-stimulated RAW 264.7 cells (**Figure 6**).

DISCUSSION AND CONCLUSION

In this study, we have shown a novel phospholipid-related mechanism underlying the anti-inflammatory effects of berberine. First, we demonstrated the aberrant activation of PLA2G4A in inflammatory responses in both *in vivo* experimental murine colitis and *in vitro* RAW 264.7 macrophages. In these *in vivo* and *in vitro* models, we showed berberine treatment significantly reduces the phosphorylation of PLA2G4A. Second, we showed berberine suppressed the expression of pro-inflammatory genes by inhibiting PLA2G4A in these models. Mechanically, we revealed that berberine

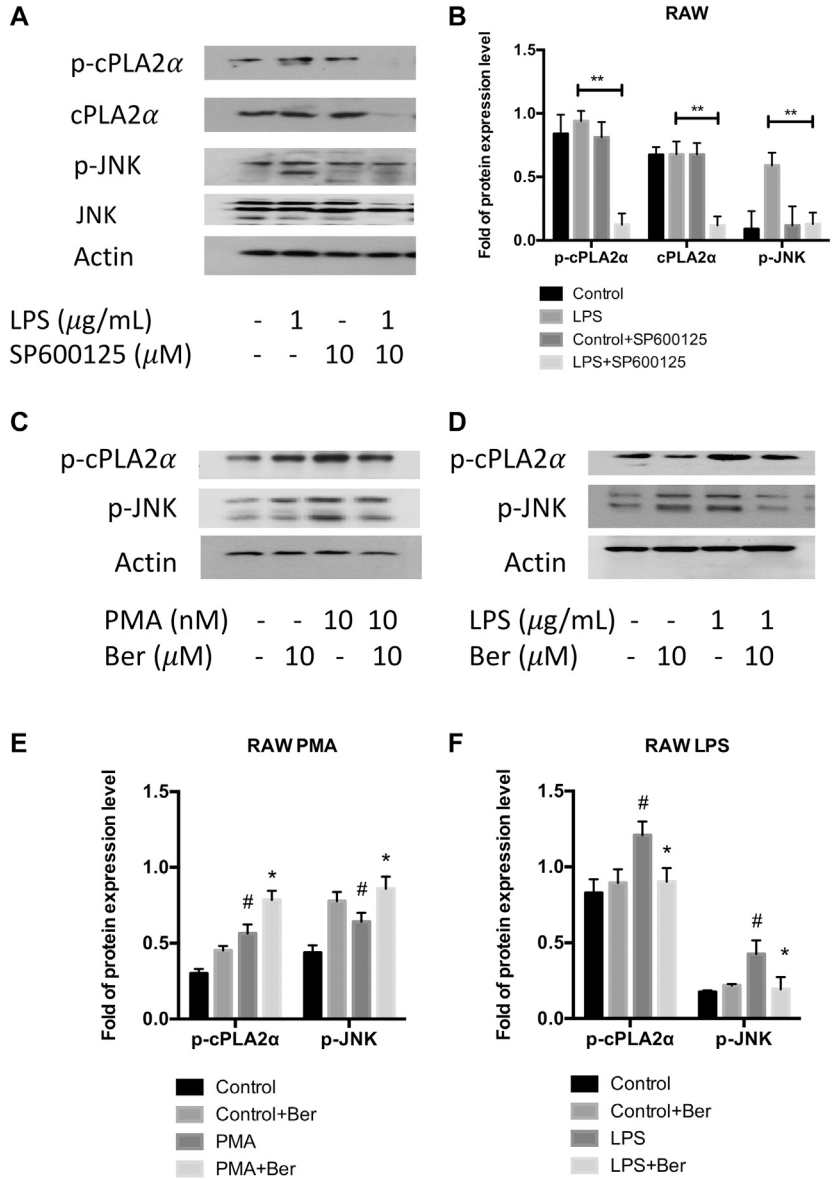

FIGURE 5 | Berberine inhibits PLA2G4A activity via the MAPK/JNK signaling pathway. **(A,B)** The immunoblot and semi-quantification results of cPLA2α, p-cPLA2α, JNK, and p-JNK in RAW cells treated with JNK inhibitor SP600125. * indicates comparisons in the model group in the absence or presence of SP600125. **(C,E)** The immunoblot and semi-quantification results of *p*-cPLA2α and *p*-JNK in RAW cells treated with berberine and JNK activator PMA. **(D,F)** The immunoblot and semi-quantification results of p-cPLA2α and p-JNK in inflamed RAW cells treated with berberine. # indicates comparisons between control group and PMA or LPS group. * indicates comparisons of PMA/LPS treatment in the absence or presence of berberine treatment. $^{*,\ \#}p < 0.05$, $^{**,\ \#\#}p < 0.01$, and $^{***,\ \#\#\#}p < 0.001$.

directly inhibits PLA2G4A activity and regulates PLA2G4A activation via the MAPK/JNK signaling pathway in inflammatory responses. Collectively, this study suggested berberine suppresses inflammatory responses through inhibition of PLA2G4A activity to ameliorate DSS-induced experimental colitis.

Numerous studies have revealed the anti-inflammatory properties of berberine in the digestive system (Habtemariam, 2016). The anti-inflammatory activity of berberine is mainly dependent on the inhibition of expression of pro-inflammatory factors including TNF-alpha, IL-6, IL-8, IFN-γ, and IL-1β (Zou et al., 2017). It has been reported the inhibitory effects of berberine on pro-inflammatory responses including TNF-alpha, IL-6, iNOS, and COX-2 were mediated through activation of AMP-activated protein kinase (AMPK) (Jeong et al., 2009). Moreover, studies have shown berberine exerts anti-inflammatory effects on DSS-induced colitis via Akt, NF-κB, and MAPK dependent signaling pathways (Amasheh et al., 2010; Remppis et al., 2010). In this study, we further investigated the pharmacological mechanism of berberine treatment in the experimental colitis. Lysophospholipids have attracted increased attention due to their importance in maintaining the function of

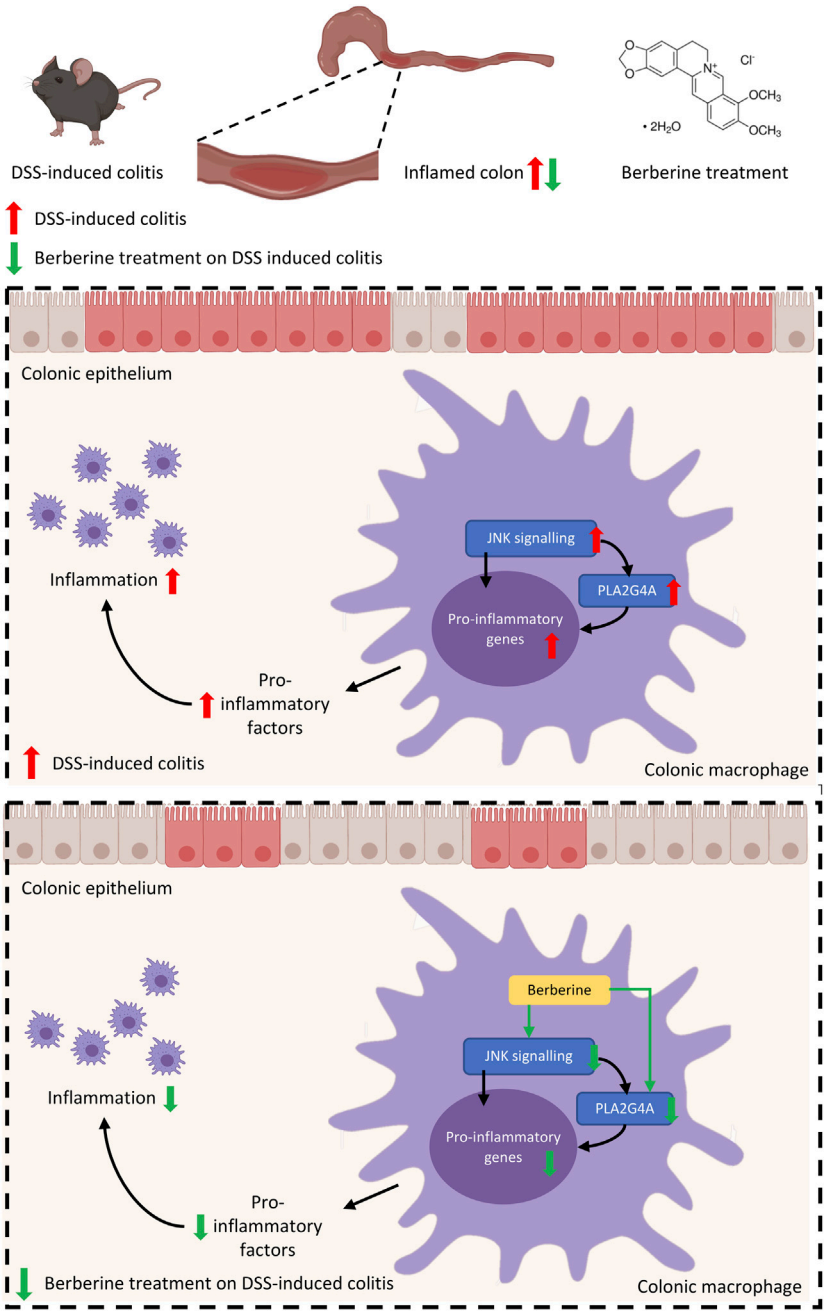

FIGURE 6 | Mechanisms of berberine anti-inflammatory effects in experimental colitis are mediated by PLA2G4A in colonic macrophages.

the intestinal mucus barrier (Wang et al., 2018). First, PC and LPC contents are intensely associated with UC in both human and animal colitis models. Patients with UC have significantly increased serum LPC content and an increased LPC/PC ratio in the colonic mucus in both remission and active disease states (Ehehalt et al., 2004; Franzosa et al., 2019). In animal models of UC, LPC (16:0) has been found elevated in the serum of TNBS-induced colitis mice (Zhang et al., 2012) and DSS-induced colitis mice (Wang et al., 2016b) through untargeted metabolomics profiling. Second, LPC may contribute to the pathophysiological progression of UC. PC has been shown with anti-inflammatory effects on the intestinal mucosal barrier (Schneider et al., 2010), while LPC has been revealed with pro-inflammatory phenotype on macrophages (Qin et al., 2014). The increased LPC/PC ratio is due to the elevated activity of catalyzed enzyme phospholipase A2α. Recent studies have indicated that cytosolic phospholipase A2α up-regulation is associated with the severity of inflammation (Gil-de-Gomez

et al., 2014; Ashley et al., 2016) and the development of murine colitis (Rosengarten et al., 2016). Herein, phospholipase A2 is considered as a potential therapeutic target for UC. Our results confirmed that berberine, as a potent anti-inflammatory agent on UC, regulates the LPC content and the PLA2G4A expression in experimental colitis mice. Similarly, one study also showed berberine (50 mg/kg) protects against LPS-induced lung injury and inhibits cytosolic phospholipase A2α in lung tissue, whereas this study lacks mechanistic insights into the berberine action on PLA2G4A (Zhang et al., 2008). In contrast, our study demonstrated the mechanisms of therapeutic effects of berberine on murine colitis is mediated by inhibiting cytosolic phospholipase A2α via direct binding and the MAPK/JNK signaling pathway.

Macrophages are responsible for innate immune responses and play an important role in mediating colonic mucosal inflammation in IBD patients (Steinbach and Plevy, 2013). Defined by the broad terms of pro-inflammatory (M1) and anti-inflammatory (M2) phenotypes, macrophages are activated toward different phenotypes depending on the stimuli (Murray et al., 2014). The colonic macrophages are mainly polarized to M1 pro-inflammatory phenotype in the colon and linked to disease severity in IBD (Lissner et al., 2015). The anti-inflammatory effects of berberine on colitis are mediated by multiple signaling pathways, such as AKT, AMPK, and MAPK/JNK signaling pathways (Cui et al., 2009; Jeong et al., 2009; Amasheh et al., 2010; Zhou et al., 2015). Nevertheless, the mechanisms of berberine treatment in suppressing inflammation in macrophages in IBD are not fully understood. On the one hand, considering berberine directly binds to secretory phospholipase A2 (Chandra et al., 2011), berberine may directly inhibit cytosolic phospholipase A2 activity. Using human PLA2G4A protein assay, we found that berberine directly inhibits its activity. On the other hand, by addressing the related references (Casas et al., 2009; Guijas et al., 2012; Lee et al., 2013), we found cytosolic phospholipase A2α is also possibly regulated by the JNK signaling pathway in IBD. Additionally, JNK is found to be up-regulated in colon tissues of DSS-induced colitis mice (Hollenbach et al., 2004; Gao et al., 2016) and inflamed mucosa of IBD patients (Docena et al., 2010; Zhou et al., 2017). JNK inhibitor has also been shown for protective effects on experimental colitis in mice (Docena et al., 2010; Reinecke et al., 2012). Besides the direct binding, we have shown that the inhibitory effect of berberine on cytosolic phospholipase A2α activity is also dependent on the MAPK/JNK signaling pathway in RAW 264.7 macrophages.

There are several limitations to this study. First, to examine the role of PLA2G4A in mediating the inflammatory responses and whether the anti-inflammatory properties of berberine treatment are through inhibition of PLA2G4A, we have used *Pla2g4a* siRNA to knock down the expression of cytosolic phospholipase A2α in *in vitro* cell models but not in *in vivo* animal models. Second, due to the lack of specific JNK activator, we used a general MAPK activator PMA to induce the activation of MAPK/JNK signaling to determine whether the inhibitory effects of berberine treatment on cytosolic phospholipase A2α are mediated by MAPK/JNK. In the future, we will establish colon-specific *Pla2g4a* knockout mice to further understand the role of colonic *Pla2g4a* in the inflammatory responses of IBD. Moreover, we will perform a screening assay of PLA2G4A to investigate the inhibitory activity of bioactive components from herbal extracts on PLA2G4A in order to provide potential therapeutic strategies for IBD.

In conclusion, this study demonstrated that berberine suppresses colonic inflammatory responses through inhibition of PLA2G4A activity to ameliorate DSS-induced experimental colitis, which enhances our understanding on the pharmacological mechanism of berberine treatment on ulcerative colitis from a perspective of lipid metabolism and signaling. This study highlights the therapeutic potential of targeting cytosolic phospholipase A2a dysfunction in the management of IBD.

DATA AVAILABILITY STATEMENT

The raw data supporting the conclusions of this article will be made available by the authors, without undue reservation, to any qualified researcher.

ETHICS STATEMENT

The animal study was reviewed and approved by Animal Care Ethics Committee, Hong Kong Baptist University.

AUTHOR CONTRIBUTIONS

Z-XB, H-TX, and C-YL designed the study and revised the manuscript. LXZ, C-YL, and P-GW conducted the animal study, cell study and wrote the manuscript. TH conducted molecular docking study. X-JH, Z-WN, and LXZ performed the lipidomics analysis. LZ, SF, HK, and HW provided technical support and advice toward this study.

FUNDING

This work was kindly funded by National Natural Science Foundation of China (Grants No. 81973538 and 81560676), Key-Area Research and Development Program of Guangdong Province (Grants No. 2020B1111110003), Shenzhen Science and Technology Innovation Committee Grant (Grants No. JCYJ20170413170320959 and JCYJ20190808164201654), and Logan Charitable Foundation.

SUPPLEMENTARY MATERIAL

The Supplementary Material for this article can be found online at: https://www.frontiersin.org/articles/10.3389/fphar.2020.576496/full#supplementary-material

REFERENCES

Aiyar, N., Disa, J., Ao, Z., Ju, H., Nerurkar, S., Willette, R. N., et al. (2007). Lysophosphatidylcholine induces inflammatory activation of human coronary artery smooth muscle cells. *Mol. Cell. Biochem.* 295, 113–120. doi:10.1007/s11010-006-9280-x

Amasheh, M., Fromm, A., Krug, S. M., Amasheh, S., Andres, S., Zeitz, M., et al. (2010). TNFα-induced and berberine-antagonized tight junction barrier impairment via tyrosine kinase, Akt and NFκB signaling. *J. Cell Sci.* 123, 4145–4155. doi:10.1242/jcs.070896

Ashley, J. W., Hancock, W. D., Nelson, A. J., Bone, R. N., Tse, H. M., Wohltmann, M., et al. (2016). Polarization of macrophages toward M2 phenotype is favored by reduction in iPLA2β Group VIA phospholipase a2. *J. Biol. Chem.* 291, 23268–23281. doi:10.1074/jbc.M116.754945

Biyyani, R. S. R. S., Putka, B. S., and Mullen, K. D. (2010). Dyslipidemia and lipoprotein profiles in patients with inflammatory bowel disease. *J. Clin. Lipidol.* 4, 478–482. doi:10.1016/j.jacl.2010.08.021

Casas, J., Meana, C., Esquinas, E., Valdearcos, M., Pindado, J., Balsinde, J., et al. (2009). Requirement of JNK-mediated phosphorylation for translocation of group IVA phospholipase A2 to phagosomes in human macrophages. *J. Immunol.* 183, 2767–2774. doi:10.4049/jimmunol.0901530

Chander, K., Vaibhav, K., Ejaz Ahmed, M., Javed, H., Tabassum, R., Khan, A., et al. (2014). Quercetin mitigates lead acetate-induced behavioral and histological alterations via suppression of oxidative stress, Hsp-70, Bak and upregulation of Bcl-2. *Food Chem. Toxicol.* 68, 297–306. doi:10.1016/j.fct.2014.02.012

Chandra, D. N., Prasanth, G. K., Singh, N., Kumar, S., Jithesh, O., Sadasivan, C., et al. (2011). Identification of a novel and potent inhibitor of phospholipase A2 in a medicinal plant: crystal structure at 1.93 Å and Surface Plasmon Resonance analysis of phospholipase A2 complexed with berberine. *Biochim. Biophys. Acta Protein Proteonomics* 1814, 657–663. doi:10.1016/j.bbapap.2011.03.002

Chen, C., Shah, Y. M., Morimura, K., Krausz, K. W., Miyazaki, M., Richardson, T. A., et al. (2008). Metabolomics reveals that hepatic stearoyl-CoA desaturase 1 downregulation exacerbates inflammation and acute colitis. *Cell Metabol.* 7, 135–147. doi:10.1016/j.cmet.2007.12.003

Cui, G., Qin, X., Zhang, Y., Gong, Z., Ge, B., and Zang, Y. Q. (2009). Berberine differentially modulates the activities of ERK, p38 MAPK, and JNK to suppress Th17 and Th1 T cell differentiation in type 1 diabetic mice. *J. Biol. Chem.* 284, 28420–28429. doi:10.1074/jbc.M109.012674

Deeth, R. J., Fey, N., and Williams–Hubbard, B. (2005). DommiMOE: an implementation of ligand field molecular mechanics in the molecular operating environment. *J. Comput. Chem.* 26, 123–130. doi:10.1002/jcc.20137

Dessen, A., Tang, J., Schmidt, H., Stahl, M., Clark, J. D., Seehra, J., et al. (1999). Crystal structure of human cytosolic phospholipase A2 reveals a novel topology and catalytic mechanism. *Cell* 97, 349–360. doi:10.1016/s0092-8674(00)80744-8

Docena, G., Rovedatti, L., Kruidenier, L., Fanning, Á., Leakey, N. A. B., Knowles, C. H., et al. (2010). Down-regulation of p38 mitogen-activated protein kinase activation and proinflammatory cytokine production by mitogen-activated protein kinase inhibitors in inflammatory bowel disease. *Clin. Exp. Immunol.* 162, 108–115. doi:10.1111/j.1365-2249.2010.04203.x

Ehehalt, R., Wagenblast, J., Erben, G., Lehmann, W., Hinz, U., Merle, U., et al. (2004). Phosphatidylcholine and lysophosphatidylcholine in intestinal mucus of ulcerative colitis patients. A quantitative approach by nanoelectrospray-tandem mass spectrometry. *Scand. J. Gastroenterol.* 39, 737–742. doi:10.1080/00365520410006233

Fan, F., Mundra, P. A., Fang, L., Galvin, A., Moore, X. L., Weir, J. M., et al. (2015). Lipidomic profiling in inflammatory bowel disease: comparison between ulcerative colitis and Crohn's disease. *Inflamm. Bowel Dis.* 21, 1511–1518. doi:10.1097/MIB.0000000000000394

Feuerherm, A. J., Dennis, E. A., and Johansen, B. (2019). Cytosolic group IVA phospholipase A2 inhibitors, AVX001 and AVX002, ameliorate collagen-induced arthritis. *Arthritis Res. Ther.* 21, 29. doi:10.1186/s13075-018-1794-6

Franzosa, E. A., Sirota-Madi, A., Avila-Pacheco, J., Fornelos, N., Haiser, H. J., Reinker, S., et al. (2019). Gut microbiome structure and metabolic activity in inflammatory bowel disease. *Nat. Microbiol.* 4, 293–305. doi:10.1038/s41564-018-0306-4

Gao, Y., Huang, Y., Zhao, Y., Hu, Y., Li, Z., Guo, Q., et al. (2016). LL202 protects against dextran sulfate sodium-induced experimental colitis in mice by inhibiting MAPK/AP-1 signaling. *Oncotarget* 7, 63981–63994. doi:10.18632/oncotarget.11742

Gil-de-Gomez, L., Astudillo, A. M., Guijas, C., Magrioti, V., Kokotos, G., Balboa, M. A., et al. (2014). Cytosolic group IVA and calcium-independent group VIA phospholipase A2s act on distinct phospholipid pools in zymosan-stimulated mouse peritoneal macrophages. *J. Immunol.* 192, 752–762. doi:10.4049/jimmunol.1302267

Guijas, C., Pérez-Chacón, G., Astudillo, A. M., Rubio, J. M., Gil-de-Gómez, L., Balboa, M. A., et al. (2012). Simultaneous activation of p38 and JNK by arachidonic acid stimulates the cytosolic phospholipase A(2)-dependent synthesis of lipid droplets in human monocytes. *J. Lipid Res.* 53, 2343–2354. doi:10.1194/jlr.M028423

Habtemariam, S. (2016). Berberine and inflammatory bowel disease: a concise review. *Pharmacol. Res.* 113, 592–599. doi:10.1016/j.phrs.2016.09.041.

Hollenbach, E., Neumann, M., Vieth, M., Roessner, A., Malfertheiner, P., and Naumann, M. (2004). Inhibition of p38 MAP kinase- and RICK/NF-kappaB-signaling suppresses inflammatory bowel disease. *FASEB J.* 18, 1550–1552. doi:10.1096/fj.04-1642fje

Hu, Y., Ehli, E. A., Kittelsrud, J., Ronan, P. J., Munger, K., Downey, T., et al. (2012). Lipid-lowering effect of berberine in human subjects and rats. *Phytomedicine* 19, 861–867. doi:10.1016/j.phymed.2012.05.009

Humphrey, W., Dalke, A., and Schulten, K. (1996). VMD: visual molecular dynamics. *J. Mol. Graph.* 14, 33–38. doi:10.1016/0263-7855(96)00018-5

Jeong, H. W., Hsu, K. C., Lee, J.-W., Ham, M., Huh, J. Y., Shin, H. J., et al. (2009). Berberine suppresses proinflammatory responses through AMPK activation in macrophages. *Am. J. Physiol. Metab.* 296, E955–E964. doi:10.1152/ajpendo.90599.2008

Kaplan, G. G. (2015). The global burden of IBD: from 2015 to 2025. *Nat. Rev. Gastroenterol. Hepatol.* 12, 720–727. doi:10.1038/nrgastro.2015.150

Karaahmet, F., Basar, O., Coban, S., and Yuksel, I. (2013). Dyslipidemia and inflammation in patients with inflammatory bowel disease. *Dig. Dis. Sci.* 58, 1806–1807. doi:10.1007/s10620-013-2614-0

Lee, I.-T., Lin, C.-C., Cheng, S.-E., Hsiao, L.-D., Hsiao, Y.-C., and Yang, C.-M. (2013). TNF-α induces cytosolic phospholipase A2 expression in human lung epithelial cells via JNK1/2- and p38 MAPK-dependent AP-1 activation. *PLoS One* 8, e72783. doi:10.1371/journal.pone.0072783.

Li, C., Xi, Y., Li, S., Zhao, Q., Cheng, W., Wang, Z., et al. (2015). Berberine ameliorates TNBS induced colitis by inhibiting inflammatory responses and Th1/Th17 differentiation. *Mol. Immunol.* 67, 444–454. doi:10.1016/j.molimm.2015.07.013

Li, Y., Xiao, H., Hu, D., Fatima, S., Lin, C., Mu, H., et al. (2016). Berberine ameliorates chronic relapsing dextran sulfate sodium-induced colitis in C57BL/6 mice by suppressing Th17 responses. *Pharmacol. Res.* 110, 227–239. doi:10.1016/j.phrs.2016.02.010

Lissner, D., Schumann, M., Batra, A., Kredel, L.-I., Kühl, A. A., Erben, U., et al. (2015). Monocyte and M1 macrophage-induced barrier defect contributes to chronic intestinal inflammation in IBD. *Inflamm. Bowel Dis.* 21, 1297–1305. doi:10.1097/MIB.0000000000000384

Liu, Y., Liu, X., Hua, W., Wei, Q., Fang, X., Zhao, Z., et al. (2018). Berberine inhibits macrophage M1 polarization via AKT1/SOCS1/NF-κB signaling pathway to protect against DSS-induced colitis. *Int. Immunopharm.* 57, 121–131. doi:10.1016/j.intimp.2018.01.049

Maier, J. K. X., and Labute, P. (2014). Assessment of fully automated antibody homology modeling protocols in molecular operating environment. *Proteins* 82, 1599–1610. doi:10.1002/prot.24576

Murase, R., Sato, H., Yamamoto, K., Ushida, A., Nishito, Y., Ikeda, K., et al. (2016). Group X secreted phospholipase A2 releases ω-3 polyunsaturated fatty acids, suppresses colitis and promotes sperm fertility. *J. Biol. Chem.* 291, 6895–6911. doi:10.1074/jbc.m116.715672

Murase, R., Taketomi, Y., Miki, Y., Nishito, Y., Saito, M., Fukami, K., et al. (2017). Group III phospholipase A 2 promotes colitis and colorectal cancer. *Sci. Rep.* 7, 12261. doi:10.1038/s41598-017-12434-z

Murray, P. J., Allen, J. E., Biswas, S. K., Fisher, E. A., Gilroy, D. W., Goerdt, S., et al. (2014). Macrophage activation and polarization: nomenclature and experimental guidelines. *Immunity* 41, 14–20. doi:10.1016/j.immuni.2014.06.008

Olofsson, K. E., Andersson, L., Nilsson, J., and Björkbacka, H. (2008). Nanomolar concentrations of lysophosphatidylcholine recruit monocytes and induce pro-inflammatory cytokine production in macrophages. *Biochem. Biophys. Res. Commun.* 370, 348–352. doi:10.1016/j.bbrc.2008.03.087

Parhofer, K. G. (2015). Interaction between glucose and lipid metabolism: more than diabetic dyslipidemia. *Diabetes Metab. J.* 39, 353–362. doi:10.4093/dmj.2015.39.5.353

Qian, Z., Wu, Z., Huang, L., Qiu, H., Wang, L., Li, L., et al. (2015). Mulberry fruit prevents LPS-induced NF-κB/pERK/MAPK signals in macrophages and suppresses acute colitis and colorectal tumorigenesis in mice. *Sci. Rep.* 5, 17348. doi:10.1038/srep17348

Qin, X., Qiu, C., and Zhao, L. (2014). Lysophosphatidylcholine perpetuates macrophage polarization toward classically activated phenotype in inflammation. *Cell. Immunol.* 289, 185–190.doi:10.1016/j.cellimm.2014.04.010

Reinecke, K., Eminel, S., Dierck, F., Roessner, W., Kersting, S., Chromik, A. M., et al. (2012). The JNK inhibitor XG-102 protects against TNBS-induced colitis. *PLoS One* 7, e30985. doi:10.1371/journal.pone.0030985

Remppis, A., Bea, F., Greten, H. J., Buttler, A., Wang, H., Zhou, Q., et al. (2010). Rhizoma coptidis inhibits LPS-induced MCP-1/CCL2 production in murine macrophages via an AP-1 and NF B-dependent pathway. *Mediat. Inflamm.* 2010, 194896. doi:10.1155/2010/194896

Rosengarten, M., Hadad, N., Solomonov, Y., Lamprecht, S., and Levy, R. (2016). Cytosolic phospholipase A2α has a crucial role in the pathogenesis of DSS-induced colitis in mice. *Eur. J. Immunol.* 46, 400–408. doi:10.1002/eji.201545848

Schneider, H., Braun, A., Füllekrug, J., Stremmel, W., and Ehehalt, R. (2010). Lipid based therapy for ulcerative colitis—modulation of intestinal mucus membrane phospholipids as a tool to influence inflammation. *Int. J. Mol. Sci.* 11, 4149–4164. doi:10.3390/ijms11104149

Song, J., Liu, K., Yi, J., Zhu, D., Liu, G., and Liu, B. (2010). Luteolin inhibits lysophosphatidylcholine-induced apoptosis in endothelial cells by a calcium/mithocondrion/caspases-dependent pathway. *Planta Med.* 76, 433–438. doi:10.1055/s-0029-1186197

Steinbach, E. C., and Plevy, S. E. (2013). The role of macrophages and dendritic cells in the initiation of inflammation in IBD. *Inflamm. Bowel Dis.* 20, 166–175. doi:10.1097/MIB.0b013e3182a69dca

Sun, G. Y., Shelat, P. B., Jensen, M. B., He, Y., Sun, A. Y., and Simonyi, A. (2010). Phospholipases A2 and inflammatory responses in the central nervous system. *Neuromolecular Med.* 12, 133–148. doi:10.1007/s12017-009-8092-z

Wang, B., Rong, X., Palladino, E. N. D., Wang, J., Fogelman, A. M., Martín, M. G., et al. (2018). Phospholipid remodeling and cholesterol availability regulate intestinal stemness and tumorigenesis. *Cell Stem Cell* 22, 206–220. doi:10.1016/j.stem.2017.12.017.

Wang, H., Klein, M. G., Snell, G., Lane, W., Zou, H., Levin, I., et al. (2016a). Structure of human GIVD cytosolic phospholipase A2 reveals insights into substrate recognition. *J. Mol. Biol.* 428, 2769–2779. doi:10.1016/j.jmb.2016.05.012

Wang, R., Gu, X., Dai, W., Ye, J., Lu, F., Chai, Y., et al. (2016b). A lipidomics investigation into the intervention of celastrol in experimental colitis. *Mol. Biosyst.* 12, 1436–1444. doi:10.1039/c5mb00864f

Wei, S., Zhang, M., Yu, Y., Lan, X., Yao, F., Yan, X., et al. (2016). Berberine attenuates development of the hepatic gluconeogenesis and lipid metabolism disorder in type 2 diabetic mice and in palmitate-incubated HepG2 cells through suppression of the HNF-4α miR122 pathway. *PLoS One* 11, e0152097. doi:10.1371/journal.pone.0152097

Zhang, H., Wang, H., Lu, D., Qi, R., Wang, Y., Yan, Y., et al. (2008). Berberine inhibits cytosolic phospholipase A2 and protects against LPS-induced lung injury and lethality independent of the alpha2-adrenergic receptor in mice. *Shock* 29, 617–622. doi:10.1097/SHK.0b013e318157ea14

Zhang, L. C., Wang, Y., Tong, L. C., Sun, S., Liu, W. Y., Zhang, S., et al. (2017). Berberine alleviates dextran sodium sulfate-induced colitis by improving intestinal barrier function and reducing inflammation and oxidative stress. *Exp. Ther. Med.* 13, 3374–3382. doi:10.3892/etm.2017.4402

Zhang, Q., Xiao, X., Feng, K., Wang, T., Li, W., Yuan, T., et al. (2011). Berberine moderates glucose and lipid metabolism through multipathway mechanism. *Evid. Based Complement. Altern. Med.* 2011. doi:10.1155/2011/924851

Zhang, X., Choi, F. F. K., Zhou, Y., Leung, F. P., Tan, S., Lin, S., et al. (2012). Metabolite profiling of plasma and urine from rats with TNBS-induced acute colitis using UPLC-ESI-QTOF-MS-based metabonomics—a pilot study. *FEBS J.* 279, 2322–2338. doi:10.1111/j.1742-4658.2012.08612.x

Zhao, L., Cang, Z., Sun, H., Nie, X., Wang, N., and Lu, Y. (2017). Berberine improves glucogenesis and lipid metabolism in nonalcoholic fatty liver disease. *BMC Endocr. Disord.* 17, 13. doi:10.1186/s12902-017-0165-7

Zhou, R., Chang, Y., Liu, J., Chen, M., Wang, H., Huang, M., et al. (2017). JNK pathway-associated phosphatase/DUSP22 suppresses CD4+ T-cell activation and Th1/Th17-cell differentiation and negatively correlates with clinical activity in inflammatory bowel disease. *Front. Immunol.* 8, 781. doi:10.3389/fimmu.2017.00781

Zhou, Y., Liu, S.-Q., Yu, L., He, B., Wu, S.-H., Zhao, Q., et al. (2015). Berberine prevents nitric oxide-induced rat chondrocyte apoptosis and cartilage degeneration in a rat osteoarthritis model via AMPK and p38 MAPK signaling. *Apoptosis* 20, 1187–1199. doi:10.1007/s10495-015-1152-y

Zou, K., Li, Z., Zhang, Y., Zhang, H., Li, B., Zhu, W., et al. (2017). Advances in the study of berberine and its derivatives: a focus on anti-inflammatory and anti-tumor effects in the digestive system. *Acta Pharmacol. Sin.* 38, 157–167. doi:10.1038/aps.2016.125

Conflict of Interest: The authors declare that the research was conducted in the absence of any commercial or financial relationships that could be construed as a potential conflict of interest.

frontiers in Pharmacology

ORIGINAL RESEARCH
published: 27 November 2020
doi: 10.3389/fphar.2020.584090

Da-Chai-Hu Decoction Ameliorates High Fat Diet-Induced Nonalcoholic Fatty Liver Disease Through Remodeling the Gut Microbiota and Modulating the Serum Metabolism

Huantian Cui[1], Yuting Li[2,3], Yuming Wang[2], Lulu Jin[2], Lu Yang[2], Li Wang[4], Jiabao Liao[5], Haoshuo Wang[2], Yanfei Peng[2], Zhaiyi Zhang[2], Hongwu Wang[2]* and Xiangguo Liu[1]**

[1]Shandong Provincial Key Laboratory of Animal Cell and Developmental Biology, School of Life Sciences, Shandong University, Qingdao, China, [2]Tianjin University of Traditional Chinese Medicine, Tianjin, China, [3]First Teaching Hospital of Tianjin University of Traditional Chinese Medicine, Tianjin, China, [4]Tianjin Second People's Hospital, Tianjin, China, [5]Jiaxing Hospital of Traditional Chinese Medicine, Jiaxing, China

The dysbiosis in gut microbiota could affect host metabolism and contribute to the development of nonalcoholic fatty liver disease (NAFLD). Da-Chai-Hu decoction (DCH) has demonstrated protective effects on NAFLD, however, the exact mechanisms remain unclear. In this study, we established a NAFLD rat model using a high fat diet (HFD) and provided treatment with DCH. The changes in gut microbiota post DCH treatment were then investigated using 16S rRNA sequencing. Additionally, serum untargeted metabolomics were performed to examine the metabolic regulations of DCH on NAFLD. Our results showed that DCH treatment improved the dyslipidemia, insulin resistance (IR) and ameliorated pathological changes in NAFLD model rats. 16S rRNA sequencing and untargeted metabolomics showed significant dysfunction in gut microbiota community and serum metabolites in NAFLD model rats. DCH treatment restored the dysbiosis of gut microbiota and improved the dysfunction in serum metabolism. Correlation analysis indicated that the modulatory effects of DCH on the arachidonic acid (AA), glycine/serine/threonine, and glycerophospholipid metabolic pathways were related to alterations in the abundance of *Romboutsia*, *Bacteroides, Lactobacillus, Akkermansia*, *Lachnoclostridium* and *Enterobacteriaceae* in the gut microflora. In conclusion, our study revealed the ameliorative effects of DCH on NAFLD and indicated that DCH's function on NAFLD may link to the improvement of the dysbiosis of gut microbiota and the modulation of the AA, glycerophospholipid, and glycine/serine/threonine metabolic pathways.

Keywords: nonalcoholic fatty liver disease, Da-Chai-Hu decoction, gut microbiota, untargeted metabolomics, correlation analysis

OPEN ACCESS

Edited by:
Yi Wang,
Zhejiang University, China

Reviewed by:
Paul F. Seke Etet,
Université de Ngaoundéré, Cameroon
Huan Chen,
Key laboratory of Microorganism Technology and Bioinformatics Research of Zhejiang Province, China

****Correspondence:***
Zhaiyi Zhang
3461285155@qq.com
Hongwu Wang
whw2009@tjutcm.edu.cn
Xiangguo Liu
xgliu0508@yahoo.com.cn

Specialty section:
This article was submitted to Ethnopharmacology, a section of the journal Frontiers in Pharmacology

Received: *16 July 2020*
Accepted: *22 October 2020*
Published: *27 November 2020*

Citation:
Cui H, Li Y, Wang Y, Jin L, Yang L, Wang L, Liao J, Wang H, Peng Y, Zhang Z, Wang H and Liu X (2020) Da-Chai-Hu Decoction Ameliorates High Fat Diet-Induced Nonalcoholic Fatty Liver Disease Through Remodeling the Gut Microbiota and Modulating the Serum Metabolism. Front. Pharmacol. 11:584090. doi: 10.3389/fphar.2020.584090

INTRODUCTION

Accumulating numbers of studies have shown that the dysbiosis in gut microbiota could contribute to the development of nonalcoholic fatty liver disease (NAFLD) (Stefano et al., 2018). The composition of gut microbiota in NAFLD patients exhibited a distinct profile when compared to healthy controls (Li et al., 2018). Redundancy analysis (RDA) has also revealed significant correlations between fecal microbiota and related clinical outcomes, such as insulin resistance (IR) and dyslipidemia (Li et al., 2018). Additionally, researchers were able to induce NAFLD in germ free (GF) mice after they received a fecal transplantation from a high fat diet (HFD)-induced NAFLD mouse model (Porras et al., 2019). Modulation of gut microbiota using probiotics has shown beneficial effects on NAFLD mice. In one study, the oral treatment of *Lactobacillus rhamnosus GG* was able to protect mice from NAFLD by inhibiting the inflammatory response and improving the gut barrier function (Ritze et al., 2014).

Currently, lipid-lowering drugs, dietary therapy and exercise are the most commonly used treatments of NAFLD (Cao et al., 2020). However, lipid-lowering drugs, such as metformin and statins, exhibit numerous side-effects including gastrointestinal disorders (Scarpello et al., 1998), hepatotoxicity, and muscle aches (Bhardwaj and Chalasani, 2007). On the other hand, non-drug therapies like encouraging healthy habits of diet and exercise can be difficult for patients to maintain. The use of traditional Chinese medicine (TCM) has shown some protective effects on NAFLD and modulation of the gut microbiota has been demonstrated to be one of its key mechanisms (Cao et al., 2020). Da-Huang-Ze-Xie decoction has been shown to alleviate HFD-induced NAFLD model rats through altering the numbers of *Desulfovibrio*, *Escherichia/Shigella*, *Bacteroides*, *Oscillibacter* and *Butyricicoccus* in gut, improving gut permeability and inhibiting the activation of the Toll-like receptor 4 (TLR4) signaling pathway in liver (Jing et al., 2017). Qu-Shi-Hua-Yu decoction has been indicated to improve blood lipid levels and hepatic steatosis in NAFLD model rats through increasing the short chain fatty acid (SCFA)-producing gut microbiota (Yin et al., 2013).

Metabolomics could identify and quantify the levels of metabolites systematically and could be used to elucidate the pathogenesis of diseases and the mechanisms of drugs on metabolic levels (Su et al., 2018). Metabolites are metabolic byproduct biomolecules with low molecular weights that serve as signaling molecules and energy sources during various biological processes. Metabolite levels could be influenced by the gut microbiota and could directly reflect the current metabolic state of organs or cells (Tremaroli and Backhed, 2012). The combination of 16S rRNA sequencing and metabolomics could elucidate the mechanisms of Chinese herbal formulas via the interactions between gut microbiota and host metabolism. Combining the 16S rRNA sequencing with metabolomics analysis, Piao et al. demonstrated that Fu-Fang-Zhen-Zhu-Tiao-Zhi capsules exhibited anti-aging effects by increasing the SCFA-producing bacteria, decreasing the hydrogen sulfide-producing bacteria, and improving glucose-lipid metabolism (Piao et al., 2020). Kang-Shuai-Lao-Pian was found to affect the numbers of *Intestinimonas*, *Oscillibacter*, *Christensenellaceae_R-7_group*, and *Lachnoclostridium_UCG-010*, *Aliihoeflea* as well as regulate lysine, dipeptide, fatty acid and purine metabolism in obese mice (Gong et al., 2020).

Da-Chai-Hu decoction (DCH), composed of *Bupleurum chinense* DC., *Scutellariae baicalensis* Georgi, *Paeonia lactiflora* Pall., *Pinellia ternata* (Thunb.) Makino, *Citrus* × *aurantium* L., *Zingiber officinale* Roscoe, *Ziziphus jujuba* Mill. and *Rheum officinale* Baill., has been shown to exhibit beneficial effects on hyperlipidaemia and hypercholesterolemia (Yoshie et al., 2004; Iizuka et al., 2013; Fan and Miao 2014). Furthermore, it has been demonstrated that DCH could decrease the level of low density lipoprotein (LDL) in hypercholesterolemia animal models through up-regulating the expression of LDL-receptor in liver (Yoshie et al., 2004). However, the exact mechanisms of DCH on NAFLD remain unclear. To better understand these mechanisms, we established a NAFLD rat model using HFD and a DCH treatment regimen. The changes of gut microbiota post DCH treatment were investigated using 16S rRNA sequencing. In addition, untargeted metabolomics was performed to investigate the metabolic regulations of DCH on NAFLD. Understanding how DCH ameliorates NAFLD will provide clinicians with another valuable therapeutic tool and help unravel the link between Chinese herbal formulas, gut microflora, and patient outcomes.

MATERIALS AND METHODS

Reagents

HFD (17.7% sucrose, 17.7% fructose, 19.4% protein and 40% fat) was obtained from Beijing Huafukang Bioscience Co., Ltd. (Beijing, China). Triglyceride (TG), total cholesterol (TC), aspartate aminotransferase (AST), alanine aminotransferase (ALT), superoxide dismutase (SOD), methane dicarboxylic aldehyde (MDA), and glutathione peroxidase (GSH-Px) assay kits test kits were obtained from Nanjing Jiancheng Biological Engineering Institute (Nanjing, China). Oil Red O Staining kit was purchased from Solarbio Biotechnology Co., Ltd. (Beijing, China). Rat insulin enzyme-linked immunosorbent assay (ELISA) kit was obtained from Multi Science Biotechnology Co., Ltd. (Hangzhou, China). Reference standards of paeoniflorin, baicalin, saikosaponin A, saikosaponin D, emodin, synephrine, succinic acid, 6-gingerol and oleanolic acid were obtained from Sichuan Weikeqi Biological Technology Co., Ltd. (Sichuan, China).

Preparation of Da-Chai-Hu Decoction

The dosage of each drug in the DCH preparation used in this study was in accordance with the record in "Treatise on Febrile Diseases", written by Zhang Zhongjing in 200 C.E.–210 C.E.. DCH contained: 12 g of *Bupleurum chinense* DC. (Tianjin traditional Chinese Medicine prepared pieces Co., Ltd, Tianjin, China, Batch number: 1907026), 9 g of *Scutellariae baicalensis* Georgi (Tianjin traditional Chinese Medicine prepared pieces Co., Ltd, Tianjin, China, Batch number: 1906002), 9 g of *Paeonia lactiflora* Pall. (Tianjin traditional Chinese Medicine prepared

TABLE 1 | Composition of chows used in current study.

	Cereal (%)	Sucrose (%)	Fructose (%)	Protein (%)	Fat(%)
Standard diet	59.40	—	—	20	4.80
HFD	—	17.70	17.70	19.40	40

Vegetable oil and lard were used as the sources of fat in the standard diet and HFD respectively.

pieces Co., Ltd, Tianjin, China, Batch number: 1901016), 9 g of *Pinellia ternata* (Thunb.) Makino (Tianjin traditional Chinese Medicine prepared pieces Co., Ltd, Tianjin, China, Batch number: 1812006), 9 g of *Citrus* × *aurantium* L. (Tianjin traditional Chinese Medicine prepared pieces Co., Ltd, Tianjin, China, Batch number: 1901016), 15 g of *Zingiber officinale* Roscoe (Tianjin traditional Chinese Medicine prepared pieces Co., Ltd, Tianjin, China, Batch number: 1903002), 12 g of *Ziziphus jujuba* Mill. (Tianjin traditional Chinese Medicine prepared pieces Co., Ltd, Tianjin, China, Batch number: 1907007), and 6 g of *Rheum officinale* Baill. (Tianjin traditional Chinese Medicine prepared pieces Co., Ltd, Tianjin, China, Batch number: 1902005). All herbs were authenticated by Pharmacist Li Wang in Department of Pharmacy of the Tianjin Second People's Hospital. The above herbs were then soaked in 300 ml water for 30 min and decocted for 30 min to obtain the aqueous extract of DCH. The aqueous extract of DCH was filtered and concentrated to a density of 0.8 g crude herb/ml.

Quality control of DCH was performed using high performance liquid chromatography (HPLC; UltiMate 3,000, Thermo Scientific™, USA) coupled with mass spectrometer (MS; Q Exactive™, Thermo Scientific™, USA). The chromatographic conditions were as follows: The chromatographic column was an Eclipse Plus C_{18} RRHD column (2.1 × 100 mm, 1.8 μm). The column temperature was maintained at 40°C and the flow rate was 0.3 ml/min. 0.1% formic acid aqueous solution (A) and acetonitrile (B) were used as the mobile phases and the injection volume was 5 μl. The mobile phase conditions were: 0 min, 5% B; 1 min, 5% B; 9 min 80% B; 12 min 100% B; 14 min 100% B; 14.1 min 5% B; 16 min 5% B. A mass spectrometer equipped with an electrospray ionization (ESI) source was used for both positive and negative ionization scan modes (m/z ranges from 100 to 1,500). The detailed parameters of MS were: spray voltage of 3,500 V (positive mode) and 3,000 V (negative mode), capillary temperature at 320°C (both positive and negative modes), sheath gas flow rate of 30 arbitrary units (both positive and negative modes), and auxiliary gas flow rate of 10 arbitrary units (both positive and negative modes).

Animals and Treatment

6-8 weeks old male Sprague-Dawley (SD) rats weighing 190–210 g, were purchased from Huafukang Animal Co., Ltd. (Beijing, China). They were acclimated in a controlled environment (12 h light/dark cycle, 21 ± 2°C with a relative humidity of 45 ± 10%) with *ad libitum* access to food and water. All animal experiments were approved by the Animal Ethics Committee at Tianjin University of Traditional Chinese Medicine.

After the acclimatization for 1 week, all animals were randomly divided into four groups (n = 10): control, model, positive control and DCH. Rats in the control group were fed with standard laboratory chow, while rats in the model, positive control, and DCH groups received HFD for 12 weeks to induce NAFLD (Li et al., 2020). The ingredients of standard chow and HFD were showed in **Table 1**. After 4 weeks of HFD feeding, rats in the positive control and DCH groups were orally treated with metformin (200 mg/kg rat weight) (Zheng et al., 2014) and DCH (8 g/kg rat weight), respectively, once per day for 8 weeks. Whereas, rats in the control and model groups received an equivalent volume of saline. At the end of 8 weeks of metformin and DCH treatment, rats were sacrificed and their livers weighed. Liver index was calculated based on the percentage of liver to body weight.

Serum Biochemical Markers Assay

Serum samples were collected at the end of 8 weeks of metformin and DCH treatment for biochemical analysis. Briefly, rats were anaesthetized and blood was harvested by a syringe from the aorta abdominalis. The blood was then centrifuged at 3,000 rpm for 15 min to isolate the serum. The levels of TG, TC, ALT, and AST in serum were analyzed according to the manufacturer's instructions provided by Nanjing Jiancheng Biological Engineering Institute (Nanjing, China) and the absorbance value was detected using a microplate reader (Varioskan Flash, Thermo Fisher, Massachusetts, USA).

H&E Staining

After euthanasia, the rat's livers were immediately removed and fixed in 10% formalin, dehydrated, and embedded in paraffin wax. The tissues were then cut into 5 μm sections using a microtome (RM2125, Leica, Buffalo Grove, USA) and were subsequently stained with hematoxylin and eosin (H&E), as has been previously described (Cui et al., 2018). The pathological severities of steatosis, lobular inflammation, and hepatocyte ballooning were determined using the NAFLD activity score (NAS) as described in our previous publication (Cui et al., 2020).

Oil Red O Staining

Livers were sectioned into 20 μm thick coronal sections using a microtome-cryostat (CM3050S, Leica, Buffalo Grove, USA). The sections were then stained with Oil Red O, following the manufacturer's instructions. The staining of lipid drops by Oil Red O was quantified using Image J to obtain the integrated optical density (IOD). The mean optical density (MOD) was calculated based on the ratio of IOD to the sum area.

Oral Glucose Tolerance Test (OGTT)

OGTT was conducted at the end of 8 weeks of metformin and DCH treatment as has been previously described (Cummings et al., 2011). Briefly, rats were fasted for 16 h and the levels of fasting blood glucose (FBG) were determined. Then, rats received 50% glucose solution (1 g/kg) intragastrically and the blood glucose levels were measured at 30, 60 and 120 min post glucose solution treatment. The area under the curve (AUC) of OGTT was then calculated.

Determination of Homeostatic Model Assessment of Insulin Resistance (HOMA-IR).

Rats were fasted as detailed above and the levels of fasting insulin (FINS) in the serum were measured using ELISA according to the manufacturer's instructions (Multi Science Biotechnology Co., Ltd., China). Additionally, the level of FBG was measured. The HOMA-IR was calculated using the following formula: HOMA-IR = FBG (mmol/L) × FINS (μU/ml)/22.5.

Analysis of Liver Biochemical Markers

0.1 g of liver tissues were immersed in 900 μl normal saline followed by ultrasonic trituration to obtain liver tissue homogenates. The homogenates were then centrifugated at 3,000 rpm for 15 min and their supernatants were used to measure the MDA level as well as the SOD and GSH-Px activities according to the manufacturer's instructions provided by Nanjing Jiancheng Biological Engineering Institute (Nanjing, China).

Fecal 16S rRNA Sequencing

At the end of 8 weeks of DCH treatment, feces from the control, model, and DCH groups were simultaneously obtained under sterile conditions in a laminar flow hood. Fecal total DNAs were extracted and their purities and concentrations were measured by agarose gel electrophoresis. The DNA samples were then diluted to 1 ng/μl and polymerase chain reaction (PCR) was conducted to amplify the V4 region of 16S rRNA of DNA samples using specific primers with the barcode (forward: GTGCCAGCMGCCGCGGTAA reverse: GGACTACHVGGGTWTCTAAT). The PCR amplification mixture of each sample consisted of 15 μl of Phusion® High-Fidelity PCR Master Mix (New England Biolabs), 0.2 μM of forward and reverse primers, and 10 ng of template DNA. The PCR products were then quantified by 2% agarose gel electrophoresis and purified using Qiagen Gel Extraction Kit (Qiagen, Germany). The sequencing libraries were generated using TruSeqRDNA PCR Free Sample Preparation Kit (Illumina, United States) and then sequenced on the NovaSeq6000 platform to generate paired-end reads.

Data Analysis of Fecal 16S rRNA Sequencing

Paired-end reads obtained from 16S rRNA sequencing were assigned to samples, truncated by cutting off the barcode and primer sequence, and merged by the FLASH V1.2.7 analysis tool (http://ccb.jhu.edu/software/FLASH/) to obtain the raw tags. The raw tags were then filtered to generate the clean tags according to the QIIME V1.9.1 quality controlled process (http://qiime.org/scripts/split_libraries_fastq.html). The chimera sequences in clean tags were detected and removed to obtain the effective tags using the UCHIME algorithm (http://www.drive5.com/usearch/manual/uchime_algo.html). The sequences of effective tags with ≥97% similarity were then assigned to the same OTUs using the Uparse V7.0.1001 software (http://drive5.com/uparse/). Representative sequences for each OTU were then screened for further annotation via the Silva database (http://www.arb-silva.de/). The relative abundances of OTUs were normalized using a standard of sequence number corresponding to the sample with the least sequences. The normalized data were then used for alpha diversity and beta diversity analysis. The gene family abundance of 16S rRNA sequencing data was predicted according to the Phylogenetic Investigation of Communities by Reconstruction of Unobserved States database (PICRUSt).

Untargeted Metabolomics Study

At the end of 8 weeks of DCH treatment, serum samples from the control, model and DCH groups were collected for metabolomics analysis. The changes in serum metabolites were screened using liquid chromatography–mass spectrometry (LC–MS) and the data were analyzed using a method described in our previous study (Cui et al., 2020).

Correlation Analysis Between Physiological Data, Untargeted Metabolomics Study and 16S rRNA Sequencing

Spearman's correlation analysis was conducted to analyze the relationship between physiological data (body weight, liver index, TG, TC, AST, ALT, AUC of OGTT, FINS, and HOMA-IR), differential serum metabolites, and gut microbiota at genus level in the control, model and DCH groups.

Statistics

All data were reported as the mean ± standard deviation (mean ± SD) for the independent experiments. Statistical differences between the experimental groups were examined using the analysis of variance (ANOVA) and SPSS software, version 20.0. A p-value < 0.05 was considered statistically significant. Curve fitting was performed using the GraphPad Prism 5 software.

RESULTS

Identification of Main Bioactive Compounds in Da-Chai-Hu Decoction by HPLC-MS Analysis

HPLC-MS analysis was conducted to investigate the chemical profiles of DCH. Synephrine, succinic acid, paeoniflorin, baicalin, saikosaponin A, 6-gingerol, saikosaponin D, emodin and oleanolic acid were used as the reference standards to validate the main bioactive compounds in DCH. The molecular formulas and chemical structures of these reference standards were shown in **Supplementary Figure S1**. The typical based peak intensity (BPI) chromatograms of DCH and the reference standards were

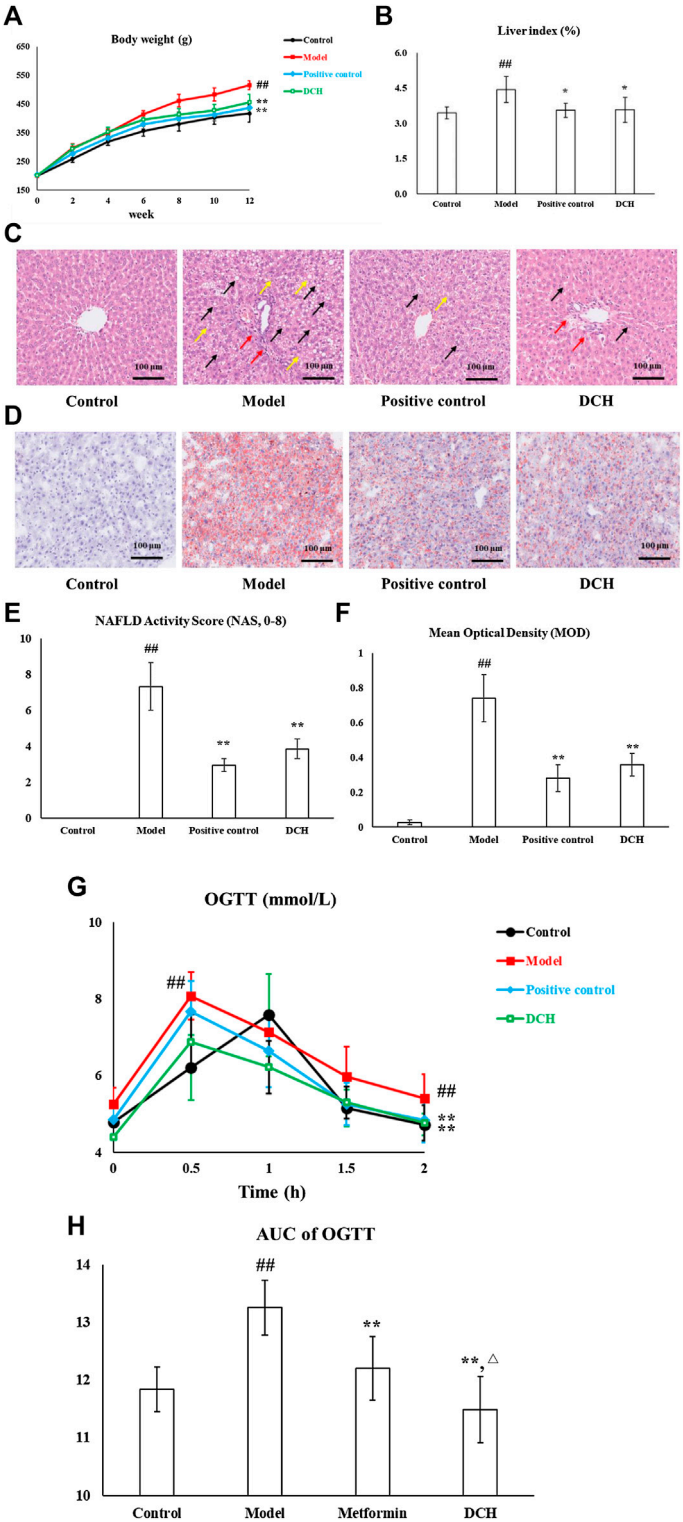

FIGURE 1 | DCH treatment improved the hepatosteatosis, IR and oxidative stress in NAFLD model rats. **(A,B)** DCH treatment decreased the body weight and liver index in NAFLD model rats. **(C,E)** H&E staining showed that DCH treatment ameliorated the hepatic steatosis, hepatocytes ballooning, and lobular inflammation in the liver. Black arrows indicate the steatosis of hepatocytes, red arrows indicate lobular inflammation and yellow arrows indicate hepatocyte ballooning (×200 magnification). **(D,F)** Oil Red O staining shows that DCH treatment improved the lipid accumulation in the liver (200×). **(G,H)** The AUC of OGTT was decreased in NAFLD model rats after DCH treatment. Control, model, positive control and DCH (n = 10 per group) groups. Data are presented as the mean ± SD. ##: $p < 0.01$ as compared to the control group; *: $p < 0.05$ as compared to the model group; **: $p < 0.01$ as compared to the model group; △: $p < 0.05$ as compared to the positive control group.

TABLE 2 | Changes in blood lipid levels and liver enzymes after DCH treatment.

Group	TC (mmol/L)	TG (mmol/L)	ALT (IU/L)	AST (IU/L)
Control	1.35 ± 0.29	0.27 ± 0.04	44.25 ± 7.59	131.02 ± 16.54
Model	2.44 ± 0.39$^{\#\#}$	1.78 ± 0.24$^{\#\#}$	159.99 ± 20.73$^{\#\#}$	197.56 ± 23.00$^{\#\#}$
Positive control	1.51 ± 0.07**	1.00 ± 0.64**	109.81 ± 17.69**	139.19 ± 12.71**
DCH	1.80 ± 0.13**,$^{\triangle\triangle}$	1.05 ± 0.28**	128.01 ± 15.59**	166.84 ± 18.15**,$^{\triangle\triangle}$

*Control, model, positive control and DCH (n = 10 per group) groups. Data are presented as the mean ± SD. $^{\#\#}$: p < 0.01 as compared to the control group; **: p < 0.01 as compared to the model group; $^{\triangle\triangle}$: p < 0.01 as compared to the positive control group.*

analyzed in both positive and negative modes (**Supplementary Figure S2**) and their characteristic fragment ions were shown in **Supplementary Table S1**. Paeoniflorin in *Paeonia lactiflora* Pall., baicalin in *Scutellariae baicalensis* Georgi, saikosaponin A and saikosaponin D in *Bupleurum chinense* DC., emodin in *Rheum officinale* Baill., synephrine in *Citrus × aurantium* L., succinic acid in *Pinellia ternata* (Thunb.) Makino, 6-gingerol in *Zingiber officinale* Roscoe and oleanolic acid in *Ziziphus jujuba* Mill. were identified as the preeminent bioactive compounds in DCH.

Effects of Da-Chai-Hu Decoction on Dyslipidemia, Liver Function, IR and Oxidative Stress in NAFLD Model Rats

After 8 weeks of metformin and DCH treatment, the body weight ($p < 0.01$, **Figure 1A**), liver index ($p < 0.01$, **Figure 1B**) and serum levels of TG, TC, AST, and ALT ($p < 0.01$, respectively, **Table 2**) were significantly increased in model group compared with the control group. Whereas, metformin and DCH treatment significantly decreased the body weight ($p < 0.01$, respectively, **Figure 1A**), liver index ($p < 0.05$, respectively, **Figure 1B**), and serum levels of TG, TC, AST, and ALT ($p < 0.01$, respectively, **Table 2**) compared to the NAFLD model rats. There were no significant differences in body weight, liver index and levels of serum ALT and TG between the positive control and DCH groups (**Table 2**), however, the levels of serum TC and AST were significantly higher in DCH group compared with those in positive control group ($p < 0.01$, respectively, **Table 2**). Notable steatosis of hepatocytes accompanied by hepatocytes ballooning and lobular inflammation was revealed by H&E staining in the model group, while metformin and DCH treatment improved the hepatic steatosis, hepatocytes ballooning, and lobular inflammation (**Figure 1C**). Likewise, the NAS score was significantly higher in the model group compared with the control ($p < 0.01$, **Figure 1E**) and H&E staining of the positive control and DCH groups showed a lower NAS score compared with the model group ($p < 0.01$, respectively, **Figure 1E**). There were no significant differences in NAS between the positive control and DCH groups (**Figure 1E**). Oil Red O staining also confirmed hepatic steatosis and increased lipid deposition in the model group ($p < 0.01$, **Figures 1D,F**), whereas the numbers of lipid-loaded hepatocytes were significantly decreased in metformin and DCH treated rats ($p < 0.01$, respectively. **Figures 1D,F**). There were no significant differences in the numbers of lipid-loaded hepatocytes between the positive control and DCH groups (**Figure 1F**).

TABLE 3 | Levels of FINS and HOMA-IR after DCH treatment.

Group	FINS (μU/ml)	HOMA-IR
Control	7.6 ± 1.33	1.14 ± 0.23
Model	16.46 ± 2.07$^{\#\#}$	3.56 ± 0.55$^{\#\#}$
Positive control	11.43 ± 1.41**	2.08 ± 0.48**
DCH	13.53 ± 1.65**	2.42 ± 0.32**

*Control, model, positive control and DCH (n = 10 per group) groups. Data are presented as the mean ± SD. $^{\#\#}$: p < 0.01 as compared to the control group; **: p < 0.01 as compared to the model group.*

TABLE 4 | The activities of SOD and GSH-Px and the levels of MDA in rat liver homogenate after DCH treatment.

Group	SOD (U/mgprot)	MDA (nmol/mgprot)	GSH-Px (U/mgprot)
Control	41.72 ± 4.39	2.78 ± 0.48	171.44 ± 3.82
Model	32.20 ± 4.94$^{\#\#}$	15.96 ± 2.01$^{\#\#}$	126.82 ± 9.87$^{\#\#}$
Positive control	39.35 ± 4.19*	7.86 ± 1.07**	159.30 ± 11.93**
DCH	38.62 ± 3.58*	8.81 ± 0.95**	154.69 ± 10.82**

*Control, model, positive control and DCH (n = 10 per group) groups. Data are presented as the mean ± SD. $^{\#\#}$: p < 0.01 as compared to the control group; *: p < 0.05 as compared to the model group; **: p < 0.01 as compared to the model group.*

IR is also an important clinical outcome of NAFLD and as such we measured the effects of DCH on IR. The AUC of OGTT was significantly increased in model group compared with the control group ($p < 0.01$, **Figures 1G,H**), whereas metformin and DCH treated rats displayed a lower AUC of OGTT compared with the NAFLD model rats ($p < 0.01$, respectively, **Figures 1G,H**). The AUC of OGTT was lower in the DCH group compared with the positive group ($p < 0.05$, **Figures 1G,H**). Additionally, the levels of FINS and HOMA-IR were higher in the model group compared with the control group ($p < 0.01$, **Table 3**) and were lower in the positive control and DCH groups compared to the model group ($p < 0.01$, respectively, **Table 3**). There were no significant differences in FINS and HOMA-IR between the positive control and DCH groups (**Table 3**).

We also investigated the anti-oxidative effects of DCH on NAFLD. Our results showed significantly lower activities of SOD, GSH-Px, and higher levels of MDA in the NAFLD model rats compared to rats in the control group ($p < 0.01$, respectively, **Table 4**). Compared with the model group, the activities of SOD ($p < 0.05$, respectively, **Table 4**) and GSH-Px ($p < 0.01$, respectively, **Table 4**) were increased and the level of MDA

($p < 0.01$, respectively, **Table 4**) was decreased in the positive control and DCH groups.There were no significant differences in SOD, GSH-Px and MDA between the positive control and DCH groups (**Table 4**).

Modulatory Effects of Da-Chai-Hu Decoction on Gut Microbiota in NAFLD Model Rats

16S rRNA sequencing was performed to detect gut microbiota changes in NAFLD model rats post DCH treatment. Overall, 2,196,489 useable reads and 1,174 OTUs were obtained from 30 samples. There were no significant differences in Chao1 index and observed species number between control and model groups, indicating that the richness of gut microbiota community was not changed after HFD treatment (**Figures 2A,B**). The Chao1 index was lower in DCH group than that in the model group, whereas there was no significant differences in observed species number between model and DCH groups (**Figures 2A,B**). The Shannon and Simpson indexes were higher in the model group compared with the control group and were lower in DCH group compared with the model group, indicating that the alpha diversity of gut microbiota community was increased in the model group compared with the control group and DCH treatment decreased the alpha diversity of gut microbiota community in NAFLD model rats (**Figures 2C,D**). Principal co-ordinates analysis (PCoA) showed significant variations of gut microbiota in each group, with a shorter distance between the control and DCH groups than between the model and DCH groups (**Figure 2E**). Likewise, system clustering tree analysis indicated that the distance from the control group to the DCH group was closer than either to the model (**Figure 2F**).

We further investigated the changes in the relative abundances of gut microbiota species. A venn diagram of the three groups demonstrated that 660 OTUs overlapped among all groups; 714 OTUs were present in the control and model groups; 775 in the control and DCH groups; and 789 in the model and DCH groups (**Figure 2G**). At the phylum level, *Firmicutes* and *Bacteroidetes* were the most abundant phyla among all samples (**Figure 2H**). The *Firmicutes* to *Bacteroidetes* (*F* to *B*) ratio was higher in the model group than in the control group ($p < 0.01$, **Figure 2I**), whereupon the *F* to *B* ratio was decreased after DCH treatment ($p < 0.05$, **Figure 2I**). At the genus level, the relative abundances of *Romboutsia, Bacteroides, Lactobacillus*, *Akkermansia*, and *Turicibacter* ($p < 0.01$, $p < 0.01$, $p < 0.01$, $p < 0.01$ and $p < 0.05$, respectively, **Figure 2J**) were signifiacntly lower and the relative abundances of *Lachnoclostridium, unidentified_Enterobacteriaceae, Allobaculum*, and *Enterococcus* ($p < 0.05$, $p < 0.05$, $p < 0.01$ and $p < 0.01$, respectively, **Figure 2J**) were significantly higher in the model group than that in the control group. Compared with the model group, DCH treatment significantly increased the relative abundances of *Romboutsia, Bacteroides, Lactobacillus*, *Akkermansia*, and *Turicibacter* ($p < 0.01$, $p < 0.05$, $p < 0.01$, $p < 0.05$ and $p < 0.05$, respectively, **Figure 2J**) and significantly decreased the relative abundances of *Lachnoclostridium* and *unidentified_Enterobacteriaceae* ($p < 0.01$ and $p < 0.05$, respectively, **Figure 2J**). Additionally, we predicted the possible pathways related to the differential gut microbiota at the genus level by PICRUSt analysis. The top 10 terms of metabolic pathways with the highest proportion and a p-value < 0.05 were listed in **Figure 2K** (control group vs. model group) and **Figure 2L** (model group vs. DCH group). Proportions of metabolic pathways that were increased in the model group but decreased in DCH group, or vice versa, were considered as differential pathways. The abundances of pentose phosphate, glycine/serine/threonine and arachidonic acid (AA) metabolic pathways as well as the valine, leucine and isoleucine biosynthesis pathways were all increased in the model group compared with the control group (**Figure 2K**). Conversely, the abundance of glycerophospholipid metabolism pathway was decreased in model group compared with the control group (**Figure 2K**). For the DCH group, the abundances of pentose phosphate, glycine/serine/threonine, and AA metabolic pathways along with the valine, leucine and isoleucine biosynthesis pathways were lower than the model group and the abundance of glycerophospholipid metabolism pathway was higher (**Figure 2L**).

Effects of Da-Chai-Hu Decoction on Serum Metabolism in NAFLD Model Rats

The changes of metabolites in serum were investigated using untargeted metabolomics. According to the principle component analysis (PCA) model, a clear group separation could be observed between the control and model groups, while the distinction between the model and DCH groups was unclear (**Figures 3A,B**). Therefore, we performed orthogonal partial least squares discriminant analysis (OPLS-DA) to further visualize the metabolic alterations occurring between the control group and model group as well as between the model group and the DCH group. The OPLS-DA models showed significant distinctions of metabolomic data between the control group and the model group as well as between the model group and the DCH group (**Figures 3C,E**). The over-fitting in the OPLS-DA model was controlled using seven-round cross validation and 200 repetitions of RPT based on the R^2 and Q^2 values. The R^2 and Q^2 values of OPLS-DA model in the comparison of control and model groups were 0.686 and −1.08, respectively. The R^2 and Q^2 values in the OPLS-DA model comparing the model group with the DCH group were 0.22 and −0.624, respectively. These results indicated that the OPLS-DA models were robust (**Figures 3D,F**). Metabolites with a VIP >1 and $p < 0.05$ between control and model groups or between DCH and model groups were considered to be differential metabolites. The numbers of differential metabolites between the control group and the model group as well as between the model group and the DCH group were visualized in **Figure 3G**. Compared with the control group, the levels of phosphatidylcholine (PC), rumenic acid, linoleic acid, eicosapentaenoic acid (EPA), L-threonine, gluconic acid, and lacto-N-tetraose were decreased and the levels of L-proline, L-lysine, L-isoleucine, L-valine, L-arginine, L-leucine, glycocholic acid, uric acid, creatinine, stearic acid, ursodeoxycholic acid, phosphatidylethanolamine (PE), L-tryptophan, 12(R)-HETE, 5-HPETE, and glycine were

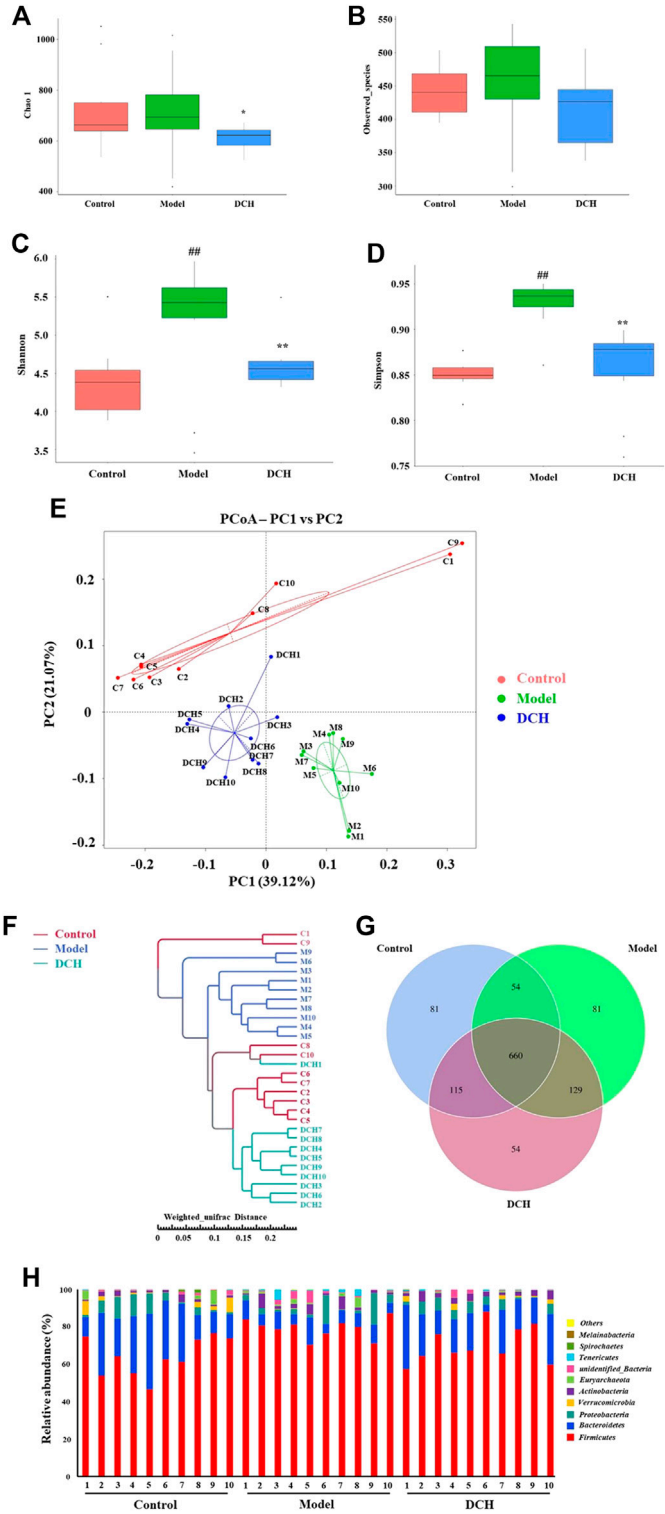

FIGURE 2 | DCH treatment affected the gut microbiota community in NAFLD model rats. **(A,B)** There were no significant differences in Chao1 index and observed species number in each group. **(C,D)** Shannon and Simpson indexes were lower in DCH group than that in the model group. **(E,F)** PCoA and system clustering tree showed more similar beta diversity between DCH and control groups than that between the model and control groups. **(G)** The different numbers of OTUs were visualized in Venn diagram. **(H,I)** At the phylum level, DCH treatment decreased the *F* to *B* ratio in NAFLD model rats. **(J)** At the genus level, DCH treatment affected the relative abundances of *Romboutsia, Bacteroides, Lactobacillus*, *Akkermansia*, *Turicibacter, Lachnoclostridium* and *unidentified_Enterobacteriaceae* in NAFLD model rats. **(K,L)** The differential metabolic pathways (written in red) of DCH on NAFLD were predicted using PICRUSt analysis based on the 16S rRNA sequencing data. Control, model and DCH (n = 10 per group) groups. Data are presented as the mean ± SD. $^{\#}$: $p < 0.05$ as compared to the control group; $^{\#\#}$: $p < 0.01$ as compared to the control group; *: $p < 0.05$ as compared to the model group; **: $p < 0.01$ as compared to the model group.

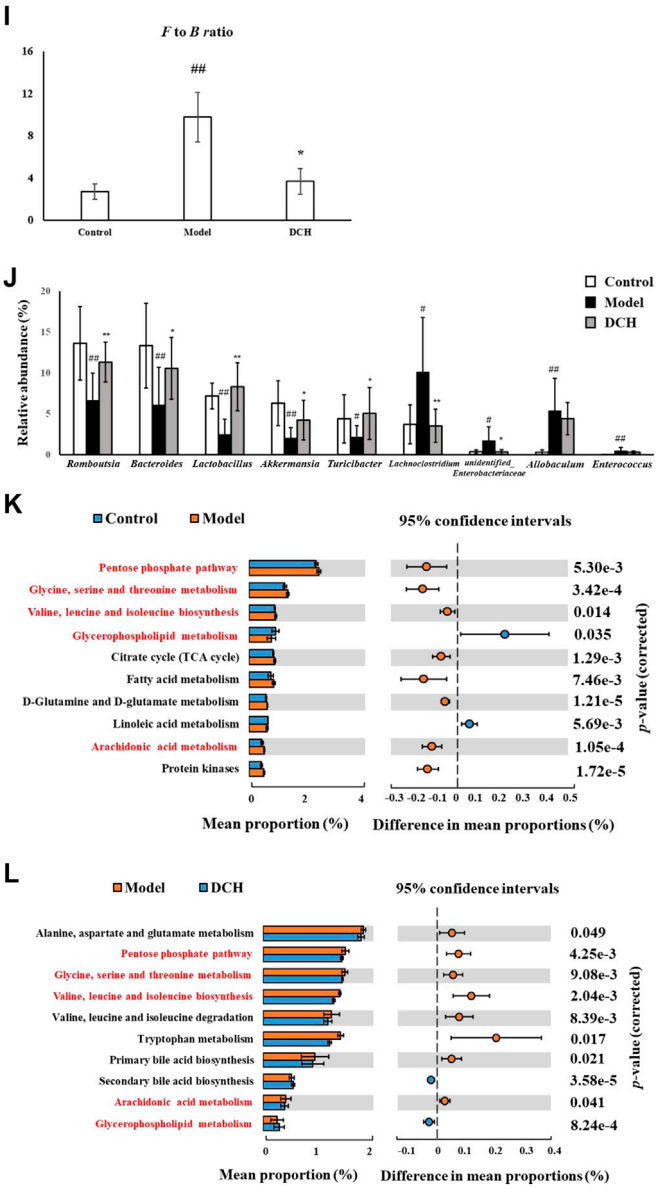

FIGURE 2 | (Continued).

increased in the model group. For the DCH group compared with the model group: the levels of linoleic acid, PC, L-threonine, and rumenic acid were increased and the levels of L-isoleucine, L-valine, L-arginine, L-leucine, stearic acid, indoleacrylic acid, THTC, 12(R)-HETE, 5-HPETE, glycine, uric acid, and PE were decreased (**Table 5**).

In addition, differential metabolites with a fold change (FC) greater than 1.2 or a FC of less than 0.8 were analyzed using MetaboAnalyst software to screen for significant metabolic pathways ($p < 0.05$, impact value >0.10). Tryptophan, AA, linoleic acid, glycerophospholipid, and glycine/serine/threonine metabolisms were identified to be significant metabolic pathways between the control and model groups (**Figure 3H**). Between the model and DCH groups, AA, linoleic acid, glycerophospholipid, and glycine/serine/threonine metabolism were identified to be significant metabolic pathways (**Figure 3I**). The same pathways obtained from both PICRUSt analysis of 16S rRNA sequencing and pathway analysis of untargeted metabolomics, including AA, glycerophospholipid, and glycine/serine/threonine metabolic pathways, were visualized in **Figure 3J** and discussed in detail.

Correlation Analysis of Physiological Data, Untargeted Metabolomics and Gut Microbiota

As shown in **Figure 4A**, *Lactobacillus* and *Romboutsia* have shown significant negative correlations with the pathological changes in NAFLD rat models, whereas *Enterococcus*,

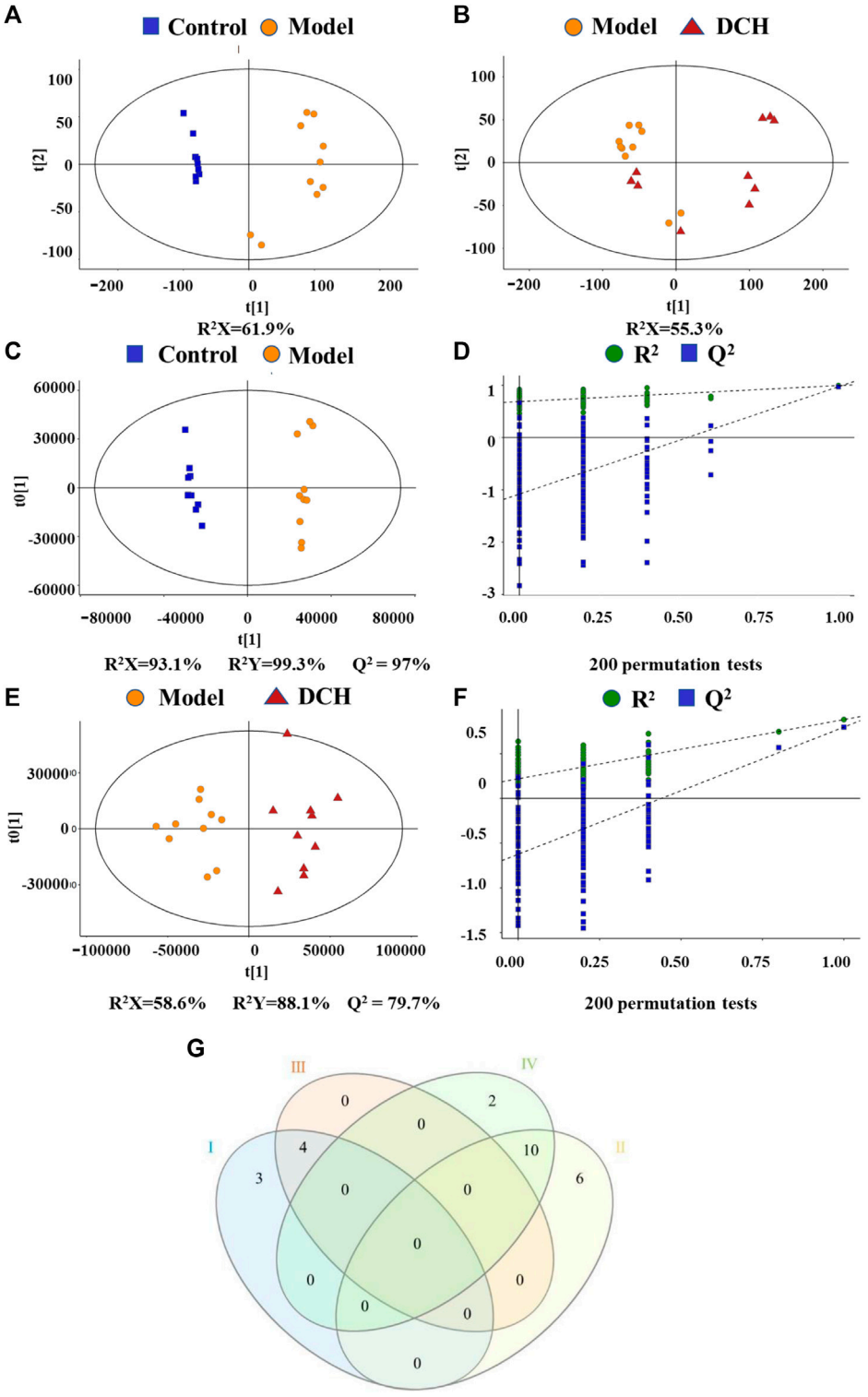

FIGURE 3 | DCH treatment regulated the serum metabolites in NAFLD model rats. **(A,B)** Scores plots of PCA between the control and model groups and the model and DCH groups. **(C,D)** Scores plots of OPLS-DA between the control and model groups and the corresponding coefficient of loading plots. **(E,F)** Scores plots of OPLS-DA between the model and DCH groups and the corresponding coefficient of loading plots. **(G)** Numbers of differential metabolites between the control and model groups and the model and DCH groups (Venn diagram). **I**: Decreased levels in the model group as compared to the control group; **II:** Elevated levels in the model group as compared to the control group; **III:** Elevated levels in the DCH group as compared to the model group; **IV:** Decreased levels in the DCH group as compared to the model group; **(H,I)** Summary of pathway analysis of serum samples between control and model groups and between model and DCH groups. **(A)** Linoleic acid metabolism; **(B)** Glycine, serine and threonine metabolism; **(C)** Glycerophospholipid metabolism; **(D)** Tryptophan metabolism; **(E)** AA metabolism. **(J)** Schematic of AA, glycerophospholipid, and glycine/serine/threonine metabolism pathways in NAFLD rats after DCH treatment. Control, model and DCH (n = 10 per group) groups.

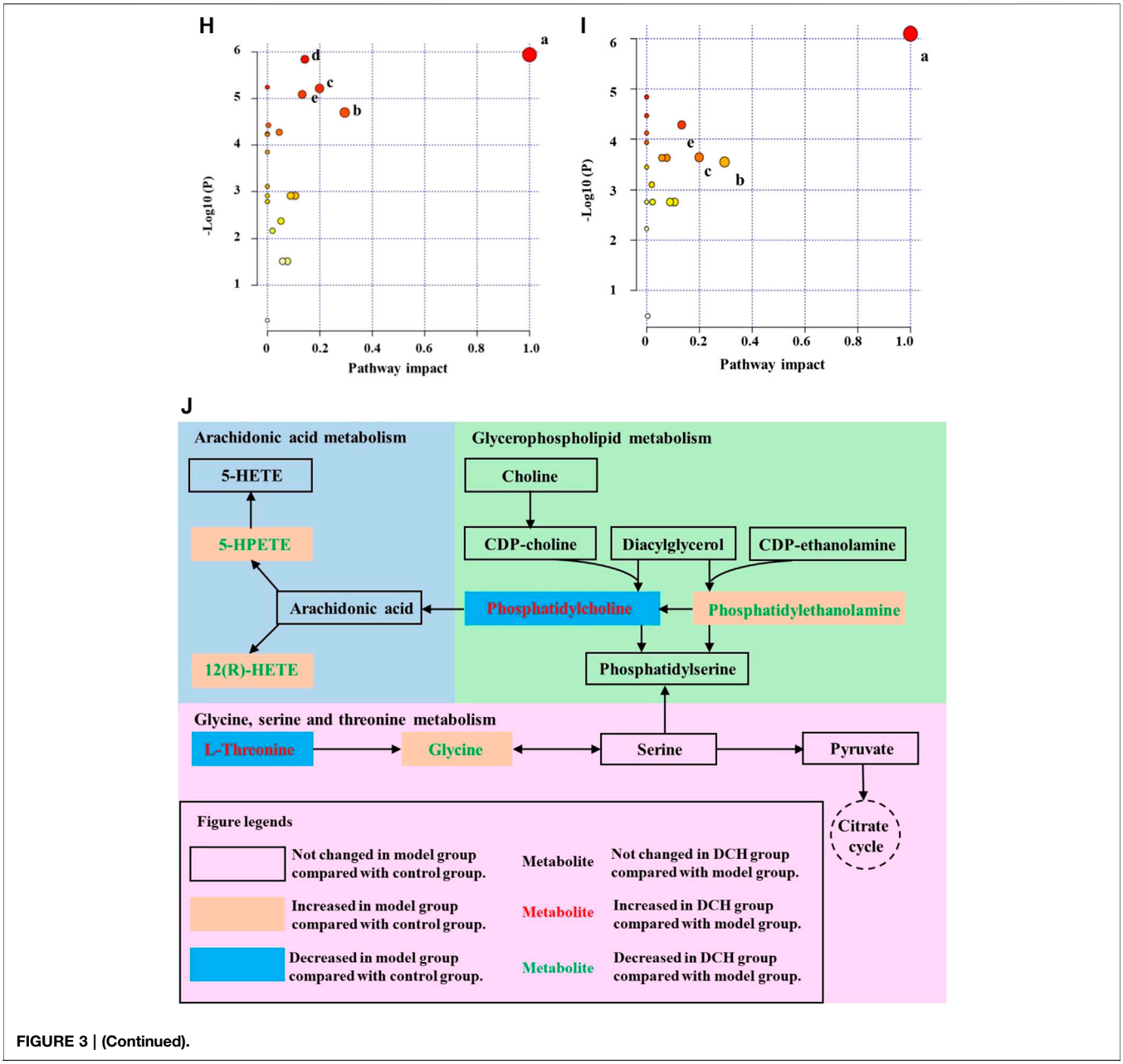

FIGURE 3 | (Continued).

Allobaculum, and *Lachnoclostridium* have shown positive correlations with the pathological changes in NAFLD rat models.

Additionally, *Lactobacillus* showed positive correlations with PC, rumenic acid, and lacto-N-tetraose and negative correlations with the majority of the amino acids and metabolites related to AA metabolism. *Enterococcus* and *Lachnoclostridium* showed positive correlations with most of the amino acid metabolites (**Figure 4B**).

DISCUSSION

In this study, NAFLD rat model was induced using HFD. Consistent with the previous studies (Li et al., 2020), rats incurred remarkable disorders in serum levels of TG, TC, ALT and AST after HFD feeding. Pathological studies also indicated clear steatosis and cellular damage of hepatocytes in the model group. DCH treatment improved dyslipidemia and ameliorated pathological changes in the liver. Due to the close relationship between IR and NAFLD (Reenam et al., 2019), we also studied the effects of DCH on IR. Our results showed decreased levels of FINS, HOMA-IR and AUC of OGTT following DCH treatment, indicating that DCH could alleviate IR in NAFLD model rats. Metformin, which has been widely used as the positive control in both NAFLD and IR studies, was served as the positive control for our study (Zheng et al., 2014; Xie et al., 2019). Clinical studies have shown that treatment of metformin for 48 days could

TABLE 5 | The differential metabolites in serum after DCH treatment.

No	Rt (min)	m/z	Formula	Metabolites	VIP		FC		Trend		Pathway
					M vs. C	D vs. M	M vs. C	D vs. M	M vs. C	D vs. M	
1	1.06	116.0703	$C_5H_9NO_2$	L-Proline	2.43	0.93	1.86	0.81	↑##	↓	—
2	0.92	120.0651	$C_4H_9NO_3$	L-Threonine	2.18	3.55	0.33	3.01	↓##	↑**	b
3	0.76	147.1121	$C_6H_{14}N_2O_2$	L-Lysine	1.38	0.69	3.24	0.92	↑##	↓	—
4	2.69	132.1014	$C_6H_{13}NO_2$	L-Isoleucine	2.94	1.49	1.98	0.67	↑##	↓*	—
5	1.43	118.0860	$C_5H_{11}NO_2$	L-Valine	2.79	2.48	2.38	0.52	↑##	↓**	—
6	0.71	281.2460	$C_{18}H_{32}O_2$	Linoleic acid	1.28	1.13	0.63	1.63	↓#	↑**	a
7	0.88	175.1181	$C_6H_{14}N_4O_2$	L-Arginine	2.77	1.31	1.94	0.66	↑##	↓**	—
8	2.92	132.1014	$C_6H_{13}NO_2$	L-Leucine	3.89	2.08	1.85	0.63	↑##	↓**	—
9	10.42	301.2171	$C_{20}H_{30}O_2$	Eicosapentaenoic acid	1.06	2.73	0.60	1.00	↓#	—	—
10	8.80	464.3011	$C_{26}H_{43}NO_6$	Glycocholic acid	1.73	0.43	2.24	0.66	↑##	↓	—
11	2.30	169.0349	$C_5H_4N_4O_3$	Uric acid	2.37	1.16	1.81	0.65	↑##	↓**	—
12	0.95	114.0659	$C_4H_7N_3O$	Creatinine	2.01	0.77	3.29	0.75	↑##	↓	—
13	14.29	283.2639	$C_{18}H_{36}O_2$	Stearic acid	2.30	1.88	2.04	0.53	↑##	↓**	—
14	9.52	391.2857	$C_{24}H_{40}O_4$	Ursodeoxycholic acid	1.66	0.64	2.25	0.75	↑##	↓	—
15	9.83	241.0560	$C_6H_{12}O_7$	Gluconic acid	1.23	0.89	0.63	0.99	↓##	↓	—
16	10.85	730.2405	$C_{26}H_{45}NO_{21}$	Lacto-N-tetraose	1.12	1.31	0.87	0.92	↓#	↓	—
17	0.83	940.8140	$C_{56}H_{112}NO_8P$	Phosphatidylcholine	2.30	2.02	0.49	1.93	↓##	↑**	c, e
18	10.99	279.2327	$C_{18}H_{32}O_2$	Rumenic acid	5.93	3.92	0.50	1.86	↓##	↑**	—
19	10.58	766.4845	$C_{45}H_{70}NO_8P$	Phosphatidylethanolamine	1.33	2.88	1.31	0.79	↑#	↓*	c
20	5.77	203.0816	$C_{11}H_{12}N_2O_2$	L-Tryptophan	1.52	0.67	1.88	0.85	↑##	↓	d
21	9.43	319.2273	$C_{20}H_{32}O_3$	12(R)-HETE	4.68	2.49	1.83	0.46	↑##	↓**	e
22	9.54	317.2116	$C_{20}H_{32}O_4$	5-HPETE	1.20	2.13	1.54	0.50	↑#	↓**	e
23	0.83	151.0721	$C_2H_5NO_2$	Glycine	1.12	2.02	1.56	0.47	↑#	↓**	b
24	5.75	188.0697	$C_{11}H_9NO_2$	Indoleacrylic acid	0.86	3.33	1.22	0.47	↑	↓*	—
25	1.72	150.0576	$C_5H_8O_2S$	THTC	0.64	1.32	1.39	0.44	↑	↓*	—

*Control, model, positive control and DCH (n = 10 per group) groups. #, p < 0.05 as compared to the control group; ##, p < 0.01 as compared to the control group; *, p < 0.05 as compared to the model group; **, p < 0.01 as compared to the model group; ↑, content increased; ↓, content decreased; vs., versus; C, control group; M, model group; D, DCH group. (a) Linoleic acid metabolism. (b) Glycine, serine and threonine metabolism. (c) Glycerophospholipid metabolism. (d) Tryptophan metabolism. (e) AA metabolism.*

decrease body weight and improve the serum levels of ALT in NAFLD and NASH patients (Loomba et al., 2009). Meta-analysis of clinical trials has also indicated that metformin could improve liver function, HOMA-IR, and body mass index (BMI) in NAFLD patients (Li et al., 2013). Although our results showed higher serum levels of TC and AST in DCH treated rats compared with those treated with metformin, a lower AUC of OGTT was observed in DCH group when compared with the metformin treated rats. Furthermore, there were no significant differences in body weight, liver index, FINS, HOMA-IR, and levels of serum TG and ALT between DCH and metformin treated rats. The minimal difference between the two therapeutic test groups suggested that DCH had the potential to serve as alternative treatment to metformin on NAFLD and IR.

NAFLD could impact the body in accordance with the two-hit hypothesis proposed by Christopher Day and Oliver James. In the first hit, excessive lipid contents accumulating in the liver triggered the dysfunction of lipid metabolism. This was followed by the second hit, where oxidative stress and lipid peroxidation caused by the dysfunction of lipid metabolism, induce cellular damage of hepatocytes (Chen et al., 2008). Our results demonstrated significant anti-oxidative effects for DCH on NAFLD model rats, inducing increased activities of SOD and GSH-Px and a decreased level of MDA. The accumulation of lipids in hepatocytes triggered the disorder of fatty acid oxidation and induced the production of reactive oxygen species (ROS). Excessive ROS could induce the peroxidation of unsaturated fatty acid to generate MDA and impair the function of mitochondria (Vander Heiden et al., 1997). SOD and GSH-Px are anti-oxidative enzymes, playing key roles in the elimination of ROS (El-Din et al., 2014). Increasing the activities of SOD and GSH-Px inhibited oxidative stress and could improve liver function in NAFLD patients (Cui et al., 2020).

In addition, we conducted 16S rRNA sequencing of fecal total DNA to investigate the changes in microbiological composition following DCH treatment. Our results showed a higher alpha diversity in the gut microbiota in the model group compared with the control group, whereas, the alpha diversity of the gut microbiota was decreased after DCH treatment. Our findings were in agreement with the studies from other researchers that HFD treatment could cause a higher alpha diversity of gut microbiota community in the animal model of NAFLD (Wu et al., 2018). PCoA and system clustering tree analysis revealed that HFD treatment affected the beta diversity of gut microbiota, conversely, the beta diversities in DCH treated rats showed a greater similarity to rats in the control group than those in the model group. The ratio between *F* to *B* is closely related to dyslipidemia (Abdallah et al., 2011). Compared to healthy controls, patients with dyslipidemia showed a significant increase in the relative abundance of *Firmicutes* and a remarkable decrease of *Bacteroidetes*: an increase in *F* to *B* ratio (Abdallah et al., 2011; Kasai et al., 2015). Decreasing the *F* to *B* ratio in patients had achieved a better clinical outcome for dyslipidemia (Xu et al., 2017). Consistent with these observations, our results indicated a substantial increase in the *F* to *B* ratio in model group, that was decreased after DCH treatment. The

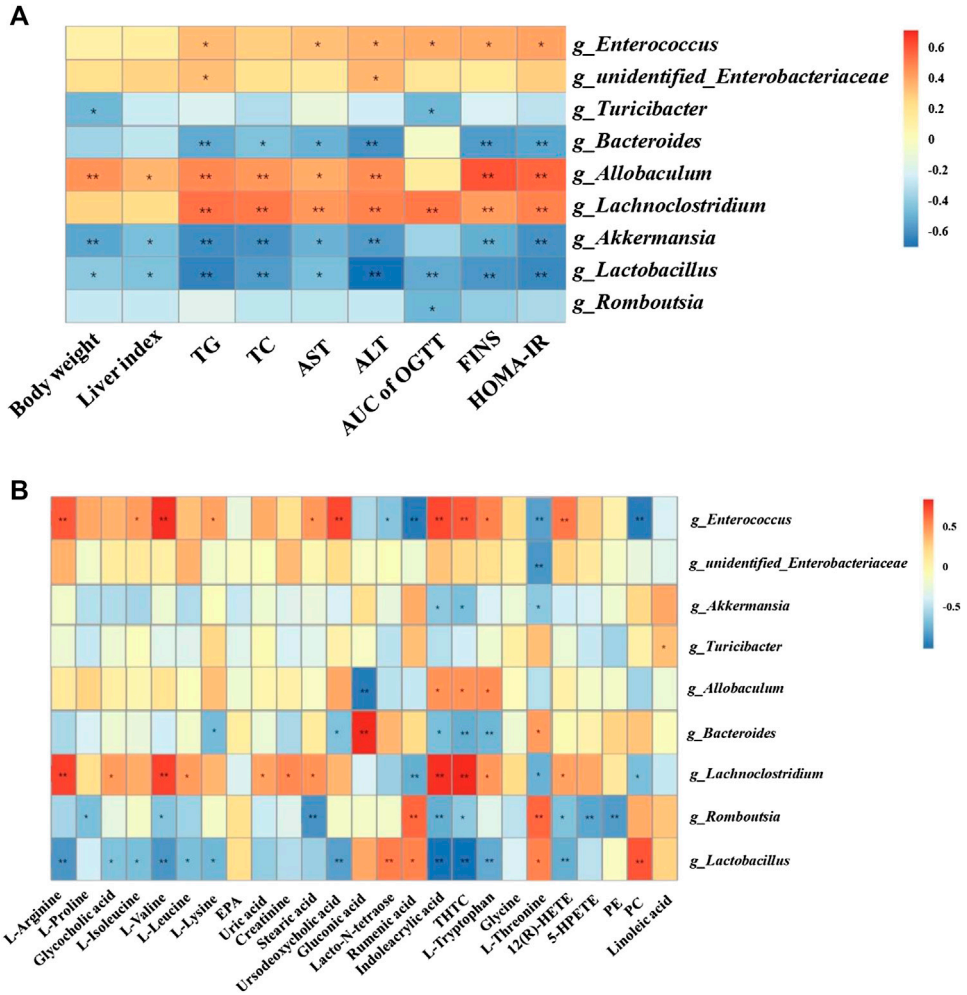

FIGURE 4 | Correlation analysis of pathological indices, untargeted metabolomics and 16S rRNA sequencing. Correlations between physiological indices and gut microbiota **(A)** and between untargeted metabolomics and gut microbiota **(B)** were analyzed using spearman's analysis (heatmap). X-axis represents the physiological indices **(A)** and differential metabolites in the serum **(B)**. Y-axis represents the gut microbiota with differential abundance. The colors of grids represent the correlation analysis value of spearman's correlation analysis. Grids in red indicate positive correlations (correlation analysis value more than 0.1), while grids in blue indicate negative correlations (correlation analysis value less than –0.1). Color coding scale indicates the correlation analysis value from heatmap, the deeper red or blue indicates higher correlation values. *: $p < 0.05$ between physiological indices and differential gut microbiota **(A)**, or between differential serum metabolites and gut microbiota **(B)**. **: $p < 0.01$ between physiological indices and differential gut microbiota **(A)**, or between differential serum metabolites and gut microbiota **(B)**.

relative abundances of *Romboutsia*, *Bacteroides, Lactobacillus, Akkermansia*, and *Turicibacter* were all increased post DCH treatment. *Bacteroides* are members in *Bacteroidetes* phylum and produce short chain fatty acids (SCFAs) through the fermentation of dietary fiber (Amabebe et al., 2020). SCFAs could be released into circulation and have been shown to help maintain the homeostasis of lipid metabolism in the liver (Nazli et al., 2004). *Lactobacillus* is a widely accepted probiotic and has used to treat dyslipidemia (Kadooka et al., 2010). *Akkermansia* has been reported to be negatively associated with inflammatory diseases and metabolic disorders (Muriel et al., 2017). In one study, supplementation with *Akkermansia* significantly improved gut barrier function, dyslipidemia, and IR in HFD-treated mice (Amandine et al., 2013). *Turicibacter* and *Romboutsia* have also been demonstrated to play beneficial roles in dyslipidemia (Kuda et al., 2017). Likewise in our study, spearman's analysis showed negative correlations for *Romboutsia*, *Bacteroides, Lactobacillus, Akkermansia*, and *Turicibacter* with body weight and biochemical markers of dyslipidemia, liver injury, and IR. Our current analysis, in concert with previous studies, indicated that one of the mechanisms for the ameliorative effects of DCH on NAFLD might be increasing the abundance of *Romboutsia*, *Bacteroides, Lactobacillus, Akkermansia*, and *Turicibacter*. In addition to increasing the relative abundance of positive gut microbiota, the relative abundances of *Lachnoclostridium* and *Enterobacteriaceae* were decreased post DCH treatment. Studies have shown that the abundance *Enterobacteriaceae* is increased in NAFLD model rats and that decreasing the abundance the *Enterobacteriaceae* in gut could improve

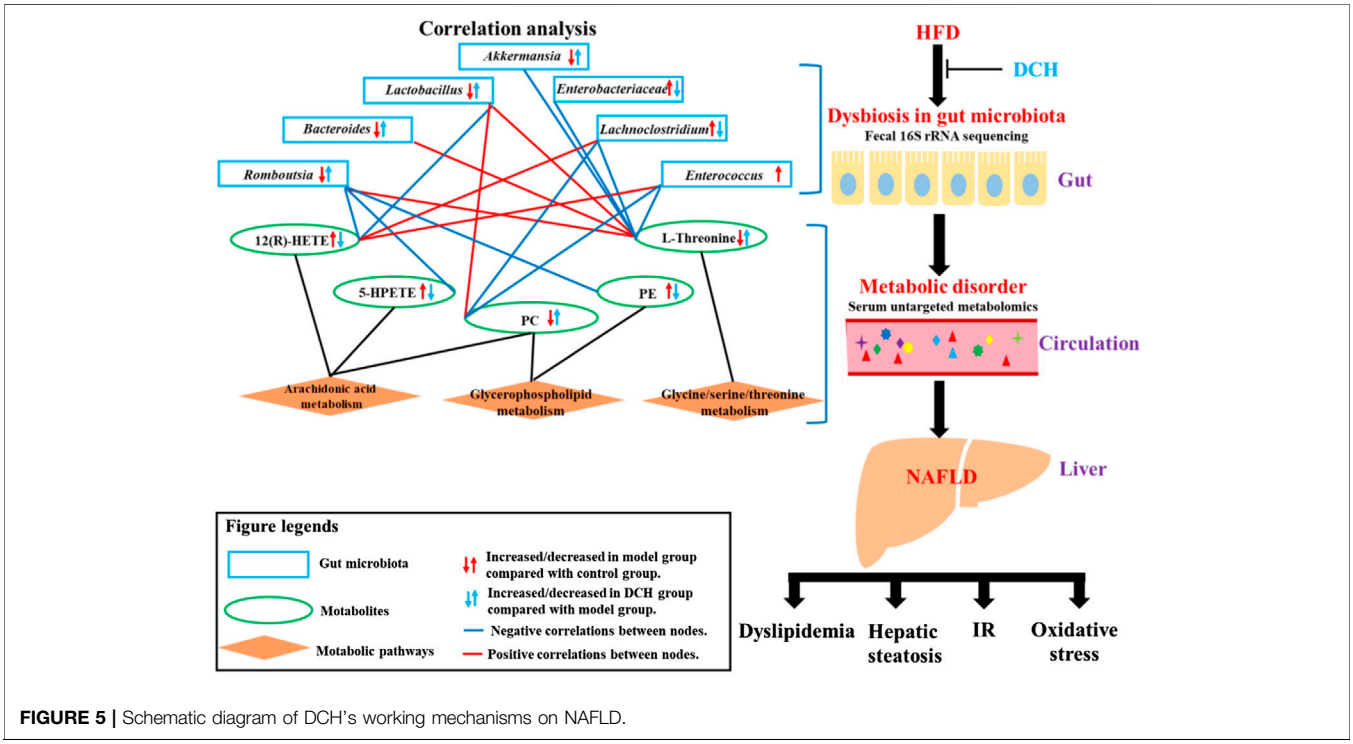

FIGURE 5 | Schematic diagram of DCH's working mechanisms on NAFLD.

NAFLD prognosis (Liang et al., 2018; Liang et al., 2018). *Lachnoclostridium* has been recently demonstrated to be associated with the progression of colorectal cancer (Liang et al., 2019). However, the role of *Lachnoclostridium* plays in NAFLD remains unclear. Our spearman's analysis showed positive correlations of *Enterococcus*, *Allobaculum*, *Lachnoclostridium*, and *Enterobacteriaceae* with the pathological changes of NAFLD. Decreasing the abundance of *Lachnoclostridium* and *Enterobacteriaceae* might be another ameliorative mechanism of DCH on NAFLD, although the impact of *Lachnoclostridium* on NAFLD needs to be further investigated to validate this supposition. Metabolic pathways related to the altered gut microbiota were also predicted using PICRUSt analysis. DCH treatment reversed the disorders in pentose phosphate, glycine/serine/threonine, AA and glycerophospholipid metabolic pathways in NAFLD model rats.

OPLS-DA of serum untargeted metabolomics showed the different metabolic profiles of the control, model and DCH groups, indicating that DCH could affect the metabolic profiles in HFD-induced NAFLD model rats. Pathway analysis of differential metabolites using MetaboAnalyst software showed that tryptophan, AA, linoleic acid, glycerophospholipid, and glycine/serine/threonine metabolic pathways were altered after HFD treatment and DCH could affect the AA, linoleic acid, glycerophospholipid, and glycine/serine/threonine metabolic pathways in NAFLD model rats. In particular, AA, glycerophospholipid, and glycine/serine/threonine metabolic pathways were identified in both PICRUSt analysis of gut microbiota studies and pathway analysis of untargeted metabolomics. Therefore, we hypothesized that DCH could regulate the disorders in AA, glycerophospholipid, and glycine/serine/threonine metabolic pathways through improving the disbiosis in gut microbiota.

AA Metabolism

The dysfunction of AA metabolism has been previously implicated in the course of metabolic disorder and inflammatory diseases (Sonnweber et al., 2018). Our results showed that the levels of 12(R)-HETE and 5-HPETE, which are metabolic products of AA, were increased in NAFLD model rats. Whereupon, DCH treatment decreased the levels of 12(R)-HETE and 5-HPETE. The serum levels of 12(R)-HETE have been positively correlated to the severity of NAFLD (Maciejewska et al., 2015). A possible mechanism of action is that increased levels of 12(R)-HETE and 5-HPETE induce the inflammatory response by recruiting neutrophil cells (Han and Corey, 2000). Dietary intervention has been shown to decrease the levels of 12-HETE and ameliorate hepatic steatosis in NAFLD patients (Dominika et al., 2015). Furthermore, negative correlations between *Lactobacillus*, *Romboutsia,* and 12(R)-HETE, 5-HPETE levels were found by our spearman's analysis. Likewise, other studies showed that excessive dietary polyunsaturated fatty acids, such as linoleic acid (LA), could augment the adipose inflammatory response in obese mice through inducing AA metabolism. Colonization of *Lactobacillus* could inhibite AA metabolism to ameliorate adipose inflammatory response and obesity through converting excessive dietary LA to 10-hydroxy-cis-12-octadecenoic acid (HYA) (Miyamoto et al., 2019). Up to now, *Romboutsia* has not been demonstrated to associate

with AA metabolism. The detailed effects and mechanisms of *Romboutsia* on AA metabolism still need to be further investigated.

Glycerophospholipid Metabolism

The dysfunction of glycerophospholipid metabolism has been shown to disturb the energy metabolism of hepatocytes (Mesens et al., 2012). Our results showed that the level of PC was decreased and the level of PE was increased in NAFLD model rats, with the inverse effect following DCH treatment. PCs comprise 40–50% of total phospholipids in mammalian cells (Vander Veen et al., 2017). The generation of PC includes two avenues. Choline is transformed into CDP-choline, an intermediate product in PC generation, and then CDP-choline interacts with diacylglycerol to form PC. PC can also be transformed from PE directly. PEs account for 15–25% of total phospholipids in mammalian cells (Vander Veen et al., 2017). PE is derived from the synthesis of diacylglycerol and CDP-ethanolamine. The decreased ratio of PC to PE, observed in NAFLD patients, could impair the permeability of cellular membrane and induce damage to hepatocytes (Li et al., 2006). Moreover, modulating the balance of PC and PE has shown beneficial effects on NAFLD (Calzada et al., 2016). Studies have demonstrated that orally treatment of *Lactobacillus*-containing probiotic formulation could increase the levels of PC in HFD-induce obese rat model (Shin et al., 2018). Negative correlations of PC (18:3), PC (20:2) and *Lachnoclostridium* have been found in obese mice (Liu et al., 2018). Our spearman's analysis also showed a positive correlation between *Lactobacillus* and PC level, and negative correlations of *Lachnoclostridium, Enterococcus* and PC. Additionally, we observed a negative correlation between PE and *Romboutsia*. Given these correlations, its likely the modulatory effects of DCH on glycerophospholipid metabolism might occur through affecting the abundances of *Lactobacillus, Lachnoclostridium* and *Romboutsia*.

Glycine/Serine/Threonine Metabolism

The dysfunction of glycine, serine and threonine metabolism has also been associated with the NAFLD-related metabolic disorders (Huang et al., 2018). Increased levels of glycine and decreased levels of L-threonine were observed in NAFLD model rats, with DCH treatment reversing the trend. L-threonine is an essential amino acid in mammal cells and has shown beneficial effects on NAFLD through inducing the synthesis of phospholipid and oxidation of fatty acids (Zhang et al., 2020). Unlike other amino acids, L-threonine can be transformed into different amino acids, such as glycine, through specific enzymatic reaction rather than through the catalysis of dehydrogenase or transamination. Glycine can be transformed into serine, which can be subsequently transformed into pyruvate through dehydration and deamination. Pyruvate can then enter the citrate cycle to generate ATP. Clinical studies showed an increase of plasma glycine levels in patients with NAFLD (Melania et al., 2018). Excessive glycine levels can disrupt the metabolism of amino acids and the citrate cycle. Spearman's correlation analysis results indicated that *Lactobacillus, Romboutsia*, and *Bacteroides* exhibited positive correlations with L-threonine, while *Akkermansia*, *Enterococcus, Enterobacteriaceae,* and *Lachnoclostridium* exhibited negative correlations. Likewise, positive corelations have been demonstrated of *Lactobacillus, Romboutsia* and L-threonine in mice after fed with *Ganoderma lucidum* spores oil (Wu et al., 2020). No bacteria examined showed significant correlations with glycine. The changes in glycine levels after DCH treatment might be caused by the transformation of L-threonine.

CONCLUSION

Overall, our study revealed the various ameliorative effects of DCH on NAFLD, including reducing the hepatic steaosis, improving dyslipidemia and IR, and enhancing the liver's anti-oxidative abilities. The mechanisms of DCH on NAFLD were likely linked to the improvement of the dysbiosis of gut microbiota and modulation of AA, glycerophospholipid, and glycine/serine/threonine metabolism (**Figure 5**). However, the detailed modulatory effects of DCH on gut microbiota and serum metabolism should be further verified using metagenomics and secondary mass spectrometry in metabolomics. Recent studies have also developed a gut microbiota depletion model using antibiotics to further verify the modulatory effects of drugs on gut microbiota (Cui et al., 2018). Fecal transplantation from drug-treated groups to experimental model groups has also been used as a novel approach to validate modulatory effects of drugs on gut microbiota (Li et al., 2018). Gut microbiota depletion and fecal transplantation could be used in future studies to validate DCH's ability to modulate the serum metabolism through improving the dysfunction of gut microbiota community. Despite the need for further specific investigation, our study has illuminated the mechanisms of DCH on NAFLD patients, and highlighted the utility of combination 16S rRNA sequencing-metabolomics to investigate the mechanisms of gut microbiota and host metabolism in Chinese herbal formulas.

DATA AVAILABILITY STATEMENT

The sequencing data in our study has been uploaded in the BioProject: PRJEB40601, https://www.ncbi.nlm.nih.gov/bioproject/PRJEB40601/.

ETHICS STATEMENT

The animal study was reviewed and approved by Animal Ethics Committee at Tianjin University of Traditional Chinese Medicine.

AUTHOR CONTRIBUTIONS

HC wrote the manuscript. HC, YL, LJ, LY, and YW conducted animal experiments. HC, LW, JL, LY, and HSW finished molecular bioassays. ZZ, HWW, XL, and YP provided

technical guidance for the whole work. All authors contributed to the article and approved the submitted version.

FUNDING

This work was supported by National Science Foundation of China (81703828), Natural Science Foundation of Tianjin (17JCYBJC42800), Science and Technology Projects in Key Fields of Traditional Chinese Medicine of Tianjin Municipal Health Commission (No. 2020006) and Public Welfare Research Projects in Jiaxing (SQ2018001355).

SUPPLEMENTARY MATERIAL

The Supplementary Material for this article can be found online at: https://www.frontiersin.org/articles/10.3389/fphar.2020.584090/full#supplementary-material

REFERENCES

Abdallah, I. N., Ragab, S. H., Abd, E. B. A., Shoeib, A. R. S., Yasser, A., and Dina, F., (2011). Frequency of firmicutes and bacteroidetes in gut microbiota in obese and normal weight egyptian children and adults. *Archives of Medical ence*. 7, 501–507. doi:10.5114/aoms.2011.23418

Amabebe, E., Robert, F. O., Agbalalah, T., and Orubu, E. S. F. (2020). Microbial dysbiosis-induced obesity: role of gut microbiota in homeostasis of energy metabolism. *Br. J. Nutr.*. 123, 1127–1137. doi:10.1017/S0007114520000380

Amandine, E., Clara, B., Lucie, G., Janneke, P. O., Céline, D., Laure, B. B., et al. (2013). Cross-talk between Akkermansia muciniphila and intestinal epithelium controls diet-induced obesity. Proc Natl Acad Sci *USA*. 110, 9066–9071. doi:10.1073/pnas.1219451110

Bhardwaj, S. S., and Chalasani, N. (2007). Lipid-lowering agents that cause drug-induced hepatotoxicity. *Clin. Liver Dis.* 11, 597–613. doi:10.1016/j.cld.2007.06.010

Stefano, B., Gianluca, I., Pina, D. M., Claudia, S., Newton, E. E., and Giovanni, C. (2018). Gut microbiota as a driver of inflammation in nonalcoholic fatty liver disease. *Mediat. Inflamm.* 1-7. doi:10.1155/2018/9321643

Calzada, E., Onguka, O., and Claypool, S. M., (2016). Phosphatidylethanolamine metabolism in health and disease. *Int. Rev. Cell Mol. Biol.* 321, 29–88. doi:10.1016/bs.ircmb.2015.10.001

Cao, M., Miao, J., Wang, L., Liu, H. Z., Cui, H. T., and Bian, Y. H. (2020) The advances of traditional Chinese medicine in the treatment of liver diseases in 2019. Tra Med Res. *online.* doi:10.12032/TMR20200520182

Chen, Z. W., Chen, L. Y., Dai, H. L., Chen, J. H., and Fang, L. Z. (2008). Relationship between alanine aminotransferase levels and metabolic syndrome in nonalcoholic fatty liver disease. *J. Zhejiang Univ. Sci. B.* 9, 616–622. doi:10.1631/jzus.B0720016

Cui, H. T., Cai, Y., Wang, L., Jia, B., Li, J., Zhao, S., et al. (2018). Berberine regulates treg/Th17 balance to treat ulcerative colitis through modulating the gut microbiota in the colon. *Front. Pharmacol.* 9, 571. doi:10.3389/fphar.2018.00571

Cui, H. T., Li, Y. T., Cao, M., Liao, J. B., Liu, X. G., Miao, J., et al. (2020). Untargeted metabolomic analysis of the effects and mechanism of nuciferine treatment on rats with nonalcoholic fatty liver disease. *Front. Pharmacol.* 11, 858. doi:10.3389/fphar.2020.00858

Cummings, B. P., Bettaieb, A., Graham, J. L., Stanhope, K. L., Dill, R., Morton, G. J., et al. (2011). Subcutaneous administration of leptin normalizes fasting plasma glucose in obese type 2 diabetic ucd-t2dm rats. *Proc. Natl. Acad. Sci. USA* 108, 14670. doi:10.1073/pnas.1107163108

Dominika, M., Piotr, O., Arleta, D., Karina, R., Dominika, J. M., Marcin, B., et al. (2015). Metabolites of arachidonic acid and linoleic acid in early stages of non-alcoholic fatty liver disease--A pilot study. *Prostaglandins Other Lipid Mediat.* 121: 184–189. doi:10.1016/j.prostaglandins.2015.09.003.

El-Din, S. H., Sabra, A. N., Hammam, O. A., Ebeid, F. A., and El-Lakkany, N. M. (2014). Pharmacological and antioxidant actions of garlic and.or onion in non-alcoholic fatty liver disease (NAFLD) in rats. *J. Egypt. Soc. Parasitol.* 44, 295–308. doi:10.12816/0006468

Fan, Y. H., and Miao, B. Q. (2014). Treatment of nonalcoholic fatty liver with Dacaihu decoction in 63 cases. *Inner. Mongolia. J. tradit. Chin. med.* 33, 9. doi:10.16040/j.cnki.cn15-1101.2014.17.014

Gong, S., Ye, T., Wang, M., Wang, M., Li, Y., Ma, L., et al. (2020). Traditional Chinese medicine formula kang shuai Lao pian improves obesity, gut dysbiosis, and fecal metabolic disorders in high-fat diet-fed mice. *Front. Pharmacol.* 11, 297. doi:10.3389/fphar.2020.00297

Han, X., and Corey, E. J. (2000). A short catalytic enantioselective synthesis of the proinflammatory eicosanoid 12(R)-hydroxy- 5(Z),8(Z),10(E),14(Z)-eicosatetraenoic acid (12(R)-HETE). *Org. Lett.* 2, 2543–2544. doi:10.1021/ol0062392

Huang, S. Z., Sun, C. J., Hou, Y. C., Tang, Y. h., Zhu, Z. B., Zhang, Z. H., et al. (2018). A comprehensive bioinformatics analysis on multiple gene expression omnibus datasets of nonalcoholic fatty liver disease and nonalcoholic steatohepatitis. *Sci. Rep.* 8, 7630. doi:10.1038/s41598-018-25658-4

Iizuka, A., Yoshie, F., Amagaya, S., Yasuda, T., Iizuka, M., Yamaguchi, H., et al. (2013). Effect of dai-saiko-to (da-chai-hu-tang) on ldl-receptor gene expression in human hepatoma cell line (hepg2). *Am. J. Plant Sci.* 4, 454–459. doi:10.4236/ajps.2013.42A058

Jing, F., Xiaoqi, S., Boyu, X., Nanyuan, F., and Min, Z. (2017). Dahuang zexie decoction protects against high-fat diet-induced nafld by modulating gut microbiota-mediated toll-like receptor 4 signaling activation and loss of intestinal barrier. *Evid. Based. Complement. Alternat. Med.* 2017, 1–13. doi:10.1155/2017/2945803

Kadooka, Y., Sato, M., Imaizumi, K., Ogawa, A., Ikuyama, K., Akai, Y., et al. (2010). Regulation of abdominal adiposity by probiotics (lactobacillus gasseri sbt2055) in adults with obese tendencies in a randomized controlled trial. *Eur. J. Clin. Nutr.* 64, 636–643. doi:10.1038/ejcn.2010.19

Kasai, C., Sugimoto, K., Moritani, I., Tanaka, J., Oya, Y., Inoue, H., et al. (2015). Comparison of the gut microbiota composition between obese and non-obese individuals in a Japanese population, as analyzed by terminal restriction fragment length polymorphism and next-generation sequencing. *BMC Gastroenterol.*. 2015, 15, 100. doi:10.1186/s12876-015-0330-2

Kuda, T., Yokota, Y., Shikano, A., Takei, M., Takahashi, H., and Kimura, B. (2017). Dietary and lifestyle disease indices and caecal microbiota in high fat diet, dietary fibre free diet, or dss induced ibd models in icr mice. *J Func Foods*. 35, 605–614. doi:10.1016/j.jff.2017.06.030

Li, F., Sun, G., Wang, Z., Wu, W., Guo, H., Peng, L., et al. (2018). Characteristics of fecal microbiota in non-alcoholic fatty liver disease patients. *Sci. China. Life. Sci.* 61, 770–778. doi:10.1007/s11427-017-9303-9

Li, J. C., Cui, H. T., Cai, Y. Z., Lin, J., Song, X., Zhou, Z. J., et al. (2018) Tong-xie-yao-fang regulates 5-HT level in diarrhea predominant irritable bowel syndrome through gut microbiota modulation. *Front. Pharmacol.* 9, 1110. doi:10.3389/fphar.2018.01110

Li, Y., Liu, L., Wang, B., Wang, J., and Chen, D. F. (2013). Metformin in non-alcoholic fatty liver disease: a systematic review and metaanalysis. *Biomed Rep*. 1, 57–64. doi:10.3892/br.2012.18

Li, Y. T., Cui, H. T., Yang, L., Jin, L. L., Wang, Y. M., Dong, X. Q., et al. (2020). Hua-Zhuo-Kai-Yu decoction inhibits apoptosis in nonalcoholic fatty liver disease. *Tradit. Med. Res.* 6, 5. doi:10.12032/TMR20200201157

Li, Z., Agellon, L. B., Allen, T. M., Umeda, M., Jewell, L., Mason, A., et al. (2006). The ratio of phosphatidylcholine to phosphatidylethanolamine influences membrane integrity and steatohepatitis. *Cell Metab.* 3, 321–331. doi:10.1016/j.cmet.2006.03.007

Liang, J. Q., Li, T., Nakatsu, G., Chen, Y. X., and Yu, J. (2019). A novel faecal lachnoclostridium marker for the non-invasive diagnosis of colorectal adenoma and cancer. *Gut.* 69, 1248–1257. doi:10.1136/gutjnl-2019-318532

Liang, Y. J., Zhang, Y. P., Deng, Y. J., Liang, S., He, Y. F., Chen, Y. N., et al. (2018). Chaihu-shugan-san decoction modulates intestinal microbe dysbiosis and alleviates chronic metabolic inflammation in NAFLD rats via the NLRP3 inflammasome pathway. *Evid Based Complement Alternat Med*. 2018, 9390786. doi:10.1155/2018/9390786

Liu, J., Yue, S., Yang, Z., Feng, W., Meng, X., Wang, A., et al. (2018). Oral hydroxysafflor yellow A reduces obesity in mice by modulating the gut microbiota and serum metabolism. *Pharmacol. Res.* 134, 40–50. doi:10.1016/j.phrs.2018.05.012

Loomba, R., Lutchman, G., Kleiner, D. E., Ricks, M., Feld, J. J., Borg, B. B., et al. (2009). Clinical trial: pilot study of metformin for the treatment of non-alcoholic steatohepatitis. *Aliment. Pharmacol. Ther.*, 29, 172–182. doi:10.1111/j.1365-2036.2008.03869.x

Maciejewska, D., Ossowski, P., Drozd, A., Ryterska, K., Jamiol-Milc, D., Banaszczak, M., et al. (2015). Metabolites of arachidonic acid and linoleic acid in early stages of non-alcoholic fatty liver disease--A pilot study. *Prostaglandins Other Lipid Mediat.* 121, 184–189. doi:10.1016/j.prostaglandins.2015.09.003

Melania, G., Fabrizia, C., Chiara, R., Emma, B., Milena, M., Veronica, D. L., et al. (2018). Altered amino acid concentrations in NAFLD: impact of obesity and insulin resistance. *Hepatology*. 67:145–158. doi:10.1002/hep.29465.

Mesens, N., Desmidt, M., Verheyen, G. R., Starckx, S., Damsch, S., De Vries, R., et al. (2012). Phospholipidosis in rats treated with amiodarone: serum biochemistry and whole genome micro-array analysis supporting the lipid traffic jam hypothesis and the subsequent rise of the biomarker BMP. *Toxicol. Pathol.* 40, 491–503. doi:10.1177/0192623311432290

Miyamoto, J., Igarashi, M., Watanabe, K., Karaki, S. I., Mukouyama, H., Kishino, S., et al. (2019). Gut microbiota confers host resistance to obesity by metabolizing dietary polyunsaturated fatty acids. *Nat. Commun.* 10, 4007. doi:10.1038/s41467-019-11978-0

Muriel, D., Clara, B., and Willem, M. V. (2017). Akkermansia muciniphila and its role in regulating host functions. *Microb. Pathog.*. 106, 171–181. doi:10.1016/j.micpath.2016.02.005.

Nazli, A., Yang, P. C., Jury, J., Howe, K., Watson, J. L., Derholm, J. D., et al. (2004). Epithelia under metabolic stress perceive commensal bacteria as a threat. *Am. J. Pathol.*. 164, 947–957. doi:10.1016/S0002-9440(10)63182-3

Piao, S. H., Zhu, Z. Q., Tan, S. Y., Zhan, H. X., Rong, X. L., and Guo, J. (2020). An integrated fecal microbiome and metabolome in the aged mice reveal anti-aging effects from the intestines and biochemical mechanism of FuFang zhenshu TiaoZhi (FTZ). *Biomed. Pharmacother.* 121, 109421. doi:10.1016/j.biopha.2019.109421

Porras, D., Nistal, E., Martínez-FlórezSusana, Olcoz., Luis, José., Jover, R., et al. (2019). Functional interactions between gut microbiota transplantation, quercetin, and high-fat diet determine non-alcoholic fatty liver disease development in germ-free mice. *Mol. Nutr. Food Res.* 63, e1800930. doi:10.1002/mnfr.201800930

Reenam, S. K., Fernando, B., Kenneth, C., and Philip, N. N. (2019). Modulation of insulin resistance in nonalcoholic fatty liver disease. *Hepatology*. 70, 711–724. doi:10.1002/hep.30429.

Ritze, Y., Bárdos, Gyöngyi., Claus, A., Ehrmann, V., Bergheim, I., Schwiertz, A., et al. (2014). Lactobacillus rhamnosus gg protects against non-alcoholic fatty liver disease in mice. *PLoS. ONE.* 9, e80169. doi:10.1371/journal.pone.0080169

Scarpello, J. H. B., Hodgson, E., and Howlett, H. C. S. (1998). Effect of metformin on bile salt circulation and intestinal motility in type 2 diabetes mellitus. *Diabet. Med.* 15, 651–656. doi:10.1002/(sici)1096-9136

Shin, J. H., Nam, M. H., Lee, H., Lee, J. S., Kim, H., Chung, M. J., et al. (2018). Amelioration of obesity-related characteristics by a probiotic formulation in a high-fat diet-induced obese rat model. *Eur. J. Nutr.*., 57, 2081–2090. doi:10.1007/s00394-017-1481-4

Sonnweber, T., Pizzini, A., Nairz, M., Weiss, Günter., and Tancevski, I.. (2018). Arachidonic acid metabolites in cardiovascular and metabolic diseases. *Int. J. Mol. Sci.*. 19: 3285. doi:10.3390/ijms19113285.

Su, G., Wang, H., Bai, J., Chen, G., and Pei, Y. (2018). A metabonomics approach to drug toxicology in liver disease and its application in traditional Chinese medicine. *Curr. Drug. Metab.* 20, 292–300. doi:10.2174/1389200220666181231124439

Tremaroli, V., and Backhed, F. (2012). Functional interactions between the gut microbiota and host metabolism. *Nature*. 489, 242–249. doi:10.1038/nature11552

Vander Heiden, M. G., Chandel, N. S., Williamson, E. K., Schumacker, P. T., and Thompson, C. B. (1997). BclxL regulates the membrane potential and volume homeostasis of mitochondria. *Cell.* 91, 627–637. doi:10.1016/S0092-8674(00)80450-X

Vander Veen, J. N., Kennelly, J. P., Wan, S., Vance, J. E., Vance, D. E., Jacobs, R. L., et al. (2017). The critical role of phosphatidylcholine and phosphatidylethanolamine metabolism in health and disease. *Biochim. Biophys. Acta Biomembr.* 1859, 1558–1572. doi:10.1016/j.bbamem.2017.04.006

Wu, S., Hu, R., Nakano, H., Chen, K., Liu, M., He, X., et al. (2018). Modulation of gut microbiota by Lonicera caerulea L. Berry polyphenols in a mouse model of fatty liver induced by high fat diet. *Molecules*. 23, 3213. doi:10.3390/molecules23123213

Wu, X., Cao, J., Li, M., Yao, P., Li, H., Xu, W., et al. (2020). An integrated microbiome and metabolomic analysis identifies immunoenhancing features of Ganoderma lucidum spores oil in mice. *Pharmacol. Res.* 158, 104937. doi:10.1016/j.phrs.2020.104937

Xie, X. H., Liao, J. B., Fang, F., Zhao, J., Cao, Y. J., Cui, H. T., et al. (2019). Jian-Gan-Xiao-Zhi decoction ameliorates high-fat high-carbohydrate diet-induced non-alcoholic fatty liver disease and insulin resistance by regulating the AMPK/JNK pathway. *Traditional Medicine Research*. 6, 1–12. doi:10.12032/TMR20191014139

Xu, P., Wang, J., Hong, F., Wang, S., Jin, X., Xue, T., et al. (2017). Melatonin prevents obesity through modulation of gut microbiota in mice. *J. Pineal Res.*. 62, e12399. doi:10.1111/jpi.12399

Yin, X. C., Peng, J. H., Zhao, L. P., Yu, Y. P., Zhang, X., Liu, P., et al. (2013). Structural changes of gut microbiota in a rat non-alcoholic fatty liver disease model treated with a Chinese herbal formula. *Syst. Appl. Microbiol.* 36, 188–196. doi:10.1016/j.syapm.

Yoshie, F., Iizuka, A., Komatsu, Y., Matsumoto, A., Itakura, H., and Kondo, K. (2004). Effects of dai-saiko-to (da-chai-hu-tang) on plasma lipids and atherosclerotic lesions in female heterozygous heritable kurosawa and kusanagi-hypercholesterolemic (khc) rabbits. *Pharmacol. Res.* 50, 223–230. doi:10.1016/j.phrs.2004.02.003

Zhang, Z. M., Zhou, Y. M., Lin, Y., Li, Y. M., Xia, B. H., Lin, L. M., et al. (2020). GC-MS-based metabolomics Research on the anti-hyperlipidaemic activity of Prunella vulgaris L. Polysaccharides. *Int. J. Biol. Macromol.*. 159: 461–473. doi:10.1016/j.ijbiomac.2020.05.003.

Zheng, L. Y., Pan, J. Q., Yang, Y. L., Lu, J. H., and Zhao, R. X. (2014). Effects total glucosides paeony on downregulating the expression ERKI/2, TLR4 and TRL9 in rats with nonalcoholic fatty liver disease. *J. Chin. Pharmaceut. Sci.*. 49, 2168–2172. doi:10.11669/cpj.2014.24.006

Conflict of Interest: The authors declare that the research was conducted in the absence of any commercial or financial relationships that could be construed as a potential conflict of interest.

frontiers in Pharmacology

ORIGINAL RESEARCH
published: 30 November 2020
doi: 10.3389/fphar.2020.578217

Chemical Fingerprint Analysis and Ultra-Performance Liquid Chromatography Quadrupole Time-of-Flight Mass Spectrometry-Based Metabolomics Study of the Protective Effect of Buxue Yimu Granule in Medical-Induced Incomplete Abortion Rats

Yan Zhang[1], Wei Li[1], Ting-Ting Chen[1], Yong Yang[1], Meng-Yao Wu[2], Jie-Ying Luo[3], Yun Gong[2,] and Liang Zou[1,4]**

[1]School of Medicine, Chengdu University, Chengdu, China, [2]Department of Pharmacology, Zhuzhou Qianjin Pharmaceutical Co., Ltd., Zhuzhou, China, [3]College of Pharmacy, Hunan University of Chinese Medicine, Changsha, China, [4]Key Laboratory of Coarse Cereal Processing of Ministry of Agriculture and Rural Affairs, School of Food and Biological Engineering, Chengdu University, Chengdu, China

OPEN ACCESS

Edited by:
Peng Li,
University of Macau,
China

Reviewed by:
Wencan He,
Université de Bordeaux, France
Jen-Tsung Chen,
National University of Kaohsiung,
Taiwan

***Correspondence:**
Yun Gong
gongyun2002@126.com
Liang Zou
zouliangcdu@126.com

Specialty section:
This article was submitted to Ethnopharmacology, a section of the journal Frontiers in Pharmacology

Received: 30 June 2020
Accepted: 09 October 2020
Published: 30 November 2020

Citation:
Zhang Y, Li W, Chen T-T, Yang Y, Wu M-Y, Luo J-Y, Gong Y and Zou L (2020) Chemical Fingerprint Analysis and Ultra-Performance Liquid Chromatography Quadrupole Time-of-Flight Mass Spectrometry-Based Metabolomics Study of the Protective Effect of Buxue Yimu Granule in Medical-Induced Incomplete Abortion Rats. Front. Pharmacol. 11:578217. doi: 10.3389/fphar.2020.578217

Medical abortion is a common method to terminate an early pregnancy and often causes serious complications such as abnormal uterine bleeding and endometritis. Buxue Yimu granule (BYG) is a well-known traditional Chinese medicine prescription composed of five kinds of drugs and is widely used in gynecology and obstetrics. The aim of the present study was to establish the quality standard of BYG and investigate its protective effect on incomplete abortion. The chemical fingerprint of BYG was established by high performance liquid chromatography (HPLC). The major compounds of BYG were determined by ultra-performance liquid chromatography with triple quadrupole mass spectrometry. An incomplete abortion rat model was induced by intragastric administration of mifepristone (8.3 $mg{\cdot}kg^{-1}$) combined with misoprostol (100.0 $\mu g{\cdot}kg^{-1}$) during early pregnancy. The serum levels of human chorionic gonadotrophin (HCG), estradiol (E_2), and progesterone (PG) were determined. The serum endogenous metabolites were analyzed by ultra-performance liquid chromatography quadrupole time-of-flight mass spectrometry (UPLC-Q-TOF/MS). Multivariate analysis, including partial least squares discriminant analysis (PLS-DA) and orthogonal partial least squares discriminant analysis (OPLS-DA), was employed to analyze the metabolic profiles, and MetaboAnalyst was used to investigate the metabolic pathways. Furthermore, hematoxylin-eosin staining (HE) was used to evaluate the histopathological changes in uterine tissue. The expression levels of VEGFA and NF-κB were detected by immunohistochemistry. The results indicated that HPLC fingerprint analysis can be successfully used to assess the quality of BYG. The medical-induced

incomplete abortion rats were clearly separated from control rats, and the biochemical changes were gradually restored to normal after administration of BYG. Moreover, 19 potential biomarkers, including N-lactoylleucine, 2-piperidinone, isobutyryl-L-carnitine, eicosapentaenoylcholine, LysoPC(14:0), LysoPC(20:5), physagulin C, LysoPC(18:3), leukotriene D5, deoxycholic acid 3-glucuronide, glycine, pregnanediol 3-O-glucuronide, LysoPC(18:2), LysoPC(17:0/0:0), N-acetyl-leukotriene E4, LysoPC(18:0), platelet-activating factor, LysoPA(24:1), and LysoPC(18:1), which were mainly related to the amino acids metabolism, lipids metabolism, and bile acid biosynthesis, were identified. Consequently, BYG exerts a potential protective role in the intervention of incomplete abortion by anti-inflammatory, promote endometrial repair, and regulate the metabolic disorders.

Keywords: Buxue Yimu granule, medical abortion, anti-inflammatory, ultra-performance liquid chromatography quadrupole time-of-flight mass spectrometry, metabolomic, fingerprint analysis

INTRODUCTION

The availability of mifepristone with misoprostol for medical abortion has been increasingly used as an alternative method to surgical intervention for early termination of pregnancy (Baiju et al., 2019). In the United States, the Food and Drug Administration (FDA) has approved this combination of medications for use at home at up to 10 weeks' gestation (Schmidt-Hansen et al., 2020). Most women believe that medical abortion has higher autonomy than surgical abortion and is more convenient, can protect privacy, and has fewer side effects than surgery (LaRoche and Foster, 2020). Despite excellent effectiveness and safety, however, previous studies have shown that the drug may still cause incomplete abortion, with a complete successful expulsion rate of 92.3% for 64–70 days of pregnancy and 86.7% for 71–77 days of pregnancy (Dzuba et al., 2020). Histopathological examination showed that the residual embryo of incomplete abortion may be the cause of other severe side-effects such as abnormal uterine bleeding (AUB), pain, and pelvic infection (Hsia et al., 2019).

From the perspective of Western medicine, uterine surgery is required for patients with an incomplete abortion. At the same time, for the treatment of complications of medical abortion, such as uterine contraction, hemostasis, and anti-infection treatments, are mainly used in the clinic (Chen and Creinin, 2015). From the perspective of traditional Chinese medicine, most women have the characteristics of weakness of Qi and blood and stagnation of blood stasis after childbirth or induced abortion. Buxue Yimu granule (BYG) is a famous prescription composed of *Leonurus japonicus* Houtt. (Yimucao), *Angelica sinensis* (Oliv.) Diels (Danggui), *Astragalus membranaceus* Bunge (Huangqi), *Citrus Reticulata* Blanco (Chenpi), and Colla corii asini (Ejiao), which has the effect of replenishing Qi and blood, promoting circulation and mitigating blood stasis. Moreover, clinical evidence has shown that BYG has a definite curative effect in the treatment of postpartum or abortion complications. However, the biological mechanisms of BYG in the treatment of obstetric complications are unclear.

Metabolomics mainly studies the changes in endogenous molecule metabolites such as fatty acids, amino acids, lipids and organic acids caused by interferences from the environment, disease status, drug intervention and other factors (Liu et al., 2012). The research concept complements the holistic view in the system theory of traditional Chinese medicine. At present, metabolomics has been widely used in the fields of food safety (Liu and Wu, 2020a), disease diagnosis (Wang et al., 2020), and drug action mechanistic studies. In particular, this technique provides a good strategy for evaluating the biological mechanism of complex classical Chinese medicine prescriptions. For instance, ^{1}H-NMR-based metabolomics has been used to study the mechanism of HuangQi-DanShen in cerebral ischemia (Liu et al., 2020b). A metabolomics study based on HPLC-MS/MS predicts that the treatment of hyperlipidemia by Si-miaoyong-an decoction is related to its antioxidant and anti-inflammatory activities and the regulation of pyruvate and taurine metabolism (Shi et al., 2020). Tianma Gouteng decoction exhibited the antihypertensive activity by regulating the metabolism of amino acids, sphingomyelin, and glycerol phospholipids (Dong et al., 2020).

In the present study, the quality standard of BYG was established by high-performance liquid chromatography (HPLC). The therapeutic effects of BYG on serum hormone levels and uterine histopathology were investigated in rats having incomplete abortions induced by mifepristone and misoprostol. Moreover, an ultra-performance liquid chromatography quadrupole time-of-flight mass spectrometry (UPLC-Q-TOF/MS)-based metabolomic method combined with multivariate analysis was applied to demonstrate and identify the potential biomarkers and the metabolic pathways.

MATERIALS AND METHODS

Chemicals and Reagents

Buxue Yimu granule was obtained from Zhuzhou Qianjin Pharmaceutical Co., Ltd. (Hunan, China). Hesperidin (batch No. C-006-191012), Astragaloside (batch No. H-013-180228),

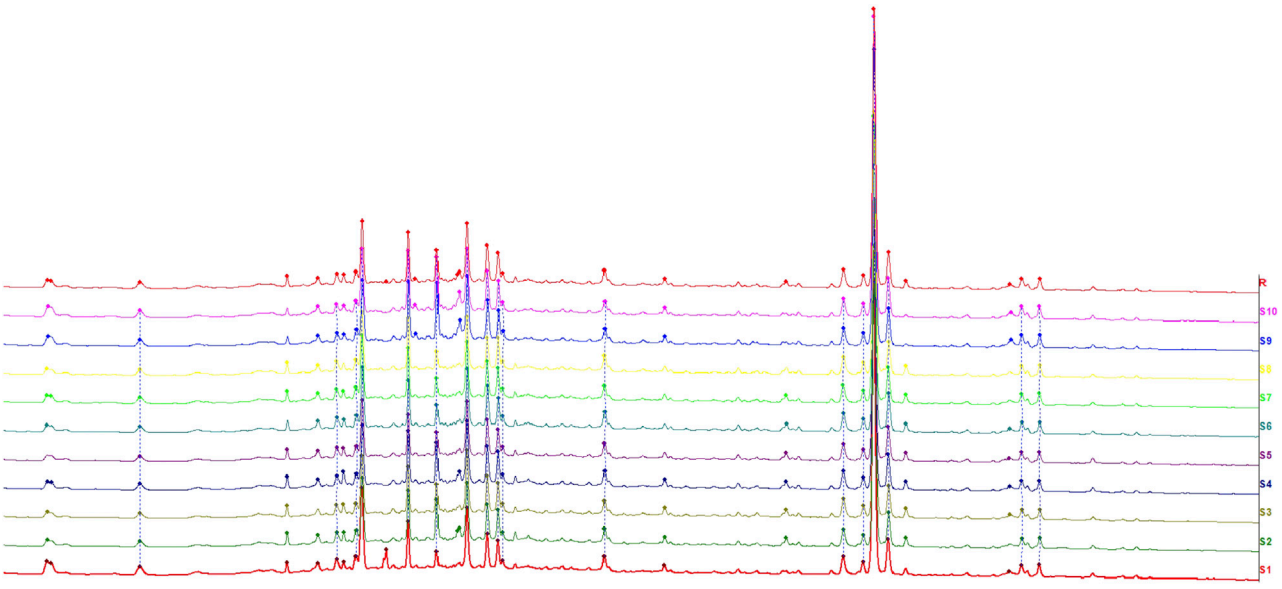

FIGURE 1 | Representative HPLC chromatograms of BYG. R: reference substance S1–S10 were 10 batches of BYG.

leonurine (batch No. Y-065-180518), ferulic acid (batch No. A-002-181216), and calycosin (batch No. M-020-190219) were obtained from Chengdu Herbpurity Co., Ltd. Senkyunolide A (batch No. wkq 20050703) was purchased from Chengdu Weikeqi Biotechnology Co., Ltd. Ligustilide (batch No. DST 191015-007) and Formononetin (batch No. DST191202-011) were obtained from Chengdu Desite Biotechnology Co., Ltd. Mifepristone and Misoprostol were obtained from Zizhu Pharmaceutical Co. (Peking, China). Pg ELISA kits (batch No. HXPZ89W47A) and E2 ELISA kits (batch No. DCZXS4SYKL) were purchased from Elabscience Biotechnology Co., Ltd. (Wuhan, China). The HCG ELISA kit (batch No. 12/2019) was purchased from Shanghai MLBIO Biotechnology Co., Ltd. (Shanghai, China). Anti-VEGFA antibody (ab9570) (batch No. 20334270) was obtained from Abcam Company Ltd. (Cambridge, MA, United States). NF-κB antibody (batch No. 00085044) was obtained from Sanying Biotechnology Co., Ltd. (Wuhan, China) HPLC-grade methanol and acetonitrile were purchased from Thermo Fisher Scientific Inc. (Iowa, United States). Formic acid was purchased from Sigma Chemical Co. (St. Louis, MO, United States). The water used in this study was prepared by an ULUP ultrapure water purification system (Chengdu, China).

Chemical Fingerprint Analysis of Buxue Yimu Granule

Buxue Yimu granules (3 g) was extracted by an ultrasonic extractor with 10 ml of water for 10 min, and then approximately 40 ml of acetonitrile was added and sonicated for 30 min. After cooling, acetonitrile was added to bring the volume to 50 ml, the solution was filtered through a 0.22 μm microporous filter membrane, and the subsequent filtrate was collected for analysis.

Chromatographic separation was carried out on an LC-16-PDA HPLC system (SHIMADZU, Japan) using a SymmetryShield™ RP C18 column (4.6 mm × 250 mm 5.0 μm, Waters, United States) with the column temperature maintained at 35°C and a detection wavelength of 254 nm. Formic acid (0.1%) in water and acetonitrile were treated as mobile phases A and B, respectively. Gradient elution was programmed as follows: 0–8 min, 95% A; 8–60 min, 95–10% A; 60–63 min, 10–2% A; 63–66 min, 2–95% A; and 66–72 min, 95% A. The sample injection volume was set at 10 μL for analysis with a flow rate of 1.0 ml·min^{-1}.

Chromatographic data were processed by the SHIMADZU Labsolutions analysis workstation, and the similarity analysis was conducted according to the similarity evaluation system of the chromatographic fingerprint of Traditional Chinese medicine (2012.130723 version, Chinese Pharmacopoeia Committee).

Determination of the Major Compounds in Buxue Yimu Granule

Chromatographic separation was carried out on a Vanquish UPLC system (Thermo Fisher Scientific, United States) using an Accucore™ C18 column (2.1 mm × 100 mm 2.6 μm, Thermo Fisher, United States) with the column temperature maintained at 35°C. Formic acid (0.1%) in water and acetonitrile were treated as mobile phases A and B, respectively. The gradient elution was programmed as follows: 0–5 min, 15–40% B; 5–10 min, 40–45% B; 10–18 min, 45–70% B; 18–18.01 min, 70–15% B and 18.01–23 min, 15% B. The sample injection volume was set at 10 μL for analysis with a flow rate of 0.2 ml·min^{-1}.

Mass spectrometry was performed on a TSQ Fortis triple quadrupole mass spectrometer system (Thermo Fisher

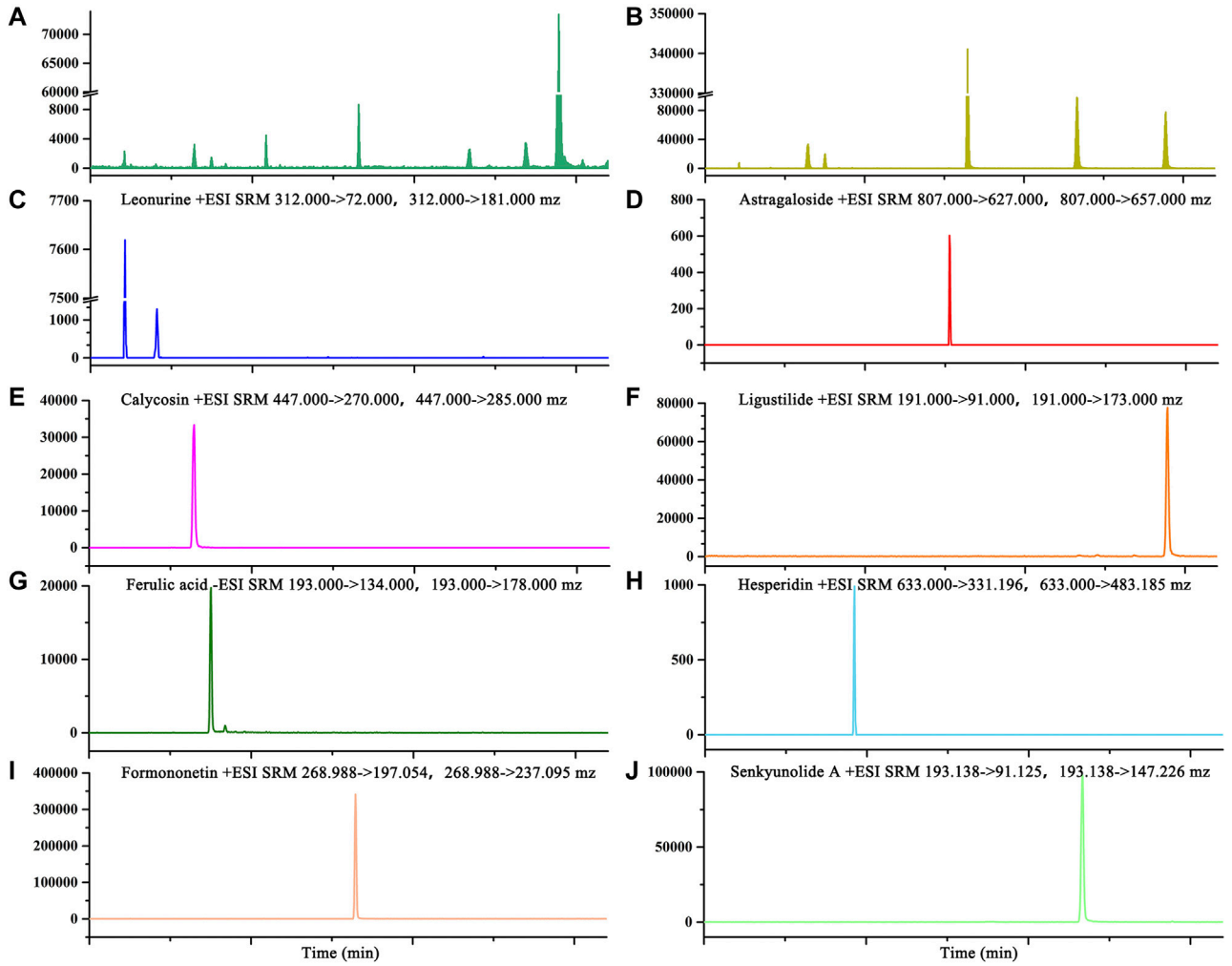

FIGURE 2 | The typical MRM chromatograms of BYG **(A)**; mixed standard reference substance **(B)**; leonurine **(C)**; astragaloside **(D)**; calycosin **(E)**; ligustilide **(F)**; ferulic acid **(G)**; hesperidin **(H)**; formononetin **(I)**, and senkyunolide A **(J)**.

Scientific, United States) equipped with an electrospray ionization source operating in positive ion mode with the following parameters: scan type, SRM; type of ion source, H-ESI; sheath gas flow rate, 35 arb; aux gas flow rate, 15 arb; spray voltage, 3.5 kV, capillary temperature, 350°C; and aux gas heater temperature, 350°C.

Medically Induced Incomplete Abortion Rat Model

Healthy, SPF-grade adult male and female Sprague-Dawley rats (180 g ± 20 g Certificate No. SCXK (Chuan) 2015-030) were supplied by the Animal Breeding Center of DaShuo Biotechnology Co., Ltd. (Chengdu, China). All rats were maintained on an alternating 12 h light/dark cycle, at the temperature of 22–25°C and humidity of 55–60%. The rats were fed with a standard diet and given free access to water. Experimental procedures were strictly in accordance with the Guide for the Care and Use of Laboratory Animals and were approved by the Animal Ethics Committee of Chengdu University.

Female SD rats in estrus were mated with male rats in a separate cage at a ratio of 2:1 overnight. Observation of sperm in vaginal secretion smears the next morning by an optical microscope was considered to be an evidence of pregnancy, and that day was recorded as the first day of gestation. On the seventh day of pregnancy, six pregnant rats were randomly selected as the control group, and the remaining rats were given mifepristone (8.3 mg·kg^{-1}, 8:00 a.m.) and misoprostol (100.0 μg·kg^{-1}, 6:00 p.m.) by intragastric administration to induce incomplete abortion (Camilleri et al., 2019; Li et al., 2020). A cotton ball of appropriate size was placed in the vagina and removed at 8:00 and 20:00 the next day. When vaginal bleeding was observed, the medical-induced incomplete abortion of early pregnancy rats was considered to be successfully replicated. The model rats were randomly divided into the model group and the BYG group (4.32 g·kg^{-1}). The BYG group was given the corresponding drugs by intragastric administration,

and the control group and the model group were given an equal volume of normal saline once a day for 7 days.

Determination of Serum Human Chorionic Gonadotrophin, Estradiol and Progesterone Levels

Blood samples were collected from the abdominal aorta after the last treatment and centrifuged at 3,500 rpm and 4°C for 10 min. Serum was aspirated and stored at −80°C until analysis of human chorionic gonadotrophin (HCG), progesterone (Pg) and estradiol (E_2) levels, which were determined by ELISA assay according to the manufacturer's instructions.

TABLE 1 | Mass spectrometry ion information of major components.

Compounds	Polarity	Precursor (*m/z*)	Product (*m/z*)	Collision energy (V)
Hesperidin	Positive	633	331.196	30.99
Hesperidin	Positive	633	483.185	31.75
Formononetin	Positive	268.988	197.054	36.63
Formononetin	Positive	268.988	237.095	26.9
Senkyunolide A	Positive	193.138	91.125	22.61
Senkyunolide A	Positive	193.138	147.226	9.34
Ligustilide	Positive	191	91	25.60
Ligustilide	Positive	191	173	15.03
Leonurine	Positive	312	72	26.86
Leonurine	Positive	312	181	21.51
Astragaloside	Positive	807	627	50.45
Astragaloside	Positive	807	657	46.70
Ferulic acid	Negative	193	134	13.47
Ferulic acid	Negative	193	178	11.53
Calycosin	Positive	447	270	38.91
Calycosin	Positive	447	285	15.57

Histopathological Examination

Uterine tissues were immediately collected after the rats were sacrificed. The left uterus tissues were fixed in 4% paraformaldehyde solution, embedded in paraffin, sectioned serially into 5 μm sections (RM2235 microtome, Leica, Germany), and stained with hematoxylin and eosin (HE). The pathological changes in the endometrium were evaluated by three randomly selected visual fields at a magnification of ×200 using optical microscopy (CX31, OLYMPUS, Japan).

Expression of Vascular Endothelial Growth Factor A and Nuclear Factor kappa-B by Immunohistochemistry

The uterine tissues were pretreated as previously described. The tissue sections (5 μm) were dewaxed with xylene for 25 min, and then treated with different concentrations of ethanol for hydration. The tissues were then incubated with 3% H_2O_2 deionized water for 10 min to inactivate the endogenous peroxidase activity. Then, tissues were rinsed again with PBS, normal goat serum blocking solution was added, and the mixtures were incubated at room temperature for 20 min. Then, the mixtures were incubated in primary antibody overnight at 4°C and incubated at 37°C for 1 h the next day. Then, the sections were rinsed three times for 5 min each with PBS, 100 μL of biotin-labeled II antibody was added, and the

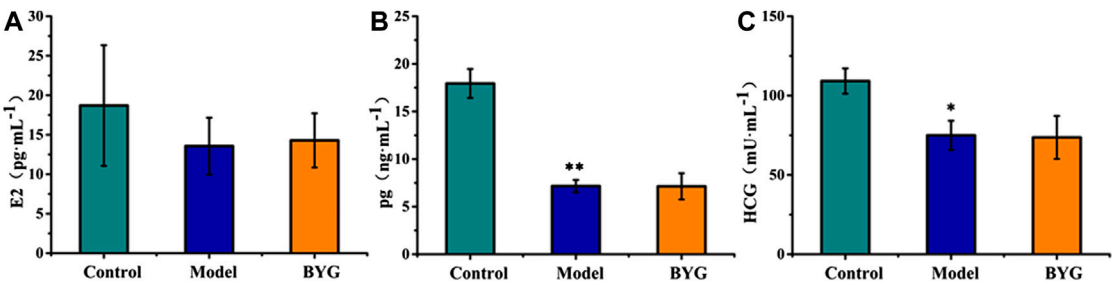

FIGURE 3 | The level of E_2 **(A)**, Pg **(B)**, and HCG **(C)** in medical-induced incomplete abortion rats. Note: VS control group, $^*p < 0.05$.

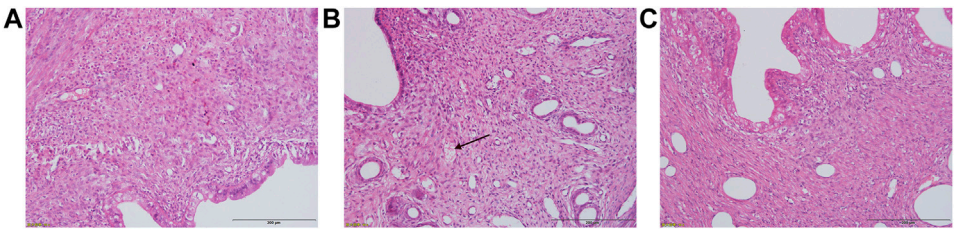

FIGURE 4 | Representative histopathological micrographs of uterine tissue. **(A)** Pregnancy control group + saline solution treatment. **(B)** Model group + saline solution treatment. **(C)** Model group + BYG treatment. H&E stain, ×200.

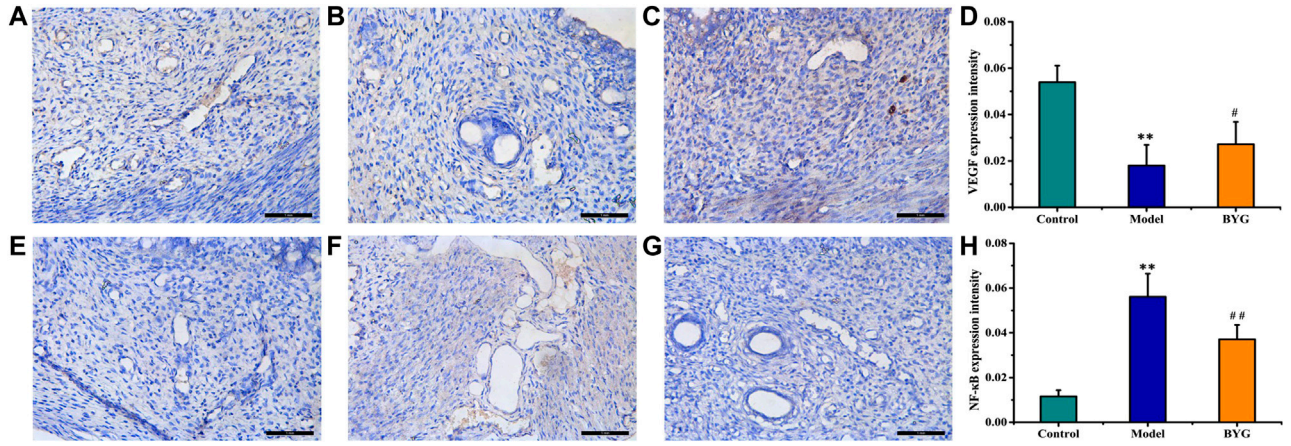

FIGURE 5 | Immunohistochemistry images of VEGFA and NF-κB in the uterus tissue. X200.

samples were kept at 37°C. After incubation for 1 h, the samples were washed for three times with PBS. The VEGFA or NF-κB proteins were stained by immersion in DAB for 10 min. The reaction was terminated by washing with tap water for 10 min. Anhydrous ethanol dehydration, xylene transparency, sealing and microscopic examination were performed. Three microscopic fields (200×) were selected for each slice, and the quantitative average optical density was analyzed by Image-Pro Plus image analysis system.

Metabolomics Serum Sample Pretreatment

For UPLC-Q-TOF/MS analysis, 400 μL of acetonitrile was added dropwise to 100 μL of the serum sample for protein-precipitation and vortexed for 3 min. The mixture was centrifuged for 10 min at 12,000 rpm, and the supernatant was used for analysis.

Ultra-Performance Liquid Chromatography Quadrupole Time-of-Flight Mass Spectrometry Condition

Metabolomics serum samples were analyzed by an UPLC-Q-TOF/MS system (Agilent, United States). An Acquity UPLC BEH C18 column (2.1 mm × 100 mm, 1.7 μm, Waters, United States) was used for separation. The gradient mobile phase was a mixture of 0.1% formic acid in water (A) and acetonitrile (B) with a flow rate of 0.35 ml·min^{-1} at 35°C. The linear gradient was as follows: 90–70% A (0–3 min) and 70–5% A (3–25 min).

The following MS parameters were employed: full scan range, 50–1,200 *m/z*; drying gas flow, 6 L·min^{-1}; source drying gas temperature, 300°C; sheath gas temperature, 320°C, sheath gas flow, 12 L·min^{-1}; nebulizer pressure, 1.0 bar; capillary voltage, 3.5 kV.

During the whole analytical process, quality control (QC) samples were analyzed every 10 samples. The stability of the analytical method was evaluated according to the relative standard deviation (RSD) of the retention time and intensity of 10 randomly selected characteristic ion peaks of QC samples.

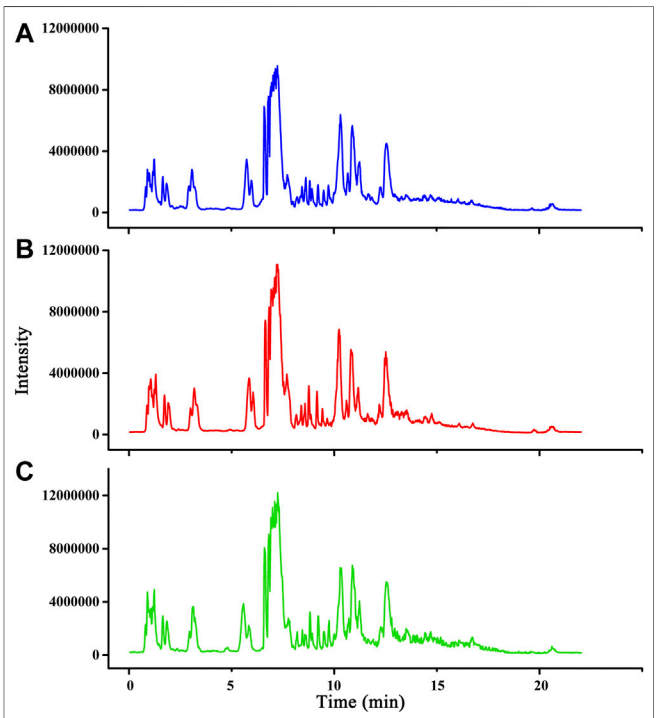

FIGURE 6 | Representative UPLC-Q-TOF/MS chromatograms of the control (blue line), model (red line), BYG treatment (green line) serum samples.

Data Analysis

Partial least-squares discriminant analysis (PLS-DA) and orthogonal partial least-squares discriminant analysis (OPLS-DA) were adopted for multivariate analysis by SIMCA. The potential biomarkers were identified with the following databases: https://hmdb.ca/, http://www.genome.jp/kegg/, http://metlin.scripps.edu/, http://www.lipidmaps.org/. All results were presented as the mean ± SD. Study data were analyzed using one-way analysis of variance (ANOVA) for significance comparison. Values of $p < 0.05$ were considered statistically significant.

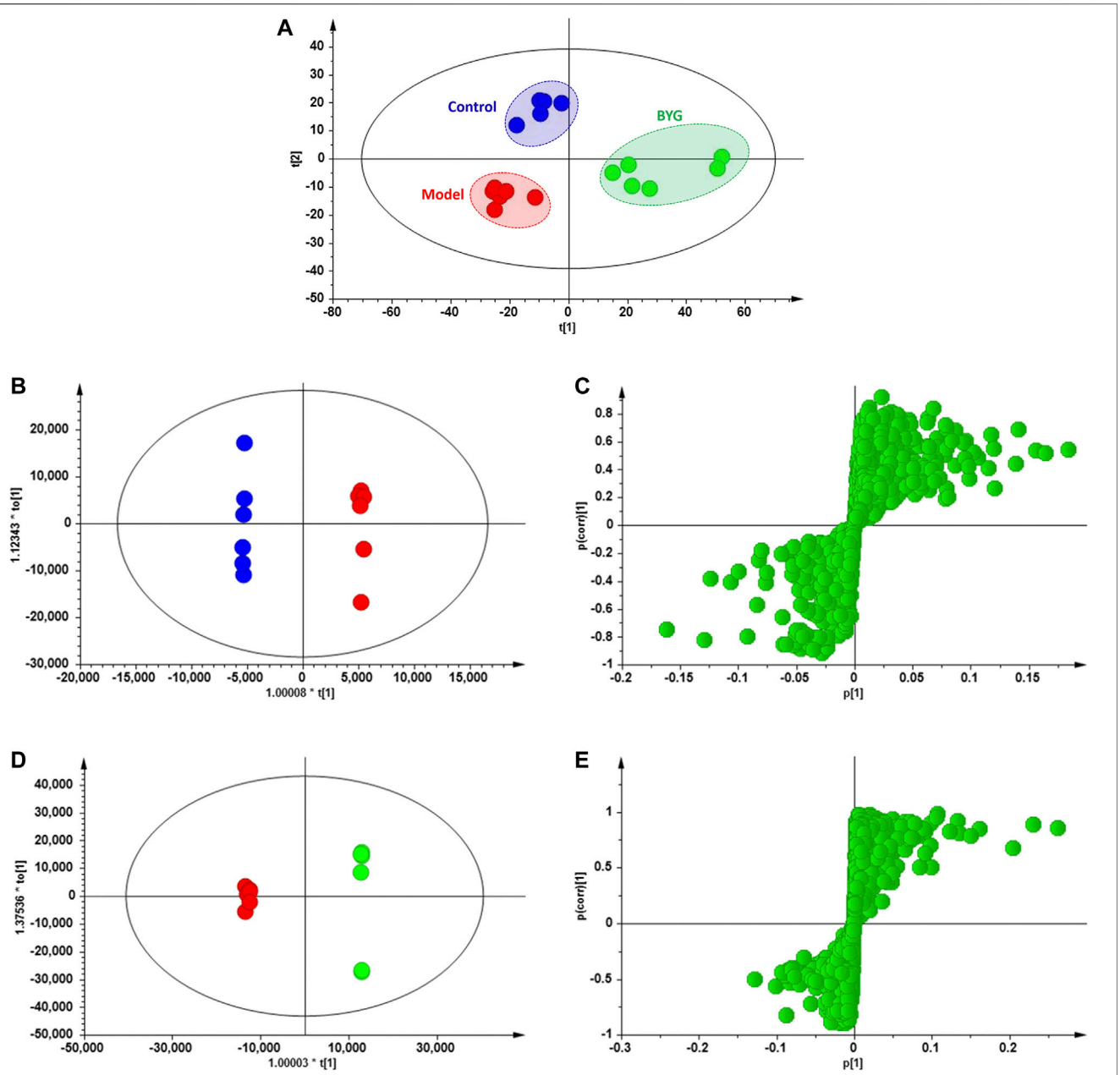

FIGURE 7 | Scores plots of PLS-DA, OPLS-DA and S-plot analysis on the serum metabolic profiles of control (blue dot), model (red dot), BYG treatment (green dot) group.

RESULTS

Chemical Fingerprint of Buxue Yimu Granule

Through the similarity comparison between the chromatograms of each sample, the common fingerprint chromatogram, namely, the reference chromatogram, was extracted, and 30 common fingerprint peaks were observed. Then the similarity of the chromatogram of each sample with the reference chromatogram was determined, and the similarity between each batch was greater than 0.99 (**Figure 1**). The experimental results showed that the similarity between the samples was high, and the preparation process was stable and controllable.

Quantitative Analysis of Major Compounds in Buxue Yimu Granule

Seven major characteristic chemical constituents from BYG were determined. A typical MRM chromatogram was shown in **Figure 2** and the mass spectrometric ion information of the major components was listed in **Table 1**. As a result, the concentrations of leonurine, calycosin, ferulic acid, hesperidin, formononetin, senkyunolide A, and ligustilide was 0.181 $mg{\cdot}g^{-1}$,

TABLE 2 | Identification results of main potential biomarkers changes.

Peak no.	R.T. (min)	Formula	Mass (*m/z*)	Biomarkers
1	1.02	$C_9H_{17}NO_4$	204.1198	N-Lactoylleucine
2	1.76	C_5H_9NO	100.0758	2-Piperidinone
3	2.31	$C_{11}H_{22}NO_4$	232.1538	Isobutyryl-L-carnitine
4	6.78	$C_{25}H_{42}NO_2$	388.3860	Eicosapentaenoylcholine
5	9.55	$C_{29}H_{41}NO_4$	468.3031	LysoPC(14:0)
6	9.60	$C_{28}H_{48}NO_7P$	542.3176	LysoPC(20:5)
7	9.73	$C_{30}H_{38}O_9$	543.3209	Physagulin C
8	9.80	$C_{26}H_{48}NO_7P$	518.3189	LysoPC(18:3)
9	10.00	$C_{25}H_{38}N_2O_6S$	495.3220	Leukotriene D5
10	10.20	$C_{28}H_{44}N_2O_8S$	569.3338	Acid 3-glucuronide
11	10.78	$C_{28}H_{52}NO_7P$	546.3472	Glycine
12	10.90	$C_{25}H_{40}N_2O_6S$	497.3346	Pregnanediol 3-O-glucuronide
13	11.07	$C_{26}H_{50}NO_7P$	520.3303	LysoPC(18:2)
14	11.36	$C_{25}H_{52}NO_7P$	510.3476	LysoPC(17:0/0:0)
15	11.89	$C_{25}H_{39}NO_6S$	482.3185	N-Acetyl-leukotriene E4
16	12.54	$C_{26}H_{54}NO_7P$	524.3638	LysoPC(18:0)
17	12.77	$C_{26}H_{54}NO_7P$	524.4282	Platelet-activating factor
18	15.90	$C_{27}H_{53}O_7P$	521.3343	LysoPA(24:1)
19	16.52	$C_{44}H_{84}NO_8P$	786.5852	LysoPC(18:1)

0.041 mg·g^{-1}, 0.050 mg·g^{-1}, 0.07 mg·g^{-1}, 0.005 mg·g^{-1}, 0.012 mg·g^{-1}, and 0.385 mg·g^{-1}, respectively. Astragaloside was not detected in Buxue Yimu granule extract.

Effect of Buxue Yimu Granule on Serum Hormone Levels

As shown in **Figure 3**, compared with those in the pregnancy control group, the HCG, E_2 and Pg levels in the model group were significantly decreased ($p < 0.05$). Compared with those in the model group, there was no significant difference between HCG, E_2 and Pg levels in the BYG group. These results indicated that BYG had no significant effect on serum hormone levels at this dose.

Effect of Buxue Yimu Granule on Pathological Endometrial Changes in Uterine Tissue

As shown in **Figure 4**, the endometrium of the pregnancy group was intact. Congestion, edema and local endometrial defects were observed in some rats in the medical-induced incomplete abortion group. Compared with model rats, except for one case of abundant endometrial blood vessels and interstitial looseness in the BYG group, the rats showed no obvious abnormal changes. Thus, BYG could ameliorate the histopathological damage.

Effect of Buxue Yimu Granule on the Expression of Vascular Endothelial Growth Factor A and Nuclear Factor kappa-B

As shown in **Figure 5**, the positive area of VEGFA was light yellow and mainly expressed in the cell membrane and cytoplasm, and the nucleus was blue. Compared with that in uterine tissue from the pregnancy control group, the expression of VEGFA in uterine tissue from the medical-induced incomplete abortion model group was decreased, and BYG treatment increased the expression of VEGFA. While the expression of NF-κB in uterine tissue from the medical-induced incomplete abortion model group was increased, and BYG treatment decreased the expression of NF-κB.

Validation of Ultra-Performance Liquid Chromatography Quadrupole Time-of-Flight Mass Spectrometry Conditions

The serum metabolite profiles were obtained from each rat group in positive ion mode. Representative UPLC-Q-TOF/MS chromatograms were presented in **Figure 6**. All the relative standard deviation (RSD %) values for the retention time and *m/z* data of the selected ions of QC sample were less than 8%, showing that the method established in this study for the analysis of rat serum metabolomics was accurate and stable.

Identification of Potential Biomarkers

As shown in **Figure 7**, the score plots from PLS-DA and OPLS-DA showed that the medical-induced incomplete abortion rat group was obviously separated from the pregnancy control group, which suggested that the administration of mifepristone and misoprostol could cause abnormalities of endogenous metabolites in rats. Moreover, compared with that of the model group, the metabolite profiles of the BYG group were gradually restored to normal.

Furthermore, 19 kind of main endogenous biomarkers, including N-lactoylleucine, 2-piperidinone, isobutyryl-L-carnitine, eicosapentaenoylcholine, LysoPC(14:0), LysoPC(20:5), physagulin C, LysoPC(18:3), leukotriene D5, deoxycholic acid 3-glucuronide, glycine, pregnanediol 3-O-glucuronide, LysoPC(18:2), LysoPC(17:0/0:0), N-acetyl-leukotriene E4, LysoPC(18:0), platelet-activating factor, LysoPA(24:1), and

LysoPC(18:1), which were mainly related to the amino acids metabolism, lipids metabolism and bile acid biosynthesis were identified according to the *m/z* results (**Table 2**). The peak area box diagram of each biomarker was shown in **Figure 8**. The analysis of potential metabolic pathways according to the identified biomarkers by MetaboAnalyst was shown in **Figure 9**. These results indicated that BYG exerts a potential protective role in the intervention of incomplete abortion by ameliorating the metabolic disorders.

DISCUSSION

Herba Leonuri, also named Chinese Motherwort, has been widely used for the treatment of dysfunctional uterine bleeding, dysmenorrhea, polycystic ovary syndrome and other gynecological diseases for hundreds of years (Lin et al., 2017; Lin et al., 2019). It has been reported that chemical components, including alkaloids, phenolic acids, flavonoids, as well as volatile oil and tannins, have been isolated and identified in Herba Leonuri (Wang et al., 2013; Wojtyniak et al., 2013). Alkaloids are considered to be the major bioactive ingredients of Herba Leonuri (Xie et al., 2015; Dong et al., 2017). Among these

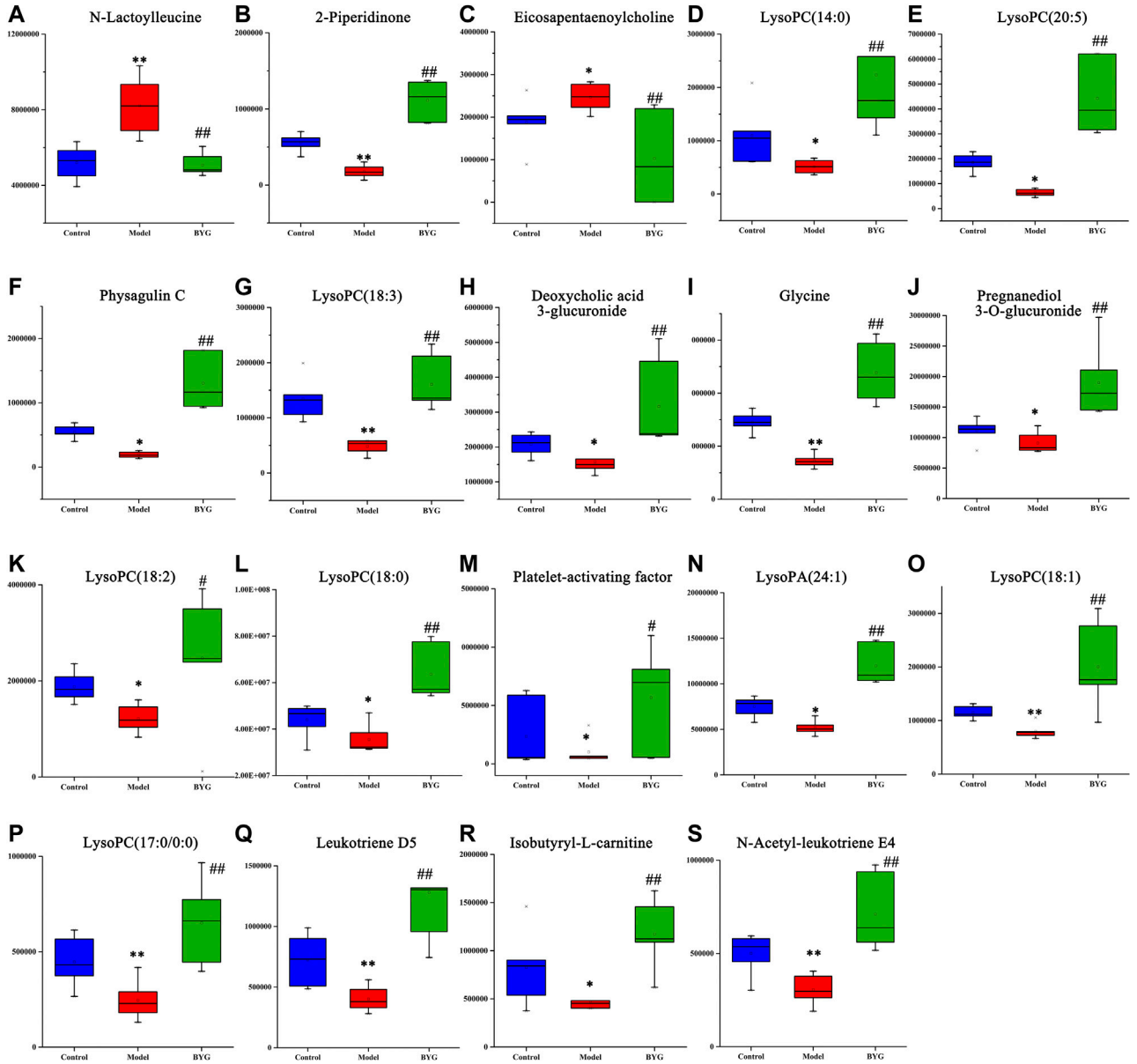

FIGURE 8 | Boxplots of identical biomarkers normalized intensity of rat plasma. Note: VS control group, $^{*}p < 0.05$ and $^{**}p < 0.01$; VS model group, $^{\#}p < 0.05$ and $^{\#\#}p < 0.01$.

components, leonurine exhibits a variety of pharmacological activities, Research has confirmed that leonurine significantly reduces the IL-1β-induced production of NO, PGE2, IL-6, and TNF-α by inhibiting the activation of the PI3K/Akt/NF-κB signaling pathway (Yin and Lei, 2018).

Angelica sinensis (Oliv.) Diels has been considered to be "female's ginseng" mainly because of its excellent therapeutic effect for gynecological diseases, such as dysmenorrhea, irregular menstruation, premenstrual, and menopausal symptoms (Huntley and Ernst, 2003; Haines et al., 2008; Hook, 2014). Ferulic acid, ligustilide and angelica polysaccharide are considered to be the main bioactive substances of Angelica (Wei and Huang 2015; Yang et al., 2019) Studies have confirmed that *Angelica sinensis* (Oliv.) Diels extract can be developed for the treatment of endometriosis by inhibiting inflammatory reactions (Xiong et al., 2020) and could significantly decrease NF-kB/β-actin and IL-6/β-actin mRNA expression in the uterus of rats with pelvic inflammation (Huang et al., 2012). In addition, metabolomics studies have shown that the volatile oil of *Angelica sinensis* can significantly inhibit the systemic inflammatory response caused by acute local stimulation, and mainly exert its anti-inflammatory activity by regulating glycine and arachidonic acid metabolic network disorders (Yao et al., 2015).

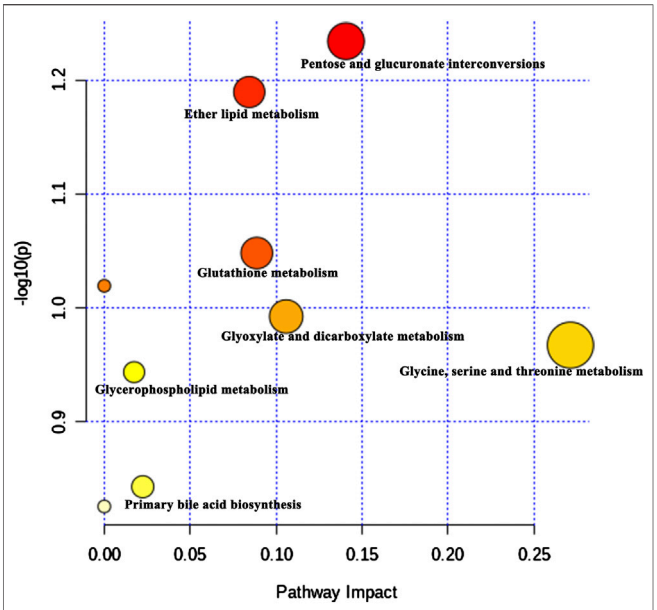

FIGURE 9 | The potential metabolic pathways according to the identified biomarkers by MetaboAnalyst.

Previous studies have shown that endometrial damage and uterine tissue inflammation are the main pathological features of abnormal bleeding after abortion (Cicinelli et al., 2017; Care et al., 2018). Inflammatory cells increase in the endometrium because of the reduction in hormone levels after incomplete abortion (Evans et al., 2011). In this study, pathological examination revealed obvious edema and congestion in the uterus of the incomplete abortion rat model and BYG intervention had a certain regulatory effect. Based on our experimental results and previous studies, we speculate that Herba Leonuri and *Angelica sinensis* (Oliv.) Diels may be the main anti-inflammatory drugs in BYG.

Vascular endothelial growth factor (VEGF), which is closely related to angiogenesis, is considered to be a key factor in endometrial repair (Sugino et al., 2002; Maybin et al., 2011). Studies have shown that leonurine, the main active component of Herba Leonuri, can promote the angiogenesis of endothelial cells by activating the mTOR/ERK pathway and enhance angiogenesis both *in vivo* and *in vitro* (Wang et al., 2018). Previous results revealed that *Angelica sinensis* can promote angiogenesis and exert anti-apoptotic effects by activating of p38 MAPK/HIF-1αα/VEGF-A signaling (Cheng et al., 2017). The current study results showed that the expression of VEGFA in uterine tissue was decreased in the medical-induced incomplete abortion model group compared to that in the control group, and BYG treatment could increase the expression of VEGFA, indicating that BYG has a certain repair effect on endometrial injury after postpartum or abortion.

Glycerophospholipids are key components of the cells and are involved in metabolism and signaling. LysoPC(20:5) is lysophospholipid, which play an important role in lipid signal transduction by acting on the lysophosphatidic receptor (LPL-R) (Lingwood and Simons, 2010). Previous studies based on metabolomics have demonstrated that the serum NMR-based metabolomics analysis method was sensitive enough to distinguish individuals having artificial abortions from healthy individuals and can provide a further understanding of the mechanism of artificial abortion complications (Wu et al., 2018). An LC/MS based serum metabolomics study indicated that women with recurrent abortions have abnormal metabolism of purine, tyrosine and amino acids (Zhang et al., 2019). In a study on the Chinese traditional medicine prescriptions Taohong Siwu Docation's intervention in the serum metabolic profile of rats with abnormal uterine bleeding, 23 biomarkers mainly involved in the metabolism of amino acids and lipids were identified (Zuo et al., 2019). Here we also observed a significant reduction in LysoPC(18:2), LysoPC(20:5), LysoPC(18:3), LysoPC(18:1), LysoPC(18:0), LysoPA(24:1) in the model group, which is consistent with the results of a previous study (Zuo et al., 2019).

N-Lactoylleucine is a lactoyl derivative of phenylalanine. An untargeted metabolomics screening study showed that the plasma levels of metabolites such as N-lactosyl-amino acids were closely correlated with the concentrations of lactate and amino acids (Jansen et al., 2015). The results of this study showed that there was abnormal amino acid metabolism in abortion rats, and the metabolite profiles of amino acids were gradually restored to normal with the treatment of BYG.

As demonstrated in the current study, in the model group, physagulin C and platelet-activating factor were significantly decreased compared to their levels in the control group, and BYG intervention could increase their levels. The most well-known pharmacological action of Angelica was enriching blood and invigorate circulation. Studies have indicated that *Angelica sinensis* can promote hematopoiesis and thrombopoiesis because of its anti-apoptotic activity through the PI3K/AKT pathway (Liu et al., 2010). Previous investigations suggested that α-pinene derivatives isolated from *Angelica sinensis* exhibited antithrombin and antiplatelet aggregation activity in vitro. (Yang et al., 2011). After administration of mifepristone and misoprostol, vaginal bleeding increased significantly in rats. The changes in these biomarkers may be closely related to the abnormal coagulation system, and BYG may reduce the amount of bleeding and shorten the bleeding time by regulating blood coagulation.

Progestational hormones, mainly progesterone, are secreted by luteal cells of the ovaries. The main metabolite of progesterone is pregnanediol. The urine excretion of pregnanediol can be used as an index to evaluate luteal function. Pregnanediol 3-O-glucuronide is a natural metabolite of pregnanediol produced by UDP glucuronosyltransferase in the liver. A metabolomics study has shown that pregnanediol 3-O-glucuronide level in placental metabolites of women that had spontaneous preterm births was significantly reduced (Elshenawy et al., 2020). Although we did not observe this effect of BYG on estradiol at the serum hormone level, based on the results of metabolomics, we speculated that BYG may also play a

certain role in regulating the abnormal hormone levels postpartum or after an abortion.

CONCLUSION

In summary, these results indicate that intragastric administration of mifepristone combined with misoprostol in early pregnancy could significantly disturb the metabolic profiles of rats. BYG exerts a potential protective role in the intervention of incomplete abortion by anti-inflammatory, promote endometrial repair, and regulate the metabolic disorders in the amino acids metabolism, lipids metabolism and bile acid biosynthesis.

DATA AVAILABILITY STATEMENT

The raw data supporting the conclusions of this article will be made available by the authors, without undue reservation.

ETHICS STATEMENT

The animal study was reviewed and approved by Chengdu University.

AUTHOR CONTRIBUTIONS

LZ, J-YL, and YG conceived and designed the experiments. YZ, WL, T-TC, and YY performed the experiments. T-TC and YZ analyzed the data. YZ and M-YW wrote the paper.

FUNDING

This work was supported by Sichuan Provincial Department of Education (17TD0010), the Youth Science Foundation of Chengdu University (2017XJZ15) and the Health and Family Planning Commission of Chengdu-Key disciplines of clinical pharmacy.

REFERENCES

Baiju, N., Achary, G., D'Antonio, F., and Berg, R. C. (2019). Effectiveness, safety and acceptability of self-assessment of the outcome of first-trimester medical abortion: a systematic review and meta-analysis. *BJOG* 126, 1536–1544. doi:10.1111/1471-0528.15922

Camilleri, C., Beiter, R. M., Puentes, L., Aracena-Sherck, P., and Sammut, S. (2019). Biological, behavioral and physiological consequences of drug-induced pregnancy termination at first-trimester human equivalent in an animal model. *Front. Neurosci.* 13, 544. doi:10.3389/fnins.2019.00544

Care, A. S., Bourque, S. L., Morton, J. S., Hjartarson, E. P., and Robertson, S. A. (2018). Reduction in regulatory T cells in early pregnancy causes uterine artery dysfunction in mice. *Hypertension* 72 (1), 177–187. doi:10.1161/hypertensionaha.118.10858

Chen, M. J., and Creinin, M. D. (2015). Mifepristone with buccal misoprostol for medical abortion: a systematic review. *Obstet. Gynecol.* 126, 12–21. doi:10.1097/AOG.0000000000000897

Cheng, C. Y., Ho, T. Y., Hsiang, C. Y., Tang, N. Y., Hsieh, C. L., Kao, S. T., et al. (2017). *Angelica sinensis* exerts angiogenic and anti-apoptotic effects against cerebral ischemia-reperfusion injury by activating p38MAPK/HIF-1 alpha/VEGF-A signaling in rats. *Am. J. Chin. Med.* 45, 1683–1708. doi:10.1142/S0192415X17500914.

Cicinelli, E., Trojano, G., Mastromauro, M., Vimercati, A., Marinaccio, M., Mitola, P. C., et al. (2017). Higher prevalence of chronic endometritis in women with endometriosis: a possible etiopathogenetic link. *Fertil. Steril.* 108, 289–295.e1. doi:10.1016/j.fertnstert.2017.05.016

Dong, H. Y., Zhang, S. Q., Du, W. X., Cong, H. L., and Zhang, L. H. (2020). Pharmacodynamics and metabonomics study of *Tianma Gouteng* decoction for treatment of spontaneously hypertensive rats with liver-yang hyperactivity syndrome. *J. Ethnopharmacol.* 253, 112661. doi:10.1016/j.jep.2020.112661

Dong, S. Y., He, J., Hou, H. P., Shuai, Y. P., Wang, Q., and Yang, W. L. (2017). Quality assessment of *Herba leonuri* based on the analysis of multiple components using normal- and reversed-phase chromatographic methods. *J. Separ. Sci.* 40, 4482–4494. doi:10.1002/jssc.201700728

Dzuba, I. G., Chong, E., Hannum, C., Lichtenberg, E. S., Hernandez, E. M. L., Ngoc, N. T. N., et al. (2020). A non-inferiority study of outpatient mifepristone-misoprostol medical abortion at 64–70 days and 71–77 days of gestation. *Contraception* 101, 302–308. doi:10.1016/j.contraception.2020.01.0096

Elshenawy, S., Pinney, S. E., Stuart, T., Doulias, P. T., Zura, G., Parry, S., et al. (2020). The metabolomic signature of the placenta in spontaneous preterm birth. *Int. J. Mol. Sci.* 21, 1043. doi:10.3390/ijms21031043.

Evans, J., Salamonsen, L. A., Winship, A., Menkhorst, E., Nie, G. Y., Gargett, C. E., et al. (2011). The regulation of vascular endothelial growth factor by hypoxia and prostaglandin during human endometrial repair. *J. Clin. Endocrinol. Metab.* 96 (8), 2475–2483. doi:10.1210/jc.2010-2971

Haines, C. J., Lam, P. M., Chung, T. K., Cheng, K. F., and Leung, P. C. (2008). A randomized, double-blind, placebo-controlled study of the effect of a Chinese herbal medicine preparation (Dang Gui Buxue Tang) on menopausal symptoms in Hong Kong Chinese women. *Climacteric* 11 (3), 244–251. doi:10.1080/13697130802073029

Hook, I. L. (2014). Danggui to Angelica sinensis root: are potential benefits to European women lost in translation? A review. *J. Ethnopharmacol.* 152 (1), 1–13. doi:10.1016/j.jep.2013.12.018

Hsia, J. K., Lohr, P. A., Taylor, J., and Creinin, M. D. (2019). Medical abortion with mifepristone and vaginal misoprostol between 64 and 70 days' gestation. *Contraception* 100,þ 178–181. doi:10.1016/j.contraception.2019.05.00

Huang, C. Y., Chen, X. P., Liu, H. M., Ren, X. P., and Xue, J. L. (2012). Effect of *Angelica sinensis* aqueous extract on uterus, ovary NF-kB/beta-actin and IL-6/beta-actin mRNA expression level in pelvic inflammation model rats. *Afr. J. Pharm. Pharmacol.* 6, 860–863. doi:10.5897/AJPP12.070

Huntley, A. L., and Ernst, E. (2003). A systematic review of herbal medicinal products for the treatment of menopausal symptoms. *Menopause* 10, 465–476. doi:10.1097/01.GME.0000058147.24036.B0

Jansen, R. S., Addie, R., Merkx, R., Fish, A., Mahakena, S., Bleijerveld, O. B., et al. (2015). N-lactoyl-amino acids are ubiquitous metabolites that originate from CNDP2-mediated reverse proteolysis of lactate and amino acids. *Proc. Natl. Acad. Sci. USA* 112, 6601–6606. doi:10.1073/pnas.1424638112

LaRoche, K. J., and Foster, A. M. (2020). "It gives you autonomy over your own choices": a qualitative study of Canadian abortion patients' experiences with mifepristone and misoprostol. *Contraception* 102, þ61–65. doi:10.1016/j.contraception.2020.04.007

Li, L. L., Huang, Q., Duan, X. C., Han, L., and Peng, D. Y. (2020). Protective effect of Clinopodium chinense (Benth.) O. Kuntze against abnormal uterine bleeding in female rats. *J. Pharmacol. Sci.* 143, 1–8. doi:10.1016/j.jphs.2020.02.004

Lin, M. J., Chen, H. W., Liu, P. H., Cheng, W. J., Kuo, S. L., and Kao, M. C. (2019). The prescription patterns of traditional Chinese medicine for women with polycystic ovary syndrome in Taiwan a nationwide population-based study. *Medicine* 98, e15890. doi:10.1097/MD.0000000000015890

Lin, Y. R., Wu, M. Y., Chiang, J. H., Yen, H. R., and Yang, S. T. (2017). The utilization of traditional Chinese medicine in patients with dysfunctional

uterine bleeding in Taiwan: a nationwide population-based study. *BMC Compl. Alternative Med.* 17, 427. doi:10.1186/s12906-017-1939-1

Lingwood, D., and Simons, K. (2010). Lipid rafts as a membrane-organizing principle. *Science* 327, 46–50. doi:10.1126/science.1174621

Liu, C., Li, J. Q., Meng, F. Y., Liang, S. X., Deng, R. X., Li, C. K., et al. (2010). Polysaccharides from the root of Angelica sinensis promotes hematopoiesis and thrombopoiesis through the PI3K/AKT pathway. *BMC Compl. Altern. Med.* 10, 79. doi:10.1186/1472-6882-10-79

Liu, P., Liu, S., Tian, D., and Wang, P. Y. (2012). The applications and obstacles of metabonomics in traditional Chinese medicine. *Evid. Based Compl. Altern. Med.* 2012, 1–4. doi:10.1155/2012/945824

Liu, S. J., and Wu, Y. N. (2020a). Application of metabonomics approach in food safety research—a review. *Food Rev. Int.* 36, 1655571. doi:10.1080/87559129.2019.1655571

Liu, Y. T., Xue, Q. Q., Li, A. P., Li, K., and Qin, X. M. (2020b). Mechanisms exploration of herbal pair of HuangQi-DanShen on cerebral ischemia based on metabonomics and network pharmacology. *J. Ethnopharmacol.* 253, 112688. doi:10.1016/j.jep.2020.112688

Maybin, J. A., Hirani, N., Brown, P., Jabbour, H. N., and Critchley, H. O. D. (2011). The regulation of vascular endothelial growth factor by hypoxia and prostaglandin $F_{2\alpha}$ during human endometrial repair. *J. Clin. Endocrinol. Metab.* 96, 2475–2483. doi:10.1210/jc.2010-2971

Schmidt-Hansen, M., Cameron, S., Lohr, P. A., and Hasler, E. (2020). Follow-up strategies to confirm the success of medical abortion of pregnancies up to 10 weeks' gestation: a systematic review with meta-analyses. *Am. J. Obstet. Gynecol.* þ222, 551. doi:10.1016/j.ajog.2019.11.1244

Shi, S., Liu, Z. Y., Xue, Z. Y., Chen, X. H., and Chu, Y. (2020). A plasma metabonomics study on the therapeutic effects of the Si-miaoyong-an decoction in hyperlipidemic rats. *J. Ethnopharmacol.* 256, 112780. doi:10.1016/j.jep.2020.112780

Sugino, N., Kashida, S., and Karube-Harada, A. (2002). Expression of vascular endothelial growth factor (VEGF) and its receptors in human endometrium throughout the menstrual cycle and in early pregnancy. *Reproduction* 123, 379–387. doi:10.1530/rep.0.1230379

Wang, C. G., Zhang, Z. J., Xu, T. Z., Lou, Y. T., Wang, Q. Q., Jin, H. M., et al. (2018). Upregulating mTOR/ERK signaling with leonurine for promoting angiogenesis and tissue regeneration in a full-thickness cutaneous wound model. *Food Funct.* 9, 2374–2385. doi:10.1039/c7fo01289f

Wang, N., Huang, X., Li, T., Wang, M., Yue, H., Chen, C. B., et al. (2020). Application of RRLC-QTOF-MS-based metabonomics and UPE for investigating Spleen-Qi deficiency syndrome with *Panax ginseng* treatment. *J. Ethnopharmacol.* 256, 112822. doi:10.1016/j.jep.2020.112822

Wang, Y., Li, B. H., Ni, Y. N., and Kokot, S. (2013). A high-performance liquid chromatography method for quality control of complex substances: analysis of marker alkaloids and flavonoids of the herb *Herba leonuri* (Yimucao). *Anal. Methods* 5, 6051–6057. doi:10.1039/c3ay40985f

Wei, W. L., and Huang, L. F. (2015). Simultaneous Determination of Ferulic Acid and Phthalides of Angelica Sinensis Based on UPLC-Q-TOF/MS. *Molecules* 20, 4681–4694. doi:10.3390/molecules20034681

Wojtyniak, K., Szymanski, M., and Matlawska, I. (2013). *Leonurus cardiaca* L. (Motherwort): a review of its phytochemistry and pharmacology. *Phytother Res.* 27, 1115–1120. doi:10.1002/ptr.4850

Wu, Z. H., Jin, L., Zheng, W. Y., Zhang, C. X., Zhang, L. W., Chen, Y. P., et al. (2018). NMR-based serum metabolomics study reveals a innovative diagnostic model for missed abortion. *Biochem. Biophys. Res. Commun.* 496, 679–685. doi:10.1016/j.bbrc.2018.01.096

Xie, J. B., Sang, L. T., Zhang, Y. Q., Fang, L. L., and Li, Y. X. (2015). Determination of stachydrine and leonurine in *Herba leonuri* and its succedaneum-herba lagopsis-with a sensitive HPLC-MS/MS method. *J. Liq. Chromatogr. Relat. Technol.* 38, 810–815. doi:10.1080/10826076.2014.973965

Xiong, Q. X., Ruan, X. Y., Deng, A. P., Liu, J., and Zhou, Q. (2020). Anti-endometriotic effect of *Angelica sinensis* (Oliv.) Diels extract in human endometriotic cells and rats. *Trop. J. Pharmaceut. Res.* 19, 817–821. doi:10.4314/tjpr.v19i4.20

Yang, F., Lin, Z. W., Huang, T. Y., Chen, T. T., Cui, J., Li, M. Y., et al. (2019). Ligustilide, a major bioactive component of Angelica sinensis, promotes bone formation via the GPR30/EGFR pathway. *Sci Rep.* 9, 6991–46. doi:10.1038/s41598-019-43518-7

Yang, N. Y., Zhou, G. S., Tang, Y. P., Yan, H., Guo, S., Liu, P., et al. (2011). Two new α-pinene derivatives from Angelica sinensis and their anticoagulative activities. *Fitoterapia.* 82, 692–695. doi:10.1016/j.fitote.2011.02.007

Yao, W. L., Zhang, L., Hua, Y. L., Ji, P., Li, P. L., Li, J. X., et al. (2015). The investigation of anti-inflammatory activity of volatile oil of *Angelica sinensis* by plasma metabolomics approach. *Int. Immunopharm.* 29, 269–277. doi:10.1016/j.intimp.2015.11.006

Yin, W. H., and Lei, Y. (2018). Leonurine inhibits IL-1 beta induced inflammation in murine chondrocytes and ameliorates murine osteoarthritis. *Int. Immunopharm.* 65, 50–59. doi:10.1016/j.intimp.2018.08.035

Zhang, L. L., Li, Y., Lin, X. Y., Jia, C. S., and Yu, X. W. (2019). Liquid chromatography/mass spectrometry based serum metabolomics study on recurrent abortion women with antiphospholipid syndrome. *PLoS One* 14, e0225463. doi:10.1371/journal.pone.0225463

Zuo, C. J., Zhang, Y., Wang, J. C., Han, L., Peng, C., and Peng, D. Y. (2019). Deciphering the intervention mechanism of Taohong Siwu Decoction following the abnormal uterine bleeding rats based on serum metabolic profiles. *J. Pharmaceut. Biomed. Anal.* 170, 204–214. doi:10.1016/j.jpba.2019.03.051

Conflict of Interest: M-YW and YG were employed by the company Zhuzhou Qianjin pharmaceutical Co., Ltd.

The remaining authors declare that the research was conducted in the absence of any commercial or financial relationships that could be construed as a potential conflict of interest.

frontiers in Pharmacology

ORIGINAL RESEARCH
published: 03 December 2020
doi: 10.3389/fphar.2020.578346

A Mass Spectrometry Based Metabolite Profiling Workflow for Selecting Abundant Specific Markers and Their Structurally Related Multi-Component Signatures in Traditional Chinese Medicine Multi-Herb Formulae

*Joëlle Houriet[1,2], Pierre-Marie Allard[1,2], Emerson Ferreira Queiroz[1,2], Laurence Marcourt[1,2], Arnaud Gaudry[1,2], Lennie Vallin[1,2], Songhua Li[3], Yu Lin[4], Ruwei Wang[5], Kenny Kuchta[6] and Jean-Luc Wolfender[1,2]**

[1]School of Pharmaceutical Sciences, University of Geneva, Geneva, Switzerland, [2]Institute of Pharmaceutical Sciences of Western Switzerland, University of Geneva, Geneva, Switzerland, [3]Izumo Clinic, Izumo-shi, Japan, [4]Kunisawa Clinic, Gotsu-shi, Japan, [5]Zhejiang Provincial Key Laboratory of Traditional Chinese Medicine Pharmaceutical Technology, Hangzhou, China, [6]Forschungsstelle für Fernöstliche Medizin, Department of Vegetation Analysis and Phytodiversity, Albrecht von Haller Institute of Plant Sciences, Georg August University, Göttingen, Germany

In Traditional Chinese Medicine (TCM), herbal preparations often consist of a mixture of herbs. Their quality control is challenging because every single herb contains hundreds of components (secondary metabolites). A typical 10 herb TCM formula was selected to develop an innovative strategy for its comprehensive chemical characterization and to study the specific contribution of each herb to the formula in an exploratory manner. Metabolite profiling of the TCM formula and the extract of each single herb were acquired with liquid chromatography coupled to high-resolution mass spectrometry for qualitative analyses, and to evaporative light scattering detection (ELSD) for semi-quantitative evaluation. The acquired data were organized as a feature-based molecular network (FBMN) which provided a comprehensive view of all types of secondary metabolites and their occurrence in the formula and all single herbs. These features were annotated by combining MS/MS-based *in silico* spectral match, manual evaluation of the structural consistency in the FBMN clusters, and taxonomy information. ELSD detection was used as a filter to select the most abundant features. At least one marker per herb was highlighted based on its specificity and abundance. A single large-scale fractionation from the enriched formula enabled the isolation and formal identification of most of them. The obtained markers allowed an improved annotation of associated features by manually propagating this information through the FBMN. These data were incorporated in the high-resolution metabolite profiling of the formula, which highlighted specific series of related components to each individual herb markers. These series of components, named multi-component signatures, may serve to improve the traceability of each herb in the formula. Altogether, the strategy provided highly informative compositional data of the TCM formula

OPEN ACCESS

Edited by:
Peng Li,
University of Macau, China

Reviewed by:
Justin J. J. van der Hooft,
Wageningen University and Research, Netherlands
Yuelin Song,
Beijing University of Chinese Medicine, China

***Correspondence:**
Jean-Luc Wolfender
jean-luc.wolfender@unige.ch

Specialty section:
This article was submitted to Ethnopharmacology, a section of the journal Frontiers in Pharmacology

Received: *30 June 2020*
Accepted: *09 October 2020*
Published: *03 December 2020*

Citation:
Houriet J, Allard P-M, Queiroz EF, Marcourt L, Gaudry A, Vallin L, Li S, Lin Y, Wang R, Kuchta K, Wolfender J-L (2020) A Mass Spectrometry Based Metabolite Profiling Workflow for Selecting Abundant Specific Markers and Their Structurally Related Multi-Component Signatures in Traditional Chinese Medicine Multi-Herb Formulae. Front. Pharmacol. 11:578346. doi: 10.3389/fphar.2020.578346

and detailed visualizations of the contribution of each herb by FBMN, filtered feature maps, and reconstituted chromatogram traces of all components linked to each specific marker. This comprehensive MS-based analytical workflow allowed a generic and unbiased selection of specific and abundant markers and the identification of multiple related sub-markers. This exploratory approach could serve as a starting point to develop more simple and targeted quality control methods with adapted marker specificity selection criteria to given TCM formula.

Keywords: multi-herb formulae, Traditional Chinese Medicine, feature-based molecular network, quality control, multi-component signature, TCM, Mass spectrometry, Chemical markers

INTRODUCTION

Multi-herb mixtures are used in many traditional medicines, such as Traditional Chinese Medicine (TCM), Japanese Kampo medicine, traditional European phytomedicine, but also in modern evidence-based herbal medicinal products (Abdel-Aziz et al., 2017). The quality assessment of such complex multi-component mixtures is challenging. The chemical quality markers are often secondary metabolites, which are frequently referred to as *components* in TCM literature (Liu et al., 2017), which is the terminology used in this study (for a glossary of terms, see **Table 1**). For individual herbs, modern pharmacopoeial monographs propose methods to check multiple chemical components both in terms of presence and relative quantification. Such methods, called *single standard to determine multi-components methods* (SSDMC), have the advantage of reducing the number of required standards, but remain limited to the verification of a single plant (Gao et al., 2009; Liang et al., 2013; Hou et al., 2019). These SSDMC methods address the limitations encountered with quality controls (QC) restricted to a single marker per herbal drug. These limitations have been highlighted by cases of adulteration and falsification, which concern all types of herbal preparations, including TCMs (Wang et al., 2018), and even more so, the huge market of food supplements (Abdel-Tawab, 2018). By being limited to a single marker or to the total amount of a given class of components, cases of falsification by adding the said marker have been reported, for example involving extracts of *Ginkgo biloba* leaves (Czigle et al., 2018). In the food supplement market, which is not submitted to specific QC, illegal additions of potentially dangerous pure substances were observed in herbal preparations (Skalicka-Wozniak et al., 2017; Kee et al., 2018).

For multi-herb TCM mixture, named formulae (**Table 1**), developing holistic analytical methods that considers their complexity is an urgent goal (Guo et al., 2015; Yang et al., 2017; Hou et al., 2019). In a formula, checking several markers representing each herb is already challenging (Yao et al., 2016). Furthermore, the pharmacopoeial marker of an herb may be ubiquitous and also present in other herbs of the same formula (Wu et al., 2018). Thus, in this complex and multifactorial context, QC of multi-herb formulae should ideally verify the presence of each herb in a specific way, as well as the absence of falsification.

To give a rationale for developing appropriate methods of QC, an in-depth investigation of the chemical composition is one of the first conditions (Hou et al., 2019). For this, liquid chromatography coupled with mass spectrometry (LC-MS) is ideal for a comprehensive chemical characterization (Hou et al., 2019). In MS, the latest generations of mass spectrometers combine sensitive detection and high mass resolution power and are capable of acquiring high resolution spectra (HRMS) alternating with fragmentation spectra (HRMS/MS). In the field of TCM, these fragmentation spectra are today mainly acquired in the data dependent acquisition mode (DDA) (Hou et al., 2019).

One of the key limitations of plant metabolite profiling still resides in the unambiguous identification of all components. At present, in-depth chemical characterizations based on UHPLC-HRMS allow potential identifications, often referred to as annotation or dereplication (Wolfender et al., 2019). Interpreting untargeted HRMS data has greatly improved thanks to dedicated software and metabolomic approaches (Wolfender et al., 2019). Furthermore, organizing HRMS/MS data by molecular networking (MN) brought a novel dimension to metabolite annotation (Wang et al., 2016a). As a way of classifying structurally related chemicals, MN is seen as a tool of interest for TCMs chemical investigation (Hou et al., 2019) and has recently begun to be employed in TCM research to annotate single herb extracts (Pan et al., 2019; Wang et al., 2019; Wang et al., 2020b). Data processing step by open-source software, such as MZmine (Pluskal et al., 2010) prior to MN has enabled the generation of so-called *feature-based molecular networks* (FBMN) (Nothias et al., 2020) (**Table 1**). Such FBMN offer the following advantages compared to classic MN: accurate mass, semi-quantitative information conservation, and isomer separation. Additionally, *in silico* prediction of fragmentation pattern has increased the number of MS/MS spectra available for annotation, which led to the generation of large databases of theoretical spectra containing more than 200,000 spectra of secondary metabolites (Allard et al., 2016).

In this exploratory study, a 10 herbs TCM formula was selected to evaluate new approaches for in-depth chemical investigation from a QC perspective. This 10 herbs formula was chosen following an open-label clinical study that evaluated three new multi-herb formulae to treat atopic dermatitis (Li et al., 2013). This affection, also called atopic eczema, is a common inflammatory skin disorder and is treated in Western medicine by topical corticosteroids and emollients (Dempster et al., 2011). The oral formula generated the best clinical outcomes (Li et al., 2013), and was therefore selected for

TABLE 1 | Terminology of terms used in this study (alphabetical order).

Anchor point	A node in a molecular network, whose formal identification is based on NMR after targeted isolation or by comparison of two independent and orthogonal data with a pure standard (i.e., retention time and *m/z*) (level 1 identification according to the Metabolomic Standard Initiative (MSI) (Sumner et al., 2007)
Bar chromatogram	A bar plot reconstituted from peak descriptors obtained after LC-HRMS data processing. The peak height is represented in bar form, as a function of retention time. The chromatographic peak is thus represented in a centroid way. This depiction allows simplifying the original chromatogram and focusing on the intensity and mean retention time of the peaks
Cluster specificity percentage	In a FBMN, average of the specificity percentages of the features grouped in a cluster for a given herb
Component	A chemical compound, also called chemical constituent, specialized or secondary metabolite, or natural product
Feature-based molecular network (FBMN)	Incorporation of LCMS features information (*m/z*, retention time, intensity) in the molecular networking of MS/MS spectra. It allows, among others, to distinguish isomers and to integrate relative quantitative information. In a FBMN, a feature is equivalent to a node (Nothias et al., 2020)
Formula	A combination of several TCM herbs (Pei et al., 2013)
Marker	A defined chemical compound for an herbal material utilized for control purposes (WHO, 2007)
Multi-component signature	A series of analogue components that are specific to one herb in a formula
Specificity percentage	Relative height intensity of one feature in a multi-herb formula. The peak height of one aligned feature in one herb is divided by the sum of the heights in all herbs

this study. It contains 10 herbs whose main pharmacological effects and TCM indications have previously been summarized (Li et al., 2013). In terms of chemical composition, these 10 herbs were previously described and several references, as well as the pharmacopoeial markers, are summarized in **Table 2**.

This study aimed at exploring the potential role of innovative UHPLC-HRMS/MS data processing tools for a comprehensive chemical characterization of such complex TCM formulae. The rationale was to select relevant specific markers for characterizing each herb in the formula from an unbiased data-driven manner. A workflow is proposed that combines state-of-the-art annotation of UHPLC-HRMS/MS metabolite profiling, FBMN, semi-quantitative Evaporative Light Scattering Detection (ELSD), as well as UV-PDA. ELSD belongs to the category of detectors which provides a proportional semi-quantitative response almost universal, but are not very sensitive (Lucena et al., 2007). In this study, ELSD was evaluated as a tool to focus on the main components from a semi-quantitative point of view. By combining these different detectors, a comprehensive view of the chemical composition of the formula was obtained by linking the detailed structural information provided by HRMS/MS and UV-PDA with the ELSD semi-quantitative information. From this comprehensive view, our workflow aimed to effectively evaluate the herb specificity of all features, to select specific and abundant markers, as well as to highlight series of related less abundant specific components of each herb marker in the formula for advanced traceability analysis. This exploratory study aims to assist in the development of routine QC methods well adapted to a given TCM formula.

RESULTS

Study Overview

The formula selected for this study contains 10 various herbal drugs from eight botanical families: *Angelica sinensis* (Oliv.) Diels (Apiaceae), *Chrysanthemum indicum* L. (Asteraceae), *Glycyrrhiza uralensis* Fisch (Fabaceae), *Isatis tinctoria* L. (Brassicaceae), *Oldenlandia diffusa* (Willd.) Roxb. (Rubiaceae), *Reynoutria japonica* Houtt. (Polygonaceae), whose synonym, *Polygonum cuspidatum* Siebold & Zucc. was used in this study to stay in line with (Li et al., 2013), *Prunella vulgaris* L. (Lamiaceae), *Scutellaria baicalensis* Georgi (Lamiaceae), *Smilax glabra* Roxb. (Smilacaceae) and *Sophora flavescens* Aiton (Fabaceae) (**Table 2**). A wide variety of different chemical classes has been described for these 10 herbal drugs, ranging from the usual flavonoids to alkaloids (*S. flavescens* (He et al., 2015), *I. tinctoria* (Mohn et al., 2009), *A. sinensis* (Jin et al., 2012; Ma et al., 2015), *O. diffusa* (Chen et al., 2016)), triterpenoids (*G. uralensis* (Wang et al., 2013), *P. vulgaris* (Bai et al., 2016), *S. flavescens* (He et al., 2015)), quinones (*P. cuspidatum* (Peng et al., 2013)), iridoids (*O. diffusa* (Chen et al., 2016)), *S. flavescens* (He et al., 2015), and phtalides (*A. sinensis* (Jin et al., 2012; Ma et al., 2015)), among others. Thus, this TCM formula is representative of typical TCM formulae and exhibits a very complex composition. In order to study the contribution of every herbal drug to this multi-herb formula and to rationally select markers representative of each of the 10 herbs, the formula and each individual herb were extracted by decoction. The 10 individual herbs and one formula are abbreviated below as 10H and 1F.

For a comprehensive metabolome characterization, the strategy applied in this study (**Figure 1**) is based on the UHPLC-HRMS/MS metabolite profiling of the formula as well as of the 10 herbal drugs included in its composition (**Figure 1.1**). The 10H and 1F are analyzed by FBMN, which allows 1) to align all HRMS features extracted by peak-picking and represent them in the form of a colored ion map (**Figure 1.3**) and 2) to group all features according to structural similarity by molecular networking (**Figure 1.3**).

Since in such an untargeted LC-MS metabolite profiling, the MS response is not proportional to the amounts of components, all extracts are analyzed by ELSD in order to highlight the main components of each herb only within the formula (**Figures 1.4, 1.5**). Altogether, this permits to localize precisely abundant markers specific to each herb in the formula.

All main components are annotated based on their corresponding HRMS and HRMS/MS spectra. The annotation strategy combined FBMN for grouping structurally related features, spectral comparisons against a comprehensive *in silico* MS/MS spectral database of secondary metabolites and

TABLE 2 | TCM herbal drugs with their proportion in the formula before decoction, their botanical name and pharmacopoeial markers.

Code	Herbs	Family	Plant part	Proportion (w/w)	Marker compound	References
A	*Angelica sinensis* (Oliv.) Diels	Apiaceae	Roots	3.4%	Ligustilide (CPh) *trans*-Ferulic acid (Ph.Eur.)	Jin et al. (2012), Ma et al. (2015)
C	*Chrysanthemum indicum* L.	Asteraceae	Flowers	6.9%	Chlorogenic acid (ChP) Luteolin (JP)	Luyen et al. (2015)
G	*Glycyrrhiza uralensis* Fisch.	Fabaceae	Roots	3.4%	Uralsaponin (ChP, Ph.Eur.)	Wang et al. (2013)
I	*Isatis tinctoria* L.	Brassicaceae	Leaves	6.9%	Indican (ChP) Arginine (Ph.Eur.)	Mohn et al. (2009)
O	*Oldenlandia diffusa* (Willd.) Roxb.	Rubiaceae	Entire plant	20.7%	Oleanolic acid (ChP)	Chen et al. (2016)
PO	*Reynoutria japonica* Houtt. (synonym *Polygonum cuspidatum* Siebold & Zucc.)	Polygonaceae	Rhizomes	10.3%	Emodin (ChP)	Peng et al. (2013)
PR	*Prunella vulgaris* L.	Lamiaceae	Fruiting tops	13.8%	Ursolic acid (ChP, Ph.Eur.)	Bai et al. (2016)
SC	*Scutellaria baicalensis* Georgi	Lamiaceae	Roots	6.9%	Baicalin (ChP, Ph.Eur.)	Karimov and Botirov (2017)
SM	*Smilax glabra* Roxb.	Smilacaceae	Rhizomes	20.7%	Octacosanol, astilbin (ChP)	Hua et al. (2018)
SO	*Sophora flavescens* Aiton	Fabaceae	Roots	6.9%	Matrine (ChP)	He et al. (2015)

ChP, Chinese Pharmacopoeia; Ph.Eur., European Pharmacopoeia; JP, Japanese Pharmacopoeia.

taxonomic filtering of the results (**Figure 1.6**). Their isolation is performed by a direct fractionation of the multi-herb formula at the gram scale (**Figure 1.7**). This process ideally both provides specific standards markers for all herbs in one step and validates the identification of annotated components (**Figure 1.8**). The isolated components are then used as anchor points in the FBMN to propagate structural information to the clustered features, which allows retrieving groups of herbal-specific components, which we refer to as specific multi-component signatures (**Figure 1.9**).

Metabolite Profiling of the Formula and Each Individual Herb

Decoctions of the 10H and 1F were prepared according to the traditional recipe and were then freeze-dried (Section *Preparation of Extracts, Formula and Enriched Formula*). The formula was first analyzed by reverse phase (RP) UHPLC-PDA-ELSD and UHPLC-HRMS using a broad linear gradient (**Figures 2A–F**). The ELSD trace revealed a high quantity of polar constituents (mainly sugars) (**Figure 2D**), while the HRMS metabolite profiling highlighted secondary metabolites (**Figures 2A–C**). An SPE enrichment procedure was implemented to improve the detection of secondary components by ELSD and PDA (**Figures 2E,G**).

To study the contribution of each herb in the formula, the 10H and 1F extracts were then profiled by UHPLC-HRMS/MS in both positive ionization (PI) and negative ionization (NI) modes using an optimized gradient in RP conditions. All analyses were performed in the data dependent mode to generate both HRMS spectra for molecular formula assignments and corresponding HRMS/MS fragmentation spectra on most detected HRMS features. Data were processed with MZmine software (Pluskal et al., 2010), to generate an aligned peak list of all features (**Figure 1.2**). This list of aligned features has been employed in two ways. On the one hand, it has been presented in the form of a 2D feature map, in which the features detected in the formula have been colored according to their occurrence in the individual herbs (**Figures 3A**, **5A** and **Supplementary Figures S1A, S2A**). This display provided a first view of a qualitative contribution of each herb to the formula. On the other hand, the list of aligned features was submitted to the Global Natural Products Social Molecular Networking (GNPS) platform to organize the HRMS/MS fragmentation spectra in clusters of features sharing similar fragmentation and thus potentially grouping structural analogues (Wang et al., 2016a; Nothias et al., 2020). In the resulting FBMN, the same color code as in the 2D feature map was applied to represent each herb (**Figure 3B** and **Supplementary Figure S1B**). Finally, peaks were annotated based on HRMS/MS spectra matches against an *in silico* database (ISDB-DNP) (Allard et al., 2016).

The FBMNs resulting from this processing allowed the organization of the metabolite profiling in both ionization modes (**Table 3**). The FBMN allowed assigning a given node to each feature for which a fragmentation spectrum was recorded. Any feature was detected in the formula and in none, one or

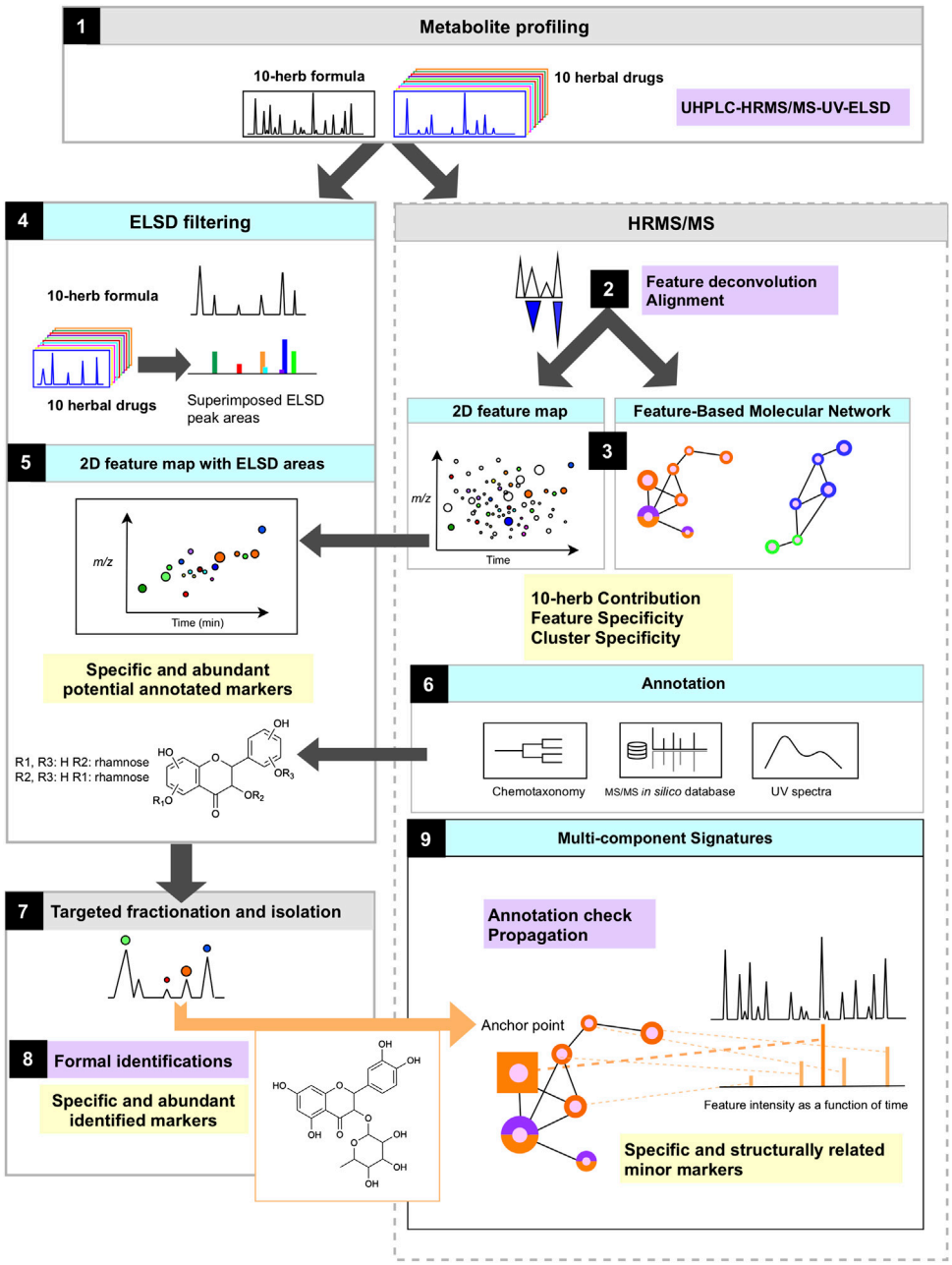

FIGURE 1 | Scheme of the study workflow and analytical strategy to evaluate the metabolome contribution of each herb, identify specific markers of the formula and establish multi-component signature of each herb.

several herbs, or in some herbs and not always in the formula. At the node level, in order to keep this information, all features were displayed by nodes having an inner circle and an external ring (legend **Figure 4**). The inner circle was of pink color if detected in the formula and of gray color if not detected in the formula but only in the individual herbs. The size of the nodes was proportional to the intensity of the peak in the formula. On each node, the external ring indicated in which individual herb(s) the feature was detected according to the corresponding herb color code. A ring with a single color was characteristic of a feature specific to a single herb (**Figures 4A,B**), while multiple colors in the ring indicated the presence of this feature in all corresponding herbs (**Figure 4C**). The colored ring area was proportional to the feature intensities in each herb.

Molecular networking allows nodes to be grouped according to the similarity of their associated HRMS/MS spectra, and thus similar structures were grouped in clusters. At the cluster level, node mapping highlighted three main types of clusters: 1) monochrome clusters with a single color on the node external ring, i.e., specific analogues series for a given herb (**Figures 3B**, **4A**), 2) multi-color clusters with a single color on

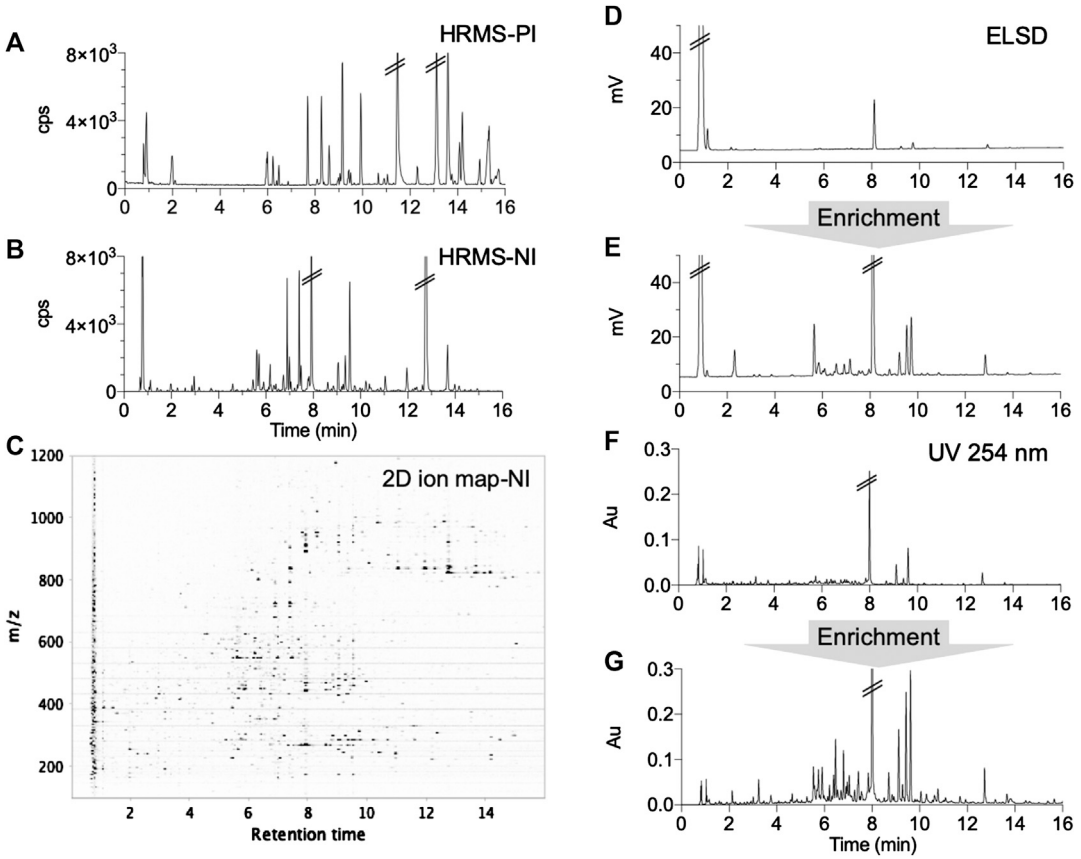

FIGURE 2 | UHPLC metabolite profiling of the formula with different detections before and after enrichment: **(A,B)** complementary positive (PI) and negative (NI) ionization chromatograms, **(C)** 2D ion map presenting all ions detected in NI, **(D,E)** ELSD chromatograms before and after SPE enrichment showing the unretained polar metabolites (mainly saccharides), **(F,G)** UV chromatograms (254 nm) before and after enrichment.

the node external ring, i.e., specific and structurally related components from different herbs (**Figures 3B**, **4B**) and 3) multi-color clusters with multiple colors of the node external rings, i.e., ubiquitous components present in different herbs (**Figures 3B**, **4E**).

The FBMN provided a very detailed view of the specificity/ubiquity of each feature and cluster across all 10H and 1F extracts. This also allowed a global qualitative vision of the contributions of each herb to the formula and the relationship between all features. In order to precisely assign the features present in the formula that were herb-specific and to identify clusters of features that showed series of analogues that were also very specific, a script was written as an alternative to the visualization classically used in FBMN. This script permitted to express the specificity numerically as a percentage of relative intensity at the node and cluster levels (Section *Node and Cluster Specificity* and **Supplementary Figure S4**)

The script considered the feature heights after the alignment of the 10 herbs of the formula and the repartition of the features in clusters. At the node level, similarly to the ring visualization, the script enabled to express as a percentage the relative height intensity of one feature in the 10 herbs (**Supplementary Figure S4**). This relative height intensity was named the *specificity percentage* of a feature (**Table 1**). Fully specific features, presenting a 100% specificity percentage, were highlighted. Due to the sensitivity of the HRMS detection and the ubiquity of natural components, in practice, the specificity percentage threshold was set at 90% for a given herb. The number of specific peaks (90% threshold) in the formula was 1,030 in PI (65%) and 734 in NI (72%) (the numbers of specific features for each herb are presented in **Supplementary Figures S5–S7**).

To visualize these specific features, all features detected in the formula were represented in the form of a 2D feature map comparable to the raw LC-HRMS ion map (**Figures 1.3**, **2C**, **3A**, **5A** for PI; **Supplementary Figures S1A, S2A** (NI)). Features detected in the formula and found in a single herb were tagged with the herb color code. Those that were not specific were represented by a white dot with a black circle. The 2D feature map also enabled to highlight chromatographic information, which are not easily visible in the FBMN.

The specific contributions varied from one herb to another: *Glycyrrhiza glabra* provided a high number of specific features (189 (18.3% of all specific features) and 168 (22.9%), respectively, in PI and NI), while the amount of dried herb represented only 3.4% of the crude herb mixture before extraction. Some of these

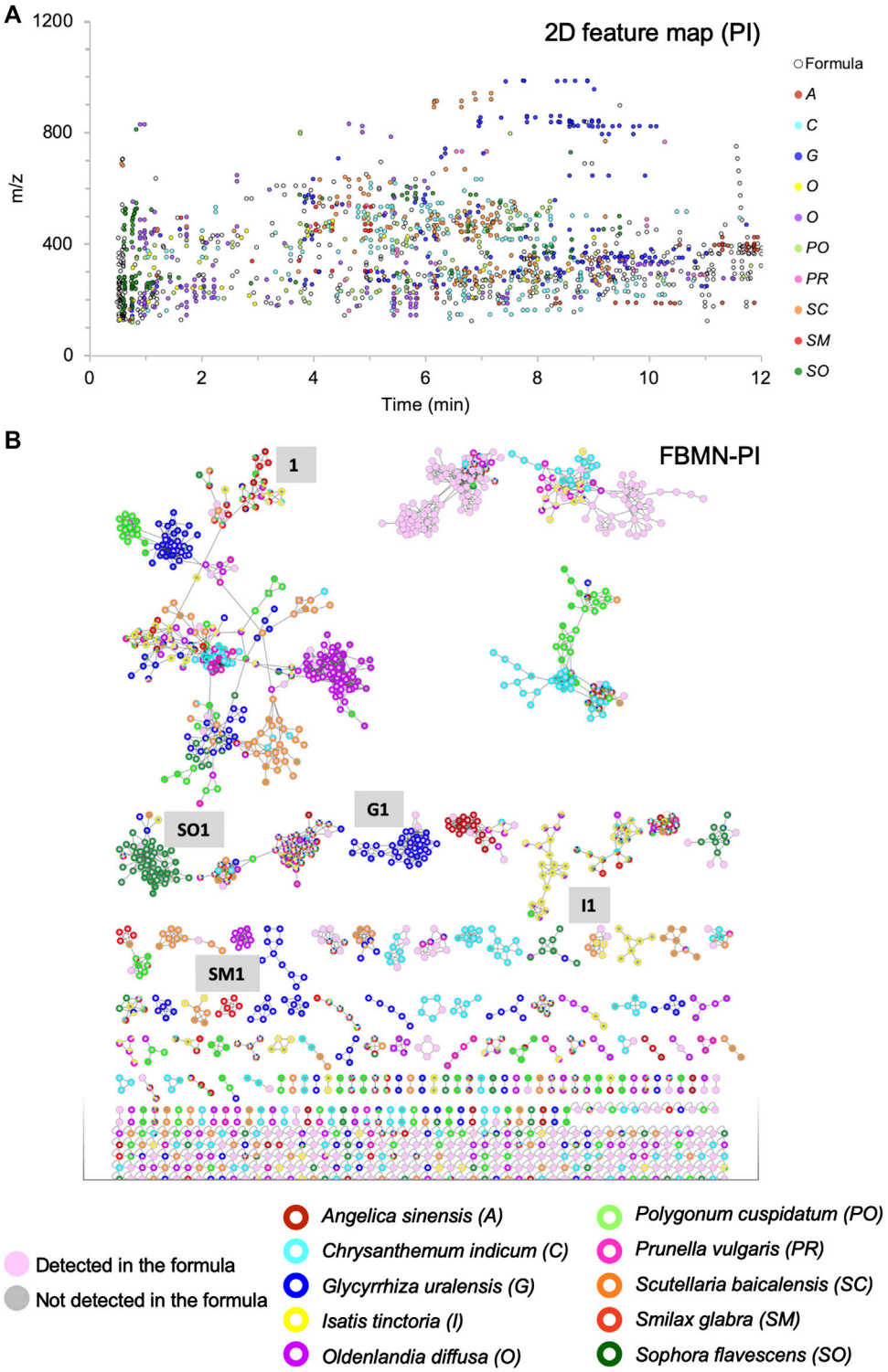

FIGURE 3 | Visualization of the contribution of the 10 herbs to the formula, in which each herb is represented by a different color: **(A)** 2D feature map in PI: each black circle represents a feature detected in the formula, the size of the circles is fixed and equal for all features. The inner color of the circle indicates that the feature is specifically detected in one of the 10 herbs (90% specificity threshold). **(B)** FBMN in PI for the organization of the MS/MS spectra of all features presented in **(A)**, with the same color coding and fixed node size.

TABLE 3 | Description of FBMNs in both ionization modes.

	Positive ionization	Negative ionization
Number of nodes	2,713	2,058
Number of clusters	148	80
Number of clustered nodes	1,258	573
Number of ISDB-DNP annotated nodes	1,698 (63%)	1,126 (55%)

specific features (blue color dots in **Figures 3A**, **5A**; **Supplementary Figures S1A, S2A**) were observed around 8 min with m/z > 800, and annotated as oleanane triterpenoids. In the FBMN, these features were organized into a specific cluster, which is highlighted by the blue color code blue (**Figure 3B**, code G1; **Supplementary Figure S1B**). In contrast, *Smilax glabra* which was one of the main dried herbs in formula (20.7%) had only 20 specific features (1.9% of all specific features) and 40 (5.4%) in PI and NI modes, respectively (red color dots mainly around 4–5 min in **Figures 3A**, **5A** and **Supplementary Figure S1A**). Some of the features from *Smilax glabra* were also organized in a specific cluster (**Figure 3B**, code SM1; **Supplementary Figure S1B**). In PI, several features of *Sophora flavescens* were highlighted before 2 min (**Figures 3A**, **5A**, dark green dots), annotated as quinolizidine alkaloids and organized in a specific cluster in the FBMN-PI (**Figure 3B**, code SO1). Overall, the feature map representation also highlighted a good spreading of all specific features across m/z and retention time dimensions.

Similarly to the treatment at the node level, the script enabled to describe with a percentage the specificity of each cluster to a given herb (*cluster specificity percentage* (**Table 1**)). For each cluster, the averages of the specificity percentages for each herb were calculated. The script also allowed to sort the clusters according to their cluster specificity percentages for each herb (**Supplementary Figure S4**). A threshold of 75% was arbitrarily chosen to identify clusters mainly specific to one of the 10 herbs. The cluster specificity percentage was also used to describe clusters whose contributions came from several herbs. Among all PI clusters, 36 clusters (24% of all clusters) were found to be specific to one of the 10 herbs. These specific clusters contained 346 nodes (13% of all nodes). In NI, 23 clusters (29% of all clusters) were found to be specific to one of the 10 herbs, which concerned 207 nodes (10% of all nodes) (**Supplementary Figure S8**).

Selection of the Most Abundant Components of Each Herb by Evaporative Light Scattering Detection Filtering

The 2D feature map and the FBMN provided a detailed visualization of the metabolome of the 10 herbs formula in terms of herb specificity and contribution which were also estimated by calculating specificity percentages. However, this analysis did not provide rational information in terms of component abundance, since untargeted HRMS/MS detection is not quantitative. To further select abundant components of interest, ELSD was used as a complement for semi-quantitative and quasi-universal detection to filter the features related to the most abundant components (**Figure 1.4**).

UHPLC-ELSD peak areas of the 10 herbs plotted in the form of bar plots (**Figures 5C,D**) highlighted 47 peaks representing the main components (**Supplementary Figures S9, S10** present the original chromatograms). Four herbs (*Scutellaria baicalensis*, *Polygonum cuspidatum*, *Glycyrrhiza uralensis*, and *Sophora flavescens*) presented rich ELSD traces with each several main components (**Figure 5C**). On the contrary, other herbs contributed only to few and low intensity UHPLC-ELSD signals (**Figure 5D**): *Isatis tinctoria* yielded two weak signals and *Smilax glabra* only one, while no signal was recorded for *Angelica sinensis* at the exception of metabolites with no retention in RP conditions (**Supplementary Figures S9, S10**).

The features of the 47 main components were localized thanks to the 2D feature maps (see Section *UHPLC-UV-PDA-HRMS/MS System* for a detailed description), and their specificity was verified as described previously. An ELSD peak was considered as specific if the corresponding feature has a specificity percentage above 90% in both ionization modes. Five main components were considered as non-specific under this criterion. In addition, five ELSD peaks were not detected in the formula decoction.

The 42 remaining abundant herb components (40 and 34 peaks, respectively, in PI and NI) were all found to be specific (90% threshold) in the formula and were highlighted in the 2D feature map and in the FBMN by mapping their ELSD intensities instead of HRMS intensities (**Figures 1.5**, **4C**,D, **5E**, **6**, **7A** and **Supplementary Figures S6E, S7**). Among them, 26 and 24 peaks had a specificity percentage of 100%, respectively, in PI and NI. Twelve and eight peaks had specificity percentages between 95 and 99%, respectively, in PI and NI and two peaks between 90 and 94% in both modes (**Supplementary Figure S3**). As shown here, the threshold of specificity percentage had to be set at 90% to consider several abundant peaks in the formula. The lack of specificity was not linked to potential carryovers effects by carefully considering the order of analysis. The low abundant detected features were thus due to minor contributions from other herbs of the TCM. However, depending on the formula composition, this threshold can be adapted.

Among the five main components that were not specific (below 90% threshold) are two main peaks of *Scutellaria baicalensis* (**SC1** and **SC2**). The component **SC1** was shared with *Oldenlandia diffusa* (94–6% in PI and 83–17% in NI) (Chen et al., 2016), while **SC2** was additionally detected in *Chrysanthemum indicum* (**Figure 7B**). Although not perfectly specific to *Scutellaria baicalensis*, these peaks were considered for further identification, being the most abundant components of the formula. The other non-specific features concerned an ELSD peak of *Chrysanthemum indicum* (**C6**), annotated as chlorogenic acid, which was shared in small amounts with three other herbs, as well as one peak from *Polygonum cuspidatum* (**PO4-F**), shared with *Smilax glabra*. Finally, one peak from *Prunella vulgaris* (**PR3**) was shared with three other herbs in small amounts. It has to be noted that these three peaks (**C6**, **PO4-F**, **PR3**) were not the main ELSD peaks for the corresponding herbs.

The features selected by ELSD filtering were all annotated in detail. The automated annotation strategy of all features

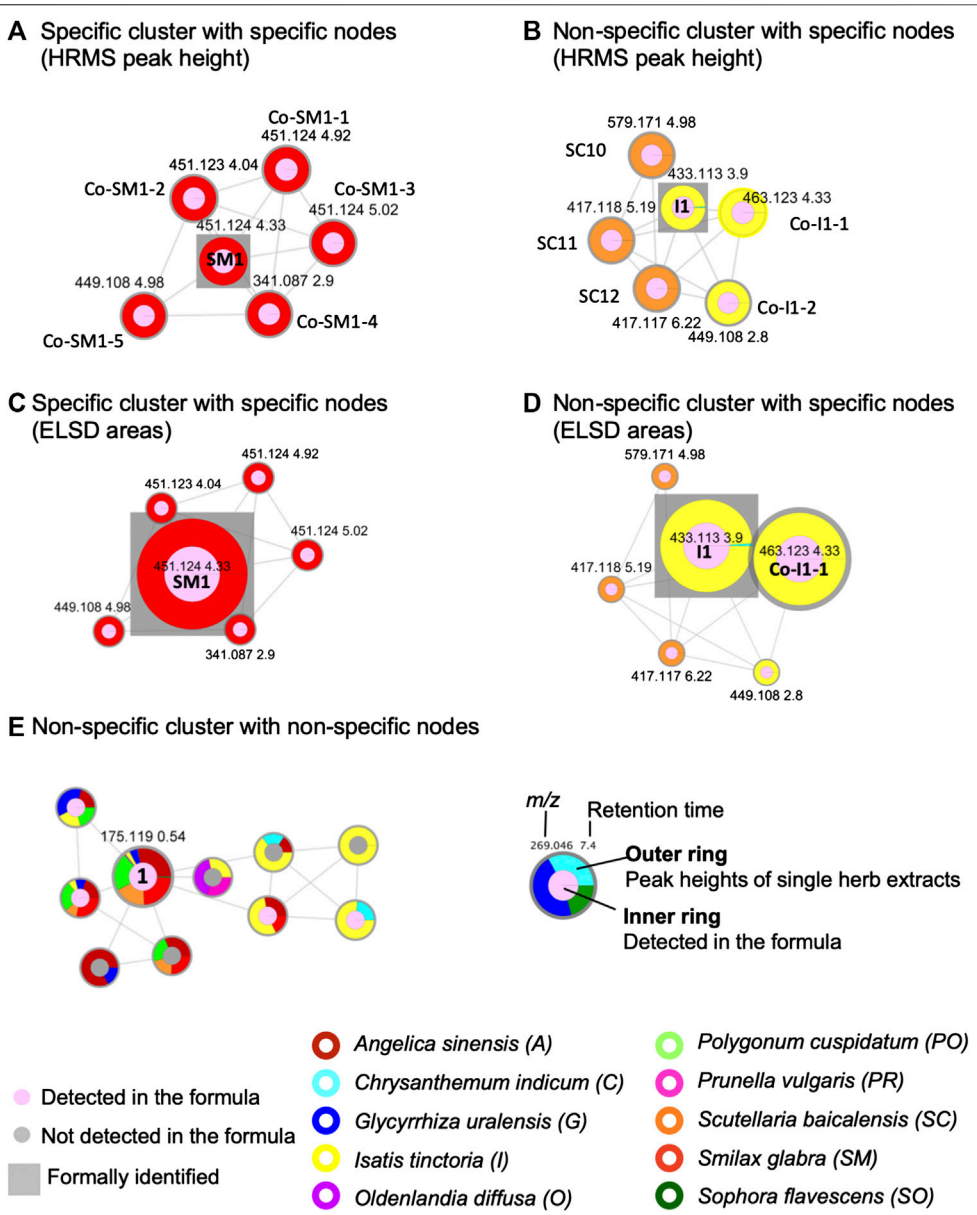

FIGURE 4 | Selected examples of cluster and node specificity in the FBMN-PI: **(A)** specific cluster for *S. glabra* (100%) exhibiting only specific nodes (the size node is proportional to the HRMS height of the peak), **(B)** non-specific cluster (50% *S. baicalensis* and 50% *I. tinctoria*), with nodes each specific to one single herb (specific components of each herb sharing common structural type for both herbs) (the size node is proportional to the HRMS height of the peak), **(C)** the same cluster as in **(A)** with the node sizes proportional to the ELSD areas, **(D)** the same cluster as in **(B)** with the node sizes proportional to the ELSD areas, **(E)** non-specific cluster common to several herbs with a node annotated as an ubiquitous component, arginine (1) (the node size is proportional to the HRMS height of the peak). For arginine (1), the colors shows the following specificity percentage: *A. sinensis* 28%, *G. uralensis* 5%, *I. tinctoria* 3%, *O. diffusa* 1%, *P. cuspidatum* 21%, *S. baicalensis* 18%, *S. glabra* 24%, *S. flavescens* 1%) (the size node is proportional to the HRMS height of the peak). Each herb is represented by a different color on the external ring. On the nodes, the numbers indicate feature *m/z* and retention time. The square is used to label formally identified components. Codes such as **Co-Sm1-2** or **SC10** referred to annotations, see **Supplementary Tables S5, S9, S10**.

combined molecular formula assignment and HRMS/MS comparison with the *in silico* spectral database. Since the filtered features (40 in PI and 34 in NI) were much less than the total number of annotated features (1,698 in PI and 1,126 in NI), their annotations were verified and completed in detail (**Supplementary Section S5** for a detailed description of the annotation workflow). For all annotations obtained, the top six structure candidates in both modes were checked for consistency in previously reported components for each herb (taxonomic consistency). When available, UV spectra were used to confirm the annotations or to discriminate them. The strategy enabled the partial annotation of all main components, however, in some

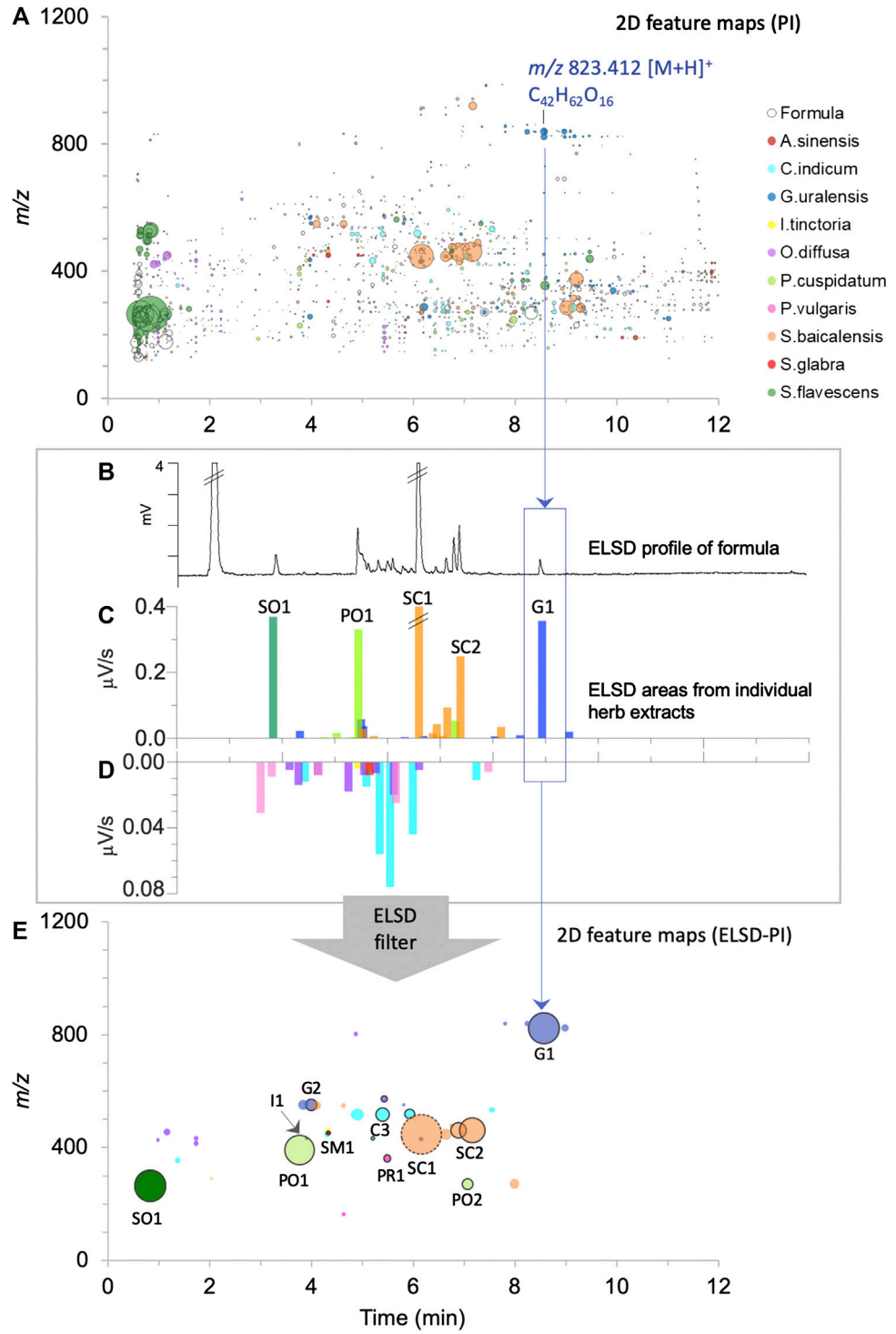

FIGURE 5 | Visualization of the contribution of the 10 herbs to the formula normalized by ELSD filtering to consider semi-quantitative relationship between components. Each herb is represented by a different color as in **Figures 3**, **4**: **(A)** 2D feature map in PI: the size of the circles is proportional to the feature height intensity in the formula, only features detected in the formula are represented. The inner coloration of the circles indicates that the feature is specifically detected in one of the 10 herbs (90% specific threshold), **(B)** ELSD profile of the formula, **(C,D)** bar plots proportional to the chromatogram retention time dimension with superimposed ELSD areas of the individual herb extracts, presented in two scales, from 0 to 0.4 µV/s in **(C)** and from 0 to 0.08 µV/s in **(D)**. **(E)** 2D feature map (PI) presenting the features to which ELSD peaks were assigned. The size of the dots is proportional to ELSD areas, with the exception of the dot with a dashed circle (SC1), where half of the area value is shown to improve visualization (very major component). The dots with a black outer circle represented components that have been formally identified.

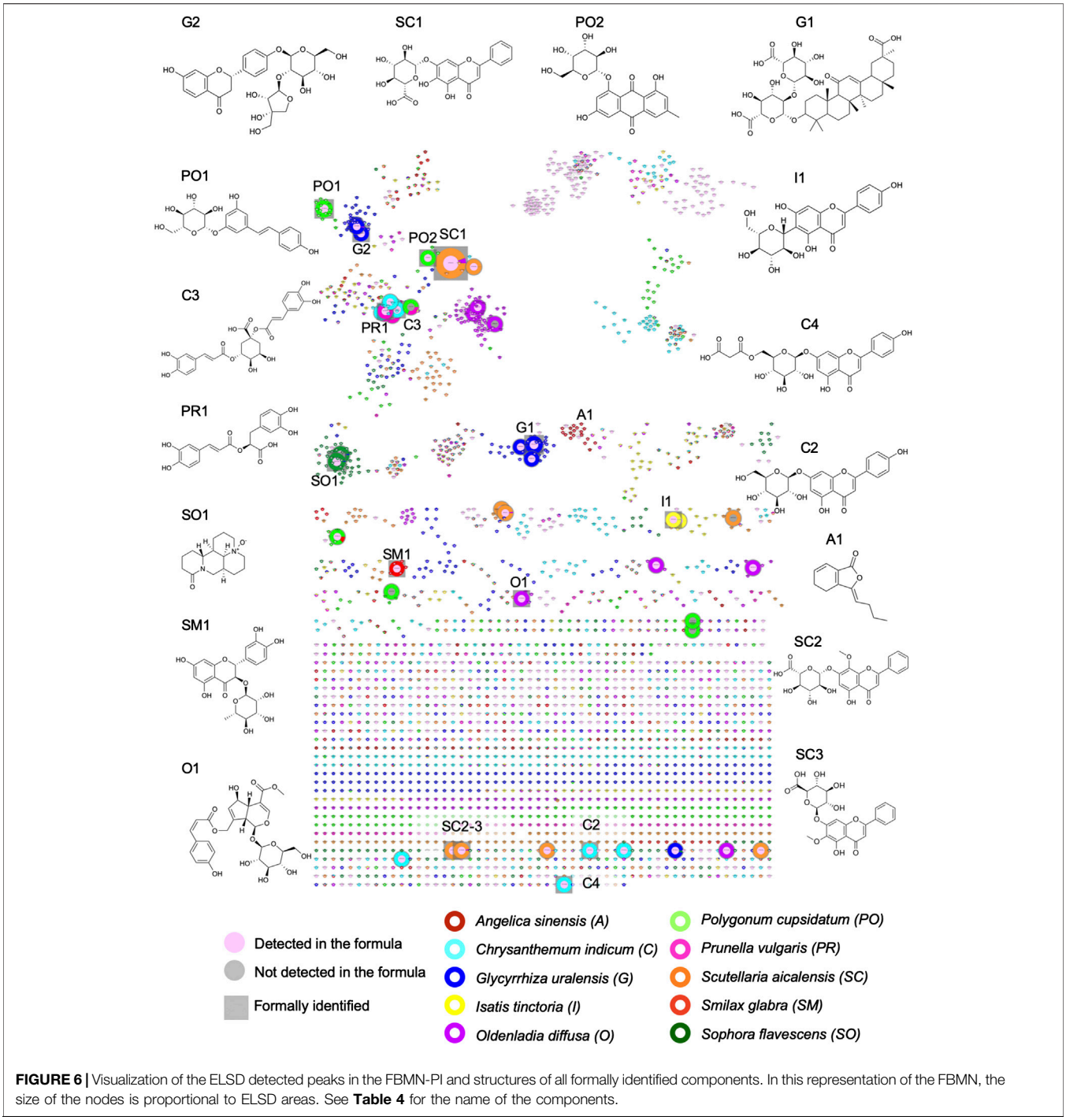

FIGURE 6 | Visualization of the ELSD detected peaks in the FBMN-PI and structures of all formally identified components. In this representation of the FBMN, the size of the nodes is proportional to ELSD areas. See **Table 4** for the name of the components.

instances, exact isomer differentiation was not possible (**Supplementary Section S5** and **Supplementary Tables S2–S11**).

At this stage of the workflow, potential markers that were both specific and ELSD detected were annotated by combining several levels of spectral and taxonomic information. This allowed the annotation of one or more potential markers for each herb, that are specific in the formula with proposals of structures that are taxonomically coherent.

Targeted Isolation of Potential Markers From the Formula

To obtain these markers rapidly in view of the standardization of the formula, the information collected was used to target their isolation from a large quantity of the formula itself rather than initiating multiple isolations on each individual herb. This step was also used to confirm the annotations made. For this, a large-scale fractionation on MPLC was attempted directly on the

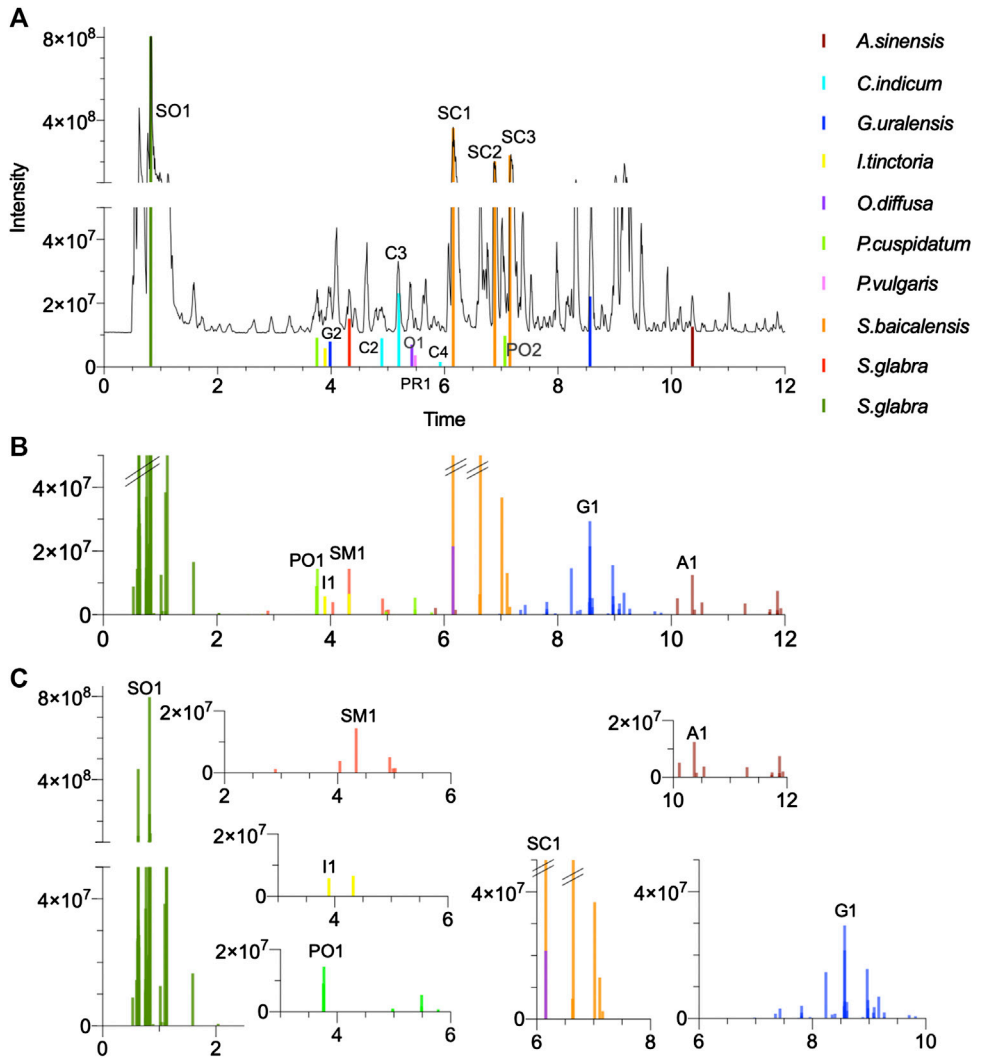

FIGURE 7 | Multi-component signatures extracted from the FBMN (**Figures 3B**, **6**) and represented in the form of bar chromatograms presenting the feature height intensity as a function of retention time in PI: **(A)** metabolite profile of the formula showing all formally identified components, **(B)** bar chromatograms showing seven multi-component signatures. **(C)** multicomponent signatures for *S. glabra* and its marker astilbin (SM1), *I. tinctoria* and isovitexin (I1), *P. cuspidatum* and *E*-piceid (PO1), *A. sinensis* and ligustilide (A1), *G. uralensis* and uralsaponin A (G1), *S. flavescens* and oxymatrine (SO1) and *S. baicalensis* and baicalin (SC1). All *X* axes represent time dimension, all *Y* axes feature height intensity. See **Supplementary Tables S2–S11** for annotations.

enriched formula extract (**Figure 1.7**). The chromatographic conditions were first optimized using an HPLC analytical column packed with the same stationary phase than the MPLC column. The optimized HPLC conditions were then geometrically transferred to the preparative scale (Challal et al., 2015) (Section *Isolation of the Markers*). The fifty MPLCs fractions were profiled by UHPLC-HRMS and ELSD in the same chromatographic conditions. Peak detection in the whole dataset with MZmine permitted the localization of the features of interest in related fractions. The ELSD traces of the selected fractions were used to assess purity. Six markers from five herbs were directly obtained from the MPLC fractions. The other markers were found in five additional fractions which were further submitted to optimized semi-preparative isolation. Altogether, the process yielded thirteen markers specific to seven herbs of the formula. These isolated components were subsequently analyzed by 1D and 2D-NMR for unambiguous identification (**Supplementary Section S7** for precise descriptions). This provided a definitive discrimination in cases where isomers could not be univocally annotated.

Based on this strategy, 13 specific standards were obtained for seven herbs of the formula. It was however not possible to obtain standards for three herbs (*Angelica sinensis*, *Prunella vulgaris* and *Isatis tinctoria*). For these herbs, the annotated features were ligustilide (**A1**) for *Angelica sinensis*, rosmarinic acid (**PR1**) and salviaflaside (**PR2**) for *Prunella vulgaris* and isovitexin (**I1**) and isoscoparin (**I2**) for *Isatis tinctoria* (**Supplementary Tables S2, S5, S8**). This difficulty was not surprising, because the ELSD profiling revealed that these components were present in low quantities. Based on the

annotations, in these cases, three standards were purchased and confirmed the annotations of **A1**, **PR1** and **I1** after comparison of their retention time and HRMS/MS spectra. All formally identified markers are summarized in **Table 4** (see their structures in **Figure 6** and their localization in the metabolite profiling in **Figure 7A** and **Supplementary Figure S15** (NI)). Finally, *Scutellaria baicalensis* and *Chrysanthemum indicum* were represented by three markers, *Glycyrrhiza glabra* and *Polygonum cuspidatum* by two markers, whereas *Angelica sinensis*, *Isatis tinctoria*, *Oldenlandia diffusa*, *Prunella vulgaris* and *Sophora flavescens* were represented by one marker.

Metabolome Analyses for Selecting Multi-Component Signatures

All formally identified markers were used as anchor points in the FBMN to correct ambiguous annotation, and to highlight minor components that could serve as potential multi-component signatures. An *anchor point* is defined as a node whose formal identification is based on NMR after targeted isolation or by comparison of two independent and orthogonal data with a pure standard (i.e., retention time and *m*/*z*) with a pure standard (level 1 identification according to the Metabolomic Standard Initiative (MSI) (Sumner et al., 2007) (**Table 1**). In a FBMN, these anchor points increase the annotation confidence for all related nodes in a given cluster. The analysis of the clusters containing such anchor points revealed some series of analogues structurally similar to the identified components and whose specificity could be rapidly evaluated. These analogues were annotated by manually propagating the information provided by the anchor points and were labeled by keeping reference to the identified marker (**Co-SC1-1**, with **Co** for co-marker) (**Supplementary Tables S2–S11**). This manual propagation consisted first in sorting the *in silico* annotation, by keeping the structures of the same chemical class as the anchor point as the most relevant. In cases of multiple relevant annotations, the sorting was done according to the chemotaxonomic relevance. Such series of clustered annotated analogues were defined as *multi-component signatures* specific to each herb marker in the formula. Together, the set of the 10 herbs multi-component signatures provide a kind of chemical passport specific to the formula. In order to visualize these multi-component signatures as a subset on the main chromatogram, the peak data from the selected clusters were exported and represented as *bar chromatograms* (**Table 1**), which presented the intensity of HRMS peaks as a function of time (**Figures 7B,C**, **8C**,D and **Supplementary Figures S15–S19**).

Several categories of multi-component signatures were distinguished: 1) herb-specific clusters containing a formally identified marker (**Figure 8** and **Supplementary Figures S16, S17, S19D**), 2) non-specific clusters containing a formally identified marker (**Supplementary Figures S17, S19B**) and 3) specific clusters with no formally identified marker and taxonomically relevant annotations (**Supplementary Figure S18**).

Category 1: Herb-Specific Clusters Containing a Formally Identified Marker

This ideal category highlighted identified markers and their structurally related analogues that are herb-specific in the formula. This was the case for seven clusters in both ionization modes with identified markers representing seven herbs (**A1** and **SO1** in PI, **SC2**, **SC3**, **C3** and **I1** in NI, **GI** and **SM1** in PI/NI) (**Supplementary Tables S2–S5, S9–11**). The analogues detected were often isomers of known markers, as shown for *Angelica sinensis* (**A1**, **Co-A1-1** and **2**), *Chrysanthemum indicum* (**C3**, **Co-C3-1** to **5**) *Glycyrrhiza uralensis* (**G1**, **Co-G1-1** to **3**) and *Smilax glabra* (**SM1**, Co-SM1-1 to 3) (**Supplementary Tables S2–S4, S10**). Concerning *Sophora flavescens*, the cluster consisted of quinolizidine alkaloids analogues of oxymatrine (**SO1**) that were not isomeric structures (**Co-SO1-1** to **6**, **Supplementary Table S11**). In the case of *Scutellaria baicalensis*, three markers were identified (**SC1**, **SC2** and **SC3**) but none were 100% specific. In order to find 100% specific makers, the nodes associated either with **SC1** or the ones associated to the cluster with **SC2** and **SC3** were inspected in detail (**Supplementary Table S9**). This revealed that the cluster with **SC2** and **SC3** had structurally related nodes that were 100% specific to the herb (**Figures 8B,C**). These nodes were annotated as analogues with additional hydroxyl or/and methyl groups. Similarly, methylated flavone aglycones were present in the same cluster.

Category 2: Non-Specific Clusters Containing a Formally Identified Marker

This type of clusters contained nodes specific to different herbs which were structurally related. This was the case for *Polygonum cuspidatum* and *Prunella vulgaris*.

For *Polygonum cuspidatum*, its marker (*E*-piceid (**PO1**), a resveratrol derivative, was detected in a large cluster shared between all herbs of the formula. Within this large cluster, several analogues of **PO1** were specific to this herb and organized in a sub cluster (**Co-PO1-1** to **4**, **Supplementary Table S7** and **Supplementary Figure S17**)). Their presence in this cluster showed that these features shared structural (at least spectral) similarities with features from other herbs.

Another mixed cluster in NI had a cluster specificity percentage of 68.9% for *Prunella vulgaris*, including **PR1**, surrounded by nodes coming from *Scutellaria baicalensis* and *Sophora flavescens* (**Supplementary Figure S19B**). The specific nodes attributed to *Prunella vulgaris* which were annotated as salviaflaside (**Co-PR1-1**) and danshensuan C (**Co-PR1-2**) were considered as co-markers of the formally identified rosmarinic acid (**PR1**) (**Supplementary Table S8**).

Category 3: Specific Clusters With No Formally Identified Marker

In some cases, a marker may be in a cluster that cannot be used for a multi-component signature. The marker of *Oldenlandia diffusa* (**O1**) represented such a case. It was linked only with features with

TABLE 4 | Formally identified markers.

Herb	Codes	Formally identified markers	Molecular formula	Class of compounds
A. sinensis	A1	Ligustilide	$C_{12}H_{14}O_2$	Isobenzofuran
C. indicum	C1	1,3-Dicaffeoyl-epi-quinic acid	$C_{25}H_{24}O_{12}$	Caffeoylquinic acid
	C2	Cosmosiin	$C_{21}H_{20}O_{10}$	Trihydroxyflavone *O*-glucosides
	C4	6″-Malonylcosmossiin	$C_{24}H_{22}O_{13}$	
G. uralensis	G1	Uralsaponin A	$C_{42}H_{62}O_{16}$	Oleanane triterpenoid
	G2	Liquiritin apioside	$C_{26}H_{30}O_{13}$	Flavanone
I. tinctoria	I1	Isovitexin	$C_{21}H_{20}O_{10}$	Flavone *C*-glucoside
O. diffusa	O1	10-*O*-*p*-*cis*-Coumaroyl scandoside methyl ester	$C_{26}H_{30}O_{13}$	Scandoside
P. cuspidatum	PO1	*E*-piceid	$C_{20}H_{22}O_8$	Stilbene
	PO2	Emodin-8-*O*-glucoside	$C_{21}H_{20}O_{10}$	Anthraquinone
P. vulgaris	PR1	Rosmarinic acid	$C_{18}H_{16}O_8$	Rosmarinic lignan
S. baicalensis	SC1	Baicalin	$C_{21}H_{18}O_{11}$	Flavone *O*-glucuronides
	SC2	Wogonoside	$C_{22}H_{20}O_{11}$	
	SC3	Oroxyloside	$C_{22}H_{20}O_{11}$	
S. glabra	SM1	Astilbin	$C_{21}H_{22}O_{11}$	Flavanone
S. flavescens	SO1	Oxymatrine	$C_{15}H_{24}N_2O_2$	Quinolizidine alkaloid

the same retention time (in-source adduct or fragment). In such a case, clusters containing only specific nodes can easily be evidenced by the proposed workflow to interpret the specificity and can, in addition to the marker, contribute to the traceability of this herb in the formula. For this herb, specific clusters contained features annotated as flavonols diglycosides (**Co-O-1** to **3** in NI and PI), which were previously described for this species and could serve as multi-component signature (**Supplementary Table S6** and **Supplementary Figure S17**).

DISCUSSION

This exploratory study enabled a comprehensive overview of the chemical composition of a 10 herb TCM formula and highlighted the contribution of each herb at the metabolite level. The proposed analytical workflow was oriented to generate useful information for the establishment of quality control (QC) methods that consider the specificity of markers, their abundance, and the presence of multi-component signatures that could serve as co-markers. The strategy combined untargeted metabolite profiling with ELSD detection, which permitted, on the one hand, identifying at least one main marker per herb and assigned its specificity in the formula. On the other hand, it permitted the extraction of specific multi-component signatures from all the information gathered in the FBMN.

Feature-Based Molecular Network for Multi-Herb Formulae Composition Assessment

To our knowledge, this study is the first to explore the potentialities of FBMN for documenting the detailed composition of a TCM multi-herb formula. Molecular networking was previously successfully used to annotate components of interest in single TCM herb extracts (Pan et al., 2019; Wang et al., 2019; Wang et al., 2020b).

Metabolite profiling processing through the FBMN workflow directly supported the visual inspection of the node and cluster specificities. However, this information-rich dataset is difficult to interpret as such. To summarize the specificity information, a script was developed to calculate the specificity of the features and clusters according to the 10 herbs and to display this information in the chromatographic dimensions (**Figures 3A**, **7** and **Supplementary Figure S4**). This generic data processing enabled all data from single herbs to be linked to the formula, provided that a careful alignment of all features was performed. This fully automated task during MZmine 2 processing was key for providing an interpretation of the contribution and specificity of each herb to the formula. Thanks to the data processing, the contribution of each herb to the formula was visualized in the form of the 2D feature map (**Figures 3A**, **5A**), which provided a qualitative and comprehensive view.

The data generated by this untargeted exploratory metabolite profiling study were used to investigate the contribution of each herb to a given formula to assist the development of improved QC methods. The same TCM metabolome dataset could also have been processed to describe the different chemical classes contained in the formula and possibly annotate as many features as possible. The proposed workflow to capture the specificity of each node and cluster could also be employed, for example, to focus on the ubiquitous features or the features present only in the formula.

Evaporative Light Scattering Detection Filtering for the Selection of Abundant Components

From the QC perspective, the semi-quantitative aspects between the different components are important (Yang et al., 2017). In this work, we decided to integrate the ELSD data into the dataset obtained from the metabolite profiling. The ELSD detection allowed us to filter the large dataset and to focus on less biased data in semi-quantitative terms. As shown in **Figures**

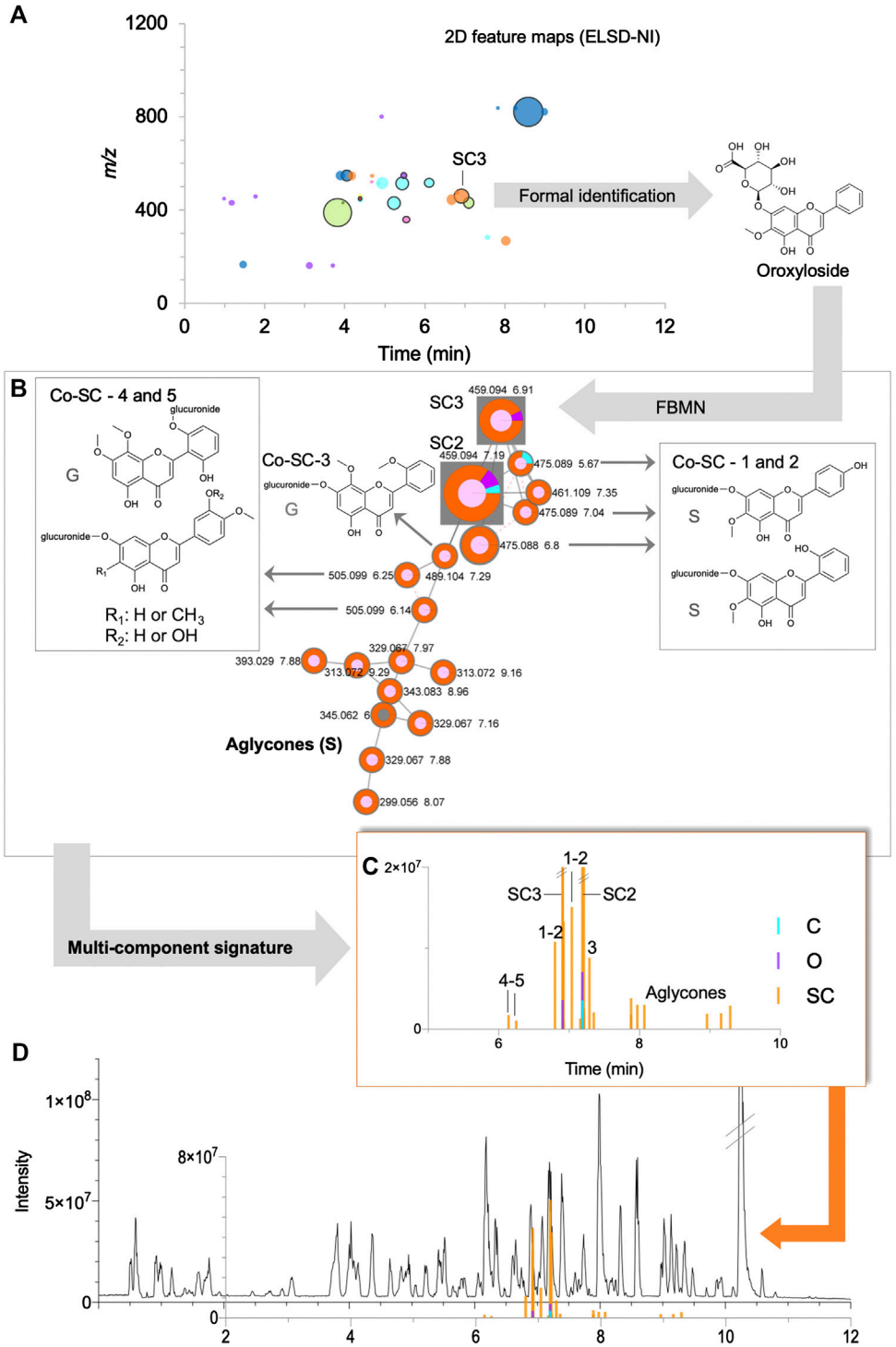

FIGURE 8 | Example of the detailed mining of a multi-component signature for *Scutellaria baicalensis* in the formula: **(A)** 2D feature map (NI) filtered by ELSD (see **Figure 5E**), **(B)** specific cluster in FBMN-NI containing the identified markers **SC2** and **SC3** and their related annotated nodes, some with structures described for the species (S) or genus (G), **(C)** bar chromatograms showing the corresponding multi-component signature with their chromatographic data, **(D)** UHPLC-HRMS/MS metabolite profile of the formula in NI in regards of the multi-component signature. Codes such as **Co-SC-2** referred to annotations, see **Supplementary Table S9**.

4A–D, **5**, **6**, complementary and simplified visualizations could be generated, which present the semi-quantitative information in addition to the contribution and specificity of each feature.

The combination of ELSD data with specific features has permitted locating potential markers precisely in the metabolite profile. This can support the targeted purifications of markers. These data can also be compared with data from the literature, and, for annotated markers, a choice among those that are commercially available is also possible to obtain specific standards and confirm the annotation process. In this study, a direct purification from the formula was attempted to identify most of the markers of interest and to obtain sufficient quantities of pure markers to develop a QC method. While this was successful for the most abundant components, the less abundant markers were obtained in small quantities or not pure enough for developing a QC method. Isolation from each individual herb would, therefore, be required for the less abundant selected markers.

Marker Selection

This workflow allowed the selections of at least one identified marker for each herb in the formula, ensuring a degree of specificity which is unique to this formula. This innovative approach is unbiased, as it is directly related to data observation. *A priori*, it can be applied to other formulae and could be generic, but further studies are needed to demonstrate it. The markers revealed by this approach are compared below with the ones proposed by the European (PhEur) and Chinese (ChP) Pharmacopoeias to evaluate their relevance. Among them, four markers were identical to the markers proposed by the Pharmacopoeias (**A1**, **G1**, **SC1**, **SM1** (**Tables 2**, **4**)) for *Angelica sinensis, Glycyrrhiza uralensis, Scutellaria baicalensis* and *Smilax glabra*. Three markers were closely related (oxymatrine (**SO1**) instead of matrine for *Sophora flavescens*, emodin-8-glucoside (**PO2**) instead of emodin for *Polygonum cuspidatum,* and 1,3-dicaffeoyl-epi-quinic acid (**C3**) instead of chlorogenic acid for *Chrysanthemum indicum*. For these three cases, the pharmacopoeial markers were detected but were less abundant based on ELSD detection or not specific. Additionally, in line with recently developed *single standard to determine multi-components methods* (SSDMC) for the QC of single TCM herb (Gao et al., 2009), our workflow highlighted wogonoside (**SC2**) as a second marker for *Scutellaria baicalensis* (Wang et al., 2017), and *E*-piceid (**PO1**) for *Polygonum cuspidatum* (Yang et al., 2015).

For the three other herbs of the formula, the pharmacopoeial markers were either not detected or/and not sufficiently specific. For *Oldenlandia diffusa* and *Prunella vulgaris*, the ChP suggested triterpene aglycones, oleanolic acid and ursolic acid, respectively. Such lipophilic compounds are difficult to extract by decoction and were not detected by RP UHPLC-HRMS/MS. Our workflow formally identified a specific scandoside derivative for *Oldenlandia diffusa* (10-*O*-*p*-*cis*-coumaroyl scandoside methyl ester (**O1**)), previously described for the genus (Otsuka et al., 1991), and whose analogues were reported for this species (Chen et al., 2016). For *Prunella vulgaris*, rosmarinic acid (**PR1**) was selected as a marker in this formula (Bai et al., 2016), since its specificity could be proved by our workflow, even if this component is reported to be occurring in many plants (Petersen and Simmonds, 2003). The analyses of the other components related to **PR1** showed the presence of specific analogues that support the herb traceability (**Supplementary Figure S19** and **Supplementary Table S8**). For *Isatis tinctoria*, the ChP marker, indican, was not detected. Its PhEur marker, arginine, was present but our approach confirmed that such a primary metabolite was not specific and occurred in several herbs of the formula (**Figure 4C**, code 1). For this herb, three flavones-*C*-glycosides were found to be specific and one of them was formally identified as isovitexin (**I1**) (**Supplementary Table S5**) (Mohn et al., 2009).

Multi-Component Signature for Improved Traceability

In addition to the single marker selection, the approach has permitted highlighting multi-component signatures for most herb markers in the formula, that were presented as bar chromatograms (**Figure 7**). For QC, the ability to demonstrate the presence of multi-component signatures (or at least a few components) is required to improve the traceability of each herb in a formula (Yang et al., 2017). Improved traceability is crucial to detect cases of adulterations that add a single marker to another herb or to a herb of poor quality (Czigle et al., 2018). If QC methods using LC-MS are not yet incorporated in the Pharmacopeias, new methods attempt to incorporate these advanced techniques. Recently, methods using LC-MS were proposed to check multiple components of a given herb used in different multi-herb formulae (Si et al., 2016), as well as multiple components representing three herbs of a given formula (Yao et al., 2016). In both cases, the selected markers were followed-up by Single Ion Monitoring (SIM). The workflow proposed by our study for unbiased and specific markers selection can thus be used prior to such targeted QC method. The data generated can be transferred to techniques adapted to routine QCs by simple MS detectors for both main markers and selected multi-component signature. For this, considering the complexity of the composition of a typical TCM, the quantitation of the specific markers could be performed by targeted MS detection, either by single ion monitoring (SIM) or multiple reaction monitoring (MRM). In addition, the targeted monitoring of the multi-component signatures can be made by selecting their SIM traces or more specifically by monitoring their MRM transition.

In addition, the metabolome of an herb can vary according to its cultivation and geographical origin (Yang et al., 2017). The choice of multi-component signatures selected in this study should be validated by comparing several batches of the same herb for example by metabolomics (Marti et al., 2014; Afzan et al., 2019; Sehlakgwe et al., 2020). As an example, for *Oldenlandia diffusa*, our workflow selected specific markers from two independent chemical classes previously described for this herb but not considered by the Pharmacopoeias. A large variation of the chemical composition of this herb was observed in different QC studies (Chen et al., 2016) and further investigation are required. Then, the reproducibility of

our observations in several batches of the formula should be conducted.

Improvement and Automation of Processing Tools

However, the proposed approach has its limitations. While FBMN approaches currently allow data integration in a fast and efficient way, automatic scripts to extract the relevant data, visualize them, and choose markers do not yet exist. In the context of this work, this data extraction was done manually and semi-automatically. Software developments should enable detailed reports to be generated from the raw data, in order to provide all the reference information needed to define specific markers adapted to each TCM formula.

Another limitation concerns the identification of markers. The annotation strategy used in this study combined HRMS/MS spectra comparison with *in silico* predicted fragmentation spectra, filtering with taxonomic data and manual evaluation of the clusters. The structural assignments of the main markers were validated by targeted isolation. The obtained matching indicated that the structure annotation of the minor associated components in the formula (at least at the precise class of compounds level) is trustworthy even if isomeric structure cannot fully be ascertained (**Supplementary Tables S2–S11**). For improving the annotation process, re-ranking the annotations considering chemotaxonomic data was recently proposed (Rutz et al., 2019), and open-access spectral databases that also incorporate chemotaxonomic data should be further developed. In this direction, the concept of Digital Reference Standard (DRS) was proposed in the TCMs area (Wang et al., 2016b) and the platform MASST was launched in GNPS to fulfill this goal (Wang et al., 2020a). Furthermore, the automatic propagation of annotations in clusters has been proposed and could complement the approach used in this study (da Silva Ricardo et al., 2018).

MATERIALS AND METHODS

Plant Materials and Chemicals

All medicinal plants were obtained from Conba company (Zhejiang CONBA Pharmaceutical and Drug Research Development Corporation, Hangzhou 310052, Zhejiang, China) which purchased them to Jinhua City, China Pharmaceuticals Co., Ltd. The raw material quality was in accordance with the *Dictionary of Traditional Chinese Medicine* and the *Chinese Pharmacopoeia* according to the laws of the Chinese government. Plant names were verified with www.theplantlist.org on April 27, 2019 and are summarized in **Table 2**, which presents the codes used in this study. For the plant *Reynoutria japonica* Houtt., the synonym *Polygonum cuspidatum* was employed in the previous study (Li et al., 2013) and was used here to avoid confusion.

Rosmarinic acid standard (≥98%) was purchased from Sigma-Aldrich Inc. (Darmstadt, Germany), ligustilide and isovitexin standards (98%) from Biopurify Phytochemicals Ltd. (Chengdu, China).

Preparation of Extracts, Formula and Enriched Formula

Extracts of each single herbal drug and the mixture for the formula were prepared according to the proportions summarized in **Table 2** and employed in Li et al. (2013). The powders of single herbal drugs (10 g) were extracted in 250 ml of boiling water and formula (5 g) in 500 ml of boiling water. The extraction was done twice for 1 h in each case. After filtration, these decoctions were freeze-dried. The yields of extraction were of: *A. sinensis* 61.8%, *C. indicum* 36.7%, *G. uralensis* 26.7%, *I. tinctoria* 36.5%, *O. diffusa* 12.2%, *P. cuspidatum* 15.9%, *P. vulgaris* 7.8%, *S. baicalensis* 55.3%, *S. glabra* 22.1%, *S. flavescens*, 28.9% and of 13.7% for the formula (w/w).

The polar compounds of the prepared formula were removed by C18 solid phase extraction (SPE 1,000 mg/12 ml, Finisterre, Teknokroma, Barcelona, Spain). 100 mg of formula solubilized in distilled water were introduced in the cartridge. 10 ml of water was used to obtain an aqueous fraction and 25 ml of methanol (Fisher Scientific, Bishop, United Kingdom) eluted the retained metabolites. After drying, the yields were 65.9% ± 2.8% (w/w) for the aqueous fraction and 17.5% ± 1.2% (w/w) for the methanolic fraction. The loss was 16.5% ± 3.1% (w/w).

For marker purification, a methanolic extract has been prepared to obtain a more enriched extract in secondary metabolites than the decoction. It was obtained from the powdered mixture (200 g) by maceration (eight times 24 h in 5 L) and evaporated, giving a yield of 18.0% (w/w). This methanolic extract was subsequently fractionated into two fractions by Vacuum Liquid Chromatography (VLC) on a RP Zeoprep 60 C18 15–25 µm (Zeochem® Silicagel, Rüti, Switzerland). After equilibration with water, 3 g of extract mixed with the solid phase (1:6) was deposited and eluted with 0.6 L of water and then by 1 L of methanol. The extraction yield was 29.7% (w/w) for the aqueous fraction and 43.4% (w/w) for the methanolic fraction.

Metabolite Profiling

Preliminary Profiles

The formula was solubilized in a solution of water and methanol (7:3), whereas the enriched extract was in water and methanol (2:8), at a concentration of 5 mg/ml for UHPLC-UV-PDA-ELSD and 1 mg/ml for UHPLC-HRMS-TOF. The solutions were sonicated (15 min) and centrifuged (10 min, 6,000 rpm) (Prism R, Labnet international, Inc., Edison, NJ, United States).

Preliminary profiles, were acquired on two independent Waters Acquity UPLC systems (Waters, Milford, MA, United States), the first equipped with a Waters Micromass LCT Premier Time-Of-Flight (TOF) mass spectrometer (Waters) with an electrospray interface (ESI) and the second with UV-PDA and ELSD detections. Chromatographic systems and TOF parameters were set as previously published (Eugster et al., 2014). The second system was controlled by Empower Software v2.0, its UV-PDA acquired from 200 to 500 nm (1.2 nm of resolution) and ELSD

Sedex 85 (Sedere LT-ELSD, Alfortville, France) was set at 45°C with a gain of 8. Chromatographic traces were exported from the proprietary format to text files to be plotted on Prism 8 (GraphPad Software, Inc.) (**Figure 2**).

Optimized Profiles

In addition to the formula, freeze-dried extracts of single herbs were prepared as above (Section *Preliminary Profiles*). Optimized profiles were acquired on two independent UHPLC systems, one equipped with three in-line detections (UV-PDA, ELSD and single quadrupole) (UHPLC-UV-PDA-QMS-ELSD) and the second with HRMS/MS.

The chromatographic conditions were the same for both systems: samples were injected (2 µL) into an Acquity UPLC BEH C18 column (1.7 µm, 2.1 mm × 100 mm; Waters) and eluted (0.4 ml/min, 40°C) with water (A) and acetonitrile (B), both containing 0.1% formic acid with the following gradient: from 15 to 75% of B from 0 to 11 min (curve 7), 75–98% from 11 to 12 min, an isocratic step at 98% for 2 min and a re-equilibration step of 2 min.

Three-Detector System

Data Acquisition

A system coupling UV-PDA detection, a single quadrupole mass spectrometer (QMS) and ELSD provided all three detections with the same pump system and thus achieved stably aligned retention times. This UHPLC-UV-PDA-QMS-ELSD system allowed the data from the three detections to be efficiently linked, and in addition, to verify via the QMS the ELSD attributions performed on the UHPLC-HRMS/MS data.

The formula, the enriched formula and the 10 single herb extracts were acquired on this three-detector system. This three-detector system, controlled by MassLynx® V4.2 (Waters), was equipped with an Acquity UPLC system (Waters), which included a binary pumping system, an auto-sampler (set at 10°C), a column manager with a pre-column heater (set at 40°C), a PDA detector and an isocratic solvent manager which directed 10% of the flow to the single quadrupole (Acquity QDA, Waters) while adding a flow of 200 µL/min of water-acetonitrile (1:1) containing 0.1% formic acid. The remaining 90% of the flow was directed to an ELSD (Büchi ELS Detector C-650), set at 45°C, gain 8. The QDA, equipped with an ESI source, was set as follows in both modes: probe temperature 600°C, ESI capillary voltage 1.2 kV, cone voltage 15 V, source temperature 120°C, acquisition range 30–1,250 Da. In this setting, the greater sensitivity of the simple quadrupole allows to obtain relevant signals on the 10% of the flow coming from the column. The isocratic pump increases the flow to ensure adequate ionization by the ESI.

Evaporative Light Scattering Detection Data Treatment

The ELSD traces of each herb were integrated with MassLynx® V4.2 (Waters) and only ELSD areas equal to or greater than 0.004 µV/s were considered. A table containing UV max and MS data was prepared in order to be compared with the HRMS data presented below. To visually compare the 10 herbs in an informative graphical representation, ELSD areas of each herb were represented using Prism software as a bar plot in a superimposed manner, each color representing an herb (**Figures 5C**,D and **Supplementary Figures 2C,D**). Two area scales were chosen to illustrate the herbs with the most intense peaks (area from 0.0 to 0.4 µV/s) (*G. uralensis*, *P. cuspidatum*, *S. flavescens*, and *S. baicalensis* (**Figure 5C**) and the herbs with less intense peaks (areas from 0.00 to 0.008 µV/s (**Figure 5D**) (*C. indicum*, *I. tinctoria*, *O. diffusa*, *P. vulgaris*, *S. glabra*). The peak areas were labeled by a letter according to their source herb and by a number in order of importance of their area, from the largest to the smallest. A total of 47 ELSD peaks were detected. The numbers of ELSD peaks for each herb were of seven for *C. indicum*, nine for *G. uralensis*, two for *I. tinctoria*, eight for *O. diffusa*, four for *P. cuspidatum*, five for *P. vulgaris,* one for *S. glabra*, ten for *S. baicalensis*, and one for *S. flavescens*. No ELSD peak was detected for *A. sinensis*. Peaks not retained under RP chromatographic conditions were not considered.

High Resolution Spectrometry Analysis

The analyses were performed on an Acquity UPLC system interfaced to an Orbitrap Q-Exactive Focus mass spectrometer (Thermo Scientific) using a heated electrospray ionization source (HESI-II) and an Acquity UPLC PDA detector. Thermo Scientific Xcalibur 2.1 software was employed for instrument control. The detailed conditions are presented in **Supplementary Section S9**.

High Resolution Spectra Data Processing

ThermoRAW MS data were converted to *.mzXML* using ProteoWizzard (Kessner et al., 2008) and loaded to MZmine 2.37 (Pluskal et al., 2010; Pluskal et al., 2012). To prepare the peak lists, the ADAP workflow was employed (Myers et al., 2017), followed by a deisotoping step and an alignment step (**Supplementary Section S10** for the precise parameters). The parameters were based on those previously used in our laboratory for single herb profiling (Barthelemy et al., 2019; Rutz et al., 2019), and no specific adaptation to a multi-herb extract has been made. Finally, the peak lists were filtered to keep only peaks with HRMS/MS scan. The HRMS level, which contained the peak height and retention time data of each feature was exported to a text file, whereas the HRMS/MS level was exported as an *.mgf* file to be submitted to the online workflow at GNPS (Wang et al., 2016a).

Feature-Based Molecular Network

Molecular network (MN) were created where edges were filtered to have a cosine score above 0.7 and more than six matched peaks. Further edges between two nodes were kept in the network if and only if each of the nodes appeared in each other's respective top 50 most similar nodes. Tolerances for precursor and fragment ions were set at 0.02 Da. The spectra in the network were then searched against GNPS spectral libraries. All matches kept between network spectra and library spectra were required to have a score above 0.7 and at least six matched peaks. The GNPS job parameters are available at https://gnps.ucsd.edu/ProteoSAFe/status.jsp?task=4cffb19303354a6a814184facb930bc0

(PI) and https://gnps.ucsd.edu/ProteoSAFe/status.jsp?task=b949d909e6484ed6b6b28db4c09109ac (NI).

The next step was to compare the experimental spectra organized in the MN against an in-house *in silico Database* (ISDB-DNP) prepared from the Dictionary of the Natural Products (DNP, 2019), according to a previously reported workflow (Allard et al., 2016). To do this, the *.mgf* file from GNPS and the *.tsv* file containing the database matches from GNPS were used. A top six consultation was employed for annotating the peaks at a tolerance of 0.005 Da and a cosinus score threshold of 0.2. FBMNs were visualized with Cytoscape 3.7.0 (**Figure 3B** and **Supplementary Figure S1B**), and annotations were displayed thanks to the Chem Viz2 1.1.0. Tables from HRMS data, GNPS library and ISDB-DNP consultations were loaded in Cytoscape.

Node and Cluster Specificity

The table gathering all information in Cytoscape was then re-exported in a text file to be evaluated by an in-house Jupyter Notebook script in terms of nodes and clusters herb-specificity (**Supplementary Figure S4**). The Jupyter Notebook and the corresponding python script are available on gitlab: https://gitlab.unige.ch/Arnaud.Gaudry/node_treater. The data loaded into the script combined the MS data obtained after the alignment of the features (called the quantification table in GNPS terminology, which contained for each aligned feature its *m*/*z*, retention time and peak height(s)), with the information related to clusters (cluster numbers, called *component indexes* in GNPS terminology). First, at the node level, the relative intensity of each feature detected in the 10 herbs was calculated, allowing the description of each node in terms of contribution of each herb, referred to as a *specificity percentage*. The lists of aligned features were then reduced to features detected in the formula (deletion of the features detected in herbs but not in the formula, as well as in the blank analyses). A threshold of 90% was applied to retrieve the specific features in an individual herb extract. The number of features specific to one herb was then counted. At the cluster level, the averages of these specificity percentages were calculated, allowing the description of each cluster according to the contribution of the 10 herbs. This percentage was named the *cluster specificity percentage*. Furthermore, this in-house script could export the HRMS data (*m*/*z*, retention time and peak height) for a specific cluster, to facilitate the link between the FBMN and the metabolite profiles. The HRMS data exported by this script were then represented against the chromatogram in the form of a bar plot with Prism 8 software (**Figures 7**, **8** and **Supplementary Section S8**), referred to as *bar chromatograms*. For the clarity of some bar chromatograms, features with the same retention time within a given cluster were deleted to avoid representing in-source features (adducts, complexes and/or fragments).

Visualization in the Feature-Based Molecular Network

To visualize the contribution of each herb to the formula, the height values of the deconvoluted peaks were represented on the nodes in two layers (legend **Figure 4**). In the center of the node, a pie chart represented the formula (pale pink) and the blank analyses (white). On the external part of the node, an external ring represented the peak heights of the feature in the single herb extracts. The node size mapped the feature heights in the formula.

2D Feature Maps

The aligned table obtained previously thanks to the in-house script was exported to a *.csv* file and loaded in Microsoft Excel 16.16.8. To prepare the 2D feature map, the feature height intensities in the formula have been assigned to the features specifically detected in one herb. Features detected below the threshold of 90% were not attributed to a given herb. This feature list was plotted as a scatter plot (arbitrary plot size for **Figure 3A** and proportional to peak height intensity in **Figure 5A** in PI; **Supplementary Section S1** for NI). Features found in the formula were plotted as black circles, whereas aligned features from each herb were plotted as dots according to a color code representing each herb. Thus, a specific aligned feature was visible as a black circle surrounding a colored dot. Finally, ELSD peak areas from the single herb extract (Sections *Evaporative Light Scattering Detection data Treatment* and *Annotation Strategy*) were manually assigned to the specific features in an additional column in the aligned table. After this manual assignment, the same plot was prepared with the attributed ELSD areas (**Figure 5E**).

Annotation Strategy

The annotation strategy combined ELSD filtering, interpretation of MS, HRMS, HRMS/MS and UV-PDA spectra with chemotaxonomy information. ELSD filtering retrieved 47 peaks (Section *Evaporative Light Scattering Detection Data Treatment*). The MS data were interpreted in parallel in both modes. First, in regard to ELSD peaks, the corresponding nominal *m*/*z* were retrieved in the QMS traces (Section *Three Detector System*). These *m*/*z* were then searched in the peak lists obtained by processing the UHPLC-HRMS/MS metabolite profiles (Section *Data Acquisition*). The specificity of the peaks highlighted by ELSD was verified. The molecular formula of the specific peaks was then calculated and searched in the DNP (DNP, 2019). The number of potential structures were recovered for the species, genus, family, if previously described. These taxonomic data were then compared with the annotation obtained on HRMS/MS data by consultation of the theoretical *in silico* MS/MS spectral database (Section *Feature-Based Molecular Network*). This annotation workflow is presented with more details in **Supplementary Section S5**. The annotation results are summarized in **Supplementary Tables S2–S11** and all associated metadata are available in the Cytoscape files in doi:10.25345/C5516P including IUPAC name and InChI key.

Isolation of the Markers

In order to rapidly isolate the makers, a fractionation at high-scale on Medium Liquid Chromatography (MPLC) was implemented. A gradient optimization was performed at High Pressure Liquid Chromatography (HPLC) scale before its transfer to MPLC

(Büchi). The enriched extract was separated thanks to a HPLC system (Agilent Technologies 1260 Infinity), controlled with the software Chemstation for LC3D (Agilent Technologies), equipped with UV-PDA detection and ELSD (Sedex LT-ELSD 85 (Sedere, Oliver, France)). A Zeoprep® column (A60 C18, 250 mm × 4.6 mm i.d., 15–25 mm, Zeochem) was used at a flow of 1 ml/min of water (A) and methanol (B) both with 0.1% of formic acid (Fisher Scientific, Bishop, United Kingdom). The optimized gradient was from 20 to 73% of B in 60 min, and then 73–100% in 20 min. Gradient transfer calculation (Challal et al., 2015) indicated the following MPLC conditions: 37 min of isocratic step at 20% of B, 747 min from 20 to 73% and 257 min from 73 to 100%, for a total of 19h30 of separation at a flow of 15 ml/min. The MPLC column (460 mm × 49 mm i.d.) was packed with the same solid phase as at HPLC scale. The enriched extract (7 g) (Section *Preparation of Extracts, Formula and Enriched Formula*) was introduced in MPLC by a dry load cell (Challal et al., 2015) and fractionated into 50 fractions. In order to monitor the MS features associated to the marker highlighted by the annotation strategy of the formula, all fractions and the enriched extract were checked in short chromatographic conditions with the same systems used for preliminary profiling (Section *Preliminary Profiles*), on one hand with UHPLC-UV-PDA-ELSD detection and on the other by UHPLC-HRMS-TOF, set as described in (Brillatz et al., 2018). HRMS data were converted to *.cdf* format through Databridge provided by MassLynx and loaded to MZmine. An aligned peak list was prepared as previously described, with specific parameters summarized in **Supplementary Section S10**. Annotated markers (**Supplementary Tables S2–S11**) were searched in the aligned table through their *m/z* in order to detect in which fraction(s) they were located. The ELSD traces of each fraction of interest were evaluated to verify the purity of the markers prior NMR analysis. Thus, seven targeted markers were identified directly in the MPLC fractions. Fraction M21 (82 mg) contained C2, fraction M34 (77 mg) and M35 (44 mg) contained mainly G1, fraction M31 (83 mg) mainly PO2, fraction 13 (199 mg) mainly SC1, fraction M25 (71 mg) mainly SC2, fraction M17 (83 mg) contained SM1. The ^{1}H and ^{13}C-NMR signal assignments are presented in **Supplementary Section S5**. The MS/MS spectra corresponding to these components in both ionization modes have been added to the GNPS library to be shared with the community.

Semi-Preparative Purification

To isolate targeted compounds that were not obtained in sufficient purity in the MPLC fractions, semi-preparatory purifications were performed from the MPLC fractions. First the chromatographic conditions were optimized at the HPLC analytical scale in the same system described in Section *Isolation of the Markers*, on an X-bridge C18 column (250 mm × 4.6 mm i.d., 5 µm) (Waters) equipped with a pre-column cartridge holder (20 × 4.6 i.d., Waters). The flow was set at 1 ml/min of water and methanol both with 0.1% of formic acid. The optimized LC conditions at the analytical level were geometrically transferred to semi-preparative scale (Guillarme et al., 2007; Guillarme et al., 2008; Challal et al., 2015). Semi-preparative HPLC was performed on an ARMEN Spot Prep System (Saint-Avé, France), with an X-bridge Prep C18 OBD column (250 mm × 19 mm i.d., 5 µm) (Waters) equipped with a UV detector and an ELSD Sedex 55 (Sedere). The flow rate was set at 17 ml/min. Fraction M6 yielded C1 (1.1 mg) (30% of methanol), fraction M23 yielded C4 (2.3 mg) and SC3 (1.0 mg) (40% of methanol). Fraction M14 yielded SO1 (2.9 mg) (1% of methanol) and PO1 (1.5 mg) (gradient from 2 to 50% of methanol in 30 min). Fraction M20 yielded O1 (8.5 mg) and SC1 (8.1 mg) (gradient from 45 to 75% of methanol in 30 min). Fraction M15 yielded G2 (8.3 mg) (gradient from 10 to 100% of methanol in 30 min). The ^{1}H and ^{13}C-NMR signal assignments are presented in **Supplementary Section S5**.

Spiking Experiments

To confirm the annotations of **A1**, **I1** and **PR1**, the retention time and spectra of the standards were compared with those observed in the corresponding herb extracts (*A. sinensis*, *I. tinctoria* and *P. vulgaris*) with the methods described in Sections *Optimized Profiles* and *Data Acquisition* (UHPLC-UV-PDA-QMS-ELSD). Spiking experiments were also performed (data not shown).

Characterization of Isolated Constituents

NMR spectra were recorded on a Bruker Avance III HD 600 MHz NMR spectrometer equipped with a CQI 5 mm Cryoprobe and a SampleJet automated sample changer (Bruker BioSpin). Chemical shift were reported in parts per million (δ) using the deuterated dimethyl sulfoxide (DMSO-d6) signal (δ_h 2.50; δ_c 39.5) as internal standards for ^{1}H and ^{13}C NMR, respectively, and coupling constants (J) were reported in hertz. Assignments were obtained based on two-dimensional (2D) NMR experiments (COSY, NOESY, HSQC and HMBC) (**Supplementary Section S7** for the precise descriptions).

CONCLUSION

This untargeted exploratory study provided a comprehensive characterization of the chemical composition of a complex TCM formula to study the specific contribution of each herb to the formula and to select quality control markers. It exemplified how metabolomics data can help to perceive the chemical contribution of each single herb to the final formula. The data-driven workflow proposed in this study for a given formula is innovative and could be used to investigate other TCM formulae in view of selecting specific markers and sub-markers. As discussed, the proposed method is certainly not to be used for a regular routine control, but it shows how far herb contribution can be monitored with state-of-the-art method in the field. Such analysis produces highly informative compositional data on representative batches, that can be used as a reference for designing appropriate and simpler quality control methods.

The extensive use of FBMN for quality control purposes needs to be evaluated in more detail. For this, methods should be developed to compare formulae, to evaluate and quantify their composition consistency in an automated and generic manner. This mainly required dedicated software development since data acquisition is ensured by most state-of-the-art available

platforms. With the rapid spread of molecular networking in many fields of plant analysis, integration of high-quality data with innovative automated methods and comprehensive natural products databases is expected and might be adopted in future by authorities and TCM producers.

DATA AVAILABILITY STATEMENT

The datasets presented in this study can be found in online repositories. The names of the repository/repositories and accession number(s) can be found below: https://massive.ucsd.edu/ProteoSAFe/dataset.jsp?task=a8219bbd768944e99257486adc672003, MassIVE MSV000085648.

AUTHOR CONTRIBUTIONS

JH designed and conceived the study, performed the experiments and interpreted the data, wrote the manuscript and created the figures. P-MA designed the HRMS/MS data interpretation and revised the manuscript. EQ designed the fractionation experiments and revised the manuscript. LM interpreted the NMR analyses of all isolated compounds. AG created the Jupyter notebook script to interpret HRMS and HRMS/MS data and revised the manuscript. LV performed part of the experiments of extraction and isolation. SL and RW developed the multi-herb formula. KK provided the multi-herb formula, was consulted during study design and revised the manuscript. J-LW conceived and designed the study, the experiments and the figures, wrote and revised the manuscript.

ACKNOWLEDGMENTS

The author JH would like to thank Adriano Rutz (Wolfender's research laboratory) for informal and constructive discussion concerning quality control during the project. The work in Göttingen is supported by the "Förderkreis der Forschungsstelle für Fernöstliche Medizin.

SUPPLEMENTARY MATERIAL

The Supplementary Material for this article can be found online at: https://www.frontiersin.org/articles/10.3389/fphar.2020.578346/full#supplementary-material

REFERENCES

Abdel-Aziz, H., Kelber, O., Lorkowski, G., and Storr, M. (2017). Evaluating the multitarget effects of combinations through multistep clustering of pharmacological data: the example of the commercial preparation Iberogast. *Planta Med.* 83 (14/15), 1130–1140. doi:10.1055/s-0043-116852

Abdel-Tawab, M. (2018). Do we need plant food supplements? A critical examination of quality, safety, efficacy, and necessity for a new regulatory framework. *Planta Med.* 84 (6-7), 372–393. doi:10.1055/s-0043-123764

Afzan, A., Wolfender, J.-L., Afzan, A., Kasim, N., Ismail Nor, H., Azmi, N., et al. (2019). Differentiation of Ficus deltoidea varieties and chemical marker determination by UHPLC-TOFMS metabolomics for establishing quality control criteria of this popular Malaysian medicinal herb. *Metabolomics* 15 (3), 35. doi:10.1007/s11306-019-1489-2

Allard, P.-M., Peresse, T., Bisson, J., Gindro, K., Marcourt, L., Pham, V. C., et al. (2016). Integration of molecular networking and in-silico MS/MS fragmentation for natural products dereplication. *Anal. Chem.* 88 (6), 3317–3323. doi:10.1021/acs.analchem.5b04804

Bai, Y., Xia, B., Xie, W., Zhou, Y., Xie, J., Li, H., et al. (2016). Phytochemistry and pharmacological activities of the genus Prunella. *Food Chem.* 204, 483–496. doi:10.1016/j.foodchem.2016.02.047

Barthelemy, M., Elie, N., Pellissier, L., Wolfender, J. L., Stien, D., Touboul, D., et al. (2019). Structural identification of antibacterial lipids from amazonian palm tree endophytes through the molecular network approach. *Int. J. Mol. Sci.* 20 (8). doi:10.3390/ijms20082006

Brillatz, T., Khamma, S., Marcourt, L., Righi, D., Queiroz Emerson, F., Wolfender, J.-L., et al. (2018). Zebrafish-based identification of the antiseizure nucleoside inosine from the marine diatom Skeletonema marinoi. *PLoS One* 13 (4), e0196195. doi:10.1371/journal.pone.0196195

Challal, S., Queiroz, E. F., Debrus, B., Kloeti, W., Guillarme, D., Gupta, M. P., et al. (2015). Rational and efficient preparative isolation of natural products by MPLC-UV-ELSD based on HPLC to MPLC gradient transfer. *Planta Med.* 81 (17), 1636–1643. doi:10.1055/s-0035-1545912

Chen, R., He, J., Tong, X., Tang, L., and Liu, M. (2016). The Hedyotis diffusa Willd. (Rubiaceae): a review on phytochemistry, pharmacology, quality control and pharmacokinetics. *Molecules* 21 (6), 710/711–710/730. doi:10.3390/molecules21060710

Czigle, S., Toth, J., Jedlinszki, N., Haznagy-Radnai, E., Csupor, D., and Tekelova, D. (2018). Ginkgo biloba food supplements on the European market—adulteration patterns revealed by quality control of selected samples. *Planta Med.* 84 (6-7), 475–482. doi:10.1055/a-0581-5203

da Silva Ricardo, R., Wang, M., Nothias, L.-F., van der Hooft Justin, J. J., Caraballo-Rodriguez Andres, M., Dorrestein Pieter, C., et al. (2018). Propagating annotations of molecular networks using in silico fragmentation. *PLoS Comput. Biol.* 14 (4), e1006089. doi:10.1371/journal.pcbi.1006089

Dempster, J., Jani, B., and Daly, T. (2011). Managing eczema in children—a treatment update. *J. Fam. Pract.* 60 (11), 660–668

DNP (2019). *Dictionary of natural products on DVD*. Boca Raton, FL: CRC Press, Taylor & Francis Group.

Eugster, P. J., Boccard, J., Debrus, B., Breant, L., Wolfender, J.-L., Martel, S., et al. (2014). Retention time prediction for dereplication of natural products (CxHyOz) in LC-MS metabolite profiling. *Phytochemistry* 108, 196–207. doi:10.1016/j.phytochem.2014.10.005

Gao, X.-Y., Jiang, Y., Lu, J.-Q., and Tu, P.-F. (2009). One single standard substance for the determination of multiple anthraquinone derivatives in rhubarb using high-performance liquid chromatography-diode array detection. *J. Chromatogr. A* 1216 (11), 2118–2123. doi:10.1016/j.chroma.2008.11.104

Guillarme, D., Nguyen, D. T., Rudaz, S., and Veuthey, J. L. (2007). Method transfer for fast liquid chromatography in pharmaceutical analysis: application to short columns packed with small particle. Part I: isocratic separation. *Eur. J. Pharm. Biopharm.* 66 (3), 475–482. doi:10.1016/j.ejpb.2006.11.027

Guillarme, D., Nguyen, D. T., Rudaz, S., and Veuthey, J. L. (2008). Method transfer for fast liquid chromatography in pharmaceutical analysis: application to short columns packed with small particle. Part II: gradient experiments. *Eur. J. Pharm. Biopharm.* 68 (2), 430–440. doi:10.1016/j.ejpb.2007.06.018

Guo, D. A., Wu, W. Y., Ye, M., Liu, X., and Cordell, G. A. (2015). A holistic approach to the quality control of traditional Chinese medicines. *Science* 347 (6219), S29–S31

He, X., Fang, J., Huang, L., Wang, J., and Huang, X. (2015). Sophora flavescens Ait: traditional usage, phytochemistry and pharmacology of an important traditional Chinese medicine. *J. Ethnopharmacol.* 172, 10–29. doi:10.1016/j.jep.2015.06.010

Hou, J. J., Zhang, J. Q., Yao, C. L., Bauer, R., Khan, I. A., Wu, W. Y., et al. (2019). Deeper chemical perceptions for better traditional Chinese medicine standards. *Engineering* 5 (1), 83–97. doi:10.1016/j.eng.2018.12.005

Hua, S., Liu, J., Dong, L., Huang, J., Fu, X., Zhang, Y., et al. (2018). Deeper chemical perceptions for better traditional Chinese medicine standards. *Engineering* 5 (1), 83–97. doi:10.1016/j.eng.2018.12.005

Jin, M., Zhao, K., Huang, Q., Xu, C., and Shang, P. (2018). Ethnomedicine, Phytochemistry and Pharmacology of Smilax glabra: An Important Traditional Chinese Medicine. *Am. J. Chin. Med.* 46 (2), 261–297. doi:10.1142/S0192415X18500143

Kee, C. L., Ge, X., Gilard, V., Malet-Martino, M., and Low, M. Y. (2018). A review of synthetic phosphodiesterase type 5 inhibitors (PDE-5i) found as adulterants in dietary supplements. *J. Pharm. Biomed. Anal.* 147, 250–277. doi:10.1016/j.jpba.2017.07.031

Karimov, A. M., and Botirov, E. K. (2017). Structural Diversity and State of Knowledge of Flavonoids of the Scutellaria L. *Genus. Russ. J. Bioorg. Chem.* 43 (7), 691–711. doi:10.1134/s1068162017070068

Kessner, D., Chambers, M., Burke, R., Agus, D., and Mallick, P. (2008). ProteoWizard: open source software for rapid proteomics tools development. *Bioinformatics* 24 (21), 2534–2536. doi:10.1093/bioinformatics/btn323

Li, S., Kuchta, K., Tamaru, N., Lin, Y., Iwasaki, S., Wang, R., et al. (2013). Efficacy of a novel herbal multicomponent traditional Chinese medicine therapy approach in patients with atopic dermatitis. *Forsch Komplementmed* 20 (3), 189–196. doi:10.1159/000351280

Liang, J., Wu, W.-Y., Sun, G.-X., Wang, D.-D., Hou, J.-J., Yang, W.-Z., et al. (2013). A dynamic multiple reaction monitoring method for the multiple components quantification of complex traditional Chinese medicine preparations: Niuhuang Shangqing pill as an example. *J. Chromatogr. A* 1294, 58–69. doi:10.1016/j.chroma.2013.04.016

Liu, C. X., Cheng, Y. Y., Guo, D. A., Zhang, T. J., Li, Y. Z., Hou, W. B., et al. (2017). A new concept on quality marker for quality assessment and process control of Chinese medicines. *Chin. Herb. Med.* 9 (1), 3–13. doi:10.1016/s1674-6384(17)60070-4

Lucena, R., Cardenas, S., and Valcarcel, M. (2007). Evaporative light scattering detection: trends in its analytical uses. *Anal. Bioanal. Chem.* 388 (8), 1663–1672. doi:10.1007/s00216-007-1344-6

Luyen, B. T. T., Tai, B. H., Thao, N. P., Cha, J. Y., Lee, H. Y., Lee, Y. M., et al. (2015). Anti-inflammatory components of Chrysanthemum indicum flowers. *Bioorg. Med. Chem. Lett.* 25 (2), 266–269. doi:10.1016/j.bmcl.2014.11.054

Ma, J.-P., Guo, Z.-B., Jin, L., and Li, Y.-D. (2015). Phytochemical progress made in investigations of Angelica sinensis (Oliv.) diels. *Chin. J. Nat. Med.* 13 (4), 241–249. doi:10.3724/sp.J.1009.2015.00241

Marti, G., Boccard, J., Mehl, F., Debrus, B., Marcourt, L., Merle, P., et al. (2014). Comprehensive profiling and marker identification in non-volatile citrus oil residues by mass spectrometry and nuclear magnetic resonance. *Food Chem.* 150, 235–245. doi:10.1016/j.foodchem.2013.10.103

Mohn, T., Plitzko, I., and Hamburger, M. (2009). A comprehensive metabolite profiling of Isatis tinctoria leaf extracts. *Phytochemistry* 70 (7), 924–934. doi:10.1016/j.phytochem.2009.04.019

Myers, O. D., Sumner, S. J., Li, S., Barnes, S., and Du, X. (2017). One step forward for reducing false positive and false negative compound identifications from mass spectrometry metabolomics data: new algorithms for constructing extracted ion chromatograms and detecting chromatographic peaks. *Anal. Chem.* 89 (17), 8696–8703. doi:10.1021/acs.analchem.7b00947

Nothias, L. F., Petras, D., Schmid, R., Duhrkop, K., Rainer, J., Sarvepalli, A., et al. (2020). Feature-based molecular networking in the GNPS analysis environment. *Nat. Methods* 17 (9), 905–908. doi:10.1038/s41592-020-0933-6

Otsuka, H., Yoshimura, K., Yamasaki, K., and Cantoria, M. C. (1991). Isolation of 10-acyl iridoid glucosides from a Philippine medicinal plant, Oldenlandia corymbosa L. (Rubiaceae). *Chem. Pharm. Bull.* 39 (8), 2049–2052. doi:10.1248/cpb.39.2049

Pan, H., Zhou, H., Miao, S., Cao, J., Liu, J., Lan, L., et al. (2019). An integrated approach for global profiling of multi-type constituents: comprehensive chemical characterization of Lonicerae Japonicae Flos as a case study. *J. Chromatogr. A* 1613, 460674. doi:10.1016/j.chroma.2019.460674

Pei, L., Bao, Y., Liu, S., Zheng, J., and Chen, X. (2013). Material basis of Chinese herbal formulas explored by combining pharmacokinetics with network pharmacology. *PLoS One* 8 (2), e57414. doi:10.1371/journal.pone.0057414

Peng, W., Qin, R., Li, X., and Zhou, H. (2013). Botany, phytochemistry, pharmacology, and potential application of Polygonum cuspidatum Sieb.et Zucc.: a review. *J. Ethnopharmacol.* 148 (3), 729–745. doi:10.1016/j.jep.2013.05.007

Petersen, M., and Simmonds, M. S. J. (2003). Rosmarinic acid. *Phytochemistry* 62 (2), 121–125. doi:10.1016/S0031-9422(02)00513-7

Pluskal, T., Castillo, S., Villar-Briones, A., and Oresic, M. (2010). MZmine 2: modular framework for processing, visualizing, and analyzing mass spectrometry-based molecular profile data. *BMC Bioinf.* 11, 395. doi:10.1186/1471-2105-11-395

Pluskal, T., Uehara, T., and Yanagida, M. (2012). Highly accurate chemical formula prediction tool utilizing high-resolution mass spectra, MS/MS fragmentation, heuristic rules, and isotope pattern matching. *Anal. Chem.* 84 (10), 4396–4403. doi:10.1021/ac3000418

Rutz, A., Dounoue-Kubo, M., Ollivier, S., Bisson, J., Bagheri, M., Saesong, T., et al. (2019). Taxonomically informed scoring enhances confidence in natural products annotation. *Front. Plant Sci.* 10, 1329. doi:10.3389/fpls.2019.01329

Sehlakgwe, P. F., Lall, N., and Prinsloo, G. (2020). H-1-NMR metabolomics and LC-MS analysis to determine seasonal variation in a cosmeceutical plant Leucosidea sericea. *Front. Pharmacol.* 11. doi:10.3389/fphar.2020.00219

Si, W., Yang, W., Guo, D., Wu, J., Zhang, J., Qiu, S., et al. (2016). Selective ion monitoring of quinochalcone C-glycoside markers for the simultaneous identification of Carthamus tinctorius L. in eleven Chinese patent medicines by UHPLC/QTOF MS. *J. Pharmaceut. Biomed. Anal.* 117, 510–521. doi:10.1016/j.jpba.2015.09.025

Skalicka-Wozniak, K., Georgiev, M. I., and Orhan, I. E. (2017). Adulteration of herbal sexual enhancers and slimmers: the wish for better sexual well-being and perfect body can be risky. *Food Chem. Toxicol.* 108 (Pt B), 355–364. doi:10.1016/j.fct.2016.06.018

Sumner, L. W., Amberg, A., Barrett, D., Beale, M. H., Beger, R., Daykin, C. A., et al. (2007). Proposed minimum reporting standards for chemical analysis. Chemical analysis working group (CAWG) metabolomics standards initiative (MSI). *Metabolomics* 3 (3), 211–221. doi:10.1007/s11306-007-0082-2

Wang, F., Wang, B., Wang, L., Xiong, Z.-Y., Gao, W., Li, P., et al. (2017). Discovery of discriminatory quality control markers for Chinese herbal medicines and related processed products by combination of chromatographic analysis and chemometrics methods: Radix Scutellariae as a case study. *J. Pharm. Biomed. Anal.* 138, 70–79. doi:10.1016/j.jpba.2017.02.004

Wang, M., Carver, J. J., Phelan, V. V., Sanchez, L. M., Garg, N., Peng, Y., et al. (2016a). Sharing and community curation of mass spectrometry data with global natural products social molecular networking. *Nat. Biotechnol.* 34 (8), 828–837. doi:10.1038/nbt.3597

Wang, M., Jarmusch, A. K., Vargas, F., Aksenov, A. A., Gauglitz, J. M., Weldon, K., et al. (2020a). Mass spectrometry searches using MASST. *Nat. Biotechnol.* 38 (1), 23–26. doi:10.1038/s41587-019-0375-9

Wang, Q., Sun, L., Liu, F., Jin, H., Yu, J., Dai, Z., et al. (2016b). Progress and challenges of reference standard and its new form: digital reference standard. *Chin. Med.* 07 (02), 77–91. doi:10.4236/cm.2016.72010

Wang, X., Zhang, H., Chen, L., Shan, L., Fan, G., and Gao, X. (2013). Liquorice, a unique "guide drug" of traditional Chinese medicine: a review of its role in drug interactions. *J. Ethnopharmacol.* 150 (3), 781–790. doi:10.1016/j.jep.2013.09.055

Wang, X.-B., Zheng, J., Li, J.-J., Yu, H.-Y., Li, Q.-Y., Xu, L.-H., et al. (2018). Simultaneous analysis of 23 illegal adulterated aphrodisiac chemical ingredients in health foods and Chinese traditional patent medicines by ultrahigh performance liquid chromatography coupled with quadrupole time-of-flight mass spectrometry. *J. Food Drug Anal.* 26. doi:10.1016/j.jfda.2018.02.003

Wang, Y. M., Fan, Q., Xiang, J., Huang, H. B., Chen, S., Liu, B. R., et al. (2020b). Structural characterization and discrimination of Paris polyphylla var. yunnanensis by a molecular networking strategy coupled with ultra-high-performance liquid chromatography with quadrupole time-of-flight mass spectrometry. *Rapid Commun. Mass Spectrom.* 34 (11). doi:10.1002/rcm.8760

Wang, Z., Kim, U., Liu, J., Cheng, C., Wu, W., Guo, S., et al. (2019). Comprehensive TCM molecular networking based on MS/MS in silico spectra with integration

of virtual screening and affinity MS screening for discovering functional ligands from natural herbs. *Anal. Bioanal. Chem.* 411 (22), 5785–5797. doi:10.1007/s00216-019-01962-4

WHO (2007). *WHO guidelines on good manufacturing practices (GMP) for herbal medicines*. Geneva, Switzerland: World Health Organization.

Wolfender, J.-L., Nuzillard, J.-M., van der Hooft, J. J. J., Renault, J.-H., and Bertrand, S. (2019). Accelerating metabolite identification in natural product research: toward an ideal combination of liquid chromatography–high-resolution tandem mass spectrometry and NMR profiling, in silico databases, and chemometrics. *Anal. Chem.* 91 (1), 704–742. doi:10.1021/acs.analchem.8b05112

Wu, X., Zhang, H. B., Fan, S. S., Zhang, Y. D., Yang, Z., Fan, S. M., et al. (2018). Quality markers based on biological activity: a new strategy for the quality control of traditional Chinese medicine. *Phytomedicine* 44, 103–108. doi:10.1016/j.phymed.2018.01.016

Yang, T.-W., Zhao, C., Fan, Y., Qi, L.-W., and Li, P. (2015). Design of ultraviolet wavelength and standard solution concentrations in relative response factors for simultaneous determination of multi-components with single reference standard in herbal medicines. *J. Pharm. Biomed. Anal.* 114, 280–287. doi:10.1016/j.jpba.2015.05.028

Yang, W., Zhang, Y., Wu, W., Guo, D., Huang, L., and Liu, C. (2017). Approaches to establish Q-markers for the quality standards of traditional Chinese medicines. *Acta Pharm. Sin. B* 7 (4), 439–446. doi:10.1016/j.apsb.2017.04.012

Yao, C., Yang, W., Si, W., Pan, H., Qiu, S., Wu, J., et al. (2016). A strategy for establishment of practical identification methods for Chinese patent medicine from systematic multi-component characterization to selective ion monitoring of chemical markers: Shuxiong tablet as a case study. *RSC Adv.* 6 (69), 65055–65066. doi:10.1039/c6ra10883k

Conflict of Interest: The authors declare that the research was conducted in the absence of any commercial or financial relationships that could be construed as a potential conflict of interest.

frontiers in Pharmacology

ORIGINAL RESEARCH
published: 14 January 2021
doi: 10.3389/fphar.2020.622787

Synergistic Effects of Cryptotanshinone and Senkyunolide I in Guanxinning Tablet Against Endogenous Thrombus Formation in Zebrafish

Jun Li[1], *Hao Liu*[1], *Zhenzhong Yang*[1], *Qingqing Yu*[2], *Lu Zhao*[1]* *and Yi Wang*[1,3]

[1]Pharmaceutical Informatics Institute, College of Pharmaceutical Sciences, Zhejiang University, Hangzhou, China, [2]The Department of Medicine, Chiatai Qingchunbao Pharmaceutical Co., Ltd., Hangzhou, China, [3]State Key Laboratory of Component-Based Chinese Medicine, Tianjin, China

Thrombosis is a key pathological event in cardiovascular diseases, and is also the most important targeting process for their clinical management. New drug development in thrombosis treatment is still in great demand. According to the traditional Chinese medicine (TCM) theory, thrombosis belongs to the syndrome of blood stasis. *Salvia miltiorrhiza* Bunge and *Ligusticum striatum* DC. are two common TCM herbs with long-term documented function in promoting blood circulation and inhibiting thrombosis, especially when used together. Guanxinning Tablet, a modern Chinese drug which contains extracts of the two herbs, also showed strong therapeutic effects in coronary heart disease. However, the pharmacological mechanism is still lacking for the compatibility of the two herbs. Here, through zebrafish-based *in vivo* fluorescence screening, we demonstrated the synergistic effects between *S. miltiorrhiza* Bunge and *L. striatum* DC. in regulating endogenous thrombosis. Moreover, combined with high-resolution mass spectrometry, the main compounds of the botanical drugs were analyzed and screened in our model system. Interestingly, cryptotanshinone and senkyunolide I, two representative compounds, respectively derived from the two herbs, also showed synergistic antithrombotic effects. Further analysis suggested that they may regulate thrombi formation at different levels *via* multiple signaling pathways, including oxidative stress, platelet activation and coagulation cascade. Taken together, our findings provided solid biological supports toward the drug compatibility theory of TCM, and suggested cryptotanshinone and senkyunolide I as promising drug candidates in thrombosis management.

Keywords: thrombosis, coronary artery disease, senkyunolide I, cryptotanshinone, oxidative stress, zebrafish, multimodal identification

OPEN ACCESS

Edited by:
Ke-Wu Zeng,
Peking University, China

Reviewed by:
Jianbo Wan,
University of Macau, China
Ying Cao,
Tongji University, China

***Correspondence:**
Lu Zhao
lzhao@zju.edu.cn

Specialty section:
This article was submitted to Ethnopharmacology, a section of the journal Frontiers in Pharmacology

Received: *29 October 2020*
Accepted: *11 December 2020*
Published: *14 January 2021*

Citation:
Li J, Liu H, Yang Z, Yu Q, Zhao L and Wang Y (2021) Synergistic Effects of Cryptotanshinone and Senkyunolide I in Guanxinning Tablet Against Endogenous Thrombus Formation in Zebrafish. Front. Pharmacol. 11:622787. doi: 10.3389/fphar.2020.622787

Abbreviations: CAD, coronary artery disease; CI, combination index; COX1, cyclooxygenase-1; fgb, fibrinogen beta chain; GXNT, guanxinning tablet; HRMS, high resolution mass spectrometry; MDA, maldondialdehyde; NETs, neutrophil extracellular traps; PHZ, phenylhydrazine; PTGS1, prostaglandin-endoperoxide synthase one; TCM, traditional Chinese medicine; tnf-α, tumor necrosis factor α; TxA2, thromboxane A2; VET, venous thromboembolism.

INTRODUCTION

Thrombosis is the key pathological process in coronary artery disease (CAD), which remains the leading cause of global DALYs for 30 years. The breakage of atherosclerosis plaque may lead to artery blockage, which triggers heart attack, stroke or sudden death. Venous thromboembolism (VET) is also a common type of cardiovascular disease, which usually develops in patients with major trauma. Besides, multiple epidemiological studies reported increased incidence of VET in patients with a history of arterial cardiovascular events or with family history of myocardial infraction (Braekkan et al., 2008; Sørensen et al., 2009). Although whether arterial and venous thrombosis are linked processes is still controversial, the comorbidity of VET in coronary artery diseases makes the treatment even more challenging.

As plaque rupture-initiated platelet activation is usually regarded as the first step in an acute coronary event, antiplatelet therapies are mainly used in the clinical management of CAD. Aspirin, for example, is a well-established antiplatelet drug in the secondary prevention of CAD patients, which irreversibly inhibits cyclooxygenase-1 (COX1), also named as prostaglandin-endoperoxide synthase 1 (PTGS1), and suppresses the biosynthesis of thromboxane A2 (TxA2) (Depta and Bhatt, 2015). Nevertheless, the intravascular imaging-based PROSPECT study only detected <5% of thin-capped fibroatheroma actually ruptured and provoked an acute coronary event during a 3.4 years observation period (Stone et al., 2011), suggesting that plaque rupture may not be the only cause. On the other hand, the role of superficial erosion of plaques was gradually recognized in CAD, which may involve multiple processes including endothelial damage and innate immune activation (Libby et al., 2019). Therefore, conjunctive therapeutic approaches, including antiplatelet agents, anti-inflammation therapies, immunoregulators, and anticoagulant drugs, may bring more benefits for CAD patients.

Traditional Chinese medicine (TCM) has millennial practical experiences in using a combination of medicinal herbs in the treatment of various diseases. For example, according to the TCM compatibility theory, the combined usage of *Salvia miltiorrhiza* Bunge (*S. miltiorrhiza*) and *Ligusticum striatum* DC. (*L. striatum*) leads to enhanced efficacy in promoting blood circulation and resolving hemostasis, and was traditionally applied in the treatment of patients with typical CAD symptoms. Indeed, Guanxinning Tablet (GXNT), which is composed of extracts from the above two plants, showed significant effects in the clinical management of CAD. A multicenter RCT study in 160 CAD patients demonstrated greatly enhanced performance in the exercise tolerance test, along with reduced angina pectoris symptoms and improved ECG results in the GXNT group, compared with the placebo group (Sun et al., 2019). Nevertheless, due to the complicate composition in naturally derived materials, whether or how the two consisting herbs of GXNT cooperatively regulate CAD is still largely unclear.

The purpose of the current study is to examine the role of GXNT, and the cooperative effects of its main components, in the treatment of thrombosis. In order to dynamically observe the endogenous blood circulation, we took advantage of the zebrafish model system. The movement of fluorescent-labeled erythrocytes can be conveniently detected in *Tg* (*LCR:eGFP*) transgenic zebrafish (Ganis et al., 2012). Besides, the capability of percutaneous oxygen absorption in early-stage zebrafish embryos allows them to survive for a long time even without functional blood circulation, which provides valuable time window for the efficacy evaluation of anti-thrombotic agents. The zebrafish thrombosis model was induced by phenylhydrazine (PHZ), which is known to cause oxidative damage and endothelial dysfunction (Jain, 1985; Sato et al., 2015) and used as a thrombosis inducer in different animal models (Sato et al., 2009; Zhu et al., 2016). Combining the methods of high-resolution mass spectrometry and the high-efficient *in vivo* screening system, we identified major chemical compounds in GXNT, and evaluated their anti-thrombotic effects in the zebrafish model. A positive combination effect between cryptotanshinone and senkyunolide I, two representative compounds from the two GXNT herbs, was identified in the regulation of thrombogenesis, which possibly functions through mediating oxidative stress, platelet activation and coagulation cascade. These findings provided biological evidences toward the pharmacological mechanism of GXNT in CADs, and suggested novel drug combinations for antithrombotic therapy.

MATERIALS AND METHODS

Animal Care Ethics

All zebrafish experiments were conducted according to the guidelines of Animal Ethics Committee of the Laboratory Animal Center, Zhejiang University.

Zebrafish Husbandry

Wildtype TU strain, *Tg* (*LCR: EGFP*) (Ganis et al., 2012) and *Tg* (*CD41: EGFP*) (Lin et al., 2005) transgenic zebrafish were all obtained from the Laboratory Animal Center of Zhejiang University. Zebrafish were maintained following standard protocols (Westerfield, 2007). E3 medium (0.29 g/l NaCl, 0.013 g/l KCl, 0.048 g/l $CaCl_2$ $2H_2O$, 0.082 g/l $MgCl_2$ $6H_2O$, pH 7.2) was used as the embryo medium. Embryos were obtained through natural spawning.

Chemicals and Reagents

PHZ (G1324044) was purchased from Aladdin company of Shanghai, China. 1-phenyl 2-thiourea (PTU, P7629) and Ethyl 3-aminobenzoate methanesulfonate (Tricaine, E10521) were purchased from Sigma-Aldrich company of United States. DCFH-DA (MA0219) and Aspirin (MB1790) were purchased from Dalian Meilun Biotechnology Company, China. MDA (S0131) was purchased from Beyotime Company of Shanghai, China. Cryptotanshinone was purchased from Winherb Medical Technology Company of Shanghai, China. Salvianolic acid B (B20261), Danshensu (B20254), Rosmarinic acid (B20862), Ferulic acid (B20007), Senkyunolide I (B21463) were

purchased from Shanghai Yuanye Biotechnology Co., Ltd. (Shanghai, China). The purity of the six compounds are all greater than 98%.

Preparation of GXNT and Herbal Extracts

GXNT and herb extracts were manufactured by Chiatai Qingchunbao Pharmaceutical Co. Ltd. (Hangzhou, China, Batch No. 201912), according to the Standard of National Medical Products Administration of China (YBZ00342016). Briefly, the rhizome of *S. miltiorrhiza* Bunge, *L. striatum* DC. or the two herbal compositions at 1:1 wt ratio (for GXNT), was collected and then extracted with water twice. The extracts were combined and concentrated, and then precipitated by adding alcohol. The insoluble substance was removed through a filter, and the filtrate was further concentrated to a relative density between 1.30 and 1.35 at 50°C. Finally, the concentrated extracts were dried to powder in a vacuum drying oven.

UPLC-HRMS Analysis

GXNT was analyzed on a UPLC (Waters, Milford, MA, United States) coupled with a Q-Exactive™ Focus mass spectrometer (Thermo Scientific, Bremen, Germany). Chromatographic separation was performed on a Waters BEH C18 (100 mm × 2.1 mm, 1.7 μm) with acidified water with 0.15% formic acid and acetonitrile with 0.15% formic acid as mobile phases A and B at 30°C. The following solvent gradient was adopted: 0 min, 2% B; 8 min, 98% B. The flow rate was set at 0.6 ml/min, and a volume of 6 μl was injected for the analysis. The parameters for mass spectrometer were as follows: curtain gas, 30 psi; Gas 1 (N2), 55 psi; Gas 2 (N2), 55 psi; ion spray voltage, 3.5 kV (positive mode); 2.5 kV (negative mode) temperature, 350°C; scan range, m/z 120–1,500.

Molecular Networking

Mass data were processed by MZmine2 and corresponding molecular networking was created according to the online workflow at GNPS (http://gnps.ucsd.edu) (Wang et al., 2016) with a parent mass tolerance of 0.02 Da and an MS/MS fragment ion tolerance of 0.02 Da, the minimum cluster size of one, run MScluster and filter precursor window tools were turned off. The network created with cosine score above 0.7 and more than four matched peaks. The spectra in the network were then searched against GNPS spectral libraries. The molecular networking data were visualized using Cytoscape (ver. 3.7.2).

Zebrafish Thrombosis Modeling and Drug Treatment

Adult, sexually mature zebrafish were used to generate embryos. Healthy fertilized embryos were selected by microscopic examination and then raised in embryo medium containing PTU (0.2 mM) at 28°C for 2 days to inhibit melanization as described before (Karlsson et al., 2001). Zebrafish embryos of 60 h post fertilization (60 hpf) were collected into a 12-well microplate (12–15 fish per well), and were treated with aspirin (30 μg/ml), GXNT (1 mg/ml), *S. miltiorrhiza* (312 μg/ml), *L. striatum* (463 μg/ml), compounds (Cryptotanshinone 1 μg/ml, Ferulic Acid 25 μg/ml, and 50 μg/ml for all the other compounds), or compound combination (Cryptotanshione 1 μg/ml + Senkyunolide I 50 μg/ml) for 24 h. The concentration of GXNT was determined by its toxicity in zebrafish embryos, and the concentration of herbs was calculated based on their respective contents in the GXNT extract. For all chemical compounds, their concentrations were determined combinedly according to their toxicity in zebrafish embryos and solubility in the embryo medium. A sub-maximal tolerable dosage without inducing any general developmental defects was chosen for each compound. Dimethyl sulfoxide (DMSO, 0.1% v/v final concentration) was used as negative control. At the 84 hpf stage, the larvae were washed three times with fish water, and treated with PHZ (0.75 μM) for another 12 h. After PHZ treatment, the embryos were anesthetized and transferred into 96-well microplate (one fish per well) and images were acquired under Leica DMI 3000B inversed microscope system (Leica Microsystems Inc., United States).

Quantification of Blood Flow and Circulating Platelets

The blood flow and circulating platelets were analyzed in *Tg* (*LCR:eGFP*) and *Tg* (*CD41:eGFP*) transgenic embryos, respectively. Embryos were anesthetized in 0.016% Tricaine during imaging. A video was taken at a speed of 50 frame/s for each embryo. For image analysis, a representative measurement area of the vein is manually located and the number of red blood cells passing through the vessel at a given point in all 50 frames is manually counted for each embryo. At least eight embryos were examined for treatment condition. Platelets were counted in the same way as erythrocytes, and the number of platelets passing through the blood vessel of representative sites was calculated in all 50 frames.

Flow Cytometry

3.5 dpf *Tg* (*LCR:eGFP*) embryos with respective treatment were collected with at least 30 embryos in each group. FACS sorting of red blood cell (GFP positive) was performed on ACEA NovoCyteTM (ACEA Biosciences, United States). All steps were performed at 4°C.

ROS Measurement

Zebrafish embryos were incubated with 10 μM DCFH-DA solution for 30 min in the dark at 28.5°C. Afterward, the embryos were rinsed with E3 media and imaged with (SparkCyto, TECAN). The fluorescence intensity of individual larva was quantified using the Image J program (v1.8.0).

MDA Analysis

Four days post fertilization embryos were collected and grinded manually in PBS. The level of MDA was analyzed by the MDA Detection Kit (S0131, Beyotime, China), and measured by Tecan Infinite M1000 PRO microplate reader (Tecan, Switzerland). At least 30 embryos were measured as one biological repeat, and three biological repeats were performed for each treatment condition.

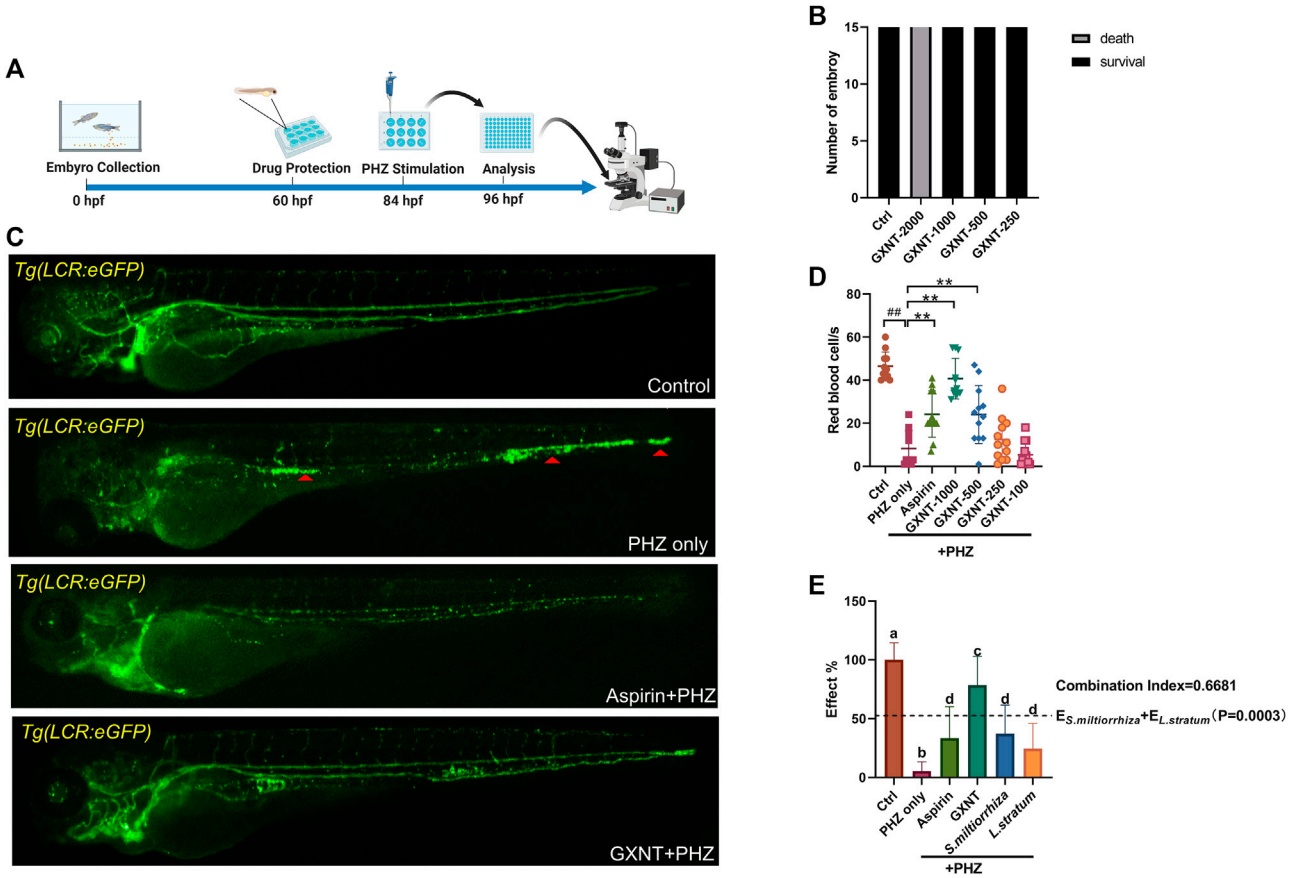

FIGURE 1 | GXNT restored blood circulation in PHZ-stimulated zebrafish thrombosis model. **(A)** Time line of drug protection and PHZ treatment. **(B)** Toxicity effects of different doses of GXNT on fish survival and general development. **(C,D)** Representative images **(C)** and quantification **(D)** of erythrocytes circulation in Tg (LCR:eGFP) fish embryos with different treatment. The concentration for the GXNT group was 1 mg/ml. Red triangles marked erythrocytes aggregation. $^{\#}$Compared with the control group; *compared with the model group; $^{\#\#}$ or $^{**}p < 0.01$. **(E)** Comparison of the therapeutic effects in blood circulation between embryos treated with single herb and GXNT. Groups labeled without a common letter were significantly different ($p < 0.05$). The p-value of t-test comparing the observed effect with the additive effect is shown on **(E)**.

mRNA Extraction and QPCR

Total RNA of zebrafish embryos was extracted by a RNA-Quick Purification Kit (RN001, ES Science), and then converted to single strand cDNA with HiFiScript cDNA Synthesis Kit (CW2569M, CWBIO). Real-time PCR was performed using the two-step quantitative RT-PCR method with 2 X SYBR Green qPCR Mater Mix (B21202, Bimake). The sequences of all primers used in the study are listed in **Supplementary Table S1**.

Statistics

All data are presented as the mean ± the standard error of the mean. Differences between two groups were analyzed using the two-tailed Student's t-test. Multiple group comparison was conducted by one-way ANOVA. A p value <0.05 was considered as statistically significant. For the test of drug combination effect, the Bliss independent model was used (Bliss, 2008; Foucquier and Guedj, 2015). For each group, the rescue effects E was calculated by (number of RBC/s in the treatment group)/(number of RBC/s in the control group) × 100%. The observed drug combination effect is expressed as E_{AB} ($0 \le E_{AB} \le 1$), and the expected additive effect is represented by the probabilistic independence general formula: $E_A + E_B(1 - E_A) = E_A + E_B - E_A E_B$, where $0 \le E_A \le 1$ and $0 \le E_B \le 1$. t-test was performed to compare the observed effect with the additive effect, and the p-value was shown on corresponding figures. The resulting Combination Index (CI) was also displayed on the figures, which can be calculated as: $CI = \frac{E_A + E_B - E_A E_B}{E_{AB}}$. When CI < 1, the combination effect is greater than the expected additive effect.

RESULTS

GXNT Restored the Circulation of Erythrocytes and Platelets in PHZ-Stimulated Zebrafish

As previously reported, the peripheral blood flow was gradually slowed down and become obviously obstructed

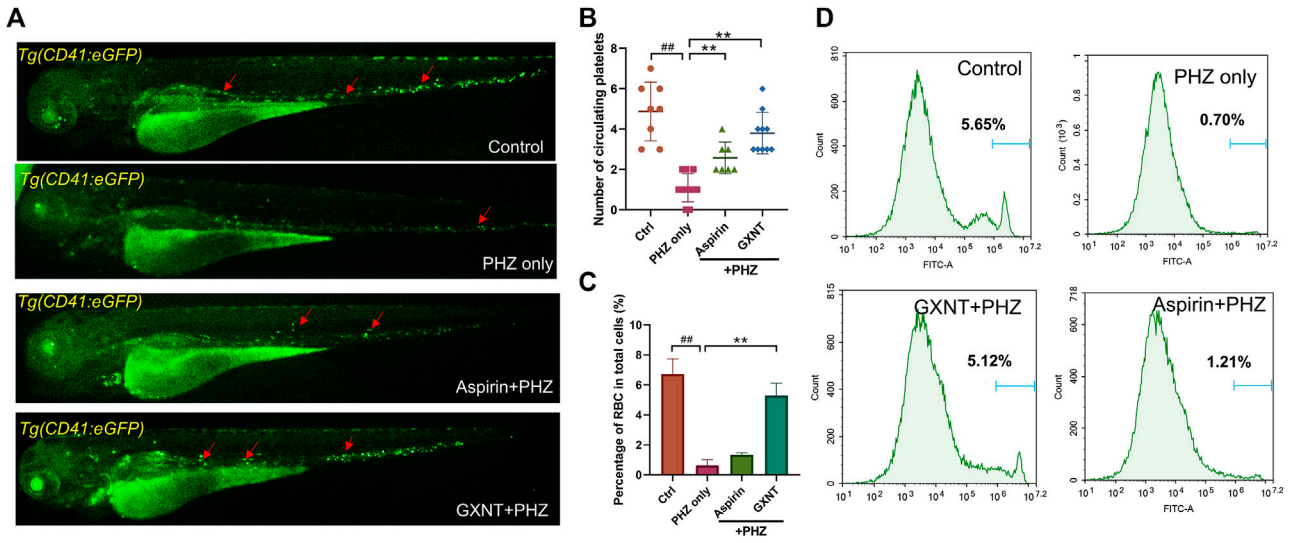

FIGURE 2 | GXNT restored platelet circulation and inhibited hemolysis in PHZ-stimulated zebrafish thrombosis model. **(A,B)** Representative images **(A)** and quantification **(B)** of platelets circulation in Tg (CD41:eGFP) fish embryos with different treatment. Red arrows marked circulating platelets. **(C,D)** Percentage of GFP labeled erythrocytes of Tg (LCR:eGFP) fish embryos with different treatment. #Compared with the control group; *compared with the model group; ## or $^{**}p < 0.01$.

in the embryos of erythrocyte-labelled *Tg* (*LCR:eGFP*) transgenic zebrafish lines after 12 h incubation in 0.75 μM PHZ solution (**Figure 1C**; **Supplementary Videos S1, S2**), indicating thrombi formation, so we continued to examine the efficacy of GXNT on this model. Toxicity analysis suggested that within a range of 100 μg/ml to 1 mg/ml, GXNT incubation from 60 to 84 hpf showed no observable effect on the survival or general development of zebrafish embryos, so the maximum concentration for subsequent studies was set to be 1 mg/ml (**Figure 1B**). Next, we added the 24-h GXNT treatment step before PHZ stimulation, and evaluated its effects on endogenous blood circulation (**Figure 1A**). Through quantification analysis of erythrocyte movement based on fluorescent imaging, a significant restoration of blood flow was observed in the embryos protected by GXNT in a dose-dependent manner, with 1 mg/ml concentration providing the best rescue effects, and 30 μg/ml aspirin was used as a positive drug (**Figure 1C,D**; **Supplementary Videos S3, S4**). In order to inquire whether platelets also participate in PHZ-induced haemostasis, the effect of GXNT was tested in the platelet-labelled *Tg* (*CD41:eGFP*) transgenic line. Noticeably, the number of circulating platelets was largely reduced after PHZ stimulation, but was strongly recovered after GXNT or aspirin treatment (**Figures 2A,B**; **Supplementary Videos S6–S9**), suggesting that platelet activation and aggregation were also involved in PHZ-induced thrombogenesis, and GXNT may negatively regulate these processes.

Aside from being a haemostasis inducer, PHZ has a well-established role in haemolysis caused by the oxidative damage to erythrocytes membrane (Chen and Collier, 1951). Indeed, considerable reduction in the number of erythrocytes was detected in PHZ treated embryos, and aspirin treatment failed to rescue the process. Interestingly, GXNT protection dramatically inhibited the haemolytic phenotype caused by PHZ, suggesting the multi-target effects of GXNT (**Figures 2C,D**).

S. miltiorrhiza and *L. striatum* Treatment Alone Showed Reduced Anti-thrombotic Effects

GXNT is consisted of extracts from two naturally derived herbs, *S. miltiorrhiza* and *L. stratum*, according to the traditional drug compatibility theory of TCM. Despite positive clinical results were reported for GXNT in the treatment of thrombotic diseases (Sun et al., 2019), whether its effect does require the combination of both herbs remains unclear from the view of modern science. In order to test the validity of this drug combination, we compared the separate effects of *S. miltiorrhiza* and *L. stratum* single treatment side-by-side with GXNT in our model system. The respective dosage of the single herb extract used in the comparison test was consistent with its respective contents in the GXNT total extract. Markedly, compared to the robust capability of GXNT in restoring the blood flow in PHZ-stimulated embryos, *S. miltiorrhiza* and *L. stratum* only have a mild to medium level anti-thrombotic effect when used by itself (**Figure 1E**). Moreover, statistical significance was detected between GXNT's effect and the additive effects of *S. miltiorrhiza* and *L. stratum*, which indicated the existence of synergistic effects between the two herbs. Thus, these results provided biological supports regarding to the combinational usage of *S. miltiorrhiza* and *L. stratum* in the regulation of thrombosis.

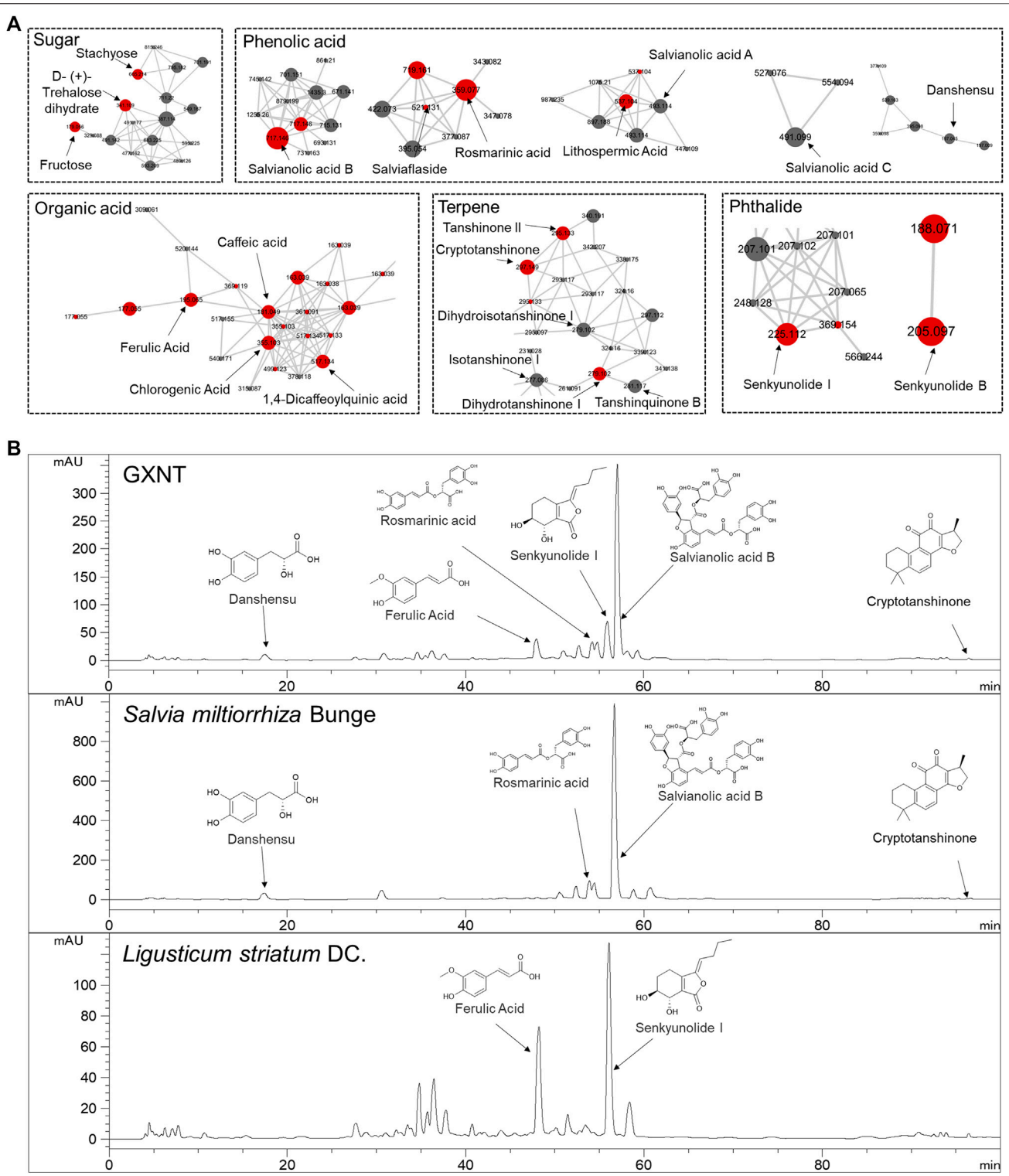

FIGURE 3 | Characterization of the chemical composition in GXNT. **(A)** Molecular networking of GXNT, the main clusters consist of sugar, phenolic acid, terpene. GNPS library annotated nodes are represented in red. **(B)** HPLC chromatogram of GXNT, *Salvia miltiorrhiza* Bunge and *Ligusticum striatum* DC.

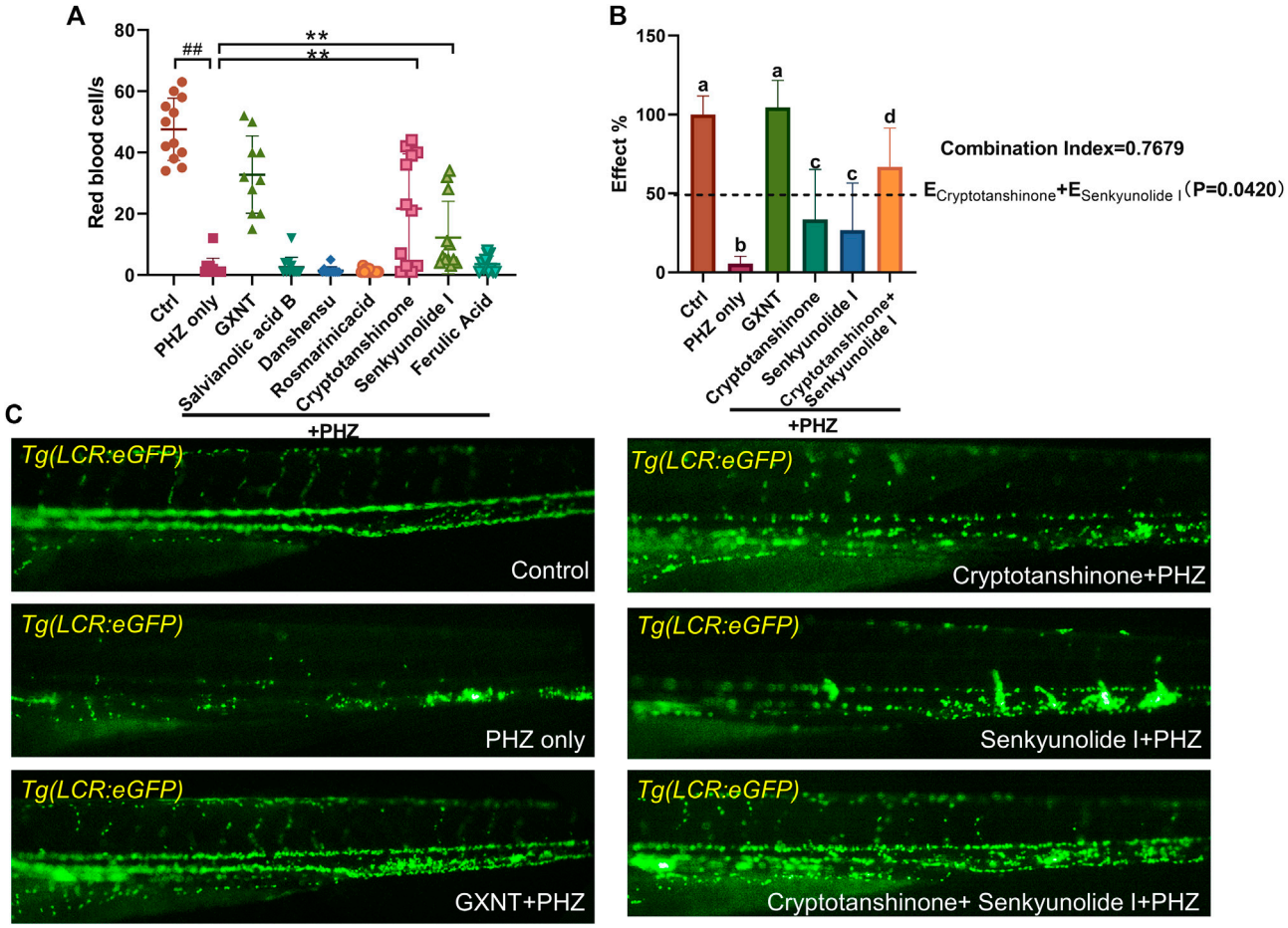

FIGURE 4 | Cyptotanshinone and senkyunolide I showed synergistic anti-thrombotic effects in PHZ-stimulated zebrafish. **(A)** Quantification of erythrocytes circulation in Tg (LCR:eGFP) fish embryos treated with different compounds. $^{\#}$Compared with the control group; *compared with the model group; $^{\#\#}$ or $^{**}p < 0.01$. **(B,C)** Representative images **(C)** and quantification **(B)** of erythrocytes circulation in Tg (LCR:eGFP) fish embryos with labeled treatment. Groups labeled without a common letter were significantly different ($p < 0.05$). The p-value of t-test comparing the observed effect with the additive effect is shown on **(B)**.

Characterization of Chemical Constituents in GXNT and Its Composing Herbs

Next, in order to inquiry what the chemical compounds are that mediate the anti-thrombotic effects of GXNT and its composing herbs, the main chemical constituents in GXNT were analysed by mass spectrometry. A rapid profiling of GXNT was performed by high resolution mass spectrometry (HRMS) on both positive and negative modes, and the mass data was processed by MZmine2 software to recognize individual ion peaks and the corresponding MS/MS data. Subsequently, the molecular networking of GXNT was created using the processed data (**Figure 3A**). After GNPS spectral libraries searching and literatures comparison based on the m/z and predicted molecular formula, a total of 43 compounds were temporary identified (**Supplementary Figure S1, Table S2**). The compounds of sugar, phenolic acid and terpene constructed the main clusters.

To further determine the composition and herbal origins of these compounds in GXNT, we optimized the chromatographic conditions on HPLC-MS for better separation, and analysed GXNT, together with its composing herbs *S. miltiorrhiza* and *L. stratum* (**Figure 3B**). As a result, danshensu, protocatechualdehyde, rosmarinic acid, lithospermic acid, salvianolic acid B, salvianolic acid A, salvianolic acid C are main GXNT compounds originated from *S. miltiorrhiza*, while senkyunolide B, chlorogenic acid, cryptochlorogenic acid, caffeic acid, ferulic acid, senkyunolide I, ligustilide are identified from *L. stratum*. Based on the results, we selected five compounds (danshensu, ferulic acid, rosmarinic acid, senkyunolide I, salvianolic acid B) of the major peaks and crytotanshinone (based on our previous findings (Sheng et al., 2020) for standard reference comparison and further study (**Supplementary Figure S2**).

In Vivo Screening Identified the Synergistic Anti-Thrombotic Effects Between Senkyunolide I and Cryptotanshinone

We continued to screen for the active GXNT compounds with anti-thrombotic effects in the zebrafish thrombosis model. The endogenous blood flow was used as the readout. Notably,

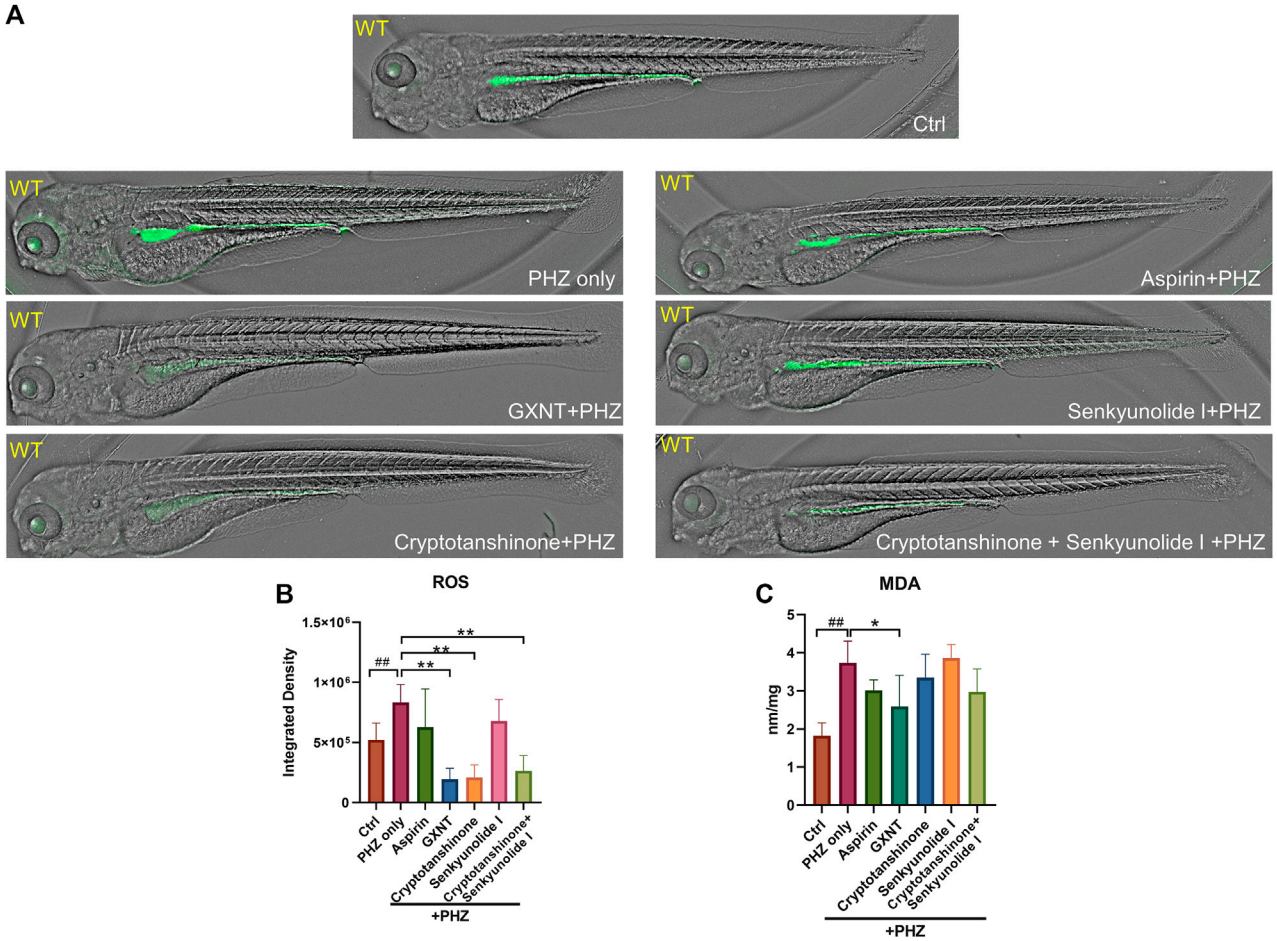

FIGURE 5 | GXNT and cryptotanshinone inhibits oxidative damages in PHZ-stimulated zebrafish. **(A,B)** Representative images **(A)** and quantification **(B)** of the fluorescence signals of DCFH-DA probe in 3.5 dpf control embryos or PHZ treated embryos with or without drug protection. **(C)** Concentration of MDA in embryos with different treatment. #Compared with the control group; *compared with the model group; *$p < 0.05$, ## or **$p < 0.01$.

senkyunolide I and cryptotanshinone were capable to significantly suppress PHZ-induced thrombogenesis, whereas the rest five compounds failed to display any detectable effects when used alone (**Figure 4A**). Since cryptotanshinone is a representative compound in *S. miltiorrhiza*, and senkyunolide I is primarily derived from *L. stratum*, we inquired if any cooperative effect exists between the two compounds, which may contribute to the synergistic effects of the two plants that we observed earlierly. Thus, the effects of combined usage of senkyunolide I and cryptotanshinone were examined and compared side-by-side with the effects of single administration. As anticipated, when used together, senkyunolide I and cryptotanshinone showed further increased effects in anti-thrombosis than that of each single compound, to a larger degree than simply additive effects (**Figures 4B,C**; **Supplementary Video S5**). Therefore, these results suggested that senkyunolide I and cryptotanshinone could be the key chemical compounds which drives the synergistic anti-thrombotic effects between *S. miltiorrhiza* and *L. stratum* in GXNT. Nevertheless, it is worth noticing that the anti-thrombotic effect of GXNT is still superior than the combined usage of cryptotanshinone and senkyunolide I, suggesting that there remain other unidentified compounds contributing to the total effect.

GXNT and Cryptotanshinone Inhibit PHZ-Induced Oxidative Damage

The oxidation of PHZ leads to the production of superoxide radicals, hydrogen peroxide, and other oxidative substances (Misra and Fridovich, 1976), which accumulation may lead to oxidative damage to the membrane of endothelial and red blood cells, eventually results in thrombosis and hemolysis. Thus, the impact of GXNT and its components on the endogenous oxidative stress after PHZ stimulation was examined by measuring the levels of free radicals and lipid peroxidation. As observed in previous studies, a moderate level of fluorescent signal was detected in the intestinal region of untreated zebrafish embryos with the ROS probe DCFH-DA, which possibly reflects the physiological level of oxidative stress

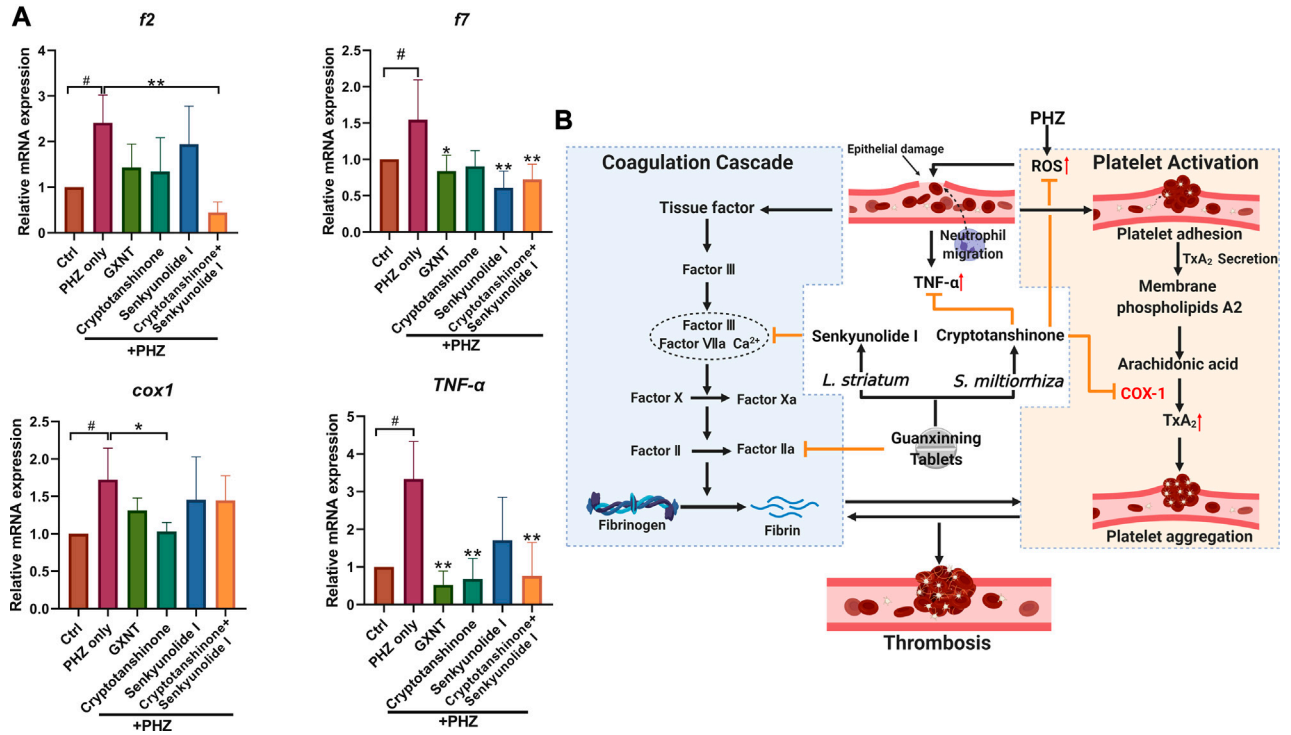

FIGURE 6 | Expression of representative factors in coagulation cascade and platelet activation in PHZ-stimulated zebrafish. **(A)** Expression of coagulation and platelet activation related factors with significant alterations in embryos with GXNT or compound treatment, compared with PHZ only stimulated group. **(B)** A proposed model showing the synergistic mechanism of GXNT and its major components in thrombosis regulation (created with BioRender.com). The complete set of data are shown in **Supplementary Figure S3**. #Compared with the control group; *compared with the model group; # or *$p < 0.05$, ## or **$p < 0.01$.

during normal intestinal development (Shi et al., 2014). The endogenous ROS signal was significantly increased after PHZ incubation, whereas GXNT protection greatly suppressed it to an even lower level than control embryos, supporting its strong anti-oxidative effect (**Figures 5A,B**). Interestingly, cryptotanshinone protection alone was sufficient to inhibit the ROS level to a comparable degree as GXNT, yet senkyunolide I treatment failed to show any effect, suggesting that the regulation of GXNT on oxidative stress may be primarily derived from the cryptotanshinone, instead of senkyunolide I. We further examined the impact of these drugs on lipid peroxidation by maldondialdehyde (MDA) analysis. The endogenous concentration of MDA increased after PHZ stimulation, and GXNT pre-incubation can effectively suppress its elevation (**Figure 5C**). Cryptotanshinone treatment also showed a tendency of MDA inhibition. Taken together, these results suggested that GXNT and its component cryptotanshinone possess strong anti-oxidative effects, which may be related to their roles in thrombosis regulation.

Cryptotanshinone and Senkyunolide I Showed Regulatory Effects on Platelet Activation and Coagulation Cascade

Finally, we investigated the influences of GXNT and its effective components on the processes of platelet activation and coagulation cascade (**Figure 6**; **Supplementary Figure S3**). The endogenous transcriptional levels of key factors in the two pathways were examined, and multiple genes showed altered expression after PHZ stimulation. Consistent with our previous findings in *Tg* (*CD41:eGFP*) fish, increased expression of *cox1* was detected in PHZ treated embryos, suggesting the role of platelet activation in our thrombosis model. Noticeably, cryptotanshinone treatment was sufficient to inhibit *cox1* expression. Besides, the expression of tumor necrosis factor α (*tnf*-α), a proinflammatory cytokine related to platelet hyperactivity, was also increased in our disease model, and was substantially inhibited by cryptotanshinone and GXNT. In the coagulation cascade, senkyunolide I was able to significantly inhibit the expression of coagulation factor VII (*f7*), which is a key component of the extrinsic factor X activating complex and is critical for the coagulation cascade in vascular endothelial injury. Downregulated expression of fibrinogen beta chain (*fgb*) was also observed in senkyunolide I protected embryos. Moreover, dramatically decreased expression of coagulation factor II (*f2*, or thrombin) was detected in embryos with combined treatment of cryptotanshinone and senkyunolide I. Collectively, these results suggested that cryptotanshinone and senkyunolide I regulated the endogenous platelet activation and coagulation cascade at multiple levels.

DISCUSSION

Different from Western pharmacological concept, which usually aimed at one compound with one or more identified specific targets, TCM was formulated through a "polypharmacologic" approach (Newman, 2020). A mixture of natural products was selected according to TCM compatibility theory, which may have limited effect when used alone, but showed enhanced or synergistic results with particular combinations. However, due to the extremely complicated chemical composition in naturally derived herbs and other materials, the pharmacological mechanism of most TCM are largely unclear, making it difficult to evaluate the validity of TCM combinations (Yuan and Lin, 2000) Nevertheless, as many single-targeted chemical drugs frequently encountered bottlenecks in the treatment of complex diseases, such as drug resistance or intolerance, the importance of multi-target and multi-pathway therapeutic strategies has been proposed in recent years (Keith et al., 2005). Re-examining classical TCM formulae, which are excel in using drug combinations, may bring us new hint.

S. miltiorrhiza and *L. striatum* are probably among the most widely used herbs with documented function in promoting blood flow, and were used in the treatment of blood stasis symptoms (primarily cardiovascular diseases) in China and some other Asian countries (Wang et al., 2017) A study in 5,284 hospitalized CAD patients in Beijing and Tianjin found that *S. miltiorrhiza* was prescribed to 63.10% of all patients, while *L. striatum* was administered to 46.36% of the patients (Gao et al., 2012). According to the TCM theory, the primary function of *S. miltiorrhiz* lies in promoting blood circulation and resolving haemostasis, and *L. striatum* is capable of enhancing energy balance and internal homeostasis. Nevertheless, despite usually prescribed together, how *S. miltiorrhiza* and *L. striatum* cooperate with each other in thrombosis regulation has little biological evidence. At the compound level, a couple of *S. miltiorrhiz* derived substances were suggested in thrombosis regulation by cell or animal studies, such as salvianolic acid A (Huang et al., 2010), salvianolic acid B (Zhang et al., 2020), dihydrotanshinone I (Park et al., 2008) and tanshinone IIA (Wang et al., 2020). Our previous study also detected the anti-thrombotic effects of cryptotanshinone (Sheng et al., 2020). The pharmacological mechanism of *L. striatum* is less examined than *S. miltiorrhiz*. The function of ligustrazine (tetramethylpyrazine) was comparatively well studied, and was indicated in multiple biological processes, including tumor metastasis, neurogenesis and thrombosis (Liu and Sylvester, 1990; Zou et al., 2018). However, ligustrazine was not identified in the *L. striatum* or GXNT extract in our mass spectrometry analysis, may be because of the difference in sample preparation or herbal species difference.

In our study, a new synergistic cooperation between cryptotanshinone and senkyunolide I in inhibiting endogenous thrombosis was proposed. There is still limited knowledge about the anti-thrombotic effects of the two compounds. Cryptotanshione was previously identified as a STAT3 inhibitor with antitumor activity (Shin et al., 2009), and the effects of senkyunolide I was mostly related to neuroinflammation (Han et al., 2018). Our findings suggested that multiple signaling pathways may be involved in the cooperative effects between cryptotanshinone and senkyunolide I in thrombosis. In our disease model, increased level of free radicals generated by PHZ oxidation is likely to be the initial pathological change, which then result in platelets aggregation and hemolysis through membranous damage of vascular endothelium and erythrocytes. Increased oxidative stress was also discovered in the development of venous and arterial thrombi in the human body, possibly through affecting the RBC membrane (Wang and Zennadi, 2020) and platelet activity (Violi et al., 2017), respectively. Cryptotanshinone showed strong inhibition on the endogenous levels of oxidative radicals and lipid peroxidation, which partially explained its anti-thrombotic activity. Besides, increased level of inflammatory cytokine TNF-α was detected in PHZ-stimulated embryos, which was greatly downregulated by cryptotanshinone or GXNT. Previous studies suggested that TNF-α, and other inflammatory cytokines such as IL-17A, may has a role in inducing the formation of neutrophil extracellular traps (NETs) (Khandpur et al., 2013), which is a specific type of cell death involved in many diseases including both VET and atherosclerosis (Mozzini et al., 2017). Whether cryptotanshinone and *S. miltiorrhiza* can regulate NETs release is interesting to test in the future. Moreover, decreased level of COX-1 was also detected in embryos protected with cryptotanshione, suggesting its possible role in platelet activation. On the other hand, the potential mechanism of senkyunolide I in thrombosis tends to be more related to the coagulation cascade. Both the expression of coagulation factor f7, which is a key factor in the extrinsic coagulation signaling, and the downstream fibrinogen were downregulated by senkyunolide I. Although still rather limited, our results suggested that cryptotanshinone and senkyunolide I may regulate thrombosis at multiple levels in different signaling pathways, which partially explained their synergistic effects.

Finally, there remain some limitations in our study. For example, only six compounds were tested in our model system for their anti-thrombotic effects. By combining the zebrafish model system with high-throughput screening platform, such as high-content analysis, we shall be able to examine the function of compounds of higher order of magnitude in the future. Besides, when testing the expression of downstream factors, whole embryo lysate extracted mRNA was used, which sensitivity can be influenced by cellular heterogeneity. Other experimental techniques, such as cell sorting, single cell sequencing, or transgenic fish reporter lines with specifically labeled downstream target, will be helpful to solve this problem.

Taken together, through zebrafish thrombotic model-based functional screening and high-resolution mass spectrometry, we investigated the effects of herb combinations and compound combinations of GXNT in the treatment of thrombosis. The synergistic effects of *S. miltiorrhiza* and *L. striatum*, as well as of their respective compound, cryptotanshinone and senkyunolide I, were firstly demonstrated in our study. Multiple signaling pathways, including oxidative stress, platelet activation and coagulation cascade were suggested to be regulated differently by these factors. Our study provides solid biological evidence toward the drug combination rationale in a TCM formulae and brings new therapeutic candidates in the management of thrombosis.

DATA AVAILABILITY STATEMENT

The original contributions presented in the study are included in the article/**Supplementary Material**, further inquiries can be directed to the corresponding author.

ETHICS STATEMENT

The animal study was reviewed and approved by Animal Ethics Committee of the Laboratory Animal Center, Zhejiang University.

AUTHOR CONTRIBUTIONS

Conception and design: LZ and YW. Acquisition of data: JL, HL, and QY. Analysis and interpretation of data: JL, HL, and ZY. Writing of the manuscript: LZ, HL, and JL.

FUNDING

This work was supported by National Key Scientific and Technological Project of China (Grant No. 2018ZX09201011), National Natural Science Foundation of China (Grant Nos. 31971088 and 81822047), and Natural Science Foundation of Zhejiang Province (Grant No. LGF21H280005).

ACKNOWLEDGMENTS

The authors are grateful for the support from ZJU PII-Tecan Joint Laboratory.

SUPPLEMENTARY MATERIAL

The Supplementary Material for this article can be found online at: https://www.frontiersin.org/articles/10.3389/fphar.2020.622787/full#supplementary-material.

REFERENCES

Bliss, C. I. (2008). The toxicity of poisons applied jointly. *Ann. Appl. Biol.* 26 (3), 585–615. doi:10.1111/j.1744-7348.1939.tb06990.x

Braekkan, S. K., Mathiesen, E. B., Njølstad, I., Wilsgaard, T., Størmer, J., and Hansen, J. B. (2008). Family history of myocardial infarction is an independent risk factor for venous thromboembolism: the Tromsø study. *J. Thromb. Haemost.* 6 (11), 1851–1857. doi:10.1111/j.1538-7836.2008.03102.x

Chen, H. L., and Collier, H. B. (1951). The action of some hemolysis accelerators upon lipid and protein monolayers. *J. Gen. Physiol.* 35 (1), 17–22. doi:10.1085/jgp.35.1.17

Depta, J. P., and Bhatt, D. L. (2015). New approaches to inhibiting platelets and coagulation. *Annu. Rev. Pharmacol. Toxicol.* 55 (1), 373–397. doi:10.1146/annurev-pharmtox-010814-124438

Foucquier, J., and Guedj, M. (2015). Analysis of drug combinations: current methodological landscape. *Pharmacol. Res. Perspect.* 3 (3) e00149. doi:10.1002/prp2.149

Ganis, J. J., Hsia, N., Trompouki, E., de Jong, J. L., DiBiase, A., Lambert, J. S., et al. (2012). Zebrafish globin switching occurs in two developmental stages and is controlled by the LCR. *Dev. Biol.* 366 (2), 185–194. doi:10.1016/j.ydbio.2012.03.021

Gao, Z. Y., Xu, H., Shi, D. Z., Wen, C., and Liu, B. Y. (2012). Analysis on outcome of 5284 patients with coronary artery disease: the role of integrative medicine. *J. Ethnopharmacol.* 141 (2), 578–583. doi:10.1016/j.jep.2011.08.071

Han, L., Liu, D. L., Zeng, Q. K., Shi, M. Q., Zhao, L. X., He, Q., et al. (2018). The neuroprotective effects and probable mechanisms of Ligustilide and its degradative products on intracerebral hemorrhage in mice. *Int. Immunopharmacol.* 63, 43–57. doi:10.1016/j.intimp.2018.06.045

Huang, Z. S., Zeng, C. L., Zhu, L. J., Jiang, L., Li, N., and Hu, H. (2010). Salvianolic acid A inhibits platelet activation and arterial thrombosis via inhibition of phosphoinositide 3-kinase. *J. Thromb. Haemost.* 8 (6), 1383–1393. doi:10.1111/j.1538-7836.2010.03859.x

Jain, S. K. (1985). *In vivo* externalization of phosphatidylserine and phosphatidylethanolamine in the membrane bilayer and hypercoagulability by the lipid peroxidation of erythrocytes in rats. *J. Clin. Invest.* 76 (1), 281. doi:10.1172/JCI111958

Karlsson, J., von Hofsten, J., and Olsson, P. E. (2001). Generating transparent zebrafish: a refined method to improve detection of gene expression during embryonic development. *Mar. Biotechnol.* 3 (6), 522–527. doi:10.1007/s1012601-0053-4

Keith, C. T., Borisy, A. A., and Stockwell, B. R. (2005). Multicomponent therapeutics for networked systems. *Nat. Rev. Drug Discov.* 4 (1), 71–78. doi:10.1038/nrd1609

Khandpur, R., Carmona-Rivera, C., Vivekanandan-Giri, A., Gizinski, A., Yalavarthi, S., Knight, J. S., et al. (2013). NETs are a source of citrullinated autoantigens and stimulate inflammatory responses in rheumatoid arthritis. *Sci. Transl. Med.* 5 (178), 178ra40. doi:10.1126/scitranslmed.3005580

Libby, P., Pasterkamp, G., Crea, F., and Jang, I. K. (2019). Reassessing the mechanisms of acute coronary syndromes. *Circ. Res.* 124 (1), 150–160. doi:10.1161/circresaha.118.311098

Lin, H. F., Traver, D., Zhu, H., Dooley, K., Paw, B. H., Zon, L. I., et al. (2005). Analysis of thrombocyte development in CD41-GFP transgenic zebrafish. *Blood.* 106 (12), 3803–3810. doi:10.1182/blood-2005-01-0179

Liu, S. Y., and Sylvester, D. M. (1990). Antithrombotic/antiplatelet activity of tetramethylpyrazine. *Thromb. Res.* 58 (2), 129–140. doi:10.1016/0049-3848(90)90170-h

Misra, H. P., and Fridovich, I. (1976). The oxidation of phenylhydrazine: superoxide and mechanism. *Biochemistry.* 15 (3), 681–687. doi:10.1021/bi00648a036

Mozzini, C., Garbin, U., Fratta Pasini, A. M., and Cominacini, L. (2017). An exploratory look at NETosis in atherosclerosis. *Intern. Emerg. Med.* 12 (1), 13–22. doi:10.1007/s11739-016-1543-2

Newman, D. J. (2020). Modern traditional Chinese medicine: identifying, defining and usage of TCM components. *Adv. Pharmacol.* 87, 113–158. doi:10.1016/bs.apha.2019.07.001

Park, J. W., Lee, S. H., Yang, M. K., Lee, J. J., Song, M. J., Ryu, S. Y., et al. (2008). 15,16-dihydrotanshinone I, a major component from *Salvia miltiorrhiza* Bunge (Dansham), inhibits rabbit platelet aggregation by suppressing intracellular calcium mobilization. *Arch. Pharm. Res.* 31 (1), 47–53. doi:10.1007/s12272-008-1119-4

Sato, H., Shinozuka, J., Tanaka, M., Fujimura, H., and Toriumi, W. (2009). Acute thrombus formation in the lungs of phenylhydrazine-treated rats. *J. Toxicol. Pathol.* 21 (4), 249–251. 10.1293/tox.21.249

Sato, H., Terasaki, N., Sakairi, T., Tanaka, M., and Takahashi, K. (2015). Gene expression profiling in the lungs of phenylhydrazine-treated rats: the contribution of pro-inflammatory response and endothelial dysfunction to acute thrombosis. *Exp. Toxicol. Pathol.* 67, 205–210. doi:10.1016/j.etp.2014.11.011

Sheng, J., Meng, Q., Yang, Z., Guan, J., Zhao, Y., Zhang, J., et al. (2020). Identification of cryptotanshinone from Tongmai to inhibit thrombosis in zebrafish *via* regulating oxidative stress and coagulation cascade. *Phytomedicine.* 76, 153263. doi:10.1016/j.phymed.2020.153263

Shi, Y., Zhang, Y., Zhao, F., Ruan, H., Huang, H., Luo, L., et al. (2014). Acetylcholine serves as a derepressor in loperamide-induced opioid-induced bowel dysfunction (OIBD) in zebrafish. *Sci. Rep*. 4, 5602. doi:10.1038/srep05602

Shin, D. S., Kim, H. N., Shin, K. D., Yoon, Y. J., Kim, S. J., Han, D. C., et al. (2009). Cryptotanshinone inhibits constitutive signal transducer and activator of transcription 3 function through blocking the dimerization in DU145 prostate cancer cells. *Cancer Res*. 69 (1), 193–202. doi:10.1158/0008-5472.can-08-2575

Sørensen, H. T., Horvath-Puho, E., Søgaard, K. K., Christensen, S., Johnsen, S. P., Thomsen, R. W., et al. (2009). Arterial cardiovascular events, statins, low-dose aspirin and subsequent risk of venous thromboembolism: a population-based case-control study. *J. Thromb. Haemost*. 7 (4), 521–528. doi:10.1111/j.1538-7836.2009.03279.x

Stone, G. W., Maehara, A., Lansky, A. J., de Bruyne, B., Cristea, E., Mintz, G. S., et al. (2011). A prospective natural-history study of coronary atherosclerosis. *N. Engl. J. Med*. 364 (3), 226–235. doi:10.1056/NEJMoa1002358

Sun, M. Y., Miao, Y., Jin, M., Dong, Y. R., Liu, S. R., Wang, M. L., et al. (2019). Effect and safety of guanxinning tablet () for stable angina pectoris patients with xin (heart)-blood stagnation syndrome: a randomized, multicenter, placebo-controlled trial. *Chin. J. Integr. Med*. 25 (9), 684–690. doi:10.1007/s11655-019-3069-8

Violi, F., Loffredo, L., Carnevale, R., Pignatelli, P., and Pastori, D. (2017). Atherothrombosis and oxidative stress: mechanisms and management in elderly. *Antioxid. Redox Signal*. 27 (14), 1083–1124. doi:10.1089/ars.2016.6963

Wang, H., Zhong, L., Mi, S., Song, N., Zhang, W., and Zhong, M. (2020). Tanshinone IIA prevents platelet activation and down-regulates CD36 and MKK4/JNK2 signaling pathway. *BMC Cardiovasc. Disord*. 20 (1), 81. doi:10.1186/s12872-019-01289-z

Wang, L., Ma, R., Liu, C., Liu, H., Zhu, R., Guo, S., et al. (2017). *Salvia miltiorrhiza*: a potential red light to the development of cardiovascular diseases. *Curr. Pharm. Des*. 23 (7), 1077–1097. doi:10.2174/1381612822666161010105242

Wang, Q., and Zennadi, R. (2020). Oxidative stress and thrombosis during aging: the roles of oxidative stress in RBCs in venous thrombosis. *Int. J. Mol. Sci*. 21 (12), 4259. doi:10.3390/ijms21124259

Wang, M., Carver, J. J., Phelan, V. V., Sanchez, L. M., Garg, N., Peng, Y., et al. (2016). Sharing and community curation of mass spectrometry data with global natural products social molecular networking. *Nat. Biotechnol*. 34 (8), 828–837. doi:10.1038/nbt.3597

Westerfield, M. (2007). *The zebrafish book : a guide for the laboratory use of zebrafish (Danio rerio)*. Eugene, OR: Inst of Neuro Science.

Yuan, R., and Lin, Y. (2000). Traditional Chinese medicine: an approach to scientific proof and clinical validation. *Pharmacol. Ther*. 86 (2), 191–198. doi:10.1016/s0163-7258(00)00039-5

Zhang, Z., Ji, J., Zhang, D., Ma, M., and Sun, L. (2020). Protective effects and potential mechanism of salvianolic acid B on sodium laurate-induced thromboangiitis obliterans in rats. *Phytomedicine*. 66, 153110. doi:10.1016/j.phymed.2019.153110

Zhu, X. Y., Liu, H. C., Guo, S. Y., Xia, B., Song, R. S., Lao, Q. C., et al. (2016). A zebrafish thrombosis model for assessing antithrombotic drugs. *Zebrafish*. 13 (4), 335–344. doi:10.1089/zeb.2016.1263

Zou, J., Gao, P., Hao, X., Xu, H., Zhan, P., and Liu, X. (2018). Recent progress in the structural modification and pharmacological activities of ligustrazine derivatives. *Eur. J. Med. Chem*. 147, 150–162. doi:10.1016/j.ejmech.2018.01.097

Conflict of Interest: Author QY was employed by the company Chiatai Qingchunbao Pharmaceutical Co., Ltd.

The remaining authors declare that the research was conducted in the absence of any commercial or financial relationships that could be construed as a potential conflict of interest.

frontiers in Pharmacology

ORIGINAL RESEARCH
published: 08 March 2021
doi: 10.3389/fphar.2021.623533

A Bioassay-Based Approach for the Batch-To-Batch Consistency Evaluation of Xuesaitong Injection on a Zebrafish Thrombosis Model

Xiangwei Ma[1], *Yanyu Chen*[2], *Shumin Jiang*[1] *and Xiaoping Zhao*[2,3]*

[1]College of Pharmaceutical Sciences, Zhejiang Chinese Medical University, Hangzhou, China, [2]School of Basic Medical Sciences, Zhejiang Chinese Medical University, Hangzhou, China, [3]Academy of Chinese Medical Science, Zhejiang Chinese Medical University, Hangzhou, China

OPEN ACCESS

Edited by:
Yi Wang,
Zhejiang University, China

Reviewed by:
Hua Yang,
China Pharmaceutical University, China
Yuelin Song,
Beijing University of Chinese Medicine, China

***Correspondence:**
Xiaoping Zhao
zhaoxiaoping@zcmu.edu.cn

Specialty section:
This article was submitted to Ethnopharmacology, a section of the journal Frontiers in Pharmacology

Received: *30 October 2020*
Accepted: *19 January 2021*
Published: *08 March 2021*

Citation:
Ma X, Chen Y, Jiang S and Zhao X (2021) A Bioassay-Based Approach for the Batch-To-Batch Consistency Evaluation of Xuesaitong Injection on a Zebrafish Thrombosis Model. Front. Pharmacol. 12:623533. doi: 10.3389/fphar.2021.623533

Quality control of Chinese medicine (CM) is mainly based on chemical testing, which sometimes shows weak correlation to pharmacological effects. Thus, there is a great demand to establish bioactivity-based assays to ensure the quality of CM. The aim of the present study was to establish a bioassay-based approach to evaluate the biological activity of Xuesaitong injection (XST) based on an *in vivo* zebrafish model. Zebrafish larvae with arachidonic acid (AA)-induced thrombus were applied to evaluate anti-thrombosis effects of XST and explore the potential mechanism of XST. Analysis of major components in normal and abnormal XST samples was performed by high performance liquid chromatography (HPLC). The results indicate that XST could significantly restore heart red blood cells (RBCs) intensity of thrombotic zebrafish in a dose-dependent manner, whilst decreasing RBCs accumulation in the caudal vein. The results were confirmed using a green fluorescence protein (GFP)-labeled zebrafish thrombosis model. Moreover, we could show that XST downregulates the expression of the *fibrinogen alpha chain* (*fga*) gene to inhibit the coagulation cascade during the process of thrombosis in zebrafish. Notoginsenoside R_1, ginsenoside Rg_1, ginsenoside Rb_1 and ginsenoside Rd, which were considered to be the major components of XST, also showed moderate anti-thrombosis efficacy. Further results showed that the zebrafish thrombosis model could efficiently distinguish five abnormal batches of XST from 24 normal batches. Furthermore, the inhibition rates of different batches were correlated with the content level of major components. Our results suggested that the proposed zebrafish thrombosis model could be successfully used to evaluate the batch-to-batch consistency of XST, which provided an alternative way for the quality control of CM.

Keywords: Chinese medicine, zebrafish thrombosis model, batch-to-batch consistency, Xuesaitong injection, quality control

INTRODUCTION

Traditional Chinese medicine (TCM) is gaining increasing attention worldwide for its distinguished efficacy and minimum side effects (Shi et al., 2018). As a TCM preparation, CM is a combination of TCM theory and modern technology, which has the advantages of high stability, convenient for transport and storage. Thus, the quality assessment of CM is an urgent task in the process of the standardization and internationalization of TCM (Wang et al., 2016; Wang et al., 2018).

Diverse analysis methods have been used for quality evaluation of CM, by determining the content of several active components, such as GC, HPLC, liquid chromatography-mass spectrometry (LC-MS), near-infrared spectroscopy (NIRS), and Raman spectroscopy (RS). A promising method for the quality control of *Astragalus mongholicus* Bunge (Astragali radix) and its products was developed by the SIM mode of ultra-performance liquid chromatography (UPLC-QDA) (Zhao et al., 2018). Wang developed a method based on HPLC coupled with a photodiode array detector for the quality evaluation of Yin Chen Hao Tang extract, which was successfully applied in the analysis of 12 different batch samples (Wang et al., 2008b). UPLC coupled with quadrupole time-of-flight mass spectrometry (UHPLC-QTOF-MS) was employed to the quality assessment of Yin-Qiao-Jie-Du tablets (He et al., 2016). A quantitative analysis model was employed to the rapid quality control of Tongkang tablets by NIRS (Pan et al., 2017).

The batch-to-batch consistency is an important part of quality evaluation of CM. Mid-infrared and ultra violet spectroscopic fingerprints were integrated for quality consistency of Weibizhi tablets (Liu et al., 2016). Li combined in-line near-infrared spectroscopy with a multivariate statistical process control method, simultaneously developed a multi-way principal component analysis model and adopted multivariate control charts for the real-time monitoring of TCM products (Li et al., 2016).

Nonetheless, the content level determination of single or multiple components cannot completely evaluate the effectiveness of CM (Wu et al., 2018), thus leaving uncertainty for quality assessment as well as therapeutic consistency. Biological assays were suggested to ensure the therapeutic consistency of botanical drug products in Botanical Drug Development Guidance for Industry promulgated by the Food and Drug Administration (FDA) (FDA, 2016). Zhang (Zhang et al., 2014) combined chemical fingerprints with biological fingerprints to detect the quality fluctuation of SHL, a herbal injection. The antioxidant capability was tested for the stability evaluation of Danhong injection based on human umbilical vein endothelial cells (HUVECs) (Li et al., 2017). Lam proposed that the quality control of a herbal product should be based on its pharmacological mechanism. They developed a platform which consisted of 18 luciferase reporter cell lines and two enzymatic assays to assess Chinese formulations and commercial products (Lam et al., 2018). Consequently, we propose the development of a model organism-based test for the consistency assessment of CM injection.

The zebrafish (*Danio rerio*), an aquatic vertebrate, is currently becoming a prevalent model organism, which is widely applied for biomedical research, toxicology studies, as well as drug discovery (Peterson and MacRae, 2012; Kalueff et al., 2014; MacRae and Peterson, 2015). Zebrafish have multiple advantages including high homology to mammals, higher fecundity, rapid development of embryos, and transparent embryos and larvae (Loehr and Hammerschmidt, 2011; Stewart et al., 2014). Zebrafish have been employed for TCM research in many aspects, for example, active ingredients screening, and toxicity evaluation (Tu et al., 2016; Yang et al., 2017). The zebrafish is a useful model in thrombosis research (Gibbins and Mahaut-Smith, 2012), because platelet function shares many characteristics with humans, such as GPIIb-IIIa, coagulation factors, and arachidonic acid metabolism enzymes (Jagadeeswaran et al., 1999; Lang et al., 2010). Thus, it is meaningful to apply the zebrafish thrombosis model for the quality evaluation of CM. Our research group has successfully established a biological quality assessment assay of Danhong injection by a thrombosis model of zebrafish (Qi et al., 2017).

Panax notoginseng (Burk.) F. H. Chen is documented from Compendium of Materia Medica to Chinese Pharmacopoeia, which has the functions of removing blood stasis and hemostasis, reducing swelling, and relieving pain. The main component of *Panax notoginseng* (Burk.) F. H. Chen is Panax notoginseng saponin (PNS). Xuesaitong injection (XST) is a freeze-dried powder injection, which is made from the PNS, is extensively applied for the treatment of cardiovascular and cerebrovascular diseases in modern medicine (Wen and Liu, 2007; Chen et al., 2014).

Our group has made a series of contributions to the chemical and pharmacological study of XST. Notoginsenoside R_1, ginsenoside Rg_1, ginsenoside Rb_1, ginsenoside Rd, and ginsenoside Re are approximately 85% of the total components in XST, whose combination possesses a considerably similar efficacy to XST in the myocardial infarction rat model (Wang et al., 2014). Wang constructed a compound-target-pathway network to explore the mechanism of XST against myocardial infarction (Wang et al., 2013). Zhao demonstrated that the cardioprotective effect of XST against ischemia/reperfusion (I/R) injury was related to myocardial energy metabolism as well as oxidative stress (Zhao et al., 2017). Wang elucidated that anti-platelet aggregation and anti-inflammation were the main mechanisms of XST involved in preventing ischemia-reperfusion injury (Wang et al., 2015). Ma established a biological evaluation method for the quality assessment of XST based on anti-inflammatory activity (Ma et al., 2019). In addition, we developed a chemical analysis method for the quality evaluation of XST (Yao et al., 2011), however there was a lack of biological assays, which was directly correlated to its pharmacological effects to ensure therapeutic consistency. In this work, a reliable method based on a zebrafish thrombosis model was developed for the quality and batch-to-batch consistency testing of XST.

MATERIALS AND METHODS

Materials

Dimethyl sulfoxide (DMSO), tricaine, 1-phenyl-2-thio-urea (PTU), and *o*-dianisdine were purchased from Sigma-Aldrich Inc. (St. Louis, MO, United States). AA was provided by the Shanghai Yuanye Bio-Technology Co., Ltd. (Shanghai, China). Ginsenoside Rg_1 (150823, purity ≥ 98%), ginsenoside Rb_1 (120120, purity ≥ 98%), ginsenoside Re (120723, purity ≥ 98%), ginsenoside Rd (120507, purity ≥ 98%), and notoginsenoside R_1 (120821, purity ≥ 99%) were purchased from the Ronghe Pharmaceutical Technology Development Co., Ltd. (Shanghai, China). Aspirin was bought from the Dalian Meilun Biological Technology Co., Ltd. (Dalian, China). Glycerol and 4% paraformaldehyde fix solution were obtained from the Sangon Biotech Co., Ltd. (Shanghai, China). Ultrahigh-purity water was produced by ELGA purelab (High Wycombe, United Kingdom). Acetonitrile and methanol were obtained from Merck KGaA (HPLC grade, Darmstadt, Germany). Acetic acid was obtained from ROE Scientific Inc. (HPLC grade, Newark, United States). The 24 normal batches of XST (lyophilized powder) were provided by the Heilongjiang Zhenbaodao Pharmaceutical Co., Ltd. (Heilongjiang, China), and the batch numbers were F704001a1, F704029a1, F704019a3, F704003a3, F701003a2, F704024a4, F704016a4, F704015a3, F701009a1, F704002a2, F704030a2, F704038a2, F704031a3, F704017a1, F701011a3, F704004a4, F704020a4, F704021a1, F704033a1, F704023a3, F704026a2, F701007a3, F704022a2, and F704025a1.

Zebrafish care, Maintenance, and Breeding

Adult wild-type Tuebingen (TU) strain zebrafish and transgenic LCR-GFP zebrafish were bought from the China Zebrafish Resource Center (Wuhan, China). Zebrafish were cultured in a light (14:10 light/dark cycle) and temperature controlled aquaculture facility. Zebrafish were fed with alive brine shrimp twice a day and dry flake once per day. Embryos and adult fish were maintained in fish water (deionized water containing 0.3% Instant Ocean Salt, temperature at 28.5°C, pH 6.9–7.2, hardness approximately 90 mg/L $CaCO_3$, conductivity 500–550 μs/cm).

The male and female adult fish were placed in a mating tank at a ratio of 1:1 (or 1:2) and separated by a baffle. The baffle was removed to allow free mating the next day. Two hours later, the embryos were collected and washed with fish water to remove dysplastic embryos and debris. The embryos were incubated in fish water containing methylene blue (inhibiting the growth of bacteria) and transferred to a 28.5°C incubator for cultivation. The fish water was changed and 2.5 μmol/L of PTU was added to inhibit melanin growth at 1dpf and 2dpf (days past fertilization, dpf).

Reagent Preparation

AA, XST, aspirin, notoginsenoside R_1, ginsenoside Rg_1, ginsenoside Re, ginsenoside Rb_1, and ginsenoside Rd were dissolved in DMSO as stock solution, and diluted in fish water containing PTU. The final concentration of XST was 400 μg/ml; the final concentration of ginsenoside Rg_1, ginsenoside Rb_1, ginsenoside Re, and notoginsenoside R_1 was 200 μmol/L, the final concentration of ginsenoside Rd was 100 μmol/L.

The abnormal batches were prepared by excluding or reducing the content of one or two components in XST (notoginsenoside R_1 accounts for 10.85%, ginsenoside Rg_1 accounts for 38.11%, ginsenoside Rb_1 accounts for 32.44%, ginsenoside Rd accounts for 4.36%, ginsenoside Re accounts for 5.16%, as shown in **Table 1**): abnormal XST-1 excluded notoginsenoside R_1; abnormal XST-2 excluded ginsenoside Rg_1; abnormal XST-3 excluded ginsenoside Rb_1; abnormal XST-4 excluded ginsenoside Rd; and abnormal XST-5 halved the content of ginsenoside Rg_1 and ginsenoside Rb_1. The components were diluted with fish water according to their content proportion in XST (400 μg/ml).

Dye working solution consisting of *o*-dianisidine (5.85 mmol/L, dissolved in ethanol), NaOAc (pH = 4.5, adjusted with pH meter (Metter-Toledo International Inc., Zurich, Switzerland)), ultrahigh-purity water, and 30% H_2O_2 was mixed at a proportion of 20:5:20:1 before use.

The Assessment of Anti-Thrombosis Effects Based on Zebrafish Thrombus Model

3dpf zebrafish larvae were used in this experiment, all zebrafish larvae were kept in fish water containing 2.5 μmol/L of PTU in the process of the experiment. The 24-well plates were used for zebrafish larvae placement, double parallel wells were established for each group totally containing 12 fish. For the establishment of the AA-induced zebrafish thrombosis model, staining, fixing, image capture, and quantitative analysis were carried out as reported previously (Qi et al., 2017).

Transgenic LCR-GFP zebrafish were adopted for model validation. After incubation with AA for an hour, the zebrafish were transferred to fish water containing 0.016% tricaine. A video of LCR-GFP zebrafish was taken with a fluorescence microscope (Leica Microsystem Inc., Wetzlar, Germany) with a magnification of ×100, the exposure time was 0.1 s, and the duration was 10 s. The software used for image capture was Andor SOLIS 4.27.30001.0 (Andor Technology Ltd., Belfast, United Kingdom). Each group was photographed under the same conditions.

Quantitative PCR Detection

Total RNA extraction from 20 zebrafish larvae per group was performed using an Ultrapure RNA kit (Beijing ComWin Biotech Co.,Ltd., Beijing, China) according to the manufacturer's protocol. Then RNA were reverse transcribed to cDNA with the HiFiScript cDNA Synthesis Kit (Beijing ComWin Biotech Co.,Ltd., Beijing, China). The qPCR was performed by using an UltraSYBR Mixture (Beijing ComWin Biotech Co.,Ltd., Beijing, China) in the Bio-Rad CFX96 real-time system (Bio-Rad Laboratories Inc., California, United States), and the samples were isolated from three independent experiments. *Ef1a* served as the housekeeping gene in each sample. The relative expression of all genes was calculated by $2^{-\Delta\Delta Ct}$. All primers sequences are listed in **Table 2**.

TABLE 1 | The content of major compounds in abnormal XST samples.

Batch	Notoginsenoside R_1 (μmol/L)	Ginsenoside Rg_1 (μmol/L)	Ginsenoside Rb_1 (μmol/L)	Ginsenoside RD (μmol/L)	Ginsenoside Re (μmol/L)
Abnormal XST-1	0.00	190.33	116.98	18.40	21.77
Abnormal XST-2	46.51	0.00	116.98	18.40	21.77
Abnormal XST-3	46.51	190.33	0.00	18.40	21.77
Abnormal XST-4	46.51	190.33	116.98	0.00	21.77
Abnormal XST-5	46.51	95.17	58.49	18.40	21.77

TABLE 2 | Sequences of primer pairs used in the qPCR.

Gene	Forward primer	Reverse primer
fga	5′-CATTCACTGCTCTGCCTG TTC-3′	5′-CGCCTCTAGGGTTCACCA C-3′
fgb	5′-CGTTGGGACGACTACCGA AG-3′	5′-AATACGGTCATTGCCCAG CC-3′
ptgs2a	5′-TCCACAGAGGAGCAGTCT CA-3′	5′-AATGTGCCCCAGATCCAC TC-3′
ptgs2b	5′-TTGTTGCTCCCATCCCTG TC-3′	5′-GAAACTCGGGTGTTGTGC AG-3′
ptgis	5′-AACCTCCGCCTGCTTATG AC-3′	5′-GCGCCGAACACTGTCAGA TA-3′
tbxa2r	5′-GCGACTACGAGGTGGAGA TG-3′	5′-AGAGCAGCAGGTATCGAA CG-3′
vwf	5′-TGGATTGTGTCAGTCTGG GC-3′	5′-GACTCGTAAGGCCTGCTG TT-3′
ef1a	5′-AGAAGGCTGCCAAGACCA AG-3′	5′-AGAGGTTGGGAAGAACAC GC-3′

HPLC Analysis of XST

Normal XST samples, notoginsenoside R_1, ginsenoside Rg_1, ginsenoside Re, ginsenoside Rb_1, and ginsenoside Rd were weighed and dissolved in 50% methanol-water solution (*v/v*) in a volumetric flask. The abnormal batches were prepared from five components of XST according to their contents in 10 mg/ml of XST (proportions refer to Reagent Preparation). The content of notoginsenoside R_1, ginsenoside Rg_1, ginsenoside Re, ginsenoside Rb_1, and ginsenoside Rd in XST (24 and 20) had been quantitatively assessed by the standard curve method.

HPLC was performed by the Agilent 1,100 Series HPLC system (Aglient Co. Ltd., Santa Clara, CA, United States) with an Agilent Zorbax SB-C18 column (250 mm × 4.6 mm, 5 μm) at 28°C. The mobile phase was composed of A (0.01% acetic acid solution) and B (0.01% acetic acid-acetonitrile) with a linear gradient elution program as follow: 0–30 min, 19–21% B; 30–35 min, 21–28% B; 35–41 min, 28–32% B; 41–52 min, 32–32% B; 52–70 min, 32–53% B; 70–80 min, 53–90% B. The injection volume was 20/5 μL. A 10 min equilibration time was adopted between HPLC runs. The flow rate was 1.0 ml/min and the detection wavelength was set at 203 nm.

Data Analysis

The heart RBCs intensity was assessed by Image-Pro Plus 6.0 (Media Cybernetios Inc., Rockvile, MD, United States). Differences of RBCs between groups were assessed by one-way analysis of variance (ANOVA), difference of inhibition rates between normal and abnormal XST groups was assessed by *t*-test, analysis was performed by GraphPad Prism six software. Peak areas were qualitatively analyzed by the Agilent ChemStation for LC Systems (Rev. B. 04. 03) (Aglient Co. Ltd., Santa Clara, CA, United States).

RESULTS

The Anti-Platelet Aggregation Efficacy of XST Based on AA-Induced Zebrafish Thrombosis Model

Zebrafish were stained with *o*-dianisidine, images were acquired through a stereomicroscope and quantified by an image software. As shown in representative images (**Figure 1A**), compared with the control group, the RBCs were significantly decreased in the heart area of zebrafish in the model group (marked by the red dashed line), apart from this, the accumulation of RBCs in the caudal vein of zebrafish (marked by the red arrow) was significantly enhanced. These results indicated that the AA-induced zebrafish thrombosis model was successfully established. Aspirin is a well-known anti-platelet aggregation drug (Warner et al., 2011). Our results showed that it had outstanding efficacy on zebrafish with thrombus at 22.5 μg/ml. XST also exerted an anti-thrombotic effect at 400 μg/ml, it significantly inhibited RBCs aggregation in caudal venous and recovered the quantity of RBCs in the heart of AA-treated zebrafish. The results of quantitative analysis are exhibited in **Figure 1B**.

In order to verify the results obtained above, LCR-GFP (locals control region-green fluorescence protein) zebrafish with GFP-labeled hemoglobin were adopted for further study. The RBCs of thrombotic zebrafish accumulated in the caudal vein, and the blood flow was discontinuous and slow, furthermore the RBCs in the heart were decreased. The situation was improved in the XST treated group. Representative images were obtained by video recording and are shown in **Figure 2**. In addition to this, XST could restore RBCs intensity in thrombotic zebrafish dose-dependently, the minimum effective dose was 280 μg/ml (**Figure 3B**). Representative images are shown in **Figure 3A.**

To further explore the potential mechanism of the antithrombotic effect of XST, the relative expressions of seven genes which are related to thrombosis were detected by qPCR. Compared with the control group, the relative expression levels of *fibrinogen alpha chain* (*fga*), *fibrinogen beta chain* (*fgb*),

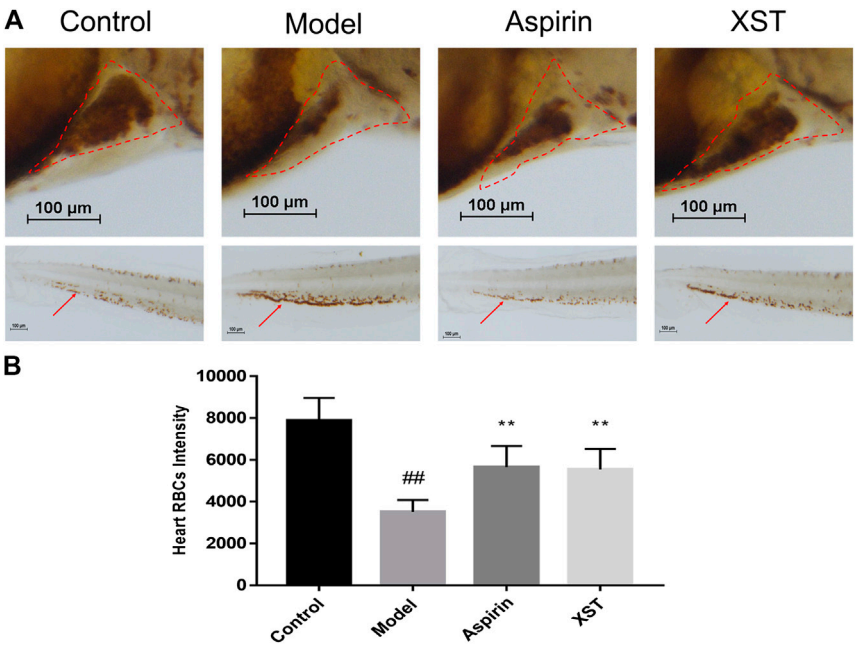

FIGURE 1 | (A) Zebrafish were stained with *o*-dianisidine in the control group, model group (AA 40 μmol/L), aspirin group (AA 40 μmol/L + aspirin 22.5 μg/ml), and XST group (AA 40 μmol/L + XST 400 μg/ml), RBCs in heart were marked by red dashed lines, caudal venous thrombus were guided by red arrows; **(B)** quantitative analysis measured the intensity of RBCs of zebrafish in heart area. The error bars represent the standard deviation of means, n = 10. All data were expressed by the mean ± SD, $^{\#\#}p < 0.01$ vs. control group; $^{**}p < 0.01$, $^{*}p < 0.05$ vs. model group.

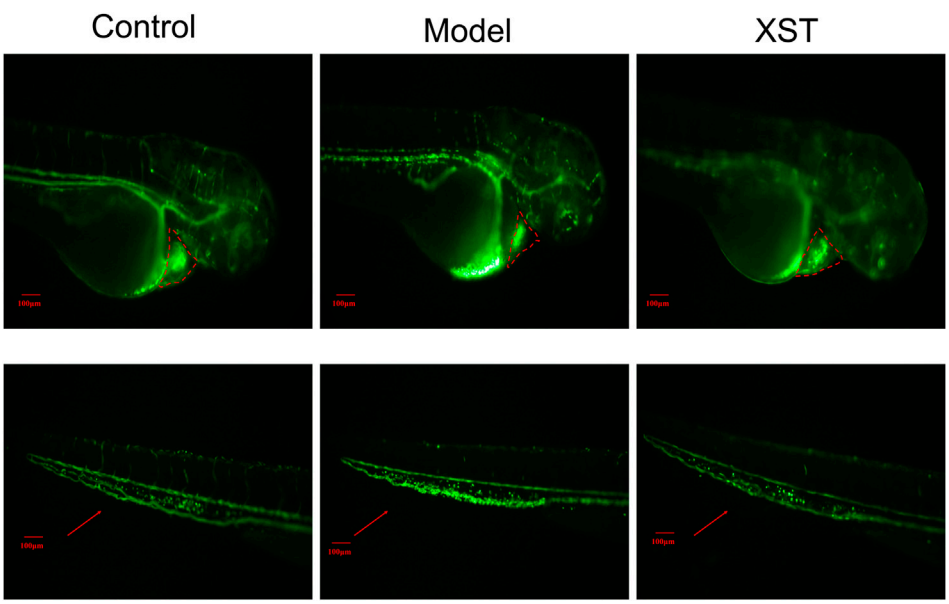

FIGURE 2 | Transgenic LCR-GFP zebrafish in the control group, model group (AA 40 μmol/L), and XST group (AA 40 μmol/L + XST 400 μg/ml), RBCs in heart were marked by red dashed lines, caudal venous thrombus were guided by red arrows. n = 10.

prostaglandin-endoperoxide synthase 2a (*ptgs2a*), *prostaglandin-endoperoxide synthase 2b* (*ptgs2b*), *prostaglandin I2 synthase* (*ptgis*) as well as *thromboxane A2 receptor* (*tbxa2r*) in the model group were significantly increased. It was noteworthy that the relative expression levels of *fga* and *ptgs2b* were obviously decreased in the XST group. Besides, the relative

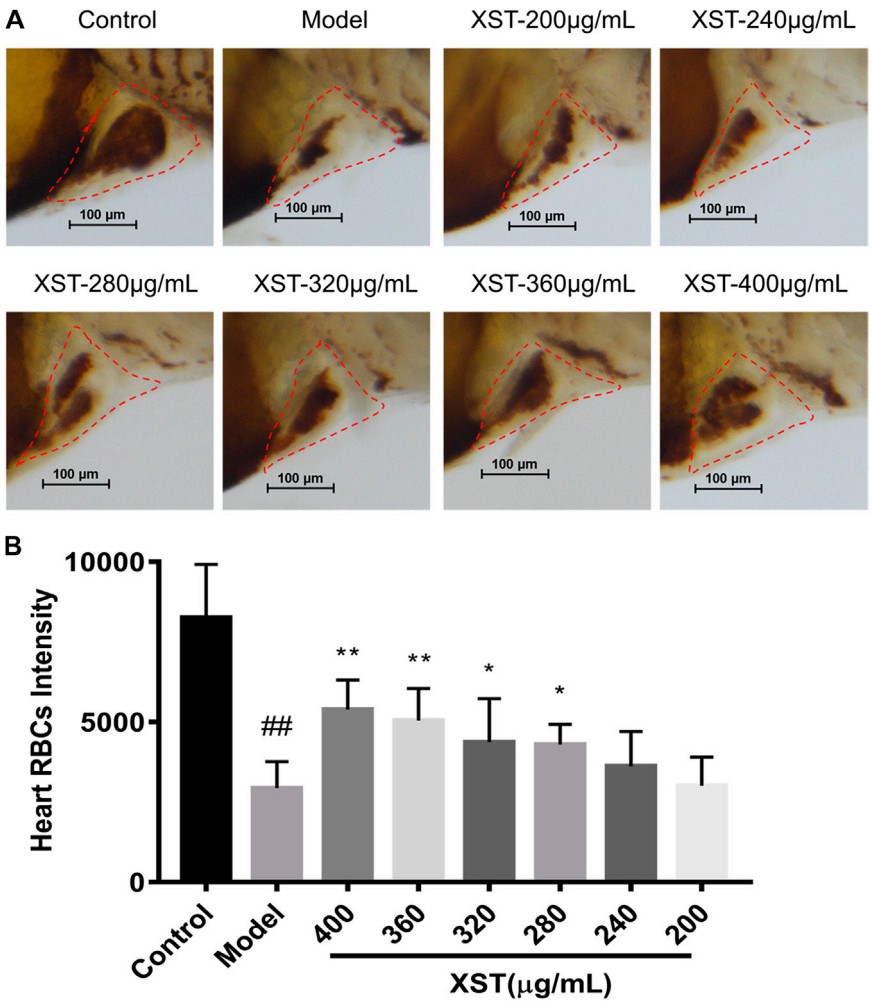

FIGURE 3 | (A) Zebrafish were stained with *o*-dianisidine in the control group, model group (AA 40 μmol/L), and XST groups of different concentrations (AA 40 μmol/L + XST 200, 240, 280, 320, 360, and 400 μg/ml), RBCs in heart were marked by red dashed lines; **(B)** quantitative analysis measured the intensity of RBCs of zebrafish in the control group, model group (AA 40 μmol/L), and XST groups of different concentrations (AA 40 μmol/L + XST 200, 240, 280, 320, 360, and 400 μg/ml) in the heart area. The error bars represent the standard deviation of means, n = 10. All data were expressed by the mean ± SD, $^{\#\#}p < 0.01$ vs. control group; $^{**}p < 0.01$, $^{*}p < 0.05$ vs. model group.

expression levels of *ptgs2a, ptgis, and tbxa2r* had a downward trend with the incubation of XST (**Figure 4**).

The Anti-thrombotic Effects of Major components in XST

Notoginsenoside R_1, ginsenoside Rg_1, ginsenoside Re, ginsenoside Rb_1, and ginsenoside Rd were the major active components of XST. To explore the anti-thrombotic components of XST, notoginsenoside R_1, ginsenoside Rg_1, ginsenoside Re, ginsenoside Rb_1 (200 μmol/L), and ginsenoside Rd (100 μmol/L) were administered to thrombotic zebrafish. As shown in **Figure 5A**, the results indicated that notoginsenoside R_1, ginsenoside Rg_1, ginsenoside Rb_1, and ginsenoside Rd had significant anti-thrombotic effects. The peaks of all five components in the HPLC chromatogram and corresponding chemical structural formulas are given in **Figure 5B**.

Comparison of Components Content and Anti-Thrombotic Efficacy of two Batches XST

In order to investigate whether anti-thrombotic effects were consistent with chemical analysis, we compared the difference of components content and anti-thrombotic efficacy of two batches of normal XST (20 and 24). HPLC was employed to determine the compounds content between two batches of XST, the chromatograms are shown in **Figure 6A**. The peaks of notoginsenoside R_1, ginsenoside Rg_1, ginsenoside Re, ginsenoside Rb_1, and ginsenoside Rd were qualitatively analyzed. As shown in **Figure 6B**, the content of major components in different batches were similar. Anti-thrombosis rate was calculated by the formula (Qi et al., 2017) and expressed in inhibition rate. The inhibition rates were counted by measuring RBCs intensity of the heart area in XST treated

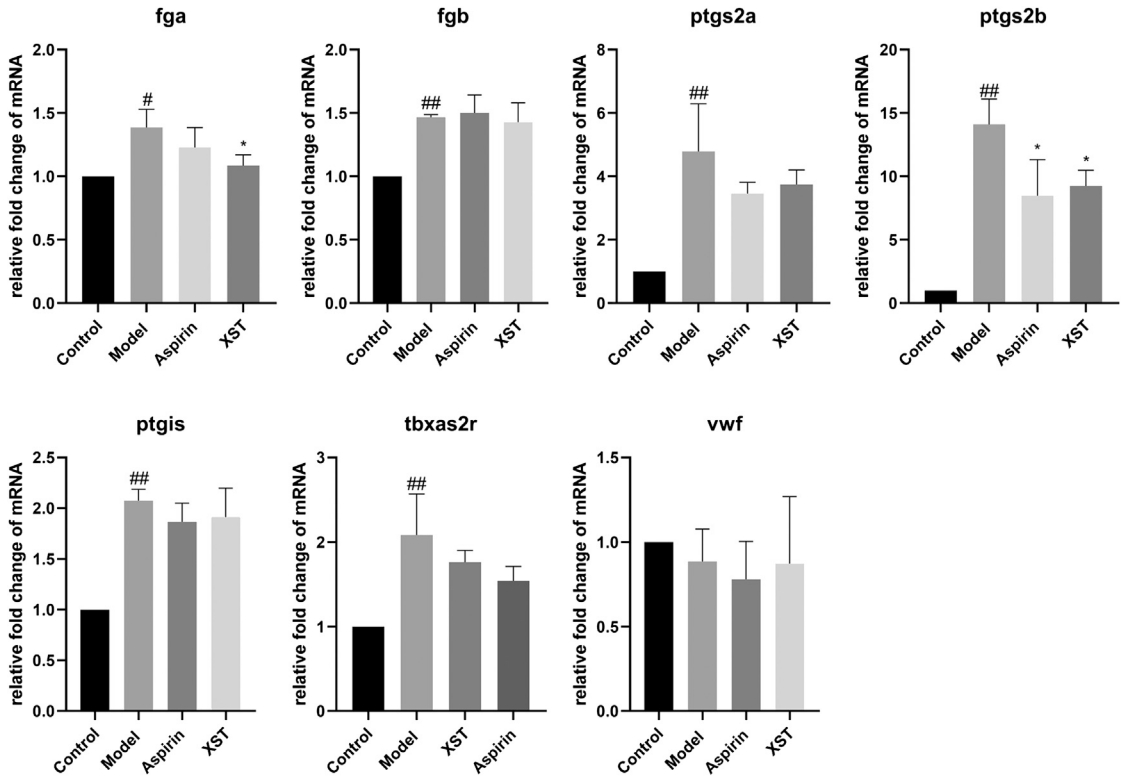

FIGURE 4 | Relative fold change of mRNA of *fga*, *fgb*, *ptgs2a*, *ptgs2b*, *ptgis*, *tbxa2r,* and *vwf* in the control group, model group (AA 40 μmol/L), aspirin group (AA 40 μmol/L + aspirin 22.5 μg/ml), and XST group (AA 40 μmol/L + XST 400 μg/ml), n = 20. All data were expressed by the mean ± SD, $^{\#\#}p < 0.01$, $^{\#}p < 0.05$ vs. control group; $^{*}p < 0.05$ vs. model group.

thrombotic zebrafish quantitatively (**Figure 6D**), representative images are shown in **Figure 6C**. The results indicate that the anti-thrombotic effect of two batches of XST were in accordance with the chemical analysis results.

An Application to Assess Batch-to-Batch Consistency of XST on Zebrafish Thrombosis Model

To explore whether the zebrafish thrombosis model was applicable to assess the quality and batch-to-batch consistency, the 24 normal batches of XST and five abnormal batches of XST were evaluated by both HPLC and the zebrafish thrombosis model. The relative percentages of notoginsenoside R_1, ginsenoside Rg_1, ginsenoside Rb_1, ginsenoside Re, and ginsenoside Rd in each XST sample were expressed as percent content by a peak area normalization method. As shown in **Figure 7A**, the area normalization percent content in normal batches were relatively consistent, while abnormal batches showed tremendous difference in components percentages. The results of the biological assay were correlated with the HPLC analysis, where abnormal XST had extremely poor anti-thrombotic effects compared with normal XST.

There was a significant difference between the average inhibition rates of normal batches and abnormal batches. The values of mean ± 2SD were considered as the limitation of normal fluctuation, nevertheless the inhibition rates of abnormal batches were below this range (**Figure 7B**). The zebrafish thrombosis model could be applied to evaluate XST effectiveness and discriminate the quality of normal and abnormal batches. For this reason, the zebrafish thrombosis model was appropriate for the batch-to-batch consistency assessment of XST.

DISCUSSION

The quality evaluation of CM has received more and more attention recently. Batch-to-batch consistency is an important part of CM quality evaluation. Current methods for consistency evaluation of CM are mainly based on chemical analysis, such as near infrared spectroscopy, HPLC fingerprints, etc. Although the conventional chemical analysis method manifests the difference in chemical markers of different batches intuitively, this cannot comprehensively reflect the bioactivity of CM for the complex composition and multifarious function. The biological assay is based on the pharmacological effects of CM, which is more consistent with clinical efficacy. More and more studies had applied pharmacological activity for the quality assessment of CM. Tsang (Tsang et al., 2019) adopted immunological activities for the quality consistency evaluation of *Dictamnus dasycarpus* Turcz. (Dictamni Cortex), an herbal medicine. Li (Li et al., 2019) established a bioassay method to evaluate the anti-platelet

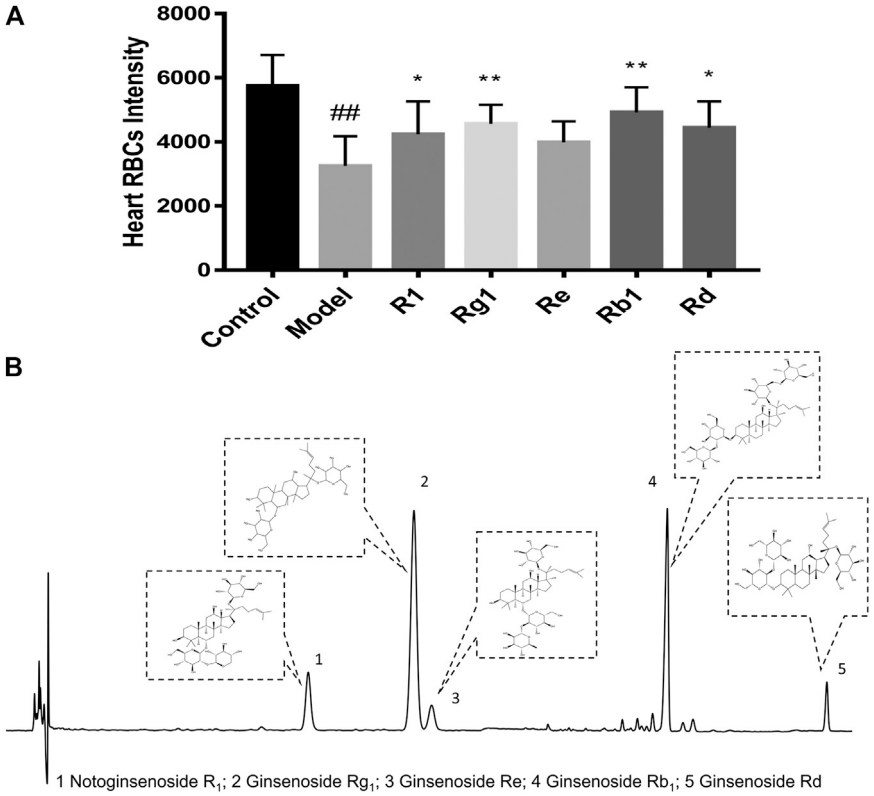

FIGURE 5 | (A) Quantitative analysis measured the intensity of RBCs of zebrafish in the control group, model group (AA 40 μmol/L), R_1 group (AA 40 μmol/L + notoginsenoside R_1 200 μmol/L), Rg_1 group (AA 40 μmol/L + ginsenoside Rg1 200 μmol/L), Re group (AA 40 μmol/L + ginsenoside Re 200 μmol/L), Rb_1 group (AA 40 μmol/L+ ginsenoside Rb_1 200 μmol/L), and Rd group (AA 40 μmol/L + ginsenoside Rd 100 μmol/L). Quantitative analysis was executed to measure the intensity of RBCs of zebrafish in the heart area. The error bars represent the standard deviation of means, n = 10. All data were expressed by the mean ± SD, $^{\#\#}p < 0.01$ vs. control group; $^{**}p < 0.01$, $^{*}p < 0.05$ vs. model group; **(B)** HPLC chromatography of XST and chemical structural formulas of notoginsenoside R_1, ginsenoside Rg_1, ginsenoside Re, ginsenoside Rb_1, and ginsenoside Rd.

aggregation efficacy of 10 *Reynoutria multiflora* (Thunb.) Moldenke (syn. *Polygonum multiflorum*) samples. Therefore, we proposed a consistency assessment of CM injection based on a model organism. In this experiment, the AA-induced zebrafish thrombosis model established by Qi (Qi et al., 2017) was successfully applied to evaluate the batch-to-batch quality of XST. As a common model organism, zebrafish have the advantages of a short breeding cycle, small volume operation, and convenient administration, so they are suitable for the screening of effective ingredients and toxic components in TCM (Liang, 2009). The zebrafish, whose platelet function has many characteristics in common with humans, is an effective model for thrombosis study. AA is an acknowledged platelet agonist (Weyand and Shavit, 2014). Prostacyclin (PGI2) and thromboxanes (TXs) are two major biologically active substances metabolized by AA through the cyclooxygenase pathway. The breaking of the TXA2/PGI2 balance is the start of platelet aggregation and vasoconstriction (Patrono et al., 1984). Our previous work demonstrated that anti-platelet aggregation was one of the primary mechanisms of XST involved in preventing ischemia-reperfusion injury (Zhao et al., 2017). The clinical dosage of XST is 200–400 mg/D. Based on clinical dosage, we found that XST alleviated cerebral I/R injury in rats with dosages of 40 mg/kg and 80 mg/kg (Wang et al., 2015). Besides, XST could improve myocardial energy metabolism in hypoxia/reoxygenation injured H9c2 cells dose-dependently (200–400 μg/ml) (Zhao et al., 2017). It has been proven that PNS could promote angiogenesis in zebrafish at 100–300 μg/ml (Hong et al., 2009). Using the concentration of 400 μg/ml, XST was able to reverse the aggregation in caudal venous and enhance the RBCs intensity of thrombotic zebrafish significantly (**Figure 1**). XST improved the blood flow and caudal vein RBCs accumulation of thrombotic transgenic LCR-GFP zebrafish (**Figure 2**). Furthermore, XST could resist AA-induced zebrafish thrombosis in a dose-dependent manner (200–400 μg/ml) (**Figure 3**). Therefore, we selected 400 μg/ml of XST as a dosage for the quality evaluation experiments.

During the development of thrombosis, the coagulation cascade is an important process, which contains a series of coagulation factors. The activation of coagulation factors will cause the formation of fibrin. The *fga* gene, which encodes

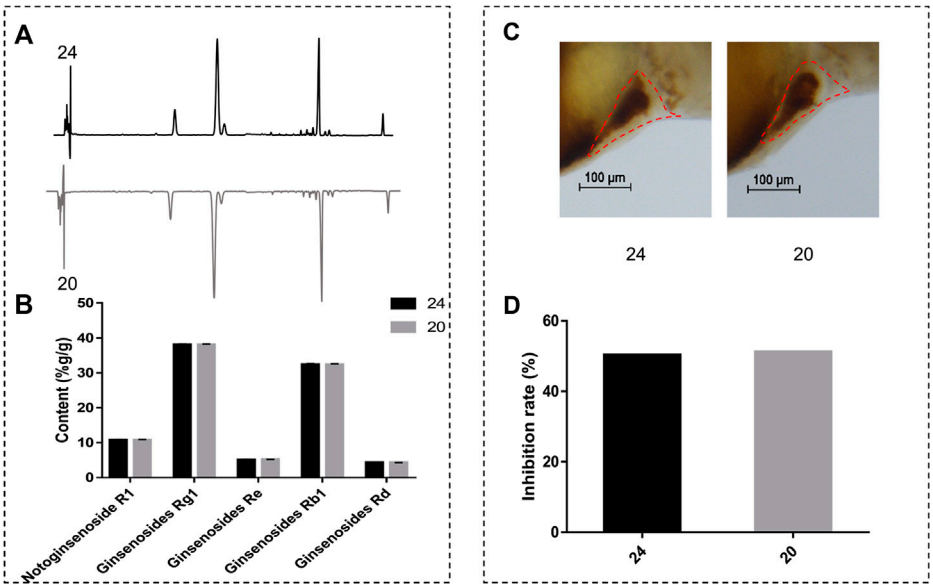

FIGURE 6 | (A) The chromatograms of XST; **(B)** content analysis results of notoginsenoside R_1, ginsenoside Rg_1, ginsenoside Re, ginsenoside Rb_1, and ginsenoside Rd of two batches of XST; **(C)** representative images of two batches of XST treated thrombotic zebrafish, RBCs were marked by red dashed lines; **(D)** inhibition rates of two batches of XST.

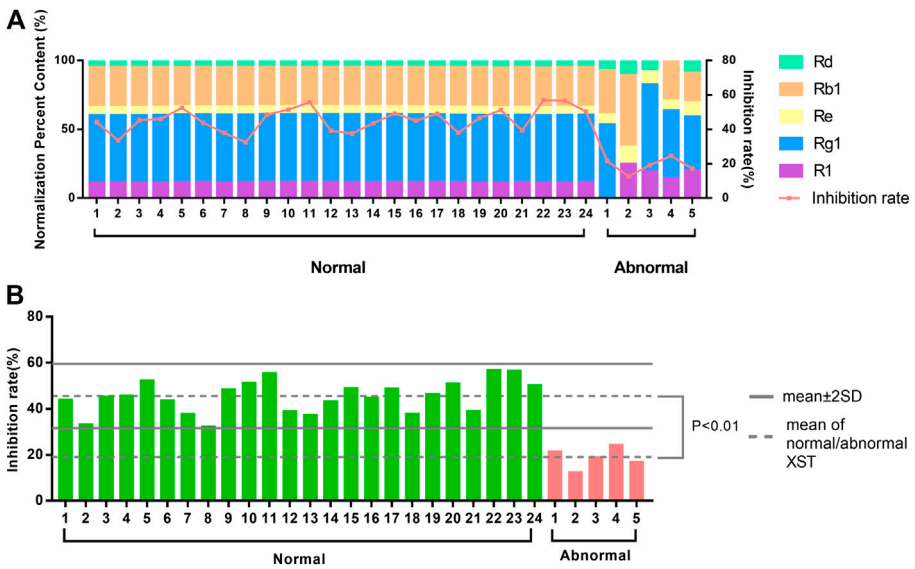

FIGURE 7 | (A) The distinction between area normalization percent content and inhibition rates of 24 normal batches of XST and five abnormal batches of XST. **(B)** The distinction between the inhibition rates of 24 normal batches of XST and five abnormal batches of XST.

fibrinogen, is one of the key genes in the coagulation cascade (Vo et al., 2013). Fibrinogen can interact with the platelet glycoprotein IIb-IIIa to cause platelet aggregation (Farrell et al., 1992). In this study, the expression of *fga* was greatly increased after AA induction, while it was significantly decreased with XST treatment. The results suggested that XST may inhibit the platelet aggregation by reducing the expression of *fga*. *Ptgs2a* and *ptgs2b* are homologous genes of prostaglandin-endoperoxide synthase 2 (*ptgs2*) in mammalian (Ishikawa et al., 2007), which play a key role in inflammatory reaction (Hellmann et al., 2015). Our results showed that AA increased the expression of *ptgs2a* and *ptgs2b* in zebrafish, while XST downregulated the expression of *ptgs2b*, which implied that XST might have an anti-thrombotic effect through ameliorating inflammatory response (**Figure 4**).

Notoginsenoside R_1, ginsenoside Rg_1, ginsenoside Rb_1, ginsenoside Rd, and ginsenoside Re occupied approximately 85% of the total ingredients in XST. Our results indicated that notoginsenoside R_1, ginsenoside Rg_1, ginsenoside Rb_1, and ginsenoside Rd had significant anti-thrombotic effects in the AA-induced zebrafish thrombosis model (**Figure 5**). Studies had been reported that PNS, notoginsenoside R_1, ginsenoside Rg_1, and ginsenoside Rb_1 could inhibit venous thrombosis induced by photochemical reaction (Wang et al., 2008a), ginsenoside Rg_1 was able to inhibit the activation of platelets and thrombosis of arterial, those results were in line with ours (Zhou et al., 2014).

In order to compare the content of major components and anti-thrombosis rate batch-to-batch, we selected two normal batches of XST for content analysis and anti-thrombotic efficacy detection (**Figure 6**). Anti-thrombotic efficacy was expressed in inhibition rate. The results showed that the component content and inhibition rates of the two batches of XST were very similar, which indicated that the anti-thrombotic effects of the two batches of XST were in accordance with the chemical analysis results.

To verify whether the zebrafish thrombosis model could distinguish normal XST and abnormal XST accurately, we prepared five abnormal batches of XST according to the ratio of the content of five main components. Each abnormal batch was obtained by reducing or excluding the content of one or two components. The 24 normal batches of XST and five abnormal batches of XST were analyzed by HPLC. The relative content of components in each sample was determined by the normalization method. The components percentages in normal batches were stable, while significant variation was observed in abnormal batches, implying the difference between normal and abnormal samples in chemical composition. The zebrafish thrombosis model was used to detect the inhibition rates of these batches and check whether the results of the two detection methods were consistent. The results showed that the inhibition rates were in accordance with the components percentages. Furthermore, the values of mean ± 2SD could distinguish the abnormal batches from the whole batches, thus the zebrafish model could significantly distinguish normal and abnormal XST. It was noteworthy that the deficiency of ginsenoside Rg_1 and ginsenoside Rb_1 causing a relatively great change of inhibition rates.

CONCLUSION

In this study, we proved the antithrombotic effects of XST and its potential mechanism. In addition, the inhibition rates of XST in the zebrafish thrombosis model were consistent with the relative percentages of main active compounds in normal or abnormal batches of XST. In short, the study provided a bioassay-based approach to evaluating the batch-to-batch consistency of XST by a zebrafish thrombosis model.

DATA AVAILABILITY STATEMENT

The raw data supporting the conclusions of this article will be made available by the authors, without undue reservation.

ETHICS STATEMENT

The animal study was reviewed and approved by the Institutional Animal Care and Use Committee of the Laboratory Animal Center, Zhejiang University.

AUTHOR CONTRIBUTIONS

XZ designed the research; XM and YC performed the research, analyzed the data; XM, YC, and SJ wrote the manuscript. All authors reviewed the manuscript.

FUNDING

This work was financially supported by the National Natural Science Foundation of China (Grant No. 82073999) and the National Standardization of Traditional Chinese Medicine Project (Grant No. ZYBZH-C-HLJ-18).

ACKNOWLEDGMENTS

We appreciate the experimental support from the Public Platform of Medical Research Center, Academy of Chinese Medical Science, Zhejiang Chinese Medical University.

REFERENCES

Chen, M., Li, H., and Qi, S. (2014). Influence of xuesaitong injection to forming of acute cerebral infarction. *Chin. J. Exp. Tradit. Med. Formulae*. 20 (10), 196–200. doi:10.13422/j.cnki.syfjx.2014100196

Farrell, D. H., Thiagarajan, P., Chung, D. W., and Davie, E. W. (1992). Role of fibrinogen alpha and gamma chain sites in platelet aggregation. *Proc. Natl. Acad. Sci. USA* 89 (22), 10729–10732. doi:10.1073/pnas.89.22.10729

FDA, U. S. (2016). Botanical drug development guidance for industry Available at: https://www.fda.gov/regulatory-information/search-fda-guidance-documents/botanical-drug-development-guidance-industry (Accessed October 28, 2020).

Gibbins, J. M., and Mahaut-Smith, M. P. (2012). *Platelets and megakaryocytes*. London, United Kingdom: Humana Press.

He, L., Chen, Y., Liang, Z., Li, Y., Zhou, M., Yuan, Z., et al. (2016). A rapid and comprehensive quality assessing method of Yin-Qiao-Jie-Du tablets using UHPLC-QTOF-MS in combination with multivariate statistical analysis. *J. Pharm. Biomed. Anal.* 124, 129–137. doi:10.1016/j.jpba.2016.02.023

Hellmann, J., Tang, Y., Zhang, M. J., Hai, T., Bhatnagar, A., Srivastava, S., et al. (2015). Atf3 negatively regulates Ptgs2/Cox2 expression during acute inflammation. *Prostaglandins Other Lipid Mediat.* 116–117, 49–56. doi:10.1016/j.prostaglandins.2015.01.001

Hong, S. J., Wan, J. B., Zhang, Y., Hu, G., Lin, H. C., Seto, S. W., et al. (2009). Angiogenic effect of saponin extract from Panax notoginseng on HUVECs *in vitro* and zebrafish *in vivo*. *Phytother Res.* 23 (5), 677–686. doi:10.1002/ptr.2705

Ishikawa, T. O., Griffin, K. J., Banerjee, U., and Herschman, H. R. (2007). The zebrafish genome contains two inducible, functional cyclooxygenase-2 genes. *Biochem. Biophys. Res. Commun.* 352 (1), 181–187. doi:10.1016/j.bbrc.2006.11.007

Jagadeeswaran, P., Sheehan, J. P., Craig, F. E., and Troyer, D. (1999). Identification and characterization of zebrafish thrombocytes. *Br. J. Haematol.* 107 (4), 731–738. doi:10.1046/j.1365-2141.1999.01763.x

Kalueff, A. V., Stewart, A. M., and Gerlai, R. (2014). Zebrafish as an emerging model for studying complex brain disorders. *Trends Pharmacol. Sci.* 35 (2), 63–75. doi:10.1016/j.tips.2013.12.002

Lam, W., Ren, Y., Guan, F., Jiang, Z., Cheng, W., Xu, C., et al. (2018). Mechanism based quality control (MBQC) of herbal products: a case study YIV-906 (PHY906). *Front. Pharmacol.* 9, 1324. doi:10.3389/fphar.2018.01324

Lang, M. R., Gihr, G., Gawaz, M. P., and Müller, I. I. (2010). Hemostasis in *Danio rerio*: is the zebrafish a useful model for platelet research?. *J. Thromb. Haemost.* 8 (6), 1159–1169. doi:10.1111/j.1538-7836.2010.03815.x

Li, C., Tu, C., Che, Y., Zhang, M., Dong, B., Zhou, X., et al. (2019). Bioassay based screening for the antiplatelet aggregation quality markers of Polygonum multiflorum with UPLC and chemometrics. *J. Pharm. Biomed. Anal.* 166, 264–272. doi:10.1016/j.jpba.2019.01.005

Li, J. P., Liu, Y., Guo, J. M., Shang, E. X., Zhu, Z. H., Zhu, K. Y., et al. (2017). A comprehensive strategy to evaluate compatible stability of Chinese medicine injection and infusion solutions based on chemical analysis and bioactivity assay. *Front. Pharmacol.* 8, 833. doi:10.3389/fphar.2017.00833

Li, W., Han, H., Cheng, Z., Zhang, Y., Liu, S., and Qu, H. (2016). A feasibility research on the monitoring of traditional Chinese medicine production process using NIR-based multivariate process trajectories. *Sens. Actuators, B* 231, 313–323. doi:10.1016/j.snb.2016.03.023

Liang, A. (2009). Zebrafish–useful model for pharmacodynamics and toxicity screening of traditional Chinese medicine. *Zhongguo Zhong Yao Za Zhi* 34 (22), 2839–2842. doi:10.3321/j.issn:1001-5302.2009.22.001

Liu, Y., Sun, G., Luan, J., Ling, J., Zhang, J., and Yang, F. (2016). A comprehensive strategy to monitor quality consistency of Weibizhi tablets based on integrated MIR and UV spectroscopic fingerprints, a systematically quantified fingerprint method, antioxidant activities and UPLC-Q-TOF-MS chemical profiling. *Rsc Adv.* 6 (1), 366–375. doi:10.1039/c5ra21468h

Loehr, H., and Hammerschmidt, M. (2011). Zebrafish in endocrine systems: recent advances and implications for human disease. *Annu. Rev. Physiol.* 73, 183–211. doi:10.1146/annurev-physiol-012110-142320

Ma, X., Jiang, S., and Zhao, X. (2019). Biological evaluation of xuesaitong injection based on multi-indicators anti-inflammatory activity. *J. Zhejiang. Chin. Med. Univ.* 43 (5), 399–406. doi:10.16466/j.issn1005-5509.2019.05.003

MacRae, C. A., and Peterson, R. T. (2015). Zebrafish as tools for drug discovery. *Nat. Rev. Drug Discov.* 14 (10), 721–731. doi:10.1038/nrd4627

Pan, W., Ma, J., Xiao, X., Huang, Z., Zhou, H., Ge, F., et al. (2017). Near-infrared spectroscopy assay of key quality-indicative ingredients of Tongkang tablets. *AAPS PharmSciTech* 18 (3), 913–919. doi:10.1208/s12249-016-0562-7

Patrono, C., Preston, F. E., and Vermylen, J. (1984). Platelet and vascular arachidonic acid metabolites: can they help detect a tendency towards thrombosis?. *Br. J. Haematol.* 57 (2), 209–212. doi:10.1111/j.1365-2141.1984.tb02888.x

Peterson, R. T., and MacRae, C. A. (2012). Systematic approaches to toxicology in the zebrafish. *Annu. Rev. Pharmacol. Toxicol.* 52, 433–453. doi:10.1146/annurev-pharmtox-010611-134751

Qi, Y., Zhao, X., Liu, H., Wang, Y., Zhao, C., Zhao, T., et al. (2017). Identification of a quality marker (Q-Marker) of Danhong injection by the zebrafish thrombosis model. *Molecules* 22 (9), 1443. doi:10.3390/molecules22091443

Shi, P., Lin, X., and Yao, H. (2018). A comprehensive review of recent studies on pharmacokinetics of traditional Chinese medicines (2014-2017) and perspectives. *Drug Metab. Rev.* 50 (2), 161–192. doi:10.1080/03602532.2017.1417424

Stewart, A. M., Braubach, O., Spitsbergen, J., Gerlai, R., and Kalueff, A. V. (2014). Zebrafish models for translational neuroscience research: from tank to bedside. *Trends Neurosci.* 37 (5), 264–278. doi:10.1016/j.tins.2014.02.011

Tsang, M. S.-M., Shaw, P.-C., Chu, I. M.-T., Cheng, L., Wong, E. C.-W., Lau, D. T.-W., et al. (2019). High-throughput immunological analysis of Dictamni Cortex: implication in the quality control of herbal medicine. *Molecules* 24 (16), 2880. doi:10.3390/molecules24162880

Tu, X., Deng, Y., Chen, J., Hu, Q., He, C., Jordan, J. B., et al. (2016). Screening study on the anti-angiogenic effects of Traditional Chinese Medicine - Part I: heat-clearing and detoxicating TCM. *J. Ethnopharmacol.* 194, 280–287. doi:10.1016/j.jep.2016.09.010

Vo, A. H., Swaroop, A., Liu, Y., Norris, Z. G., and Shavit, J. A. (2013). Loss of fibrinogen in zebrafish results in symptoms consistent with human hypofibrinogenemia. *PLoS One* 8 (9), e74682. doi:10.1371/journal.pone.0074682

Wang, F., Liu, Y., Liu, L., Zeng, Q., Fan, J., Wang, C., et al. (2008a). Inhibitory effect of panax notoginseng saponins, panax notoginseng saponins R1, ginsenoside Rb1, ginsenoside Rg1 on photochemical reaction induced mesenteric venous thrombosis in rats——the main component of Panax notoginseng inhibits venous thrombosis. *World Sci. Technology-Modernization Traditional Chin. Med. Materia Med.* 10 (3), 106–111. doi:10.3969/j.issn.1674-3849.2008.03.022

Wang, L., Li, Z., Zhao, X., Liu, W., Liu, Y., Yang, J., et al. (2013). A network study of Chinese medicine xuesaitong injection to elucidate a complex mode of action with multicompound, multitarget, and multipathway. *Evid. Based Complement. Alternat Med.* 2013, 652373. doi:10.1155/2013/652373

Wang, L., Li, Z., Shao, Q., Li, X., Ai, N., Zhao, X., et al. (2014). Dissecting active ingredients of Chinese medicine by content-weighted ingredient-target network. *Mol. Biosyst.* 10 (7), 1905–1911. doi:10.1039/c3mb70581a

Wang, L., Yu, Y., Yang, J., Zhao, X., and Li, Z. (2015). Dissecting Xuesaitong's mechanisms on preventing stroke based on the microarray and connectivity map. *Mol. Biosyst.* 11 (11), 3033–3039. doi:10.1039/c5mb00379b

Wang, J., Guo, Y., and Li, G. L. (2016). Current status of standardization of traditional Chinese medicine in China. *Evid. Based Complement. Alternat. Med.* 2016, 9123103. doi:10.1155/2016/9123103

Wang, N., Li, Z.-Y., Zheng, X.-L., Li, Q., Yang, X., and Xu, H. (2018). Quality assessment of kumu injection, a traditional Chinese medicine preparation, using HPLC combined with chemometric methods and qualitative and quantitative analysis of multiple alkaloids by single marker. *Molecules* 23 (4), 856. doi:10.3390/molecules23040856

Wang, X., Lv, H., Sun, H., Jiang, X., Wu, Z., Sun, W., et al. (2008b). Quality evaluation of Yin Chen Hao Tang extract based on fingerprint chromatogram and simultaneous determination of five bioactive constituents. *J. Sep. Sci.* 31 (1), 9–15. doi:10.1002/jssc.200700376

Warner, T. D., Nylander, S., and Whatling, C. (2011). Anti-platelet therapy: cyclo-oxygenase inhibition and the use of aspirin with particular regard to dual anti-platelet therapy. *Br. J. Clin. Pharmacol.* 72 (4), 619–633. doi:10.1111/j.1365-2125.2011.03943.x

Wen, Y., and Liu, L. (2007). 80 cases of acute myocardial infarction treated by xuesaitong injection. *Shaanxi. J. Tradit. Chin. Med.* 10, 1289–1290. doi:10.3969/j.issn.1000-7369.2007.10.011

Weyand, A. C., and Shavit, J. A. (2014). Zebrafish as a model system for the study of hemostasis and thrombosis. *Curr. Opin. Hematol.* 21 (5), 418–422. doi:10.1097/moh.0000000000000075

Wu, X., Zhang, H., Fan, S., Zhang, Y., Yang, Z., Fan, S., et al. (2018). Quality markers based on biological activity: a new strategy for the quality control of traditional Chinese medicine. *Phytomedicine* 44, 103–108. doi:10.1016/j.phymed.2018.01.016

Yang, W., Ma, L., Li, S., Cui, K., Lei, L., and Ye, Z. (2017). Evaluation of the cardiotoxicity of evodiamine *in vitro* and *in vivo*. *Molecules* 22 (6), 943. doi:10.3390/molecules22060943

Yao, H., Shi, P., Shao, Q., and Fan, X. (2011). Chemical fingerprinting and quantitative analysis of a Panax notoginseng preparation using HPLC-UV and HPLC-MS. *Chin. Med.* 6, 9. doi:10.1186/1749-8546-6-9

Zhang, L., Ma, L., Feng, W., Zhang, C., Sheng, F., Zhang, Y., et al. (2014). Quality fluctuation detection of an herbal injection based on biological fingerprint combined with chemical fingerprint. *Anal. Bioanal. Chem.* 406 (20), 5009–5018. doi:10.1007/s00216-014-7918-1

Zhao, M., Dai, Y., Li, Q., Li, P., Qin, X. M., and Chen, S. (2018). A practical quality control method for saponins without UV absorption by UPLC-QDA. *Front. Pharmacol.* 9, 1377. doi:10.3389/fphar.2018.01377

Zhao, X., Zhang, F., and Wang, Y. (2017). Proteomic analysis reveals Xuesaitong injection attenuates myocardial ischemia/reperfusion injury by elevating pyruvate dehydrogenase-mediated aerobic metabolism. *Mol. Biosyst.* 13 (8), 1504–1511. doi:10.1039/c7mb00140a

Zhou, Q., Jiang, L., Xu, C., Luo, D., Zeng, C., Liu, P., et al. (2014). Ginsenoside Rg1 inhibits platelet activation and arterial thrombosis. *Thromb. Res.* 133 (1), 57–65. doi:10.1016/j.thromres.2013.10.032

Conflict of Interest: The authors declare that the research was conducted in the absence of any commercial or financial relationships that could be construed as a potential conflict of interest.

The handling editor declared a past co-authorship with the authors XZ and XC

frontiers in Pharmacology

ORIGINAL RESEARCH
published: 19 April 2021
doi: 10.3389/fphar.2021.622744

Pure Total Flavonoids From Citrus Protect Against Nonsteroidal Anti-inflammatory Drug-Induced Small Intestine Injury by Promoting Autophagy *in vivo* and *in vitro*

Shanshan Chen[1†], *Jianping Jiang*[2,3†], *Guanqun Chao*[4], *Xiaojie Hong*[1], *Haijun Cao*[1] and *Shuo Zhang*[1*]

[1]First Affiliated Hospital, Zhejiang Chinese Medical University, Zhejiang, China, [2]Department of Pharmacy, School of Medicine, Zhejiang University City College, Zhejiang, China, [3]Zhejiang You-du Biotech Limited Company, Quzhou, China, [4]Sir Run Run Shaw Hospital, Zhejiang, China

OPEN ACCESS

Edited by:
Peng Li,
University of Macau, China

Reviewed by:
Jia Liu,
China Academy of Chinese Medical Sciences, China
Gianfranco Natale,
University of Pisa, Italy

***Correspondence:**
Shuo Zhang
zhangshuotcm@163.com

[†]These authors have contributed equally to these work

Specialty section:
This article was submitted to Ethnopharmacology, a section of the journal Frontiers in Pharmacology

Received: 29 October 2020
Accepted: 24 March 2021
Published: 19 April 2021

Citation:
Chen S, Jiang J, Chao G, Hong X, Cao H and Zhang S (2021) Pure Total Flavonoids From Citrus Protect Against Nonsteroidal Anti-inflammatory Drug-Induced Small Intestine Injury by Promoting Autophagy in vivo and in vitro. Front. Pharmacol. 12:622744. doi: 10.3389/fphar.2021.622744

Small intestine injury is an adverse effect of non-steroidal anti-inflammatory drugs (NSAIDs) that urgently needs to be addressed for their safe application. Although pure total flavonoids from citrus (PTFC) have been marketed for the treatment of digestive diseases, their effects on small intestine injury and the underlying mechanism of action remain unknown. This study aimed to investigate the potential role of autophagy in the mechanism of NSAID (diclofenac)-induced intestinal injury *in vivo* and *in vitro* and to demonstrate the protective effects of PTFC against NSAID-induced small intestine disease. The results of qRT-PCR, western blotting, and immunohistochemistry showed that the expression levels of autophagy-related 5 (Atg5), light chain 3 (LC3)-II, and tight junction (TJ) proteins ZO-1, claudin-1, and occludin were decreased in rats with NSAID-induced small intestine injury and diclofenac-treated IEC-6 cells compared with the control groups. In the PTFC group, Atg5 and LC3-II expression, TJ protein expression, and the LC3-II/LC3-I ratio increased. Furthermore, the mechanism by which PTFC promotes autophagy *in vivo* and *in vitro* was evaluated by western blotting. Expression levels of p-PI3K and p-Akt increased in the intestine disease-induced rat model group compared with the control, but decreased in the PTFC group. Autophagy of IEC-6 cells was upregulated after treatment with a PI3K inhibitor, and the upregulation was significantly more after PTFC treatment, suggesting PTFC promoted autophagy through the PI3K/Akt signaling pathway. In conclusion, PTFC protected intestinal barrier integrity by promoting autophagy, which demonstrates its potential as a therapeutic candidate for NSAID-induced small intestine injury.

Keywords: autophagy, pure total flavonoids from citrus, non-steroidal anti-inflammatory drugs, PI3K-AKT pathway, small intestine injury

INTRODUCTION

Non-steroidal anti-inflammatory drugs (NSAIDs), such as diclofenac and aspirin, are the most prescribed drugs worldwide and are commonly used in the treatment of chronic pain, tumor chemoprevention, and cardio-cerebrovascular diseases (Gwee et al., 2018). The expanding use of capsule endoscopy and double-balloon enteroscopy have increased the incidence of adverse effects on the digestive tract, including small intestine injury, that is currently receiving increased attention. A recent study confirmed that the incidence of NSAID-induced lower digestive tract injury is higher than that of the upper digestive tract (Sostres et al., 2013). Injury to the small intestine induced by NSAIDs is characterized by intestinal mucosal erosion, ulceration, stricture, and even bleeding, which can be severely harmful to the health of the individual (Shin et al., 2017). Therefore, small intestine injury is an adverse event associated with NSAID treatment that urgently needs to be addressed to allow for the safe administration of these drugs.

Dysfunction of the mechanical barrier of the intestinal mucosa is considered to play a vital role in the occurrence and development of NSAID-induced lower digestive tract injury (Bjarnason et al., 2018). Furthermore, intestinal mucosa permeability increases in NSAID-induced enteropathy, which causes intestinal bacteria, toxins, bile acids, and proteolytic enzymes to penetrate intestinal epithelial cells and cause intestinal mucosal erosion and ulceration, leading to a series of symptoms (Ravikumar et al., 2004). However, the mechanism by which the intestinal mucosa mechanical barrier is impaired has not been clarified. Elucidating its regulatory mechanism would facilitate the identification of effective strategies to prevent and treat NSAID-induced intestinal injury. Previous studies have determined that expression of intestinal tight junction (TJ) proteins, including zonula occludens-1 (ZO-1), claudin-1 (CLDN-1), and occludin (OCLN), and cytoskeleton-related proteins decreases in NSAID-induced small intestine injury. Destruction of the intestinal epithelial cytoskeleton and TJs increases intestinal epithelium permeability, which in turn causes intestinal mucosa damage (Chao and Zhang, 2012).

A recent study showed that autophagy is closely involved in the barrier function of the intestinal mucosa and regulation of intestinal epithelial TJs (Wong et al., 2019). Autophagy is generally considered a process by which cells are renewed. It degrades senescent organelles, long-lived proteins, and invading pathogens through lysosomes and recycles the degradation products to maintain the physiological processes required for basic life activities (Mizushima and Komatsu, 2011; Galluzzi et al., 2014). Recent studies have found that autophagy is affected in various diseases by the regulation of AMP-activated protein kinase (AMPK), mitogen-activated protein kinase (MAPK), Beclin-1/B-cell lymphoma (Bcl)-2, and the mammalian target of rapamycin (mTOR) pathway (Mohammadinejad et al., 2019). However, the mechanism underlying the intestinal mucosal mechanical barrier impairment has not been clarified.

Citrus flavonoids have been studied in recent years owing to their beneficial characteristics, such as anti-oxidative, anti-inflammatory, and pro-cardiovascular activities (Bondonno et al., 2018; Vazhappilly et al., 2019). Pure total flavonoids from citrus (PTFC) are flavonoids isolated and purified from the dry and ripe peels of citrus species (Citrus Changshan-huyou Y.B Chang; Qu Zhi Qiao), which are mainly produced in Changshan and Quzhou in Zhejiang Province, China. PTFC consist of four flavonoids, naringin, neohesperidin, narirutin, and hesperidin. Naringin plays an antioxidant role in improving liver injury and downregulates inflammatory mediators (Adil et al., 2015). *In vitro* studies have shown that naringin decreases hepatic stellate cell activity and inhibits liver fibrosis by inhibiting mTOR-autophagy (Shi et al., 2016). Narirutin inhibits the production of inflammatory mediators via NF-kB and MAPKs in lipopolysaccharide (LPS)-stimulated macrophages (Ha et al., 2012). In addition, naringin can increase the level of antioxidants *in vivo* to protect the liver and small intestine from oxidative damage caused by free radicals (Wu et al., 2017). To date, only a few studies have investigated the potential implication of citrus flavonoids in intestinal mucosal barrier repair (Stevens et al., 2019), making further investigation needed. Furthermore, the effects of PTFC on autophagy remain unknown. To elucidate this important interaction, we investigated whether improvement in NSAID-induced small intestine injury by PTFC is mediated by its promotion of autophagy.

MATERIALS AND METHODS

PTFC Extraction and Purification

PTFC were prepared as previously described (Jiang et al., 2019). Briefly, 1,000 g of Qu Zhi Qiao (*Citrus Paradisi cv. Changshanhuyou*) fruit peel was extracted twice with 0.10% calcium hydroxide [$Ca(OH)_2$] solution at 100°C for 1.5 h. Filtrates were mixed and decompressed. The total flavonoid preparations were at a concentration of 3.83 mg/ml. The total flavonoids were separated and enriched using HPD-300 macroporous resin. The amounts of loaded samples and the method of eluting the samples were as described above. The eluant was collected and concentrated by drying for use in subsequent experiments.

PTFC Flavonoid Content

The PTFC composition was analyzed by high-performance liquid chromatography (HPLC) using a system that included a quaternary gradient pump, an online degasser, a UV detector, and a column thermostat produced by Shimadzu Corporation. Chromatographic separation was performed at 25°C on a Hypersil SB C18 column (Thermo Fisher Scientific, MA, United States). The mobile phase was water-acetonitrile and the samples were eluted using a gradient method consisting of the following elution gradient: 0–15 min, 20% acetonitrile; 15–35 min, 60–100% acetonitrile; 42–45 min, 100–20% acetonitrile; 45–50 min, 20% acetonitrile. The flow rate of the mobile phase was 1.0 ml/min, the wavelength was 283 nm, and the injection volume was 10 μl. The flavonoids in the samples were identified based on the chromatographic peaks of the

standard substances that constitute PTFC (neohesperidin, naringin, narirutin, and hesperidin).

The total flavonoid content of PTFC was determined as previously described (Jiang et al., 2019). Briefly, each flavonoid extract was dissolved in methanol (1:1, w/v). Then, 0.5 ml of 10% $Al(NO_3)_3$ solution was added followed by 0.5 ml of 5% $NaNO^2$ solution. The absorbance of the samples was measured at 0, 5, and 10 min at a wavelength of 510 nm. The total flavonoid content in the PTFC was calculated using a standard curve.

Animals

Eight-week-old male Sprague–Dawley rats (220 ± 20 g) were obtained from Zhejiang Chinese Medical University and were fed standard laboratory chow and provided tap water. The rats were randomly divided into three groups and housed in cages (four rats per cage) in climate-controlled rooms at 20 ± 2°C and 50–60% humidity on a 12 h light/dark cycle. The study was approved by the local Animal Ethics Committee of Zhejiang Chinese Medical University (Zhang et al., 2019).

Diclofenac-Induced Small Intestine Injury and Treatments

Intestinal injury was induced using diclofenac based on a method previously developed in our laboratory (Chao and Zhang, 2012). The treatment course and dose of diclofenac were chosen as it causes small intestine injury similar to those induced by NSAIDs in humans. To establish the experimental model, non-fasted rats (n = 8 per group) were treated by intragastric administration of diclofenac (7.5 mg/kg) twice a day for 5 days. The control groups were treated with intragastric administration of 2 ml of saline twice a day for 5 days. PTFC (100 mg/kg/day), which was supplied by Zhejiang Chinese Medical University, was administered 9 days before the initial diclofenac administration and then both drugs were co-administered on the final 5 days. All rats were anesthetized by an intraperitoneal injection of 50 mg/kg sodium pentobarbital after the drug treatment, the small intestines were harvested for observation, and the tissue prepared for subsequent experiments.

Cell Culture and Treatments

IEC-6 cells were purchased from American Type Culture Collection (ATCC, Manassas, VA, United States) and cultured in Dulbecco's Modified Eagle Medium (DMEM), high glucose medium supplemented with penicillin (100 U/ml), streptomycin (100 mg/L), 10% fetal bovine serum (FBS), and insulin (0.1 U/ml). The cells maintained in a 37°C incubator containing 5% CO_2. The experiments consisted of the four following groups:

Model group: When the cell confluence reached approximately 60%, diclofenac sodium was added to each well at a final concentration of 60 μM. After 48 h of induction, the cells were collected for western blot analysis and immunofluorescence staining.

PTFC group: During the second 24 h of the 48 h cell modeling period, PTFC were added for continuous treatment at a final concentration of 1 mg/ml.

PI3K inhibition group: During the second 24 h of the 48 h cell modeling period, PI3K inhibitor LY294002 was added for continuous treatment at a final concentration of 20 μM.

PTFC + PI3K inhibition group: During the second 24 h of the 48 h cell modeling period, both the PI3K inhibitor LY294002 (final concentration of 20 μM) and PTFC (final concentration of 1 mg/ml) were added.

General Tissue Examination

General examination of the small intestine was performed on a 10 cm portion dissected from the ileocecal region. Injury to the small intestine tissue was evaluated and the ulcer index determined based on scoring of ulcer measurements using vernier calipers. The Reuter score was also used to quantify the intestinal damage according to the degree of adhesion (Endo et al., 2010). The total score of intestinal damage was the sum of both measurements (**Table 1**).

RNA Extraction and Real-Time Reverse Transcription Polymerase Chain Reaction (qRT-PCR) Analysis

Intestinal tissues and IEC-6 cells were collected and total RNA extracted using a TRIzol® Plus RNA Purification Kit (Thermo Fisher Scientific) according to the manufacturer's protocol. Complementary DNA (cDNA) was synthesized from the extracted RNA using SuperScript III First-Strand Synthesis SuperMix (Thermo Fisher Scientific) following the manufacturer's instructions. Real-time PCR was performed using PowerUp™ SYBR™ Green Master Mix (Applied Biosystems, United States) according to the manufacturer's instructions. The cycling conditions used were 95°C for 2 min, followed by 40 cycles of amplification at 95°C for 15 s and 60°C for 1 min. Relative expression of the target genes was normalized to glyceraldehyde 3-phosphate dehydrogenase (GAPDH) expression, evaluated using the $2^{-\Delta\Delta Ct}$ method (Livak and Schmittgen, 2001), and expressed as a ratio to the control values in the experiment. The PCR rat primer sequences used in this study are listed in **Table 2**.

Western Blot Analysis

Proteins from the small intestine tissue samples and IEC-6 cells were extracted using radioimmunoprecipitation assay (RIPA) buffer (Thermo Fisher Scientific) supplemented with a protease and phosphatase inhibitor cocktail (Thermo Fisher Scientific) and then quantified using a BCA protein assay kit (Beyotime Biotechnology, China). Approximately 50 μg of protein was loaded onto each lane of an acrylamide gel and separated by sodium dodecyl sulfate-polyacrylamide gel electrophoresis (SDS-PAGE). The electrophoretically separated protein bands were transferred onto a Hybond-P polyvinylidene fluoride (PVDF) membrane (GE Healthcare, United States). After blocking with 5% non-fat milk in Tris-buffered saline containing 0.1% Tween-20, the membranes were incubated at 4°C overnight with the following primary antibodies: rabbit anti-light chain 3 (LC3, 1:1,000, Cell Signaling Technology, United States), rabbit anti-ZO1 (1:

TABLE 1 | Ulcer score and Reuter score determination.

Reuter score		
i) Ulcer scores	0	No ulceration occurred
	1	Local hyperemia, no ulceration
	2	Ulceration without congestion or bowel wall thickening
	3	Ulceration and inflammation in one area
	4	Two or more areas of ulcer with inflammation <1 cm
	5	Several ulcers ≥1 cm and inflammation
ii) adhesion score	0	No adhesion
	1	Light adhesion, slight force required to separate the colon from other tissues
	2	Heavy adhesion

TABLE 2 | Polymerase chain reaction (PCR) primers.

Gene	GenBank accession	Primer sequences (5–3′)	Amplicon size (bp)
GAPDH	NM_017008.4	F: AAGGTCGGTGTGAACGGATTTG R: CATGTAGACCATGTAGTTGAGGTCA	127
Atg5	NM_001,014,250.1	F: TCAGCTCTGCCTTGGAACATCA R: AAGTGAGCCTCAACTGCATCCTT	95
Z O -1	NM_001,106,266.1	F: GACCCTGACCCAGTGTCTGATAA R: CTATCCCTTGCCCAGCTCTTCT	119
CLDN 1	NM_031699.2	F: GGATGGATCGGCTCTATCGTCA R: GATGGCCTGAGCAGTCACGAT	90
OCLN	NM_031329	F: CCAACGGCAAAGTGAATGGCAAGA R: CCACGGACAAGGTCAGAGGAATCT	105

GAPDH, glyceraldehyde 3-phosphate dehydrogenase; Atg5, autophagy-related 5; ZO-1, zonula occludens; CLDN-1, claudin-1; OCLN, occludin; F, forward; R, reverse; bp, base pair.

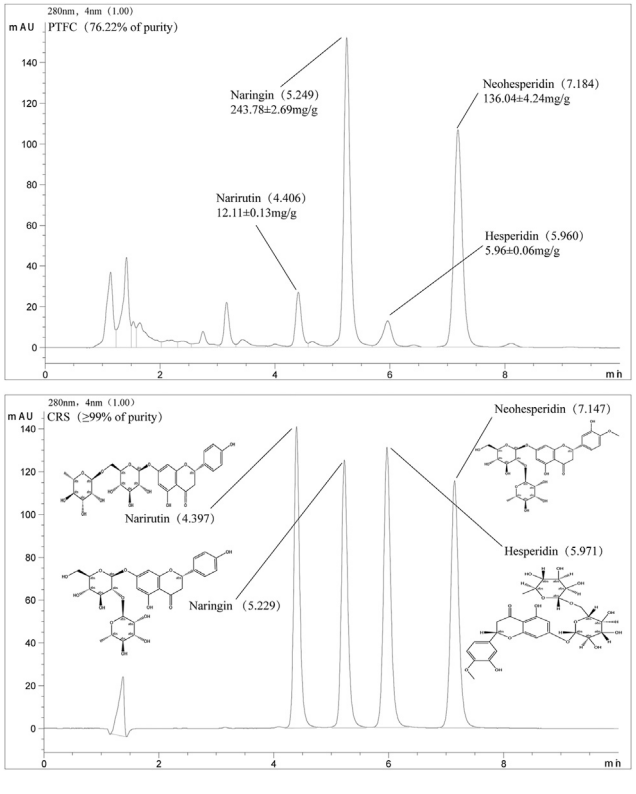

FIGURE 1 | HPLC chromatographic profile of PTFC and standard flavanones narirutin, naringin, neohesperidin, and hesperidin.

500, Abcam, United Sttaes), rabbit anti-CLDN1 (1:500 and 1: 1,000, Abcam), rabbit anti-OCLN (1:1,000, Abcam), rabbit anti-PI3K (1:500, Abcam), rabbit anti-PI3K p85 alpha (phospho Y607, 1:500, Abcam), rabbit anti-Akt (1:1,000, Cell Signaling Technology), rabbit anti-Akt (phosphor Ser473, 1:1,000, Cell Signaling Technology), rabbit anti-mTOR (1:1,000, Cell Signaling Technology), or rabbit anti-mTOR (phosphor Ser2448, 1:1,000, Cell Signaling Technology). Rabbit anti-GAPDH (1:10,000, Abcam) was used as an internal control. The membranes were then washed and incubated with a horseradish peroxidase (HRP)-labeled goat anti-rabbit secondary antibody (1:5,000, Thermo Fisher Scientific). The HRP was detected using the luminol-based enhanced chemiluminescent SuperSignal West Dura Extended Duration Substrate (Thermo Fisher Scientific). Protein expression was visualized using X-ray film and the band intensities were quantitated using Image Pro Plus 6.0 software (Media Cybernetics, United States). Data are presented as ratios of the optical density (OD) of the target protein band to that of the GAPDH band. For the p-PI3K, p-Akt, and p-mTOR subunits, the data are presented as ratios of the OD of phosphorylated bands to that of the total subunit band.

Histopathology and Histological Examination

The small intestine tissue samples were fixed with 10% formalin in phosphate-buffered saline (PBS), embedded in paraffin, cut as

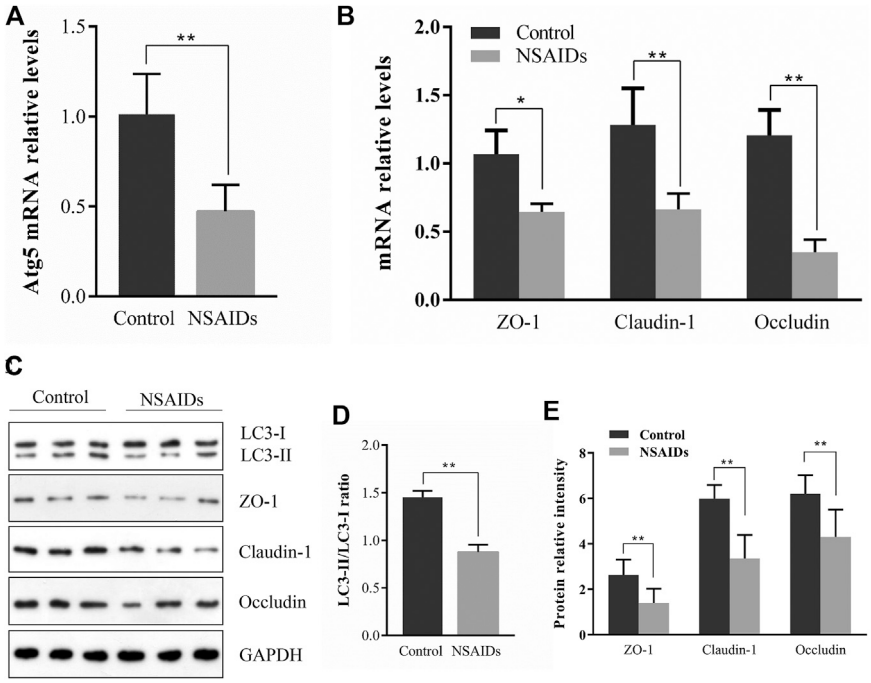

FIGURE 2 | Relationship between autophagy and tight junction (TJ) barrier in nonsteroidal anti-inflammatory drug (NSAID)-induced small intestine injury. Levels of mRNA were determined in the NSAID model group and control group using quantitative reverse transcription-polymerase chain reaction (qRT-PCR) for **(A)** autophagy-related 5 (Atg5) and **(B)** zonula occludens (ZO-1), claudin (CLDN)-1, and occludin (OCLN) **(C)** Glyceraldehyde 3-phosphate dehydrogenase (GAPDH) was used as a loading control (**D,E**) Western blotting was used to analyze protein levels in the NSAID model group and control group **(D)** Protein levels of light chain 3 (LC3) forms LC3-II and LC3-I were determined using ImageJ software and the signal density ratios of LC3-II/LC3-I were calculated **(E)** Protein levels of ZO-1, CLDN-1, and OCLN. $^{**}p < 0.01$.

3 μm-thick sections, mounted onto microscope slides, and stained with hematoxylin and eosin (H&E) for histological examination according to standard techniques. The stained sections were then examined using a light microscope (Olympus, Japan) to histologically evaluate the small intestine injuries.

Immunohistochemical (IHC) Assay

Paraffin-embedded small intestine tissue sections (5 μm) were deparaffinized in xylene and then rehydrated through a graded series of ethanol and distilled water. The rehydrated tissue sections were microwaved for antigen retrieval, treated with 3% hydrogen peroxide (H_2O_2) for 5 min, blocked with 5% bovine serum albumin. The blocked tissue sections were incubated at 4°C overnight with the following antibodies: rabbit anti-LC3 (1:1,000, Cell Signaling Technology), rabbit anti-ZO 1 (1:75, Santa Cruz, United States), rabbit anti-OCLN (1:100, Abcam), and rabbit anti-CLDN1 (1:200, Abcam). The antibody binding to their respective target antigens were detected using an Envision™ Detection Kit (DAKO, Denmark). All sections were counterstained with hematoxylin and examined under an light microscope. In addition, quantitative IHC analysis was performed using Image Pro Plus 6.0 software (Media Cybernetics). Data are shown as the fold-change of the average integrated OD (IOD) per area.

Immunofluorescence Staining

IEC6 cells (3×10^4) were seeded onto glass coverslips in 12-well plates and cultured overnight at 37°C in a 5% CO_2 incubator. After treatment with diclofenac sodium and PTFC, the cells were fixed with 4% paraformaldehyde for 30 min, followed by three PBS washes. The cells were subsequently permeabilized with 0.5% Triton X-100 solution for 5 min, blocked with 10% normal donkey serum for 1 h at room temperature. The cells were then incubated at 4°C overnight with primary antibody rabbit anti-LC3 (1:200, Cell Signaling Technology). After three washes with PBS, the cells were incubated for 1 h with Alexa Fluor® 488 Donkey Anti-Rabbit IgG (1:200; Jackson ImmunoResearch, United States). Finally, the cells were counterstained with DAPI (Beyotime, China) for 5 min and the coverslips were mounted in 10 μl of FluroGuard anti-fade solution (Bio-Rad, United States). The positive control group of cells were treated with chloroquine at a final concentration of 60 μM for 48 h.

Statistical Analysis

All data were analyzed using the Statistical Package for the Social Sciences (SPSS) 17.0 software and expressed as mean ± standard error of the mean (SEM). Comparisons between two groups were performed using a two-tailed *t*-test. Differences between multiple groups were assessed by one-way analysis of variance (ANOVA). Test results showing $p < 0.05$ (*) and $p < 0.01$ (**) were considered statistically significant.

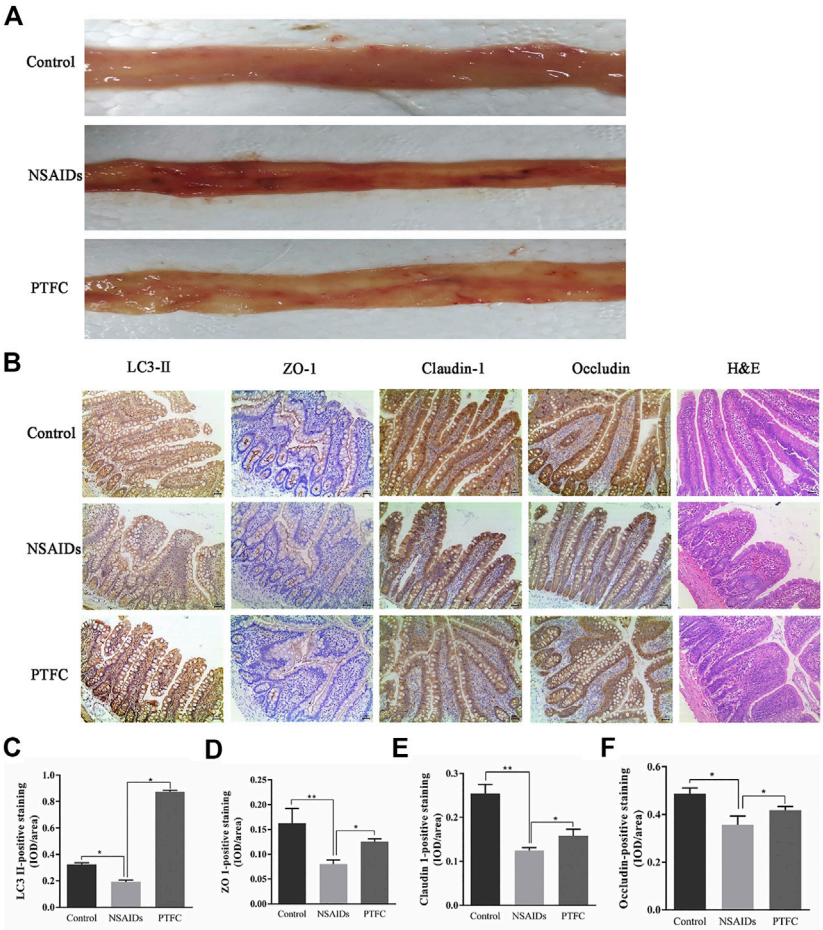

FIGURE 3 | Morphological examination of various experimental groups or rats **(A)** Morphological changes in the intestinal mucous membrane were observed **(B)** Hematoxylin and eosin (H&E) staining revealed severe injuries in the small intestines of rats in NSAID model group, whereas the PTFC group showed significant improvement in bowel lesions (×200 magnification). Immunohistochemistry (IHC) was used to evaluate expression of **(C)** light chain 3 (LC3)-II **(D)** zonula occludens (ZO)-1 **(E)** claudin (CLDN)-1, and **(F)** occludin (OCLN) in control, NSAID model, and PTFC groups of rats.

TABLE 3 | Macroscopic examination of small intestine injury in rats.

Experimental groups (n = 8 per group)	Reuter score
Control (A)	0.00 ± 0.00
Model (B)	5.25 ± 0.886[a,b]
PTFC (C)	1.125 ± 0.641[a,c]

[a]p < *0.05, compared with the control (A) group.*
[b]p < *0.05, compared with PTFC (C) groups.*
[c]p < *0.05, compared with model (B) group.*

RESULTS

PTFC Total Flavonoid Content

The HPLC chromatogram profile of PTFC is shown in **Figure 1**. The HPLC chromate-graphic profile revealed that narirutin, naringin, neohesperidin, and hesperidin were present in the PTFC sample, with retention time peaks of 4.397, 5.229, 5.971, and 7.147 min, respectively. The total flavonoid content (purity) of PTFC as rutin equivalents was 76.22%. Based on the standard curve, the narirutin, naringin, neohesperidin, and hesperidin content in PTFC were 12.11 ± 0.12 mg/g, 243.78 ± 2.69 mg/g, 5.96 ± 0.06 mg/g, and 136.04 ± 4.24 mg/g, respectively.

In vivo Inhibition of Autophagy and Down Regulation of TJ-Related Proteins in the Diclofenac-Treated NSAID Model Group

According to qRT-PCR analysis of mRNA levels, Atg5 expression in the diclofenac-treated NSAID rat model group with enhanced small intestine injury was lower than that in the untreated (uninjured) control group (**Figure 2A**). Meanwhile, qRT-PCR and western blot analysis of ZO-1, CLDN-1, and OCLN showed that expression levels of these major TJ-related proteins were lower in the NSAID model group than that in the control group (**Figures 2B,E**). Western blot analysis of the autophagy marker LC3-II showed that the NSAID model group exhibited

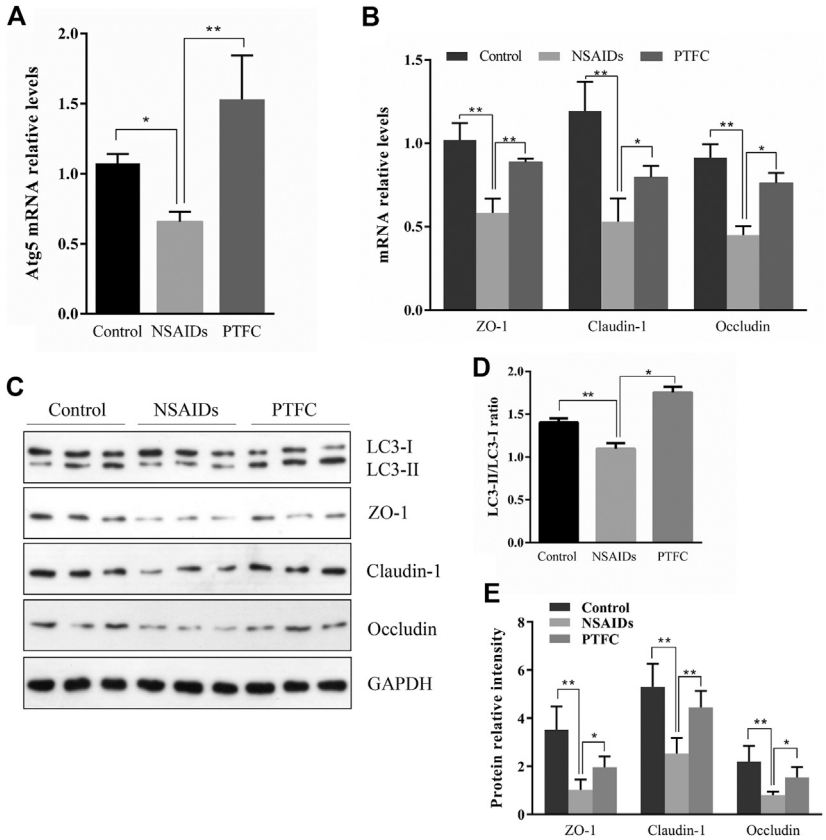

FIGURE 4 | PTFC increases TJ-related protein levels and inhibits NSAID-induced small intestine injury progression in rats. Levels of mRNA were evaluated in the NSAID model group, PTFC group, and control group of rats using quantitative reverse transcription-polymerase chain reaction (qRT-PCR) for **(A)** autophagy-related 5 (Atg5) and **(B)** ZO-1, CLDN1, and OCLN **(C)** Western blot analysis was used to determine protein expression levels in the groups of rats **(D)** Levels of light chain 3 (LC3) were determined and the signal intensity ratio of LC3-II/LC3-I was calculated using ImageJ software (**$p < 0.01$) **(E)** Protein expression of ZO-1, CLDN1, and OCLN were measured in all groups using western blotting (*$p < 0.05$ and **$p < 0.01$).

significantly lower LC3-II protein levels than those of the control group, and the LC3-II/LC3I ratio was also lower (**Figure 2D**).

PTFC Increased TJ-Related Protein Expression and Inhibited NSAID-Induced Small Intestine Injury Progression *in vivo* and *in vitro*

General tissue examination revealed that in the experimentally established NSAID-induced rat model, the mucosa was congested, edematous, eroded, and even ulcerated (**Figure 3A** and **Table 3**). In contrast, the PTFC group showed only mild hyperemia and edema. H&E staining showed that the small intestines of rats in the diclofenac-treated NSAID model group were severely injured with marked atrophy of the villi, irregular arrangement of glands, and considerable inflammatory cell infiltration. In contrast, the PTFC group exhibited significant improvements in small bowel lesions. IHC analysis revealed that LC3 expression levels were highest in the cytoplasm (**Figure 3B**). The LC3 signal showed low levels of cytoplasmic staining in the NSAID-induced model group, whereas strong staining was observed in the PTFC group. The IHC signal intensities for TJ proteins were consistent among groups. In the small intestines of rats and IEC-6 cells, expression levels of TJ proteins ZO-1, CLDN-1, and OCLN were decreased in the model group compared to that in the control group according to both qRT-PCR and western blotting, and they exhibited a greater degree of small intestine injury. Administration of PTFC attenuated the decrease in TJ protein expression and was associated with intestinal mucosal barrier repair in the NSAID-induced small intestine injury model (**Figures 4B**,**E**; **Figures 5B**,**E**).

QRT-PCR results revealed that Atg5 mRNA levels in the PTFC group were higher than those in the control group (**Figure 4A**; **Figure 5A**), whereas levels in the diclofenac-treated NSAID model group were lower. Western blot analysis of LC3-II protein expression in all three groups showed that the PTFC group exhibited a significant increase in LC3-II protein levels and the LC3-II/LC3-I ratio, whereas the diclofenac-treated NSAID model group exhibited decreased values (**Figure 4D**; **Figure 5D**).

PTFC Treatment Increased Autophagosome Formation *in vitro*

In order to evaluate the effect of PTFC on the formation of autophagosomes, immunofluorescence staining for LC3-II was

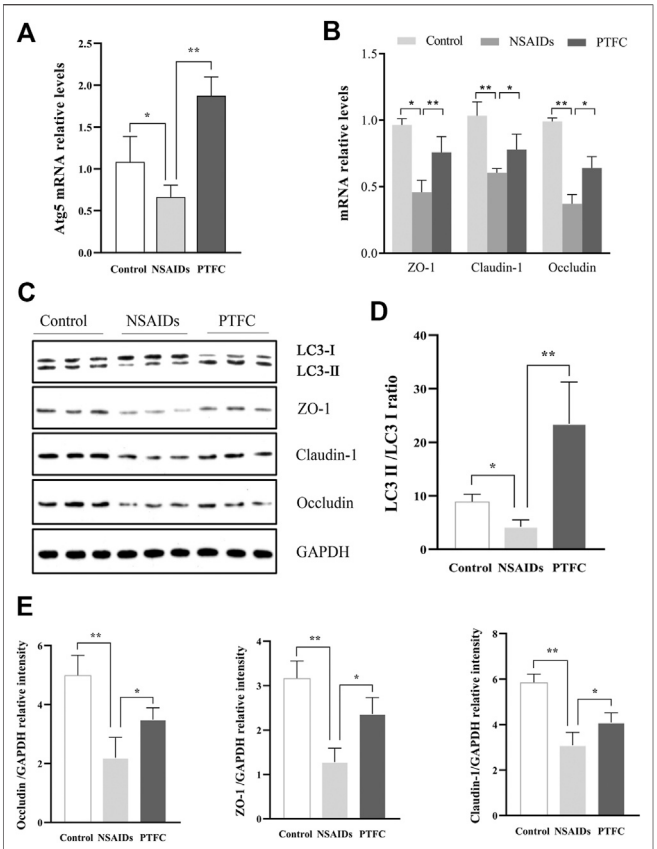

FIGURE 5 | PTFC promotes autophagy and increases TJ-related protein levels in IEC-6 cells. IEC-6 cells were untreated for the 48 h of culture (Control), treated with diclofenac for the 48 h of culture (NSAID), or treated with diclofenac for the 48 h of culture plus treatment with PTFC for the final 24 h or culture (PTFC). The mRNA levels were then detected in all groups using quantitative reverse transcription-polymerase chain reaction (qRT-PCR) **(A)** mRNA levels of autophagy-related 5 (Atg5) **(B)** mRNA levels of ZO-1, CLDN1, and OCLN **(C)** Western blot analysis was used to determine protein expression levels in the groups of cells **(D)** Levels of light chain 3 (LC3) were determined and the signal intensity ratio of LC3-II/LC3-I density ratio was calculated using ImageJ software (**$p < 0.01$) **(E)** Protein expression of ZO-1, CLDN1, and OCLN was measured in all groups using western blotting (*$p < 0.05$ and **$p < 0.01$).

performed in IEC-6 cells (**Figure 6**). The results showed the LC3-II signal in the diclofenac-treated model group was significantly decreased compared with that in the control group. Furthermore, the positive signal in the PTFC treatment group was significantly enhanced.

PTFC Increased Autophagy Through PI3K/Akt/mTOR Signaling *in vivo* and *in vitro*

Expression levels of p-PI3K, PI3K, p-Akt, Akt, p-mTOR, and mTOR were determined in the small intestine of rats by western blot analysis (**Figure 7A**). In addition, the ratios of phosphorylated to unphosphorylated proteins (p-PI3K/PI3K, p-Akt/Akt, and p-mTOR/mTOR) were calculated for all groups (**Figure 7B**). The results revealed higher values in the NSAID model groups and lower values in the PTFC groups compared to those in the control group. The ratios of phosphorylated to unphosphorylated proteins (p-PI3K/PI3K and p-Akt/Akt) in IEC-6 cells treated with the PI3K inhibitor LY294002 and PTFC were significantly lower than those in the NSAID model group (**Figures 8C,D**). The PTFC + PI3K inhibitor group demonstrated the most significant decrease. Phosphorylation of LC3-II showed the opposite trend (**Figure 8B**). This suggested that PTFC promotes autophagy through PI3K/Akt signaling.

DISCUSSION

In the present study, we used a diclofenac-induced small intestine injury rat model to explore the role of autophagy in the regulation of intestinal mucosal barrier repair by determining the expression levels of LC3-II and Atg5. The induction of autophagy may protect the intestinal mucosal barrier. LC3-II expressed on the autophagosome membrane is a classic marker of autophagy, and the presence of LC3 in autophagosomes and the conversion of LC3-I to LC3-II are considered indicators of autophagy (Sakiyama et al., 2009; Yu et al., 2013; Zhu et al., 2015).

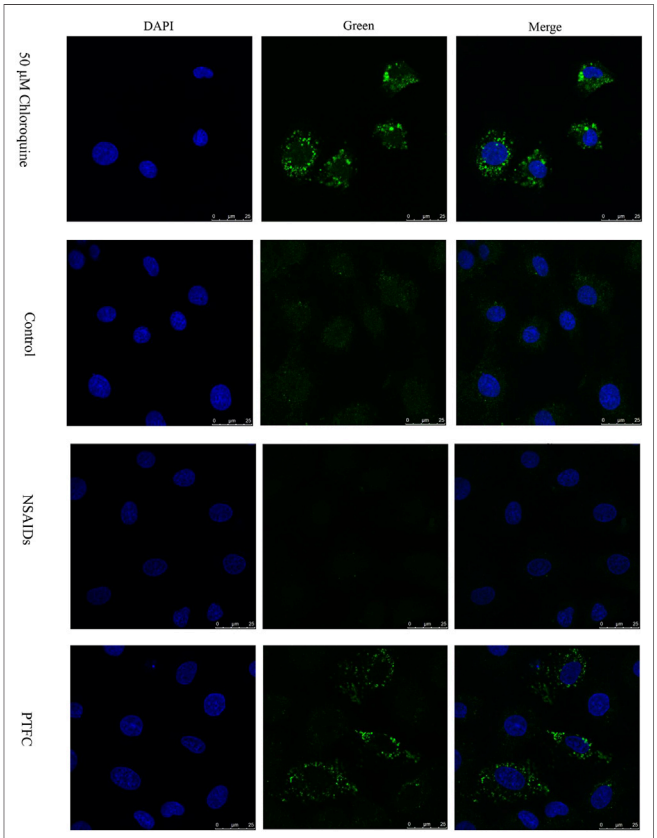

FIGURE 6 | Effect of PTFC on the formation of autophagosome in IEC-6 cells. Immunofluorescence staining of LC3-II (Green) was performed. Nuclei were stained with DAPI. Chloroquine (50 μM) was used as positive control. The results revealed that the LC3-II signal in the diclofenac-treated model group (NSAIDs) was significantly decreased compared with that in the untreated group (Control), but the positive signal in the PTFC treatment group (PTFC) was significantly enhanced.

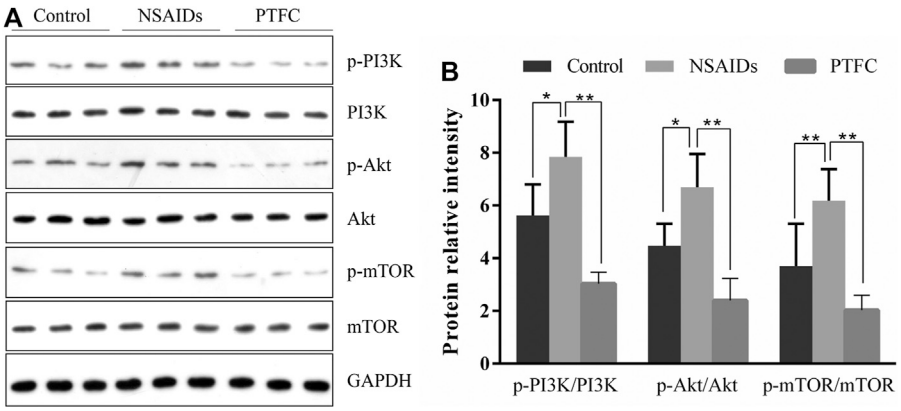

FIGURE 7 | PTFC increases autophagy in rats through PI3K/Akt Signaling **(A)** Western blot analysis was performed to determine expression levels of phosphoinositide 3-kinase (PI3K), phosphorylated-PI3K (p-PI3K), Akt, phosphorylated-Akt (p-Akt), mechanistic target of rapamycin (mTOR), and phosphorylated mTOR (p-mTOR) in the NSAID model group, PTFC group, and Control group of rats **(B)** Density ratios of phosphorylated to unphosphorylated proteins (p-PI3K/PI3K, p-Akt/Akt, and p-mTOR/mTOR) were calculated using ImageJ software. Glyceraldehyde 3-phosphate dehydrogenase (GAPDH) was used as a loading control (*$p < 0.05$ and **$p < 0.01$).

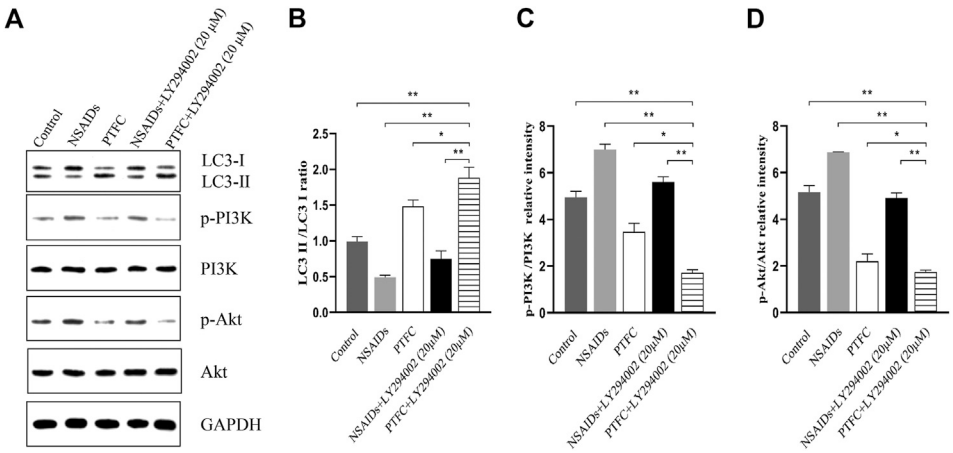

FIGURE 8 | PTFC increases autophagy through PI3K/Akt Signaling in IEC-6 cells **(A)** Western blot analysis was performed to determine expression levels of levels of light chain 3 (LC3), phosphoinositide 3-kinase (PI3K), phosphorylated-PI3K (p-PI3K), Akt, and phosphorylated-Akt (p-Akt) **(B–D)** Density ratios of LC3-II/LC3-I and phosphorylated/unphosphorylated proteins (p-PI3K/PI3K, p-Akt/Akt) were calculated using ImageJ software. Glyceraldehyde 3-phosphate dehydrogenase (GAPDH) was used as a loading control (*$p < 0.05$ and **$p < 0.01$).

Furthermore, among the Atg proteins, Atg5 is indispensable for autophagic vesicles and its knockout inhibits autophagy, suggesting that it has a central role in autophagy (Saha et al., 2018). Our results demonstrated lower expression levels of Atg5, LC3-II, and TJ proteins ZO-1, CLDN-1, and OCLN, as well as lower LC3-II/LC3-I ratios in the NSAID-induced small intestine injury rat model group compared to those in the control group. This indicated that autophagy may have affected TJ protein expression in NSAID-induced intestinal injury.

Understanding how NSAIDs modulate autophagy will help elucidate the role of autophagy in intestinal homeostasis and NSAID enteropathy. Recent reports suggest that autophagy in various diseases is affected by the regulation of the AMPK, MAPK, MAPK, Beclin-1, Bcl-2, and mTOR pathways (Mohammadinejad et al., 2019). The serine/threonine kinase mTOR, which is mainly regulated by PI3K/Akt signaling, is a crucial suppressor of autophagy (Datta et al., 2014). A recent study showed that the PI3K/AKT/mTOR signaling pathway is closely related to the regulation of autophagy and intestinal mucosal barrier function (Tanaka et al., 2008; Chen et al., 2017).

There is currently no effective therapeutic or preventative strategy for small bowel injury caused by NSAIDs (Utzeri and Usai, 2017). As a number of flavonoids participate in the regulation of intestinal TJ barrier integrity, they may be promising therapeutic agents. This regulation of intestinal TJ barrier integrity may partially contribute to the flavonoid-mediated biological effects on human health (Noda et al., 2012). Many natural products are rich in flavonoids and possess protective activities against intestinal inflammation, barrier integrity, and changes in gut microbiota (Gil-Cardoso et al., 2016). PTFC used in the present study were prepared from Qu Zhi Qiao (fruit of *Citrus Paradisi cv.*

Changshanhuyou) which is one of the new "Zhejiang eight flavors." Qu Zhi Qiao was collected by "Standard for Processing Traditional Chinese Medicine in Zhejiang Province"which has the function of alleviating depression to regulate qi and relieving flatulence. In the current study, the PTFC contained narirutin, naringin, neohesperidin, and hesperidin, with a total flavonoid content of 76.22%. In recent years, underlying beneficial characteristics of PTFC and their metabolites have been investigated, including optimization of barrier permeability, positive balance of gut microbiota, and immunomodulation, as well as inhibition of oxidative stress and inflammation in gut, hepatoprotective and pro-cardiovascular activities (Vazhappilly et al., 2019; Shi et al., 2020; Wang et al., 2021). Evidence pointed to the health-promoting properties of hesperidin and narirutin, the most abundant citrus flavanones in citrus genus, on the intestinal barrier and human health (Shen et al., 2019; Guirro et al., 2020). In animal models with drug-induced intestinal epithelial damage, hesperidin manifested its protective effect by maintaining the intestinal epithelial barrier, most researchers stated the molecular basis for the effects seems to be mediated via decreased inflammatory mediators pathway (Tejada et al., 2018), but it may get involved in the autophagy pathways as well, though proposed in pathogenesis of diabetes via targeting TGF-β signaling presently (Heydarpour et al., 2020). Additionally, even hesperetin, the aglycones of hesperidin, has also been shown to ameliorate the epithelial barrier damage via increased expressions of TJ proteins ZO-1 and OCLN (Zhang et al., 2020), which is consistent with our findings. The similarly enhancement of TJ integrity *in vivo* and *in vitro*, induced by citrus-derived flavonoids, naringin, was also demonstrated. That exerted significant effects on alleviating sepsis-induced intestinal mucosal injury and improving impaired intestinal permeability (Li et al., 2018). Our previous study even directly proved its protective effect on small intestine injury in NSAIDs related enteropathy (Chao et al., 2021). More importantly, emerging research reported that naringin attenuated the severity of colitis by suppressing endoplasmic reticulum stress-induced autophagy in colorectal mucosal cells (Pei et al., 2020), and regulated autophagy mediated by PI3K-Akt-mTOR pathway to ameliorate endothelial cell dysfunction induced by high glucose/high fat stress (Wang et al., 2020), or decrease hepatic stellate cell activity in liver fibrosis (Shi et al., 2016), the same as the autophagy regulatory pathway of NSAIDs intestinal disease in this study. While another component, neohesperidin, also derived from flavonoids, though a study indicatied that it might not affect the TJ (Nakashima et al., 2020), it offered virtually complete protection against the autophagy-inhibitory effect of okadaic acid. Therefore, these four compounds may play key roles in regulating autophagy and the integrity of the intestinal TJ barrier. First, our data showed that expression levels of Atg5 and LC3-II and the ratio of LC3-II/LC3-I decreased in the NSAID model group compared to those in the control group, whereas the PTFC group exhibited opposite results. Second, our results showed that the expression levels of p-PI3K, p-Akt, p-mTOR, and p-PI3K/PI3K as well as the ratios of p-Akt/Akt and p-mTOR/mTOR were higher in the NSAID model group and lower in the PTFC group compared to those in the control group. These findings suggest that PTFC activated autophagy and inhibited the progression of NSAID-induced small intestine disease, which was mediated, at least partly, by the PI3K/AKT signaling pathway.

CONCLUSION

Our data presents new information regarding increased autophagy levels, which protected rats against NSAID-induced small intestine disease. In addition, the PI3K/AKT pathway was identified to be functionally vital for attenuating autophagy. Our results also indicate that pretreatment with PTFC attenuated NSAID-induced small intestine injury and protected the intestinal mucosal barrier of rats. These findings have the potential for translation into novel protective strategies. Finally, PTFC may be considered a therapeutic candidate for NSAID-induced small intestine injury. Future clinical trials will be needed to confirm the effective human dose of PTFC.

DATA AVAILABILITY STATEMENT

The raw data supporting the conclusions of this article will be made available by the authors, without undue reservation, to any qualified researcher.

ETHICS STATEMENT

The animal study was reviewed and approved by the Institutional Animal Care and Use Committee of Zhejiang Chinese Medical University.

AUTHOR CONTRIBUTIONS

Participated in research design:SC and SZ; Conducted experiments: JJ and XH; Performed data analysis: HC and JJ; Wrote or contributed to the writing of the manuscript: SC and GC. All authors agreed the submission of this manuscript and agreed to be accountable for all aspects of this work.

FUNDING

This work was supported in part by the National Natural Science Foundation (81973598, 82074186, 82074214). Funding was also provided by the Medical Research Development Fund Project of the Beijing Kangmeng Charity Foundation under Grant No. WS686F, the Key Program of Administration of Traditional Chinese Medicine of Zhejiang Province (2020ZZ007) and "Ten thousand plan"-high level talents special support plan of Zhejiang province (No. ZJWR 0108035).

SUPPLEMENTARY MATERIAL

The Supplementary Material for this article can be found online at: https://www.frontiersin.org/articles/10.3389/fphar.2021.622744/full#supplementary-material.

REFERENCES

Adil, M., Kandhare, A. D., Visnagri, A., and Bodhankar, S. L. (2015). Naringin ameliorates sodium arsenite-induced renal and hepatic toxicity in rats: decisive role of KIM-1, Caspase-3, TGF-β, and TNF-α. *Ren. Fail.*, 37, 1396–1407. doi:10.3109/0886022x.2015.1074462

Bjarnason, I., Scarpignato, C., Holmgren, E., Olszewski, M., Rainsford, K. D., and Lanas, A. (2018). Mechanisms of damage to the gastrointestinal tract from nonsteroidal anti-inflammatory drugs. *Gastroenterology* 154, 500–514. doi:10.1053/j.gastro.2017.10.049

Bondonno, N. P., Bondonno, C. P., Blekkenhorst, L. C., Considine, M. J., Maghzal, G., Stocker, R., et al. (2018). Flavonoid-rich apple improves endothelial function in individuals at risk for cardiovascular disease: a randomized controlled clinical trial. *Mol. Nutr. Food Res.* 62, 1700674–1700710. doi:10.1002/mnfr.201700674

Chao, G., Dai, J., and Zhang, S. (2021). Protective effect of naringin on small intestine injury in NSAIDs related enteropathy by regulating ghrelin/GHS-R signaling pathway. *Life Sci.* 266, 118909. doi:10.1016/j.lfs.2020.118909

Chao, G., and Zhang, S. (2012). Therapeutic effects of muscovite to non-steroidal anti-inflammatory drugs-induced small intestinal disease. *Int. J. Pharmaceutics* 436, 154–160. doi:10.1016/j.ijpharm.2012.05.063

Chen, T., Xue, H., Lin, R., and Huang, Z. (2017). MiR-126 impairs the intestinal barrier function via inhibiting S1PR2 mediated activation of PI3K/AKT signaling pathway. *Biochem. Biophysical Res. Commun.* 494, 427–432. doi:10.1016/j.bbrc.2017.03.043

Datta, K., Suman, S., and Fornace, A. J., Jr. (2014). Radiation persistently promoted oxidative stress, activated mTOR via PI3K/Akt, and downregulated autophagy pathway in mouse intestine. *Int. J. Biochem. Cel Biol.* 57, 167–176. doi:10.1016/j.biocel.2014.10.022

Endo, H., Iijima, K., Asanuma, K., Ara, N., Ito, H., Asano, N., et al. (2010). Exogenous luminal nitric oxide exposure accelerates columnar transformation of rat esophagus. *Int. J. Cancer* 127, 2009–2019. doi:10.1002/ijc.25227

Galluzzi, L., Pietrocola, F., Levine, B., and Kroemer, G. (2014). Metabolic control of autophagy. *Cell* 159, 1263–1276. doi:10.1016/j.cell.2014.11.006

Gil-Cardoso, K., Ginés, I., Pinent, M., Ardévol, A., Blay, M., and Terra, X. (2016). Effects of flavonoids on intestinal inflammation, barrier integrity and changes in gut microbiota during diet-induced obesity. *Nutr. Res. Rev.* 29, 234–248. doi:10.1017/S0954422416000159

Guirro, M., Gual-Grau, A., Gibert-Ramos, A., Alcaide-Hidalgo, J. M., Canela, N., Arola, L., et al. (2020). Metabolomics elucidates dose-dependent molecular beneficial effects of hesperidin supplementation in rats fed an obesogenic diet. *Antioxidants* 9, 79–19. doi:10.3390/antiox9010079

Gwee, K.-A., Goh, V., Lima, G., and Setia, S. (2018). Coprescribing proton-pump inhibitors with nonsteroidal anti-inflammatory drugs: risks versus benefits. *Jpr* 11, 361–374. doi:10.2147/JPR.S156938

Ha, S. K., Park, H.-Y., Eom, H., Kim, Y., and Choi, I. (2012). Narirutin fraction from citrus peels attenuates LPS-stimulated inflammatory response through inhibition of NF-κB and MAPKs activation. *Food Chem. Toxicol.* 50, 3498–3504. doi:10.1016/j.fct.2012.07.007

Heydarpour, F., Sajadimajd, S., Mirzarazi, E., Haratipour, P., Joshi, T., Farzaei, M. H., et al. (2020). Involvement of TGF-β and autophagy pathways in pathogenesis of diabetes: a comprehensive review on biological and pharmacological insights. *Front. Pharmacol.* 11, 1–21. doi:10.3389/fphar.2020.498758

Jiang, J., Yan, L., Shi, Z., Wang, L., Shan, L., and Efferth, T. (2019). Hepatoprotective and anti-inflammatory effects of total flavonoids of Qu Zhi Ke (peel of Citrus changshan-huyou) on non-alcoholic fatty liver disease in rats via modulation of NF-κB and MAPKs. *Phytomedicine* 64, 153082–153089. doi:10.1016/j.phymed.2019.153082

Li, Z., Gao, M., Yang, B., Zhang, H., Wang, K., Liu, Z., et al. (2018). Naringin attenuates MLC phosphorylation and NF-κB activation to protect sepsis-induced intestinal injury via RhoA/ROCK pathway. *Biomed. Pharmacother.* 103, 50–58. doi:10.1016/j.biopha.2018.03.163

Livak, K. J., and Schmittgen, T. D. (2001). Analysis of relative gene expression data using real-time quantitative PCR and the $2^{-\Delta\Delta}$CT method. *Methods* 25, 402–408. doi:10.1006/meth.2001.1262

Mizushima, N., and Komatsu, M. (2011). Autophagy: renovation of cells and tissues. *Cell* 147, 728–741. doi:10.1016/j.cell.2011.10.026

Mohammadinejad, R., Ahmadi, Z., Tavakol, S., and Ashrafizadeh, M. (2019). Berberine as a potential autophagy modulator. *J. Cel Physiol.* 234, 14914–14926. doi:10.1002/jcp.283252019

Nakashima, M., Hisada, M., Goda, N., Tenno, T., Kotake, A., Inotsume, Y., et al. (2020). Opposing effect of naringenin and quercetin on the junctional compartment of MDCK II cells to modulate the tight junction. *Nutrients* 12 (11), 3285–3317. doi:10.3390/nu12113285

Noda, S., Tanabe, S., and Suzuki, T. (2012). Differential effects of flavonoids on barrier integrity in human intestinal Caco-2 cells. *J. Agric. Food Chem.* 60, 4628–4633. doi:10.1021/jf300382h

Pei, R., Liu, X., and Bolling, B. (2020). Flavonoids and gut health. *Curr. Opin. Biotechnol.* 61, 153–159. doi:10.1016/j.copbio.2019.12.018

Ravikumar, B., Vacher, C., Berger, Z., Davies, J. E., Luo, S., Oroz, L. G., et al. (2004). Inhibition of mTOR induces autophagy and reduces toxicity of polyglutamine expansions in fly and mouse models of Huntington disease. *Nat. Genet.* 36, 585–595. doi:10.1038/ng1362

Saha, S., Panigrahi, D. P., Patil, S., and Bhutia, S. K. (2018). Autophagy in health and disease: a comprehensive review. *Biomed. Pharmacother.* 104, 485–495. doi:10.1016/j.biopha.2018.05.007

Sakiyama, T., Musch, M. W., Ropeleski, M. J., Tsubouchi, H., and Chang, E. B. (2009). Glutamine increases autophagy under basal and stressed conditions in intestinal epithelial cells. *Gastroenterology* 136, 924–932. doi:10.1053/j.gastro.2008.12.002

Shen, C.-Y., Wan, L., Wang, T.-X., and Jiang, J.-G. (2019). Citrus aurantium L. var. amara Engl. inhibited lipid accumulation in 3T3-L1 cells and *Caenorhabditis elegans* and prevented obesity in high-fat diet-fed mice. *Pharmacol. Res.* 147, 104347–104412. doi:10.1016/j.phrs.2019.104347

Shi, H., Shi, H., Ren, F., Chen, D., Chen, Y., and Duan, Z. (2016). Naringin in Ganshuang Granule suppresses activation of hepatic stellate cells for anti-fibrosis effect by inhibition of mammalian target of rapamycin. *J. Cel. Mol. Med.* 21, 500–509. doi:10.1111/jcmm.12994

Shi, Z., Li, T., Liu, Y., Cai, T., Yao, W., Jiang, J., et al. (2020). Hepatoprotective and anti-oxidative effects of total flavonoids from Qu Zhi Qiao (fruit of Citrus Paradisi cv.Changshanhuyou) on nonalcoholic steatohepatitis *in vivo* and *in vitro* through Nrf2-ARE signaling pathway. *Front. Pharmacol.* 11, 1–13. doi:10.3389/fphar.2020.00483

Shin, S. J., Noh, C.-K., Lim, S. G., Lee, K. M., and Lee, K. J. (2017). Non-steroidal anti-inflammatory drug-induced enteropathy. *Intest. Res.* 15, 446–455. doi:10.5217/ir.2017.15.4.446

Sostres, C., Gargallo, C. J., and Lanas, A. (2013). Nonsteroidal anti-inflammatory drugs and upper and lower gastrointestinal mucosal damage. *Arthritis Res. Ther.* 15, S3. doi:10.1186/ar4175

Stevens, Y., Rymenant, E. V., Grootaert, C., Camp, J. V., Possemiers, S., Masclee, A., et al. (2019). The intestinal fate of citrus flavanones and their effects on gastrointestinal health. *Nutrients* 11, 1464–1517. doi:10.3390/nu11071464

Tanaka, Y., Sekiguchi, F., Hong, H., and Kawabata, A. (2008). PAR2 triggers IL-8 release via MEK/ERK and PI3-kinase/Akt pathways in GI epithelial cells. *Biochem. Biophysical Res. Commun.* 377, 622–626. doi:10.1016/j.bbrc.2008.10.018

Tejada, S., Pinya, S., Martorell, M., Capó, X., Tur, J. A., Pons, A., et al. (2019). Potential anti-inflammatory effects of hesperidin from the genus citrus. *Cmc* 25, 4929–4945. doi:10.2174/0929867324666170718104412

Utzeri, E., and Usai, P. (2017). Role of non-steroidal anti-inflammatory drugs on intestinal permeability and nonalcoholic fatty liver disease. *Wjg* 23, 3954–3963. doi:10.3748/wjg.v23.i22.3954

Vazhappilly, C. G., Ansari, S. A., Al-Jaleeli, R., Al-Azawi, A. M., Ramadan, W. S., Menon, V., et al. (2019). Role of flavonoids in thrombotic, cardiovascular, and inflammatory diseases. *Inflammopharmacol* 27, 863–869. doi:10.1007/s10787-019-00612-6

Wang, K., Peng, S., Xiong, S., Niu, A., Xia, M., Xiong, X., et al. (2020). Naringin inhibits autophagy mediated by PI3K-Akt-mTOR pathway to ameliorate endothelial cell dysfunction induced by high glucose/high fat stress. *Eur. J. Pharmacol.* 874, 173003–173045. doi:10.1016/j.ejphar.2020.173003

Wang, M., Zhao, H., Wen, X., Ho, C. T., and Li, S. (2021). Citrus flavonoids and the intestinal barrier: interactions and effects. *Compr. Rev. Food Sci. Food Saf.* 20, 225–251. doi:10.1111/1541-4337.12652

Wong, M., Ganapathy, A. S., Suchanec, E., LaidlerMa, L. T., Ma, T., and Nighot, P. (2019). Intestinal epithelial tight junction barrier regulation by autophagy-related protein ATG6/beclin 1. *Am. J. Physiology-Cell Physiol.* 316, C753–C765. doi:10.1152/ajpcell.00246.2018

Wu, L., Yan, M., Jiang, J., He, B., Hong, W., and Chen, Z. (2017). Pure total flavonoids from citrus improve non-alcoholic fatty liver disease by regulating TLR/CCL signaling pathway: a preliminary high-throughput 'omics' study. *Biomed. Pharmacother.* 93, 316–326. doi:10.1016/j.biopha.2017.04.128

Yu, Y., Shiou, S. R., Guo, Y., Lu, L., Westerhoff, M., Sun, J., et al. (2013). Erythropoietin protects epithelial cells from excessive autophagy and apoptosis in experimental neonatal necrotizing enterocolitis. *PLoS One* 8, e69620. doi:10.1371/journal.pone.0069620

Zhang, J., Lei, H., Hu, X., and Dong, W. (2020). Hesperetin ameliorates DSS-induced colitis by maintaining the epithelial barrier via blocking RIPK3/MLKL necroptosis signaling. *Eur. J. Pharmacol.* 873, 172992–173027. doi:10.1016/j.ejphar.2020.172992

Zhang, S., He, Y., Shi, Z., Jiang, J., He, B., Xu, S., et al. (2019). Small intestine protection of mica against non-steroidal anti-inflammatory drugs-injury through ERK1/2 signal pathway in rats. *Front. Pharmacol.* 10, 1–6. doi:10.3389/fphar.2019.00871

Zhu, Y., Lin, G., Dai, Z., Zhou, T., Li, T., Yuan, T., et al. (2015). L-Glutamine deprivation induces autophagy and alters the mTOR and MAPK signaling pathways in porcine intestinal epithelial cells. *Amino Acids* 47, 2185–2197. doi:10.1007/s00726-014-1785-0

Conflict of Interest: The author JJ was employed by the Zhejiang You-du Biotech Limited Company.

The remaining authors declare that the research was conducted in the absence of any commercial or financial relationships that could be construed as a potential conflict of interest.

frontiers in Pharmacology

ORIGINAL RESEARCH
published: 29 June 2021
doi: 10.3389/fphar.2021.685575

Microscopic Mass Spectrometry Imaging Reveals the Distribution of Phytochemicals in the Dried Root of *Isatis tinctoria*

Li-Xing Nie[1,2], Jing Dong[3], Lie-Yan Huang[2], Xiu-Yu Qian[2], Chao-Jie Lian[2], Shuai Kang[2,4], Zhong Dai[2] and Shuang-Cheng Ma[1,2]**

[1]Chinese Academy of Medical Science and Peking Union Medical College, Beijing, China, [2]National Institutes for Food and Drug Control, National Medical Products Administration, Beijing, China, [3]Shimadzu China Innovation Center, Beijing, China, [4]College of Pharmacy, Hebei University of Chinese Medicine, Shijiazhuang, China

OPEN ACCESS

Edited by:
Peng Li,
University of Macau, China

Reviewed by:
Pavel Klouček,
Czech University of Life Sciences Prague, Czechia
Hossein Hashempour,
Azarbaijan Shahid Madani University, Iran
Zhitao Liang,
Department of Health (Hong Kong), China

***Correspondence:**
Shuai Kang
kangshuai@nifdc.org.cn
Shuang-Cheng Ma
masc@nifdc.org.cn

Specialty section:
This article was submitted to Ethnopharmacology, a section of the journal Frontiers in Pharmacology

Received: 25 March 2021
Accepted: 25 May 2021
Published: 29 June 2021

Citation:
Nie L-X, Dong J, Huang L-Y, Qian X-Y, Lian C-J, Kang S, Dai Z and Ma S-C (2021) Microscopic Mass Spectrometry Imaging Reveals the Distribution of Phytochemicals in the Dried Root of Isatis tinctoria. Front. Pharmacol. 12:685575. doi: 10.3389/fphar.2021.685575

The dried root of *Isatis tinctoria* L. (Brassicaceae) is one of the most popular traditional Chinese medicines with well-recognized prevention and treatment effects against viral infections. Above 300 components have been isolated from this herb, but their spatial distribution in the root tissue remains unknown. In recent years, mass spectrometry imaging (MSI) has become a booming technology for capturing the spatial accumulation and localization of molecules in fresh plants, animal, or human tissues. However, few studies were conducted on the dried herbal materials due to the obstacles in cryosectioning. In this study, distribution of phytochemicals in the dried root of *Isatis tinctoria* was revealed by microscopic mass spectrometry imaging, with application of atmospheric pressure–matrix-assisted laser desorption/ionization (AP-MALDI) and ion trap–time-of-flight mass spectrometry (IT-TOF/MS). After optimization of the slice preparation and matrix application, 118 ions were identified without extraction and isolation, and the locations of some metabolites in the dried root of *Isatis tinctoria* were comprehensively visualized for the first time. Combining with partial least square (PLS) regression, samples collected from four habitats were differentiated unambiguously based on their mass spectrometry imaging.

Keywords: mass spectrometry imaging, *Isatis tinctoria*, atmospheric pressure–matrix-assisted laser desorption/ionization, ion trap–time-of-flight mass spectrometry, traditional Chinese medicine

INTRODUCTION

Natural products have always benefited the health care of people worldwide and are used as herbal medicines commonly (He et al., 2020). Among them, traditional Chinese medicine (TCM) has made significant contributions to the treatment of human disease from ancient times to present (Wang et al., 2021). For instance, the dried root of *Isatis tinctoria* L. (*Isatis indigotica* Fortune ex Lindl.) (Isatidis Radix in Latin, Isatis root in English, and Banlangen in Chinese) has been widely used as the remedy for fever and infection in China and other countries (Zhou and Zhang, 2013). It is well recognized for prevention and treatment effects against a variety of viral infections, such as seasonal flu (Speranza et al., 2020), severe acute respiratory syndrome (Lin et al., 2005), and H1N1 flu epidemic (Li and Tao, 2013; Luo et al., 2019). As the important ingredient in the so-called Three Drugs and Three Prescriptions, the dried root of *Isatis tinctoria* has also been playing an active role in fighting against the novel corona virus disease 2019 (COVID-19) (Li et al., 2020b; Li and Xu, 2021).

TABLE 1 | Sample collection information of the dried root of *Isatis indigotica*.

Sample no	Habitat	Collection time
GS1	Gansu	Sep., 2019
GS2	Gansu	Sep., 2019
GS3	Gansu	Sep., 2019
HLJ1	Heilongjiang	Oct., 2019
HLJ2	Heilongjiang	Oct., 2019
HLJ3	Heilongjiang	Nov., 2019
XJ1	Xinjiang	Sep., 2019
XJ2	Xinjiang	Oct., 2019
XJ3	Xinjiang	Oct., 2019
NMG1	Neimengu	Nov., 2019
NMG2	Neimengu	Oct., 2019
NMG3	Neimengu	Oct., 2019

Till now, more than 300 components have been isolated from the root of *Isatis indigotica*, including alkaloids, sulfur-containing compounds, phenylpropanoids, amino acids, nucleosides, organic acids and esters, flavonoids, quinones, terpenes, sterols, saccharides, aromatics, peptides, alcohols, aldehydes and ketones, nitriles, and sphingolipids. Although chemical composition and pharmacological activities of phytochemicals in the dried root of *Isatis tinctoria* have been extensively investigated by Lin et al. (2005); Speranza et al. (2020), the analysis of their spatial distribution in tissue has not yet been done.

Unraveling the tissue-specific localization of molecules in medicinal herbs can provide straightforward clues to understand their biological functions. Technologies for this aim face challenges and are still under development. Conventional investigations have enabled the comprehensive chemical profiling of metabolites from the dried root of *Isatis tinctoria*, applying separation and identification techniques such as high-performance liquid chromatography (HPLC) (Zou et al., 2005), ultra-performance liquid chromatography (UPLC) (Shi et al., 2012), and ultra-performance liquid chromatography–quadrupole–time-of-flight mass spectrometry (UPLC-Q-TOF/MS) (Guo et al., 2020a). However, the microscopic localizations of components in samples are largely ignored during the homogenization and purification process.

By directly detecting the ion beams of components on a sample surface, mass spectrometry imaging (MSI) can achieve the chemical distribution information. With the aid of the optical microscope, MSI can link morphological features with chemical profiling, thus providing untargeted, label-free, and multiplexed approach for molecular imaging. In recent years, it has become a fascinating tool for capturing the spatial accumulation and localization of metabolites in plants (Shimma and Sagawa, 2019; Li et al., 2020a; Li et al., 2020c), but only a few studies had been conducted on the dried herbal materials (Ng et al., 2007; Wu et al., 2007; Yi et al., 2012; Liang et al., 2014a; Liang et al., 2014b), which are extremely difficult to sectioning.

In the present study, distribution of phytochemicals in the dried root of *Isatis tinctoria* was revealed by microscopic mass spectrometry imaging, using atmospheric pressure–matrix-assisted laser desorption/ionization (AP-MALDI) combined with ion trap–time-of-flight mass spectrometry (IT-TOF/MS). In particular, the slice preparation method directly associated with the quality of the mass spectrometry imaging (MSI) results was optimized for the dried woody sample. Numerous constituents, including alkaloids, sulfur-containing compounds, phenylpropanoids, amino acids, nucleosides, organic acids, flavonoids, terpenes, saccharides, aromatics, peptides, and sphingolipids, were comprehensively visualized in the dried root of *Isatis tinctoria* for the first time. Moreover, samples from different habitats were distinguished based on their mass spectrometry imaging and the partial least square (PLS) regression.

FIGURE 1 | A photograph of the dried root of *Isatis indigotica* **(A)** and the magnified image of its transverse section **(B)**.

MATERIAL AND METHODS

Chemicals and Samples

2′, 5′-Dihydroxyacetophenone (2, 5-DHAP), 2, 5-dihydroxybenzoic acid (DHB), α-cyano-4-hydroxycinnamic acid (CHCA), 1, 5-naphthalenediamine (1, 5-DAN), 9-aminoacridine (9-AA), 1, 8-bis(tetramethylguanidino)naphthalene (TMGN), 1, 2-bis (trimethoxysilyl)ethane (BTME), gelatin, formic acid (LC-MS grade), ethanol (HPLC grade), and methanol (LC-MS grade) were purchased from Sigma-Aldrich (St. Louis, MO, United States). De-ionized water was purified by a Milli-Q system (Millipore, Bedford, MA, United States). Optimum cutting temperature (OCT) compound was purchased from Leica (Nussloch, Germany). The samples of the dried root of *Isatis tinctoria* were collected from four main habitats in China, Gansu, Heilongjiang, Xinjiang, and Neimenggu. The sample collection information could be found in **Table 1**, and the typical macroscopic images of the herb and its transverse section are shown in **Figure 1**. All samples were authenticated by Associate Professor Shuai Kang, who is in charge of the Traditional Chinese Medicine Herbarium, National Institutes for Food and Drug Control. The voucher specimens were deposited in National Institutes for Food and Drug Control (NIFDC), Beijing, China.

Slice Preparation and Optical Imaging

A piece 1 cm in length was cut from the dried root of *Isatis tinctoria* using a blade, and then embedded in 0.1 g/ml gelatin solution before freezing at −20°C. The frozen sample embedded with gelatin was axially fixed on a cryomicrotome (Leica CM 1950, Nussloch, Germany) by OCT compound carefully to avoid contamination on the surface of the sample. The

gelatin on the top was peeled off to expose the surface of the cross section of the root before one side of the double-sided conductive tape (3M, St. Paul, MN, United States) was adhered to the root surface. Then the tissue was sectioned into a 40-μm slice with the tape at −18°C. Finally, the slice was fixed carefully on an indium tin oxide (ITO)-coated glass slide (Matsunami Glass, Osaka, Japan) with another side of the tape. Before matrix coating, the optical image of the tissue was captured by a charge-coupled device (CCD) camera of the optical microscope embedded to the imaging mass microscope system (Shimadzu iMScope, Kyoto, Japan).

Matrix Application

After optimization, 2′, 5′-dihydroxyacetophenone (2, 5-DHAP) and 1, 5-naphthalenediamine (1, 5-DAN) were chosen as the matrix for positive and negative ion detection, respectively, and were applied in the mode of spraying. The matrix solution of 2′, 5′-dihydroxyacetophenone (2, 5-DHAP) was prepared at a concentration of 10 mg/ml in methanol and water (all containing 0.1% formic acid) at a ratio of 8:2, and 1, 5-naphthalenediamine (1, 5-DAN) was prepared as a saturated solution in ethanol–water (70:30). For spraying, 1 ml of matrix solution was added to the cavity of the handle airbrush. Then the solution was sprayed on the sample surface using the airbrush, keeping a distance at about 10 cm. For each glass, the airbrushing was repeated 10 cycles every 60 s. Finally, the sprayed glass slide was kept in the fume hood for 5 min to vaporize the solvent.

Microscopic Mass Spectrometry Imaging

Microscopic mass spectrometry imaging of the tissue was performed using the iMScope instrument (Shimadzu, Kyoto, Japan) equipped with an optical microscope, an atmospheric pressure chamber for matrix-assisted laser desorption/ionization (AP-MALDI) source, and an ion trap–time-of-flight mass spectrometer. The acquisition region was defined with the help of the optical microscope, and the tissue was irradiated with a diode-pumped 355 nm Nd:YAG laser with 5 ns pulse width. The laser diameter was 80 μm, and the data were collected at an interval of 80 μm. The tissue surface was laser-irradiated with 100 shots (1,000 Hz repetition rate) for each pixel. All the data were acquired in the positive and negative modes with sample voltage of 3.5 and 3.0 kV, respectively. The mass ranges were *m*/*z* 100–500 and *m*/*z* 500–1,000, while the detector voltage was 1.97 kV for all the samples. Three repetitions for each sample were performed, and two slices were prepared for each repetition in order to measure the positive and negative ions separately.

Data Analysis

Mass image reconstruction and data analysis were performed using IMAGEREVEAL™ MS (Shimadzu, Kyoto, Japan). All images were reconstructed by linear smoothing and displayed in absolute intensity after total ion current (TIC) normalization. Statistical analysis including principal component analysis (PCA) and partial least squares (PLS) regression was carried out by IMAGEREVEAL™ MS for differentiation of samples from different habitats.

RESULTS

Phytochemical Profiles of the Dried Root of *Isatis tinctoria*

Figure 2 showed the typical overall average mass spectra of the dried root of *Isatis tinctoria* gained by matrix-assisted laser desorption/ionization and ion trap–time-of-flight (MALDI-IT-TOF) mass spectrometry imaging (MSI) under positive and negative/ionization modes. Positive ions were mainly detected in the mass range of *m*/*z* 100–400 and *m*/*z* 400–800, while negative ions were mainly observed in the mass range of *m*/*z* 100–200, *m*/*z* 400–500, and *m*/*z* 400–700. The putative identification of the components was based on the accurate mass-to-charge ratio with reference to the isotopic peak, the reference standards, and/or the literatures and data bases. As could be seen from **Table 2**, the detected phytochemicals belong to a wide range of chemical compound classes such as alkaloids, sulfur-containing compounds, phenylpropanoids, amino acids, nucleosides, organic acids, flavonoids, terpenes, saccharides, aromatics, peptides, and sphingolipids. In the positive ion mode, the detected ions were prominently in the protonated adduct form of all amino acids, most of the alkaloids, some of the phenylpropanoids and the nucleosides, majority of the aromatics, minority of the sulfur-containing compounds, several sphingolipids, as well as organic acids with basic group. Also sodium or potassium adducts of some nucleosides and a few alkaloids, peptides, and sulfur-containing compounds were found. In the negative ion mode, majority of the sulfur-containing compounds and the organic acids, some of the phenylpropanoids, minority of the aromatics, a few saccharides, flavonoids, nucleosides, as well as alkaloids with acid group were readily detected as $[M-H]^-$ form of ions.

Visualization of the Distribution of Phytochemicals in the Dried Root of *Isatis tinctoria*

The optical images in **Figures 3**, **4** showed the main compartments of the cross section of the dried root of *Isatis tinctoria*: cork and cortex, phloem, cambium, and xylem as well as the distinctive spatial distribution of various kinds of characteristic constituents. The most abundant class of chemical components isolated from *Isatis tinctoria* is alkaloid. They were mostly detected as the positive ions and presented a variety of distributions. As could be seen from **Figure 3B**, sodium adduct of oxindole (*m*/*z* 156.0416), an indole alkaloid, was located exclusively in xylem. Another ion of *m*/*z* 458.2167 (**Figure 3C**) was found to have a different distribution in the specific region of phloem. This ion was assigned to the potassium adduct of 3-[2′-(5′-hydroxymethyl) furyl]-1(2*H*)-isoquinolinone-7-*O*-β-*D*-glucoside, an isoquinolinone alkaloid glycoside. Sulfur-containing compounds are characteristic secondary metabolites occurring in cruciferous plant, and they

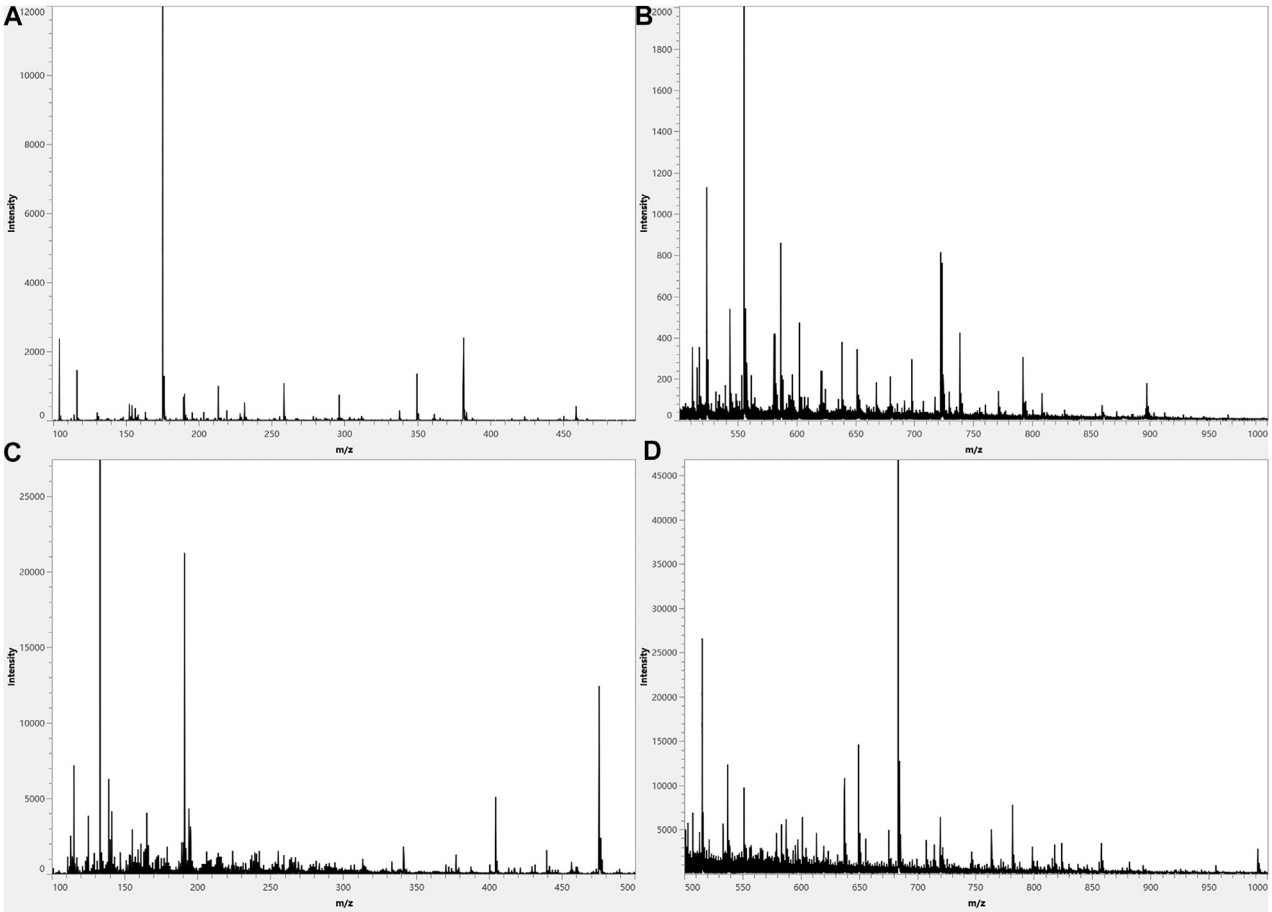

FIGURE 2 | Typical overall average mass spectra acquired from a cross section of the dried root of *Isatis indigotica* by matrix-assisted laser desorption and ion trap–time-of-flight (MALDI-IT-TOF) mass spectrometry imaging (MSI) in the spectral ranges of *m/z* 100–500 in a positive mode **(A)**, *m/z* 500–1,000 in a positive mode **(B)**, *m/z* 100–500 in a negative mode **(C)**, and *m/z* 500–1,000 in a negative mode **(D)**.

are the second abundant class of chemical components in *Isatis tinctoria*. Taking isatindigoside F (*m/z* 476.1258), a typical glucosinolate, as an example (**Figure 4B**), sulfur-containing compounds were mainly detected as the negative ions which accumulated mostly in phloem of the dried root of *Isatis tinctoria*. Dozens of phenylpropanoids are also found in *Isatis indigotica*, and they can be detected in positive or negative modes. **Figure 3D** and **Figure 4C** showed the spatial distribution of the ions of *m/z* 343.1371 and *m/z* 683.2479, which corresponded to the $[M+H]^+$ and $[M-H]^-$ forms of the ions of coniferin and clemastanin B, a phenylpropanoid glycoside and a lignan diglucoside, respectively. Regardless of the form of the ions, the majority of the phenylpropanoids presented the highest abundance near the lateral area of the root, including phloem, cortex, and cork. *Isatis* root produces several nucleosides, which are normally observed as positive ions. MSI results suggested that the ion of *m/z* 152.0588 was assigned to the protonated adduct of guanine. As noticeable in the ion, it was located almost exclusively in xylem of the root. Moreover, mass spectrometry imaging (MSI) study on the constituents of the dried root of *Isatis tinctoria* revealed the presence of a variety of organic acids. The negative ions assigned as $[M-H]^-$ form of maleic acid (*m/z* 115.004), malic acid (*m/z* 133.0147, **Figure 4E**), and citric acid (*m/z* 191.0191, **Figure 4F**) were found at very high intensities in the area of phloem. Amino acids are widespread primary metabolites in plants, and they showed diversified distribution in the dried root of *Isatis tinctoria* in the form of the proton adducts. The protonated adduct of histidine at *m/z* 156.0786 (**Figure 3F**) was more abundant at the inner side of the cambium. On the contrary, another ion image concerned the distribution of proline at *m/z* 116.0709 (**Figure 3G**) with the highest abundance at the outer side of the cambium. Interestingly, the ion of arginine at *m/z* 175.1188 (**Figure 3H**) was located with prominent abundance in all tissues except regions of cambium, cortex, and cork. Ions based on phytochemicals belonging to minor groups in *Isatis* root like peptides, saccharides, flavonoids, and aromatics were also analyzed. It could be judged from **Figure 3I** that the highest concentration of a cyclic peptide named cyclo (*L*-Phe–*L*-Tyr) in the form of potassium adduct at *m/z* 349.2320 was in xylem and phloem. Sucrose is a nutritional ingredient that naturally occurs in many plants. Its negative ion at *m/z* 341.1089 (**Figure 4G**) was located mainly in the outer part of the root corresponding to the

TABLE 2 | Assignment of ions observed in the matrix-assisted laser desorption and ion trap–time-of-flight (MALDI-IT-TOF) mass spectrometry imaging (MSI) of the dried root of *Isatis indigotica* with references regarding shown compounds.

No	Compound	Chemical class	Ion formula	Theoretical m/z	Observed m/z	Mass accuracy (ppm)	Refs
1	*r*-Aminobutyric acid	Amino acids	$C_4H_9NO_2$+H	104.0712	104.0709	2.9	Pan, (2014)
2	Choline	Alkaloids	$C_5H_{14}NO^+$	104.1075	104.1066	8.6	The Metabolomics Innovation Center, (2020)
3	Proline	Amino acids	$C_5H_9NO_2$+H	116.0712	116.0709	2.6	Wu et al. (1997)
4	Valine	Amino acids	$C_5H_{11}NO_2$+H	118.0869	118.0865	3.4	Chen et al. (2012)
5	Leucine/isoleucine	Amino acids	$C_6H_{13}NO_2$+H	132.1025	132.1018	5.3	Zhao, (2015)
6	Adenine	Nucleosides	$C_5H_5N_5$+H	136.0624	136.0613	8.1	Chen et al. (2012)
7	Aminobenzoic acid	Organic acids	$C_7H_7NO_2$+H	138.0556	138.0545	8.0	Wang et al. (2013)
8	4-(2-Hydroxyethyl) phenol	Aromatics	$C_8H_{10}O_2$+H	139.0760	139.0773	9.3	Wang et al. (2013)
9	Hexyl isothiocyanate	Alkaloids	$C_7H_{13}NS$ + H	144.0848	144.0853	3.5	Condurso et al. (2006)
10	3-Formylindole	Alkaloids	C_9H_7NO + H	146.0607	146.0614	4.8	Zhao, (2015)
11	Glutamine	Alkaloids	$C_5H_{10}N_2O_3$+H	147.0770	147.0758	8.2	Pan, (2014)
12	Lysine	Amino acids	$C_6H_{14}N_2O_2$+H	147.1154	147.1132	1.4	Pan, (2014)
13	Uracil	Nucleosides	$C_4H_4N_2O_2$+K	151.1256	151.1243	8.6	Pan et al. (2013)
14	Guanine	Nucleosides	$C_5H_5N_5O$ + H	152.0573	152.0588	9.9	Pan et al. (2013)
15	Dopamine	Alkaloids	$C_8H_{11}NO_2$+H	154.0791	154.0790	0.6	HighChem LLC, (2020)
16	Oxindole	Alkaloids	C_8H_7NO + Na	156.0426	156.0416	6.4	Wang et al. (2013)
17	Histidine	Amino acids	$C_6H_9N_3O_2$+H	156.0774	156.0786	7.7	Pan, (2014)
18	Hypoxanthine	Nucleosides	$C_5H_4N_4O$ + Na	159.0283	159.0275	5.0	Xiao et al. (2003)
19	3-Indoleformic acid	Alkaloids	$C_9H_7NO_2$+H	162.0556	162.0553	1.9	Yang et al. (2014b)
20	Phenylalanine	Amino acids	$C_9H_{11}NO_2$+H	166.0869	166.0853	9.6	Pan, (2014)
21	Acetovanillone	Aromatics	$C_9H_{10}O_3$+H	167.0709	167.0709	0.0	Wang et al. (2013)
22	Isatin	Alkaloids	$C_8H_5NO_2$+Na	170.0218	170.0221	1.8	Zou and Koh, (2017)
23	2,5-Dihydroxyindole	Alkaloids	$C_8H_7NO_2$+Na	172.0375	172.0388	7.6	Li, (2010a)
24	Arginine	Amino acids	$C_6H_{14}N_4O_2$+H	175.1196	175.1188	4.6	Zeng et al. (2010)
25	3-Indoleacetonitrile	Alkaloids	$C_{10}H_8N_2$+Na	179.0585	179.0592	3.9	Wang et al. (2013)
26	Tyrosine	Amino acids	$C_9H_{11}NO_3$+H	182.0818	182.0800	9.9	Pan, (2014)
27	Dihydroconiferyl alcohol	Phenylpropanoids	$C_{10}H_{14}O_3$+H	183.1022	183.1036	7.6	Wang et al. (2013)
28	4-Hydroxyindole-3-carboxaldehyde	Alkaloids	$C_9H_7NO_2$+Na	184.0375	184.0368	3.8	Li et al. (2010b)
29	2,4(1H,3H)-Quinazolinedione	Alkaloids	$C_8H_6N_2O_2$+Na	185.0327	185.0326	0.5	Wang and Liu, 2008
30	Deoxyvasicinone	Alkaloids	$C_{11}H_{10}N_2O$ + H	187.0872	187.0864	4.3	Zhao, 2015
31	1-Methoxy-3-indoleformic acid	Alkaloids	$C_{10}H_9NO_3$+H	192.0661	192.0648	6.8	Yang et al. (2014b)
32	(1′*R*,2′*R*,3′*S*,4′*R*)-1,2,4-triazole	Nucleosides	$C_7H_{11}N_3O_4$+H	202.0829	202.0841	5.9	Pan, (2014)
33	Tryptophan	Amino acids	$C_{11}H_{12}N_2O_2$+H	205.0978	205.0959	9.3	Pan, (2014)
54	*L*-targinine	Peptides	$C_7H_{16}N_4O_2$+Na	211.1165	211.1150	7.1	The Metabolomics Innovation Center, (2020)
35	(–)-(*R*)-2-(4-Hydroxy-2-oxoindolin-3-yl)-acetamide	Alkaloids	$C_{10}H_{10}N_2O_3$+Na	229.0589	229.0576	5.7	Chen et al. (2012)
36	2′-Deoxyuridine	Nucleosides	$C_9H_{12}N_2O_5$+H	229.0825	229.0842	7.4	Pan, (2014)
37	(+)-(*S*)-2-(3-Hydroxy-4-methoxy-2-oxoindolin-3-yl)-acetamide	Alkaloids	$C_{11}H_{12}N_2O_4$+H	237.0876	237.0899	9.7	Chen et al. (2012)
38	2′-Deoxycytidine	Nucleosides	$C_9H_{13}N_3O_4$+Na	250.0804	250.0824	8.0	Pan, (2014)
39	(*S*)-(–)-Spirobrassinin	Sulfur-containing compounds	$C_{11}H_{10}N_2OS_2$+H	251.0314	251.0335	8.4	Zhang et al. (2020b)
40	Pyrraline	Amino acids	$C_{12}H_{18}N_2O_4$+H	255.1339	255.1332	2.7	The Metabolomics Innovation Center, (2020)
41	Indiforine C	Alkaloids	$C_{12}H_{14}N_2O_3$+Na	257.0902	257.0918	6.2	Liu et al. (2018b)
42	Indirubin/indigotin	Alkaloids	$C_{16}H_{10}N_2O_2$+H	211.0813	211.0821	3.0	Chen et al. (2012)
43	Thymidine	Nucleosides	$C_{10}H_{14}N_2O_5$+Na	265.0801	265.0824	8.7	Pan, (2014)
44	Adenosine	Nucleosides	$C_{10}H_{13}N_5O_4$+H	268.1047	268.1011	6.0	Zhao, (2015)
45	Inosine	Nucleosides	$C_{10}H_{12}N_4O_5$+H	269.0887	269.0905	6.7	Pan et al. (2013)
46	Tryptanthrin	Alkaloids	$C_{15}H_8N_2O_2$+Na	271.0484	271.0488	1.5	Chen et al. (2012)
47	2′-*O*-Methyladenosine	Nucleosides	$C_{11}H_{15}N_5O_4$+H	282.1203	282.1221	6.4	Zhang et al. (2019a)
48	Indican	Alkaloids	$C_{14}H_{17}NO_6$+H	296.0925	296.0935	3.4	Zou and Koh, (2017)
49	Guanosine	Nucleosides	$C_{10}H_{13}N_5O_5$+Na	306.0815	306.0824	2.9	Xiao et al, (2014)
50	(–)-(2′*S*)-Isatiscaloids E/(+)-(2′*R*)-isatiscaloids E	Alkaloids	$C_{14}H_{19}N_3O_5$+H	310.1404	310.1428	7.7	Wang et al. (2009)
51	Isatiscaloids A	Alkaloids	$C_{15}H_{22}N_2O_5$+H	311.1608	311.1627	6.1	Wang et al. (2009)

(Continued on following page)

TABLE 2 | (*Continued*) Assignment of ions observed in the matrix-assisted laser desorption and ion trap–time-of-flight (MALDI-IT-TOF) mass spectrometry imaging (MSI) of the dried root of *Isatis indigotica* with references regarding shown compounds.

No	Compound	Chemical class	Ion formula	Theoretical m/z	Observed m/z	Mass accuracy (ppm)	Refs
52	Indiforine F	Alkaloids	$C_{14}H_{18}N_2O_5$+Na	317.1114	317.1138	7.6	Liu et al. (2018b)
53	Evofolin-B	Phenylpropanoids	$C_{17}H_{18}O_6$+H	319.1182	319.1160	6.9	Wang et al. (2013)
54	Isatiscaloids B	Alkaloids	$C_{16}H_{20}N_2O_5$+H	321.1451	321.1458	2.2	Wang et al. (2013)
55	Adenosine-3′,5′-cyclic monophosphate	Nucleosides	$C_{10}H_{12}N_5O_6P$ + H	330.0604	330.0618	4.2	Pan, (2014)
56	Indole-3-acetonitrile-6-*O*-β-*D*-glucopyranoside	Alkaloids	$C_{16}H_{18}N_2O_6$+H	335.1244	335.1240	1.2	He et al. (2006a)
57	Isatisindigoticanine K	Alkaloids	$C_{19}H_{13}N_3O_2$+Na	338.0906	338.0927	6.2	Zhang et al. (2020c)
58	Coniferin	Phenylpropanoids	$C_{16}H_{22}O_8$+H	543.1394	543.1371	6.7	Zhang et al. (2019a)
59	Isaindigodione	Alkaloids	$C_{18}H_{18}N_2O_4$+Na	549.1165	549.1133	9.2	Xiao et al. (2014)
60	Cyclo (*L*-Phe–*L*-Tyr)	Peptides	$C_{18}H_{18}N_2O_3$+Na	549.2300	549.2320	5.7	Wang et al. (2013)
61	Indole-3-acetonitrile-2-*S*-β-*D*-glucopyranoside	Sulfur-containing compounds	$C_{16}H_{18}N_2O_5S$ + H	351.1015	351.1005	2.8	Yang et al. (2014b)
62	Qingdainone	Alkaloids	$C_{23}H_{13}N_3O_2$+ H	364.1087	364.1079	2.2	He et al. (2006a)
11	Isatindigotindoline C	Alkaloids	$C_{23}H_{21}N_3O_4$+H	404.1611	404.1602	2.2	Liu et al. (2018a)
64	Isatisindigoticanine A	Alkaloids	$C_{22}H_{18}N_2O_6$+H	407.1244	407.1215	7.1	Zhang et al. (2019b)
65	Isatindigobisindoloside G	Sulfur-containing compounds	$C_{24}H_{21}N_3O_5S$ + H	455.1278	455.1238	8.8	Zhang et al. (2020a)
66	3-[2′-(5′-hydroxymethyl)furyl]-1(2H)-isoquinolinone-7-*O*-β-*D*-glucoside	Alkaloids	$C_{20}H_{21}NO_9$+K	458.2199	458.2167	7.0	He et al. (2006b)
67	Isatisindigoticanine I	Sulfur-containing compounds	$C_{24}H_{21}N_3O_5S$ + H	464.1281	464.1245	7.8	Zhang et al. (2020a)
68	Isatindigoside F	Sulfur-containing compounds	$C_{25}H_{23}N_3O_5S$-H	476.1279	476.1258	4.4	Zhang et al. (2020a)
69	Isatigotindolediosides B	Alkaloids	$C_{20}H_{25}NO_{11}$ + Na	478.1326	478.1307	4.0	Meng et al. (2017b)
70	Isatigotindolediosides A	Alkaloids	$C_{21}H_{27}NO_{12}$ + H	486.1612	486.1579	6.8	Meng et al. (2017b)
71	Isatindigoside J	Alkaloids	$C_{25}H_{27}N_3O_8$+H	498.1877	498.1892	3.0	Zhang et al. (2020c)
72	Isatithioetherin A/isatithioetherin B	Sulfur-containing compounds	$C_{20}H_{26}N_4O_4S_3$+Na	505.1014	505.1058	8.7	Guo et al. (2020b)
73	Bisindigotin	Alkaloids	$C_{32}H_{18}N_4O_2$+Na	513.1328	513.1278	9.7	Wei et al. (2005)
74	Isatigotindolediosides D	Alkaloids	$C_{22}H_{28}N_2O_{13}$ + H	529.1670	529.1111	7.4	Meng et al. (2017b)
75	Isatithioetherin C/isatithioetherin E	Sulfur-containing compounds	$C_{20}H_{26}N_4O_4S_4$+Na	537.0735	537.0784	9.1	Guo et al. (2020b)
76	(+)-(7*R*,7′*R*,8*S*,8′*S*)-Neo-olivil	Phenylpropanoids	$C_{26}H_{54}O_{12}$ + H	539.2129	539.2143	2.6	Kikuchiand Kikuchi, (2005)
77	(2*S*,3*R*)-3-Hydroxymethyl-*N*-(2′-hydroxynonacosanoyl)-trideca-9*E*-sphingenine	Sphingolipids	$C_{43}H_{85}NO_5$+H	696.6507	696.6565	8.3	Li et al. (2007)
78	1-O-β-D-Glucopyranosyl-(2*S*,3*R*)-*N*-(2′-hydroxyhe xacosanoyl)-octadeca-11*E*-sphingenine	Sphingolipids	$C_{50}H_{97}NO_9$+H	856.7242	856.7292	5.8	Sun et al. (2009)
79	Propanedioic acid	Organic acids	$C_3H_4O_4$-H	103.0031	103.0040	8.7	Li, (2010)
80	Pyrocatechol	Aromatics	$C_6H_6O_2$-H	109.0289	109.0294	4.6	Wang et al. (2013)
81	Maleic acid/fumaric acid	Organic acids	$C_4H_4O_4$-H	115.0031	115.0040	7.8	Peng et al. (2005b)
82	Nicotinic acid	Organic acids	$C_6H_5NO_2$-H	122.0241	122.0254	5.7	Li, (2010)
83	3-Methylfuran-2-carboxylic acid	Organic acids	$C_6H_6O_3$-H	125.0238	125.0243	4.0	Zeng et al. (2010)
84	Goitrin/epigoitrin	Sulfur-containing compounds	C_5H_7NOS-H	128.0169	128.0162	5.5	Wang et al. (2014)
85	Malic acid	Organic acids	$C_4H_6O_5$-H	133.0136	133.0147	8.3	Liu et al. (2010)
86	Salicylic acid	Organic acids	$C_7H_6O_3$-H	137.0238	137.0241	2.2	Zhao, (2015)
87	Vanillin	Aromatics	$C_8H_8O_3$-H	151.0394	151.0388	4.0	Sun et al., 2007
88	Fructose/glucose	Saccharides	$C_6H_{12}O_6$-H	179.0555	179.0554	0.6	Liu et al. (2010)
89	Mannitol	Saccharides	$C_6H_{14}O_6$-H	181.0711	181.0697	7.7	He et al., 2006b
90	2-Amine-4-quinlinecarboxylic acid	Alkaloids	$C_{10}H_8N_2O_2$-H	187.0507	187.0517	5.3	Pan, (2014)
91	Citric acid	Organic acids	$C_6H_8O_7$-H	191.0191	191.0191	0.0	Liu et al. (2010)
92	Glucuronic acid	Organic acids	$C_6H_{10}O_7$-H	193.0548	193.0338	5.2	Liu et al. (2010)
93	Syringic acid	Organic acids	$C_9H_{10}O_5$-H	197.0461	197.0449	6.1	Wang et al. (2009)
94	Isatindosulfonic acid E	Sulfur-containing compounds	$C_9H_9NO_3S$-H	210.0224	210.0233	4.3	Meng et al. (2017a)
95	Isatindosulfonic acid C	Sulfur-containing compounds	$C_{10}H_{11}NO_4S$-H	240.0330	240.0318	5.0	Meng et al. (2017a)
96	Palmitic acid	Organic acids	$C_{16}H_{32}O_2$-H	255.2323	255.2542	7.4	Kizil et al. (2009)

(Continued on following page)

TABLE 2 | (*Continued*) Assignment of ions observed in the matrix-assisted laser desorption and ion trap–time-of-flight (MALDI-IT-TOF) mass spectrometry imaging (MSI) of the dried root of *Isatis indigotica* with references regarding shown compounds.

No	Compound	Chemical class	Ion formula	Theoretical m/z	Observed m/z	Mass accuracy (ppm)	Refs
97	Emodin	Flavonoids	$C_{15}H_{10}O_5$-H	269.0449	269.0450	0.4	Li, (2010)
98	Linolenic acid	Organic acids	$C_{18}H_{30}O_2$-H	277.2167	277.2172	1.8	Kizil et al. (2009)
99	Calycosin	Flavonoids	$C_{16}H_{12}O_5$-H	283.0606	283.0111	8.8	Wang et al. (2013)
100	Stearic acid	Organic acids	$C_{18}H_{36}O_2$-H	283.2116	283.2646	3.5	Kizil et al. (2009)
101	Sucrose	Saccharides	$C_{12}H_{22}O_{11}$-H	541.1083	541.1089	1.8	Liu et al. (2010)
102	Sinensetin	Flavonoids	C20H20O7- H	371.1130	371.1103	7.3	Li, (2010)
103	Gluconapin	Sulfur-containing compounds	$C_{11}H_{19}NO_9S_2$-H	372.0422	372.0429	1.9	Mohn et al. (2007)
104	Isatindigotindoloside C/ Isatindigotindoloside D	Sulfur-containing compounds	$C_{17}H_{20}N_2O_6S$-H	379.0911	379.0938	6.6	Liu et al. (2015b)
105	Progoitrin/epiprogoitrin	Sulfur-containing compounds	$C_{11}H_{19}NO_{10}S_2$-H	388.0371	388.0355	4.1	Mohn et al. (2007)
106	Glucotropaeolin	Sulfur-containing compounds	$C_{14}H_{19}NO_9S_2$-H	408.0422	408.0418	1.0	Mohn et al. (2007)
107	Isovitexin	Flavonoids	$C_{21}H_{20}O_{10}$-H	431.0977	431.1012	8.1	Zhao, (2015)
108	Glucobrassicin	Sulfur-containing compounds	$C_{16}H_{19}N_2O_9S_2$-H	447.0531	447.0537	1.3	Guo et al. (2020a)
109	Isatindigobisindoloside A/ isatindigobisindoloside B	Alkaloids	$C_{24}H_{23}N_3O_6$-H	448.1508	448.1554	5.8	Liu et al. (2015a)
110	Isatindigoside F	Sulfur-containing compounds	$C_{25}H_{23}N_3O_5S$-H	476.1279	476.1258	4.4	Zhang et al. (2020a)
111	Isatigotindolediosides F	Sulfur-containing compounds	$C_{21}H_{27}NO_{12}S$-H	516.1175	516.1153	4.3	Meng et al. (2017b)
112	Isatigotindolediosides E	Sulfur-containing compounds	$C_{22}H_{28}N_2O_{11}S$-H	527.1335	527.1284	9.7	Meng et al. (2017b)
113	Isatigotindolediosides D	Sulfur-containing compounds	$C_{22}H_{28}N_2O_{13}$-H	527.1512	527.1538	4.9	Meng et al. (2017b)
114	Glucoisatisin/epiglucoisatisin	Sulfur-containing compounds	$C_{21}H_{26}N_2O_{12}S_2$-H	561.0848	561.0830	3.2	Mohn and Hamburger, (2008)
115	Isovitexin	Flavonoids	$C_{21}H_{20}O_{10}$-H	431.0977	431.1012	8.1	Zhao, (2015)
116	Linarin	Flavonoids	$C_{28}H_{32}O_{14}$-H	591.1713	591.1674	6.6	Peng et al. (2005a)
117	Neohesperidin	Flavonoids	$C_{28}H_{54}O_{15}$-H	609.1819	609.1801	3.0	Peng et al. (2005a)
118	Clemastanin B	Phenylpropanoids	$C_{32}H_{44}O_{16}$-H	683.2550	683.2489	8.9	Yang et al. (2014a)

location of phloem, cortex, and cork. Similar distribution pattern was observed for the ion assigned to isovitexin (*m*/*z* 431.1012, **Figure 4H**), a representative flavone glycoside from *Isatis* root. Compounds belonging to aromatics are also isolated from *Isatis* root. This group includes vanillin, whose negative ion could be found at *m*/*z* 151.0388. In contrast to the above-discussed localization of two ions, this component accumulated at the area corresponding to xylem mainly (**Figure 4I**).

Differentiation of the Habitats of the Dried Root of *Isatis tinctoria*

Three repetitions for twelve samples of the dried root of *Isatis tinctoria* from Gansu, Xinjiang, Heilongjiang, and Neimenggu were first classified according to their habitats as groups 1, 2, 3, and 4, respectively. Mass spectrometry imaging (MSI) data of the whole tissues within two spectral ranges (*m*/*z* 100–500 and *m*/*z* 500–1,000) in positive and negative modes were input to establish four partial least square (PLS) regression models separately. Partial least square (PLS) regression was performed by importing the information of all detected ions to the *X*-matrix, while the actual groups of habitats were imported to the *Y*-matrix. As shown in **Figure 5**, good correlation between the predicted and actual groups of habitats of the dried root of *Isatis tinctoria* was found with all regression coefficients (R^2) above 0.99, which indicated an excellent discrimination ability of the mass spectrometry imaging (MSI) method.

DISCUSSION

In this study, iMScope, the optical microscope, in combination with the atmospheric pressure–matrix-assisted laser desorption/ionization (AP-MALDI) and the ion trap–time-of-flight mass spectrometry (IT-TOF/MS), was first applied to visually clarify the distribution of phytochemicals in the dried root of *Isatis tinctoria*. Nowadays, there have been increasing reports on the applications of mass spectrometry imaging (MSI) in the investigation of animal or human tissues (Wu et al., 2019), but with less focus on plants (Davison et al., 2019; Sun et al., 2020; Zhang et al., 2020d), not to mention traditional Chinese medicine (TCM). In addition, most of the research works were performed

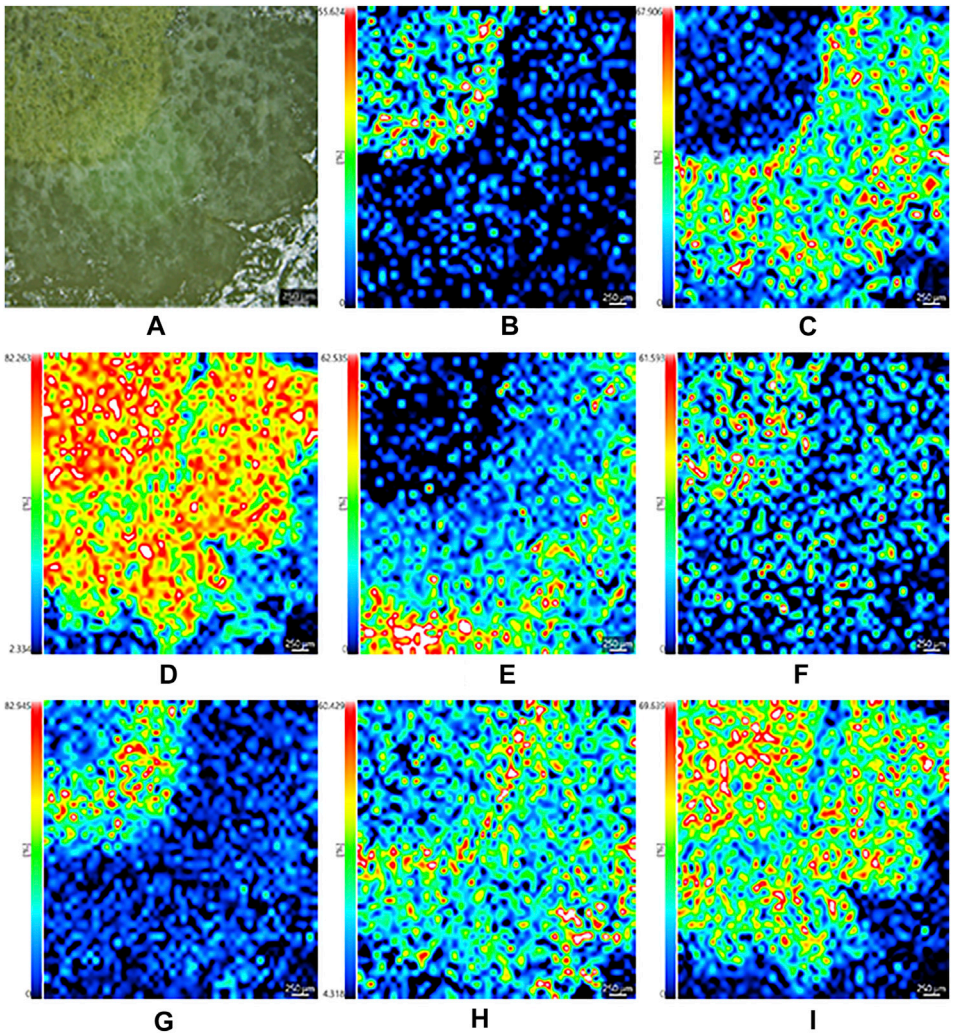

FIGURE 3 | Optical image of the dried root of *Isatis indigotica* **(A)** and the mass spectrometry images of the positive ions of oxindole **(B)**, 3-[2′-(5′-hydroxymethyl) furyl]-1(2*H*)-isoquinolinone-7-O-β-D-glucoside **(C)**, coniferin **(D)**, guanine **(E)**, histidine **(F)**, proline **(G)**, arginine **(H)**, and cyclo (*L*-Phe–*L*-Tyr) **(I)**.

with the fresh herbs (Fowble et al., 2017; Lange et al., 2017; Freitas et al., 2019) due to the obstacles in the sectioning of the dried material. To reveal the spatial localization of phytochemicals in traditional Chinese medicine (TCM) in the form of actually sold in the market and used in clinic, the dried root of *Isatis tinctoria* was chosen as the imaging subject. As expected, the cryosectioning of the hard and fragile woody root presented great challenges.

First, the thickness of the tissue was optimized in the range from 20 to 80 μm. It was apparent that the thicker the slice, the more integrated the tissue, but thinner slice posed more sensitive detection of ions. Taking a comprehensive consideration of the integrity of the tissue and the quality of the mass data, a thickness of 40 μm was selected. Next, the temperature for cryosectioning of the frozen tissue was assessed in the range of −12–−22°C. It was found that the section would rupture when the temperature was too low, while when the temperature was too high, the section would wrinkle. Numerous trials indicated that satisfactory result could be obtained with a temperature of −18°C, which was coincident with the reported optimum cryosectioning parameter for the roots of *Panax* genus (Wang et al., 2016). Since the thin slice of the dried root of *Isatis tinctoria* was easy to fall off from the glass slide, a double-sided adhesive tape was utilized. To better avoid tissue break and movement during the sectioning, the sample surface was adhered by one side of the tape before cutting.

Subsequently, several matrices were evaluated as follows: 2′, 5′-dihydroxyacetophenone (2, 5-DHAP), 2, 5-dihydroxybenzoic acid (DHB), α-cyano-4-hydroxycinnamic acid (CHCA), and 1, 5-naphthalenediamine (1, 5-DAN) for the positive ion mode, and 1, 5-naphthalenediamine (1, 5-DAN), 9-aminoacridine (9-AA), 1, 8-bis(tetramethylguanidino) naphthalene (TMGN), and 1, 2-bis(trimethoxysilyl)ethane (BTME) for the negative ion mode. Briefly, comprehensive detection of molecules was achieved when using 2′, 5′-dihydroxyacetophenone (2, 5-DHAP) and 1, 5-naphthalenediamine (1, 5-DAN) as the matrixes in positive

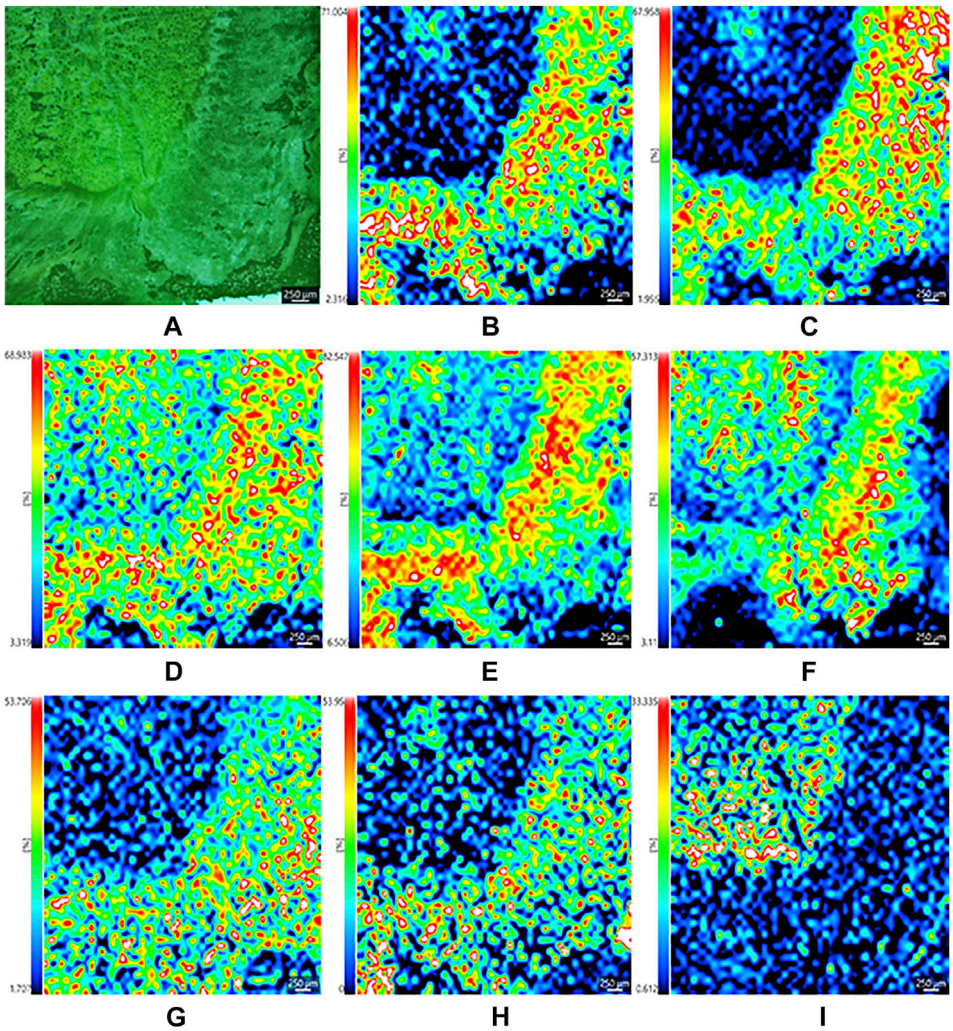

FIGURE 4 | Optical image of the dried root of *Isatis indigotica* **(A)**, and the mass spectrometry images of the negative ions of isatindigoside F **(B)**, clemastanin B **(C)**, maleic acid **(D)**, malic acid **(E)**, citric acid **(F)**, sucrose **(G)**, isovitexin **(H)**, and vanillin **(I)**.

and negative ion modes, respectively. It was unexpected that DHB, the regular matric used in MALDI MSI of small molecules in plants, was not the most fitted matric for the dried root of *Isatis tinctoria*. In addition, two matrix-coating modes, air-assisted spraying and sublimation, were compared, and the results indicated that spraying presented stronger signal intensity and miner analyte delocalization.

As a result, 118 ions in the dried root of *Isatis tinctoria* were assigned as 10 classes of components including some bioactive molecules. Not surprisingly, the majority of the identified phytochemicals belonged to alkaloids and sulfur-containing compounds. The second most detected components were nucleosides, organic acids, and amino acids. A few aromatics, flavonoids, phenylpropanoids, saccharides, peptides, and sphingolipids were also found. On the contrary, esters, quinones, terpenes, sterols, alcohols, aldehydes, ketones, and nitriles from *Isatis indigotica* were not detected by mass spectrometry imaging (MSI) this time. Like fructose and glucose, several alkaloids, sulfur-containing compounds, amino acids, and saccharides were grouped together in **Table 2** since they hold isomeric relationship and could not be differentiated by their exact mass. Hence, further work should be done for the separation of the detected isomers. The presence of most of the identified components was previously found in *Isatis indigotica* except choline, dopamine, *L*-targinine, and pyrraline, which might be caused by the loss during the extraction and separation process in routine methods. Therefore, the matrix-assisted laser desorption/ionization and ion trap–time-of-flight (MALDI-IT-TOF) mass spectrometry imaging (MSI) in a single run covered not only the natural products that were commonly detected but also less reported molecules, illustrating the high throughput and high sensitivity of the method. It was also delighted to find that a couple of important bioactive molecules (references could be seen in **Table 2**) from *Isatis indigotica*, such as uracil, adenine, hypoxanthine, 4(3*H*)-quinazolinone, deoxyvasicinone,

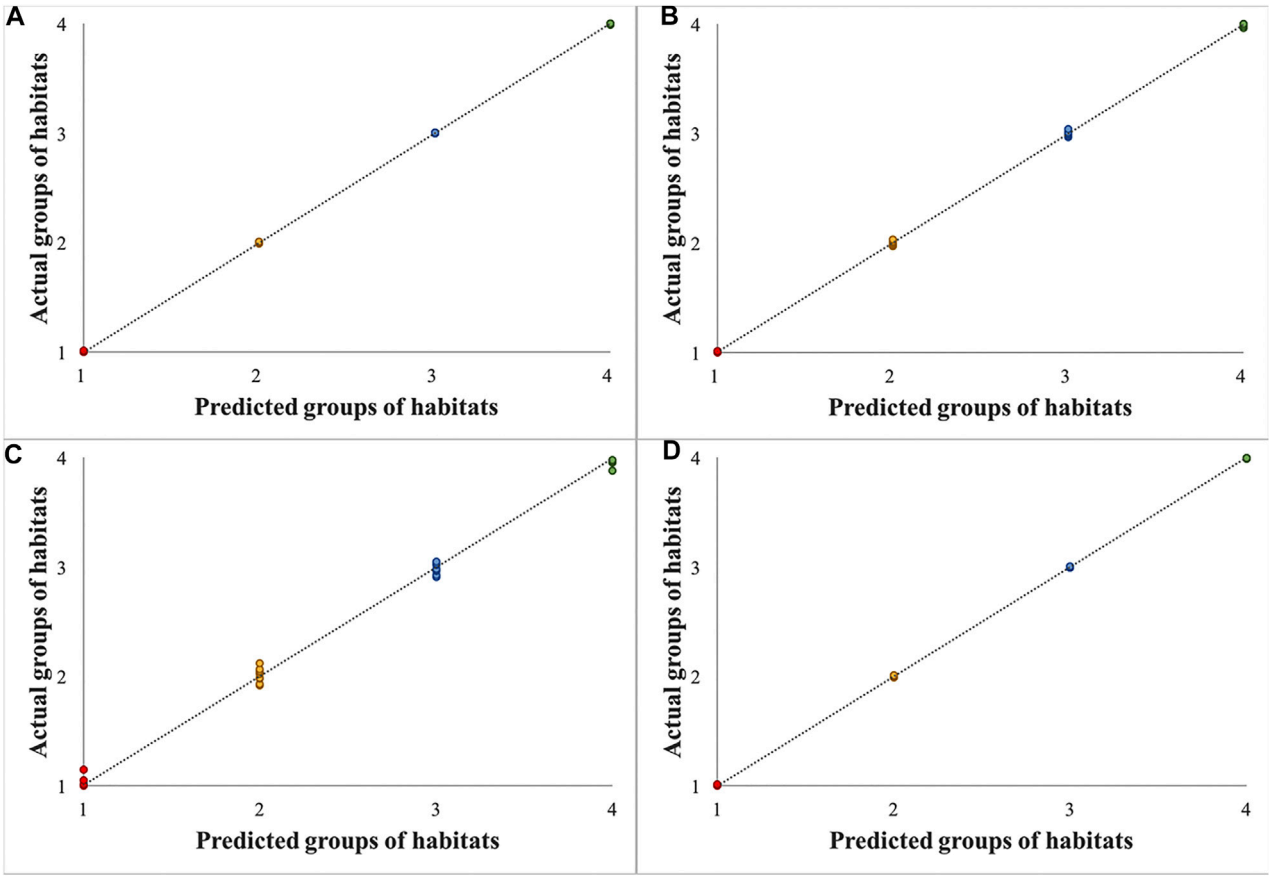

FIGURE 5 | Results of partial least square (PLS) regression models for samples of the dried root of *Isatis indigotica* from four habitats based on mass spectrometry imaging (MSI) data in the spectral ranges of *m/z* 100–500 in a positive mode **(A)**, *m/z* 500–1,000 in a positive mode **(B)**, *m/z* 100–500 in a negative mode **(C)**, and *m/z* 500–1,000 in a negative mode **(D)**.

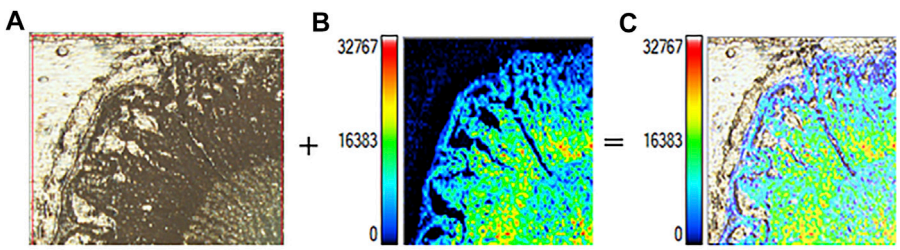

FIGURE 6 | Optical image **(A)**, mass spectrometry image **(B)**, and overlay image **(C)** of the dried root of *Isatis indigotica*.

2,4(1*H*,3*H*)-quinazolinedione, isalexin, guanine, indirubin, and indigotin, were identified in an untargeted, label-free, and multiplexed way without extraction or isolation. Among them, uracil, adenine, guanine, indirubin, and indigotin are often used as the chemical markers for authentication of the root of *Isatis indigotica*, and they were detected in all the investigated samples. Using mass spectrometry imaging, the herb could be identified in a rapid way with multiple indexes, comparing to routine TLC or HPLC methods.

As indicated in **Figure 6**, the optical microscope embedded in the iMScope made it possible to acquire optical images and ion distribution images in the same instrument. The convenient assessment allowed for an unprecedented visualization of the spatial distribution of phytochemicals in the dried root of *Isatis indigotica*. Consequently, the localization and spatial information of some molecules in the root tissue were elucidated, which were related to the botanical structure of the herb. In all, a majority of the phytochemicals were shown to be more abundant in phloem,

the nutrition-storing tissue of *Isatis indigotica*, than in xylem, the principle water-conducting tissue. Nevertheless, the signals for some identified constituents were considerably lower, and their mass spectrometry imaging (MSI) localization was therefore not so distinctive. Comparing with the LC-MS analysis after laser microdissection, microscopic mass spectrometry imaging using matrix-assisted laser desorption can reveal the spatial distribution of compounds in a more precise and direct way. Besides, segmentation and dissection might bring uncontrollable pollution, compound migration, or denaturation. However, the differentiation of isomers and absolute quantitation were not available by MALDI-MSI currently.

Finally, based on the ion images, data were collected from the whole tissue and analyzed by partial least squares (PLSs), and the dried root of *Isatis indigotica* from four habitats was differentiated unambiguously. Spectra collected from the whole tissue, the outer part of the tissue (cork, cortex, and phloem), and the inner part of the tissue (cambium and xylem) were also inputted for principal component analysis (PCA). However, no distinct cluster was observed for samples from different habitats.

Among other possibilities, the results from this study can be applied to increase the extraction yield of a given active component in *Isatis indigotica*, which is promising in research fields, such as pharmaceutical applications and industrial production. Moreover, the location of specific metabolites is helpful to improve the understanding of the relationship between compound distribution and plant structure as well as function. Combining with the chemometric method, mass spectrometry imaging (MSI) provides a simple and rapid approach for distinguishing habitats of traditional Chinese medicine (TCM) and exploring the environmental effects of plant growth. Finally, similar studies on other traditional Chinese medicine (TCM) are underway in our laboratory.

DATA AVAILABILITY STATEMENT

The raw data supporting the conclusion of this article will be made available by the authors, without undue reservation, to any qualified researcher.

AUTHOR CONTRIBUTIONS

LN designed and performed the experiments, analyzed the data, and wrote the manuscript. JD, LH, CL, and XQ assisted in performing the experiments. SK collected and authenticated the dried root of *Isatis indigotica*. ZD and SM revised the manuscript. All authors read and approved the final manuscript.

FUNDING

This work was supported by the National Natural Science Foundation of China (grant no. 81303194).

ACKNOWLEDGMENTS

The authors gratefully acknowledge the technical advice provided by Shuang-shuang Di and Honggang Nie from Beijing National Laboratory for Molecular Sciences, College of Chemistry and Molecular Engineering, Peking University.

REFERENCES

Chen, M., Gan, L., Lin, S., Wang, X., Li, L., Li, Y., et al. (2012). Alkaloids from the Root of Isatis Indigotica. *J. Nat. Prod.* 75, 1167–1176. doi:10.1021/np3002833

Condurso, C., Verzera, A., Romeo, V., Ziino, M., Trozzi, A., and Ragusa, S. (2006). The Leaf Volatile Constituents of Isatis Tinctoria by Solid-phase Microextraction and Gas Chromatography/mass Spectrometry. *Planta Med.* 72, 924–928. doi:10.1055/s-2006-946679

Davison, A. S., Strittmatter, N., Sutherland, H., HughesHughes, A. T. J., Hughes, J., Bou-Gharios, G., et al. (2019). Assessing the Effect of Nitisinone Induced Hypertyrosinaemia on Monoamine Neurotransmitters in Brain Tissue from a Murine Model of Alkaptonuria Using Mass Spectrometry Imaging. *Metabolomics*. 15, 68–77. doi:10.1007/s11306-019-1531-4

Fowble, K. L., Teramoto, K., Cody, R. B., Edwards, D., Guarrera, D., and Musah, R. A. (2017). Development of "Laser Ablation Direct Analysis in Real Time Imaging" Mass Spectrometry: Application to Spatial Distribution Mapping of Metabolites along the Biosynthetic Cascade Leading to Synthesis of Atropine and Scopolamine in Plant Tissue. *Anal. Chem.* 89, 3421–3429. doi:10.1021/acs.analchem.6b04137

Freitas, J. R. L., Vendramini, P. H., Melo, J. O. F., Eberlin, M. N., and Augusti, R. (2019). Assessing the Spatial Distribution of Key Flavonoids in Mentha × Piperita Leaves: An Application of Desorption Electrospray Ionization Mass Spectrometry Imaging (DESI-MSI). *J. Braz. Chem. Soc.* 30, 1437–1446. doi:10.21577/0103-5053.20190039

Guo, Q., Sun, Y., Tang, Q., Zhang, H., and Cheng, Z. (2020a). Isolation, Identification, Biological Estimation, and Profiling of Glucosinolates in Isatis Indigotica Roots. *J. Liquid Chromatogr. Relat. Tech.* 43, 645–656. doi:10.1080/10826076.2020.1780605

Guo, Q., Xu, C., Chen, M., Lin, S., Li, Y., Zhu, C., et al. (2018b). Sulfur-enriched Alkaloids from the Root of Isatis Indigotica. *Acta Pharmaceutica Sinica B* 8, 933–943. doi:10.1016/j.apsb.2018.08.005

He, L. W., Li, X., Chen, J. W., and Sun, D. D. (2006a). Studies on Water-Soluble Chemical Constitutions in Radix Isatidis. *Chin. Pharm. J.* 17, 232–234. doi:10.3969/j.issn.1001-0408.2006.03.034

He, L. W., Li, X., Chen, J. W., Sun, D. D., Jü, W. Z., and Wang, K. C. (2006b). [Chemical Constituents from Water Extract of Radix Isatidis]. *Yao Xue Xue Bao*. 41, 1193–1196. doi:10.1097/00024382-200610001-00089

He, Y. Q., Zhou, C. C., Yu, L. Y., Wang, L., Deng, J. L., Tao, Y. L., et al. (2020). Natural Product Derived Phytochemicals in Managing Acute Lung Injury by Multiple Mechanisms. *Pharmacol. Res.* 163, 105224. doi:10.1016/j.phrs.2020.105224

HighChem, L. L. C. (2020). *MzCloud Mass Spectral Library*. Available at: https://www.mzcloud.org/((Accessed 12, 2020)

Kikuchi, M., and Kikuchi, M. (2005). Studies on the Constituents of Swertia Japonica MAKINO II. On the Structures of New Glycosides. *Chem. Pharm. Bull.* 53, 48–51. doi:10.1248/cpb.53.48

Kizil, S., Turk, M., Çakmak, Ö., Özgüven, M., and Khawar, K. M. (2009). Microelement Contents and Fatty Acid Compositions of Some Isatis Species Seeds. *Not. Bot. Horti. Agrobot. Cluj. Napoca.* 37, 175–178. doi:10.15835/nbha3713115

Lange, B. M., Fischedick, J. T., Lange, M. F., Srividya, N., Šamec, D., and Poirier, B. C. (2017). Integrative Approaches for the Identification and Localization of Specialized Metabolites in Tripterygium Roots. *Plant Physiol.* 173, 456–469. doi:10.1104/pp.15.01593

Li, J.-g., and Xu, H. (2021). Chinese Medicine in Fighting against COVID-19: Role and Inspiration. *Chin. J. Integr. Med.* 27, 3–6. doi:10.1007/s11655-020-2860-x

Li, M., Wang, X., HanJia, L. L., Jia, L., Liu, E., Li, Z., et al. (2020a). Integration of Multicomponent Characterization, Untargeted Metabolomics and Mass Spectrometry Imaging to Unveil the Holistic Chemical Transformations and Key Markers Associated with Wine Steaming of Ligustri Lucidi Fructus. *J. Chromatogr. A*. 1624, 461228. doi:10.1016/j.chroma.2020.461228

Li, R. F., Hou, Y. L., Huang, J. C., Pan, W. Q., Ma, Q. H., Shi, Y. X., et al. (2020b). Lianhuaqingwen Exerts Anti-viral and Anti-inflammatory Activity against Novel Coronavirus (SARS-CoV-2). *Pharmacol. Res.* 156, 104761. doi:10.1016/j.phrs.2020.104761

Li, S., Zhu, N., Tang, C., Duan, H., Wang, Y., Zhao, G., et al. (2020c). Differential Distribution of Characteristic Constituents in Root, Stem and Leaf Tissues of Salvia Miltiorrhiza Using MALDI Mass Spectrometry Imaging. *Fitoterapia*. 146, 104679. doi:10.1016/j.fitote.2020.104679

Li, T., and Tao, P. (2013). Traditional Chinese Herbal Medicine as a Source of Molecules with Antiviral Activity. *Antivir. Res.* 97, 1–9. doi:10.1186/s13020-016-0074-0

Li, X. (2010). *Chemical Constituents and Quality Control of Radix Isatidis. [master's Thesis]*. [Changzhi (Shanxi)]: Shanxi Medicinal University

Li, X., Chen, A. J., and Li, C. (2010). Studies on Water-Soluble Chemical Constituent in Radix Isatidis. *Chin. J. Exp. Tradit. Med. Form.* 16, 64–67. doi:10.13422/j.cnki.syfjx.2010.05.037

Liang, Z., Chen, Y., Xu, L., Qin, M., Yi, T., Chen, H., et al. (2014a). Localization of Ginsenosides in the Rhizome and Root of Panax Ginseng by Laser Microdissection and Liquid Chromatography-Quadrupole/time of Flight-Mass Spectrometry. *J. Pharm. Biomed. Anal.* 105, 121–133. doi:10.1016/j.jpba.2014.12.005

Liang, Z., Oh, K., Wang, Y., Yi, T., Chen, H., and Zhao, Z. (2014b). Cell Type-specific Qualitative and Quantitative Analysis of Saikosaponins in Three Bupleurum Species Using Laser Microdissection and Liquid Chromatography-Quadrupole/time of Flight-Mass Spectrometry. *J. Pharm. Biomed. Anal.* 97, 157–165. doi:10.1016/j.jpba.2014.04.033

Lin, C.-W., Tsai, F.-J., Tsai, C.-H., Lai, C.-C., Wan, L., Ho, T.-Y., et al. (2005). Anti-SARS Coronavirus 3C-like Protease Effects of Isatis Indigotica Root and Plant-Derived Phenolic Compounds. *Antiviral Res.* 68, 36–42. doi:10.1016/j.antiviral.2005.07.002

Li, X., Sun, D.-D., Chen, J.-W., He, L.-W., Zhang, H.-Q., and Xu, H.-Q. (2007). New Sphingolipids from the Root of Isatis Indigotica and Their Cytotoxic Activity. *Fitoterapia*. 78, 490–495. doi:10.1016/j.fitote.2007.03.017

Liu, S., Yan, J., Li, H. L., Song, F. R., Liu, Z. Y., Liu, Z. Q., et al. (2010). Studies on Chemical Constituents of Compound Indigowoad Root Granule by Mass Spectrometry. *Chem. J. Chin. Univ.* 31, 1137–1142. doi:10.1016/S1872-2040(09)60019-0

Liu, S.-F., Lin, B., Xi, Y.-F., Zhou, L., Lou, L.-L., Huang, X.-X., et al. (2018a). Bioactive Spiropyrrolizidine Oxindole Alkaloid Enantiomers from Isatis Indigotica Fortune. *Org. Biomol. Chem.* 16, 9430–9439. doi:10.1039/C8OB02046A

Liu, S.-F., Zhang, Y.-Y., Zhou, L., Lin, B., Huang, X.-X., Wang, X.-B., et al. (2018b). Alkaloids with Neuroprotective Effects from the Leaves of Isatis Indigotica Collected in the Anhui Province, China. *Phytochemistry* 149, 132–139. doi:10.1016/j.phytochem.2018.02.016

Liu, Y.-F., Chen, M.-H., Guo, Q.-L., LinXu, S. C. B., Xu, C.-B., Jiang, Y.-P., et al. (2015a). Antiviral Glycosidic Bisindole Alkaloids from the Roots ofIsatis Indigotica. *J. Asian Nat. Prod. Res.* 17, 689–704. doi:10.1080/10286020.2015.1055729

Liu, Y.-F., Chen, M.-H., Lin, S., Li, Y.-H., Zhang, D., Jiang, J.-D., et al. (2015b). Indole Alkaloid Glucosides from the Roots of Isatis Indigotica. *J. Asian Nat. Prod. Res.* 18, 1–12. doi:10.1080/10286020.2015.1117452

Luo, Z., Liu, L. F., Wang, X. H., Li, W., Jie, C., Chen, H., et al. (2019). Epigoitrin, an Alkaloid from *Isatis Indigotica*, Reduces H1N1 Infection in Stress-Induced Susceptible Model *In Vivo* and *In Vitro*. *Front. Pharmacol.* 10, 78. doi:10.3389/fphar.2019.00078

Meng, L., Guo, Q., Liu, Y., Chen, M., Li, Y., Jiang, J., et al. (2017a). Indole Alkaloid Sulfonic Acids from an Aqueous Extract of Isatis Indigotica Roots and Their Antiviral Activity. *Acta Pharmaceutica Sinica B* 7, 334–341. doi:10.1016/j.apsb.2017.04.003

Meng, L.-J., Guo, Q.-L., Xu, C.-B., Zhu, C.-G., Liu, Y.-F., Chen, M.-H., et al. (2017b). Diglycosidic Indole Alkaloid Derivatives from an Aqueous Extract of Isatis Indigotica Roots. *J. Asian Nat. Prod. Res.* 19, 529–540. doi:10.1080/10286020.2017.1320547

Mohn, T., Cutting, B., Ernst, B., and Hamburger, M. (2007). Extraction and Analysis of Intact Glucosinolates-A Validated Pressurized Liquid Extraction/liquid Chromatography-Mass Spectrometry Protocol for Isatis Tinctoria, and Qualitative Analysis of Other Cruciferous Plants. *J. Chromatogr. A* 1166, 142–151. doi:10.1016/j.chroma.2007.08.028

Mohn, T., and Hamburger, M. (2008). Glucosinolate Pattern inIsatis tinctoriaandI. indigoticaSeeds. *Planta Med.* 74, 885–888. doi:10.1055/s-2008-1074554

Ng, K.-M., Liang, Z., Lu, W., Tang, H.-W., Zhao, Z., Che, C.-M., et al. (2007). *In Vivo* analysis and Spatial Profiling of Phytochemicals in Herbal Tissue by Matrix-Assisted Laser desorption/Ionization Mass Spectrometry. *Anal. Chem.* 79 (7), 2745–2755. doi:10.1021/ac062129i

Pan, Y. L. (2014). *Study the Chemical Composition of Effective Extraction of Isatidis Radix and its Composition Analysis of Different Regions. [master's Thesis]*. [Nanjing (Jiangsu)]: Nanjing University of Traditional Chinese Medicine

Pan, Y., Xue, P., Li, X., ChenLi, J. J., and Li, J. (2013). Determination of Nucleosides and Nucleobases in Isatidis Radix by HILIC-UPLC-MS/MS. *Anal. Methods*. 5, 6395–6400. doi:10.1039/C3AY40841H

Peng, S. P., and Gu, Z. L. (2005a). Recent Progress in the Studies of Chemical Constituents and Pharmacological Effects on Roots of Isatis Indigotica, *Chin. Wild Plant Res.* 24, 4–7. doi:10.3969/j.issn.1006-9690.2005.05.002

Peng, Y., Zhang, L. P., Song, H., Pan, W. S., and Sun, Y. Q. (2005b). The Chemical Constituents from Isatis Indigotica Fort, I. *Chin. J. Med. Chem.* 15, 371–372. doi:10.14142/j.cnki.cn21-1313/r.2005.06.017

Shi, Y.-H., Xie, Z.-Y., Wang, R., Huang, S.-J., Li, Y.-M., and Wang, Z.-T. (2012). Quantitative and Chemical Fingerprint Analysis for the Quality Evaluation of Isatis Indigotica Based on Ultra-performance Liquid Chromatography with Photodiode Array Detector Combined with Chemometric Methods. *Int J Mol Sci.* 13, 9035–9050. doi:10.3390/ijms13079035

Shimma, S., and Sagawa, T. (2019). Microscopy and Mass Spectrometry Imaging Reveals the Distributions of Curcumin Species in Dried Turmeric Root. *J. Agric. Food Chem.* 67, 9652–9657. doi:10.1021/acs.jafc.9b02768

Speranza, J., Miceli, N., Taviano, M. F., Ragusa, S., Kwiecień, I., Szopa, A., et al. (2020). Isatis Tinctoria L. (Woad): A Review of its Botany, Ethnobotanical Uses, Phytochemistry, Biological Activities, and Biotechnological Studies. *Plants*. 9, 298. doi:10.3390/plants9030298

Sun, C., Wang, F., Zhang, Y., Yu, J., and Wang, X. (2020). Mass Spectrometry Imaging-Based Metabolomics to Visualize the Spatially Resolved Reprogramming of Carnitine Metabolism in Breast Cancer. *Theranostics*. 10, 7070–7082. doi:10.7150/thno.45543

Sun, D. D., He, L. W., Li, X., Chen, J. W., and Ding, L. (2007). Study on Chemical Constituents of Radix Isatidis. *Chin. Pharm. J.* 18, 172–173.

Sun, D., Dong, W., Li, X., and Zhang, H. (2009). Isolation, Structural Determination and Cytotoxic Activity of Two New Ceramides from the Root of Isatis Indigotica. *Sci. China Ser. B-chem.* 52, 621–625. doi:10.1007/s11426-008-0146-9

The Metabolomics Innovation Centre (2020). *The Human Metabolome Database*. Available at: https://hmdb.ca/(Accessed December 12, 2020)

Wang, R., Runco, J., Yang, L., Yu, K., Li, Y., Chen, R., et al. (2014). Qualitative and Quantitative Analyses of Goitrin-Epigoitrin in Isatis Indigotica Using Supercritical Fluid Chromatography-Photodiode Array Detector-Mass Spectrometry. *RSC Adv.* 4, 49257–49263. doi:10.1039/c4ra02705a

Wang, S., Bai, H., Cai, Z., Gao, D., Jiang, Y., Liu, J., et al. (2016). MALDI Imaging for the Localization of Saponins in Root Tissues and Rapid Differentiation of Three Panax Herbs. *Electrophoresis* 37, 1956–1966. doi:10.1002/elps.201600027

Wang, W. Y., Zhou, H., Wang, Y. F., Sang, B. S., and Liu, L. (2021). Current Policies and Measures on the Development of Traditional Chinese Medicine in China. *Pharmacol. Res.* 163, 105187. doi:10.1016/j.phrs.2020.105187

Wang, X., Zheng, W., Xie, G., Qiu, M., and Jia, W. (2009). [Determination of Salylic Acid, Syringic Acid, Benzoic Acid and Anthranilic Acid in Radix Isatidis by HPCE]. *Zhongguo Zhong Yao Za Zhi* 34, 189–192. doi:10.3321/j.issn:1001-5302.2009.02.019

Wang, X. F., and Liu, Y. H. (2008). Anti-endotoxic Effects of 3-(2'-Carboxyphenyl)-4(3h)-Quinazolinone from Radix Isatidis. *Lishizhen Med. Mat. Med. Res.* 19, 262–264. doi:10.3969/j.issn.1008-0805.2008.02.002

Wang, X. L., Chen, M. H., Wang, F., Pu, P. B., Lin, S., Zhu, C. G., et al. (2013). Chemical Constituents from Root of Isatis Indigotica. *China J. Chin. Mate. Med.* 38, 1172–1182. doi:10.4268/cjcmm2013081210.1080/03632415.2013.848346

Wei, X. Y., Leung, C. Y., Wong, C. K. C., Shen, X. L., Wong, R. N. S., Cai, Z. W., et al. (2005). Bisindigotin, a TCDD Antagonist from the Chinese Medicinal HerbIsatis Indigotica. *J. Nat. Prod.* 68, 427–429. doi:10.1021/np049662i

Wu, H., Dai, Z., Liu, X., Lin, M., Gao, Z., Tian, F., et al. (2019). Pharmacodynamic Evaluation of Shenfu Injection in Rats with Ischemic Heart Failure and its Effect on Small Molecules Using Matrix-Assisted Laser Desorption/Ionization-Mass Spectrometry Imaging. *Front. Pharmacol.* 10, 1424. doi:10.3389/fphar.2019.01424

Wu, W., Liang, Z., Zhao, Z., and Cai, Z. (2007). Direct Analysis of Alkaloid Profiling in Plant Tissue by Using Matrix-Assisted Laser Desorption/ionization Mass Spectrometry. *J. Mass. Spectrom.* 42 (1), 58–69. doi:10.1002/jms.1138

Wu, X., Qin, G., Cheung, K. K., and Cheng, K. F. (1997). New Alkaloids from Isatis Indigotica. *Tetrahedron* 53, 13323–13328. doi:10.1016/S0040-4020(97)00846-6

Xiao, S., Bi, K., and Sun, Y. (2007). Identification of Chemical Constituents in the Root of Isatis Indigotica Fort. By LC/DAD/ESI/MS/MS. *J. Liquid Chromatogr. Relat. Tech.* 30, 73–85. doi:10.1080/10826070601034295

Xiao, S. S., Jin, Y., and Sun, Y. Q. (2003). Recent Progress in the Studies of Chemical Constituents, Pharmacological Effects and Quality Control Methods on the Roots of Isatis Indigotica. *J. Shenyang Pharm. Univ.* 20, 455–459. doi:10.14066/j.cnki.cn21-1349/r.2003.06.020

Yang, L., Jiang, H., Wang, G., Wang, M., Ding, L., Chen, L., et al. (2014a). Phenylpropanoids and Some Nitrogen-Containing Constituents from the Roots of Isatis Indigotica Fort. (Cruciferae). *Biochem. Syst. Ecol.* 54, 313–315. doi:10.1016/j.bse.2014.03.004

Yang, L., Wang, G., Wang, M., Jiang, H., Chen, L., Zhao, F., et al. (2014b). Indole Alkaloids from the Roots of Isatis Indigotica and Their Inhibitory Effects on Nitric Oxide Production. *Fitoterapia.* 95, 175–181. doi:10.1016/j.fitote.2014.03.019

Yi, L., Liang, Z.-T., Peng, Y., Yao, X., Chen, H.-B., and Zhao, Z.-Z. (2012). Tissue-specific Metabolite Profiling of Alkaloids in Sinomenii Caulis Using Laser Microdissection and Liquid Chromatography-Quadrupole/time of Flight-Mass Spectrometry. *J. Chromatogr. A.* 1248, 93–103. doi:10.1016/j.chroma.2012.05.058

Zeng, J., Guo, Z., Xiao, Y., Wang, C., Zhang, X., and Liang, X. (2010). Purification of Polar Compounds from Radix Isatidis Using Conventional C18 Column Coupled with Polar-Copolymerized C18 Columncation of Polar Compounds from Radix Isatidis Using Conventional C_{18} Column Coupled with Polarcopolymerized C_{18} Column. *J. Sep. Sci.* 33, 3341–3346. doi:10.1002/jssc.201000417

Zhang, D. D., Li, Q. Y., Shi, H. Y., Chen, K. X., Li, Y. M., and Wang, R. (2019a). Glycosides from Roots of Isatis Indigotica. *Chin. Tradit. Herb. Drugs*. 50, 3575–3588. doi:10.7501/j.issn.0253-2670.2019.15.009

Zhang, D., Shi, Y., Li, J., Ruan, D., JiaZhu, Q. W. L., Zhu, W., et al. (2019b). Alkaloids with Nitric Oxide Inhibitory Activities from the Roots of Isatis Tinctoria. *Molecules*. 24, 4033–4042. doi:10.3390/molecules24224033

Zhang, D., Ruan, D., Li, J., Chen, Z., Zhu, W., Guo, F., et al. (2020a). Four Undescribed Sulfur-Containing Indole Alkaloids with Nitric Oxide Inhibitory Activities from Isatis Tinctoria L. Roots. *Phytochemistry* 174, 112337. doi:10.1016/j.phytochem.2020.112337

Zhang, D. D., Ruan, D. Q., Li, Q, Y., Chen, K. X., Li, Y. M., and Wang, R. (2020b). Study on Alkaloids from Alcohol Extract of Radix Isatidis. *CJTCMP*. 35, 2287–2291. CNKI:SUN:BXYY.0.2020-05-018

Zhang, D., Sun, Y., Chen, Z., JiaZhu, Q. W. L., Zhu, W., Chen, K., et al. (2020c). Bisindole Alkaloids with Nitric Oxide Inhibitory Activities from an Alcohol Extract of the Isatis Indigotica Roots. *Fitoterapia*. 146, 104654. doi:10.1016/j.fitote.2020.104654

Zhang, J., Du, Q., SongGao, X. S. S., Gao, S., Pang, X., Li, Y., et al. (2020d). Evaluation of the Tumor-Targeting Efficiency and Intratumor Heterogeneity of Anticancer Drugs Using Quantitative Mass Spectrometry Imaging. *Theranostics*. 10, 2621–2630. doi:10.7150/thno.41763

Zhao, N. (2015). *Study on the Serum Pharmacochemistry of Banlangen Based on the LC-MS. [master's Thesis]*. [Haerbin (Heilongjiang)]: Heilongjiang University of Traditional Chinese Medicine

Zhou, W., and Zhang, X.-Y. (2013). Research Progress of Chinese Herbal Medicine Radix Isatidis (Banlangen). *Am. J. Chin. Med.* 41, 743–764. doi:10.1142/s0192415x1350050x

Zou, P., Hong, Y., and Koh, H. L. (2005). Chemical Fingerprinting of Isatis Indigotica Root by RP-HPLC and Hierarchical Clustering Analysis. *J. Pharm. Biomed. Anal.* 38, 514–520. doi:10.1016/j.jpba.2005.01.022

Zou, P., and Koh, H. L. (2007). Determination of Indican, Isatin, Indirubin and Indigotin inIsatis Indigotica by Liquid Chromatography/electrospray Ionization Tandem Mass Spectrometry. *Rapid Commun. Mass. Spectrom.* 21, 1239–1246. doi:10.1002/rcm.2954

Conflict of Interest: The authors declare that the research was conducted in the absence of any commercial or financial relationships that could be construed as a potential conflict of interest.

Advantages of publishing in Frontiers

OPEN ACCESS
Articles are free to read for greatest visibility and readership

FAST PUBLICATION
Around 90 days from submission to decision

HIGH QUALITY PEER-REVIEW
Rigorous, collaborative, and constructive peer-review

TRANSPARENT PEER-REVIEW
Editors and reviewers acknowledged by name on published articles

Frontiers
Avenue du Tribunal-Fédéral 34
1005 Lausanne | Switzerland

Visit us: www.frontiersin.org
Contact us: frontiersin.org/about/contact

REPRODUCIBILITY OF RESEARCH
Support open data and methods to enhance research reproducibility

DIGITAL PUBLISHING
Articles designed for optimal readership across devices

FOLLOW US
@frontiersin

IMPACT METRICS
Advanced article metrics track visibility across digital media

EXTENSIVE PROMOTION
Marketing and promotion of impactful research

LOOP RESEARCH NETWORK
Our network increases your article's readership